THE UNIVERSITY *of* EDINBURGH

Improving the Performance of Hybrid Wind-Diesel-Battery Systems

Leong Kit Gan

Doctor of Philosophy

The University of Edinburgh

2016

Abstract

Off-grid hybrid renewable energy systems are known as an attractive and sustainable solution for supplying clean electricity to autonomous consumers. Typically, this applies to the communities that are located in remote or islanded areas where it is not cost-effective to extend the grid facilities to these regions. In addition, the use of diesel generators for electricity supply in these remote locations are proven to be uneconomical due to the difficult terrain which translates into high fuel transportation costs. The use of renewable energy sources, coupling with the diesel generator allows for the diesel fuel to be offset. However, to date, a common design standard for the off-grid system has yet to be found and some challenges still exist while attempting to design a reliable system. These include the sizing of hybrid systems, coordination between the operation of dissimilar power generators and the fluctuating load demands, optimal utilisation of the renewable energy resources and identifying the underlying principles which reduce the reliability of the off-grid systems.

In order to address these challenges, this research has first endeavoured into developing a sizing algorithm which particularly seeks the optimal size of the batteries and the diesel generator usage. The batteries and diesel generator function in filling the gap between the power generated from the renewable energy resources and the load demand. Thus, the load requirement is also an important factor in determining the cost-effectiveness of the overall system in the long run. A sensitivity analysis is carried out to provide a better understanding of the relationship between the assessed renewable energy resources, the load demand, the storage capacity and the diesel generator fuel usage.

The thesis also presents the modelling, simulation and experimental work on the proposed hybrid wind-diesel-battery system. These are being implemented with a full-scale system and they are based on the off-the-shelf components. A novel algorithm to optimise the operation of a diesel generator is also proposed. The steady-state and dynamic analysis of the proposed system are presented, from both simulation and an experimental perspective. Three single-phase grid-forming inverters and a fixed speed wind turbine are used as a platform for case studies. The

grid-forming inverters adopt droop control method which allows parallel operation of several grid-forming sources. Droop control-based inverters are known as independent and autonomous due to the elimination of intercommunication links among distributed converters. Moreover, the adopted fixed speed wind turbine employs a squirrel cage induction generator which is well known for its robustness, high reliability, simple operation and low maintenance. The results show a good correlation between the modelling, the experimental measurements, and the field tested results.

The final stage of this research explores the effect of tower shadow on off-grid systems. Common tower designs for small wind turbine applications, which are the tubular and the lattice configurations, are considered in this work. They generate dissimilar tower shadow profiles due to the difference in structure. In this research, they are analytically modelled for a wind turbine which is being constructed as a downwind configuration. It is proven that tower shadow indeed brings negative consequence to the system, particularly its influence on battery lifetime within an off-grid system. This detrimental effect occurs when power generation closely matches the load demand. In this situation, small frequent charging and discharging cycles or the so called microcycles, take place. The battery lifetime reduction due to these microcycles has been quantified and it is proven that they are not negligible and should be taken into consideration while designing an off-grid hybrid system.

Declaration

I declare that the work contained in this thesis is my own except where clearly stated otherwise in the text. This work has not been submitted elsewhere for any other degree or professional qualification except as specified. Parts of the work have been presented at conferences and published in journals.

_____

Leong Kit Gan

June 2016

Acknowledgements

Firstly, I would like to thank my supervisor, Dr. Jonathan Shek for giving all kinds of support, guidance and encouragement to me while carrying out my research. He has devoted his valuable time for discussions and efforts in keeping me on track in the project with the correct directions and within the allowable time frame. I would also like to thank my co-supervisor, Professor Markus Mueller who is always supportive, encouraging and keeping me motivated throughout the project.

I am very grateful and would like to thank the Commonwealth Scholarship Commission from the UK, Energy Technology Partnership (ETP) and Gaia Wind Ltd. and The University of Edinburgh for funding my studies. Without these scholarships, it would be impossible for me to complete such an insightful programme from this prestigious university.

I would like to extend my gratitude to my colleagues from the Institute for Energy Systems at the University of Edinburgh have helped me and ensured that my research life was not a lonely process. Particularly, they include Juan Pablo Echenique Subiabre, Haw Wooi Chuan, Ozan Keysan, Marios Sousounis, Paul Bonar, Renaldi Renaldi, Yew Chuan Chong, Xiao Yun Rong, Faheem Akhter, Okechukwu Ubani and Nisaar Ahmed. A special note of thanks goes to Douglas Carmichael for his assistance in the laboratory and his help in keeping me safe in dealing with high voltage devices.

In addition to the above, I would like to thank my wife and my mother for their emotional encouragement and moral support during my studies. My final thanks go to my little daughter, Abby Zyi En Gan, who has been a good company and brings me a lot of joy in my life.

Table of Contents

List of Figures

Figure No. ***Page***

List of Tables

Table No. ***Page***

Abbreviations

AC	Alternating Current
ARE	Alliance for Rural Electrification
BEM	Blade Element Model
CAES	Compressed Air Energy Storage
CCM	Continuous Conduction Mode
CFD	Computational Fluid Dynamics
CO_2	Carbon Dioxide
CPU	Central Processing Unit
CRT	Cathode Ray Tube
DC	Direct Current
DG	Distributed Generator
DFIG	Doubly Fed Induction Generator
DoD	Depth of Discharge
DOL	Direct On-line
DR	Demand Response
EE	Energy Efficiency
EMS	Energy Management System
EREC	Engineering Recommendation
EU	European Union
EV	Electric Vehicle
ESS	Energy Storage System
FFT	Fast Fourier Transform
FNN	Fuzzy Neural Network
GA	Genetic Algorithm
GHG	Greenhouse Gases
GUI	Graphical User Interface
GTO	Gate Turn-off Thyristor
HESS	Hybrid Energy Storage System
HEV	Hybrid Electric Vehicle
HRES	Hybrid Renewable Energy System
ICE	Internal Combustion Engine
IEA	International Energy Agency
IEC	International Electrotechnical Commission
IGBT	Insulated Gate Bipolar Transistor
IPCC	Intergovernmental Panel on Climate Change
LED	Light Emitting Diode
LOLP	Loss of Load Probability
MPC	Model Predictive Control
NREL	National Renewable Energy Laboratory

O&M	Operation and Maintenance
PCC	Point of Common Coupling
PFC	Power Factor Correction
PHES	Pumped Hydro Energy Storage
PHEV	Plug-in Hybrid Electric Vehicle
PID	Proportional-Integral-Derivative
PLL	Phase-Locked Loop
PMSG	Permanent Magnet Synchronous Generator
PRG	Gross Production
PWM	Pulse Width Modulation
PV	Photovoltaic
RAM	Random Access Memory
RES	Renewable Energy Sources
RESF	Renewable Energy Sources Fraction
RMS	Root Mean Square
SI	Sunny Island
SOC	State of Charge
SOH	State of Health
SMES	Superconductive Magnetic Energy Storage
SMPS	Switch Mode Power Supplies
SR	Spinning Reserve
STATCOMS	Static Synchronous Compensator
SWCC	Small Wind Certification Council
SVC	Static Var Controller
TOU	Time of Use
TSR	Tip Speed Ratio
UK	United Kingdom
VPP	Virtual Power Plant
VSI	Voltage Source Inverter

Nomenclature

a_n	Harmonics coefficient (dimensionless)
A_R	Rotor disk plan area with radius R (m^2)
B (x,y)	Beta function (dimensionless)
BRE	Battery relative efficiency (dimensionless)
C_d	Cycles to failure at depth of discharge *d* (dimensionless)
C_P	Peukert capacity (Ah)
C_o	Cost of an item (£)
C_1	Input capacitor (F)
C_2	Output capacitor (F)
C_d	Drag coefficient of the tower (dimensionless)
C_p	Aerodynamic power coefficient of the turbine (dimensionless)
d	Depth of discharge (%)
D	Tower diameter (m)
E_{EXC}	excess energy (kWh)
E_L	Load energy (kWh)
f_s	Switching frequency (Hz)
f_c	PWM carrier frequency (dimensionless)
$H_{vonKarman}$	Von Karman shaping filter transfer function (dimensionless)
$H_{Nichita}$	Nichita approximated transfer function (dimensionless)
J_1	Inertia of the turbine rotor ($kg.m^2$)
J_r	Reflected moment of inertia ($kg.m^2$)
J_m	Momentum deficit behind the tower ($kg.ms^{-1}$)
k	Peukert constant (dimensionless)
k_σ	Constant of proportionality (dimensionless)
K	Kinematic momentum ($kg.ms^{-1}$)
K_w	Number of wind turbines (dimensionless)
K_p	Proportional constant (dimensionless)
K_i	Integral constant (dimensionless)
K_d	Derivative constant (dimensionless)
K_P	Active power drooping gradient (W)
K_Q	Reactive power drooping gradient (VAr)
K_F	Gain constant of the von Karman shaping filter (dimensionless)
L_1	Input inductor (H)
L_2	Output inductor (H)
L	Turbulence length (m)
N	Gear ratio (dimensionless)
P	Active power (W)
P_{wind}	Wind Turbine Output Power (kW)
P_{gen}	Power generated (W)

P_{dem}	Power demand (W)
P_a	Cumulative present worth factor (dimensionless)
PW	Present worth (dimensionless)
P_r	present worth factor (dimensionless)
P_{absorb}	Power absorbed by the load (W)
$P_{nominal}$	Nominal power of the load (W)
P_m	Rotor mechanical power (W)
$P_{out,AC}$	AC output power of the inverter (W)
$P_{in,DC}$	DC input power of the inverter (W)
P_R	Active power transferred (W)
PF	Power factor (dimensionless)
PRG	Gross production (dimensionless)
Q_R	Reactive power transferred (VAr)
Q	Reactive power (VAr)
r	Radial distance (m)
$RESF$	Renewable energy sources fraction (dimensionless)
S	Apparent power (VA)
$S_{VV}(\omega)$	Von Karman power spectrum (dimensionless)
$S_w(\omega)$	White noise power spectral density function (dimensionless)
t	Theoretical time to discharge the batteries (hours)
t’	Modified discharge time (hours)
T_{dp}	Active power decoupling delay (s)
T_{dQ}	Reactive power decoupling delay (s)
T_F	Time constant of the von Karman shaping filter (s)
T_s	Sampling period (s)
TI	Turbulence intensity (dimensionless)
$u(x, \eta)$	Axial velocity component of the wind (m/s)
U	Mean wind speed (m/s)
U_0	Free stream velocity (m/s)
$v(x, \eta)$	Lateral velocity component of the wind (m/s)
V	Wind Velocity (m/s)
V_{out}	Output voltage (V)
V_{in}	Input voltage (V)
V_0	Voltage magnitude reference at no load (V)
V_{peak}	Single-phase voltage peak reference (V)
V_s	PWM carrier voltage magnitude (V)
V_{actual}	Actual voltage experienced by the load (V)
$V_{nominal}$	Nominal voltage of the load (V)
V_{diff}	Voltage difference between two voltage sources (V)
V_{PCC}	Voltage at point of coupling (V)
V_{ext}	Voltage at external voltage source (V)
V_w	Wind speed (m/s)

ω_0	Frequency reference at no load (Hz)
W	Total battery life fraction consumed (dimensionless)
W_{gen}	Energy generated (kWh)
W_{dem}	Energy demand (kWh)
x	Non-dimensional Cartesian co-ordinates in the tower cross section (dimensionless)
y	Non-dimensional Cartesian co-ordinates in the tower cross section (dimensionless)
ρ	Air density (kg/m^3)
σ	Empirical constant (dimensionless)
σ_{TI}	Turbulence intensity (dimensionless)
σ_w	Unitary variance (dimensionless)
σ_{sf}	Colored noise transfer function (dimensionless)
λ	Tip speed ratio (dimensionless)
$\eta_{inverter}$	Efficiency of the inverter (%)
θ	Azimuthal angle (degree)
θ_{diff}	Phase angle difference between the two voltage sources (degree)

Chapter 1 Introduction

1.1 Background

Globally, conventional fossil fuel-based electrical power systems are facing the problems of poor energy efficiency and contributing to environmental pollution. Over the period of power systems development, the concentrations of carbon dioxide (CO_2) in the atmosphere have been increasing significantly [1]. The use of energy has been identified as the largest source of overall anthropogenic greenhouse gases (GHG) emissions. Within the energy sector, CO_2 emission is primarily due to the combustion of carbon-based fuels during the process of power generation. From the Intergovernmental Panel on Climate Change (IPCC) fifth assessment report [2], it is stated that the climate change can be linked to the phenomenon of global warming resulting from GHG emissions. In another occasion, people who are settling in small villages located far away from the utility grid have been utilising small diesel generators to electrify their homes. These diesel generators are categorised as fossil fuel-based power generators which contribute to the overall GHG emissions [3]. The COP21, also known as the 2015 Paris Climate Conference which involved 196 nations has formalised a legally binding and universal agreement on aiming to limit global warming to "well below 2° Celsius (C) above pre-industrial levels and to pursue efforts to limit the temperature increase to 1.5 °C" [4]. Developed and developing countries are no longer separated into distinct groups as in the Kyoto Protocol and all parties are expected to undertake the ambitious climate action, with the recognition that developing countries will require additional support for the ambitious implementation [4].

Renewable energy technologies have been developed rapidly and they are being adopted from countries all over the world in order to combat climate change [5]. The year 2015 was extraordinary for renewable energy as the rate of deployment [4] was the largest [6]. Globally, this is dominated by large (e.g., megawatt-scale and up) generators that are owned by utilities or large investors [6], despite it has been shown that these are insufficient in providing electricity services to the energy-poor

communities [7]. Meanwhile, the market for distributed, small-scale generation has started to accelerate in both developing and developed countries. In developing countries, the rapid expansion of small-scale renewable systems is associated with rural electrification for people living far from the grid. On the contrary, significant growth is observed in developed countries from residential and industry in response to a demand for self-sufficiency and the desire to become 'prosumers' [6].

At present, approximately 1.2 billion people, or 17% of the global population, living without access to electricity [6]. Majority of these populations live in sub-Saharan Africa and developing Asia. Such an energy outlook is unacceptable and the lack of affordable and reliable electricity supply is a major impediment to the development of many rural communities, particularly those remote from the existing electricity grid. Therefore, off-grid electrification systems are often the only practical solution for electricity generation for these communities. Traditionally, off-grid electrification systems rely solely on diesel generators, but the remained instability and volatility of the oil market [8] [9] bring uncertainties to the consumers with regards to the future diesel fuel cost. The developments in renewable generation technologies allows the use of natural resources (wind, hydro, or photovoltaic (PV)) as alternative energy sources. However, their intermittency typically results in the inability to maintain the power balance between supply and demand [10]. The remedy to this problem is to combine RES with conventional diesel generation and batteries [11] [12]. This combined system forms a so-called hybrid renewable energy system (HRES) which may provide reliable electricity supply [13]. Other form of energy storage systems (ESSs) such as capacitors, supercapacitors, flywheels and superconductive magnetic energy storage (SMES) are known as fast-response ESSs. However, these ESSs do not have high energy density. Therefore, they are more suitable to be used for regulating the grid frequency and mitigating flicker effects in the scenario of sudden power changes from the load and the short-term fluctuations from renewable generations [14]. On the other hand, pumped hydro energy storage (PHES), compressed air energy storage (CAES) and thermal ESSs can deliver power in the magnitude of megawatts to gigawatts for several hours. In addition, they possess

slow response time and are not ideal to be operated with rapid mode changes due to the associated large inertia [14].

Despite the positive outcomes obtained from the existing HRES, some challenges and reliability issues are yet to be addressed. This research attempts to solve several practical problems on current HRESs, working in collaboration with a small wind turbine company, Gaia-Wind Limited. As part of their growth plans, Gaia-Wind are constantly exploring new renewable energy solution for small scale projects. These include sizing of batteries and diesel generator, optimally control of the operation of the diesel generator, hybrid system laboratory setup and the tower shadow effects on the battery lifetime within a hybrid wind-diesel-battery system. Gaia-Wind Ltd. have over 20 years of design experience from the Danish wind industry and have utilised this in their current product – the 133-11kW wind turbine. This wind turbine is well-known for its high energy production, quiet operation and long track record of reliability. As part of its expansion growth, Gaia-Wind is exploring the possibility of developing HRESs using their wind turbine for off-grid applications.

One of the most expensive components in HRESs is the batteries as very often they are oversized to increase system autonomy. A diesel generator on the other hand is used as a backup whenever there is an energy deficit in the system. If a diesel generator is oversized, it will experience low part load efficiency and in the long term this will be detrimental to the engine system. Both batteries and diesel generator are seen to be trade-offs from each other. Intuitively, if a higher capacity battery system is being installed, the diesel generator's operation will be less frequent and vice versa. In addition, many project managers experience the challenge in optimally sizing these components for different sites. This is due to the different availability of RES and load demand for different locations. In order to address this problem, this research utilises the annual historical RES and load demand information, characteristics of renewable energy devices and the lifecycle cost of HRES components while performing the sizing studies. A graphical user interface (GUI) is suitable to be developed as it has been used as a tool to ease carrying out the sizing process and to perform sensitivity analysis [15] [16]. The aim of the sizing tool is to seek the optimum configuration of the hybrid system, based on the minimum cost of

electricity. The corresponding batteries and diesel generator's yearly operation which can be simply linked to their technical performance are analysed and discussed. One of the main benefits of developing the sizing GUI is to ease the hybrid system sizing process while allowing one to understand the underlying principles to achieve that. This is an important step prior to the implementation of the real system as unnecessary capital investment may be spent in over-sizing the batteries or diesel generators.

In an off-grid hybrid wind-diesel-battery system, the diesel generator is often not utilised efficiently, therefore compromising its lifetime. In particular, running the diesel generator at more than 40% of its rated capacity is often unmet. This is due to the variation in power demand and wind speed which needs to be supplied by the diesel generator. In addition, the frequent start-stop cycles of the diesel generator leads to additional mechanical wear and fuel wastage [17] [18]. With a given day-ahead forecast of local renewable energy resource and load demand, it is possible to optimise the operation of a diesel generator, subjected to other pre-defined constraints. Thus, the utilisation of the RES to supply electricity can be maximised. Usually, the optimisation studies of a HRES are being conducted through simple analytical modelling, coupled with a selected optimisation algorithm to seek the optimised solution. The obtained solution is not verified using a more realistic system model, for instance the physical modelling approach. This often leads to the question of applicability of such optimised operation in reality. In order to take a step further, model-based design using Simulink is employed in this research to perform a comparison through a physical modelling approach. The Simulink model has the capability to incorporate the electrical and mechanical (Simscape) physical characteristics into the simulation, which are often neglected by other authors when performing such a study. Therefore, HRES simulation models are built according to the system proposed in the work. Finally, sensitivity analyses are performed as a means of testing the designed hybrid system against wind and load forecast errors. The simulation methodology provides insight in terms of electrical performances of the proposed control algorithm. Besides being able used as a tool to assist hardware development, developers are able to simulate other desired scenarios using the

simulation model and check the correctness of the algorithm before executing them on the expensive hardware.

Since a hybrid wind-diesel-battery system involves the rotation of the wind turbine blades, additional protection and risk assessment would be required if it was tested in the field. This is due to the lack of initial understanding of the level of operational safety of a newly proposed system. In addition, reproducibility is a challenge in the field, for instance, it is nearly impossible to obtain the exact same wind speed profile in the field to be used as a test input. This adds to the challenge while tuning the controller or to troubleshoot any faults within the system. The additional time which is required to perform certain tests in the field further justify the additional human resource cost in the project development. As part of a product development cycle, laboratory testing is believed to present a more controlled test environment and its performance is close to the real system compared to computer simulations. After conducting simulation studies, a laboratory platform is required to validate the steady-state and dynamic performances of the proposed hybrid system through a series of functional tests. The construction of a hybrid system in the laboratory provides low cost and safer testing and verification of the wind turbine, which would otherwise be costly in the field. In this research, a full-scale HRES system is established and characterised in a modular basis and the implementation process is explained in detailed. The test rig is designed based on the hybrid of real-time simulation and the hardware components. In particular, the drive train (aerodynamic profile of the blades and the gearbox) and the braking mechanism of the wind turbine are implemented using computer modelling. The hybrid approach of utilising both software and hardware simplifies the test rig design for the purpose of laboratory testing and at the same time contribute to cost saving on expensive hardware components. The developed hardware platform allows engineering issues and their underlying dynamics to be investigated. For example, the non-ideal aerodynamic effects (wind shear, tower shadow and others) of the wind turbine imposing on other hybrid system components, different types of battery along with their respective performances and the off-grid system's power quality can be studied. Additionally, the prototype also can be used to validate the simulation model.

In an off-grid hybrid wind-diesel-battery system, the battery lifetime is often optimistically over-predicted by hybrid system designers and battery manufacturers. This is due to the underestimation of battery wear as a result of short charge-discharge cycles, otherwise known as microcycles [19] [20]. The detrimental effect of microcycles on a battery-based standalone renewable energy system has been investigated previously. It was studied based on the short-term fluctuations of RES such as solar and wind [20]. Microcycles are known to take place, especially when power generation closely matches the load demand. However, this research provides new insight on battery lifetime reduction due to microcycles which are mainly attributed to tower shadow phenomena. In particular, the downwind wind turbines are considered here as their tower shadow effects are more significant compared to the upwind counterpart. Simulation and experimental results have shown that the wind speed deficit due to this non-ideal effect is important in a standalone hybrid system. In addition, the effects of tower shadow occur typically two to three times per revolution, depending on the number of blades. The modelling of the tower shadow profiles for tubular and four-leg tower configurations are conducted, respectively. Typically, these towers are used in small wind turbine applications. The tower shadow profiles are emulated experimentally using the built test rig with the emulated tower shadow characteristics being explained. Moreover, the quantification of the battery lifetime reduction is analysed through several case studies. A sensitivity analysis of the battery lifetime reduction for different tower configurations, operating at different load conditions is performed. This study seeks the relationship between the tower shadow effects and the battery lifetime reduction in an off-grid situation while serving as an as awareness for HRES designers when selecting the types of tower for their wind turbines. Besides, it may be used for HRES sizing studies in order to avoid the battery being optimistically assumed to last longer than reality.

1.2 Outline of Thesis

Chapter 2 provides a background and literature review on the difference between grid-connected and isolated HRES, the hardware components involved and their

associated design considerations in an off-grid system, the architectures of off-grid HRES and a discussion on battery technologies for off-grid systems.

Chapter 3 describes the sizing methodology in finding an optimum configuration of the HRES, based on the calculated life-cycle cost over the 20 years period chosen in this work. Attention is given in finding the trade-offs between the cost of battery storage system and the diesel generator fuel usage over the considered period. One of the reasons of choosing 20 years is that the Gaia wind turbines are designed for a lifetime of 20 years [21]. It is acknowledged that wind turbines are known to have a much higher capital cost per kW compared to fossil fuel-based generators, such as the diesel generators [22]. However, the capital cost of a wind turbine can only be recovered (payback period) after it operates for a certain amount of time [23] (depending on the site average wind speed) and the cost of electricity (COE) is expected to reduce further when the wind turbine continues to operate. In this case, if fewer years were to be considered in the sizing study, the remaining "unused" lifetime of the wind turbine will cause the computed COE to be higher.

Chapter 4 presents the modelling and simulation of the HRES in detail. The modelling of the battery grid-forming system, fixed-speed wind turbine, diesel generator and turbulent wind speed model are described individually. An integrated system is successfully being simulated and the system performances are discussed.

Chapter 5 proposes a new optimised control algorithm on the diesel generator usage within an off-grid HRES, based on the forecasted wind and load models. A new methodology of simulating a long-term operation of the HRES using the Simulink physical modelling is proposed. It is compared and contrasted with the conventional means of performing optimisation of the hybrid system which uses the simplified mathematical modelling.

Chapter 6 explains the experimental setup of the off-grid hybrid system proposed in this work. It is based on the off-the-shelf components currently available in the market, coupled with the necessary software developed from this research. Each of these components is characterised individually and the test procedures are shown. The steady-state and dynamic performances of the completed test rig are discussed.

Chapter 7 investigates the tower shadow effect from both tubular tower and lattice tower point of view. These were modelled analytically and were tested with the developed test rig. The limitations of the test rig in emulating the tower shadow profiles are discussed. Finally, the tower shadow effect on the batteries lifetime within an off-grid system is demonstrated.

Chapter 8 summarises the work undertaken in this thesis and its contribution to the knowledge gap in the field of hybrid system. Finally, recommendations for future work are provided.

1.3 Component Power Ratings and Specifications

In order to ease readers in referencing the component power ratings used throughout this thesis, Table 1.1 summarises the components and their power ratings in each chapter. The Gaia wind turbine is rated at 11 kW and the grid-forming inverter system is rated at 18 kW and they remain the same throughout this thesis. Variations in diesel generator power rating, battery capacity, load profile, battery state of charge (SOC) limits, hybrid system safety precautions are observed in different chapters. The differences are attributed to the purpose of studies (long term sizing and short-term optimised control) and limited laboratory facilities for the experimental work. The detail descriptions on component specifications and how the results may change due to the discrepancies are provided in the appropriate sections.

Chapter	Wind turbine (kW)	Diesel generator (kW)	Battery capacity (kWh)	Inverter (kW)	Load profile	Battery SOC limits (%)	Hybrid system safety-pre-cautions
3	11	11	150	18	3 households	$40 \leq SOC \leq 100$	NA
4	11	8	15	18	Fixed balance and unbalance	NA	NA
5	11	8	45	18	3 households	$20 \leq SOC \leq 100$	• 3 kW load turn on at SOC = 85% and off at SOC = 80% • 5 kW load turn on at SOC = 95% and off at SOC = 90% • Diesel generator support when SOC < 15%
6	11	Emulate from grid	5.088	18	Fixed balance and unbalance	$20 \leq SOC \leq 100$	SMA SI 8.0H synchronises to utility grid when SOC beyond limits
7	11	Emulate from grid	5.088	18	Fixed balance	$20 \leq SOC \leq 100$	SMA SI 8.0H synchronises to utility grid when SOC beyond limits

Table 1.1: Hybrid system component's nominal power ratings in each chapter

Chapter 2 Background and Literature Review

In the process of designing a HRES, it is important to first have a good understanding on its technologies, architectures and design challenges. A HRES can be designed in various forms, depending on the applications involved. In particular, designers need to consider the types of load, which mainly can be categorised into alternating current (AC) or direct current (DC). Typical home appliances are AC powered whereas specific applications such as telecommunication and data centres require DC supply. Geographical location of the load (islanded or grid-connected) will further define the types of technologies, sizing and configurations of the system to be involved. This chapter compares and contrasts a grid-connected and an isolated hybrid system. The system design and operation challenges being associated with both systems are different and hence will need to be analysed in greater detail. Further on, the design considerations of batteries, diesel generators and inverters are discussed. An off-grid HRES can be designed in three configurations, depending on the applications involved. These are mainly the AC system, DC system and mixed AC-DC system. Battery technologies which are available and suitable to be implemented in a hybrid system are discussed. Then, a literature review on HRES topologies (both modelled and implemented) considered by others is discussed. The cost of hybrid system components, which include wind turbines, bidirectional inverters, diesel generators, batteries are reviewed. This will be used in Chapter 3 for the hybrid system sizing cost calculations. Finally, energy management systems for HRESs proposed by other authors are discussed.

Due to the space and time constraints, it is not possible to cover all the aspects of off-grid renewable energy systems. Therefore, only the vital topics which enable the reader to appreciate this research are presented.

2.1 Grid-connected versus Isolated Hybrid Renewable Energy Systems

2.1.1 System Capability

A HRES can be referred to small generators or decentralised generations which can either be used as a standalone unit at an isolated area (e.g. remote areas) or utility-connected systems. When a HRES is grid-connected, it is typically coupled to a medium voltage e.g. 11 – 66 kV or low voltage e.g. 110 – 690 V networks, depending on the location and total installed capacity of the distributed generators (DGs) [24]. A utility owned HRES can be used to improve power supply flexibility and quality and hence improving system stability. A HRES with a power converter interface can act as an active and reactive power supplier, correcting the power factor at local nodes and in certain cases to track their maximum power point from renewable generations (wind turbines and PV arrays) [24]. From the utility perspective, the investment on transmission and distribution infrastructures upgrade can be deferred by having HRES to supply the unexpected high load growth on certain areas.

2.1.2 Communication Devices

In anticipating the future energy system to be interconnected with various units of HRESs, advanced information and communication devices are expected to be heavily involved. In such an energy system, the HRES units can be aggregated and viewed as the "virtual power plant (VPP)" that can be treated as a single entity [25] [26]. Given the fact that these pools of HRES are located at multiple locations with different generation technologies, it is easy to see how the information and communication technologies play a major role in facilitating the grid control mechanism [24]. In this case, the power system will rely upon software systems to remotely and automatically dispatch and optimise generations, managing load demand and storage systems in a secure web-connected system [24]. On the other hand, an isolated HRES requires minimal or no communication devices, hence simplifying the design and overall operation of the HRES [27].

2.1.3 Mode of Operations

From the control point of view, a HRES which is connected to the strong grid has small variations in voltage and frequency. In this operational mode, the strong grid dictates the grid voltage magnitude and frequency and each DG unit can be viewed as a current source, whose power can be varied by varying the reference current [28]. In an isolated system, the inverter should be operated as a voltage source inverter (VSI) and forms the grid. As the references from the main grid are lost, a new reference voltage must be internally generated by the DG unit controllers in order to maintain good power quality. In this case, the DG units are working as a voltage-controlled source whose outputs should be proportionally shared in meeting the load demand [27]. The power sharing schemes should be designed so as not to overstress any individual unit, where no single dominant energy source is present in the system.

2.1.4 Protection Systems

Protection system design can be very dissimilar for a HRES which is capable of working as both grid-connected mode and islanded mode compared to a HRES that only operates as islanded mode. From the literature, the fault current magnitude when operating as a grid-connected mode is significantly different from an islanded HRES [29] [30]. Therefore, conventional approaches to tackle the protection system problem cannot be reused in such highly dynamic HRES. Typically, the fault current values for a DG unit with power electronics converter interface is limited to around 2 – 3 per unit of their rated currents [31] [32]. It is important to note that these are simulated values and not being validated experimentally. In the grid-connected mode, the protection relays isolate the HRES from the main grid in order to protect the DG units and loads. In islanding mode, the protection relays act to isolate the smallest part of the HRES during fault clearing [24]. More protection system challenges are being associated with a HRES operating in both modes; hence a proper coordination between the DG units, protective equipment and loads is required to ensure a safe operation of the HRES.

When used as a standalone system, the HRES serves small houses such as single to several households, remote island resorts or supporting more specific applications. These include the communication centres and mining sites. A HRES is economically

advantageous compared to diesel-only solution for supplying these remote areas where supplies from the national grid system are either difficult to avail due to complicated terrain or frequency disruptions caused by inclement weather conditions or man-made disturbances. Table 2.1 compares the characteristics between grid-connected and isolated HRES.

Attributes	Grid-connected HRES	Isolated HRES
Typical voltage connection	• Low voltage: 110 – 690 V • Medium voltage: 11 – 66 kV	• Low voltage: 110 – 690 V
Benefits to the utility grid	• Supply electricity to local loads during utility grid fault occurrence • Correct power factor at local nodes	• Investment deferral in grid infrastructure to meet higher load capacity
Communication technology	• Advanced information and communication devices required to facilitate grid control	• Minimal or no communication devices
Control strategy	• Operate as current-controlled source during grid-connected mode and voltage-controlled source during isolated mode	• Operates at voltage-controlled source
Protection relays capabilities	• Isolate the HRES from the main grid • Isolate the smallest part of the HRES during fault clearing	• Isolate the smallest part of the HRES during fault clearing

Table 2.1: Comparison of grid-connected and isolated hybrid renewable energy systems

2.2 Design Considerations of Off-grid Hybrid Systems

The previous section briefly lays out the comparison between a grid-connected and an isolated HRES. Since this work focusses on isolated HRESs, it is worth discussing the design considerations when designing a HRES for a remote location. However, the discussion is broken down into different sub-sections based on the components available in a HRES. Since this thesis is about hybrid wind-diesel with battery storage system, the discussion is limited to the components available in such system.

2.2.1 Wind Resource

Besides having a good annual average wind speed, the wind should have smooth and laminar flow in order maximise the energy generated. Otherwise, it could lead to the potential discouragement of deploying wind energy systems due to the fact that turbulent wind deteriorates the performance of the wind turbine's capability of capturing energy from the wind [33]. In addition, it is best to avoid excessive high-

intensity turbulent wind speed as it increases the mechanical stress on the wind turbines. For this reason, wind turbines are recommended to be positioned away from any obstacles as much as possible. However, these wind potential areas are scarce and not easily to be identified. The choice of wind turbines for different wind sites can be referenced from the International Electrotechnical Commission (IEC) Standard 61400-1:2005 [34].

A simple and common approach to represent a wind profile and its output power is by treating samples of wind velocity as a random variable with a Weibull distribution [35], [36]. In the sizing process of distributed energy sources, the wind uncertainty is represented by the Weibull probability density function [37]. This approach can be visualised in Figure 2.1 [38]. The energy output can be computed by multiplying the formed Weibull distribution with the wind turbine power curve. However, it was observed that there were some discrepancies in the fitted Weibull distribution curve [36]. In addition, this approach would not be used to perform time series simulation as the yearly wind profile was statistically modelled. Thus, the overall optimisation of the hybrid system can be compromised as a result this inaccuracy [39].

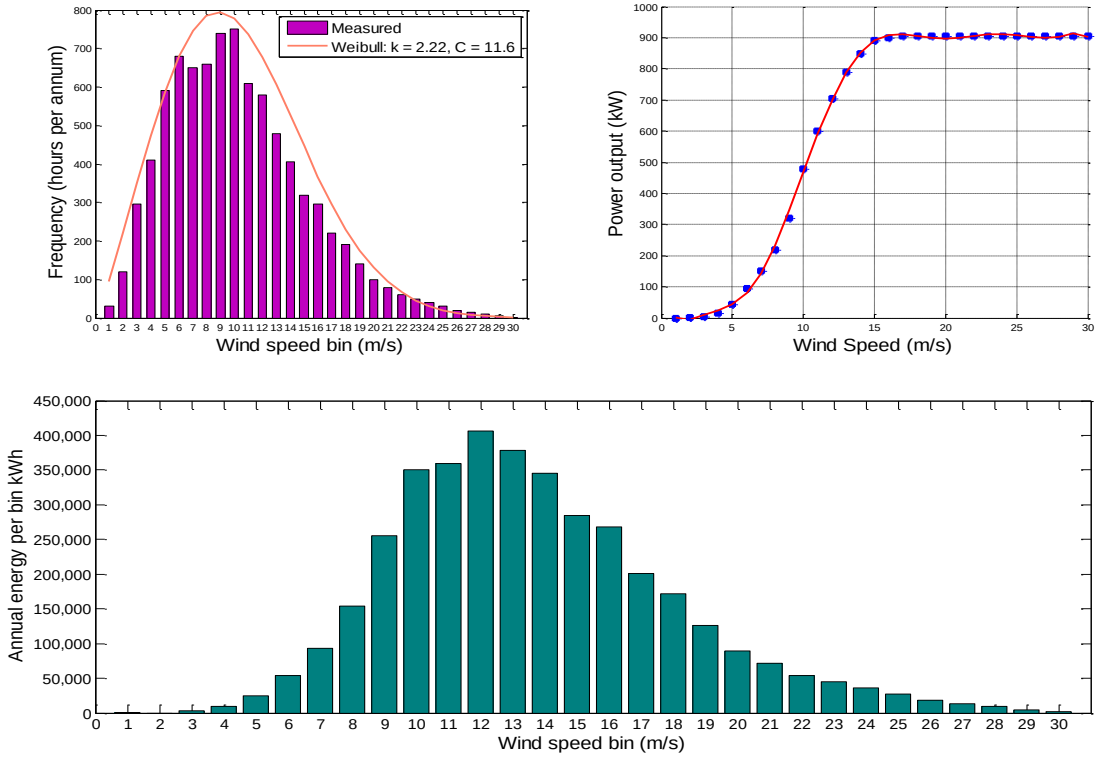

Figure 2.1: (a) annual wind speed distribution, (b) wind turbine power curve, (c) annual power output [38]

2.2.2 Wind Turbines

Modern wind turbine is a machine that converts kinetic energy from wind into electrical power which can be used by the consumers. According to the IEC standard 61400-2:2013 [40], a small wind turbine has a rotor swept area of smaller than 200 m^2. In the UK, this class of wind turbine is rated between 1.5 kW and 50 kW [41]. The physics of small wind turbines are noted to be similar to those classified as high-power wind turbines [42]. In order to keep the cost low and to meet the simple maintenance requirements, small wind turbines usually have a fixed pitch angle [42]. Generally, wind turbines can be operated in fixed-speed or variable-speed. Fixed-speed wind turbines can only operate at a constant speed (or almost constant) for all wind speeds with predefined frequency power injection into the grid. The fixed-speed system is optimised at only a single speed, normally representing the maximum energy capture potential for a given site [43]. Usually an induction generator which is utilised in a fixed-speed system is complemented with reactive power compensators such as static VAR controllers (SVCs) or static synchronous compensators (STATCOMS).

On the contrary, the variable-speed operation of wind turbines is often desired to achieve maximum aerodynamic efficiency over a wide range of wind speeds [44]. For every wind speed, there is a single maximum power point which can be extracted from the wind turbine. By connecting all the points together, a peak power curve is obtained, as illustrated in Figure 2.2 [45]. The variable-speed operation can be configured as a doubly fed induction generator (DFIG), a permanent magnet synchronous generator (PMSG), or an electrically excited synchronous generator.

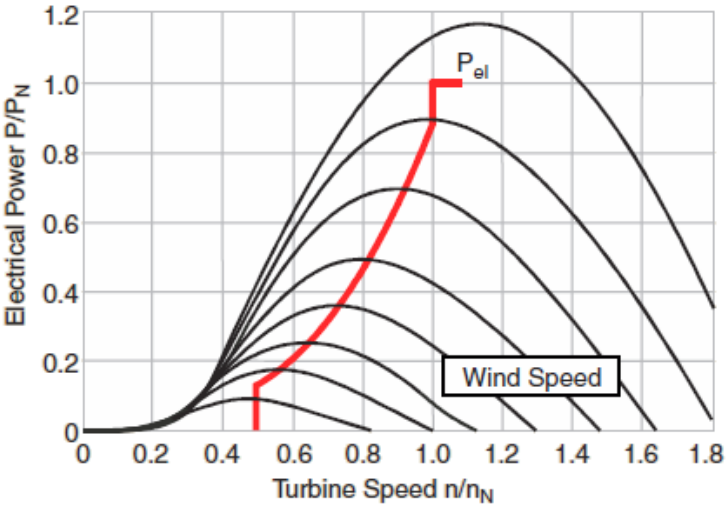

Figure 2.2: Electrical output power as a function of turbine speed. Parameter curves are plotted for different wind speeds. Maximum power point tracking (red curve) can be realised with a variable speed system [45]

In the DFIG topology, the stator terminals are connected directly to the grid and the rotor is connected to the grid via slip rings and partially rated back-to-back voltage source converter that controls both the rotor and the grid currents. The DFIG systems are more prone to failures due to the use of slip rings [43]. The PMSG has a higher efficiency than an induction generator and has no gearbox power losses. In addition, it eliminates the usage of slip rings. However, the variable-speed operation requires a fully rated back-to-back power converter to be interfaced between the generator and the grid. Furthermore, a direct drive system which uses multipole PMSG is physically much larger than generators used with gearboxes [44]. Cogging torque is known to occur, particularly at the low wind speeds [46]. Finally, the variable-speed operation increases system control complexity.

From the author's point of view, although there is no clear distinct winner in the small wind turbine technologies, the use of fixed-speed wind turbines in remote areas is relatively more advantages over its variable-speed counterpart in an off-grid scenario. In remote areas, the accessibility to the horizontal-axis wind turbine's (dominant in small wind turbines [42]) nacelle to perform maintenance and repair is a challenge. Therefore, failure of wind turbine components can lead to significant

maintenance costs being incurred. The fixed-speed wind turbines can be reasoned as a preferred choice in rural areas.

2.2.3 Battery Bank

For an off-grid system, a battery bank is used to store excess energy generated from the DGs or/and used to form the electricity grid if the diesel generator is not set to perform such a task. The durability of each battery depends on the way they are operated and to external conditions, in particular ambient temperature. For instance, a typical lead-acid battery which is designed for solar applications will lose between 15% to 20% of its lifespan (the number of charge/discharge cycles they can perform) for each 5ºC above the standard temperature of 25 ºC [47].

Another consideration is that the lifespan of a battery is reduced when it is discharged deeper at each cycle (depth of discharge(DoD)). From past experiences, in order to avoid damaging the battery, the SOC should not drop below 45%, and should never reach less than 25%. The mentioned figures refer to lead acid battery technology as reported in 2011 [48]. This indicates that to reach an optimal battery lifespan, a sufficiently large battery bank should be installed to achieve a suitable DoD. Considering that a battery bank constitutes a substantial proportion of the hybrid system cost, it is reasonable to design the system in such a way that allows batteries to operate for a minimum of at least six years and ideally eight to ten years before being replaced [47].

A diesel generator can be started up to mitigate the battery bank DoD problem when the specified low SOC threshold is reached. However, the diesel generator's lifetime is also compromised by the frequent on/off cycles [17] [18]. In practice, the management system should start the diesel generator whenever the specified battery SOC is reached until the battery is fully charged again. This widely used management strategy does possess some disadvantages aside from its simplicity. An interesting example can be found in the village of Akkan in Morocco, whereby a hybrid PV-diesel-battery system was implemented by Trama TechnoAmbiental [48]. It consists of a system combining PV, diesel generator and a battery bank with 4 days of back-up capacity. In this case, the diesel generator was started up when the SOC

level (below 45%) was low late at night. It runs the whole night continuously until the battery was fully charged. When the sun was rising in the morning, the PV generation was only partially used (catering for actual consumption) because the battery was already charged. Hence, unnecessary fuel expenses are involved. This case study has demonstrated the importance of the energy management system (EMS) in handling the energy flow within a hybrid system more efficiently and preserving the lifetime of the equipment. Along with this, another consideration is whether to run the EMS automatically or manually by a local operator. Unpredictable consumer behaviour can result in under-voltage on the battery system, pushing the community to complete black out as a consequence of running an automatic EMS. This can seriously endanger the battery state of health (SOH) as a result of these high-stress situations. On the other hand, a manual EMS can be run poorly if insufficient training are given to the local operators.

A battery's total capacity is reduced when a higher discharge current takes place. The greater the discharge rate, the lower the delivered capacity. This phenomenon is known as Peukert's law [49] [50]. This law is firstly presented by a Germen scientist, Peukert in 1897 and provided an empirical equation that provides assistance in determining the battery capacity based on the rate that it is being discharged. If the load growth is taken place in a remote area, the battery throughput is increased throughout the year. Eventually, the battery will not only be depleted more quickly but also its total capacity gets reduced by higher discharge current.

2.2.4 Diesel Generator

A diesel generator has low upfront investment cost but suffers from the costly long term usage of diesel fuel. As a general rule, renewable generations should first be utilised before running a diesel generator. The marginal cost of generation with renewables is zero whereas each kWh produced by the diesel generator requires fuel and increases the price of electricity. For this reason, the diesel generator is most suitable to be used for back-up when the production of renewables is insufficient to meet the load demand or when the battery has a low SOC, rather than being used as a grid forming device. A hybrid system which is operating in a rural area also reflects the area has limited road access and is sometimes surrounded by challenging terrain

conditions. Therefore, additional cost is being associated for both fuel transportation and operation and maintenance in these locations. In addition, heavy reliance on the diesel generator is not ideal as the transport of diesel fuel to these areas can take a long time besides suffering from increasing fuel prices from time to time.

The lifetime of a diesel generator is mainly affected by the number of on/off cycles and the operating capacity (partly or fully loaded). A fixed speed diesel generator is recommended to run at least 40% of its rated capacity to prolong the lifetime of the diesel engine. Moreover, when running at part load, the efficiency reduces and it is lower compared to its variable speed diesel generator counterpart [51]. The typical load curve for a housing area is composed of a prominent peak in the morning and evening when the occupants are at their most active time at home. The base load or idle load is generally present most of the time, contributed from appliances and equipment in off or "standby" mode while drawing power. Typical examples are refrigerators and communication devices such as modem. In many cases, the peak load is several times higher than the base load. During the night hours, a limited load level is observed and is generally the lowest throughout the day. From the described load profile, it can be concluded that the diesel generator will suffer from degradation and inefficient in utilising the diesel fuel as a result of huge load variation throughout the day [47]. Cascaded diesel generators with smaller power ratings can be used however with the compromise of increasing the complexity in terms of control and overall cost due to the use of synchronisers.

Despite the above mentioned challenges of using a diesel generator in a remote area, it is frequently regarded as a useful device as a back-up and it functions well in complementing the intermittent generations from the renewables. Major maintenance operations should be carefully planned with respect to the cost and unavailability of the equipment. Typically, diesel generators would need to conduct maintenance operation after 15,000 to 25,000 running hours [47].

2.2.5 Inverter

Sizing an inverter for an off-grid system is very different from sizing a grid-connected inverter. A grid-connected inverter simply converts all the DC from

renewable energy generations (PV or rectified wind energy) into AC power, which is fed back into the house usage or back to utility if there is energy surplus. Hence, the sizing of the grid-connected inverter is based on the power rating of the DGs. It is not responsible for meeting all the AC load power requirements since practically unlimited power is available from the utility. An off-grid inverter must be capable of meeting the needs of the rated loads (running simultaneously) and also their surge needs. Considering the case of an off-grid system as shown in Figure 2.3, the bidirectional inverter is connecting between the AC and DC buses. This inverter is operated as a grid-forming device which is able to guarantee a stable set of voltage and frequency despite the variations in renewable energy generation and load demand. It also needs to provide the required start-up current for the induction generator-based wind turbine. In addition, some house loads with induction motors such as washing machines, pumps, and power tools can have large start-up current, up to seven times their rated power. Although it is common that these households are equipped with soft-starting devices, the limited in-rush currents are still relatively higher than their nominal values [52] [53].

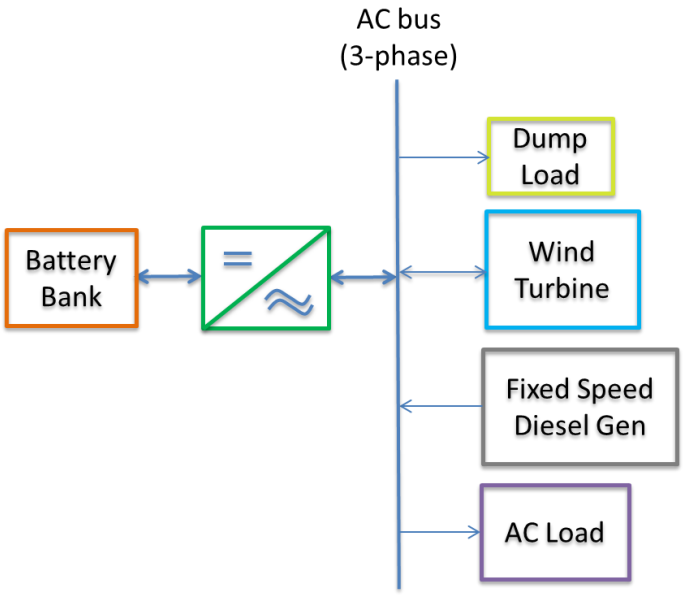

Figure 2.3: Off-grid hybrid wind-diesel system

However, it is important to note that the inverter of the off-grid system should not be oversized due to several reasons. Figure 2.4 depicts the common efficiency curve of a single-phase inverter, rated at 4.6 kW [54]. It is observed that the “peak” efficiency

does not occur at its rated operating condition. In this case, the peak efficiency is reached at about half of the inverter's rated output power, and decreases by a relatively small amount as the output power approaches its rated value [55] [56]. More significantly, if the inverter is utilised less than 10% of its rated capacity, huge energy losses are expected to be experienced. Therefore, it is desired to size the inverter which operates within the highest efficiency region.

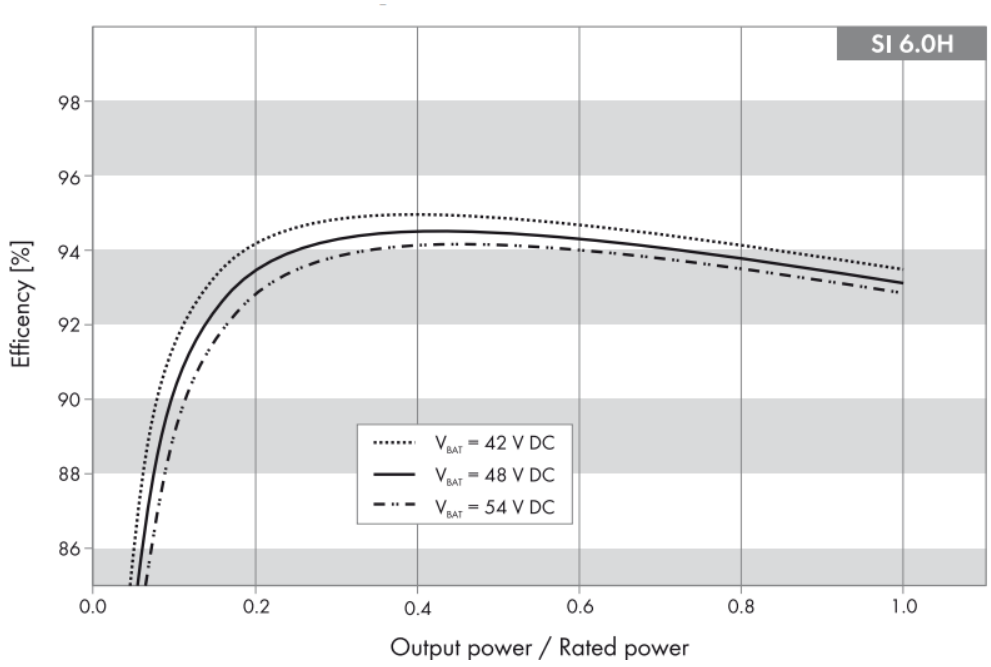

Figure 2.4: SMA Sunny Island 6.0H characteristic efficiency curve [54]

Another consideration is the no-load power consumption of the inverter. Since there may be long periods of time when no power is required by the loads, this can accumulate to a substantial amount of energy drain on the system. Table 2.2 tabulates the energy consumption for various inverter power ratings in no-load operation [54]. The consumption in no-load operation is increased by more than 40% when the power rating of the inverter is doubled. For the case of Sunny Island 6.0H with a 25.8 W of no-load power consumption, 619.2 Wh is consumed within a day. On small systems, this figure has a relatively considerable impact on the overall power consumption.

	Sunny Island 3.0M	*Sunny Island 4.4M*	*Sunny Island 6.0H*	*Sunny Island 8.0H*
Consumption in no-load operation and in discharge mode	18.0 W	18.0 W	25.8 W	25.8 W

Table 2.2: Series of Sunny Island inverters energy consumption in no-load operation

An inverter's lifespan can be extended to more than ten years, but this component is a sophisticated product and the repair or part replacement has to be undertaken by a specialist technician from the supplying company.

2.2.6 System Design

Based on the abovementioned design considerations being associated with the use of diesel generator, battery bank and inverter, the operational strategy of the system should be focused on satisfying all their needs as much as possible. Mainly, the efficiency and prolongation of their operational life can be treated as the criteria or constraints while operating the system. For this purpose, optimising the operational strategies of the diesel generator, battery and inverter and the utilisation of wind energy are important and have a strong influence on the life cycle cost of the system [57].

Looking from a wider perspective, the system design is very much dependent on the selection of bus bar (AC or DC) for the hybrid system. In the next section, the discussion is focused on different configuration models as well as their advantages and limitations.

2.3 Architecture of Off-grid Hybrid Systems

The configurations of hybrid systems can mainly be categorised into three types; AC system, DC system and mixed AC/DC system [58] [59]. The choice of the bus bar depends on the generation technologies to be integrated and the type of load to be supplied. While PV panels and batteries supply DC power, electrical generators found in diesel generators, small wind turbines and low head hydro turbines produce AC power. The definition of each hybrid configuration with their advantages and their limitations are discussed.

2.3.1 AC System

A typical AC coupled configuration is shown in Figure 2.5. In this configuration, different energy sources are connected to the AC bus through appropriate power electronics devices. If DC storage such as a battery bank is utilised, it is connected to the bus via a bidirectional converter. AC loads are directly connected to the bus while DC loads need AC/DC power converters in order to be connected to the AC network. Within the AC system, the choice of single-phase or three-phase distribution system will need to be carefully considered. Single-phase distribution grids are relatively cheaper than the three-phase ones, without the existence of unbalanced condition which is typically a major problem in mini-grid systems. On the contrary, the latter systems allow greater opportunity for commercial purposes to obtain power and the possibility of future interconnection to the national grid [59].

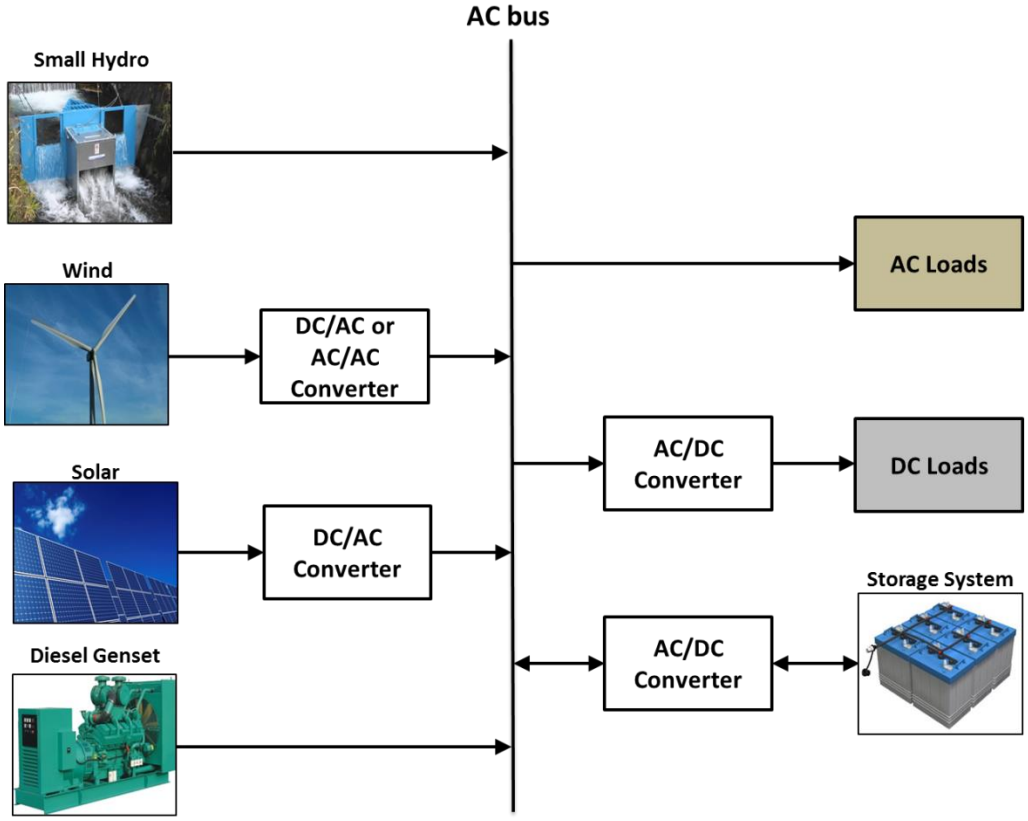

Figure 2.5: AC coupled configuration of hybrid wind-solar-small hydro-diesel system

AC power network has been the standard choice for commercial energy systems since the late 19th century. The easy transformation of AC voltage into different

levels for various applications, the capability of transmitting power over long distances and its inherent characteristic from the fossil-based driven rotating machine have made the AC power network to become the main choice. To date, AC networks have existed for more than one century. Therefore, it is not surprising that AC loads have been the dominating technology in the market. It has been used to power the incandescent lamps and motor-based household products such as fans, air-conditioners, washing machines and refrigerators. If a DC system were to be used, radical upgrade/reinstallation on these appliances or an inverter at the entry point of each household is needed and hence further contributing to a higher upfront development cost.

On the other side, challenges still remain within the AC network despite its development for a long time. In particular, in-rush currents caused by transformers, induction motors and generators and difficulty in voltage control, decoupling of reactive power from active power in a high R/X line impedance ratio and system stability are still among the challenges seen contrary to the DC system [60] [61]. In addition, advanced frequency and voltage control techniques are required to maintain AC power quality and stability when islanded, grid-connected and in transient modes.

The implementation of AC microgrid systems can be observed around the world [59]. Researchers focused the study of AC microgrid in the area of droop control (load sharing), harmonics filtering, line impedance effect and stability of the overall system [27] [62] [63] [64]. The parallel operation of the inverters in an isolated scenario was claimed to improve compared to the conventional droop control method as it took into consideration of the line R to X impedance ratio [27]. Similarly, another study has experimentally validated that the line impedance consideration can compensate the non-uniformity of the inverters [62]. From the control system point of view, literature [63] studied the angle droop control instead of the conventional frequency droop. Although it ensures proper load sharing, the overall stability is negatively impacted by the high gain angle droop control. Hence, the work proposed a supplementary control loop to stabilise the system for a range of operating conditions while ensuring satisfactory load sharing. In [64], a cooperative harmonic filtering strategy for converters operating in an isolated system is proposed. In

particular, the harmonic conductance-harmonic Q-V droop which may effectively damp harmonic resonances is integrated into the conventional frequency and voltage droop controls.

2.3.2 DC System

Since the concept of smart grid was introduced, the utilisation of DC system for industrial power supply and commercial buildings are increasing. With the vast deployment of DC-based DGs such as PV panels and small wind turbines (which are operating with permanent magnet generators that require rectification), the option of connecting consumer electronics devices to a DC bus system is viable. Figure 2.6 shows the block diagram of a typical DC coupled hybrid system. This configuration has one DC bus and all the DGs are connected to the bus via power electronics interfacing circuits. Generally, the DGs require unidirectional power converters whereas the ESS is connected to the DC bus via bidirectional converter. In this scheme, the storage system is used to form a constant DC bus voltage as the renewable energy-based DGs are not producing power all the time. Their energy production is dependent on the availability of RES. If a diesel generator is chosen to form the grid, it needs to be running all the time. Discussion earlier has shown that this is not the best approach to use a diesel generator due to the low load factor and the difficulty in transporting diesel fuel to remote areas. Usually, the low load factor situations occur when the consumers are away to work during the day or are sleeping during the night. Several DC loads such as computers, mobile phones and light-emitting diode (LED) lighting can be connected directly to the DC bus via DC/DC converters which produce a constant DC voltage. On the other hand, AC loads are supplied through an inverter. Rather than using a single high power rated inverter, several smaller rating inverters can be cascaded to achieve the former. This methodology is adopted to improve the overall supply reliability [65].

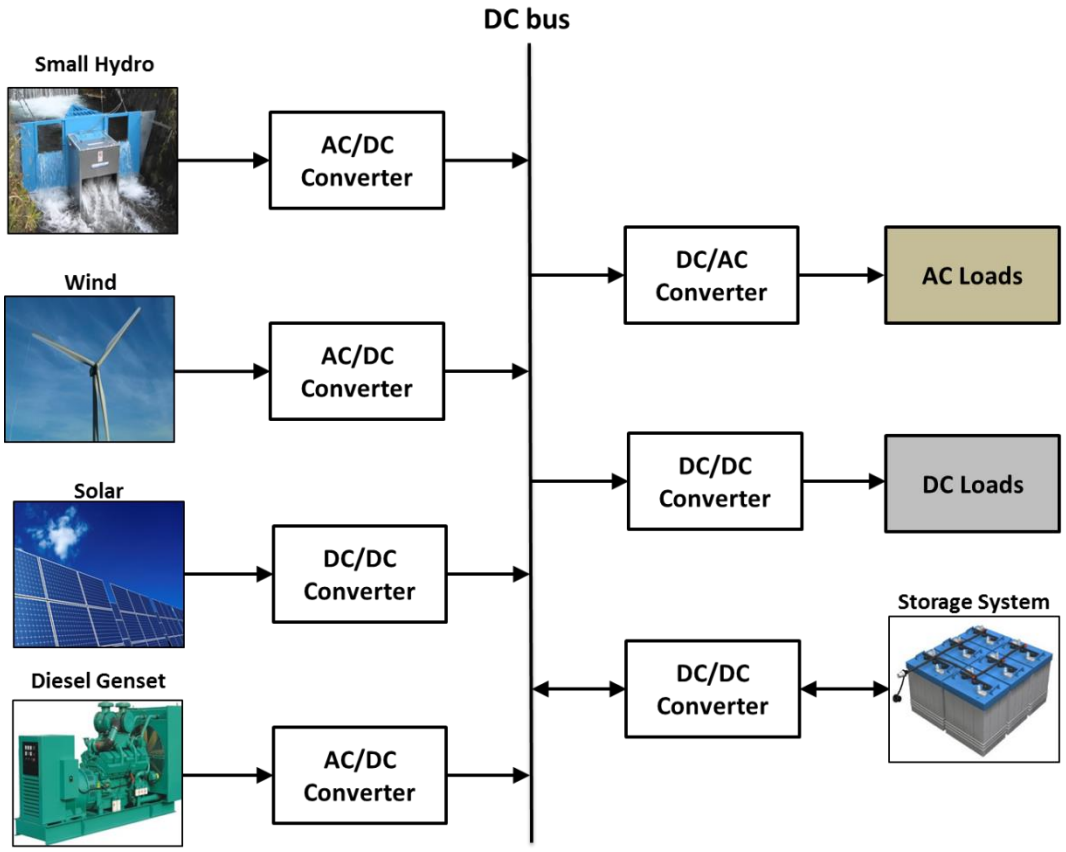

Figure 2.6: DC coupled configuration of hybrid wind-solar-small hydro-diesel system

The most apparent advantage of using a DC system is its simplicity as synchronisation is not required to integrate various energy sources [65]. Therefore, frequency and phase control is not required. In addition, there are challenges in the synchronisation of frequencies and voltage control during islanding operation [66] [67] [68]. Moreover, DC power converters do not use a transformer to step-up or step-down voltage, hence reducing the system physical size.

Consumer devices (computers, LED lighting and mobile phones) need DC power for their operation [69]. However, a conversion stage from the available AC power into DC is required for use. Typically, this is achieved using inefficient rectifiers [70]. Moreover, the power generated from the PV systems must first be converted to AC to be tied up to the existing AC bus, only later to be converted to DC for end users. These DC-AC-DC power conversion stages result in substantial energy losses. Eliminating this waste, by some estimates, could improve PV system performance by as much as 25% [70]. In addition, the presence of an electric vehicle (EV) with a

charging system in the home increases the attractiveness of having the DC system. The car batteries are even permitted to be used as a back-up power without the use of costly inverter technology. However, an individual DC system cannot completely eliminate the losses in multiple stage conversions, though it was reported that the DC supplying system demonstrated has a greater efficiency than the standard AC one [71]. The report was aiming to provide a comparison between DC and AC supplying systems for office buildings, from the perspective of cables and converters efficiencies [71]. In addition, a year of loss evaluation on DC microgrid system for residential houses was also simulated and compared with the loss in an AC system [72]. The considered system comprises a PV system, a gas engine cogeneration and 20 residential houses. Figure 2.7 shows the calculated system losses of both systems in each month [72]. The results demonstrated that the losses in the DC microgrid are lower than the AC microgrid all year round. The losses between the two systems are about 15% [72].

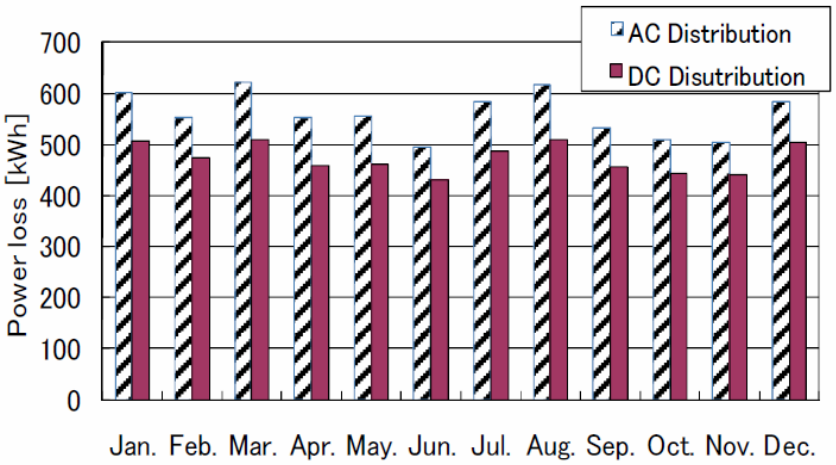

Figure 2.7: Total losses in each month [72]

Although the DC system presents several advantages over its AC counterpart, it requires substantial replacement of existing AC-based electronic products. At present, many consumer electronic products are compatible with AC voltage standards. It is impossible to replace all these technologies in a short time and without a huge amount of monetary investment involved. Currently, the main challenge being associated with the DC system is the protection design, directed primarily to the end-

user inverter, customer network faults including inverter switching transients and double-fault situations between different networks (AC and DC) [24] [73]. Commonly available fuses and automatic relays are also difficult to use with power converters. This is due to the fact that power converters do not produce sufficient and long enough short-circuit currents for the fuses to react [32] [74]. Therefore, a different protection scheme is utilised along with the DC system, in particular with different fault-detection and grounding methods. These protection systems consist of current interrupting devices, protection relays, measuring equipment and grounding systems [75] [76] [77].

Literature [78] proposed a distributed model predictive control (MPC) approach to extract optimal power from the PMSG-based WECSs, in a cooperative manner rather than competing with each other. Simulation results showed that the control scheme is especially useful in coordinating the load sharing between multiple PMSGs in a situation whereby the ESS is limited or when it runs out of its capacity, with the aim of stabilising grid DC voltage. A low-voltage bipolar-type DC microgrid has also been proposed to supply power via the three-wire distribution system [79]. The bipolar DC bus concept increases supply reliability and it allows user's loads to choose the source voltage from either bus. A laboratory-scaled system has been constructed to examine the fundamental characteristics of the proposed system [79]. At the University of Bath, UK, a DC microgrid demonstration project was built to power part of their library [80] . The main loads are computers and priority LED lighting.

2.3.3 Mixed AC/DC System

A mixed scheme has both an AC and a DC bus. Figure 2.8 presents the configuration of such a system. All the DC energy sources (PV panels and battery banks) are coupled to the DC bus via a DC-DC converter. DC electrical loads are directly supplied through the DC bus. On the other hand, rotating generator-based DGs (hydro, wind turbine, diesel generator) are connected to an AC bus with AC loads supplied through this bus. A bidirectional DC-AC converter is required to interface the DC and AC buses. The main objective of this bidirectional converter is to maintain a smooth power transfer between the DC and AC buses. Power flows from

the DC bus to the AC bus if the power generated in DC bus is greater than the AC bus and vice versa. In addition, this converter is used to maintain stable voltages along the buses under varying generation and load conditions. This mixed AC/DC system is more beneficial to facilitate the connection of various AC and DC power sources and loads in order to minimise conversion losses [81].

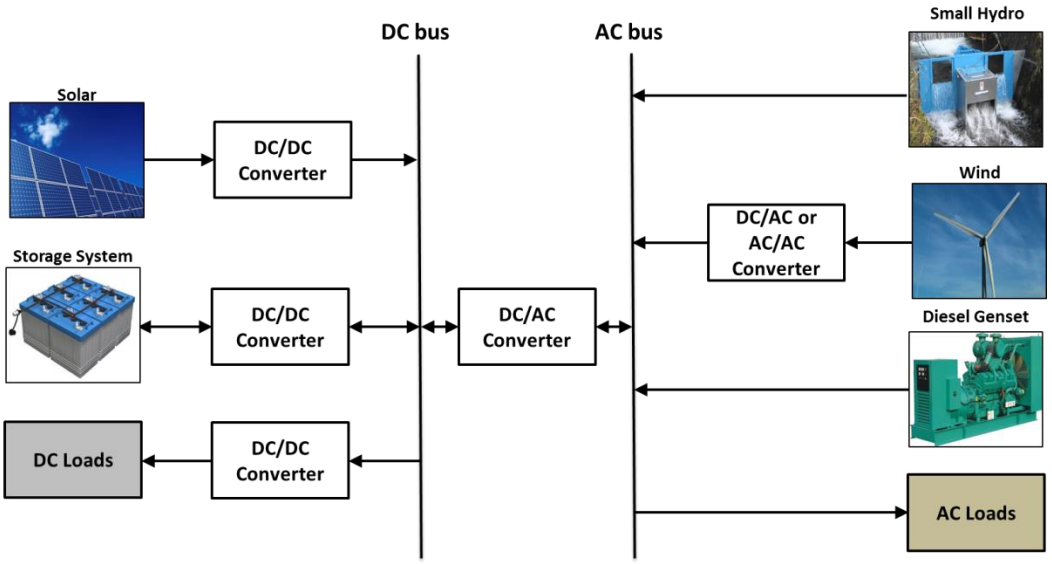

Figure 2.8: Mixed AC/DC configuration of hybrid wind-solar-small hydro-diesel system

Despite the shift in technologies of some electronic products that can potentially be operated in DC (for instance from cathode ray tube displays (CRT) to LED television), there are still devices/appliances (air conditioners, refrigerators and freezers), which are much more efficient to operate in an AC configuration [70]. Therefore, generators and loads should be connected to their respective bus bar, depending on their most efficient technology (AC or DC) in nature. With this approach, conversion losses are minimised as power converter stages are reduced. As a result of the simplification of equipment, the mixed AC/DC system has lower cost and higher energy efficiency compared to DC only and AC only systems. In addition, the elimination of power factor correction (PFC) in power electronics loads when connecting to DC bus indicates significant cost reduction in end users equipment.

The power quality of the AC grid within the mixed AC/DC system can be enhanced without having the DC loads being connected to the AC grid. The DC loads will not

inject harmonics to the DC bus due to the full controllability of the bidirectional inverter which links the AC and DC buses. The capability to control unsymmetrical current within the mixed AC/DC system is improved since the negative and zero sequence current problems caused by unbalanced loads in the AC grid can be mitigated by the DC grid [82].

Although there are many benefits of a mixed AC/DC system, as described above, there are practical problems that exist in implementing it. Due to the differences in control philosophy and characteristics of an AC and a DC system, the control and energy management within the mixed system is more complicated than individual AC or DC systems. As a result, such scheme is considered as a long-term process. It is relatively easier to integrate the mixed AC/DC system within new buildings than old buildings that need to upgrade their distribution systems. New metering, protection and grounding equipment are also required for the mixed AC/DC system [82].

Meanwhile, in Tagajo campus of Tohoku Gakuin University, Japan, a mixed AC/DC isolated microgrid was developed for researchers as an experimental equipment to conduct microgrid related research and development [83]. The DC bus integrates the PVs, a wind turbine, a diesel generator, a variable DC load, EVs and an ESS which consists of secondary batteries and electrical double-layer capacitor (ELDC). An inverter is interfaced between the DC bus and AC bus and it serves the AC load. Since most of the generations and loads are connected to the DC bus, the work focuses on stabilising the DC voltage within an acceptable range using the proposed "Coordinated Band Control" strategy. In particular, the battery, ELDC and diesel generator play a role in stabilising the DC voltage. In another study, multiple bidirectional power converters are used in the mixed AC/DC microgrid system [84]. The authors proposed a distributed coordination control method to enable the power flow between AC and DC buses in both grid-connected and islanded modes. The control strategy was verified using a real-time hardware-in-loop (HIL) system.

2.4 Off-grid Energy Storage Systems

The introduction of ESSs can be beneficial by allowing time-shifting between electricity generation and consumption in an electricity network. Fluctuating and/or intermittent energy production from the renewables was in most cases found to be unable to adjust to the profile of electricity demand from the consumer. Its impact on power quality and power system dynamics reflects the need to couple ESSs with renewable generations. In the case of an off-grid system, the benefits of adopting ESSs can be summarised as the exploitation of otherwise wasted amounts of energy (excess energy from the renewables), the increase in overall system reliability in delivering high quality of power to the consumer and the improved operation of the power system. In this section, the discussion is focused on the battery technologies and their suitability for off-grid systems. Their technical characteristics together with their range of applications in off-grid systems are analysed.

2.4.1 Classification of Energy Storage Technologies

The types of energy storage can be categorised into different forms; mainly mechanical, electrical, electrochemical, thermal and virtual natures. The flowchart as shown in Figure 2.9 categorises the typical types of energy storage available in the market. However, only the battery technology for off-grid hybrid systems will be discussed here.

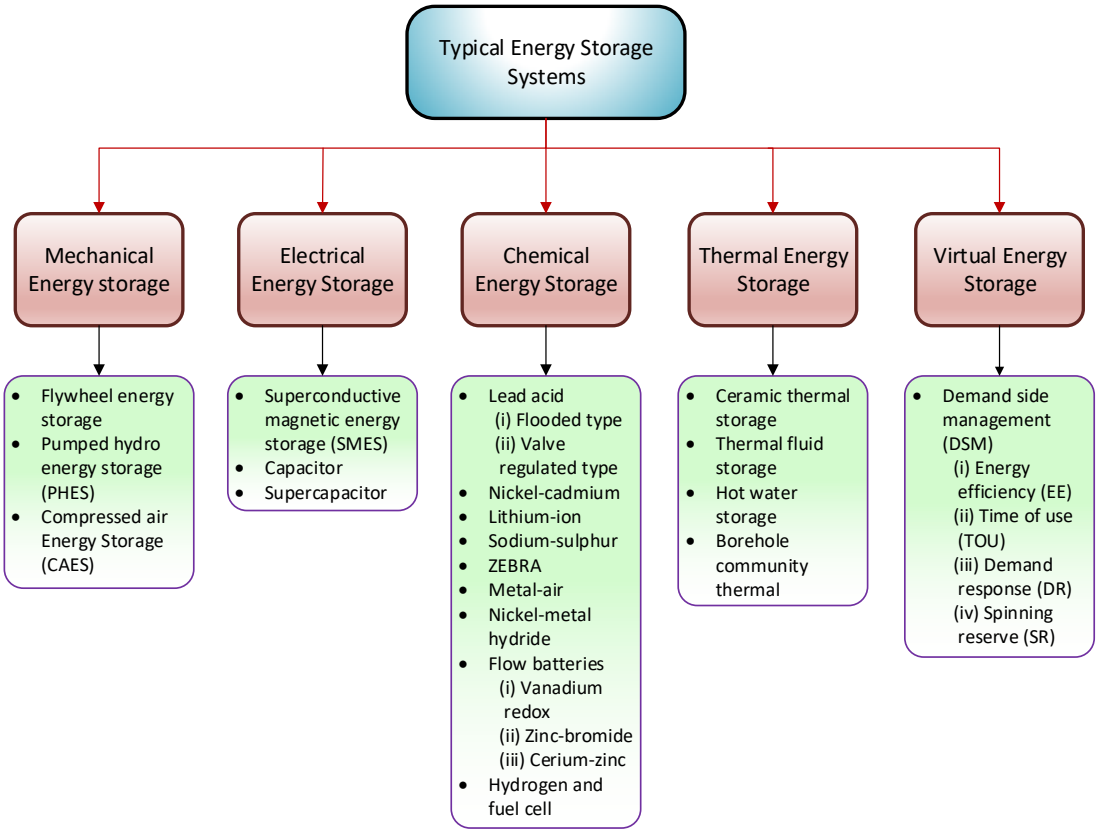

Figure 2.9: Types of energy storage

First of all, the energy and power density distinguish the types of energy storage technology. Essentially, it is a trade-off between the choice of high energy density or high power density for all technologies that are available in the market. Figure 2.10 [14] graphically illustrates the comparison between each energy storage technology as a function of system power rating and their corresponding rated energy capacity. The chart further divides the technologies diagonally, demonstrating the discharge time duration at power rating. In the case of off-grid systems for small remote communities, the interested energy storage's power ratings lie within the range of kilowatts (*kW*).

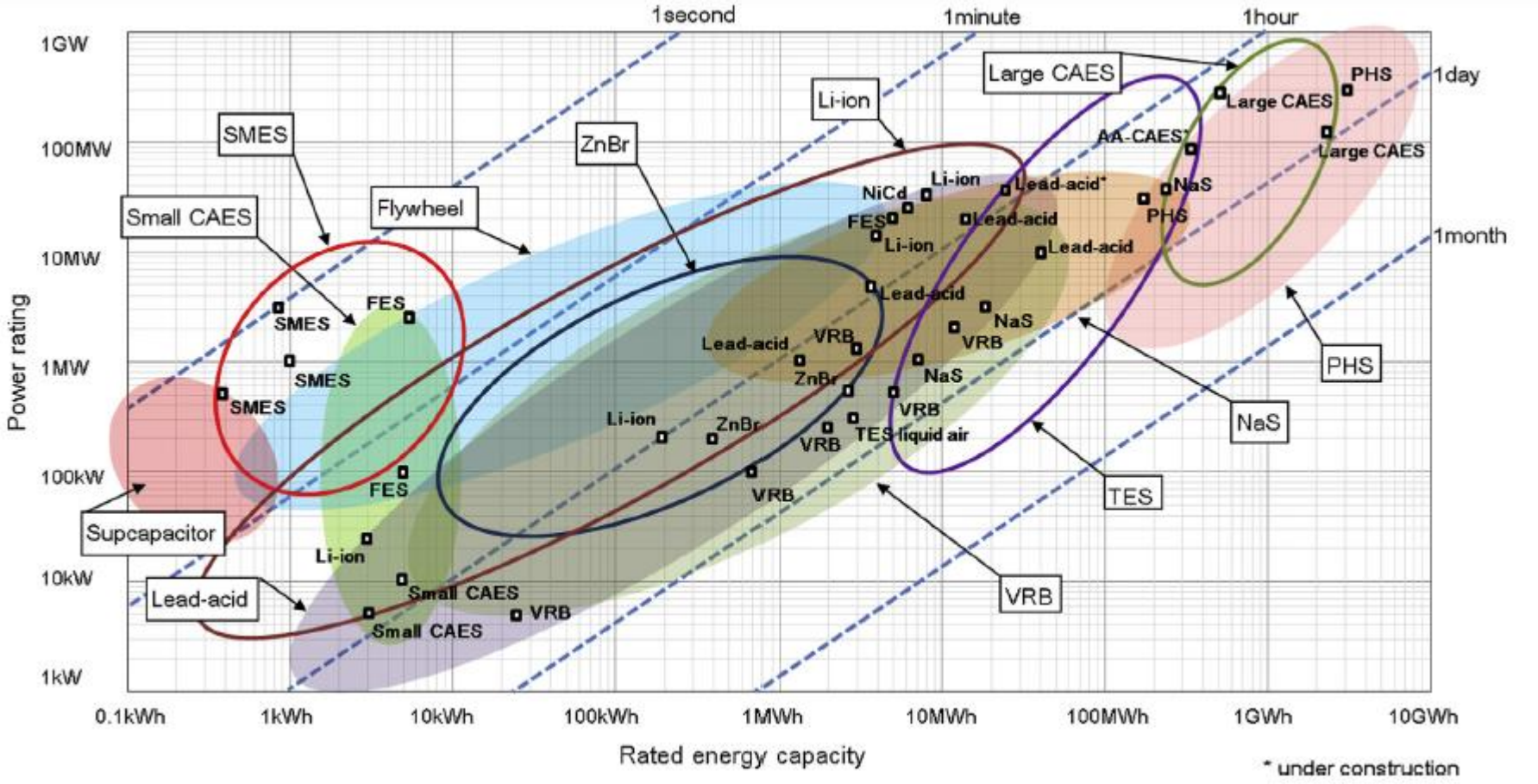

Figure 2.10: Energy Storage Power and Energy Density [14]

Batteries are the most widely adopted energy storage technology, especially in rural areas of developing countries and in some cases, they are also considered as the main electricity carrier [85]. Within these regions, the low-income households have been using batteries to power their light loads, such as radios and TVs for a few hours during the night [86]. Most batteries deliver power in the range of few *kW* to more than 100 *MW* for few minutes to several hours. The existence of numerous types of battery technologies, each with its own special characteristics, allows a wide range of applications to be covered, from power equality to energy management. In the off-grid systems, batteries are commonly utilised to improve power quality, performing black start capability and small-scale storage (typically up to a few days of remote communities load consumption). Table 2.3 tabulates the advantages and disadvantages of the battery technologies discussed so far which is suitable for renewable energy applications [87]. This is referenced from Energy Storage Association (ESA), a non-profit organisation [87]. However, it is not known if ESA is in any way being associated with companies which may be biased in their publication. Generally, it can be observed that all the batteries are relatively suitable to handle power management except the metal-air type which is more ideal for energy management. Among the battery ESSs, flow batteries, metal-air and NaS have proved to be good at carrying out the role of energy management. However, it is believed that lead-acid and Ni-Cd are more ideal for small-scale battery storage systems for off-grid applications. They are described as mature technology with known performance characteristics, relatively low capital cost (lead-acid), low maintenance requirement (Ni-Cd) and do reasonably well in both power and energy management, although the main negative feature of these technologies is the used of environmentally unfriendly content [88] [89] [90].

Technology	Advantages	Disadvantages	Power application	Energy application
Flow batteries: **PSB** **Vanadium redox** **ZnBr**	High capacity, independent power and energy ratings	Complicated system requirements of pumps, sensors and control units	Reasonable for this application	Fully capable and reasonable
Metal-air	Very high energy density	Electric charging is difficult	Not feasible or economical	Fully capable and reasonable
NaS	High power and energy densities, high efficiency	Production costs, safety concerns (addressed in design)	Fully capable and reasonable	Fully capable and reasonable
Li ion	High power and energy densities, high efficiency	High production cost, requires special charging circuit	Fully capable and reasonable	Feasible but not quite practical and economical
Ni-Cd	High power and energy densities, high efficiency		Fully capable and reasonable	Reasonable for this application
Other advanced batteries	High power and energy densities, high efficiency	High production cost	Fully capable and reasonable	Feasible but not quite practical and economical
Lead-acid	Low capital cost	Limited cycle life when deeply discharged	Fully capable and reasonable	Feasible but not quite practical and economical

Table 2.3: Comparison of battery technologies [87]

Over the decades, many research activities have been focusing on the development of new battery and supercapacitor technology, usually aiming to enhance the power capacity or the energy capacity [91]. However, despite significant improvements in relation to these energy storage technologies, an ultimate all-round energy technology which transcends any other in all aspects such as cost, efficiency, power/energy capacity, weight/volume and cycle life is not likely to be materialised in the near future [91]. Therefore, it can be concluded that a homogenous ESS is subjected to limited characteristics. On the other hand, a hybrid energy storage system (HESS) which typically consists of heterogeneous energy storage elements is a viable solution for a practical ESS with currently available technologies. They have the potential to overcome the limitations of single-technology ESS by exploiting only the advantages of heterogeneous energy storage technologies while hiding their drawbacks [91]. HESS is known to be a system-level design methodology to enhance ESS performance through the efficient use of current storages even without the major progress of the particular storage technology. For instance, the supercapacitor technology has the advantage of a long cycle life, high cycle efficiency, short response time, and high power capacity can be used to compensate the limitations of the conventional battery system [91]. Despite the potential benefits that can be tapped from a battery-based HESS, the development of such system is beyond the scope of this research.

2.5 Literature review

The following sections discuss the literature review on different topologies of hybrid RES schemes proposed by various authors (both modelled and implemented), the choice of components (available in the market) for hybrid system proposed in this work, a brief overview of battery degradation models and the energy management systems in HRESs.

2.5.1 Topologies of Hybrid Renewable Energy Systems

This section reviews the modelled (techno-economic and sizing) and implemented off-grid HRESs around the world. It is aimed to perform a comparison of the sizes and schemes against the choice of technology and subsequently provide a general

idea and justification on the size of load (community) that the HRES proposed in this work may service realistically. In view of this, several HRESs proposed in the past have been selected for comparison.

It is acknowledged that remote communities live in different levels of poverty and economic capability, which varies between countries. This affects their affordability on housing appliances and ultimately their load usage pattern. In addition, there is a discrepancy in the level of monetary subsidisation on the supplied off-grid systems from local government or institutes. Therefore, it is important to note that the value of a direct comparison on the proposed HRES schemes from various authors against the serviced load demand is limited. The extracted case studies here serve as a general awareness and the optimal system is case-based specific. To the best knowledge of the author, the information on the selected case studies is the latest at the point of writing. Readers are recommended to refer to the most recent literature for further power generation infrastructure upgrades or changes of the load demand.

The inclusion of all reported projects is beyond the scope of this thesis. In this section, seven samples of modelled and five samples of implemented HRESs are briefly summarised, as tabulated in Table 2.4. The considered community size or load is from a single household to a small village (about 173 households). Generally, PV technology is widely used across the world due its cost-effectiveness and low maintenance [92]. Except case study number 4 (in Cameroon), all the other considered HRESs in Table 2.4 use PV arrays to generate electricity. Wind turbine technology is also a popular choice among the considered HRESs. The limited use of hydro generation can be associated with the high dependence on geographical location, whereby a running river with a certain head is required. In all cases, battery storages are used to store excess generation and supply power deficit to the load demand. To a certain extent, diesel generators are used as a back-up to enhance the reliability of the power supply system to consumers. A fuel cell system was used in Cangucu, Brazil as part of their research and demonstration project. As previously mentioned, the installed renewable energy devices, energy storage and the load demand vary across projects. However, in many case studies, a household on average consumes 5 kWh/day. In addition, the average renewable power generation

(combined wind and solar PV) required for a household is approximately between 1 kW to 4 kW (depending on household income level). Again, the exact figures are dependent on several factors such as the available capital cost for the project, geographical locations, type of RESs available, environmental impacts, societal level (hence income) of the consumers and the energy policy of a particular country.

Case number	Modelling / Implemented	Study/Project location	Technology	Load Type	Design capacity	Remarks	Source
1	Modelling	6 remote sites in Algeria	Wind, PV, Diesel, Battery	Single household for 6 rural sites	300 W - 1kW solar-PV 1 kW - 6kW Wind 4.5 kW Diesel Battery - not mentioned	i. The optimal hybrid system configurations to meet the load demand depend largely on renewable energy sources. ii. For high wind potential sites, more than half of the total power generation is provided by the wind turbines. iii. A diesel generator is used as a backup.	[93]
2	Modelling	Vadodara, India	Wind, PV, Battery	AC home appliances, 5 kWh/day	2 kW solar-PV 1 kW Wind 2.4 kWh Battery	i. An hourly time series simulation for every configuration is performed for 1 year period. ii. The hybridisation of wind turbine and solar PV proved to be more economics in terms of COE compared to standalone wind or solar-PV system	[94]
3	Modelling	Dhahran, Saudi Arabia	Wind, PV, Diesel, Battery	Twenty typical 2-bedroom families in Dhahran (126 kW peak)	100 kW - 200 kW Wind 100 m^2 - 1000 m^2 solar-PV 16 kW - 128 kW Diesel 126 - 3024 kWh Battery	i. Investigate the performance of hybrid systems consisting different power rating of wind farms, PV areas and storage capacities together with a diesel back-up while satisfying a predefined specific annual load demand. ii. Best wind energy utilisation factor when the wind turbines are rated slightly less than the load demand. iii. Doubling the wind farm capacity did not double the utilised wind energy and has resulted in about 25% decrease of diesel generator energy used.	[95]
4	Modelling	Far North Province, Cameroon	Wind, Diesel, Battery	Isolated rural households/ schools/ small villages (0.19 kWh/day – 7.08 kWh/yr)	180 W - 870 W Wind 2.5 kW - 5 kW Diesel 0 - 37.8 kWh Battery	i. Due to small wind turbine capacity, the renewable energy fraction for all cases were greater than 70% ii. However, the effect of battery systems has not been investigated as well as the unit cost of energy produced by the wind/diesel system.	[96]
5	Modelling	Madhya Pradesh, India	Wind, PV, Battery	Typical village load of 43.2 kWh/day	8 kW solar-PV 7 kW Wind 44.29 kWh Battery	i. The combination of deterministic and probabilistic approaches was used to size the system ii. Optimum configuration for 80% reliability consists of solar-PV, wind turbine and batteries	[97]
6	Modelling	3 remote sites in Bangladesh	PV, Diesel, Battery	50 kWh/day with 11 kW peak for 50 households	6 kW solar-PV 10 kW Diesel 16 kWh Battery	i. The wind-diesel-battery, wind-PV-diesel-battery, PV-diesel-battery and diesel generator only systems were investigated for rural electrification in Bangladesh ii. The solar irradiation, wind speed and load profiles were synthesised using HOMER software. iii. Diesel generator only system is not feasible due to the high diesel cost.	[98]

7	Modelling	Remote site of Abuja, Nigeria	PV, Diesel, Battery	175 kWh/day for 24 households	54.15 kW solar-PV 25 kVA Diesel 540 kWh Battery	i. Various classes of individuals residing in the considered location; they are federal civil servants, lecturers, teachers, traders and students. These people are supposedly more civilised than typical rural dwellers and hence this affects their perceptions and way of life, including the type of domestic appliances. ii. The hybrid system model was developed using DIgSILENT software; the design methodologies and analyses are based on the global engineering standards and practical experience.	[99]
8	Implemented	Kythonos Island, Greece	PV, Diesel, Battery	12 holiday houses	11 kW solar-PV 9 kVA Diesel 76.8 kWh battery	i. Intelligent load controllers were used to controlling the operation of non-critical loads (water pumps) ii. SMA grid-forming inverters (three single-phase) regulate system voltage and frequency, perform load shedding, manage diesel generator start-up and de-rate PV generation when system frequency rises. iii. Batteries were replaced after 8 years of operation. iv. Lesson learnt: PV arrays should be mounted at least 2 meters high from the ground, far from bushes and trees in order to avoid destruction.	[100]
9	Implemented	Makawanpur District, Nepal	Wind, PV, micro-hydro, Battery	173 households (approx. 4.67 kWh/day for each household)	5 kW solar-PV 3 kW Wind 20 kW Hydro Battery - not mentioned	i. A novel idea of hybridizing solar-PV, wind and hydro energy sources. The energy sources are located in two villages and linked with an 11 kV network. ii. It is important to note that the average electricity consumption at the considered villages in Nepal is far lower than in developed countries iii. The challenge of synchronizing two mini-grids is highlighted, however, the reliability of the system increased.	[101]
10	Implemented	Cangucu Research Center, Brazil	PV, Battery, Fuel-cell	65 kWh/day	19.09 kW solar-PV 5 kW Fuel cell 21.12 kWh Battery	i. The hybrid system combines four Sunny Island 4248U inverters and four Sunny Boy 6000U inverters to provide AC on demand and to control the battery charging and discharging process. ii. Different possible hybrid system configurations were studied and compared under actual operational conditions in the Legal Amazon. iii. Considering the use of 100% renewable energy sources, where the wind is not available, the PV-batteries proved to be the most favourable	[102]
11	Implemented	Isle of Eigg, Scotland	Wind, PV, hydro, Diesel, Battery	225 kW (38 households and 5 commercial properties)	54 kW solar-PV 24 kW Wind 119 kW Hydro 160 kW Diesel 211 kWh Battery	i. Diesel generation is a critical component to ensure reliable supply to consumers. ii. Seasonal output variations from each generation are coped with the mixed of renewable energy sources. iii. Demand management and participation of users helped the island in sustaining its off-grid solution.	[103], [104]

12	Implemented	Isle of Foula, Scotland	Wind, PV, hydro, Diesel, Battery	22 kW (island population of 25 residents)	19.2 kW solar-PV 30 kW Wind 15 kW Hydro 60 kW Diesel 164.88 kWh Battery	i. Because of its northerly latitude and hence long hours of daylight during the summer months, PV system is expected to be significant ii. Battery storage has been sized to supply a small overnight load, which is assumed to consist of fridges, freezers, central heating pumps and a few lights. iii. Load controllers are used to turning on water and space heaters when the batteries are fully charged and there is a surplus of energy.	[103]

Table 2.4: Comparison of modelled and implemented off-grid HRES around the world

Although in the literature many different HRES schemes are being deployed, the one used as a basis for this thesis is the hybrid wind-diesel-battery scheme as this was pre-specified by the wind turbine manufacturer (PhD project collaborator: Gaia-Wind Ltd.). One of the aims of this work is to study the feasibility and approach to adapt the existing utility grid-connected Gaia wind turbine in an off-grid system. The advantages of this scheme are:

- Simpler control strategy compared to the case where more renewable power generators are integrated. Fewer variables to be considered whilst performing optimal operation
- With the existence of battery storage, and if it is properly sized, wind energy can be utilised as much as possible
- With the existence of battery storage, diesel generator can be used sparingly and avoid the frequent turning on and off because such switching pattern can lead to fatigue stress on the mechanical parts

However, the disadvantages are:

- Rely heavily on single RES, i.e. wind energy. If wind energy is unavailable for an extended period of time and the batteries are fully discharged, diesel generator will need to be turned on to fully supply the system
- Wind velocity fluctuates continuously both in a daily cycle and seasonally. Hence, the sized energy storage and diesel generator are sometimes not being used optimally
- Complementary RES to wind energy, for instance solar PV, which is available in most parts of the world is not utilised

2.5.2 A Review on Hybrid Wind-Diesel-Battery System Components

In this section, the main components of the considered hybrid system, i.e. wind turbines, off-grid grid-forming inverters, batteries and diesel generators from different manufacturers are surveyed. A few models of each component were selected for comparison purposes. The component specifications and cost are briefly discussed. With this, the components with different technologies which are available in the market are identified, further justifying their choices for this project.

a) Wind Turbines

The following discussion is not for the justification on wind turbine selection for this project as the project collaborator's (Gaia Wind Ltd.) fixed-speed wind turbine has to be used as case studies, modelling, simulation and experimental work in this research. However, it is worth acknowledging the existence and technologies of other small wind turbines (similar power ratings) offered from the market. Six wind turbine manufacturers and their corresponding model, cost, specifications are tabulated in Table 2.5. The selected small wind turbines are rated around Gaia's wind turbine (11 kW), except for the case of Britwind and Kingspan wind turbines. They are useful to provide a cost per kW comparison relative to other higher power rating wind turbines.

From Table 2.5, it is noticed that several manufacturers offer their wind turbines to be connected to single-phase systems. These include Britwind, Kingspan and FuturEnergy. The cost per kW is generally lower for larger power rating wind turbines, as can be explained by the economics of scale. The large cost range for the Bergey wind turbine is attributed to the tower type and height selection offered by the manufacturer. All the considered wind turbines are 3-bladed except Gaia wind turbine. It is also observed that the blade area of the Gaia wind turbine is at least twice larger than other manufacturers. This is an advantage as the larger area may result in more wind energy being captured.

Since the Gaia wind turbine utilises an induction generator for power generation, it requires a gearbox as the wind turbine rotor rotates at a much lower speed (nominally at 56 rpm) compared to its generator (synchronous speed at 1000 rpm) [105]. The other wind turbine manufacturers adopt direct-drive PMSGs, which allow variable speed operation and hence maximum power point tracking is achievable. On the other hand, a fixed-speed wind turbine only captures optimal power at one wind speed. The cut-in wind speed for all the considered wind turbines ranged between 2.5 m/s and 3.5 m/s. Gaia-Wind 133 has a cut-out wind speed of 25 m/s and the others operate continuously.

Manufacturer	Model	Estimated cost (incl. VAT)	Phase	Power Rating	£ / kW	Number of blades	Blade Area	Gearbox	Generator	Cut-In Wind Speed	Cut-Out Wind Speed	Source
Britwind (formerly Evance)	R9000	£31,500	Single / Three	5 kW	6,300.00	3 (upwind)	approximately 24 m^2	None	PMSG	3 m/s	None - continuous generation to survival wind speed (60 m/s)	[106], [107]
Kingspan	KW6	£31,600	Single / Dual / Three	6.1 kW	5,180.30	3 (downwind)	approximately 25 m^2	None	PMSG	3.5 m/s	None - continuous generation	[108], [109]
FuturEnergy	AirForce 10	£47,250	Single / Three	13 kW	3,634.62	3 (upwind)	approximately 51 m^2	None	PMSG	about 3 m/s	None - continuous generation	[110], [111]
Fortis	Alizé	£42,040	Three	10 kW	4,204.00	3 (upwind)	31.42 m^2 / 34.2 m^2 / 37.4 m^2	None	PMSG	3 m/s	None - continuous generation	[112], [113]
Bergey Windpower	Bergey Excel 10	£34,416 - £49,660	Three	12.6 kW	2,731-3,941	3 (upwind)	approximately 39 m^2	None	PMSG	2.5 m/s	None - continuous generation	[114], [115]
Gaia-Wind	Gaia-Wind 133	£46,000	Three	11 kW	4,181.82	2 (downwind)	133 m^2	Two stage, gear ratio 18:1	Induction Generator	3.5 m/s	25 m/s	[105], [116]

Table 2.5: Selected small wind turbines specifications and costs comparison

b) Bidirectional Inverters

For an AC-connected hybrid system, the grid is established by one of the generating sources. This needs to be a reliable source with high availability. Typically, the diesel generator or the battery grid-formed inverter is used to perform this role. Here, it is desired to minimise diesel use; hence, the inverter will be used to form the grid. This inverter has a major role as it must be able to control all the power flows in the system.

As it is the interest of Gaia-Wind Ltd. to utilise an off-the-shelf grid-forming inverter system in the proposed hybrid system, few commercially available units are compared and contrasted. The criteria for selecting the appropriate inverter system is its modularity, user friendliness and functionally stable while operating in conjunction with a Gaia wind turbine. In order to ensure the three-phase, 11 kW induction generator (which is used in the Gaia wind turbine) to start-up properly, a three-phase grid, rather than a single-phase grid is required and its power rating should be sufficiently higher than the generator. Therefore, the five selected inverter manufacturers for comparison purposes are rated (total power rating for 3-phase system) between 18 kW and 21 kW, as shown in Table 2.6. They are a single-phase unit, specifically designed for off-grid applications. Therefore, a three-phase grid would require 3 units.

Manufacturer	Model	Estimated cost (incl VAT)	Phase	Power Rating	Estimated cost for 3-phase system (incl VAT)	£ / kW	Supported batteries	Battery voltage	Source
OutBack	Radian 7000 VA	£5,496	Single	7 kW	£16,488	786	Lithium ion, Aqueous ion, Flow chemistry	48 V	[117]
SMA	SI 8.0H	£3,602	Single	6 kW	£10,806	600	Flooded, VRLA, Lithium-ion	48 V	[118]
Studer	Xtender XTH 6000	£5,266	Single	6 kW	£15,798	878	VRLA, Gel	48 V	[119]
Schneider	Conext XW+ 6848	£3,710	Single	6.8 kW	£11,130	546	Flooded, Gel, AGM, Lithium-ion	48 V	[120]
Victron	Quattro 8000 VA	£2,936	Single	7 kW	£8,808	420	Gel. AGM	48 V	[121]

Table 2.6: Selected off-grid inverter specifications and costs comparison

The cost per kW varies considerably although their power ratings are similar. This can be attributed to the battery charger technology, types of batteries supported by the inverter and the brand of the product. Studer (Swiss made) off-grid inverter has the highest cost compared to other products, although the supported batteries are commonly supported by other off-grid inverter manufacturers. It is noticed that the OutBack inverter supports more advanced batteries, which includes lithium-ion, aqueous ion and flow batteries. A 48 V DC voltage is required to be connected at the DC side of the inverters.

Besides being modular, easy to use and capable of supporting the Gaia wind turbine, another important consideration from the research perspective is the availability of disseminated literature, on both modelling and implemented systems. Furthermore, the chosen system should also offer sufficient flexibility on programming and system monitoring. After reviewing the options from Table 2.6 and several discussions with Gaia-Wind Ltd., it is agreeable that the Sunny Island (SI) 8.0H grid-forming inverter, from SMA is the preferred option, despite its higher cost per kW than Schneider's and Victron's. The choice is also supported with the literature availability on modelling of the Sunny Island devices [54] [122] [123] [124] and the case studies on implemented projects [102] [100] [103] [104], which were performed by other researchers in collaboration with SMA.

In general, the modular design of the SMA off-grid inverters results in the possibility to extending the power capability of the system up to 300 kW using the SMA Multicluster boxes. Maintenance can be performed on a cluster basis and the availability of the entire system is enhanced with the modular structure. However, it is not as compact as a dedicated three-phase inverter of similar rating. The operation of the diesel generator can be automatically triggered or the utility grid being automatically connected (for the on-grid system) during the unavailability of RESs and when the battery SOC is low. As the synchronisation module is already embedded in the SI inverter, the need to purchase additional synchronisation equipment is unnecessary. Following synchronisation, the SI system is seen as an extra load on the system as it charges the battery banks. Hence, the diesel generator

operates at maximum output for as long as possible, minimising diesel generator run-time and optimising efficiency.

Another advantage of the SI system is that it can be configured as a mixed AC/DC system. The DC-based generators (for instance PV) and DC loads can be connected to the battery terminals via DC/DC converters, if required. A sample electrical wiring diagram of the SI system, coupling with other power generators and loads is shown in Figure 2.11 [125]. A remote control and data logging system can be integrated in the SI system, which provides the flexibility for users to configure settings such as nominal voltage and frequency of the system operating in off-grid scenario, type of batteries used and their corresponding protection limits, timings for turning on/off external sources (diesel generator/utility grid supply), limiting the amount of power drawn from external sources and controlling the load shedding contactors. The web-based control and monitoring option is a crucial feature for some remote areas where accessibility is proven to be a challenge.

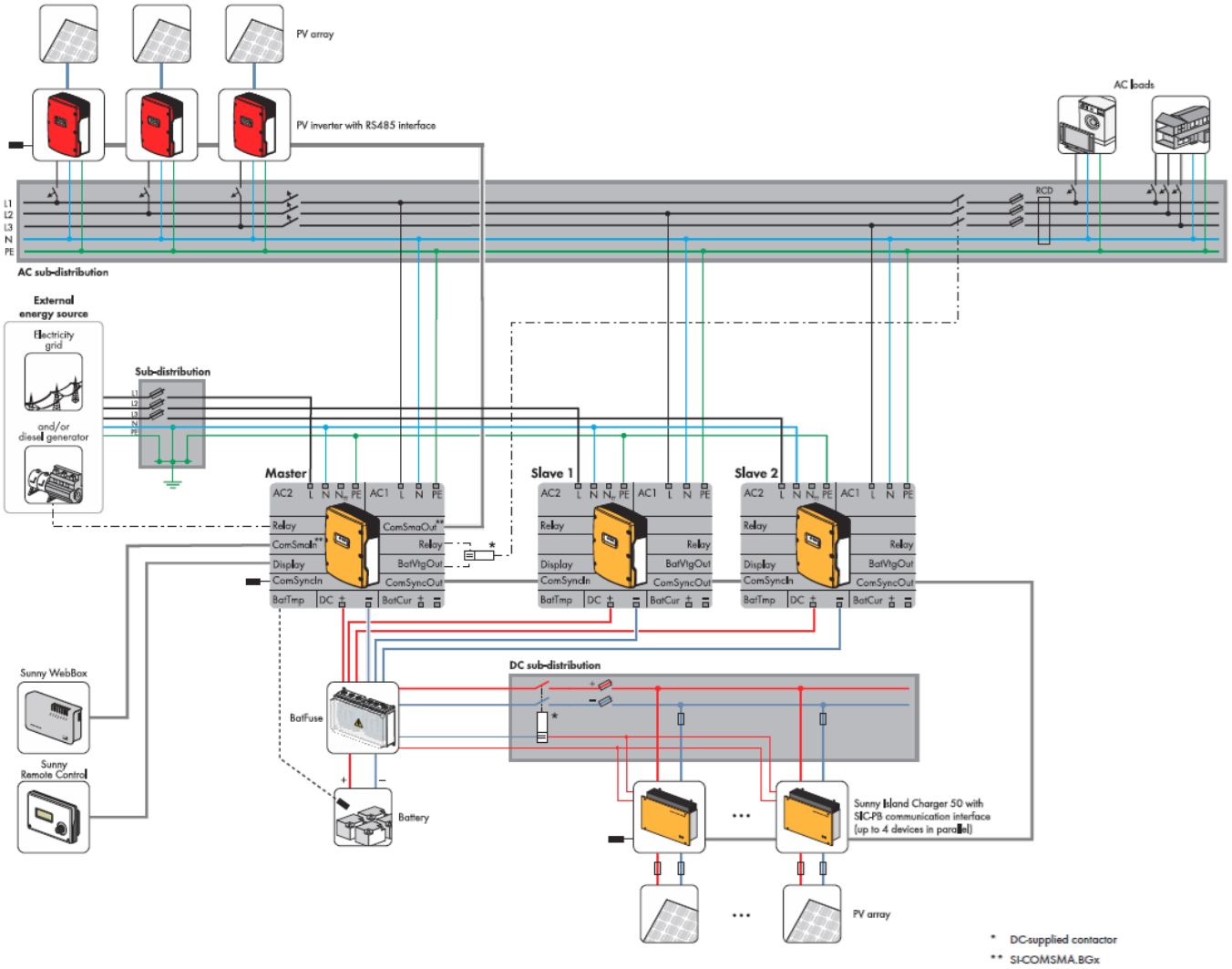

Figure 2.11: A sample of electrical wiring diagram of an off-grid system using SI inverters [125]

c) Diesel Generator

In this project, a diesel generator is used as a backup when the battery SOC is low and the electricity generation from renewables is insufficient to supply the load demand. At present, fixed-speed generators still vastly outnumber variable-speed generators and they are commonly used in off-grid applications. The 3-phase diesel generators with the power capacity up to 20 kW are considered in this work. In addition, a price comparison on different manufactures on similar product range is performed. Table 2.7 shows the diesel generator cost comparison offered by Harrington Generators International (HGI), Hyundai, Pramac and SDMO. The prices are influenced by the specifications such as noise level and fuel capacity. For residential application, the low noise level is of great importance, especially during the night. It is noticeable that SDMO unit offers the quietest and longest run time compared to other manufacturers.

Manufacturer	Model	Price (incl VAT)	Continuous kW	£ / kW	Run Time (hours)	Noise Level	Fuel Capacity
HGI	SKD100T3	£4,999.99	8 kW	£625.00	10	70 dba @ 7m	22 L
Hyundai	DHY11KSE	£4,670.00	8 kW	£583.75	12	65 dba @ 7m	42 L
Pramac	P9000	£4,065.00	7.2 kW	£564.58	12	72 dba @ 7m	24 L
SDMO	XP-T12K	£6,399.99	8.4 kW	£761.90	20	58 dba @ 7m	50 L

Table 2.7: Diesel generator costs comparison on selected manufacturers [126]

In order to study the economics of the diesel generator, Table 2.8 compares the cost for different power ratings. All the diesel generators possess similar noise levels, between 65 dba and 68 dba at 7m away. The cost per kW demonstrates a more meaningful insight and from Table 2.8, a decreasing trend is observed as the power rating increases. However, it is known that the capital cost of a diesel generator is not significant compared to its lifetime fuel consumption.

Manufacturer	Model	Price (incl. VAT)	Continuous kW	£ / kW	Run Time (hours)	Noise Level	Fuel Capacity
Pramac	P6000	£3,189.99	4.45 kW	£716.85	17	67 dba @ 7m	24 L
Hyundai	DHY11KSE	£4,670.00	8 kW	£583.75	12	65 dba @ 7m	42 L
Hyundai	DHY14KSE	£5,574.00	10 kW	£557.40	18	67 dba @ 7m	77 L
Hyundai	DHY22KSE	£6,129.00	16 kW	£383.06	13	68 dba @ 7m	77 L
Hyundai	DHY28KSE	£7,351.00	20 kW	£367.55	12	68 dba @ 7m	93 L

Table 2.8: Diesel generator cost comparison at different power ratings [126]

A typical small diesel generator (rated at 5 kW) efficiency curve is shown in Figure 2.12 [102]. If a diesel generator is sized much larger than the average load demand, the probability of it operating at part load efficiency is higher. Long term operation at this efficiency region may deteriorate the lifetime of a diesel generator and the diesel fuel usage will be inefficient. As a result, a possible solution to mitigate this drawback is to employ dual diesel generator system [127]. The smaller generator is used during light load condition. As the load demand increases, the other larger generator takes over the electricity supply system.

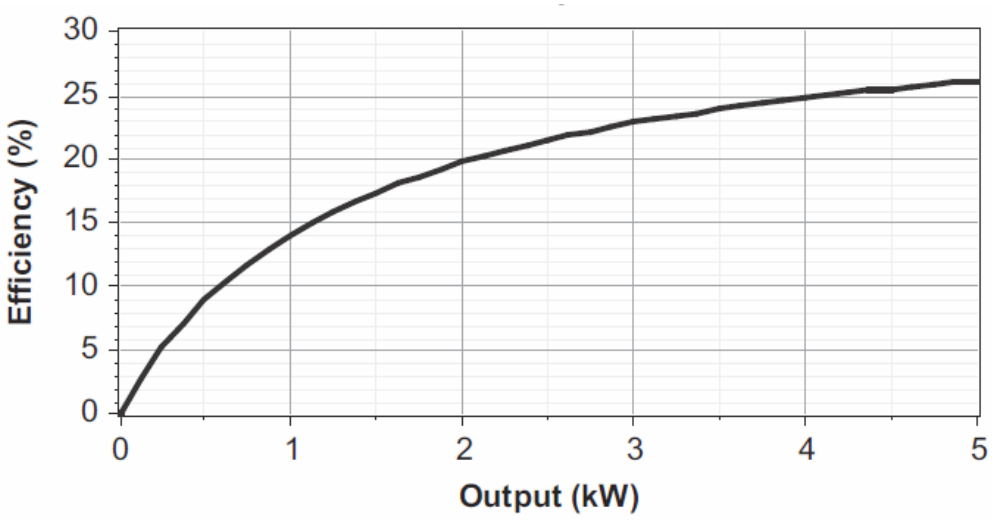

Figure 2.12: A 5 kW diesel generator efficiency curve [102]

d) Battery

As discussed in the background section, there are many types of batteries available in the market for the use of ESSs. However, since the SMA Sunny Island inverter system is agreed to be utilised, the supported batteries are limited to lead-acid and lithium-ion. Moreover, as an initial phase of the project, Gaia-Wind was more interested in cost saving and demonstrating the workability of the proposed hybrid system, rather than choosing the optimum energy storage technology. Therefore, lead-acid batteries were the preferred option. However, for the sake of completeness, lead-acid and lithium-ion batteries from the selected manufacturers were compared, as shown in Table 2.9. The cost and technological comparison for all types of batteries are beyond the scope of this work. A more comprehensive cost review for different kinds of energy storages can be found in the literature [14].

Manufacturer	Model	Battery Type	Nominal Voltage	Price (incl VAT)	Capacity at C20 (kWh)	£ / kWh	Lifetime	Key features
Rolls	4000 Series (RB-T12136)	Lead-acid	12 V	£277.00	1.632	£169.73	1280 cycles to 50% DoD	Flooded deep cycle
Rolls	OpzV Gel (RB-S2-855GEL)	Lead-acid	2 V	£426.00	1.71	£249.12	3200 cycles to 50% DoD	High impact resistance casing, maintenance free
Rolls	AGM Series 5 (RB-S12-160AGM)	Lead-acid	12 V	£388.00	1.74	£222.99	1250 cycles to 50% DoD	Deep cycling, maintenance free
Trojan	Premium Line (TB-T105RE)	Lead-acid	6V	£213.00	1.35	£157.78	1700 cycles to 50% DoD	Flooded deep cycle
Victron	Victron Lithium Battery (VLB-12/90BMS)	Lithium-ion	12.8 V	£1,022.00	1.152	£887.15	5000 cycles to 50% DoD	Integrated cell balancing, temperature and voltage control
LG Chem	RESU 3.3 (LG-RESU3-3)	Lithium-ion	48 V	£2,699.00	3.3	£817.88	6000 cycles to 90% DoD	Built-in DC circuit breaker

Table 2.9: Lead-acid and lithium-ion batteries cost comparison [128] [129] [130]

The Rolls OpzV Gel battery has more cycles than the 4000 series and AGM series. However, it has a low nominal voltage of 2 V. This means that in order to meet the 48 V requirement of the Sunny Island inverter, at least 24 batteries connected in series are required, which is very costly for the initial stage. From the energy capital cost (£/kWh) column of Table 2.9, it is observed that the lithium-ion batteries are significantly more expensive than the lead-acid. However, the number of cycles is noticeably higher for lithium-ion batteries. Besides that, their higher prices may also be attributed to the additional battery management systems and DC circuit breaker being integrated into the battery systems. For the purpose of project demonstration and to keep the initial cost low, the Rolls 4000 Series (RB-T12136) batteries are adopted in this work. In particular, the four units are connected in series to form a DC link of 48 V to meet the SI 8.0H DC input specification.

After selecting the battery system to be adopted in the hybrid system research, another aspect is to choose an appropriate battery degradation model. It is expected that the lifetime of a battery is an important parameter whilst analysing the overall performance of an off-grid system. Therefore, it is useful to identify and understand the fundamentals of different battery degradation models available in the literature, although it is not the intention of this work to go in depth in each of them.

The battery ageing phenomena are hard to quantify accurately due to the diversity and complexity of the processes taking place in all conditions during its lifetime. The clear degradation indicators are the capacity fade, resistance augmentation and loss of available peak power [131], which can influence the battery utilisation characteristics. The ageing process can be divided into two types, i.e., calendar and cycle ageing [132]. Calendar ageing is recurrently influenced by temperature, storage SOC and time. On the other hand, change in SOC, cycle number, charge/discharge voltage and factors which are coming from utilisation mode have an impact on cycle ageing. The variables interact with one another and the relationship can become highly complexed [133], making the ageing phenomena a difficult task to comprehend and quantify. Various methodologies from different fields such as electrochemical models, performance models and statistical models [134] have been proposed to deal with battery lifetime estimation [135]. It is important to note that there is no single objective method of characterising the different approaches to battery ageing – the one outlined here was proposed by [135], but since different approaches may share certain characteristics but not others, other means of categorising these approaches are possible.

Table 2.10 summarises the battery ageing estimation methods and their respective performance aspects [135]. Direct measurement is straightforward as it does not require a battery model in its implementation. It is suitable to be performed on all types of batteries. However, the measurement duration is too high for real-time implementation and therefore, it is not an ideal approach to estimate the ageing evolution. Electrochemical and the equivalent circuit models are powerful tools to understand the different interactions between the different physical phenomena and ageing as a result of various operating conditions. However, they cannot be directly adapted by other batteries due to the difference in battery technology, design and materials. Moreover, the equivalent circuit based models require a large and diverse data set to estimate the electrical network parameters accurately.

Performance-based models simply provide a fixed relationship between stress factors and the remaining useful life of a battery, without involving a detailed understanding of the processes that contribute to the degradation. As a result, each contributing

stress factor has to be investigated independently which results in significant experiment effort. The accelerated testing procedure from some battery manufacturers further leads to significant errors in predicting the battery lifetime because this is not necessarily representative of actual usage [136]. Similar to the electrochemical and equivalent circuit-based models, the performance-based model cannot be directly adopted by other battery technologies.

An analytical model with empirical data is formulated based a large set of data from experiments. The model parameters are evaluated based on a large number of data sets and the accuracy of measurement plays a major role in the model precision. Lastly, statistical methods do not utilise the knowledge of battery chemistry and their degradation mechanisms. Hence, it is easily adjustable to different batteries and able to give an ageing diagnosis in real time. As implied by its name, statistics requires an extensive data set to be effective. In addition, it only works for one battery as each ageing will be different due to the dependence on battery usage pattern.

Types of battery degradation model	Modelling remarks	Adaptation	Precision	Operate without data	Real time	Prediction
Direct measurement	• Do not need battery hypothesis as it is a direct estimation • Performs for all kinds of battery usage	Excellent	Excellent	Excellent	Very poor	Very poor
Electrochemical models	• Degradation mechanisms can be related to material properties • Cell performance can be represented by physical equations by fitting parameters using the macroscopic observations	Very poor	Excellent	Fair	Fair	Fair
Equivalent circuit-based models	• Identification of internal battery parameters (resistance and capacitance) is required	Very poor	Fair	Good	Good	Fair
Performances-based models	• Uses simple correlations between stress factors and capacity fade/impedance rise • Most studies consider calendar and cycle ageing separately • Calendar ageing - main variables are time, temperature and SOC • Cycle ageing - involves more complex independent variables such as temperature, cycle number, DoD, current and voltage (which further relate to battery utilisation). Consider ageing a damage-accumulation model (fatigue approach)	Very poor	Good	Poor	Fair	Good
Analytical model with empirical data fitting	• Based on large experimental data sets to evaluate or predict ageing estimator values • Model parameters and direct ageing estimator can be determined empirically	Very poor	Good	Poor	Poor	Poor
Statistical methods	• Do not need any prior knowledge on the ageing mechanisms and no hypothesis made on the factors • Do not use any chemical or physical formulation	Fair	Good	Very poor	Good	Good

Table 2.10: Battery ageing estimation methods and performances comparison for five principle approaches [135]

2.5.3 Review of Energy Management Systems for Standalone Applications

Whenever more than one energy sources exist within a hybrid renewable energy system, an energy management system (EMS) is required to guide the power flow within the system effectively. Ideally, an EMS aims to maximise the utilisation of renewable energy, reduce the stress level experienced by the ESSs, minimise the COE and maintain the stability and reliability of the system by supplying the load in all conditions. In general, an EMS can be implemented with conventional rule-based strategy or intelligent-based strategy with optimization algorithms. However, it is worth noting that an EMS which works well for certain HRESs may not be optimised for other configurations. In addition, it is acknowledged that there are many possibilities for an EMS to manage the power flow within a system, depending on the objectives and criteria defined by users. This section reviewed some of the EMS approaches which have been proposed for different hybrid system configurations.

Case number	Modelling / Implemented	System topology	EMS approach	Remarks	Source
1	Modelling	PV-wind-diesel-battery	MPC	• The renewable energy is maximised while minimising the operation cost and battery's charge-discharge cycles. • However, the diesel generator was scheduled to operate at part load condition within the considered timeframe.	[137]
2	Modelling	Wind-diesel-battery	MPC	• The solar energy is maximised, with the aim of reducing the diesel generator use. Nevertheless, frequent diesel generator power output variations were observed from the simulated results.	[138]
3	Modelling	Wind-diesel-battery	Predictive strategy	• An idealised predictive strategy, based on perfect wind and load forecasts are developed. • The EMS is benchmarked against other non-predictive dispatch strategies (load following, frugal dispatch, SOC set-point and full power/minimum run time), using life-cycle cost as the indicator.	[139]
4	Modelling	Wind-diesel-battery	Stochastic dynamic multi-stage model	• The diesel generator dispatch was optimised and was compared against the load following and full-power strategies. • In order to reduce the computational burden while seeking the optimal solution of the complex model, hourly time steps were considered. Hence, the short-term peaks in the load demand were not considered.	[140]
5	Modelling	PV-wind-diesel-battery	Receding horizon optimisation	• An optimised hybrid system which integrates demand response schemes and day-ahead forecasting of renewable energy resources and load demand were studied. • However, it is noticed that the diesel generator was frequently changing its output power throughout the day. The optimisation strategy was carried out over a moving time-horizon in order to determine the optimal power references for various energy generation sub-systems.	[141]
6	Modelling	PV-wind-battery-fuel-cell	Constrained rule-based strategy	• PV and wind are the main supply and the fuel-cell serves as the back-up source. • The power management strategy was designed to maximise the battery efficiency by operating fuel-cell to store excess energy, whilst operating within the specified battery SOC limits.	[142]
7	Implemented	PV-wind-battery-fuel-cell	Constrained rule-based with hysteresis band	• The battery SOC is the parameter that determines the operation of the electrolyser and the fuel-cell. • The integration of hysteresis band provides larger operation flexibility and protecting the fuel-cell and electrolyser from frequent start-stops.	[143]

8	Modelling	PV-battery-fuel-cell-supercapacitor	Constrained rule-based central power flow controller and local load power management	• The main aim of the EMS is to reduce the stress on the generators whilst satisfying load demand with the access to controllable load. • The central controller acquires data through sensors and produces reference power for converters which are interfacing the generators and the grid. • The local load management algorithm controls the load shedding operation based on the energy balance situation in the system	[144]
9	Modelling	PV-wind-battery-fuel-cell-bioethanol	State-machine based decision making	• The dispatch strategy is defined based on load requirements, battery SOC, and the availability of renewable energy sources • The wind turbine is the primary generator whilst the PV system is the secondary source of energy due to the high availability of wind resource for the considered location.	[145]
10	Modelling and Implemented	PV-wind-battery	Constrained rule-based strategy	• The EMS consists of a fast loop control for energy conversion and an external supervisor controller for energy management strategy. • The supervisor controller is responsible for managing the mode of operation which is determined by the energy balance between the total generation and the total demand, whilst maintaining the DC bus voltage and battery SOC within the limits.	[146]
11	Modelling and Implemented	PV-wind-diesel-battery-supercapacitor	Constrained rule-based strategy	• The proposed EMS control the power flow within the system according to the frequency of the power generation (from wind or PV). • High-frequency power flow is met by the supercapacitors to minimise power fluctuations to the battery, with the aim of improving lifetime. Polynomial control method was adopted for microcontroller implementation.	[147]
12	Modelling	PV-wind-micro hydro-diesel-battery	Multi-agent system with game theory	• The distributed EMS fulfill the load demand by making decisions based on the availability of renewable resources, system parameter variations and maximising system efficiency • The authors benchmarked the proposed EMS against a typical centralised topology under different circumstances. The authors concluded that the distributed EMS performs better in terms of power generators efficiency within the considered system.	[148]
13	Modelling	PV-wind-diesel-battery	Mixed integer linear programming	• The EMS utilises two-day ahead forecast of RESs and predictions of electrical load and water consumption to compute an optimised power dispatch solution based on rolling horizon strategy (15 minutes sampling time). • The EMS delivers power generation set points for each generation unit, water pump to keep the elevated water tank level within pre-defined limits and send signals to consumers for demand side management (DSM). Historical data from a remote location in Chile was selected for simulation purposes.	[149]

2.6 Summary

As a concluding remark, this chapter has given the basic background on the underlying principles of off-grid HRESs and their associated design challenges. The overview on HRES architecture (AC, DC and mixed AC/DC) and battery technology were also presented. It is then followed by the review of existing literature on HRES topologies, the cost of components (wind turbines, bidirectional inverters, diesel generators, batteries), battery degradation models and energy management systems for HRESs.

In order to design an optimum hybrid system, it is common to begin with the system sizing. Therefore, the next chapter discusses the proposed sizing work and the analyses involved aim to provide a better understanding of the subject.

Chapter 3 Sizing of Hybrid Renewable Energy Systems

Traditionally, the HRES sizing approach is attributed to the rule-of-thumb methods that are based on expertise's knowledge and experiences in the field [150]. Clearly, this is not an ideal approach as the lack of optimum sizing or oversizing of components within a hybrid renewable energy system can often lead to high installation costs [151]. The technical and economic analyses of a hybrid system in accordance with the local load demand and availability of local RESs are essential for feasibility justification before a particular project is being implemented. Due to the complexity of multiple generations and the variability nature of RESs and load demand, seeking an optimum system becomes more challenging as many variables or factors need to be considered. Fortunately, various sizing tools have been developed over the years with the aim of easing the process of sizing off-grid renewable energy systems. A comprehensive review of the hybrid renewable energy systems sizing tools is reported by authors in [152]. It is worth to summarise the popularly used sizing tools by highlighting their key features, advantages and disadvantages. However, not all of the sizing tools are still being used and their availabilities are unknown, hence they are excluded here. These include the HYBRIDS, Remote Area Power SIMulator (RAPSIM), Simulation and Optimization Model for Renewable Energy Systems (SOMES), SOLSTOR, HySim, Integrated Power System (IPSYS), Hybrid Power System Balance Analyser (HySys), Dymola/Modelica, Autonomous Renewable Energy Systems (ARES) and SOLSIM. Detailed description on these sizing tools can be obtained from literature [152]. In this work, the discussed ones are Hybrid Optimization Model for Multiple Energy Resources (HOMER), HYBRID 2, RETScreen, Improved Hybrid Optimization by Genetic Algorithm (iHOGA), Integrated Simulation Environment Language (INSEL), Transient Energy System Simulation Program (TRNSYS), improved Grid-connected Renewable HYbrid Systems Optimization (iGRHYSO) and HybSim, as summarised in Table 3.1.

The sizing tools which are capable of performing both technical and economic analysis are HOMER, HYBRID 2 and iGRHYSO. Thermal energy systems can be analysed through HYBRID 2, INSEL and TRNSYS. One of the main advantages of RETScreen and iGRHYSO is the connection of meteorological database from National Aeronautics and Space Administration (NASA). It is important to highlight that INSEL and TRNSYS are programming languages and they do not generate the optimal configuration of HRESs with user's input data. Besides RETScreen, all the other sizing tools listed in Table 3.1 are priced at full versions. Nevertheless, demo versions with limited features or time usage are available. HOMER was found to be the most widely hybrid sizing tool in the literature. It has been used by researchers around the world to analyse hybrid systems at different scale levels [152]. HOMER is known to be user-friendly and easy to understand with its intuitive GUI. In addition, it provides efficient graphical approaches for analysing simulated results. Nonetheless, the code and underlying principles in computing the optimal configuration are not transparent to users. Although this reduces the complications one has to encounter, it hinders more advanced users to alter the programme to meet specific requirements. Furthermore, the hidden details do not allow one to learn the tactics to model hybrid system components and developing code for computing the optimal hybrid system configurations.

Software	Remarks	Advantages	Disadvantages
HOMER	• Developed by NREL • Capable of performing pre-feasibility studies, optimization and sensitivity analysis in several possible system configurations, for both on-grid and off-grid systems. • Able to perform one-year simulation, with hourly sampling rate. • Feasible configurations are sorted by net present cost (NPC).	• User-friendly GUI shortens the learning curve for new users. • Display simulation results in a wide variety of tables and graphs which assist users in comparing and evaluating each configuration based on economic and technical merits. • The software keeps updating and being supported.	• "Black box" code used. • Only allow single objective function for minimising NPC, hence incapable of solving multi-objective problems • Does not rank the hybrid system based on levelised COE • Does not consider any degradation in batteries, regardless of its usage. For example, higher DoD may decrease the battery lifetime more than low and infrequent DoD. • Does not consider intra-hour variability • Requires paid license for professional version and the license pricing increases with additional libraries
HYBRID 2	• Developed by Renewable Energy Research Laboratory (RERL) of the University of Massachusetts, USA with support from NREL • Adopts probabilistic/time series approach to perform detailed long-term performance and economic analysis on a wide variety of hybrid power systems.	• A variety of different control strategies which includes the interactions between diesel generator dispatch and batteries. • Statistical methods to account for inter time step variations in the wind and load in order to improve the accuracy of prediction for diesel generator dispatch.	• May not work with Windows platforms later than Windows XP • Software is not updated and not supported from developer • Limited access to parameters and lack of flexibility
RETScreen	• Developed by Ministry of Natural Resources, Canada for evaluating both financial and environmental costs and benefits of different renewable energy technologies for any location in the world. • RETScreen 4 - Microsoft excel-based technical and financial analysis tool on hybrid renewable energy system projects • RETScreen Plus - a Window-based software tool to evaluate energy management performances.	• It has a global climate database of more than 6000 ground stations • Accessible in more than 30 languages • It is linked to NASA climate database	• Does not take into consideration of ambient temperature while evaluating PV performance. • Unable to import user's time series data for simulation • Limited visualisation features • Data sharing problems • Does not support more advanced calculations
iHOGA	• Developed by the University of Zaragoza, Spain. • Multi or single objective optimisation can be performed using genetic algorithm (GA) • Can be used to analyse on-grid and off-grid system	• It was claimed to be low in computation time • Allows probability analysis	• Professional version is priced and only limited features is provided for education version • Requires internet connection to run professional version

INSEL	• Developed by University of Oldenburg • Uses general purpose graphical programming language to simulate renewable energy systems • Capable of creating models and configurations of electrical and thermal energy systems	• The software is fully compatible with Matlab/Simulink • Has a meteorological database of 2000 locations worldwide • Database of various hybrid system components from different manufacturers is available.	• Free trial version is only limited to 30 days, payment is required for full license • Familiarity with new programming language is required • Does not provide optimal configuration of the studied hybrid system
TRNSYS	• Jointly developed by the University of Wisconsin and University of Colorado • TRNSYS is made up of two parts; kernel and library of components • Kernel reads and processes input file, iteratively solves the system, determines convergence and plots system variables • The standard library includes approx. 150 models ranging from pumps to multizone buildings, wind turbines and electrolyzers, weather data, economics routines and basic HVAC equipment.	• Long track of history with 35 years of being commercialized • Capable of simulating transient behaviour with vast variety of available components in the library • Can assess the performance of thermal and electrical energy system simultaneously	• Demo version has limited capability and full version is priced • Does not provide optimal configuration of the studied hybrid system
iGRHYSO	• Developed by University of Zaragoza • It is developed for the optimisation of grid-connected renewable energy system and considers different types of network sales of the electricity market	• Adopted rainflow calculations on battery lifetime • Connected to NASA database to obtain weather data • Takes into consideration of ambient temperature while calculating the power outputs from PV and wind turbines	• Only available in the Spanish language • Software is priced and trial version is not available • Not ideal for the analysis of off-grid power systems
HybSim	• Developed by Sandia National Laboratories • HybSim is a tool to design and evaluate the economic and environmental benefits of integrating renewable energy generators to fossil fuel-based generation in off-grid scenarios. • Software GUI is developed using Microsoft Excel	• Development platform is Microsoft Excel which is available for most users	• Discrepancies between simulation and measurement results is expected as the software is not intended to emulate the exact response of the components

Table 3.1: Analysis of hybrid renewable energy system sizing tools

Besides the HRES sizing tools described above, several other researchers who have undertaken the research on this topic are noticed. Earlier work simply shows the generation capacity is determined to best match the power demand by minimising the difference between total power generation and load demand over a period of 24 hours [153]. The author iteratively optimised the components by using hourly average data of wind speed and solar irradiation in meeting a specific load demand. In [154], the authors further utilised linear programming technique to optimise the sizing of the hybrid system components (battery capacity and diesel fuel usage) within the 24 hour period. Kaldellis pointed out that focusing on the installation cost is insufficient for a hybrid system sizing methodology which is based on simplified cost analysis [22]. Operation and maintenance (O&M) costs take up a large proportion of the overall cost of the system over its lifetime. Thus, Kaldellis has developed a method to calculate the long-term energy production cost for a wind-diesel hybrid system by taking into consideration fixed and variable costs of maintenance, operation and financing, and initial costs. Several differences between the above-mentioned literature are acknowledged. In particular, the work in [153] and [22] were using load-following strategy to calculate the optimum hybrid system while the authors in [154] sought optimum configuration based on electricity cost minimisation by maximising the utilisation of renewables. In addition, literature [22] considers short and long term cost while the other two literature studies their system based on a day's operation. Nevertheless, a fixed battery and diesel generator replacement period are adopted in the literature [22], which does not necessarily present the most realistic situation. Recognising the fact that the battery replacement cost is high over the lifecycle of a hybrid system, a battery degradation model is used in this work to evaluate the battery lifetime at different battery capacities. Finally, the topology considered in this work is slightly distinct from the literature whereby grid-forming inverters are used and they may have a different cost function compared to the uninterruptible power supply (UPS) [22].

Alternatively, the authors in [35] have developed an algorithm to optimally size a standalone hybrid wind-diesel system by considering the total system reactive power balance condition. In another mean of selecting the optimal combination of a hybrid renewable energy system to meet the demand, evaluation was conducted on the basis

of reliability of the system by considering the loss of load probability (LOLP) [155]. The LOLP sensitivity analysis on total installation cost has been demonstrated in [156] for the considered hybrid system. In a different perspective, the authors in [157] described an optimal energy storage sizing method by considering the compensation cost of wind power and load curtailment.

In hybrid electric vehicle (HEV) research, battery sizing has also been given attention. Similar to off-grid HRES, a hybrid propulsion system is powered by fossil fuel-based internal combustion engine (ICE) and/or battery storage. However, the HEV battery sizing is influenced by several other factors, such as the user driving pattern, power management strategy, the charging/discharging profile (if it is a plug-in hybrid electric vehicle (PHEV)), weight of the batteries, availability of charging infrastructure etc. An integrated optimisation framework on battery sizing, charging and power management for PHEV has been proposed by the authors in [158]. The framework assessed the interactions between the three control variables, while minimising the CO_2 emissions. In another study, the relationship of sizing the batteries along with power-split strategies between ICE and the electric drive was investigated [159]. From the simulation study, the rules for proper power splitting were extracted based on the acceleration rate and the driving speed. An analysis has been conducted on choosing the battery size of the EVs and PHEVs which was based on statistical data of a fleet of vehicles with realistic driving patterns [160].

In this work, a tool specifically for sizing off-grid HRESs has been developed. The main feature of this tool is to assist project managers to visualise and evaluate the trade-offs between batteries and diesel generator usage, given a site specific resource availability and load demand. As far as the author is aware, other hybrid system sizing tools do not have the capability of demonstrating their results with the proposed approach. The process of seeking the optimum configuration is demonstrated graphically which allows the hybrid system developer to understand the sizing methodology and trade-offs in a system. A similar graphical approach has been adopted in [22] and [161] as part of their result's analysis, however it has not been used for analysing the trade-offs between batteries and diesel generator usage. In this research, the methodology of sizing the hybrid system which considers

financial viability and technical performances are outlined. The hybrid system components and life-cycle cost modelling utilised in this work are first explained. In particular, the wind turbine is represented mathematically with their coefficients obtained empirically from the measured wind speed and its respective output power data. Then, the optimum configuration of a hybrid system is obtained based on minimum life-cycle cost. It is then followed by the load sensitivity towards the cost and the overall performance of the hybrid system. The corresponding sensitivity analysis on batteries and diesel generator utilisation throughout the year are shown as part of the discussion.

3.1 Modelling of Hybrid System Components

As mentioned before, a graphical user interface (GUI) has been developed which assists the project manager to analyse the long term costs of energy production of a hybrid system. This potentially helps developers to make a justifiable components sizing decision by taking into consideration the financial, renewable resources and technical factors. Figure 3.1 shows the block diagram of the proposed hybrid system implemented in this work. The power flow directions are indicated by the arrows. In this research, the wind turbine system is modelled using empirical data, which directly correlates the relationship between wind speed and generated power output. Thus, the losses of the system are accounted in the equation. Similarly, the efficiency of the diesel generator is related to its power production and its fuel consumption. The modelling approach of these systems will be further described in the following sections. For the case of the grid-forming inverter, it is assumed that it has an average operational efficiency of 95%. The widely employed lead-acid batteries are considered in this study. As discussed in the previous chapter, in order to keep the initial project cost low, it is agreeable with Gaia-Wind Ltd that lead-acid batteries would be employed in this research. In addition, the DC voltage of 48 V can be formed from the lead-acid batteries without imposing constraints on the experiments which will be discussed in later chapters. In particular, the Rolls 4000 Series (RB-T12136) lead-acid batteries (Table 2.9) are adopted in this sizing study. Hypothetically, if the lithium-ion batteries were chosen in this study, the battery replacement cost over the operational period will be lesser as more cycles are

allowed before its end of life. However, the initial cost is relatively higher than the lead-acid batteries (which has lesser number of cycles to failure). Although at this point it is unknown which option is more economical, the cheaper battery option will be sized larger and this can influence the diesel generator usage by storing and utilising more wind energy in this case. Conversely, the more expensive battery option will be sized at a smaller scale and the diesel generator will be used more frequently.

The overall battery efficiency is specified by two efficiencies; the coulombic efficiency and the voltage efficiency. The product of these two is the battery energy efficiency. The coulombic losses happen as a result of charge transfer to facilitate electrochemical reaction. In addition, the battery self-discharge phenomenon is considered as part of the coulombic losses. Another form of loss in the electrochemical systems is the over-potential, which is defined by the ratio between the voltage during discharging and voltage during charging [162]. Lead-acid batteries typically have coulombic (Ah) efficiencies of around 85% and energy (Wh) efficiencies of around 70% over most of the state of charge (SOC) range [163]. These parameters are determined by the details of design and duty cycle to which they are exposed [163]. In the following case studies, an average energy efficiency of 70% is adopted. This value excludes the auxiliary power requirement such as battery management system, fan ventilation etc.

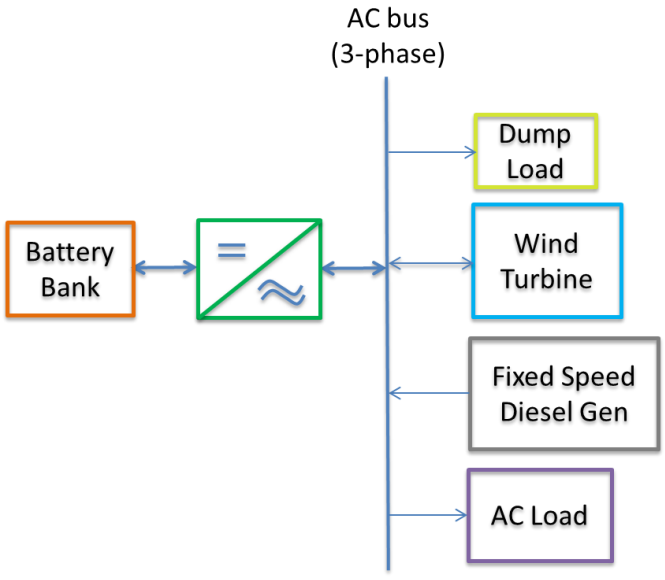

Figure 3.1: Proposed hybrid wind-diesel-battery system

The layout of the GUI is demonstrated in Figure 3.2. The load profile, the amount of wind turbines, battery parameters, inflation and discount rate, the cost of components, and wind turbine power curve coefficients can be altered before performing life-cycle cost simulation. In addition, the user is able to use any yearly wind speed profile for a particular site. In order to simplify matters, the renewable energy resource and load were assumed to be the same throughout the 20 years lifetime. With all the information given to the GUI programme, the optimal batteries and diesel generator sizes were sought. The following subsections describe the modelling and costs of the hybrid system components, the adopted battery and diesel generator degradation model and the constraints of system operation.

It is important to note that the developed sizing tool is generic and it is suitable to be used for different types of wind turbines. In addition, generalised wind turbine power curves can be used if needed. This can be achieved by keying in the appropriate power curve's coefficients within the GUI. However, the author has adopted a Gaia-Wind wind turbine as an example of this work due to the data availability. The modelling approach and analysis carried out in the following sections can serve as a reference and can be modified to suit any other systems of interest.

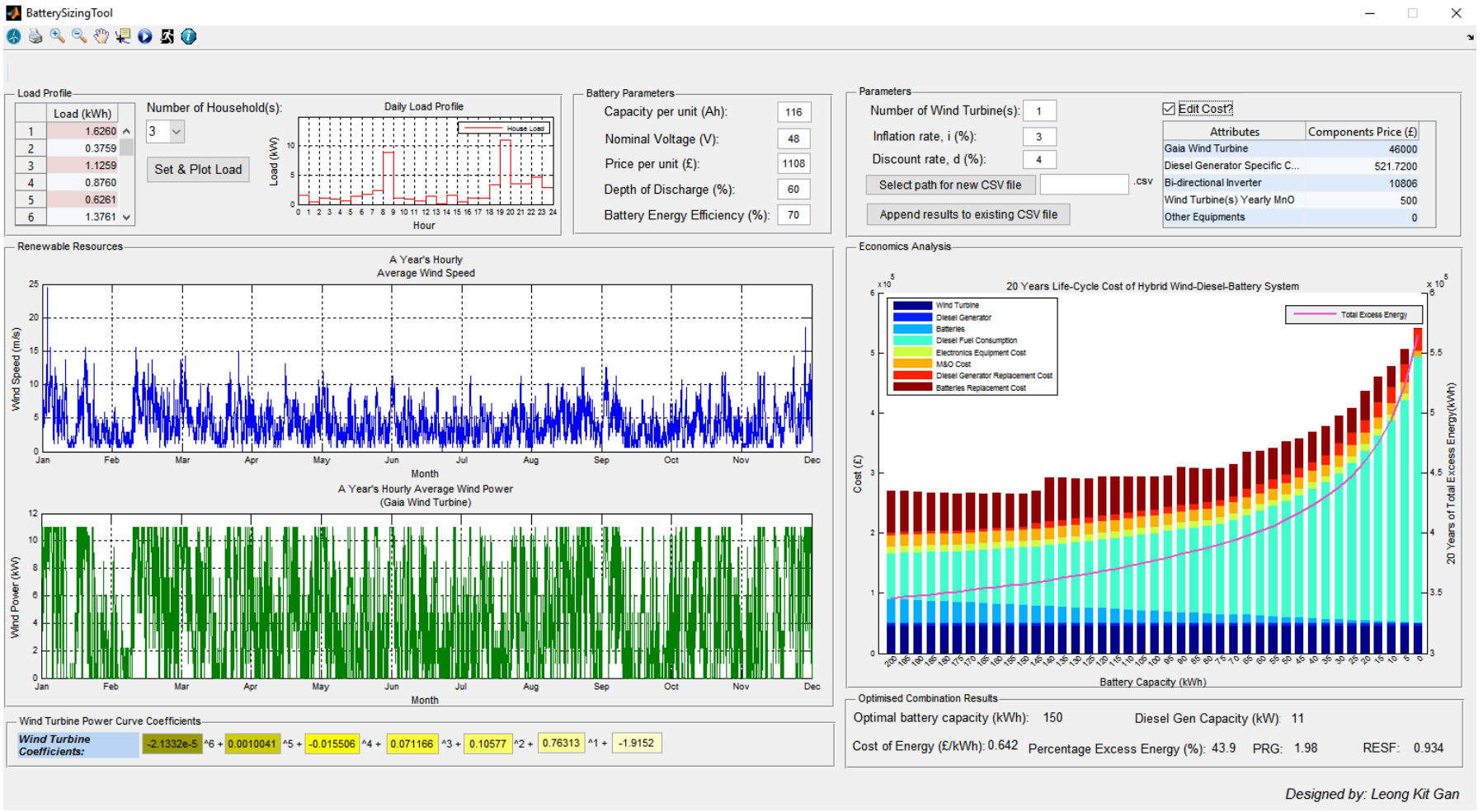

Figure 3.2: GUI for calculating long term cost of hybrid system operation

3.1.1 Wind Energy Modelling

As stated before, the wind energy conversion systems are represented with the power curve's coefficients. For the case of wind energy systems, most of the small wind turbine manufacturers do provide their wind turbine power curves as part of the associated data sheets. By plotting an estimated power curve and interpolating it with a polynomial equation, the coefficients can be obtained. Higher resolution power performance data are published and readily available if the wind turbines are accredited by certification bodies such as TUV NEL, Small Wind Certification Council (SWCC) and National Renewable Energy Laboratory (NREL).

The wind turbine's generated power here is modelled based on Gaia-Wind's wind turbine power curve as shown in Figure 3.3. The fixed speed wind turbine was rated at 11 kW and it utilises an induction machine to generate electricity. The power curve in Figure 3.3 is formulated empirically using Gaia-Wind's measured wind speed and power output of the wind turbine.

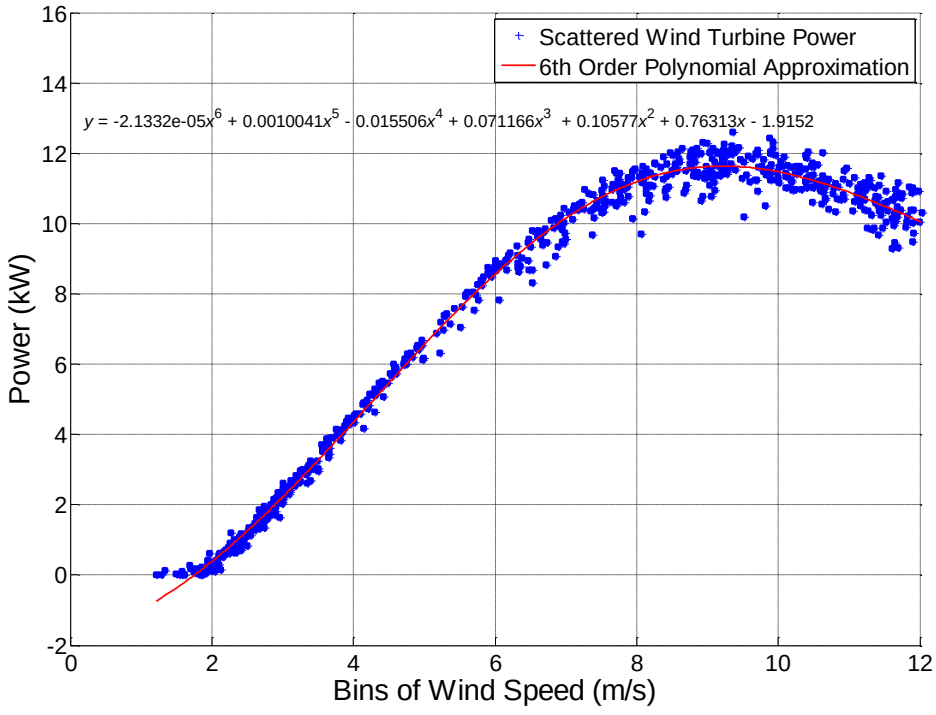

Figure 3.3: Gaia's Wind Turbine Approximated Power Curve

Thus, the output power from Gaia's wind turbine can be computed at any given wind speed using a polynomial function. A polynomial is a function describing the form of a length of line which is constructed out of known constants and variables. This function uses the operations of addition, subtraction, multiplication and non-negative integer exponents to describe the form of the line. The equation is a function of wind velocity, given as:

$$P_{wind} = -2.13e^{-5}V^6 + 0.001V^5 - 0.0155V^4 + 0.0712V^3 + 0.1058V^2 + 0.7631V - 1.9152 \quad (3.1)$$

where:

P_{wind}: Wind Turbine Output Power (kW)
V: Wind Velocity (m/s)

The equation (3.1) is used from wind speed of 3.5 m/s onwards as power generation starts at wind speeds above 3.5 m/s (cut-in speed) and the rated wind speed is 9.5 m/s. For wind speeds exceeding 25 m/s, the turbine has to be stalled (hence no power generated) to prevent structural damage [105].

In order to simulate the operation of the hybrid system [164], [165], the measured data of hourly wind speed is utilised. The benefit of using annual hourly data is that the peaks and troughs of the wind speed profile are included, thus reflecting a more realistic situation. Moreover, variations in seasonal wind speed are also taken into account when running the simulation. Hourly wind speed data measured at Bishopton [166], which is situated in the north-east of Renfrewshire, Scotland is depicted in Figure 3.4. The first hour begins on 1/1/2012 at 00:00. Nevertheless, a period of low wind speeds is observed in February and the zoomed-in wind speed in this month is demonstrated in the bottom plot of Figure 3.4. The wind is measured in open terrain at the height of 10 m above ground level [166]. Since the hub height of the Gaia wind turbine is 18 m above ground level, the wind speed profile at this height is estimated from the measured wind speed at 10 m, using the Log Law, with an estimated roughness length of 0.25 m (many trees, hedges and few buildings) [44]:

$$U(z) = U(z_r)\frac{\ln(\frac{z}{z_0})}{\ln(\frac{z_r}{z_0})} \tag{3.2}$$

where:

$U(z)$	: wind speed at height z (m/s)
$U(z_r)$	: wind speed at reference height z_r (m/s)
z	: height above ground level for wind velocity $U(z)$ (m/s)
z_0	: roughness length (m)

As the Gaia-Wind 11 kW wind turbine is used in this study; hence the power curve from Figure 3.3 is used to compute the power output of the turbine. The corresponding wind power over a one year period is shown in Figure 3.5. This took into account the cut-in and cut-off wind speed supplied by the manufacturer. For simplicity purposes, the power output is programmatically regulated at 11 kW. It is believed that the wind speed at Renfrewshire is slightly higher than the average wind speed in the UK and this will impact the annual energy generated from the wind turbine and hence the sizing results.

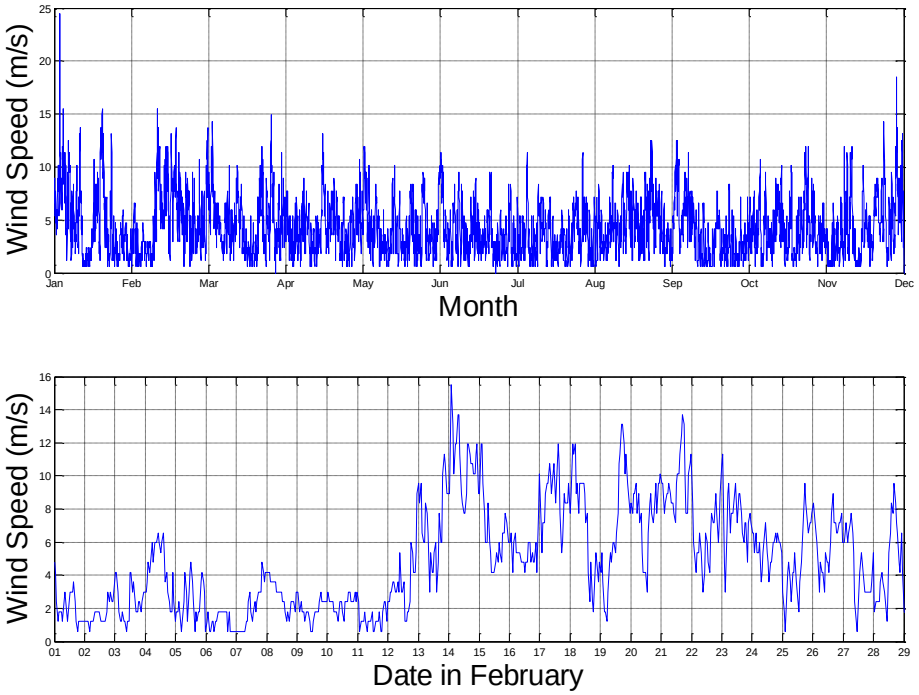

Figure 3.4: Converted yearly (top) and zoomed in February (bottom) wind speed at hub height, 18 m in Bishopton, 2012

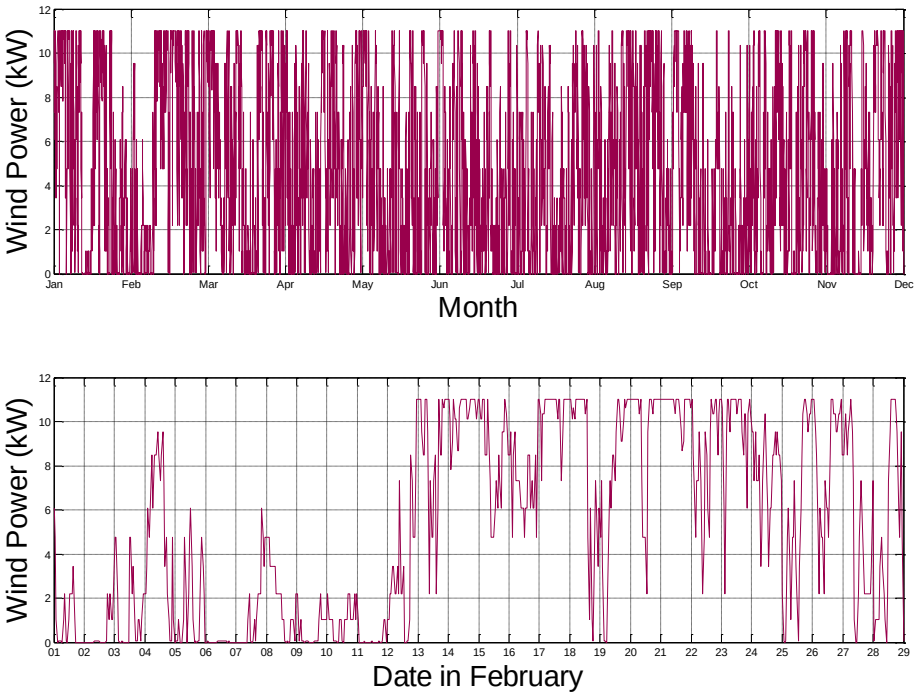

Figure 3.5: Corresponding Gaia wind turbine yearly (top) and zoomed in February (bottom) power output in Bishopton, 2012

3.1.2 Load Profile Modelling

The hourly averaged consumer load profile is shown in Figure 3.6. The detailed bottom-up load model which was developed in [51] can be found in Appendix A. For simplicity, it was being repeated 365 times to emulate annual demand. However, if a more accurate load model is desired, it can be formulated from historical measurements with the incorporation of load growth factors. Considering a single to a few households of electricity demand to be supplied from the off-grid system, the simplified load model here is suffice as the load growth factor has a stronger influence on the design of large-scale power systems. The diversity of the residential load within a distribution network has been studied in the past with the introduction of coincidence factor for quantification purposes [167]. It was concluded that the peak demand coincidence factor decreases as the number of customer increases [168]. Similarly, from the point of view of an off-grid power system in rural areas, it has been stated that the diversity of aggregate demand becomes greater as the

number of households rises [169]. Since the sizing study here considers less than 10 households and the sampling time is one hourly, the variability between each household is not being reflected in the load aggregation while performing sensitivity studies in later sections. It is common that the household load adopts single phase systems. However, in this work, it is assumed that the load is shared between the three phases in proportion and the simulation dealt with net energy in and energy out of the households.

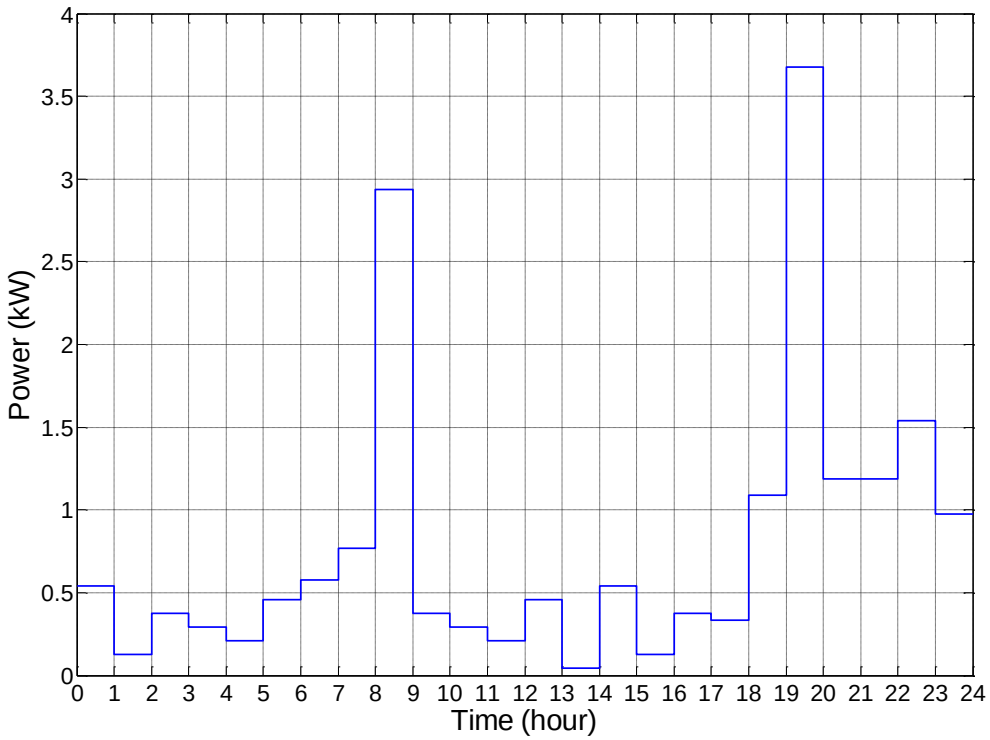

Figure 3.6: Load profile (consumer plus Gaia's wind turbine start-up)

In addition to the consumer load profile, the induction generator which Gaia-Wind wind turbine utilises requires a high inrush current during the start-up process. Therefore, the average start-up energy of the wind turbine in an hour is provided by the manufacturer as:

$$P = \sqrt{3} \times 415V \times 100A = 71.88\ kW \tag{3.3}$$

$$E = \frac{71.88\ kW \times 7.5s}{3600s} = 0.15\ kWh \tag{3.4}$$

The start-up stator current is given as 100 A. Without a soft-starter, the start-up process is completed approximately 7.5 seconds. The wind turbine start-up process will take place whenever the wind turbine is in stall position and the wind speed goes to more than 3.5 m/s. In the sizing algorithm, this condition is checked hourly and an energy value of 0.15 kWh is added to the load profile if a start-up is detected.

3.1.3 Battery Storage Calculations

In a hybrid wind-diesel-battery system, battery banks are electrochemical devices that store energy from other AC or DC sources for later use. The batteries serve as a platform to maximise the usage of renewable energy by storing excess energy whenever the supply from the wind turbine(s) exceeds the load demand. Furthermore, a properly-sized battery bank is capable of reducing the number of start-stop cycle of the diesel generator, along with a reduction in fuel consumption. As discussed in the previous chapter, the chosen grid-forming inverter system in this project is the Sunny Island 8.0H, which require a battery DC voltage of 48 V. Since the Rolls 4000 Series (RB-T12136) battery (116 Ah at C10), with each rated at 12 V is selected for this work, a string of 4 units (connected in series) is required to meet the 48 V requirement. Each string has the capacity of 5.568 kWh, and its cost is £ 1,108 (inc VAT).

When determining the SOC for an energy storage device, the following constraint must be satisfied.

$$SOC_{\min} \leq SOC \leq SOC_{\max} \tag{3.5}$$

where $SOC_{\min}$ and $SOC_{\max}$ are the minimum and maximum state of charge respectively. This research assumes that $SOC_{\min}$ and $SOC_{\max}$ are equal to 40% and 100% respectively. In other words, 60% DoD is allowed at all times. Note that the diesel generator is switched-on only whenever the energy in the batteries is fully dissipated in addition to insufficient generation from the renewables to meet the demand. Since the diesel generator is not used to charge the batteries here, the energy

generated from the diesel generator should be excluded in the battery storage calculation.

The battery SOC is updated based on the following equations. When wind turbine generation is greater than the load demand and the batteries are not fully charged, *SOC (n)* is defined as:

$$SOC(n) = SOC(n-1) + \left[\frac{(E_{\text{wind}}(n) - E_{\text{load}}(n))(\eta_{battery})(\eta_{inverter})}{E_{\text{battery}}}\right] \times 100\% \qquad (3.6)$$

On the other hand, when load demand is greater than wind turbine generation and the battery SOC is more than 40%, *SOC (n)* is defined as:

$$SOC(n) = SOC(n-1) - \left[\frac{E_{\text{load}}(n) - E_{\text{wind}}(n) \Big/ (\eta_{battery})(\eta_{inverter})}{E_{\text{battery}}}\right] \times 100\% \qquad (3.7)$$

where:

SOC (n-1)	: battery SOC level at previous hour (%)
E_{load} *(n)*	: energy demand (kWh)
E_{wind} *(n)*	: wind energy generation (kWh)
E_{battery}	: total installed battery capacity (kWh)
η_{battery}	: one-way battery energy efficiency (p.u.)
η_{inverter}	: one-way grid-forming inverter efficiency (p.u.)

In a battery-based off-grid hybrid renewable energy system, the remaining useful life of the batteries is largely influenced by the DoD. Theoretically, a large battery capacity would experience smaller DoDs compared to smaller batteries, for the same operating conditions. This in turn affects the frequency of replacing batteries during the lifetime of the HRES, for instance 20 years. Being able to predict the lifetime of a battery is of great importance in the initial stage of hybrid system design as it involves the decision of determining the operating conditions and planning replacement intervals for batteries [170]. Manufacturers cannot test their batteries for a full range of applications due to the huge amount of time and costs involved, in addition to the lack of detailed knowledge concerning the use of batteries in various applications [170]. Various kinds of battery lifetime models are available, as

discussed in Chapter 2. However, it is not practical to consider highly sophisticated battery lifetime models which include many ageing processes and various extreme non-linear stress factors. Fortunately, simplified battery life estimation has been developed such as the rain-flow cycle counting model [171]. This method assumes that battery lifetime is primarily a function of depth of charge/discharge cycles [172]. Experimental validations have been conducted against several other battery life models and the results show that the cycle counting algorithm generates a fairly accurate ranking on the lifetime of batteries with respect to the different levels of battery usage (different current profiles) [171]. In renewable energy applications, such method of predicting the battery lifetime have been successfully employed in [173] and [174]. In addition, this algorithm is chosen to be implemented in a hybrid system sizing commercial software, known as the HYBRID2 [172]. This methodology requires the following assumptions which are made in fatigue analysis to be taken into consideration [170]:

1. The stress events can be defined to induce only a small amount of incremental loss of lifetime. It can frequently occur until the battery fails.
2. The loss of lifetime caused by a stress event is independent of the previous stress events and the present battery state-of-health.
3. The process of deteriorating the battery is either independent of the sequence of the stress events or the stress events which occur are distributed statistically throughout the lifetime of the battery. This also means that the battery is not assumed to be operated first at float operation for half of its lifetime and then subsequently cycled for the other half of its lifetime, but float operation and cycling happen more or less alternatively.

In this work, a cycle-to-failure versus DoD curve was employed and it is shown in Figure 3.7 [173]. The corresponding relationship which was approximated by a polynomial curve fit is shown as [173]:

$$C_d = -1.345e^{-12}d^{-4} + 1.495e^{-7}d^{-3} - 0.001507d^{-2} + 601.5d^{-1} - 122.5 \quad (3.8)$$

where:

C_d: Cycles to failure at a depth of discharge d

d: Depth of discharge

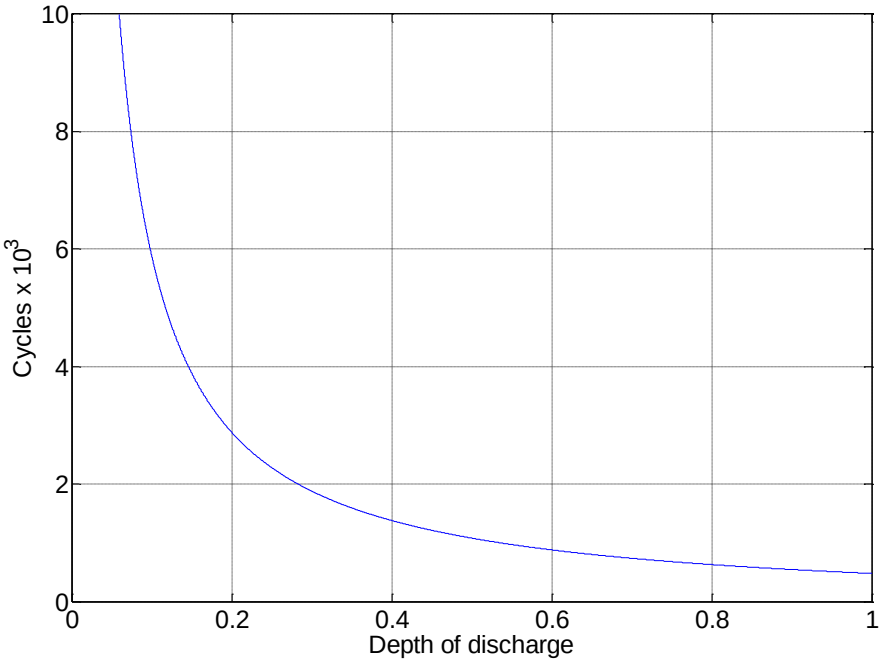

Figure 3.7: Cycles-to-failure versus depth of discharge for a typical deep-cycle lead-acid battery

If the number of cycles-to-failure for a given depth of discharge d is C_d, then the fraction of battery life used in one full cycle of range, d can be written as $1/C_d$. If i different cycle ranges are considered each with N_i cycles, the total battery life fraction consumed, W can be computed as a summation of each individual cycle as [173]:

$$W = \sum_{i=\,i_{min}}^{i=i_{max}} \frac{N_i}{C_{di}} \tag{3.9}$$

After sufficient cycles have passed and the accumulated fraction is equal to 1.0, the battery is assumed to reach its end of life and it needs to be substituted with a new one.

3.1.4 System Operation Modelling

The following energy-production scenarios exist within the hybrid system:

- The energy is produced by the wind turbine is directly sent to the consumer load.
- The diesel generator is operated (brought online) at times when wind power fail to satisfy load demand and when battery storage is depleted.
- The surplus energy from the wind turbine (not absorbed by consumer load) is stored in the batteries via the bi-directional inverters.
- The stored energy in batteries is used to cover the energy deficit.
- The excess energy is dissipated by a dump load if the batteries SOC are at their maximum level.
- The average energy which is used to start-up the wind turbine is added to the load profile if the start-up condition is met (previous hour(s) wind speed less than 3.5 m/s and current hour wind speed more than 3.5m/s).

The magnitude difference between generated power (P_{gen}) and the demand (P_{dem}) over a given period of time is:

$$\Delta P = P_{\text{gen}} - P_{\text{dem}} \tag{3.10}$$

The power equation can then be translated into energy generated and demanded (W_{gen}, W_{dem}) over a period of a year (8760 hours) and be written as:

$$W_{\text{gen}} = \sum_{n=1}^{8760} [(\Delta T)(K_{\text{w}} P(n)_{\text{w}})] \tag{3.11}$$

$$W_{\text{dem}} = \sum_{n=1}^{8760} [(\Delta T)(P(n)_{\text{dem}})] \tag{3.12}$$

where K_{w} represents the number of wind turbines used, n is the sampling time (hour of year), and ΔT is the time between the samples (in this case one hour). The energy balance within the hybrid system is sequentially calculated throughout the year. It is important to note that in reality, power generation and load demand change sub-hourly and this may affect the final results. Furthermore, since this study considers only one wind turbine and a few households, the averaging effect is not greater than

those which consider larger scale generation and load demand of many households. However, if a high sampling rate is applied, the computational time will increase. It is acknowledged that the hourly sampling rate adopted in this work is a limitation and it may contribute to the average energy excess and energy deficit errors.

3.2 Life-cycle Cost Modelling

This section describes the life-cycle cost modelling for the considered case study. These include the hybrid system hardware cost, operation and maintenance (O&M) cost and long-term diesel fuel cost.

3.2.1 Hybrid Wind-Diesel-Battery System Hardware Cost Estimation

The initial estimated cost of components involved in implementing the hybrid wind-diesel-battery system is listed in Table 3.2. They can be referenced from Table 2.5, Table 2.6, Table 2.8, Table 2.9 and the reasons for selecting these are discussed in Chapter 2. From Table 3.2, it is observed that the wind turbine's capital cost per kW is much higher than the diesel generator. However, a wind turbine generates power with wind which does not incur any cost. On the other hand, a diesel generator consumes costly diesel fuel over its lifetime. The high cost incurred by the SMA bi-directional inverters was due to the topology proposed in this work i.e. battery grid-formed requirement. During the start-up process of the induction generator, high current would be transferred from the batteries. The high power transferred translates to the high cost of the converter.

Components	**List Price (£)**	**£ per kW or £ per kWh**
Gaia-Wind wind turbine system	46,000.00/unit	4181.81 £/kW
3-Phase SMA grid-forming inverter cluster	10,806.00/unit	600.33 £/kW
3-Phase diesel generator	521.72/kW	521.72 £/kW
A string (4 units) of Rolls RB-T12136 battery (48 V, 116 Ah)	1,108/string	198.99 £/kWh

Table 3.2: Hardware cost estimation of a hybrid wind-diesel-battery system [116] [118] [126] [128]

3.2.2 Operation and Maintenance (O&M) Cost Estimation

The O&M cost of a hybrid wind-diesel-battery system can be significant when considering for a long term operation as highlighted in [22]. In the case of studying

economics between batteries and diesel generator capacity (directly proportional to fuel consumption), the consideration of O&M cost is important as they inherit different price characteristics. Rather than replacing the batteries at a fixed period, in this work, the battery replacement period is dependent on their DoD cycling. The battery lifetime model adopted is described in the Section 3.1.3. For the same amount of energy flow in the hybrid system, a smaller battery capacity would incur more frequent DoD than a larger battery capacity over their lifetime, hence the replacement period would be shorter for the former. Longer lifetime is possible to be achieved with careful operation of the batteries, such as limited charge rates, limited weekly cycling, occasional re-conditioning of the batteries, and controlled temperature [175]. Similarly, a diesel generator has a lifetime commonly determined by a number of operational hours. Here, it is assumed that an off-grid diesel generator has a running time of 10,000 hours. Once this number is reached, replacement is required [102]. The assumptions made here are based on past experiences. As the technologies improve over time, these assumptions should be altered accordingly.

The O&M costs are incurred at later times, thus it is convenient to refer all costs to the time of acquisition i.e., present worth. The inflation rate, *i* and discount rate, *d* are the two factors which affect the value of money over time. The present worth factor of an item that will be purchased *n* years later is given by [176]:

$$P_{\mathrm{r}} = \left(\frac{1+i}{1+d}\right)^{n} \tag{3.13}$$

The present worth (PW) is thus:

$$PW = (P_{\mathrm{r}})C_{\mathrm{o}} \tag{3.14}$$

where C_{o} is cost of an item at the time the investment was made.

Sometimes it is necessary to determine the present worth of a recurring expense, the cumulative present worth factor can be derived as [176]:

$$P_a = \left(\frac{1-x^n}{1-x}\right) \tag{3.15}$$

where $x = \left(\frac{1+i}{1+d}\right)$

If the recurring purchase does not begin until the end of the first year, and if the last purchase occurs at the end of the useful life of the system, there will still be *n* purchases, but the cumulative present worth factor becomes

$$P_{a1} = xP_a \tag{3.16}$$

In this work, the 20 years cumulative maintenance cost of the wind turbine utilised the present worth factor, P_{a1}. The wind turbine yearly maintenance cost is £ 500. It is assumed that the grid forming inverters needed to be replaced in 10 years [177]. For the given inflation rate of 3 % and discount rate of 4%, x = 0.9904, P_a = 18.27, and P_{a1} = 18.1. So Table 3.3 can now be generated. Note that the battery and diesel generator O&M costs vary scenario by scenario. It is expected that in a scenario whereby a large battery capacity is installed, the incurred diesel generator O&M cost is less as the diesel generator running time reduces.

Component	**Initial Cost (£)**	**Present Worth (£)**
Gaia wind turbine maintenance for 20 years	500/year	9050
Battery replacement	1108/string	Vary depending on replacement period
Diesel generator	521.72/kW	Vary depending on replacement period
SMA grid-forming inverters at year 10	10,806.00/unit	9,812 /cluster

Table 3.3: Operation and maintenance cost [116] [118] [126] [128]

3.2.3 Diesel Generator Fuel Consumption Modelling

In order to justify the long-term economics of diesel generators in a hybrid system, it is important to understand the diesel fuel consumption for different generator capacities and also the future diesel price.

Unfortunately at present, most of the small diesel generator (sufficient for single household) manufacturers do not include the ¼, ½, ¾ and full load fuel consumption in their data sheet. Thus, the fuel consumption for various sizes was approximated using the following approach. Figure 3.8 shows the plots of approximated diesel generator fuel consumption (litres/hour) at ¼, ½, ¾ and full load, starting from a power rating of 20 kW up to 200 kW. Rather than using a specific manufacturer's diesel fuel consumption data, these empirical data were obtained from Diesel Service

& Supply Ltd (more than 30 years of history), which it was believed to be realistic and not brand bias [178].

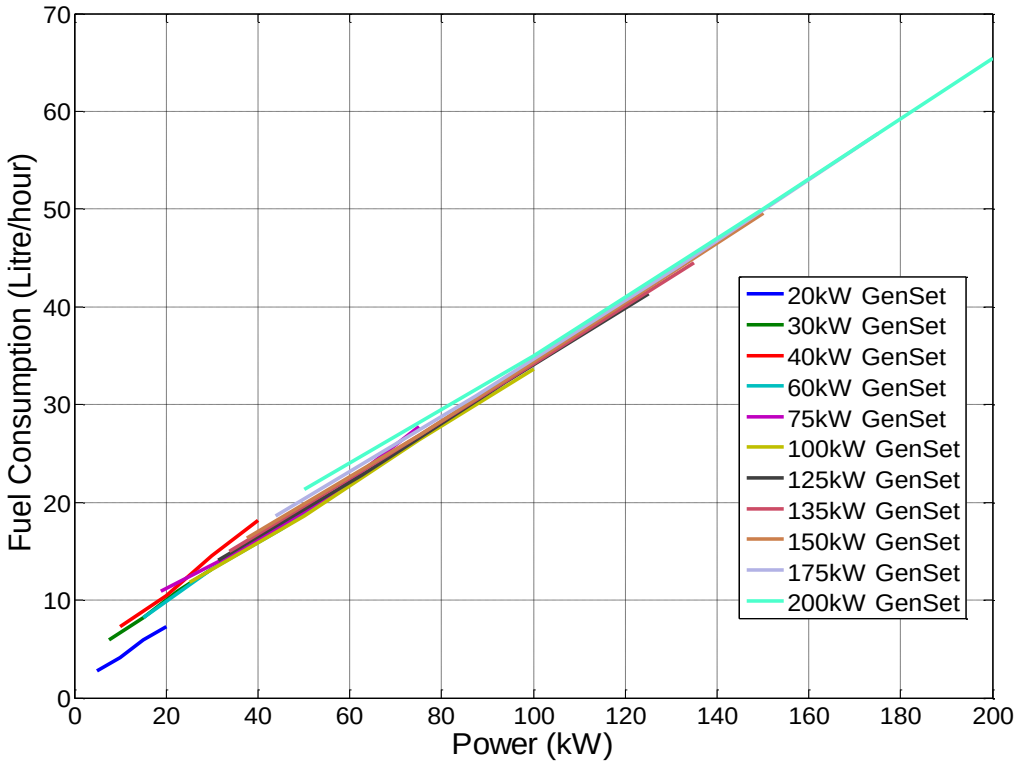

Figure 3.8: Diesel generator fuel consumption for various capacity

It is observed that the fuel consumption coincides with each other. From here, all the generator's fuel consumption points are plotted and linear fitting is performed, as shown in Figure 3.9.

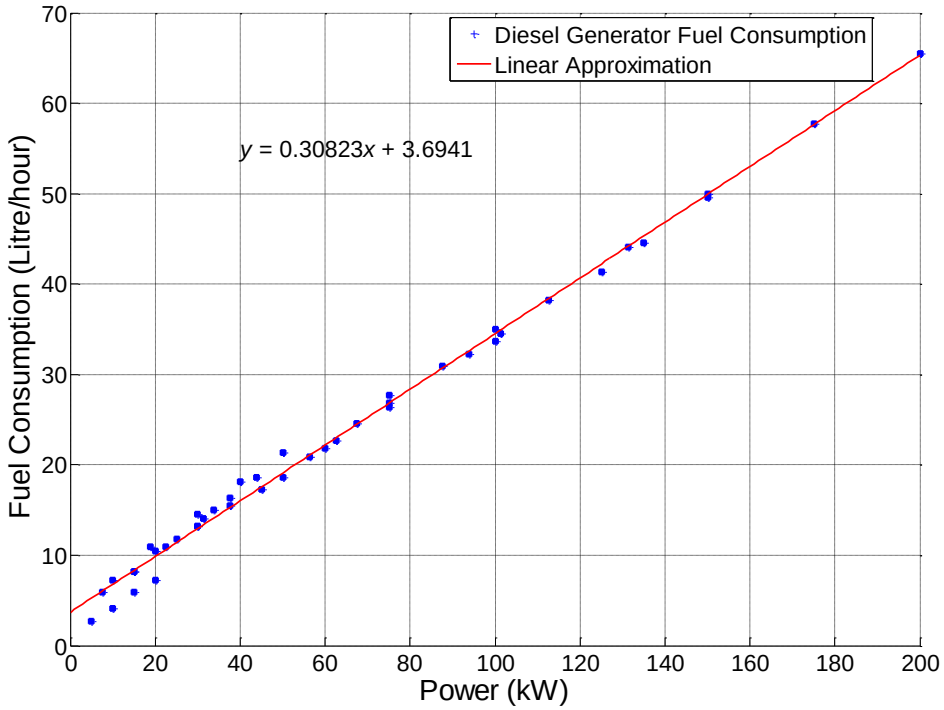

Figure 3.9: Linear fit of diesel generator fuel consumption

The approximated fuel consumption equation as a function of power, given as:

$$F = 0.30823P + 3.6941 \tag{3.17}$$

In order to verify the accuracy and reasonability of the obtained fuel consumption equation, it was compared with other available sources i.e. Cummins Power Generation's diesel generator set datasheet and Hardy Diesel Ltd [179] [180]. A first derivative of the above function gives the change in fuel consumption of the power rating range (0 – 200 kW), as shown in Figure 3.10 (blue curve).

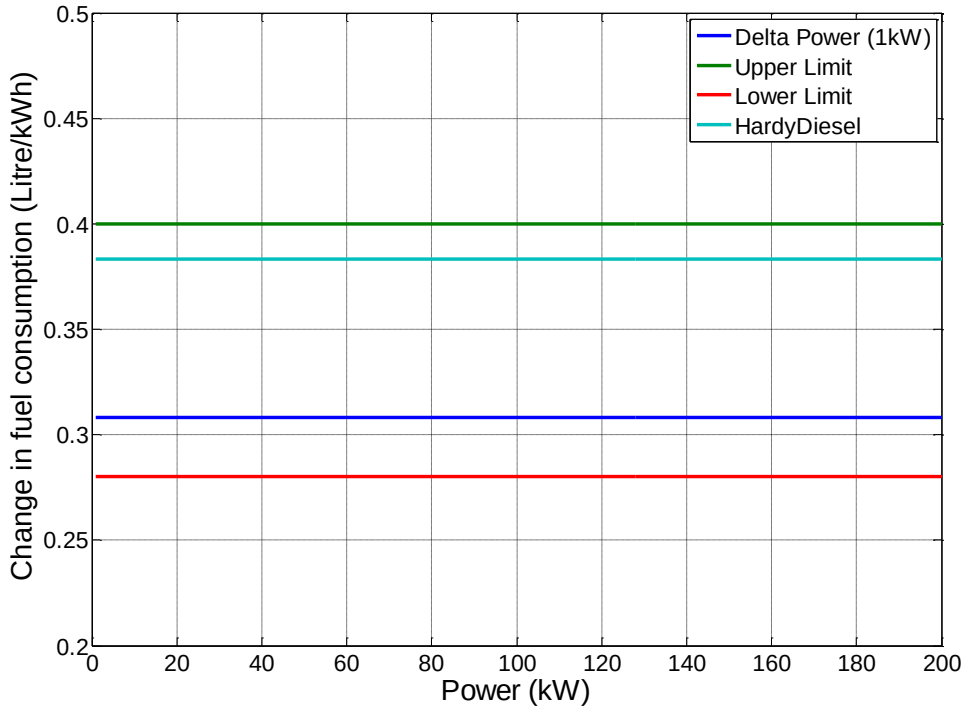

Figure 3.10: Comparison of first derivative and other sources fuel consumption plots

Based on literature [178] and [179], a diesel generator typically consumes between 0.28 and 0.4 litres of fuel per kilowatt hour at the generator terminals, which are marked as red (Lower Limit) and green (Upper Limit) constant lines respectively. On top of that, Hardy Diesel Ltd uses 0.383 litres of fuel per kilowatt for their reference in calculating fuel consumption [180]. Therefore, it can be seen that the diesel generator set's fuel consumption estimation from this work is within the boundary compared to other sources.

For this case study, it is desired to estimate the long-term energy production (from the year 2016 - 2035) cost involved in running the hybrid system. Therefore, predicting the future diesel fuel price is essential. Figure 3.11 shows the projected diesel fuel price (pence per litre) in the UK [181], based on the past 10 years diesel historical fuel prices. For simplicity, a linear approximation line was extrapolated to 2040. The future diesel price might be lower than the predicted values as renewable energy penetration becomes higher in the future.

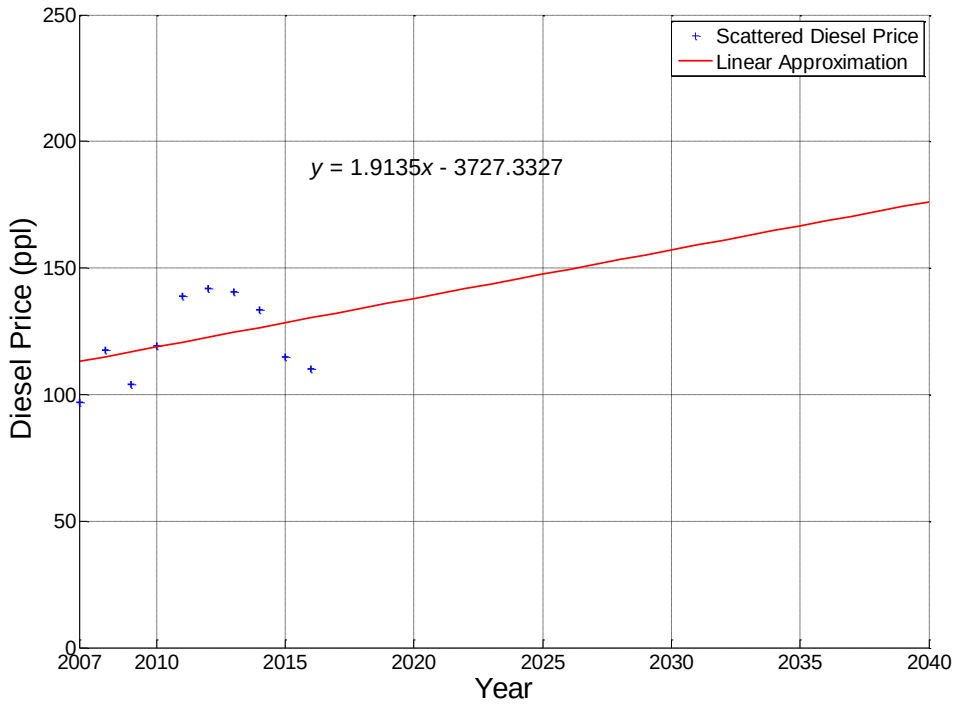

Figure 3.11: Linear extrapolation of diesel fuel price (pence per litre)

The diesel price as a function of year is given as:

$$Price = 1.9135 \times (Year) - 3727.3327 \tag{3.18}$$

With the fuel consumption and diesel price equations, the cost of running the diesel generators for various capacities was computed in different years. Intuitively, if a lower diesel fuel price than the projected fuel price (Figure 3.11) is used to seek the optimal system, the diesel generator will be "encouraged" to run more frequently and the optimal battery storage would be sized smaller in capacity. An averaged diesel price of the past 10 years (121.703 pence per litre) is simulated in the next section as a comparison with a linearly increase diesel fuel price projection (Figure 3.11).

3.3 Results and Discussion

3.3.1 Base case (Diesel generator-only)

As a base case and for COE comparison purposes, the diesel generator only solution in supplying electricity to a single household is simulated using the developed sizing

tool. The screenshot of the solution is shown in Figure 3.12. The wind power generation is zero throughout the year although wind speed input is provided. The diesel generator is programmed to operate with a load-following strategy to supply the load demand, hence no additional or short of energy is being generated at all times. The diesel generator is sized according to the peak load demand, which is around 4 kW in this case. Since no battery storage is utilised, the generated solutions are the same for all scenarios (from the bar chart). The computed COE is approximately £ 7.66/kWh. The simulation was simply rerun for a different number of households and their respective COE and the required diesel generator capacity is shown in Figure 3.13. It is noticed that the COE reduces when the number of household increases. This can be explained by the more efficient consumption of diesel fuel as the loading capacity increases, as demonstrated in Figure 3.9.

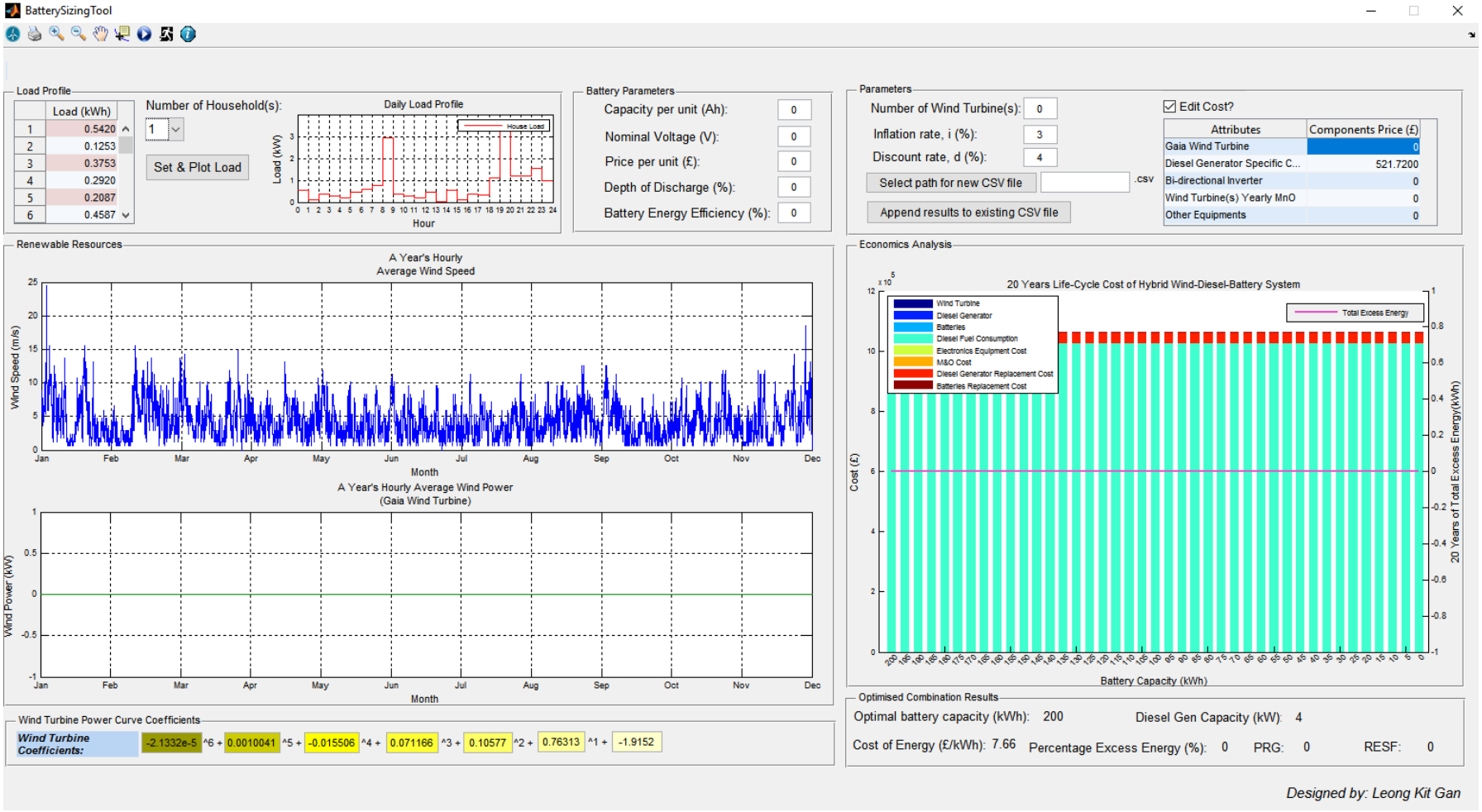

Figure 3.12: Life-cycle cost analysis of diesel-generator only system in Bishopton area (one household)

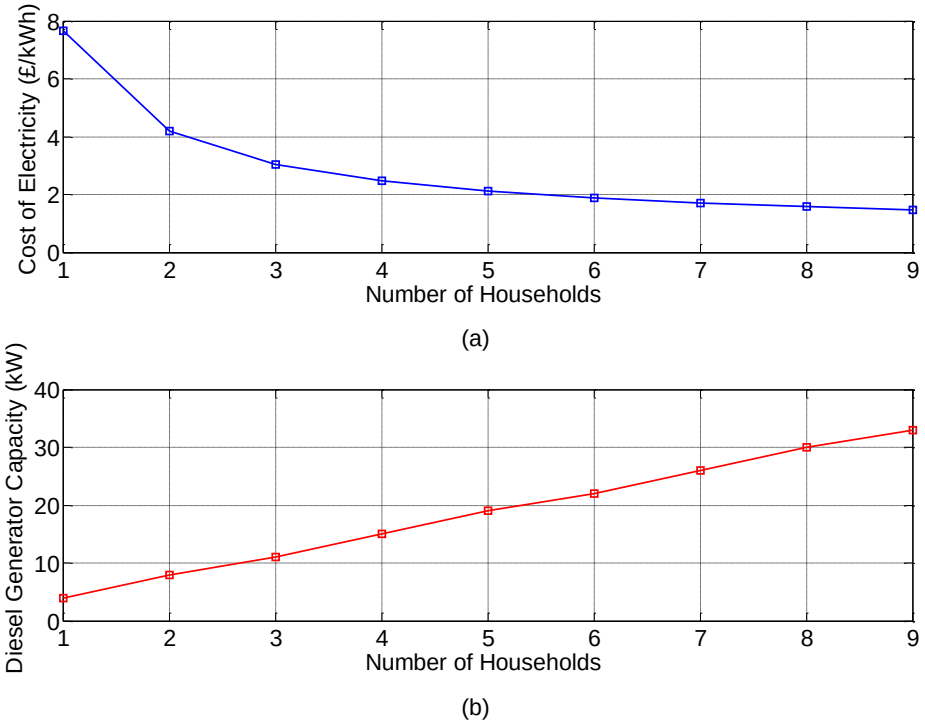

Figure 3.13: Diesel generator only solution a) cost of energy (£/kWh), (b) diesel generator capacity (kW)

3.3.2 Scenario Analysis

Using the abovementioned models and costs, various combination sets of batteries and diesel fuel consumption have been simulated, as depicted in Figure 3.14. Each bar shows the lifetime cost (from 2016 to 2035) of running the off-grid hybrid wind-diesel-battery system in the Bishopton area for a single household. All the scenarios utilised an 11 kW Gaia-Wind wind turbine. The storage capacity was linearly reduced from the leftmost bar until zero-battery solution at the rightmost bar, as shown in the third stack (light blue colour) from the bottom. The y-axis on the left is the total cost, while the y-axis on the right is the corresponding total energy dissipated in dummy loads. It is interesting to note that the diesel generator unit cost is relatively low compared to its fuel consumption, depending on usage. Thus, it is important for both consumer and project manager to look at life-cycle cost analysis, which points out the high cost being associated with diesel fuel and not the hardware itself.

The 200 kWh battery scenario (extreme left column stack) simulates most batteries compared to other scenarios, thus dumping least energy throughout the 20-year period. In addition, the diesel fuel consumption is zero and this can be attributed to a large amount of renewable energy and low load demand. It seemed that this is ideal as the load was fully supplied by renewable sources. However, the slight higher battery cost does not justify its financial attractiveness as the most optimal solution. Between scenarios with battery capacities of 155 kWh and 120 kWh, the batteries were not replaced at all because they have not been cycled to reach their end of life. When the battery capacity is set at 150 kWh onwards, they need to be replaced once in 20 years. However, it is important to note that the battery replacement cost at year 10 is slightly lower than the initial capital cost due to the present worth factor being taken into consideration. As the battery capacity is further reduced to 55 kWh, they need to be replaced twice over the period of 20 years. On the contrary, the zero-battery solution demonstrated that the power deficit was fully met with a diesel generator and wind turbine. However, the diesel generator is replaced more frequently compared to other scenarios as it is switched on whenever the wind energy is lower than the load demand. The zero-battery configuration presents the highest COE due to the heavy reliance on diesel generator and poor utilisation of excess wind energy compared to other scenarios. Furthermore, the surplus energy equally is the highest as there are no batteries to store excess energy from the wind turbine. Nevertheless, small relative change in excess energy over the scenarios is observed, considering that the scale of the y-axis on the right is enlarged. The analysis here clearly demonstrates the trade-off between the battery capacity and diesel generator usage. The amount of batteries is inversely proportional to the diesel fuel consumption.

From Figure 3.14, it is observed that the optimum configuration for the hybrid system is the 155 kWh battery storage and without diesel generator. The optimal solution cost is approximately two-third less than the zero-battery solution. However, the COE (£/kWh) is approximately £ 0.77/kWh, exceeding the cost of utility-generated electricity. Nevertheless, this is much lower than the base case (diesel generator only system) which simulated the COE of £ 7.66/kWh (single household

scenario). Further analysis showed that about 80 % of the excess energy generated by the RES was not being utilised. This can be explained by the low load demand in the system - generation far exceeded demand. For that reason, the load to be supplied should be increased to reduce excess energy in the system. In addition, it was also noted that most of the simulated scenarios did not justify the use of a diesel generator due to the large amount of excess energy existing within the system. The next section analyses the effects of the load demand changes on the performance of the hybrid system.

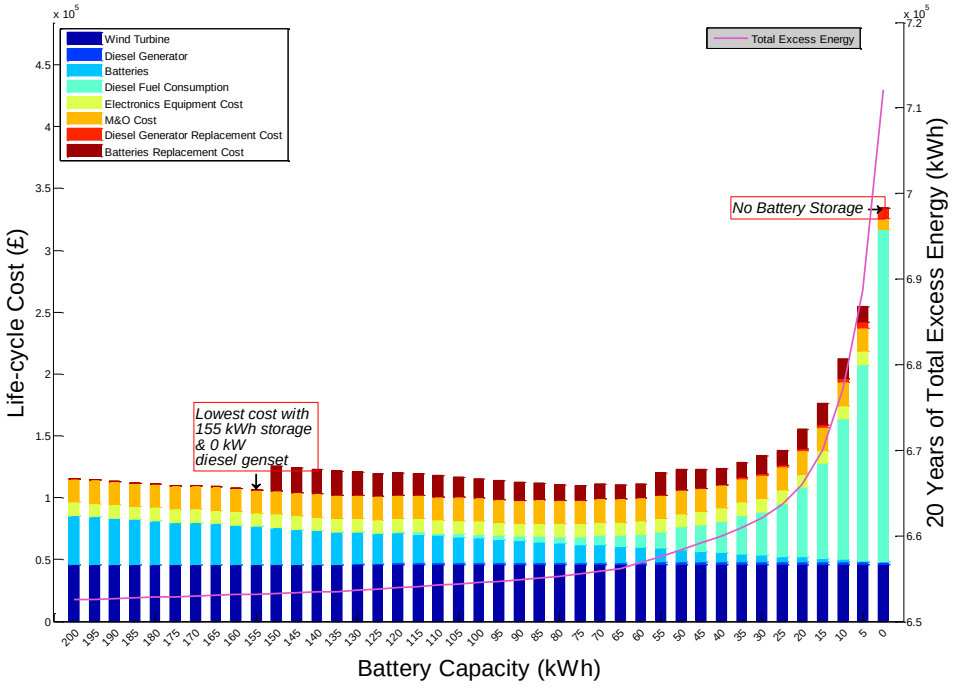

Figure 3.14: Life-cycle cost analysis of hybrid wind-diesel-battery system in Bishopton area (single household)

3.3.3 Load Sensitivity

The performance of renewable energy systems can be characterised by two performance indicators [90]:

i. Renewable energy sources fraction (RESF), defined by:

$$RESF = \frac{E_{\mathrm{WT}} - E_{\mathrm{EXC}}}{E_{\mathrm{WT}} - E_{\mathrm{EXC}} + E_{\mathrm{AUX}}} \tag{3.19}$$

where E_{EXC} is the excess energy which have been produced and dissipated in resistors and not used for the main load. E_{AUX} is the energy generated by auxiliary generator, which in this case is diesel generator.

The RESF parameter is also often called solar fraction because wind energy comes from the sun. If RESF = 1, it means all the loads are satisfied by RES and no diesel fuel is used.

ii. Gross production (PRG), originating from a solar source (wind) in units of load energy (E_{L}) is defined by:

$$PRG = \frac{E_{\mathrm{WT}}}{E_{\mathrm{L}}} \tag{3.20}$$

Here, the investigation was carried out on the effects of increasing the load linearly (number of households) towards the performance and financial attractiveness of the hybrid system. Simulations were performed and only the lowest life-cycle cost solution would be selected for each set of load demand. Figure 3.15 a – e shows the plots of the described parameters versus the number of households.

From Figure 3.15a, it is observed that the COE dropped about 26% when the household increased from one to two. This proved the hypothesis made in the previous section i.e. as the generation capacity matches closer to the load demand, less energy is being dumped (Figure 3.15b) and thus driving towards better economics of the hybrid system. Interestingly, as the number of households continues to increase, the COE picks up while the optimal battery capacity lies between 145 kWh and 200 kWh. The rise in COE is due to the heavier reliance of diesel generator in supplying the increase in load demand. In other words, the reduction of renewable energy contribution in the system as the load demand increases is portrayed in Figure 3.15c. The PRG (ratio of renewable energy generation to load demand) decreased algebraically as the load increasing linearly, as shown in Figure 3.15d.

Based on the COE plot, the optimum number of households to be supplied by the defined hybrid system is two. Nonetheless, it is observed that by a slight increase (about 3.5 %) in battery capacity, another household can be supported optimally. In addition, the amount of energy being wasted will fall by 16.5%. However, the COE will be marginally increased, resulting £ 0.642/kWh as demonstrated in Figure 3.15a. From the author's point of view, two to three households are reasonable loads to be supported by the system. Due to the necessity to reach an LOLP equal to zero (giving total autonomy), the obtained configuration produces more energy than the load demand and quite significant amount of the energy produced by the wind turbine cannot be stored. It would be better off if part of the excess energy is used for non-critical load like electric heater or refrigeration.

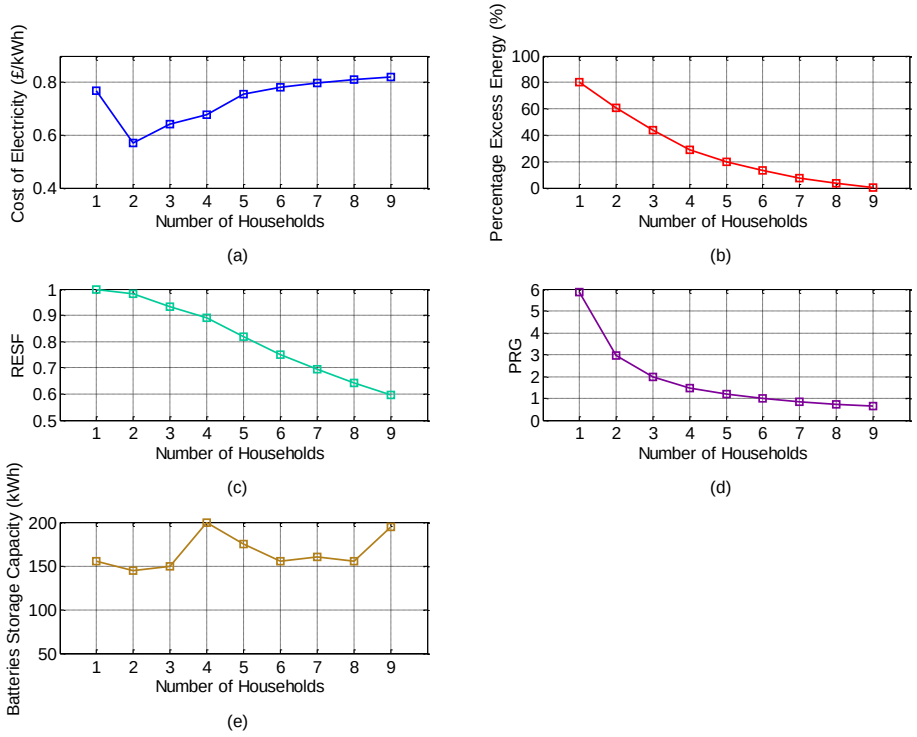

Figure 3.15: Performance indicators (a) cost of energy (£/kWh), (b) percentage excess energy, (c) RESF, (d) PRG, (e) number of batteries against number of households

3.3.4 Hybrid System Technical Performance Analysis

It is worth exploring the hybrid system operation performance, in particular the batteries SOC and diesel generator start-stop variations. In this section, three households load allocation were used as the case study. The corresponding life-cycle cost scenarios are shown in Figure 3.16. Inevitably, the obtained configuration has struck the balance of batteries and diesel generator usage, giving the lowest cost solution when the battery's installed capacity is 150 kWh. It is mentioned that as the battery capacity becomes lower, it charged and discharged more frequently. Smaller storage also mean that lower SOC are reached more frequently, which shorten batteries lifetime and hence more replacements over the considered 20 years period. The zero-oil solution is not shown in this diagram as it can be imagined that the battery storage required to meet the load demand would be very large and costly.

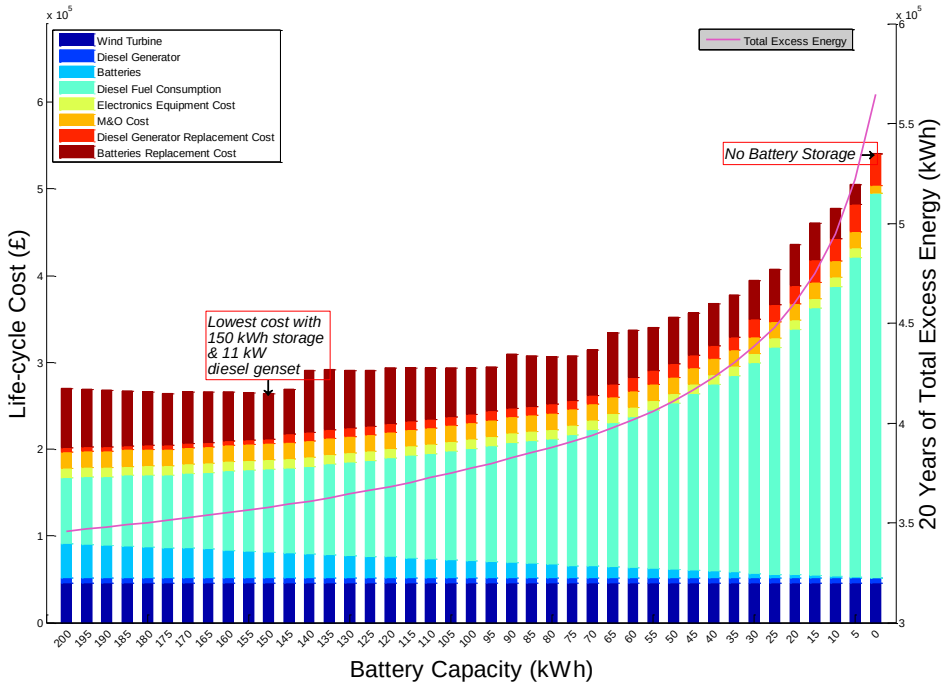

Figure 3.16: Life-cycle cost analysis of hybrid wind-diesel-battery system in Bishopton area (three households)

Figure 3.17 shows the energy flow of each component within the optimally sized hybrid system (three households), which was simulated between 25/1/2012 and 31/1/2012 (one week). Low wind period (hence minimal wind energy) is observed during the mid-week and energy from the battery is first being utilised to supply the load demand. Just before the end of 28/1/2012, the battery energy level drops to 60 kWh (which is equivalent to 40 % SOC for a 150 kWh battery capacity). From this point onwards, the diesel generator is switched on to supply the energy deficit within the system. The extracted energy flow diagram has proven that despite a large battery capacity and a wind turbine with high power rating being installed, a few days of low wind situation can discharged the battery to a low SOC level and eventually trigger the diesel generator to operate.

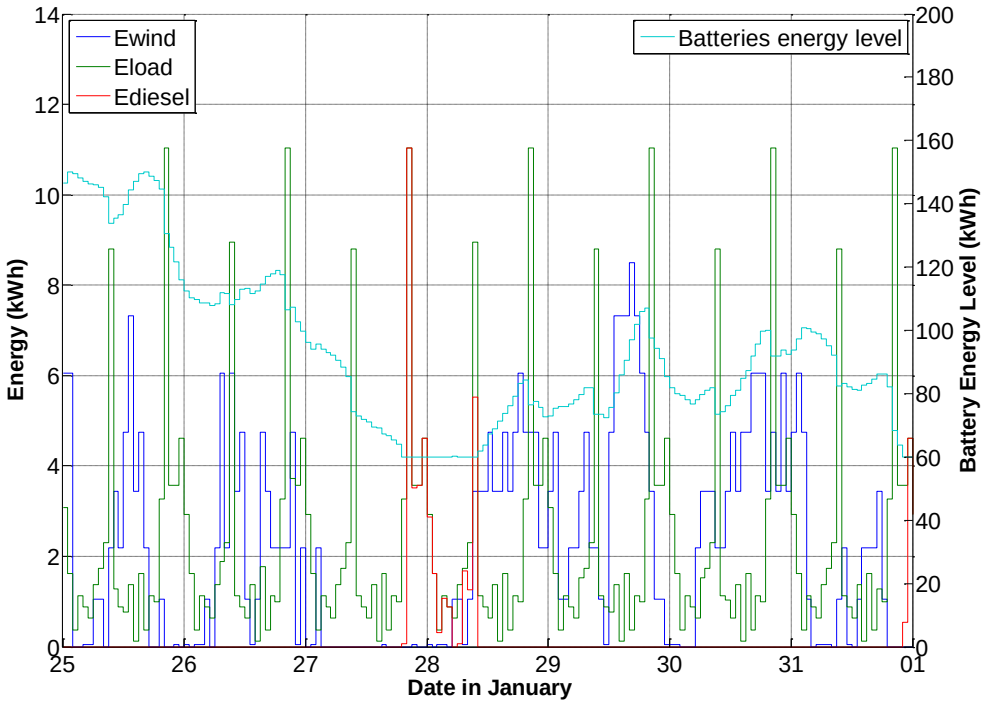

Figure 3.17: Energy flow within the hybrid system during low wind period

Few scenarios (with different battery capacities) were selected to demonstrate the yearly batteries SOC cycles. Figure 3.18 shows the yearly batteries SOC cycling with installed battery capacity of 200 kWh, 155 kWh, 105 kWh and 55 kWh, respectively. Intuitively, the batteries discharge and reach the allowable DoD level more

frequently as the installed battery capacity is reduced. The frequent charge and discharge cycles experienced by the 55 kWh batteries are more detrimental to its lifetime, compared to larger installed battery capacities.

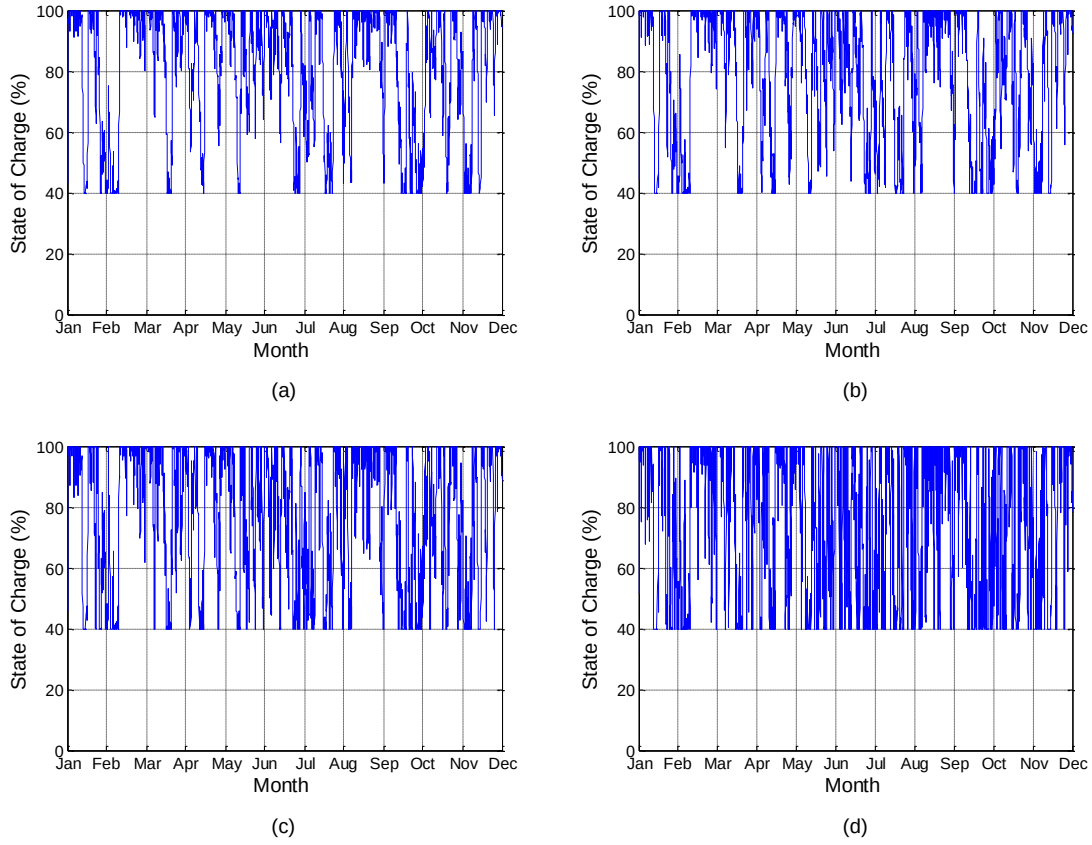

Figure 3.18: Yearly batteries SOC for a) 200 kWh, b) 155 kWh, c) 105 kWh and d) 55 kWh battery installed capacity (three households)

Figure 3.19 shows the diesel generator's operating capacity (in percentage of rated capacity) with installed battery capacity of 200 kWh, 155 kWh, 105 kWh and 55 kWh. It is a well-known fact that a fixed speed diesel engine needs to run at least 20-40% of its rated capacity because of technical limitations running it at lower loads in addition to the economics of fuel utilisation [90]. Fortunately, most of the time, the diesel generator is operating at more than 20% of its rated capacity for all simulated scenarios. Furthermore, it is observed that the diesel generator runs more frequently as the installed batteries capacity decreases.

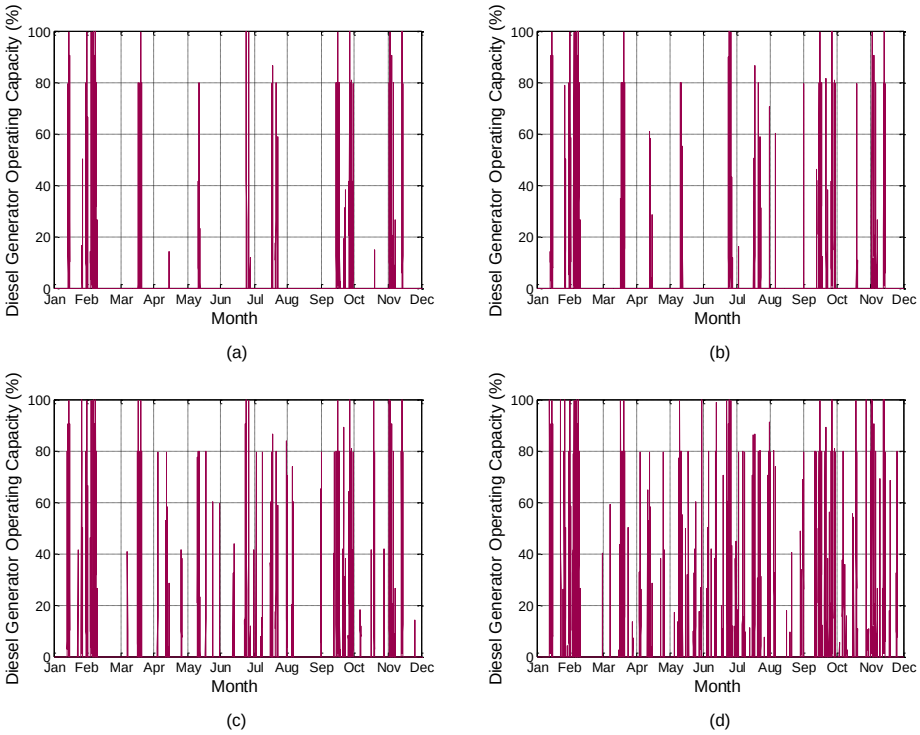

Figure 3.19: Yearly diesel generator operation for a) 200 kWh, b) 155 kWh, c) 105 kWh and d) 55 kWh battery installed capacity (three households)

Based on the abovementioned analysis, it seems more beneficial for a hybrid system to be sized with a larger battery storage capacity to achieve less frequency charge and discharge sequence and to reduce the start-stop process of the diesel generator. However, a balance should be made between the use of diesel generator and the size of batteries capacity, considering the substantial initial investment and also long term economics of the system. From the author's point of view, the optimum results computed from Figure 3.16 represents the lowest life-cycle cost and at the same time demonstrates a balance in diesel generator and batteries utilisation.

3.3.5 Hybrid System Configuration Analysis

In this section, the financial attractiveness of a hybrid wind-diesel-battery system is compared with diesel generator only system and wind-diesel system. A scenario with an average fixed diesel price of 121.70 pence per litre is simulated. The COE and performance comparison is tabulated in Table 3.4. The COE is reduced by more than 50 % when the wind turbine is coupled to the diesel generator. The incorporation of a

properly sized battery system further reduces the COE by approximately half compared to the wind-diesel system. This demonstrates that a wind-diesel-battery system is a viable off-grid power system solution from the economics perspective. In addition, the wind energy is better utilised as the battery can store excess energy for later use, resulting in lower renewable energy being wasted. This is also indicated by the higher RESF for the wind-diesel-battery systems.

As mentioned previously, it is worth investigating the effect of diesel price on the system sizing. If the diesel price does not change in the future, the computed COE is lower than the case whereas diesel price is forecasted to increase linearly. Nevertheless, the computed battery capacities are the same for both cases. This is due to the small average diesel price difference (26.76 pence) between both cases. In all cases, the diesel generator is sized to meet the peak load demand when the wind speed is insufficient for power generation and the stored energy in the battery is fully utilised. Nonetheless, the diesel generator capacity can be reduced if an optimal energy management system is used. For instance, the diesel generator can be used to charge the batteries in earlier hours so that the peak load can also be supported by the batteries.

System Configuration	COE (£/kWh)	Excess energy (%)	RESF	PRG	Battery capacity (kWh)	Diesel Gen capacity (kW)
Diesel generator only system (linearly increase diesel price)	3.04	0	0	0	0	11
Wind-diesel system (linearly increase diesel price)	1.36	69.2	0.608	1.98	0	11
Wind-diesel-battery system (fixed diesel price)	0.60	43.9	0.934	1.98	150	11
Wind-diesel-battery system (linearly increase diesel price)	0.64	43.9	0.934	1.98	150	11

Table 3.4: Optimal sizing for PV alone, wind alone and PV-wind hybrid systems in Bishopton (three households)

3.4 Summary

This chapter has given some insight and considerations that need to be taken into account when sizing storage capacity for hybrid wind-diesel-battery systems. The described methodology managed to take into consideration the peaks and troughs of a wind profile. The hybrid wind-diesel-battery system is justified to be a feasible

solution and it generates a lower COE compared to the diesel generator only and wind-diesel generator systems. More complex modelling and hardware testing are needed if a more accurate estimation of batteries and diesel generator sizing is desired. Finally, the developed GUI can potentially be employed as a tool for project managers to size the hybrid system accordingly for various climates and load demand characteristics. In the next chapter, a slightly different aspect of the hybrid system is focussed, which is the modelling of a complete hybrid system using the Simulink software. The system performance in terms of electrical point of view can be investigated through the use of physical modelling, which is available in Simulink as part of the MATLAB product.

Chapter 4 Hybrid System Modelling and Simulation

In order to perform detailed analysis of the hybrid system, simulation models have been created. The hybrid system model was developed in MATLAB-Simulink, based on commercially available components. In this project, bi-directional battery inverters are utilised to form an isolated three-phase grid. A fixed speed wind turbine and a diesel generator connect to the AC grid. This chapter describes in detail the modelling and simulation of individual components of the hybrid system. Finally, a simulation of the full system model is carried out.

4.1 Sunny Island Bidirectional Inverter

In this thesis, the bi-directional battery inverter Sunny Island (SI) 8.0H was chosen to form the three phase isolated grid. It is important to note that some information used to model the SI 8.0H refers to previous models of SI inverters which are similar in design and functionality. The functionalities and key components were identified before modelling work was carried out. First of all, the SI inverters have three different operating modes [182]. They are the grid-tied mode, the grid forming mode and the droop-mode. In the grid-tied mode, the inverters follow the voltage and frequency defined by an external power source. This can be a diesel generator or the utility grid. In this case, the SI inverters control the current they draw from the grid to charge the battery. In contrast, they keep the grid voltage and the frequency at a constant level in grid-forming mode. A grid former is considered as a voltage source. In this operating mode, there are no other components within the grid that control the voltage or the frequency [182]. Parallel operation with the utility grid or diesel generator with droop control is not possible in this mode. Other grid components operating in parallel with the grid-forming inverter are considered to be current sources [122]. Finally, the droop mode allows parallel operation of several SI inverters and grid-forming power sources for instance diesel generator.

The droop control method is known to enable distributed converters to operate independently and autonomously without relying on intercommunication links [183].

Such a system will behave in many respects similarly to the conventional large utility grid. If the available power on the AC bus is higher than the demand, the inverters will operate as active rectifiers and charge their batteries, allowing the AC frequency to rise marginally. On the other hand, if the demand is larger than the available power, the deficit will be fed via the inverters, slightly reducing the AC frequency [182]. The focus of this thesis is on the droop mode of the SI inverters which will be explained in detail later. The AC and DC electrical specifications of the SI 8.0H (single unit) are given in Table 4.1 and Table 4.2 respectively [54]. Three units of the SI 8.0H (rated at 18 kW) are needed to form the three-phase grid and provide the wind turbine start-up current.

Parameters	***Values***
Rated Power	6,000 W
Maximum AC power	12,000 W
AC power for 30 minutes at 25°C	8,000 W
AC power for 5 minutes at 25°C	9,100 W
AC power for 1 minute at 25°C	9,600 W
Maximum AC power for 3 seconds at 25°C	11,000 W
Maximum connectable power of the PV inverters*	12,000 W
Maximum connectable power of the wind power inverters*	6,000 W
Rated grid voltage	230 V
AC voltage range	202 V … 253 V
Rated frequency	50 Hz
Frequency range	45 Hz … 65 Hz
Frequency tolerance of the set range	±5 Hz
Rated current	26.1 A
Maximum output current as a peak value for 60 milliseconds	120 A
Total harmonic factor of the output voltage	4%
Displacement power factor cosφ	-1 … +1

Table 4.1: Sunny Island 8.0H AC Specifications

* For every 1,000 W of power of the wind power inverters, the maximum connectable power of the PV inverters decreases by 2,000 W.

Parameters	***Values***
Rated input voltage	48 V
DC voltage range	41 V … 63 V
Rated DC charging current	115 A
Rated DC discharging current	136 A
Maximum battery charging current	140 A
Battery type	Flooded Lead Acid, Valve Regulated Lead-Acid
Battery capacity range	100 Ah … 10,000 Ah
Recommended minimum battery capacity C10	250 Ah
Recommended minimum battery capacity C10 for every 1,000 W of power of the AC sources in the stand-alone grid*	100 Ah

Table 4.2: Sunny Island 8.0H DC Specifications

* For every 1,000 W_p in PV plants

Figure 4.1 shows the principle structure of the SI 4500 battery inverter [122] [184], which is a predecessor of SI 8.0H. The SI 4500 inverter requires a nominal DC input voltage of 60 V, whereas SI 8.0H has a rated DC input of 48 V. In this work, the inverter structure shown in Figure 4.1 is adopted and assumed to be the same as the SI 8.0H, except that the nominal battery voltage is 48 V for the SI 8.0H. The battery is connected to a bidirectional Ćuk-Converter which boosts the DC voltage of the battery to a higher level [123]. The single phase AC voltage is obtained by inverting the DC voltage via the single phase inverter. From the literature [122], the topology used for the inverter is a bridge circuit. In addition, from the Sunny Island 8.0H's user manual [54], it is able to perform synchronisation with external power source. It can be concluded from the literature that an SI inverter mainly consists of a bidirectional Ćuk converter, a bi-directional inverter and a synchronisation controller. Modelling for each of these components will be discussed in detail in the following sections.

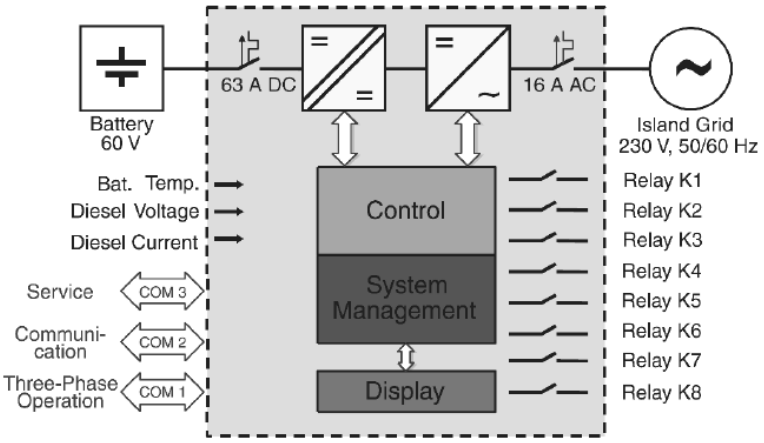

Figure 4.1: Structure of previous Sunny Island 4500 battery inverter [122]

The SI 8.0H utilised in this project works with a battery DC voltage of 48 V and having the same AC output voltage of 230 V. Based on this available information, the stepped up DC voltage of the Ćuk converter can be calculated with the assumption that the inverter is working with a modulation index, $m = 0.8$.

4.1.1 Bidirectional Ćuk Converter

The inverter utilises a Ćuk converter (shown in Figure 4.2) to step up the battery voltage from 48 V to 800 V and allow the power flow in both directions. The Ćuk converter can be synthesised by cascading the boost converter, and buck converter [185]. It comprises an input inductor L_1, an energy transfer capacitor C_1, a filter inductor L_2, a filter capacitor C_2, a switching device (for example MOSFET) and a diode. The capacitor C_1 is used as the main energy storage element and it transfers energy from L_1 to L_2 via the commutation of the switching device and the diode. The operation of the Ćuk converter can be analysed in two states. When the switch is turned on and the diode is off, the energy in capacitor C_1 is discharged into the load by the inductor (L_2) current. With the switch in off state and the diode is forward biased, capacitor C_1 is charged via inductor , L_1 [186].

An important advantage of this topology is the continuous current at both the input and output of the converter [186]. The continuous output current of the Ćuk converter ensures the inverter to be able to draw current more consistently. This enables the inverter's controller parameters to have a wider margin during the tuning

process. On the contrary, it requires a high number of reactive components and it incurs high current stresses on the switch, the diode and the capacitor C_1 [186]. It is an inverting converter, so the output voltage is inversed polarity with respect to the input voltage. In continuous conduction mode (CCM), the voltage transfer function of the Ćuk converter is as shown in equation 4.1 [187]. Detailed operation and steady-state analysis are presented in [123] and [187].

$$\frac{V_{\text{out}}}{V_{\text{in}}} = \frac{-D}{1-D} \tag{4.1}$$

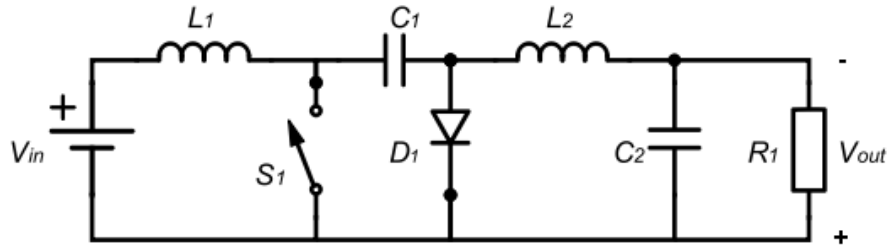

Figure 4.2: Schematic of unidirectional Ćuk converter

In order to allow bidirectional power flow, diode (D_1) from Figure 4.2 needs to be replaced with an active switching device, resulting in a circuitry shown in Figure 4.3.

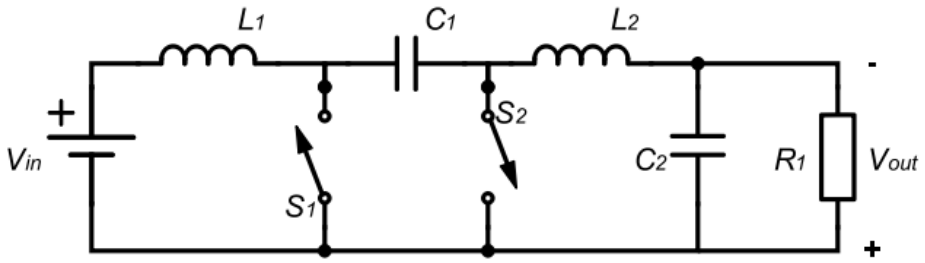

Figure 4.3: Schematic of bidirectional Ćuk converter

The control topology of the bidirectional Ćuk converter adopted in this work is voltage-mode control [186] [188], as depicted in Figure 4.4. It is a closed loop control system with negative feedback. The output DC voltage of the Ćuk converter tracks the desired reference voltage. The converter output voltage is feedback and subtracted from the desired reference voltage, producing an error to the proportional-integral-derivative (PID) controller. A control voltage is produced and compared

with the high-frequency sawtooth waveform. The comparator generates a pulse width modulation (PWM) signal which is fed to the switches in the Ćuk converter. Note that the PWM signal and its complementary form are fed to switches, S_1 and S_2, respectively. The duty ratio of the PWM signal changes over time in such a way that the error between the reference voltage and the output voltage of the Ćuk converter is minimal. The PID controller reacts fast to changes in the converter output voltage, thus voltage-mode control provides good load regulation [186].

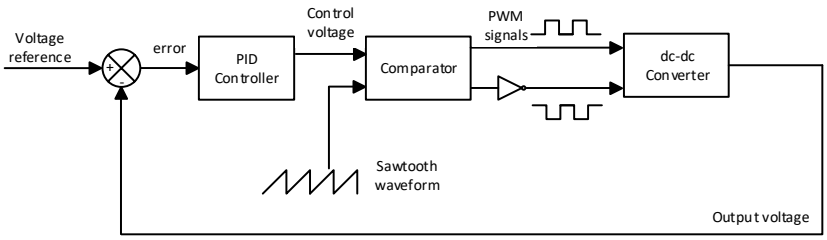

Figure 4.4: Control of the bidirectional Ćuk converter

The Ćuk converter Simulink implementation is shown in Figure 4.5. It consists of three main sections; Ćuk converter circuitry, a controller which controls the switching on and off of the MOSFETs S_1 and S_2 and the DC load. Its parameters were designed and selected as shown in Table 4.3. Note that the PID gains were determined manually by trial and error method due to time constraint. If time is permitted, a more rigorous approach would be used to tune the parameters, such as the Ziegler-Nichols method [189].

It is noted that the Ćuk converter modelled in this work was based on an unrealistic trial and error approach with a boost ratio of approximately 20 (48 V to 800 V), which is also unrealistic for the converter topology shown. However, the simplistic model for the purposes of this study has little impact on the final results as the output DC voltage is maintained at about 800 V, which then becomes an input to the SI inverter. Furthermore, since inverter output is controlled by another control loops, the transient performance of the Ćuk converter may not be "seen" by the load.

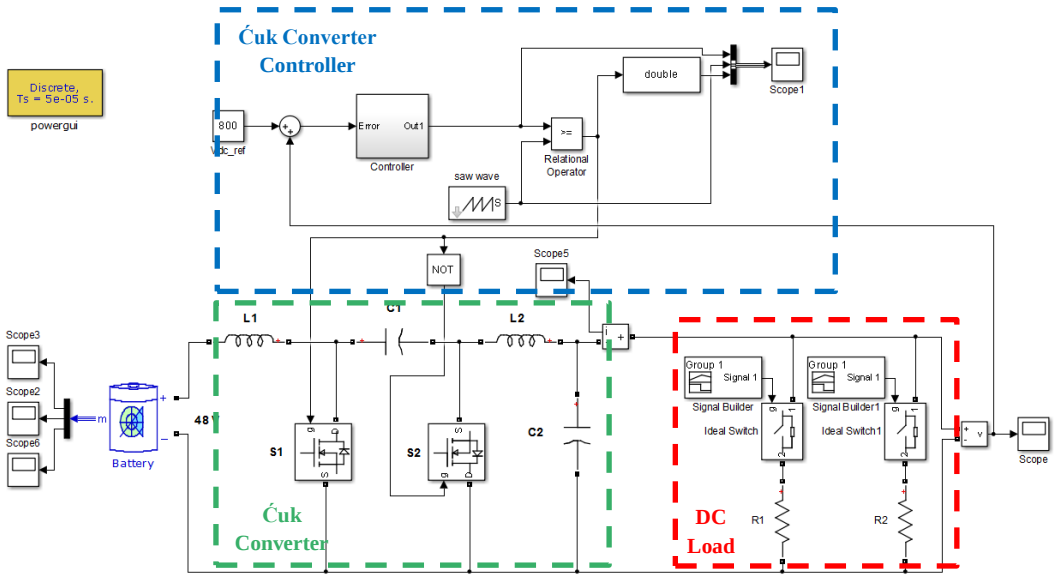

Figure 4.5: Simulink model of the bidirectional Ćuk converter

Parameters	***Values***
Switching frequency, f_s	10 kHz
Input inductor, L_1	6.3 mH
Output inductor, L_2	31.6 mH
Input capacitor, C_1	25.034 mF
Output capacitor, C_2	0.165 F
Proportional constant, K_p	0.0001
Integral constant, K_i	0.019
Derivative constant, K_d	0.012

Table 4.3: Ćuk converter parameters

In this work, the built-in battery model which is available in SimPowerSystems Simulink library [190] is used with the hybrid system simulations. It is a generic dynamic rechargeable battery model which provides a set of predetermined charge behaviour for lead-acid, lithium-ion, nickel-cadmium and nickel-metal-hydride. The model was validated experimentally and it claimed to have a maximum error of 5%

(when SOC is between 10% and 100%) for charge (current between 0 and 2C) and discharge (current between 0 and 5C) dynamics [190]. Nevertheless, several assumptions were made in the battery modelling.

- The internal resistance is assumed to be constant during the charge and discharge cycles and does not vary with the current amplitude.
- The parameters of the model are deduced from the discharge characteristics and assumed to be for the same for charging.
- The capacity of the battery does not change with the current amplitude (no Peukert effect being taken into consideration).
- The self-discharging of the battery is not represented.
- The battery has no memory effect.

A more detailed battery model can be used instead. However, the increase in complexity would require more computational effort which may lead to longer simulation time. For the purpose of this work, the simple battery model in Simulink is appropriate as the analysis performed hereafter may be considered from a system point of view whilst the detailed battery behavioural characteristics are beyond the scope of this work. The predefined battery parameters in the following simulations are tabulated in Table 4.4. In order to reduce the simulation period while at the same instance being able to observe the dynamics of certain parameters such as voltage, current, and battery SOC, a relatively smaller battery capacity (15 kWh) compared to Chapter's 3 optimally sized batteries is adopted in this chapter.

Parameters	***Values***
Nominal voltage	48 V
Rated capacity	15 kWh
Initial SOC	50%
Maximum capacity	325.52 Ah
Fully charged voltage	52.26 V
Nominal discharge current	62.5 A
Internal resistance	0.001536 Ω

Table 4.4: Lead-acid battery parameters

In order to test the Ćuk converter's capability of performing power flow in both directions, positive and negative loads are used in this case. Initially, both R_1 = 80 Ω (positive load) and R_2 = -40 Ω (negative load) were disconnected. The positive load draws current from the battery whereas the negative load emulates current flowing from the load to the battery. Positive and negative resistive loads were used instead of DC voltage sources due to the fact that the resistive loads do not interfere the Ćuk converter's output voltage. The total simulation time is 500 seconds (s). At 80 s, R_1 was connected. At 200 s, R_1 was disconnected and R_2 was connected.

Figure 4.6, Figure 4.7 and Figure 4.8 show the output DC voltage, load current and battery SOC respectively. The converter took approximately 50 s to reach a steady state of 800 V at its output. At 80 s, the load R_1 was connected, drawing 10 A from the converter as shown in Figure 4.7. During this period, the battery SOC dropped linearly. At 200 s, it can be observed that the current was flowing in the opposite direction, with a magnitude of 20 A. This was due to the connection of the negative load of 40 Ω. Thereafter, the battery SOC increased linearly as shown in Figure 4.8. Thus, the simulation has demonstrated that the designed Ćuk converter is capable of stepping up and stepping down the voltage, further allowing power flow in both directions with a minimal transient.

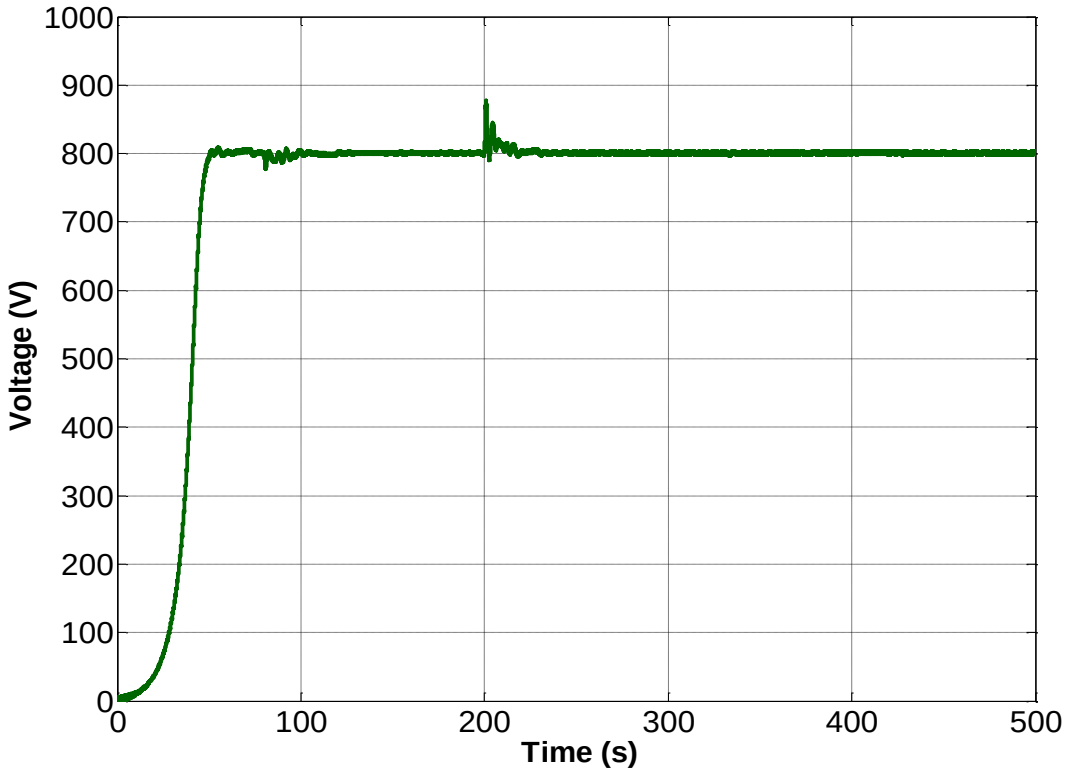

Figure 4.6: Output DC voltage of the Ćuk converter

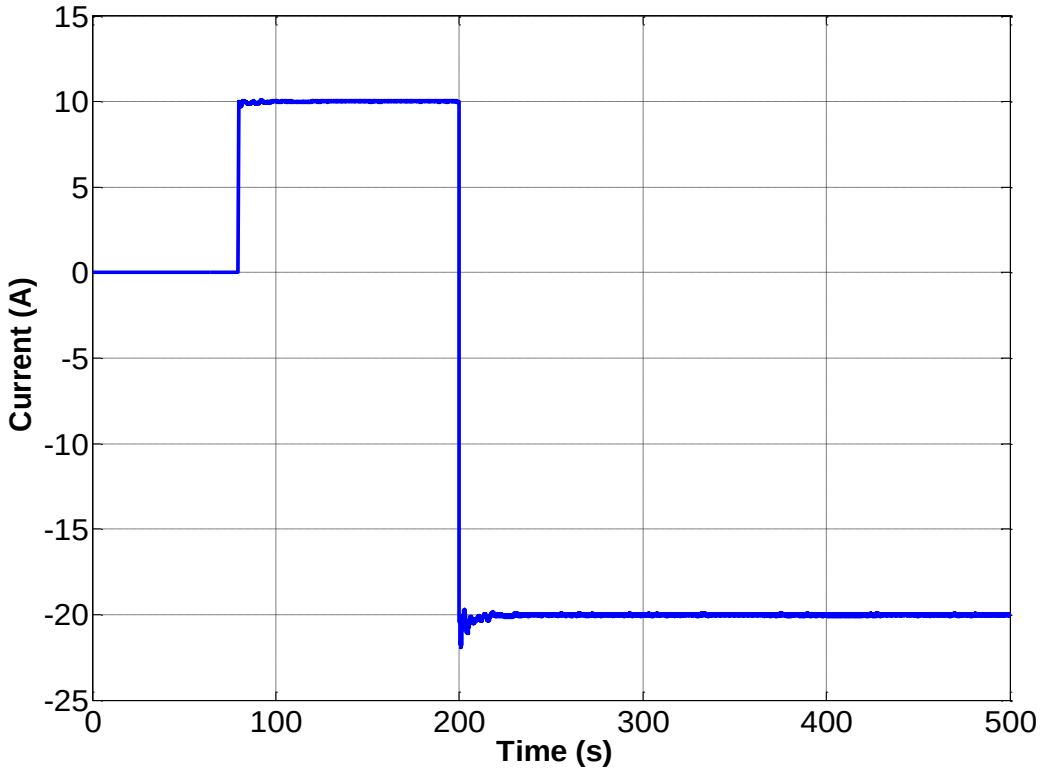

Figure 4.7: Load current

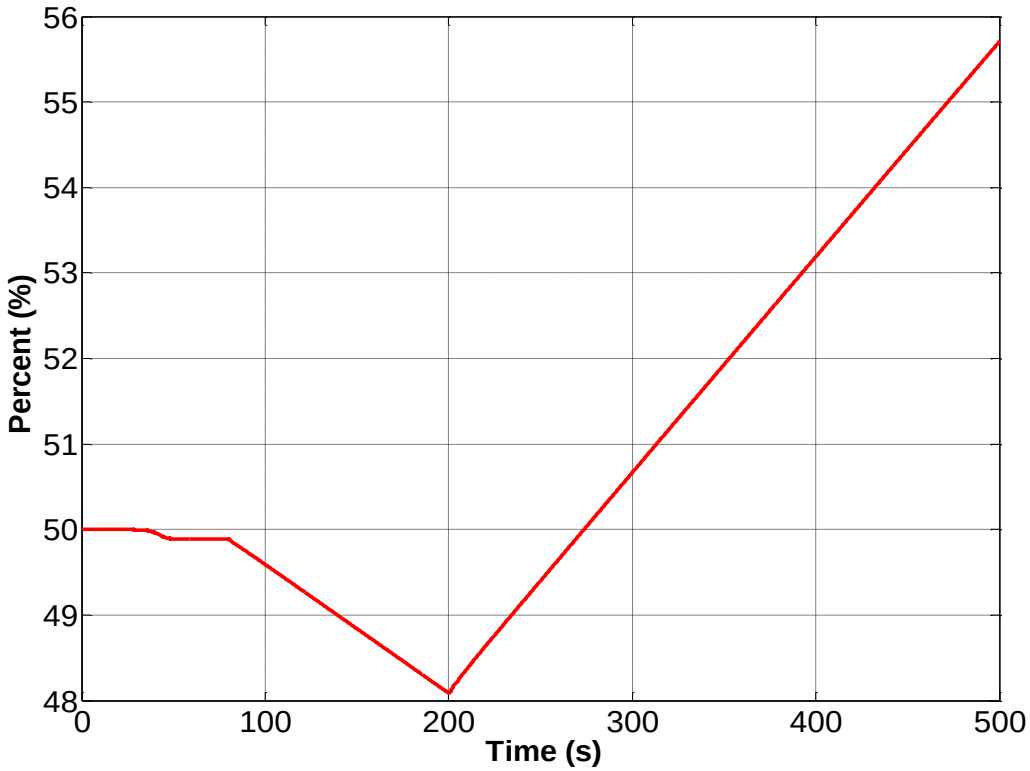

Figure 4.8: Battery state of charge

4.1.2 Bidirectional Inverter

An inverter is an electrical device which changes the DC to AC through the proper switching of solid-state power electronics such as gate turn-off thyristors (GTOs) or insulated gate bipolar transistors (IGBTs). Effectively, it performs the opposite function of a rectifier. Since the input is a dc voltage source, the SI 8.0H inverter is also referred as VSI. This section focuses on the control strategy for the three single-phase inverters, in which one unit works as the master device and the other two units are slaves. As mentioned before, the droop control of the SI inverter will be the focus of this work. The idea behind this control philosophy is to emulate the conventional behaviour of a synchronous machine by controlling the voltage and frequency on the AC system [191]. The measured voltage and frequency quantities can be used for coordination, thus replacing the need for expensive communication lines [124] [192]. An increase in the active/reactive power demand is accompanied by a reduction in the frequency/voltage. However, the difference between the power electronics based inverter and the conventional synchronous machine is the absence of machine inertia

for the case of the former. Fortunately, this is a desirable property as it reacts to load changes or variations quickly, hence reducing the transient time.

When at least two VSIs are paralleled, it uses two droop control equations to deduce its converter reference frequency ω and voltage amplitude V from the measured active power, P and reactive power, Q, respectively. These equations are shown in (4.2) and (4.3) and their corresponding illustration is shown in Figure 4.9.

$$\omega = \omega_0 - K_\mathrm{P} \times P \tag{4.2}$$

$$V = V_0 - K_\mathrm{Q} \times Q \tag{4.3}$$

where

ω_0 – frequency reference at no load
V_0 – voltage magnitude reference at no load
K_P – active power drooping gradient
K_Q – reactive power drooping gradient

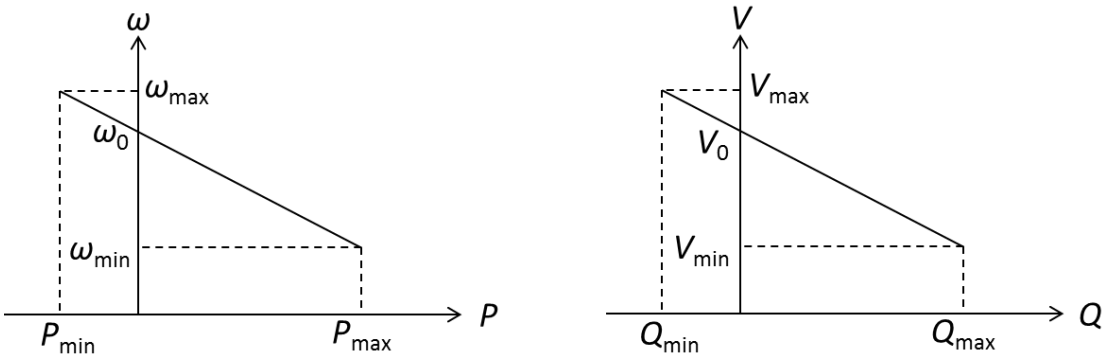

Figure 4.9: P-ω and Q-V droop characteristics

At idle frequency (ω_o), the inverter active power output is zero. This corresponds to a no load condition. An increase in the load power will cause frequency reduction as demonstrated from the negative slope, whilst power reduction will lead to a rise in frequency. In order to keep the magnitude and frequency of the voltage within the acceptable bounds, the gradients K_P and K_Q are to be less gradual. However, this would compromise the load sharing accuracy. The best trade-off would therefore require a careful study of the particular system, before tuning K_P and K_Q accordingly [63]. Fortunately, the SMA's SI inverter droop settings are available in the literature and are referenced as shown in Figure 4.10.

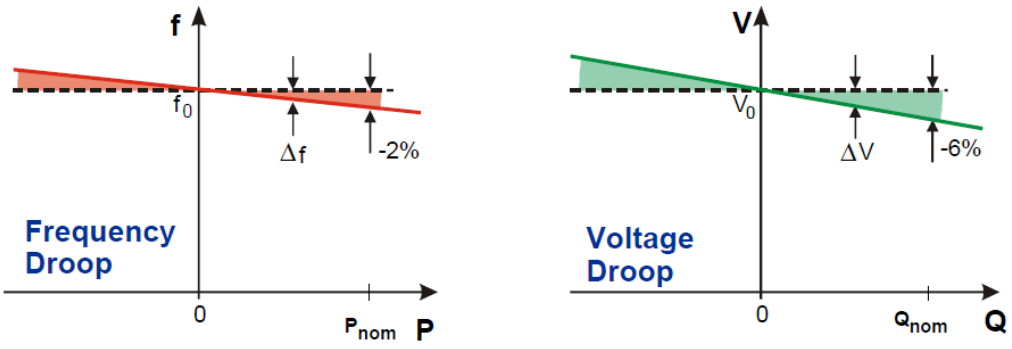

Figure 4.10: SMA Sunny Island droop characteristics [122]

If a cluster of VSI operates in parallel during autonomous mode, frequency variation leads automatically to power sharing. For a system with *n* inverter(s), the following equality holds [193]:

$$\Delta P = \sum_{i=1}^{n} \Delta P_i \tag{4.4}$$

where ΔP_i being the power variation in the *ith* inverter. The frequency variation of a single inverter can be computed as:

$$\Delta\omega = K_{Pi} \times \Delta P_i \tag{4.5}$$

This shows that when multiple converters operate simultaneously within a system, the total load shared by all the units is dependent on their individual droop settings, K_{Pi}. It is important to state that this principle effectively creates an efficient communication link among the local DGs in terms of power sharing and eliminates the need for communication systems [27]. This reduces the system's complexity and maintenance requirements, which is ideal for isolated self-sustaining communities. Similar thoughts can be applied to voltage/reactive power control mode which is also based on the droop characteristics [191]. However, as the voltage has local characteristics, network cable impedances prevent precise reactive power sharing within a network.

The control structure of the SI inverter is shown in Figure 4.11. As aforementioned, the three-phase voltages are formed with three single-phase inverters, in this case which are represented by three rows. The first column shows the voltage and current measurement of each phase. The second column, 'PQ Computation' block computes

the active and reactive power based on the measured voltage and current [191] [194] [195] [196]. This can be done through the power transfer relationship in the d-q reference frame after doing Park's transformation [197]. The measuring stage introduces a delay for decoupling purposes [191]. Another output signal is the measured power converter's output current. The third column contains the droop controllers of the SI, a master droop controller for phase A and a slave droop controller for phase B and phase C respectively. The master droop controller generates voltage references for each phase from the droop characteristics. The synchronising signals for phase B and C are generated from master's droop controller and being sent to both slave's droop controller respectively [122]. These synchronisation signals contain voltage phase and frequency information. The reference voltages are fed to the inner current loop and outer voltage loop. These control loops consist of PID controllers which effectively minimise the errors between the measured voltage and current from the power converter output and their reference values. Subsequently, the computed three-phase voltages are the reference signals to the PWM generator block which controls the switching sequence of the switching devices GTOs/IGBTs, generating AC voltage [191] [194] [195]. Finally, the voltage which contains harmonics needs to be cleaned by employing appropriate filters which typically constructed using several series and parallel LC filter sections. The described inverter control topology is generally used in autonomous operation of microgrids and parallel operation of the inverters [198] [199] [200] [201].

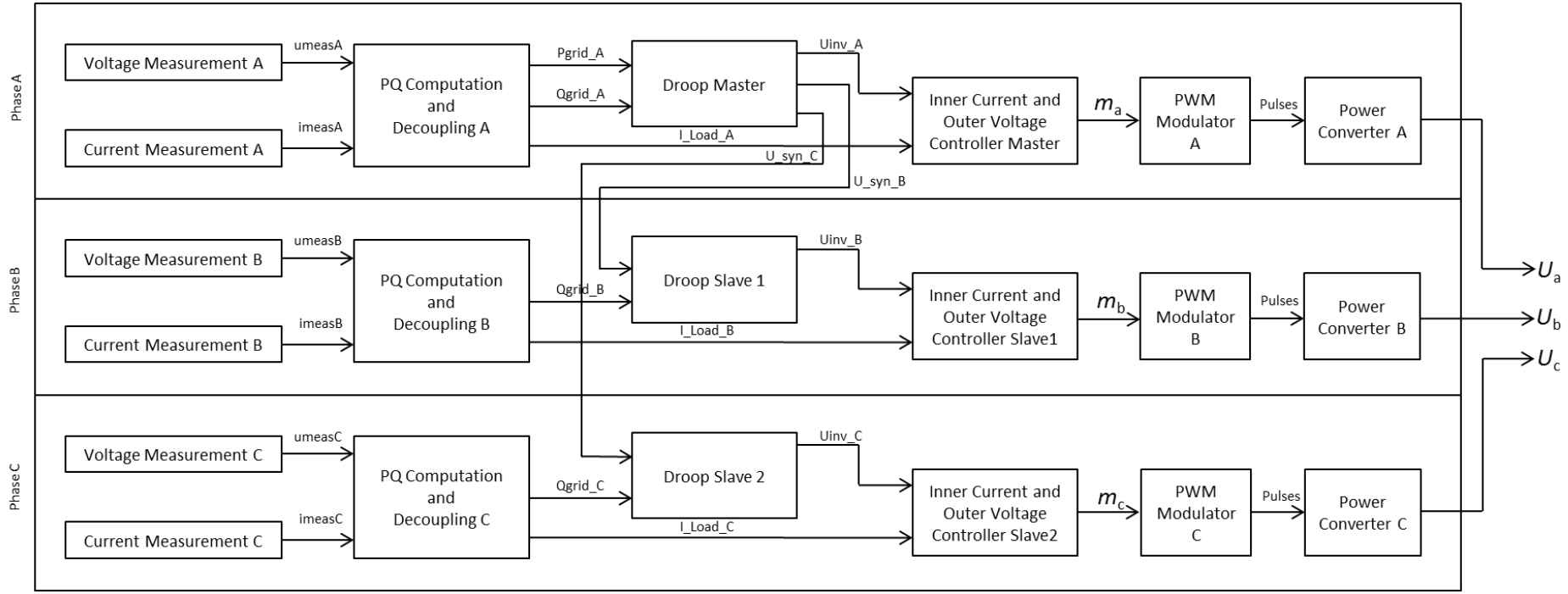

Figure 4.11: SMA Sunny Island main structure [122]

A three-phase SI Simulink model was built and tested with the load configuration as shown in Figure 4.12. Each unit of the SI inverter model is represented as Figure 4.13. The estimated parameters are tabulated in Table 4.5. At this stage, the synchroniser is not included in the model. The objective of this simulation is to analyse the performance of the model when operating in no load, maximum balanced load, and unbalanced load conditions. These represent the extreme cases. The load switching sequence is portrayed in Table 4.6. At 100 s, a load of 1 kW was switched on, followed by 17 kW load switched on at 150 s for 30 s. This has resulted in the SI inverters to operate at rated condition, i.e. 18 kW between 150 s and 180 s. All the loads were turned off at 180 s. Finally, a pre-set unbalanced load was turned on at 200 s. It is noted from previous studies that the Ćuk converter needs approximately 50 s to stabilise its output DC link. Therefore, the following simulation results were recorded after the DC link voltage was being established. Note that the required 50 s settling time is unique to this model and may not be representative in a real converter.

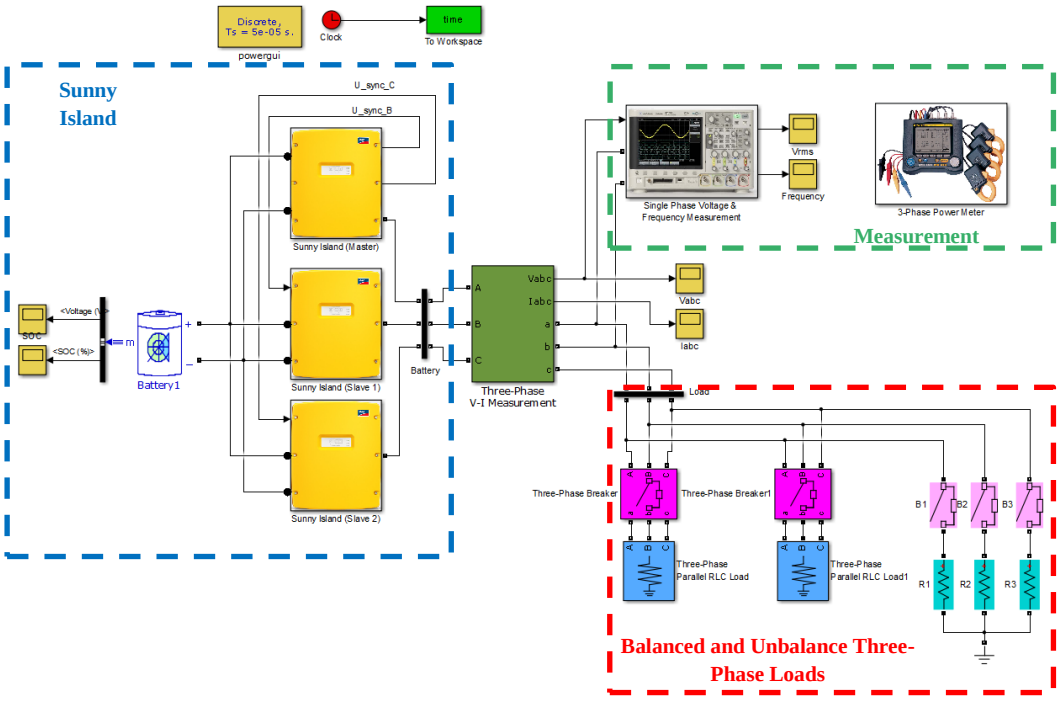

Figure 4.12: Simulink model of the Sunny Island Inverter with loads

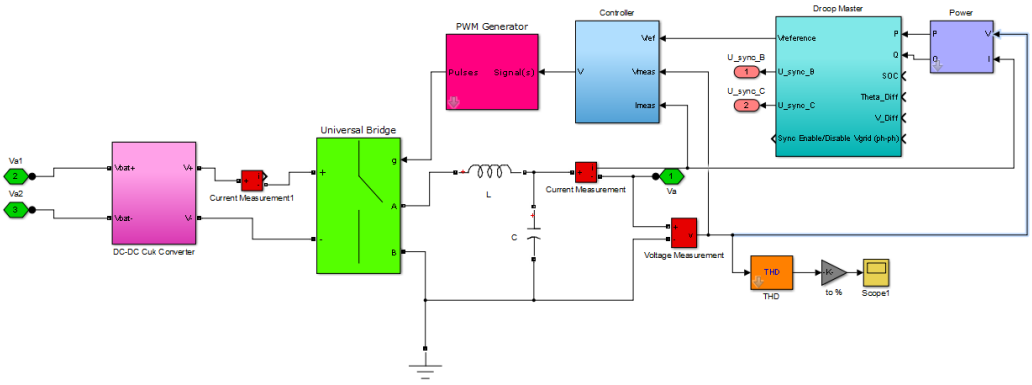

Figure 4.13: Detailed Simulink model of Sunny Island Inverter

Parameters	***Values***
Active power decoupling delay, T_{dp}	0.05 s
Reactive power decoupling delay, T_{dQ}	0.05 s
Active Power Droop, K_P	0.1667 x 10^{-3} rad/sW
Reactive Power Droop, K_Q	2.3 x 10^{-3} V/Var
Phase feed-forward gain, K_{ff}	-5 x 10^{-6} rad/W
Single-phase voltage peak reference, V_{peak}	325 V
PWM carrier voltage magnitude, V_s	400 V
PWM carrier frequency, f_c	1050 Hz
Inverter output filter inductor, L	21.132 mH
Inverter output filter capacitor, C	1.2 mF
Voltage controller proportional constant, K_{vp}	0.8
Voltage controller integral constant, K_{vi}	0.1
Voltage controller derivative constant, K_{vd}	10
Current controller proportional constant, K_{ip}	500
Current controller integral constant, K_{ii}	0
Current controller derivative constant, K_{id}	10

Table 4.5: Estimated Sunny Island controller parameters

Time (seconds)	0 - 100	100 - 150	150 - 180	180 - 200	200 -300
Load 1 (3-Phase balance), 1 kW	OFF	**ON**	**ON**	OFF	OFF
Load 2 (3-Phase balance), 17 kW	OFF	OFF	**ON**	OFF	OFF
Load 3a (1-phase load), 6 kW Load 3b (1-phase load), 0 kW Load 3c (1-phase load), 6 kW	OFF	OFF	OFF	OFF	**ON**

Table 4.6: Load sequence for a total simulation time of 300 seconds

The root mean square (RMS) phase voltage of the SI is shown in Figure 4.14. It was evident that there was a small voltage reduction at 100 s and a significant voltage drop was observed at 150 s which occurred due to the rise in the load demand. However, it can be seen that the voltage was kept within the statutory limits despite the load changing conditions. According to the UK Engineering Recommendation (EREC) G59 [202], the DGs should be able to operate in parallel with the distribution system (utility grid) based on the following voltage and frequency range:

Voltage range:

The maximum voltage of 258.2 V with no time limit, 269.7 V for 0.98s and of 277.7 V for 0.48s.

The minimum voltage of 204.1 V with no time limit, 188 V for 2.48s and 180 V for 0.48s.

Frequency range:

The maximum frequency 51.3 Hz with no time limit, 51.8 Hz for 89.98s and 52.2 Hz for 0.48s

The minimum frequency 47.7 Hz with no time limit, 47.2 Hz for 19.98s and 46.8 Hz for 0.48s

During islanding operation, it is also recommended the DG operations remain within the statutory limits. However, it was also mentioned that when the DGs are remote from a network voltage control point it may be required to withstand voltages outside the normal statutory limits [202]. Although this work focuses on off-grid power systems, they may be connected to the distribution system in the future and hence the recommended statutory limits should be followed as close as possible.

Figure 4.15 illustrates the frequency of the system voltage. The frequency drops negligibly at 100 s and at a higher magnitude at 150 s for the same reason, i.e. rose in load demand. It was noticeable that there are slightly more frequency fluctuations

occurring just after 50 s, where the DC link voltage began to settle. This is demonstrated in Figure 4.16. Overall, the frequency fluctuations were mainly because of the existence of harmonics which have not been entirely filtered out. However, the frequency was within the statutory limits for various load conditions. The voltage and frequency rise to their nominal values, 230 V and 50 Hz, respectively after the loads are turned off at 180 s. Based on these two performance indicators, it can be concluded that the droop characteristics for voltage and frequency were successfully implemented.

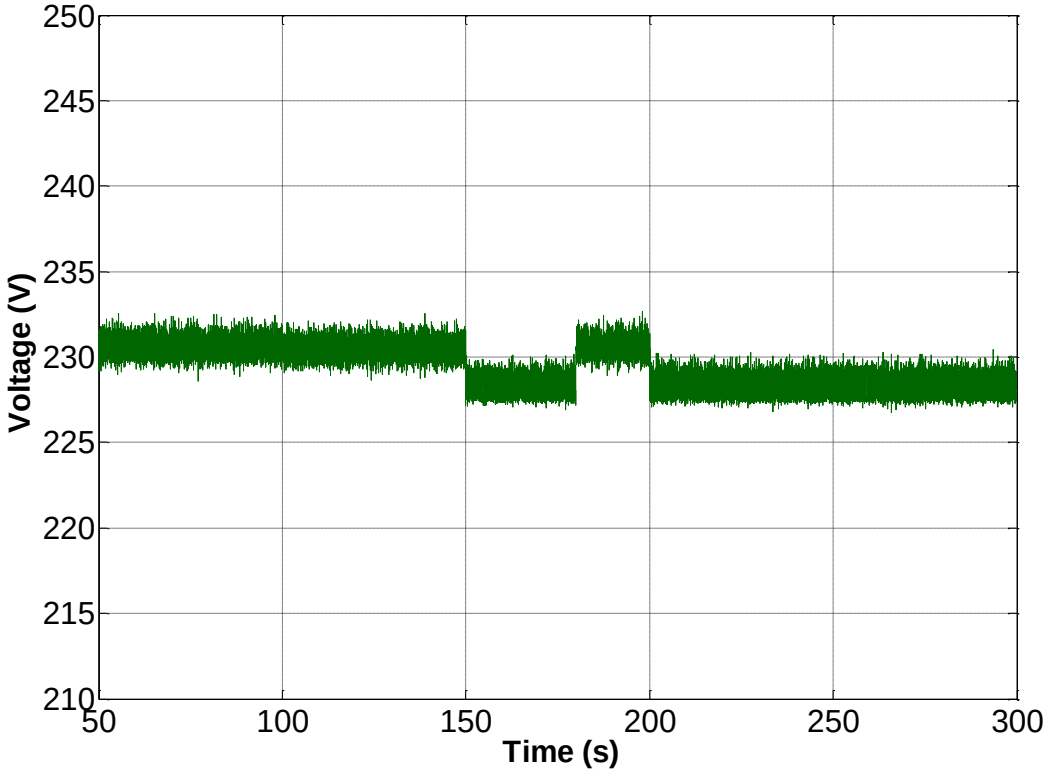

Figure 4.14: RMS voltage of the Sunny Island output

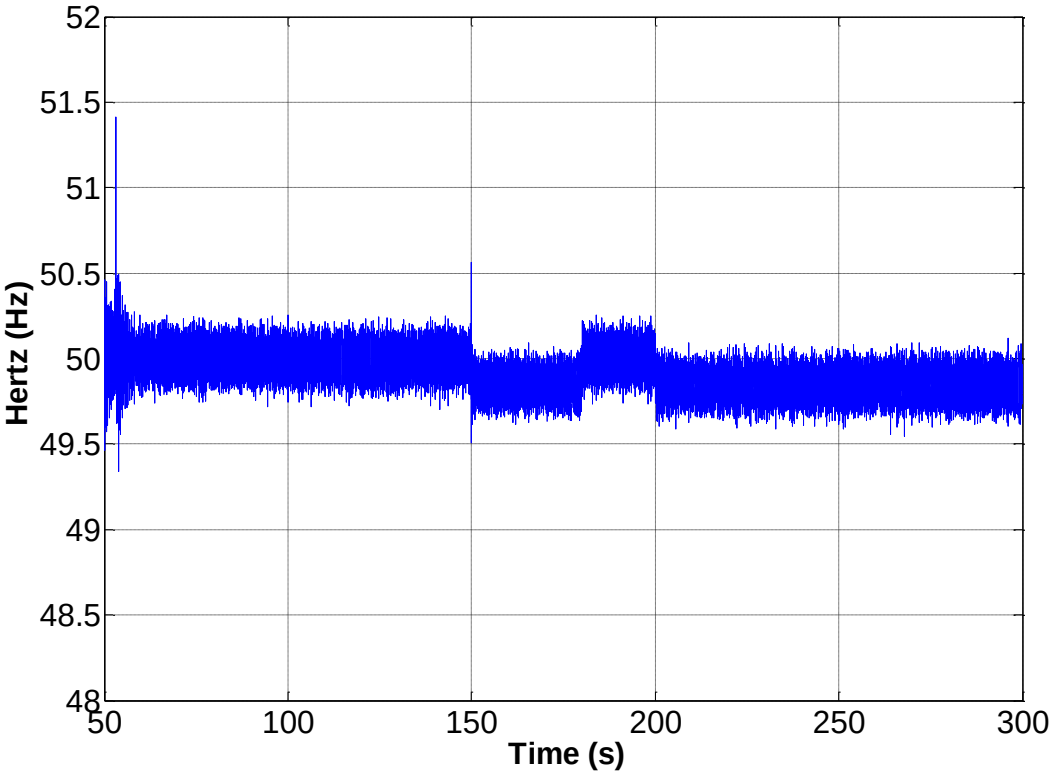

Figure 4.15: Frequency of the Sunny Island output

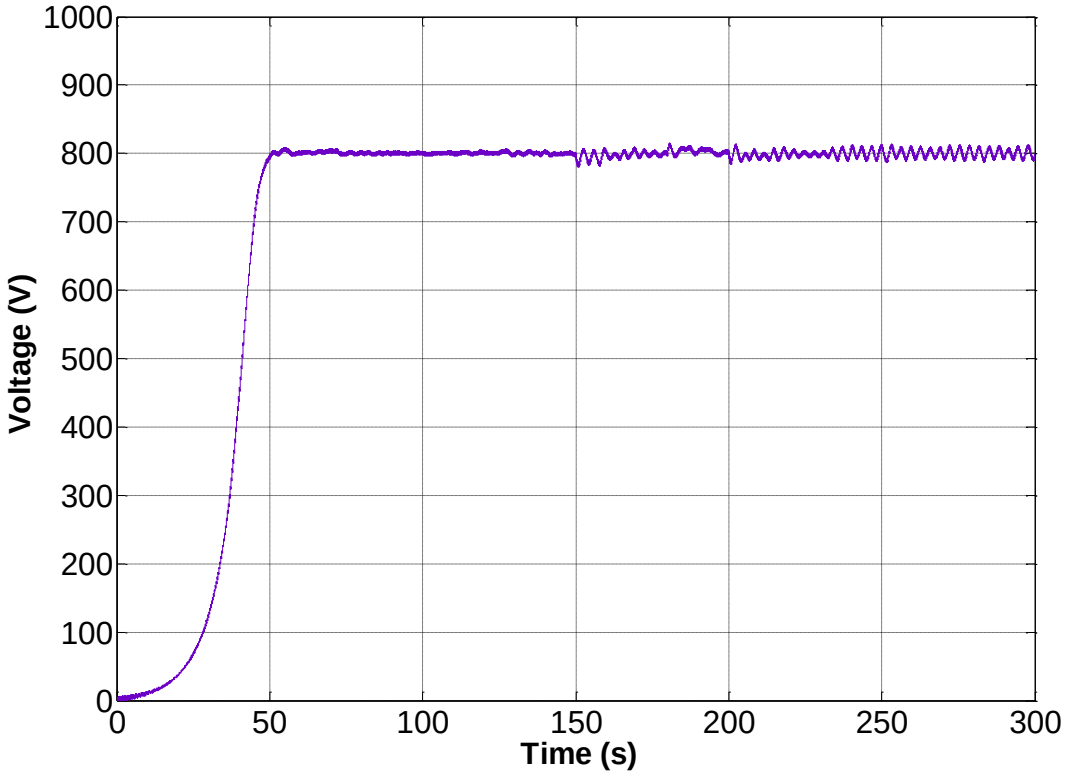

Figure 4.16: DC link voltage begins to settle at 50s

Figure 4.17 shows the steady state three-phase current waveform at no load and unbalanced load conditions. It can be clearly seen from the sinusoidal waveforms deteriorated marginally at the high-frequency edges after moving to an unbalanced load condition. This can also be attributed to the high current being drawn from the system.

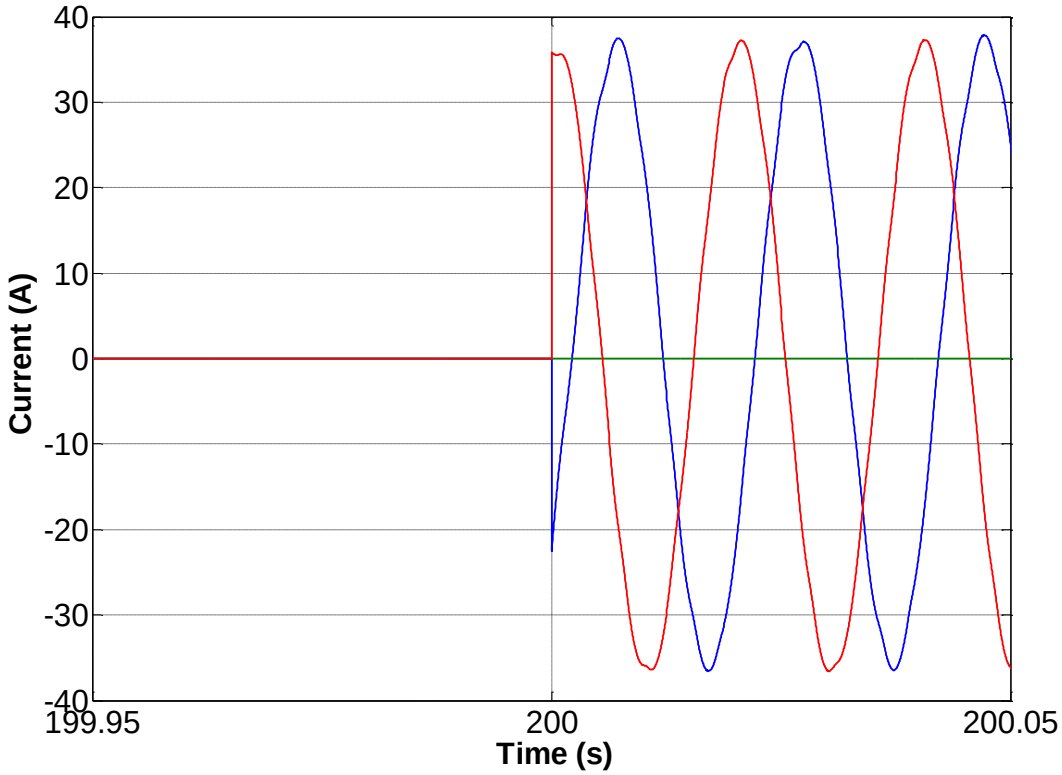

Figure 4.17: Transient from no load to unbalanced load condition

Figure 4.18 illustrates the SOC of the battery throughout the simulation period. The discharging curve is relatively linear and the steepness reflects the amount of power being drawn from the battery. Obviously, in this instance, the highest discharging rate occurred between the period of 150 s and 180 s.

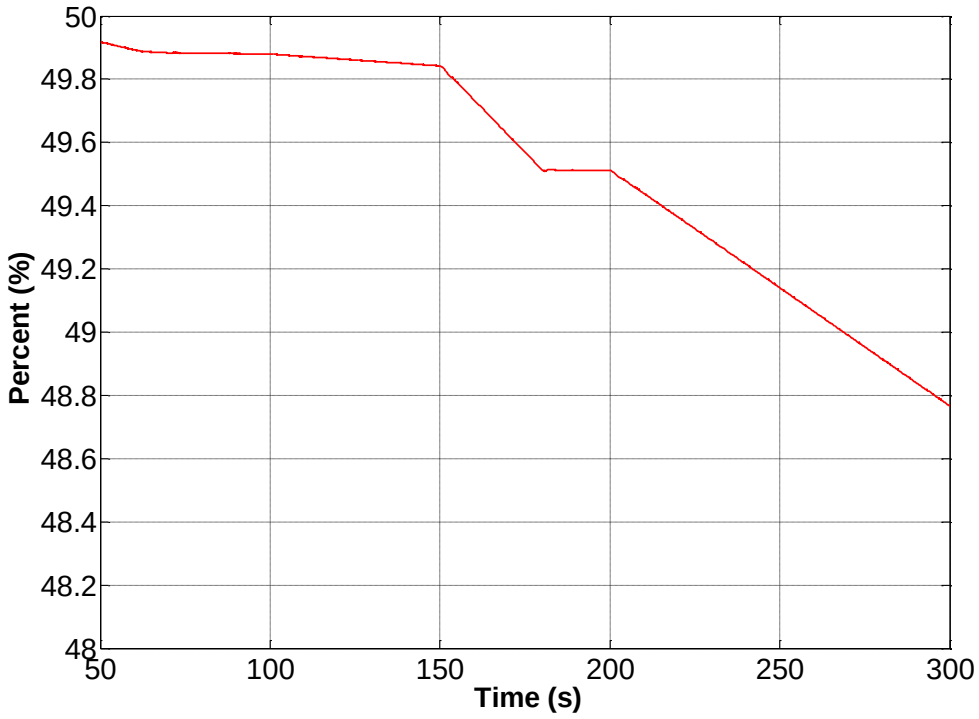

Figure 4.18: State of charge of the batteries

Figure 4.19 shows the total power dissipated by the resistive loads. Between 150 s and 180 s, a maximum load of 18 kW was supplied from the inverters. This load value is the rated power of the three-phase SI 8.H system. However, due to the drop in voltage profile as shown in Figure 4.14, the load could not dissipate its nominal power. This can be verified based on the relationship:

$$\frac{P_{dissipated}}{P_{nominal}} = \left(\frac{V_{actual}}{V_{nominal}}\right)^2 \tag{4.6}$$

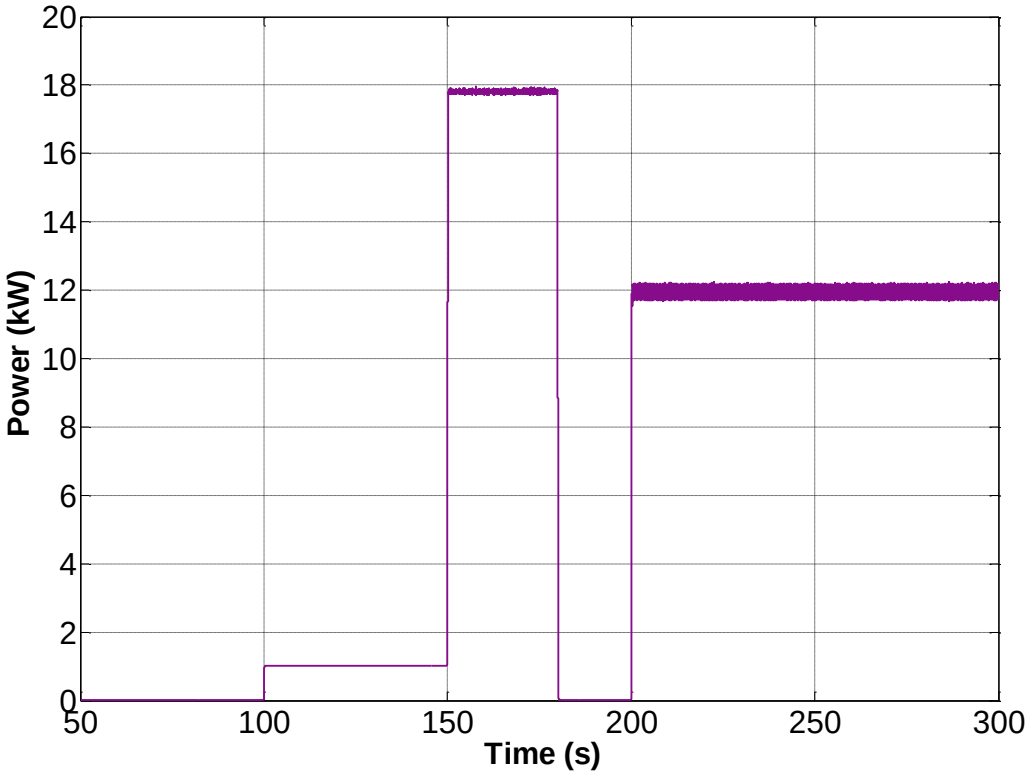

Figure 4.19: Total power dissipation by the resistive loads

4.1.3 Synchronisation Controller

A hybrid wind-diesel system can operate as a standalone wind-only system or together with a diesel generator when there is insufficient wind power generation. Switching between these two modes is an important feature for a hybrid system to operate flexibly. Particularly, synchronisation control is the key process in connecting two or more voltage sources. The synchronisation algorithm adopted in this work can be found in Appendix B.

4.2 Wind Turbine

In this work, the Gaia Ltd's 133-11kW fixed speed wind turbine was modelled. It consists of 4 main components: the blades, the step-up gearbox, the induction generator and the power electronics for grid connection. The Gaia wind turbine specifications are tabulated in Table 4.7.

Parameters	***Values***
Rotor diameter	13 m
Hub height	18.2 m
Tower type	Lattice or tubular
Rated electrical power	11 kW
Cut-in wind speed	3.5 m/s
Rated wind speed	9.5 m/s
Cut-out wind speed	25 m/s
Rotor speed range	56-62 rpm
Fixed or variable pitch	Fixed blade, variable tip
Number of blades	2
Blade type	Glass fiber
Blade tip pitch angle	90º
Gearbox	Two stage, gear ratio 1:18

Table 4.7: Gaia Wind Turbine Specifications

The theory of wind turbine aerodynamic is of importance for a designer to optimise power extraction from the wind. Its most fundamental formula is the mechanical power extraction of the rotor which is shown in equation (4.7) and the detail derivation of this formula can be found in [203].

$$P_{\mathrm{m}} = \frac{1}{2}.\rho.A_{\mathrm{R}}.V_{\mathrm{W}}^{3}.C_{\mathrm{P}}(\lambda,\beta) \tag{4.7}$$

where:

P_{m}: Rotor mechanical power (W)
ρ: Air density (kg/m^3)
$A_{\mathrm{R}} = \pi \mathrm{R}^2$: Rotor disk plan area with radius R (m^2)
V_{w}: Wind speed (m/s)
C_{p}: Aerodynamic power coefficient of the turbine

Based on equation (4.7), the converted mechanical power from a wind stream is a function of air density (ρ), the surface area of the rotor (A_{R}), the wind velocity (V_{w})

and also the power coefficient (C_p). Wind velocity has a significant influence on the power output due to its cubic property. The aerodynamic modelling to be adopted in this work can be explained by the blade element model (BEM) theory. The limitations of this theory such as wind shearing profile and tower shadow are clearly laid out in [44]. To design highly accurate models, vortex models or computational fluid dynamics (CFD) models (appropriate for unsteady aerodynamics) which are more rigorous than the BEM theory should be utilised. These highly computational models are elaborated in [204]. For simplicity and practical purposes, the BEM theory is being adopted in this modelling.

The power coefficient, $C_p(\lambda, \beta)$ is used to quantify the ratio of power extracted from the wind turbine to the theoretical power available in the wind. However, it does not represent a direct measure of the efficiency of the turbine. It is computed as a function of, tip speed ratio (TSR), λ which can be defined as equation (4.8) and pitch angle of the blades, β in degrees.

$$\lambda = \frac{R.\omega_R}{V_W} \tag{4.8}$$

where:

ω_R: Angular speed of the wind turbine rotor (rad/s)

It is worth mentioning the importance of the TSR in the design of wind turbine generators. When a rotor blade passes through the air it leaves turbulence in its wake. If the next arriving blade reaches this point while the air has yet to recover from the wind turbulence, that particular blade will not be extracting power efficiently. However, if the rotor rotates at a lower angular speed in order to avoid turbulent air and also if it is operating at a lower TSR than its optimum value, it will not be able to extract the optimum power from the wind. Therefore, the TSR is chosen to be at an optimum level so that the blades are extracting maximum power [205].

Typically, the optimal power coefficient C_p, lies between 0.4 - 0.5, while it can be derived that the theoretical maximum value of C_p is equal to 0.593, which is also called the "Betz Limit" [203]. This is an important limit because it defines the upper limit of any rotor disk type energy-extracting device that is placed in the flow of a fluid [203]. In this thesis, the C_P for the Gaia's wind turbine is derived using the

experimental data provided in a report by TUV NEL [206]. Using the available data, the λ values are derived accordingly. The C_p-λ curve is shown in Figure 4.20. It was modelled as a look-up table in Simulink. The curve of the C_p-λ characteristic demonstrates, as shown in Figure 4.20, two zero crossings:

- When λ is equal to approximately 2 (which corresponds to wind speed of about 19.5 m/s), the wind turbine is stalled and thus transfers no power, so $C_P = 0$ must also apply. In this case, the air masses flow through the turbine without being slowed down.
- When λ is about 11, the corresponding wind speed is 3.5 m/s. This is also the cut-in wind speed of the wind turbine.

Between these two points, the power coefficient is positive and it demonstrates a relatively narrow maximum of $C_{Popt} \approx 0.26$ at a tip speed ratio of $\lambda_{opt} \approx 7$. The C_p-λ characteristic is dependent on the turbine design, mainly the choice of airfoil, chord length and twist along the blade [44].

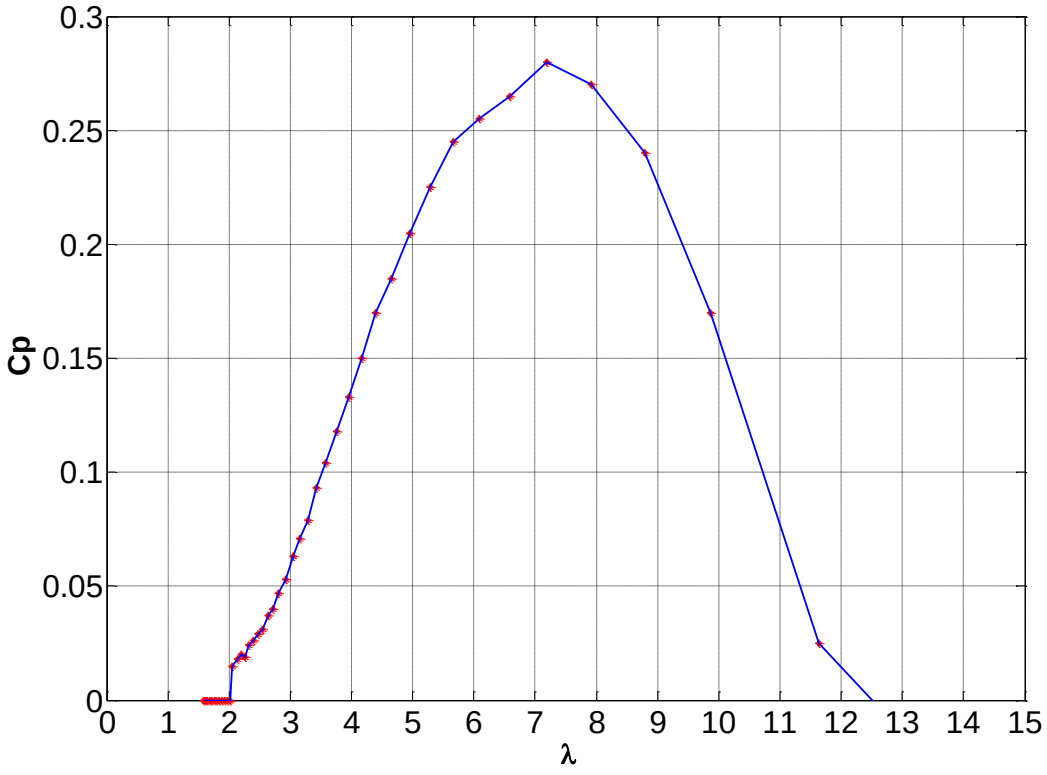

Figure 4.20: C_P-λ curve for 133-11kW turbine

The step-up gearbox is represented by a simple mathematical function with the mechanical torque at the low speed shaft and the rotational speed of the generator as inputs. A 1:18 ratio gives the rotational speed at the rotor blades; the input power at the low speed shaft is then used to calculate the mechanical torque at the high speed shaft. The generator is an 11 kW 6 pole machine. The Simulink asynchronous machine model is used and it is a state-space model to represent the electrical part and a second-order system for the mechanical part. The stator and rotor quantities are in the arbitrary two-axis reference frame. The corresponding equivalent circuit parameters are set according to the generator's manufacturer, WEG.

The moment of inertia of the drive train is represented as a single element at the generator. Therefore, the moment of the inertia of the turbine rotor reflected back through the gearbox is required. This can be calculated using the following equation:

$$J_{\mathrm{r}} = \frac{J_1}{N^2} \tag{4.9}$$

The reflected moment of inertia J_{r} is the load inertia of the turbine rotor (J_1) divided by the square of the gear ratio (N). J_1 and N are given from the Gaia report on aeroelastic loads [207]. The gearbox greatly reduces the moment of inertia "seen" by the generator, although the value of 6.265 kg.m^2 means that the inertia of the generator rotor is still insignificant.

With the abovementioned specifications, a Simulink model of the wind turbine was built and it is shown in Figure 4.21. In order to characterise the power curve of the wind turbine model, a linear increasing wind speed was fed to the turbine. Thereafter, the turbine computed its mechanical torque accordingly, by referring to the variations of wind speed and the C_{P}-λ look-up table. The turbine's mechanical torque was then translated through the gearbox which matches the rotational speed of the induction generator. In this simulation, the three-phase terminals of the induction generator were directly connected to the three-phase SI output as depicted in Figure 4.22. The simulation began with the SI start-up process which took approximately 50 s. At 60 s, the generator was connected through the three-phase circuit breaker and operated as a motor until near synchronous speed at 1000 rpm. At 80 s, the wind speed was linearly increased from 0 m/s. Power output from the generator was being measured

at the same time. Through this approach, the power curve of the wind turbine model was obtained.

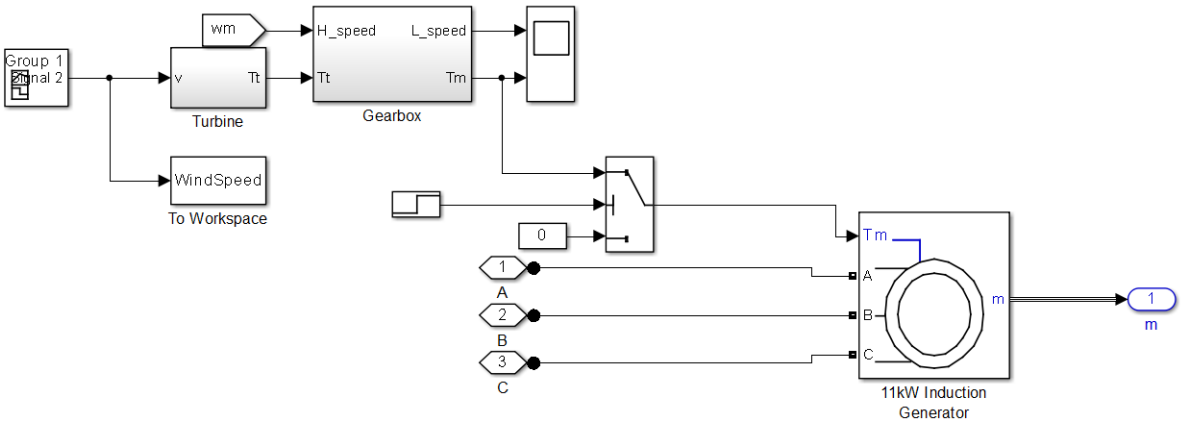

Figure 4.21: Simulink model of Gaia Wind Turbine with linear increasing wind speed input

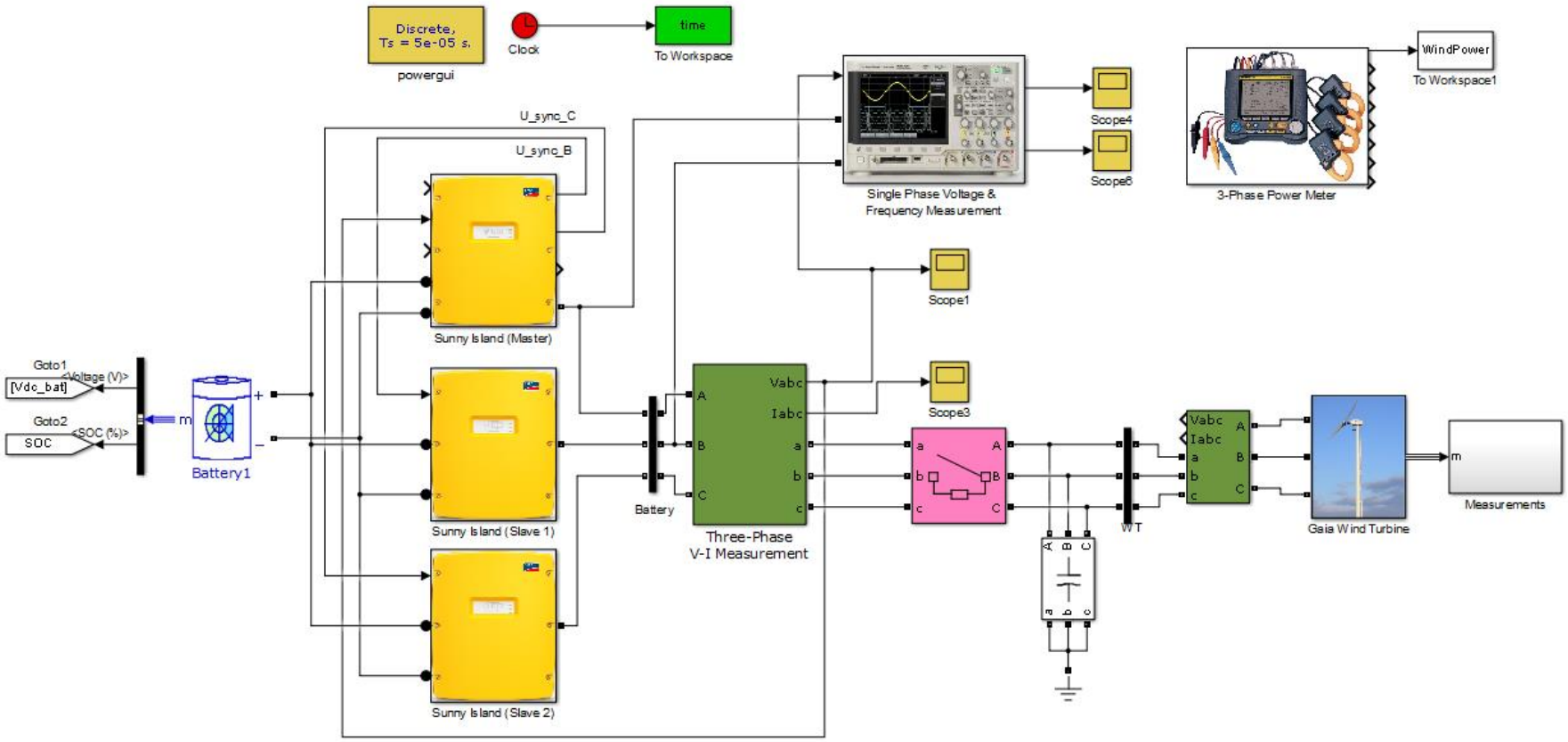

Figure 4.22: Simulink model of the Sunny Island connecting to Gaia wind turbine through a three-phase circuit breaker

Figure 4.23 shows the comparison between the Simulink model's (blue line) and the TUV NEL's (red line) measured power curves. The curve matches with each other relatively well except for some discrepancies at wind speed approximately 17 m/s onwards. It can be pointed out that these are due to several reasons. First of all, the TUV NEL's power curve was formulated with the wind turbine connected to utility grid (strong grid), in contrast to the off-grid scenario (weak grid) in Simulink. The difference in grid strength gives a dissimilar dynamics after connection of generator to the grid. A drop in voltage and frequency are more apparent with the case of weak grid. In addition, the difference between the simulated rotational speed and the actual rotational speed being modelled in the C_P-λ look-up table also contribute to the mismatch. The mismatch occurred at higher wind speed can be explained by the power equation of the wind turbine, i.e. the power output of a wind turbine is more sensitive to the wind speed as they have a cubic relationship. When the wind speed is about 19.5 m/s, the wind turbine stops generator power and goes into stall position.

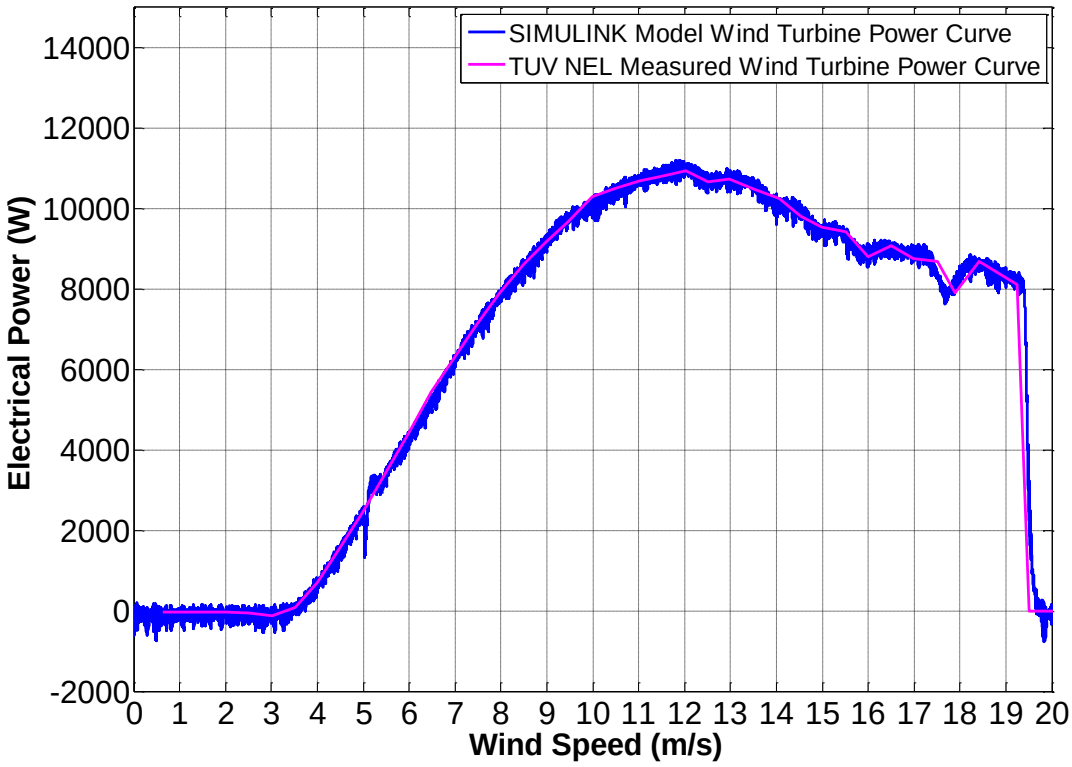

Figure 4.23: Simulink model and TUV NEL [208] power curve

Figure 4.24 shows the rotational speed and electromagnetic torque of the induction generator for different wind speed inputs. When the three-phase terminals of the induction generator were connected to the SI inverters at 60 s, it ran as a motor, reaching near synchronous speed at about 75 s. At 80 s, the wind speed started to increase linearly. At about 95 s, the rotational speed of the induction generator rose steadily, operating at super-synchronous mode. This is in line with power curve shown in Figure 4.23, which indicates the wind turbine started generating power at wind speed 4 m/s.

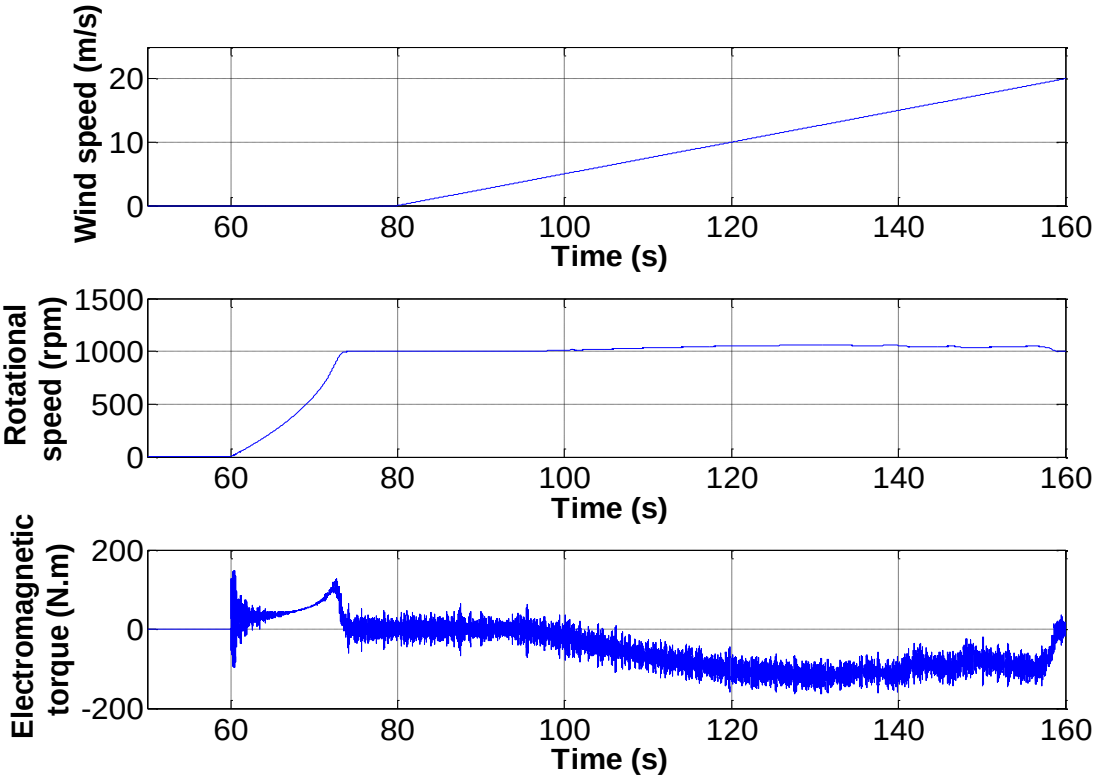

Figure 4.24: Input of linear increasing wind speed to the wind turbine, rotor rotational speed and electromagnetic torque of the induction generator

Figure 4.25 shows the stator current and the stator voltage of the induction generator, using the direct on-line (DOL) starting method. At the point of connection to the grid, the start-up RMS current was about 40 A and it lasted slightly less than 15 s. This is by far the most common starting method available on the market since it is the most fundamental solution. The starting equipment of such approach consists only the main contactor and a thermal or electronic overload relay [209]. However,

the disadvantage of this method is that it gives the highest possible starting current. According to Table 4.1, the RMS current rating for each SI 8.0H is 26.1 A. Therefore, the high inrush current during the start-up process should be reduced to an appropriate level to avoid the inverters being overloaded and eventually damage. Several starting methods exist in the market which can be chosen to mitigate such problem. These include the star-delta start, the electronic starter (soft-starter), the frequency converter, the series-parallel starter and the reduced voltage auto-transformer starter [209], [210]. However, each of them is only suitable for certain specific applications and it has its own advantages and disadvantages [209], [210]. In this thesis, the electronics soft-starter has been adopted for starting the induction generator. The next section describes the principle of operation, modelling and simulation of the soft-starter in the Gaia's fixed speed wind turbine application.

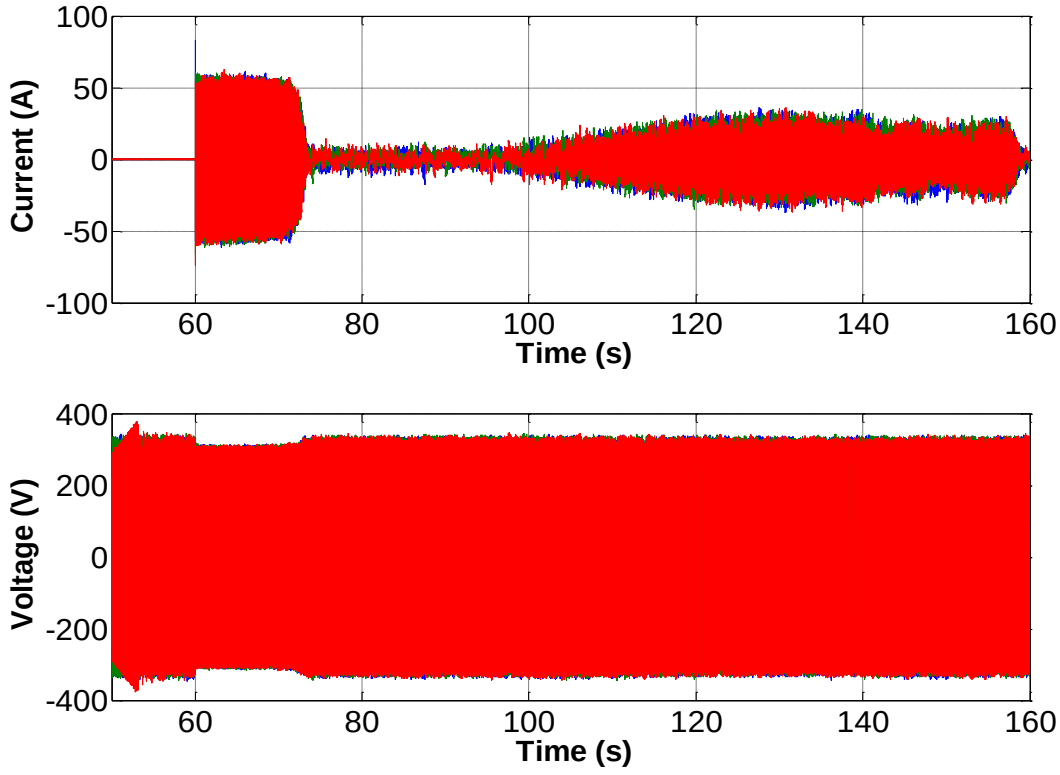

Figure 4.25: Stator current and voltage of the induction generator

4.3 Soft-starter

Induction machines, especially squirrel cage type make up a large part of industrial applications due to their simplicity of construction, reliability, economy and relatively high efficiency [211]. However, it is a well-known fact that the DOL starting method can result in mechanical wear through the rapid acceleration and the voltage dips in the supply. The voltage dip scenarios are more apparent in weak grids. A risk of overload relay tripping may take place due to the high inrush current and one may not be able to start the induction machine without giving it a significant time to cool down. There is also a magnetization peak that can be over 20 times the rated current since the motor is not energised from the first moment [209]. It is not a trivial task to predict the starting current and the starting torque as they can be hugely different between manufacturers for the same power rating of the machine. This can be attributed to the different motor design [209]. In general, modern machines have a higher inrush current than the older ones due to the lower resistance in the windings [209]. A soft-starter with appropriate settings may mitigate the mechanical stress experienced by the induction machine, therefore, avoiding unnecessary heating and alleviate voltage dips and brownout conditions [211]. Subsequently, the need for service and maintenance are reduced.

A frequency converter (also known as variable speed drive) may also be used as a smooth accelerator, however with the expense of higher cost and bigger physical size. More importantly, Gaia's wind turbines are running at fixed speed and it would be unnecessary to continuously regulate the speed of the generator. Therefore, a simple soft-starter is sufficient for this application since only start-up of the generator requires smooth acceleration.

The common topology of a soft-starter is shown in Figure 4.26. It has three pairs of thyristors connected in an anti-parallel configuration. The soft-starter is placed in between the supply and the load. The output voltage of the soft-starter is regulated by controlling the firing angle, α, allowing a proportion of the current to pass through as shown in the picture. A larger firing angle gives a smaller average voltage, hence a smaller current value to be drawn by the load. Typically, a soft-starter can be configured into two modes of operation; i.e., voltage ramp mode (open-loop control)

and current limiter mode (closed loop control). In the voltage ramp mode, the voltage profile is produced independent of the current drawn or the speed of the motor [211]. This method is not able to limit the current of the motor during start-up. On the left of Figure 4.27 shows the voltage profile of such scheme with an initial voltage and ramp duration set by the user. On the other hand, the closed loop current limiter control monitors the current level and modifies the voltage profile so that the current limit is not exceeded. As shown on the right of Figure 4.27, the voltage is fixed at a certain level when the current drawn is reached at the pre-defined limit.

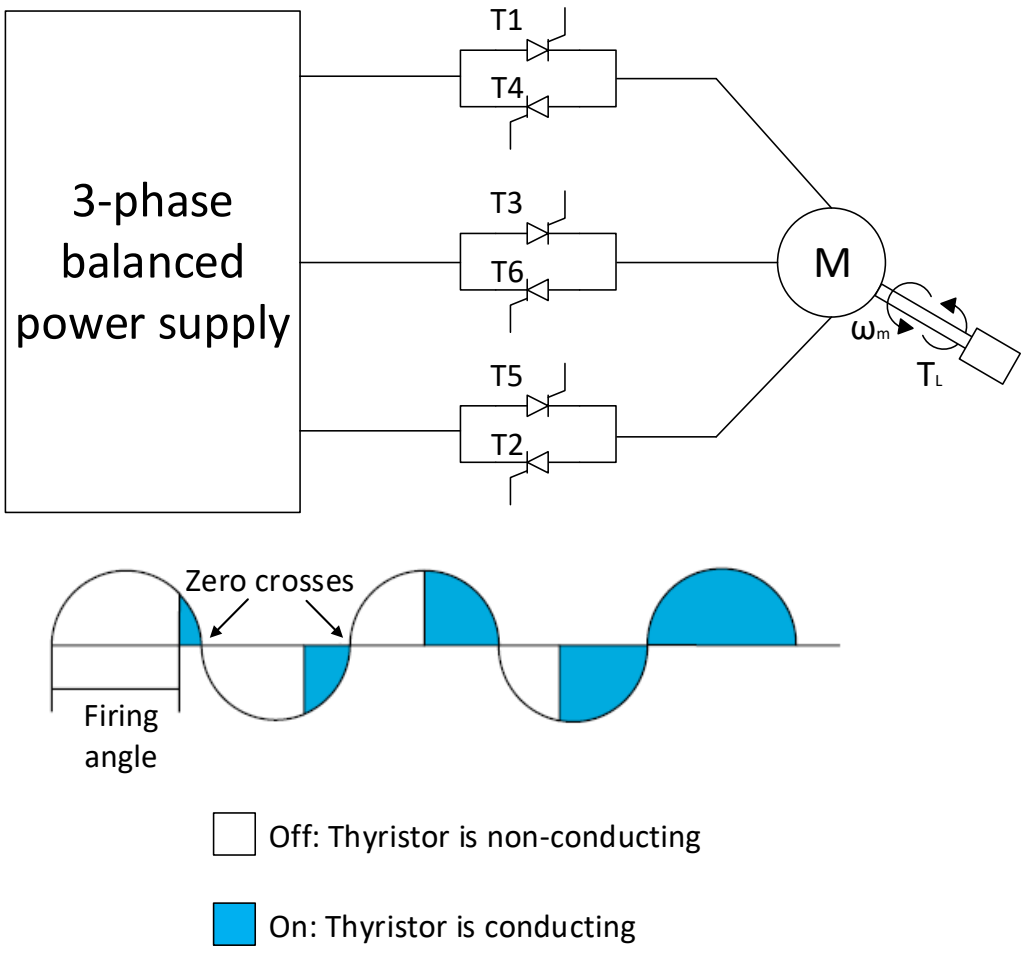

Figure 4.26: Thyristors connected in an anti-parallel fashion and conduction profile across time

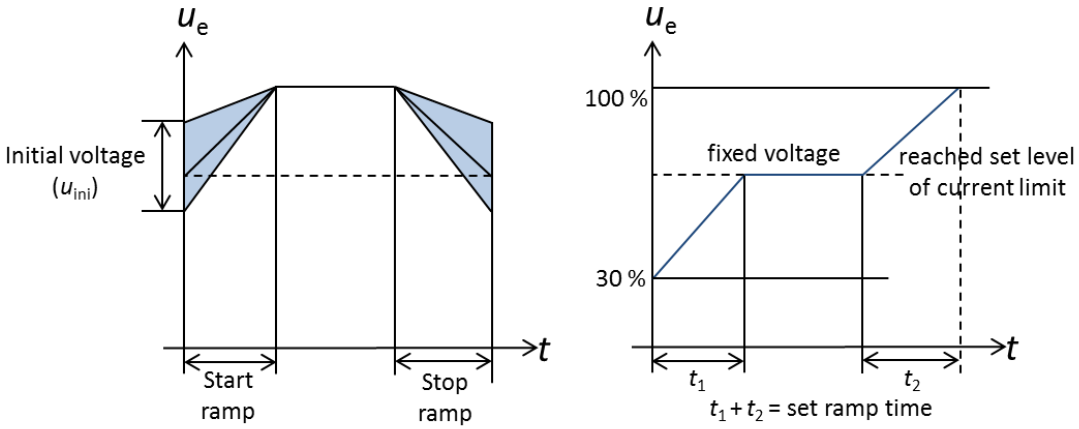

Figure 4.27: *(Left)* Voltage profile of voltage ramp mode; *(Right*) Voltage profile of current limiter mode

In this work, the three-phase WEG SSW-07 soft-starter which uses the common topology, as described previously is adopted in this work [212]. More detailed explanations on the architecture and hardware testing are described in Chapter 6. The soft-starter with the configuration as shown in Figure 4.26 was modelled in Simulink. Figure 4.28 shows the Simulink model of the stand-alone wind system with a soft-starter being incorporated into the system. It is mainly being used to reduce the start-up current of the generator. The soft-starter modelling was setup based on the configuration shown in Figure 4.26. The control of the voltage ramp mode is a simple linear ramp up signal fed to the pulse generator block. As the alpha angle decreases, the voltage increases, eventually reaching full voltage after pre-determined ramp duration. Once the rated voltage was achieved, the bypass switch was closed to reduce losses incurred by the thyristors. The modelling of such soft-starter is shown in Figure 4.29.

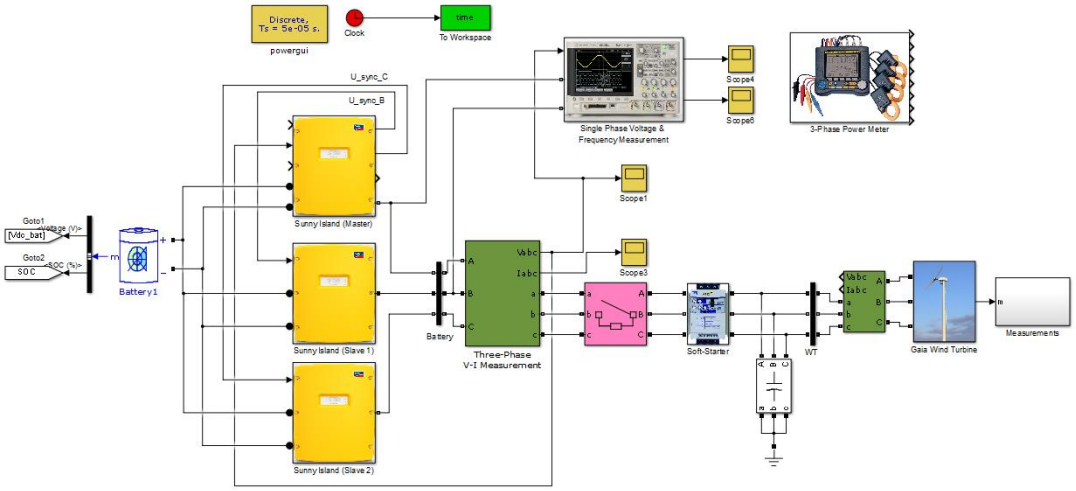

Figure 4.28: Simulink model of the Sunny Island connecting to Gaia wind turbine with a soft-starter

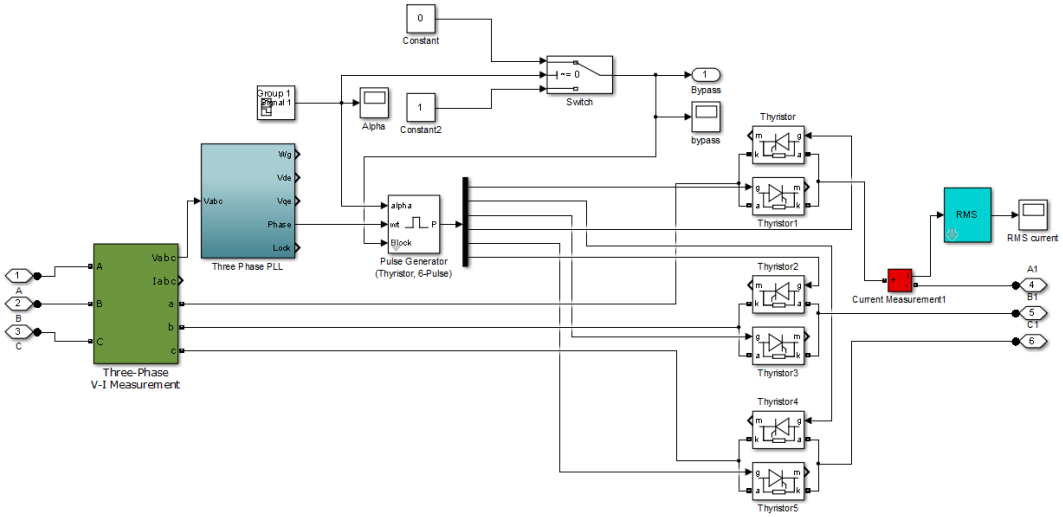

Figure 4.29: Simulink model of soft-starter in voltage ramp mode

In reality, the appropriate settings (initial voltage, ramp time, etc) of the soft-starter can be found through empirical approach. This is particularly true for the case of voltage ramp mode due to the uncontrolled current drawn by the motor. Most machine manufacturers design their machines with different specifications. This adds to the challenge of estimating the current drawn during the start-up [209]. Furthermore, a different point of connection of the motor gives different voltage and frequency dynamics to the network. Thus, it is important to first characterise the soft-starter settings together with the load-connected machine.

The simulations were performed with different ramp duration. They were 120 s, 80 s, and 40 s respectively. The initial voltage for these simulations was 50% of the rated voltage which corresponds to 90 degree firing angle. In addition, a simulation of 120 s ramp time and the initial voltage of approximately 30% of the rated voltage, which corresponds to 130 degree firing angle, was also conducted. For comparison purposes, the DOL method (without using a soft-starter) for weak grid and strong grid conditions were simulated. The weak grid in this case was represented by the three-phase supply formed with SI inverters. On the contrary, the strong grid was emulated with an ideal three-phase voltage source, which is also an infinite bus. The simulation begins with the SI's DC link being established, which took approximately 50 s. At 60 s, the soft-starter was turned on and the generator starts to increase its speed and operates as a motor until near synchronous speed at 1000 rpm. Figure 4.30 shows the current drawn as a function of rotational speed of the induction machine.

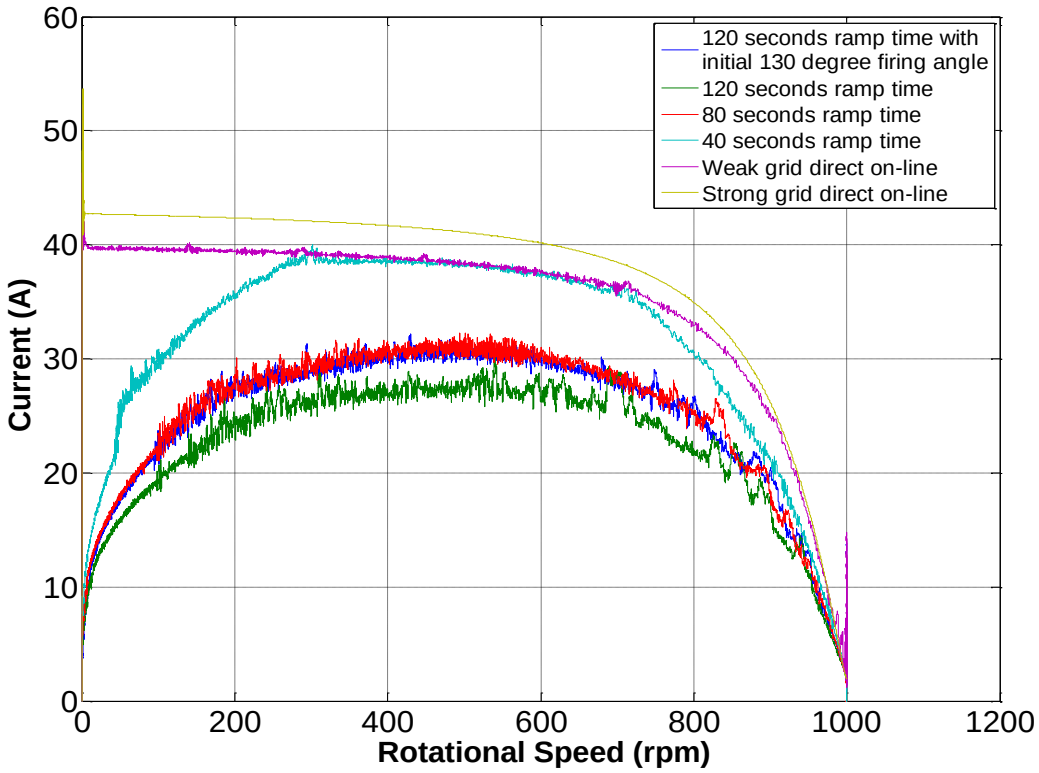

Figure 4.30: Current drawn vs rotational speed characteristic curves (voltage ramp mode)

It can be observed that the start-up current was lower when the ramp time was larger, in this case 120 s. The machine was able to overcome its inertia and had sufficient time to accelerate, thus drawing less current compared to the extreme case of DOL method. The DOL with strong grid drew the highest inrush current, slightly larger than the weak grid case due to the ideal voltage in the former. The weak grid experienced a sudden voltage dip when the circuit breaker was closed, thereby limiting the power being absorbed by the machine. It was also noted that 120 s ramp time with 30% initial voltage (blue line) and 80 s ramp time with 50% initial voltage (red line) were relatively similar in terms of current drawn and electromagnetic torque generated in the machine. From this, it can be concluded that several settings can be tuned to achieve the same start-up current magnitude. However, the former setting requires an additional of 40 s to achieve the same results by increasing the initial voltage to 50% of its rated value.

Figure 4.31 demonstrates the electromagnetic torque-speed characteristics of the induction machine. As expected, the DOL method with strong grid delivers the

highest available motor torque, followed by the weak grid DOL's scenario. In general, there is more torque pulsation at low speed for the weak grid supply which can be mainly attributed to the system performance (voltage and frequency) as shown in Figure 4.32 and Figure 4.33.

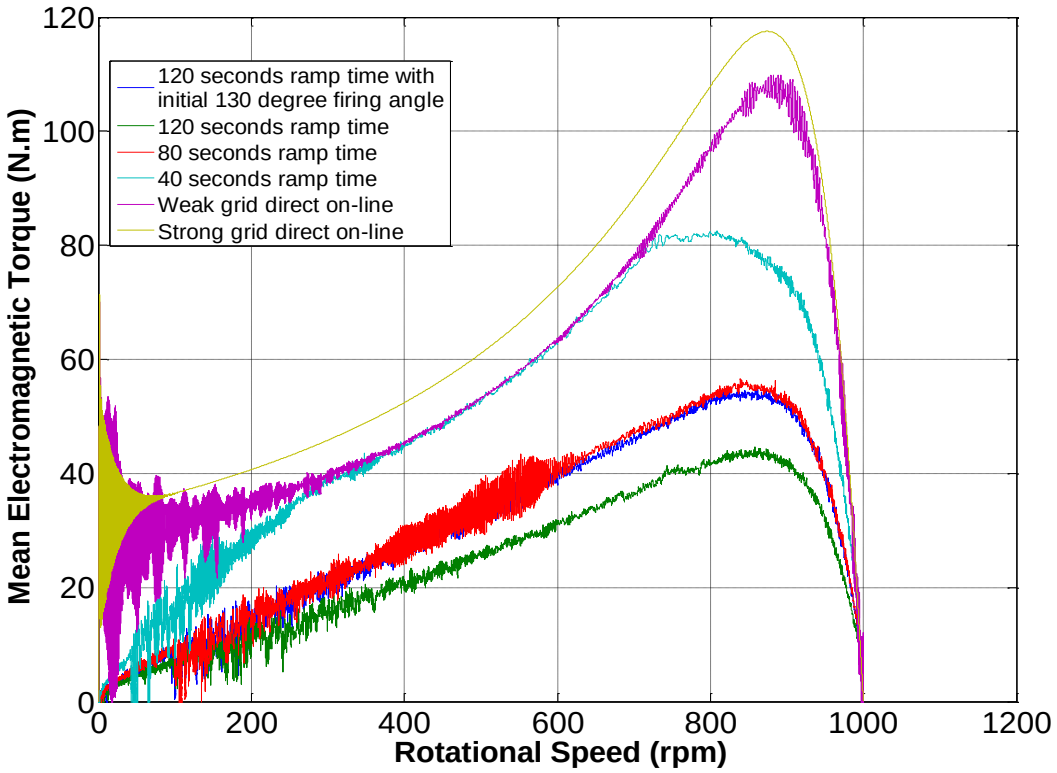

Figure 4.31: Mean electromagnetic torque vs rotational speed characteristic curves (voltage ramp mode)

It can be clearly seen from Figure 4.32 that the DOL method at weak grid has the highest magnitude of voltage dip but for the shortest duration compared to the rest. It is not advisable to use DOL method especially in a very weak grid condition due to the possibility occurrence of severe voltage dip which can easily violate the statutory voltage limits. Larger ramp time with the appropriate initial voltage setting reduces the voltage dip. In this case, the 120 s ramp time with 50% initial voltage has the lowest voltage dip during start-up. Once the induction machine runs near synchronous speed, the voltage recovers. The steady state voltage profile after connecting the induction machine was slightly lower than before the circuit breaker was closed due to the reactive power required to run the machine. This can be

explained from the droop characteristics (Figure 4.9) within the inverter system as previously discussed. An interesting point can be noted from Figure 4.32 is that for the 120 s ramp time with 30% initial voltage scenario, the voltage did not drop immediately after the circuit breaker is closed at 60 s. In fact, it was waiting the voltage at the output of the soft-starter to reach to a higher level before it dropped. In another perspective, the system voltage started to drop when the machine was accelerating at 100 s, which is shown in Figure 4.34. It is important to highlight the voltage dip analysis especially in an off-grid system because there are loads that have the tendency to suffer more with such circumstances. For instance, a well-known phenomenon such as the light flicker effects (incandescent or fluorescent) may be experienced by users [213] [214].

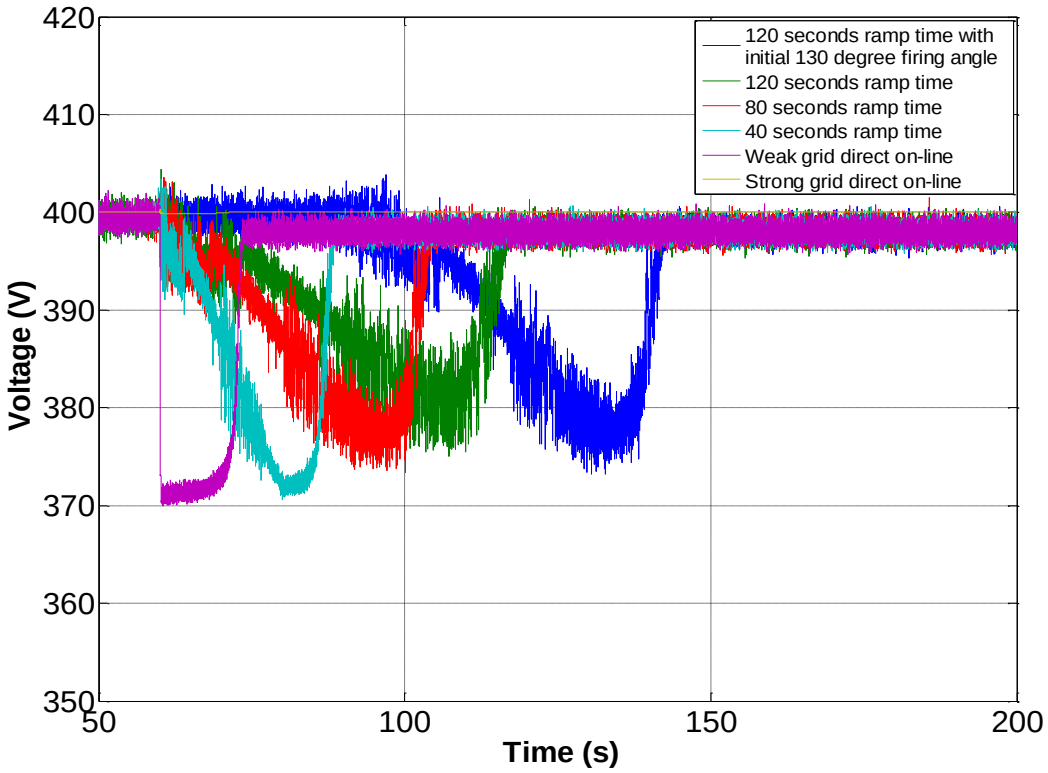

Figure 4.32: Grid line-line voltage profile (voltage ramp mode)

The frequency profiles are shown in Figure 4.33. The frequency spike occurred just after 50 s is attributed to the voltage settling of the modelled DC-DC converter, as explained in section 4.1.2. Note that this may not be reflected in the real system. From Figure 4.33, the frequency drop starting from 60 s can be observed more

significantly for the case of weak grid DOL method. It recovered to slightly less than the nominal level when the speed of the induction machine reached near synchronous speed. For other cases, the frequency fluctuated more significantly during start-up because of the harmonics generated by the thyristors switching of the soft-starter. Due to the temporary existence of these harmonics, the analysis of the harmonics content for soft-starter applications is actually in general not relevant at all [210]. The harmonic concerns are usually relevant for drive applications where harmonics are generated continuously and a filter is always required to mitigate them [210].

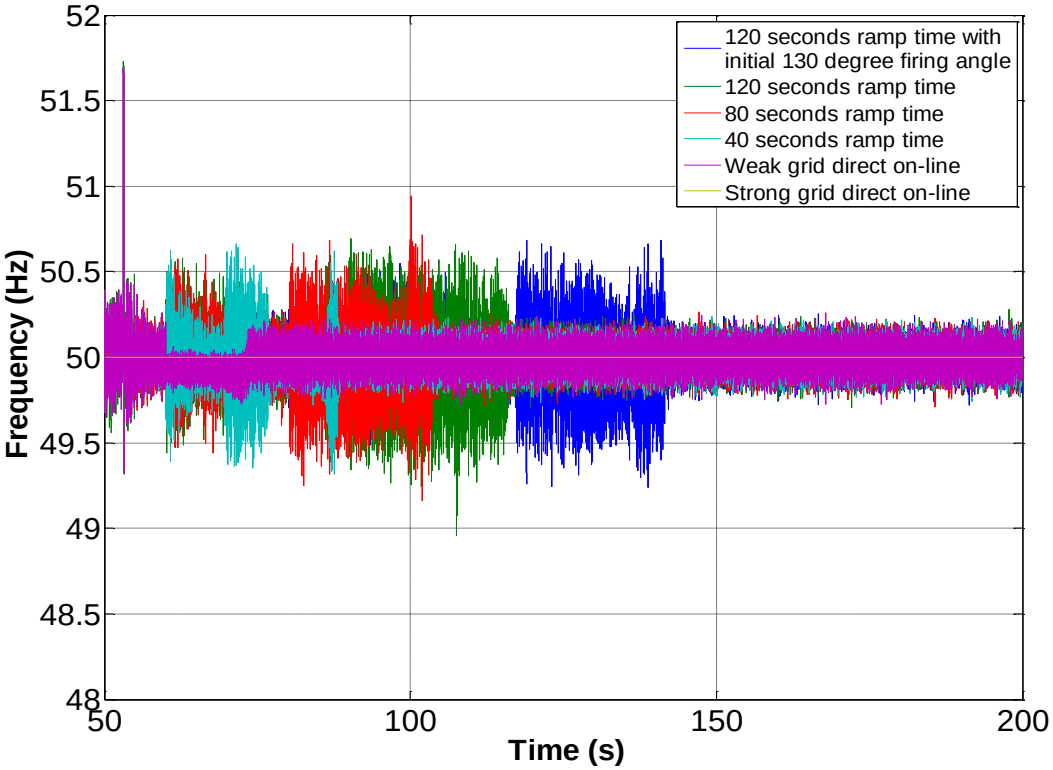

Figure 4.33: System frequency profile (voltage ramp mode)

Figure 4.34 shows the rotational speed of the induction machine for all the scenarios. In general, the induction machine accelerated immediately after the circuit breaker was closed except for the case of 120 s ramp time with only 30% of its rated voltage. The insufficient voltage hence insufficient current to overcome its inertia forbids the induction to accelerate. During this period, unnecessary heating of the machine was experienced. Therefore, it is vital to set the appropriate initial voltage, allowing almost immediate acceleration of the induction machine to avoid unnecessary

heating. Table 4.8 summarises the time taken for the induction machine to accelerate from the start to near synchronous speed for various settings. However, it is noted that the ramp time demonstrated in Figure 4.34 and Table 4.8 is lower than the set ramp time. This is due to the induction machine already gained sufficient energy to achieve near synchronous speed before the stator voltage (supply voltage) reached its rated value (400 $V_{line\text{-}to\text{-}line}$). Finally, Figure 4.35 portrays the firing angle of the thyristors for the scenarios which were using a soft-starter.

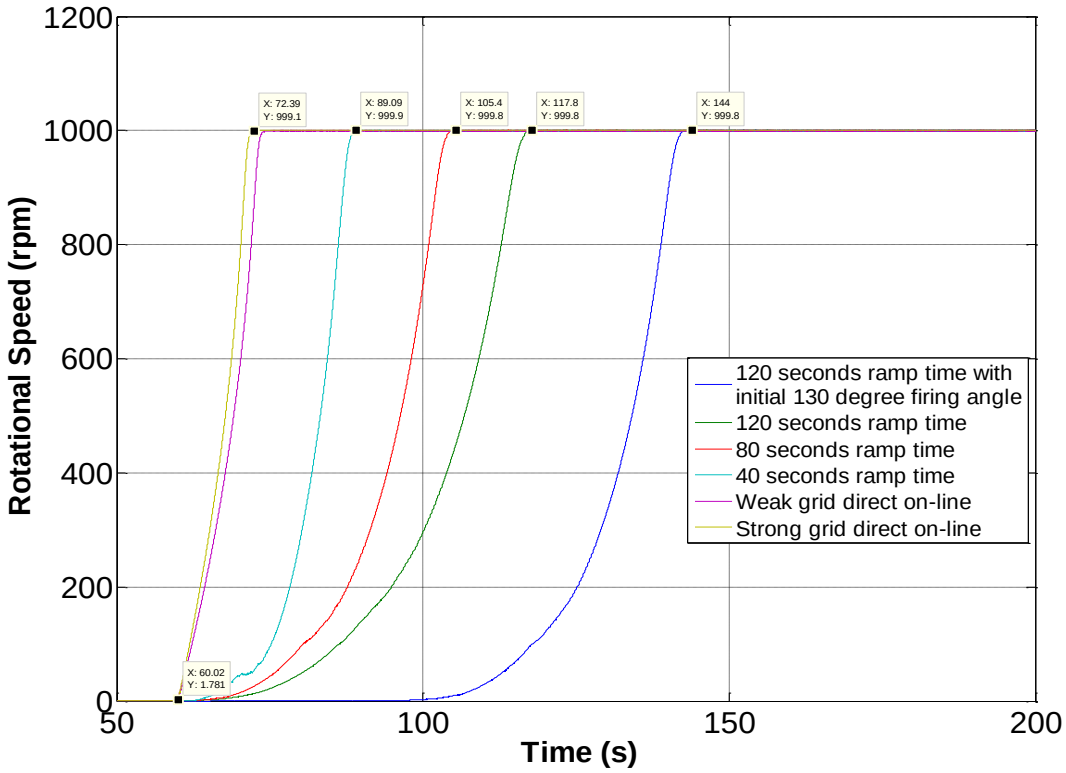

Figure 4.34: Rotational speed of the induction machine (voltage ramp mode)

Scenario	Time (s)
Strong grid DOL	12.37
Weak grid DOL	15.32
40 s ramp time	29.07
80 s ramp time	45.38
120 s ramp time	57.78
120 s ramp time with initial 130 degree firing angle	83.98

Table 4.8: Acceleration time of the induction machine for various soft-starter settings (voltage ramp mode)

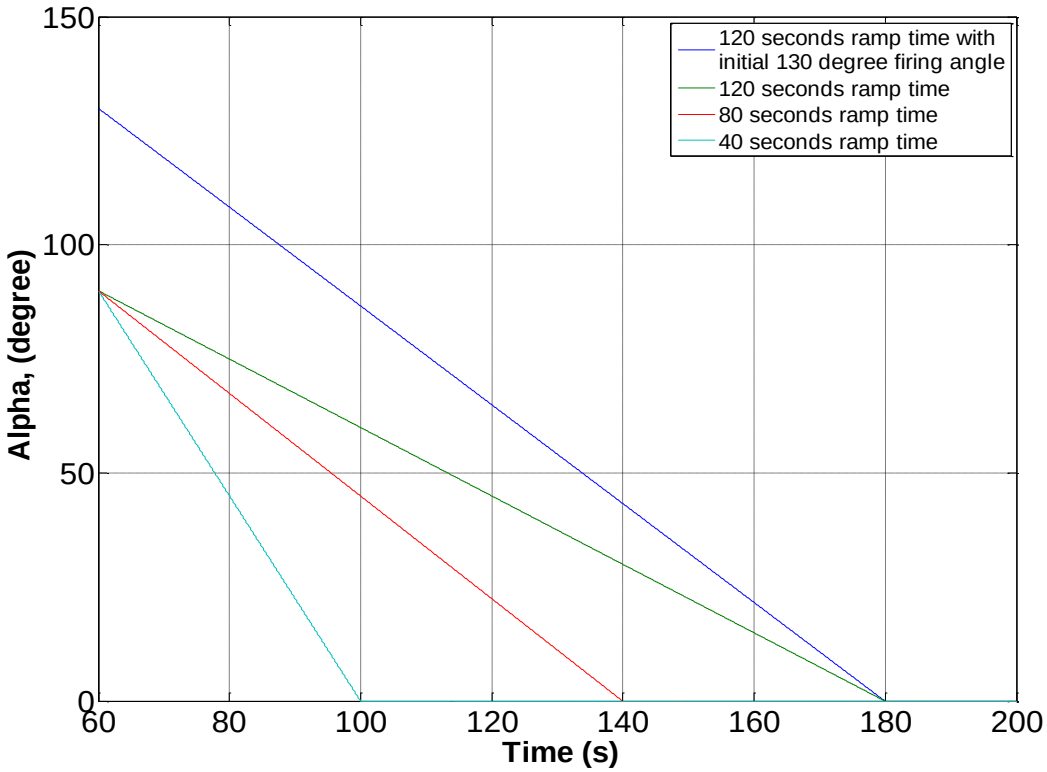

Figure 4.35: Firing angle of the thyristors (voltage ramp mode)

The Simulink model of the soft-starter operating in current limiter mode is shown in Figure 4.36. The output current of the soft-starter was measured and fed back to the control circuit.

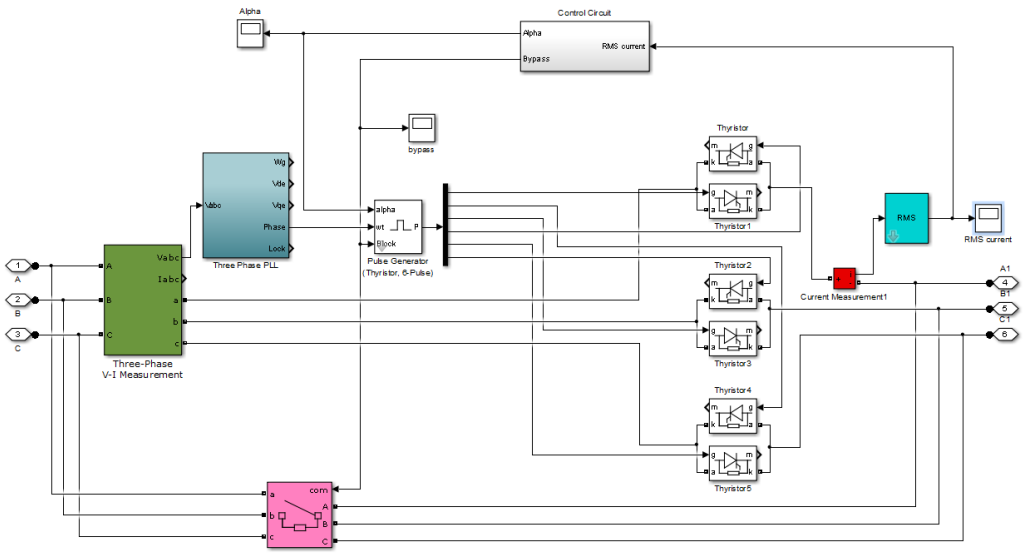

Figure 4.36: Simulink model of soft-starter in current limiter mode

When the current limit was reached during start-up, the firing angle stopped decreasing hence the voltage was fixed at a certain value. As the machine accelerated, the slip decreased and the current across the rotor was reduced. The firing angle then continued to decrease and eventually achieved the rated voltage when the firing angle was zero. As soon as the voltage was at its rated magnitude, the by-pass contactor was closed to reduce losses. In the current limiter mode, there was no voltage ramp time setting. However, there is a locked rotor time setting which is mainly used to protect the induction machine from being overheated if the limited current was insufficient to accelerate the machine to full speed.

The simulations were performed with 25 A, 20 A and 15 A current limit. These values were below the rated current of the SI 8.0H. For performance comparison purposes, the DOL method (without using a soft-starter) for weak grid and strong grid conditions were included. Figure 4.37 shows the current drawn from the induction machine as a function of its rotational speed. It can be noticed that the controller was able to limit the current relatively well according to the pre-defined level. The 15 A current limit setting has the least current fluctuations during machine acceleration. This smooth acceleration can also be reflected from Figure 4.38, where it has the lowest torque perturbation at low speed compared to other current limit settings. However, the available motor torque was much smaller when the current is being limited further. Care should be taken when setting the current limit for the start-up operation to avoid locked rotor situation.

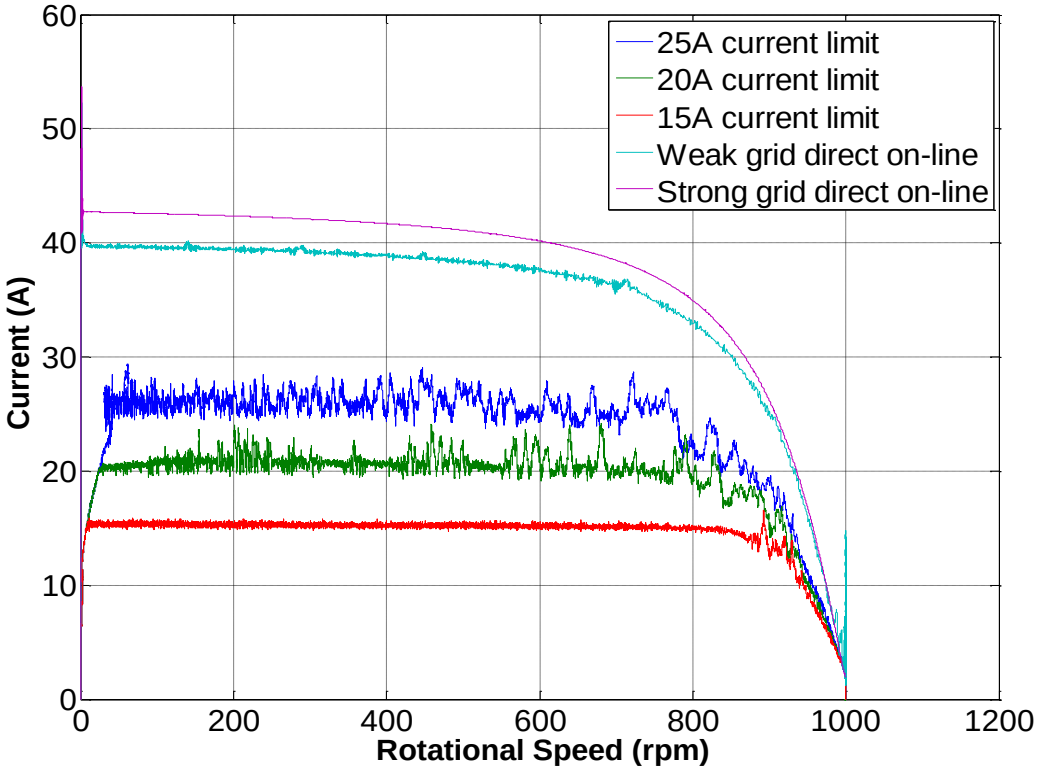

Figure 4.37: Current drawn vs rotational speed characteristic curves (current limiter mode)

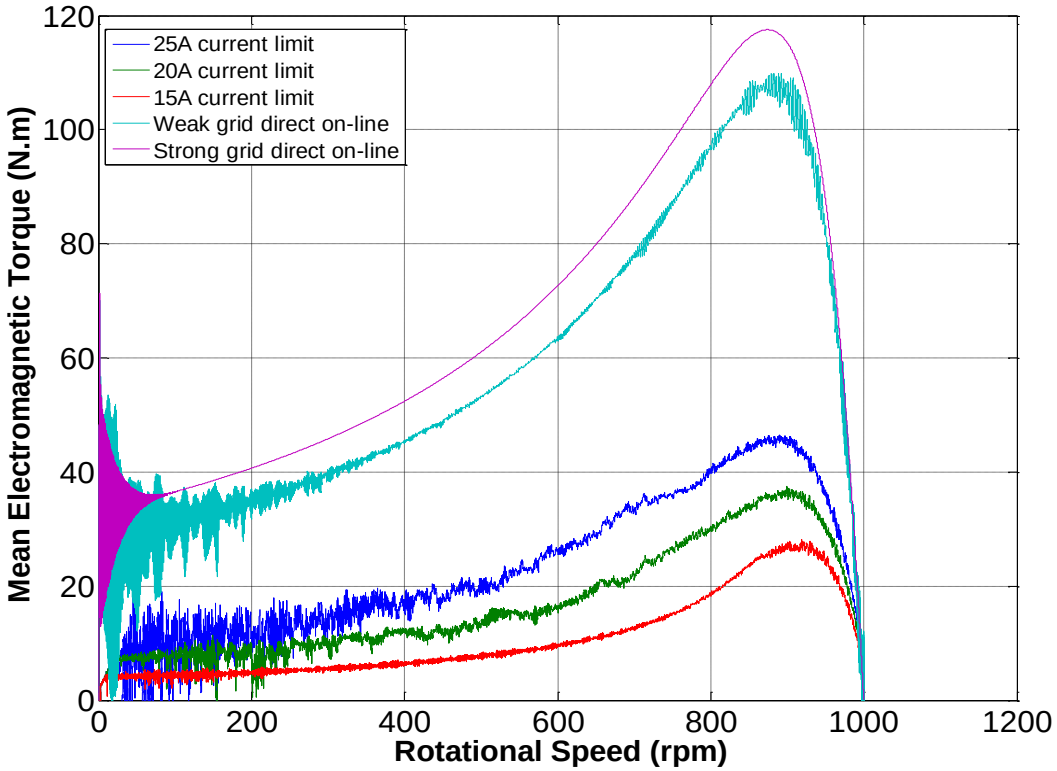

Figure 4.38: Mean electromagnetic torque vs rotational speed characteristic curves (current limiter mode)

Figure 4.39 shows the voltage profile in current limiter mode. As expected, lower current drawn from the network reduces the voltage dip, therefore meeting the statutory voltage limits. However, this comes with the compromise of longer voltage dip duration due to the slow motor acceleration. Comparing to the voltage ramp mode's voltage profile (Figure 4.32), the current limiter mode has a better performance control in the magnitude of grid voltage dip.

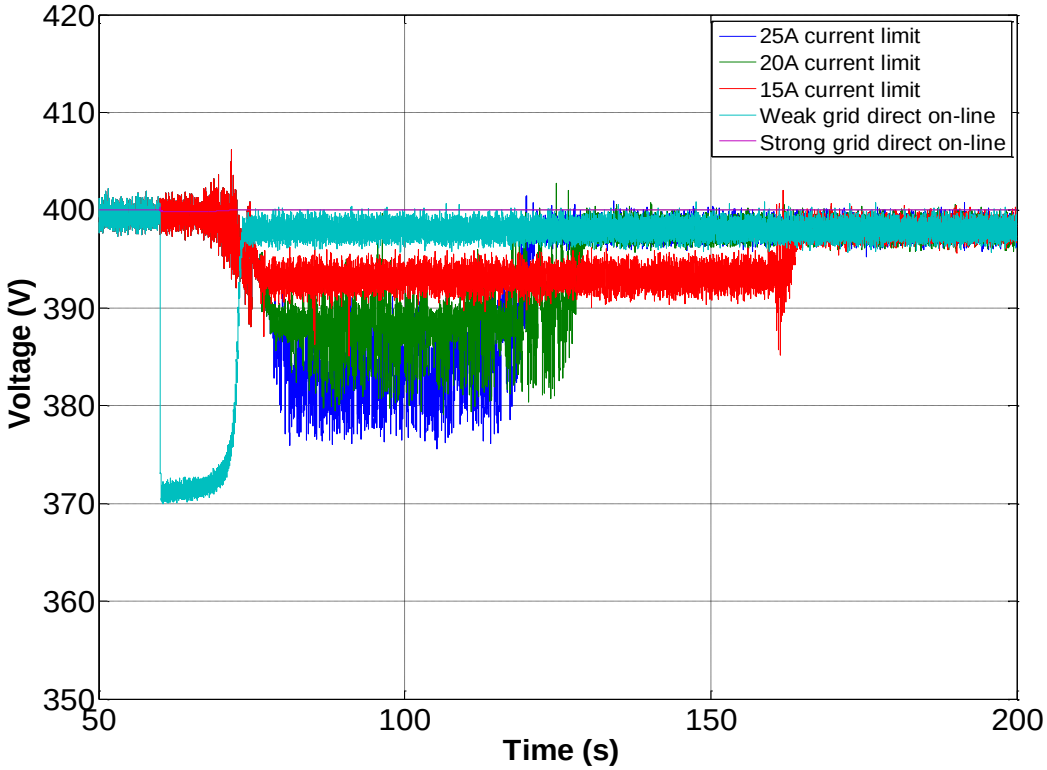

Figure 4.39: Grid line-line voltage profile (current limiter mode)

The frequency profiles for the current limiter mode are shown in Figure 4.40. The frequency spike occurred just after 50 s is attributed to the voltage settling of the modelled DC-DC converter, as explained in section 4.1.2. Note that this may not be reflected in the real system. The lowest current limit setting indeed provided the least frequency fluctuations as shown in Figure 4.40. The fluctuations occurred only during the initial acceleration and when the by-pass contactor was closed at the end of the start-up process. In contrast, the frequency fluctuated throughout the start-up period for the 25 A and 20 A current limit settings. Nevertheless, they were all within the off-grid system's statutory limits which tend to be relatively less stringent

compared to utility grid. Figure 4.41 shows the rotational speed of the induction machine for all scenarios. The time taken for the start-up process is summarised in Table 4.9.

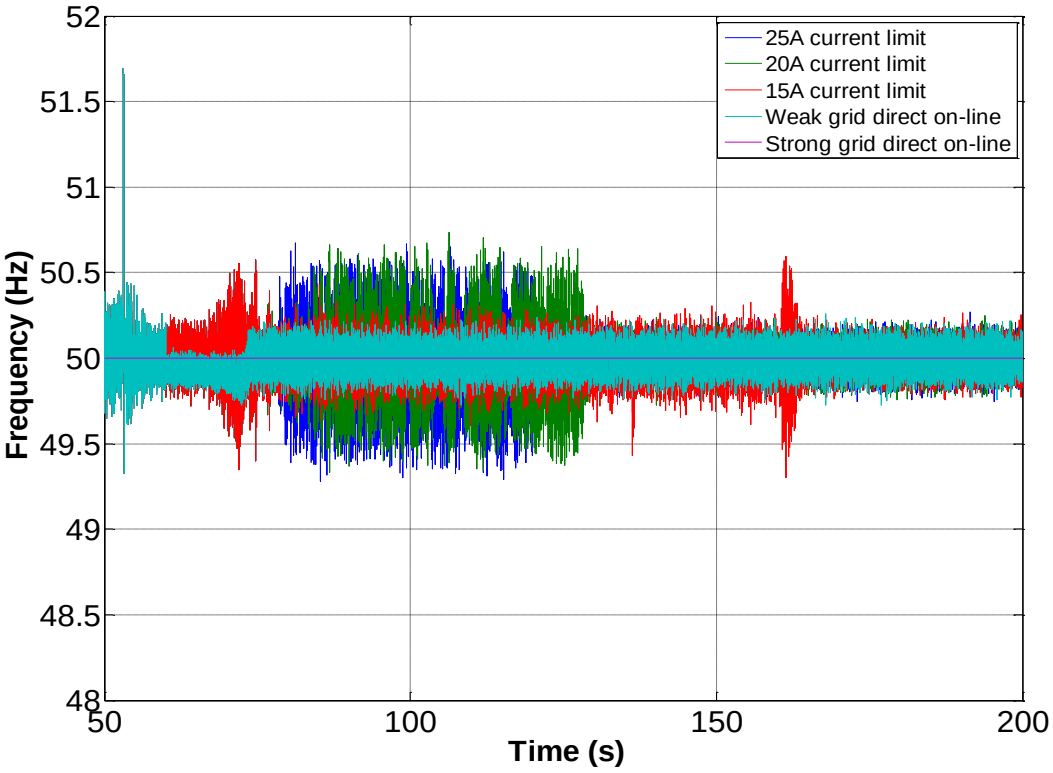

Figure 4.40: System frequency profile (current limiter mode)

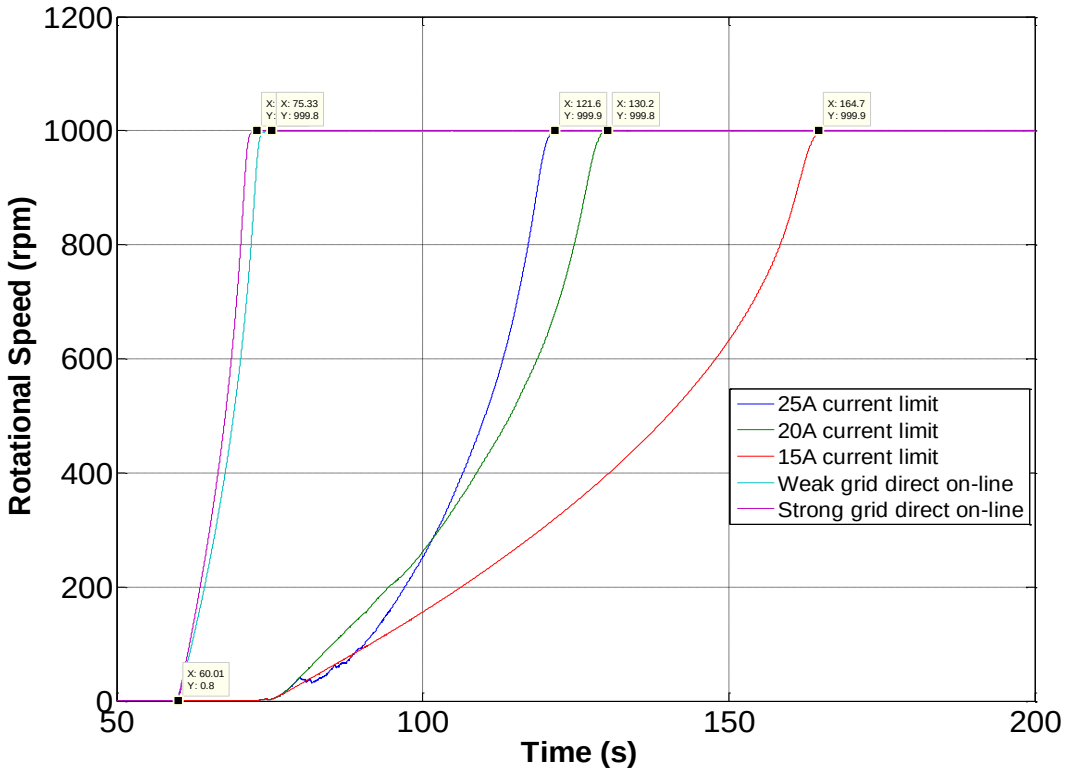

Figure 4.41: Rotational speed of the induction machine (current limiter mode)

Scenario	Time (s)
Strong grid DOL	12.37
Weak grid DOL	15.32
25A current limit	61.59
20A current limit	70.19
15A current limit	104.69

Table 4.9: Acceleration time of the induction machine for various soft-starter settings (current limiter mode)

Figure 4.42 shows the firing angle of the thyristors in current limiter mode. Initially, the output voltage of the soft-starter increased linearly (firing angle was decreasing linearly). As soon as the stator current started to exceed the pre-determined limit, the firing angle stopped decreasing momentary. The motor was accelerated with a fixed

value of current and the firing angle continued to decrease until the rated voltage of the stator was achieved.

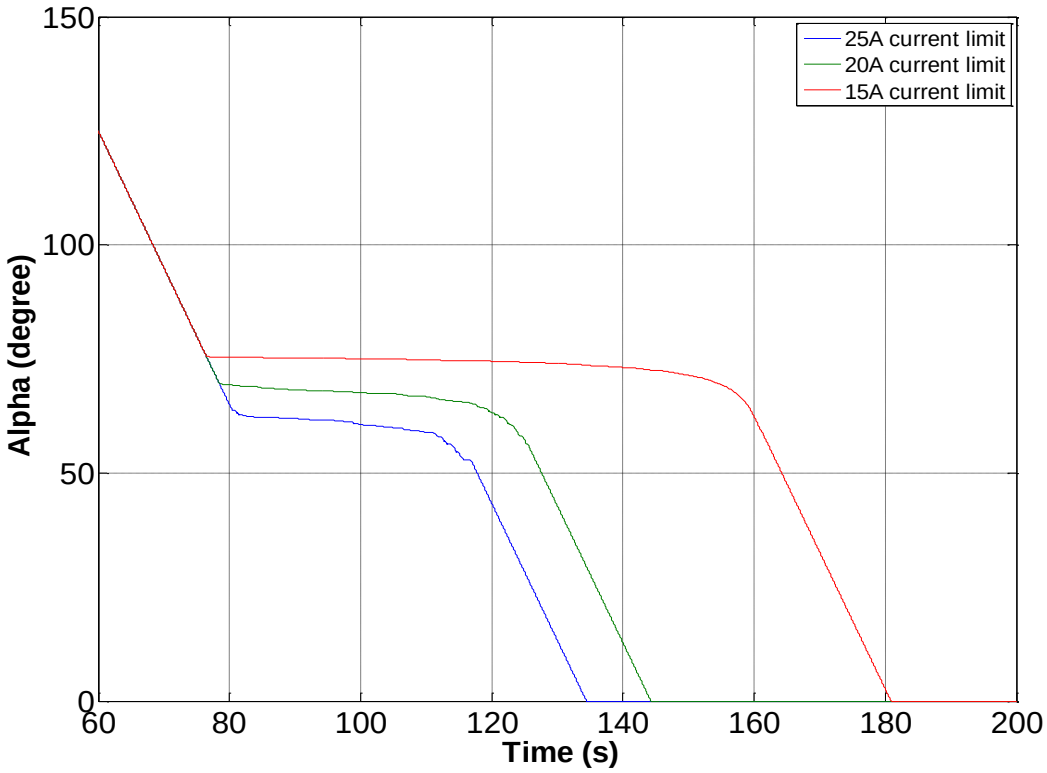

Figure 4.42: Firing angle of the thyristors (current limiter mode)

4.4 Wind Speed Generator

To model the wind energy conversion system, it requires not only the model of the turbine, generator, and its associated power electronics converter but also an accurate model of the wind itself. Atmospheric motions applied for wind energy vary in both time (seconds to months) and space (centimetres to thousands of kilometres) are summarised in Figure 4.43.

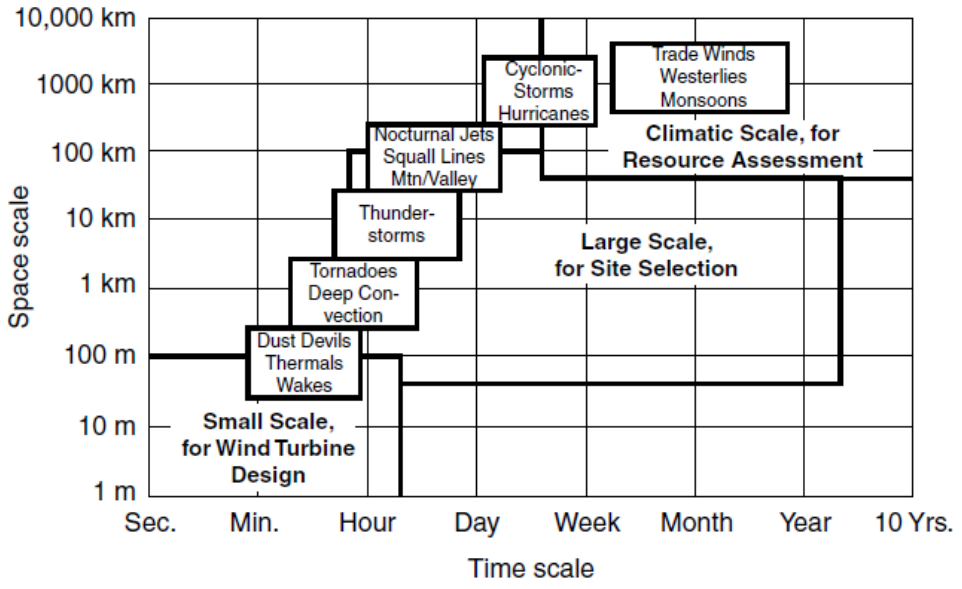

Figure 4.43: Time and space scales of atmospheric motion [215]

For wind energy applications, three major time scale can be considered, i.e., hourly, minutes and seconds as highlighted in Figure 4.43. In this work, the average wind speed of 10 minutes was taken directly from the historical measurement. Therefore, the turbulent wind speed variations (over time intervals of seconds) are of interest here. In particular, the turbulent fluctuations in the flow need to be quantified. Turbulence occurs in the Ekman layer, a boundary layer between the earth's surface and the troposphere [216]. It is caused by the dissipation of the wind's kinetic energy into thermal energy via the creation and destruction of progressively smaller eddies (or gusts). Mathematically, the turbulent wind can be thought of as random wind speed fluctuations imposed on the averaged short-term wind speed [44]. The short-term period usually taken to be ten minutes with a sampling rate of about 1 second [44] [217] [218]. In this work, wind models based on a spectral analysis of the turbulent wind component which have been developed in the past [216] [217] [218] are adopted. It is vital to note that these turbulent fluctuations can have a significant effect on the turbine's aerodynamic efficiency, and hence its generating capacity [216]. Thus, the examination of turbine's dynamic response with turbulence should be taken into consideration based on the abovementioned facts.

A number of power spectral density functions are used as models in wind energy engineering when the turbulence power spectral densities are unavailable for a given

site. In the literature, the two widely used wind speed models exist, namely Van der Hoven's model [219] and von Karman model, used in [218]. The Van der Hoven spectral model is shown in Figure 4.44. The horizontal wind speed data in this spectrum obtained from meteorological tower of the Brookhaven National Laboratory [219] ranges between 0.0007 and 900 cycles/h. Such a frequency range designates the medium and long-term variations, as well as the spectral range of the turbulence component [217].

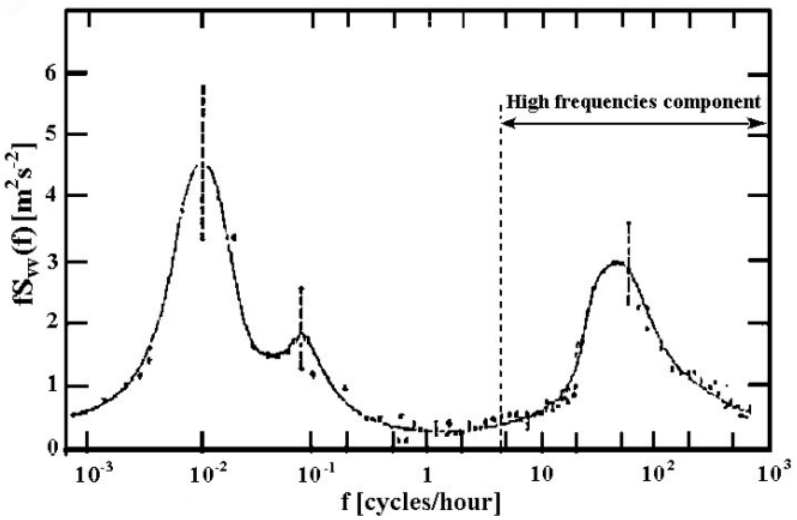

Figure 4.44: Van der Hoven's spectral model [217]

Authors in [217] have pointed out the drawbacks of the Van der Hoven model based on their simulated wind speed (Figure 4.45) using this approach. In particular, the Van der Hoven model cannot be used for a complete description of the wind speed over a time scale of seconds, minutes and hours because this model treats the turbulence component as a stationary random process. Its properties do not depend on the mean value variations of the wind. As observed from Figure 4.45, the magnitude of the turbulence is almost identical regardless of the mean wind speed over a period of time.

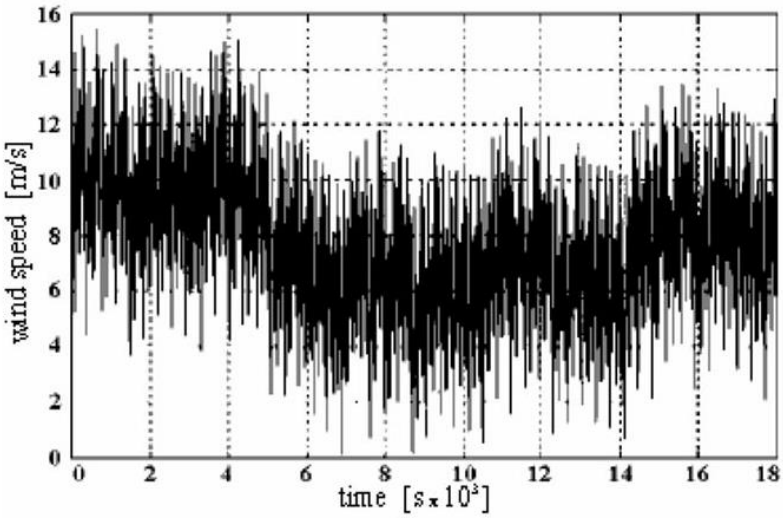

Figure 4.45: Van der Hoven's model based simulation of the wind speed for a time horizon of 5 hours [217]

On the other hand, the basic model of the von Karman power spectrum describing the turbulence component is given as:

$$S_{\mathrm{vv}}(\omega) = \frac{0.475\sigma_{TI}^2 \frac{L}{U}}{\left[1 + \left(\frac{\omega L}{U}\right)^2\right]^{5/6}} \tag{4.10}$$

where:

σ_{TI}: Turbulence intensity
L: Turbulence length (m)
U: Mean wind speed (m/s)

This model shows that the turbulent component is dependent on the value of the mean wind speed, U. In [216] and [218], the authors have successfully formulated a simulation scheme where the non-stationary turbulence component is modelled using a signal shaping filter with white noise input. The schematic of the turbulent wind model is shown in Figure 4.46. As mentioned, the "driving force" of the turbulent component is a random number generator, which produces normally distributed white noise. The discrete-time signal produced in this manner has a mean value of zero and a normalised standard deviation of one. However, as the wind speed for physical reasons, cannot be changed abruptly, but rather continuously, the white

noise has to be smoothed using a carefully designed signal-shaping filter in order to achieve correct spectral distribution. In essence, the shaping filter must be chosen to best characterise the true spectrum of the wind [216] [217] [218] to emulate a more realistic situation. The gain and time constant of the shaping filter are designed to ensure the standard deviation of the coloured noise also equal to one. Then, this transformed signal is multiplied with the respective wind-speed-dependent standard deviation, σ_u to produce an appropriate turbulent wind component. Finally, the turbulent wind profile is synthetically generated by adding the turbulent component to the mean wind speed.

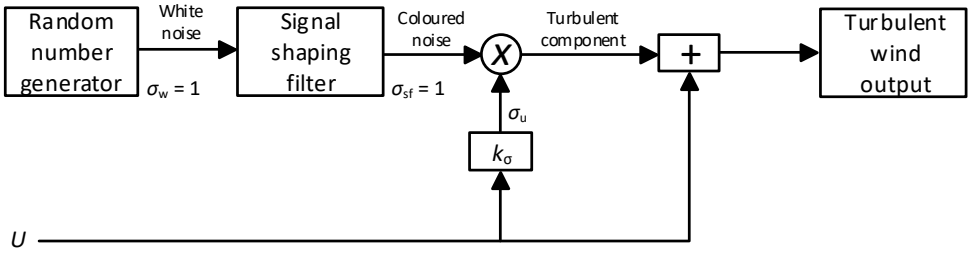

Figure 4.46: Turbulent wind model block diagram

The transfer function of the von Karman shaping filter in Figure 4.46 can be written as:

$$H_{\text{vonKarman}}(s) = \frac{K_F}{[1 + sT_F]^{5/6}} \tag{4.11}$$

where K_F and T_F are the gain and time constant of the filter.

However, in order to reduce the computational time and being able to implement this transfer function in Simulink, the 5/6-order filter is approximated with a rational transfer function. Nichita [217] states that an acceptable solution for the model approximation can be made by the second order transfer function:

$$H_{\text{Nichita}}(s) = K_F \frac{m_1 T_F s + 1}{(T_F s + 1)(m_2 T_F s + 1)} \tag{4.12}$$

where $m_1 = 0.4$ and $m_2 = 0.25$.

The time constant, T_F of the shaping filter is related to the turbulence length scale, L and the mean wind speed, U by:

$$T_F = \frac{L}{U} \tag{4.13}$$

The static gain, K_F of the filter is to be determined so that its output should have a normalised standard deviation ($\sigma_{sf} = 1$). The input white noise of the filter with a sampling period T_s and unitary variance ($\sigma_w = 1$). Note that in simulation, the white noise power spectral density function, $S_w(\omega)$ has a finite sampling time (for e.g. $T_s = 1$), hence it is band-limited:

$$S_w(\omega) = S_{w0}\,, \qquad \omega \in \left[-\frac{\pi}{T_s}, +\frac{\pi}{T_s}\right] \tag{4.14}$$

By definition, the integral over all frequencies of a signal is equal to its total variance. Applying this definition to the white noise power spectral density, the following derivations are obtained:

$$\sigma_w^2 = \frac{1}{2\pi}\int_{-\pi/T_s}^{+\pi/T_s} S_w(\omega)\, dw = 1 \tag{4.15}$$

Substituting equation (4.14) into (4.15):

$$\sigma_w^2 = \frac{1}{2\pi}\int_{-\pi/T_s}^{+\pi/T_s} S_{w0}\, dw = 1 \tag{4.16}$$

which gives:

$$S_{w0} = T_s \tag{4.17}$$

By imposing the condition that the variance of the coloured noise should be equal to 1 and using the integration principle, the equation below is formulated:

$$\sigma_{sf}^2 = \frac{1}{2\pi}\int_{-\pi/T_s}^{+\pi/T_s} |H_F(jw)|^2 S_{w0}\, dw = 1 \tag{4.18}$$

Replacing the white noise transfer function which is found to be equivalent to the constant sampling time, T_s, we obtain:

$$\sigma_{\mathrm{sf}}^2 = \frac{T_\mathrm{s}}{2\pi}\int_{-\pi/T_\mathrm{s}}^{+\pi/T_\mathrm{s}} |H_\mathrm{F}(jw)|^2\, dw = 1 \tag{4.19}$$

Substituting the von Karman shaping filter's transfer function from equation (4.11) into equation (4.19):

$$\sigma_{\mathrm{sf}}^2 = \frac{T_\mathrm{s}}{2\pi}\int_{-\pi/T_\mathrm{s}}^{+\pi/T_\mathrm{s}} \left|\frac{K_\mathrm{F}}{[1+j\omega T_\mathrm{F}]^{5/6}}\right|^2 dw = 1 \tag{4.20}$$

$$\sigma_{\mathrm{sf}}^2 = \frac{1}{2\pi}\int_{-\pi/T_\mathrm{s}}^{+\pi/T_\mathrm{s}} \frac{K_\mathrm{F}^2 T_\mathrm{s}}{[1+(\omega T_\mathrm{F})^2]^{5/6}} dw = 1 \tag{4.21}$$

The above equation can be solved using the general integral solution [220]

$$\int_{-\infty}^{\infty} \frac{1}{[1+(\omega T_\mathrm{F})^2]^{5/6}} dw = \frac{1}{T_\mathrm{F}} B\left(\frac{1}{2},\frac{1}{3}\right) \tag{4.22}$$

where *B (x,y)* designates the beta function:

$$B(x,y) = \int_0^1 t^{x-1}(1-t)^{y-1} dt \tag{4.23}$$

As the Nyquist frequency of the band-limited white noise signal is considerably higher than that of coloured noise signal, the limits of the integration can be approximated with infinities [218]. Thus, substituting equation (4.22) into equation (4.21), we obtain:

$$\sigma_{\mathrm{sf}}^2 = \frac{1}{2\pi}\frac{K_\mathrm{F}^2 T_\mathrm{s}}{T_\mathrm{F}} B\left(\frac{1}{2},\frac{1}{3}\right) = 1 \tag{4.24}$$

Rearranging equation (4.24), the static gain, K_F can be written as:

$$K_F = \sqrt{\frac{2\pi}{B\left(\frac{1}{2},\frac{1}{3}\right)}\cdot\frac{T_\mathrm{F}}{T_\mathrm{s}}} \tag{4.25}$$

σ_u increases proportional with the mean wind speed with a relation of:

$$\sigma_u = k_\sigma U \tag{4.26}$$

where the constant of proportionality, k_σ, depends on the terrain conditions. It can be estimated with from the terrain conditions table (Table 4.10) or measured directly for a particular field.

Terrain type	k_σ
Coastal areas	0.123
Lakes	0.145
Open	0.189
Built up areas	0.285
City centres	0.434

Table 4.10: Values of k_σ for various terrains at the height of 10 m [221]

Figure 4.47 shows the turbulent wind generator implemented in Simulink. In order to demonstrate that the generated wind profile's turbulence intensity is indeed dependent on the mean wind speed, Figure 4.48 shows the evolution of the wind speed during two-time intervals of 10 minutes each. These intervals have been chosen so that the medium to long-term component (mean wind speed) has different values: 5 m/s and 13 m/s.

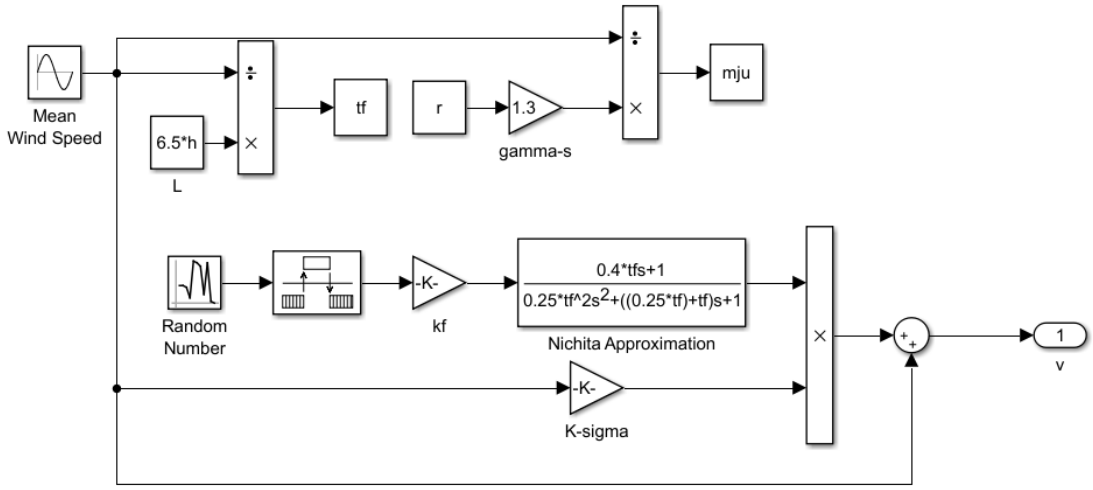

Figure 4.47: Simulink model of turbulent wind generator

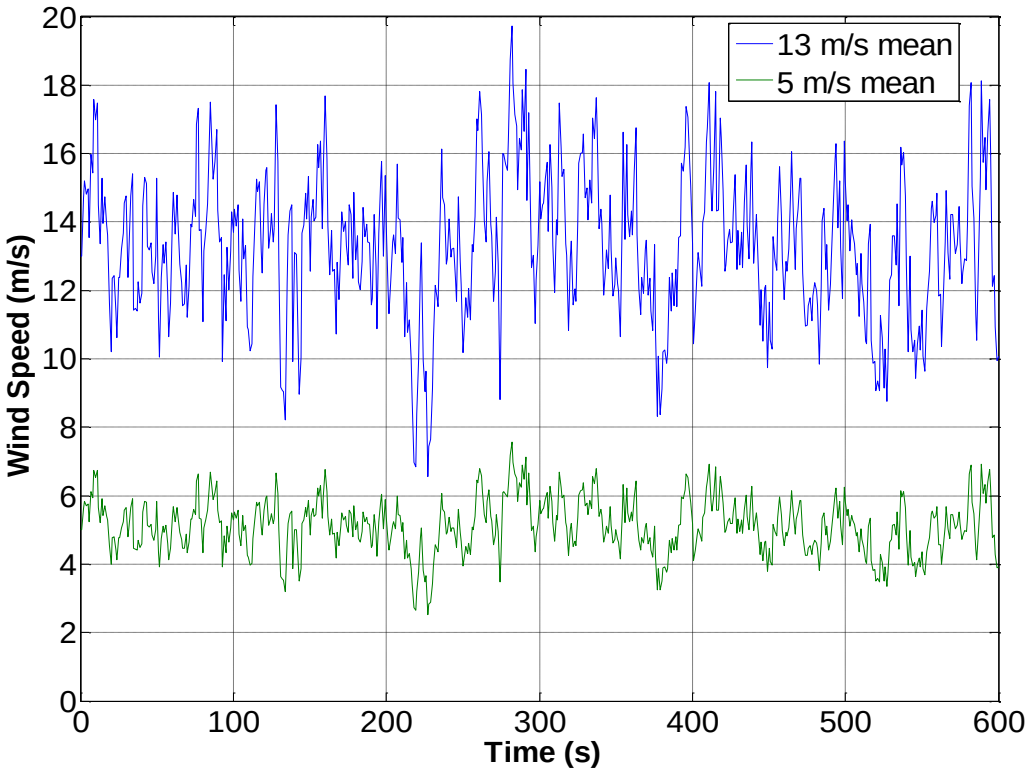

Figure 4.48: Short-term wind profile generated with mean wind speed of 5 m/s and 13 m/s respectively

The random number generator was pre-set with the same seed setting to produce same random pattern for both scenarios. Visual inspection shows that both wind profiles had the same fluctuations (rise and fall) at the same time, however by means of different magnitudes. A way to quantified this was to use the turbulence intensity definition [44]:

$$TI = \frac{\sigma_{\mathrm{u}}}{U} \tag{4.27}$$

where σ_{u} is the standard deviation of the turbulent wind, given in the sampled form by:

$$\sigma_{\mathrm{u}} = \sqrt{\frac{1}{N_{\mathrm{s}} - 1}\sum_{i=1}^{N_{\mathrm{s}}}(u_i - U)^2} \tag{4.28}$$

The computed turbulence intensities were 0.1598 and 0.1579 for mean wind speed of 13 m/s and 5 m/s cases respectively.

4.4.1 Effect of Turbulence on Real Wind Turbines

In reality, the wind affects wind turbines in a number of ways which the spectral method of wind modelling discussed above does not take into consideration. Stannard has identified that the major effect which has be considered is the disc averaging as it depends on the mean wind speed [216].

As the turbine rotates, it experiences an average of the turbulent wind passing through its blades. This smoothing effect can be modelled by a spatial filter [216]:

$$W_{\mathrm{AV}}(s) = \frac{(\sqrt{2} + \mu s)}{(\sqrt{2} + \sqrt{0.55}\mu s)(1 + (\mu s/\sqrt{0.55}))} \tag{4.29}$$

where μ, the decay factor is expressed as:

$$\mu = \frac{\gamma_{\mathrm{s}} R}{U} \tag{4.30}$$

The effect of disc averaging on Gaia's 13 m diameter wind turbine is depicted in Figure 4.49. It was simulated with a mean wind speed of 13 m/s for 160 seconds. It is observed that the sharp edges (high-frequency components) of the turbulent wind were filtered after passing through the turbine. In addition, a small delay (phase shift) was noticed after the disc averaged effect. This is in-line with the filter response which practically representing the real scenario of the turbine requiring some time to "experience" the wind.

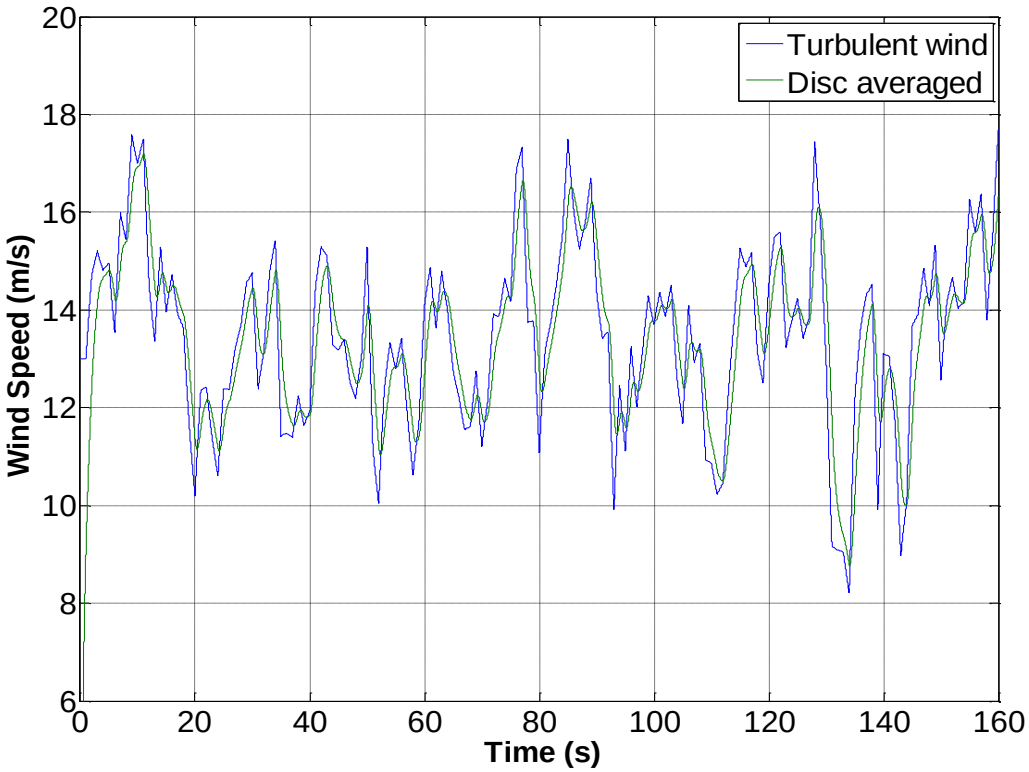

Figure 4.49: Effect of disc-averaging filter in the time domain

4.5 Diesel Generator

Diesel engines are widely used applications in our everyday lives especially in the field of automobiles. In the case of electricity generation, its fast prime mover response time is the desired characteristic to meet the fast varying load demands. The diesel generator can serve as a useful backup or emergency generator especially during the peak demand, where there is a lack of power generation from the utility. For a hybrid wind-diesel system point of view, the diesel generator is ideal for relieving the wind intermittency effects as encountered by consumers. However, it is important to note that the wind energy should first be utilised before starting up a diesel generator due to the high diesel fuel prices and also its environmental impacts.

A typical diesel generator structure is portrayed in Figure 4.50 which consists of an ICE and a synchronous generator coupled on the same shaft [222]. The generator used is generally either a permanent magnet or a wound-field synchronous machine. The wound field generators require an exciter and a voltage regulator to control the

output AC voltage [222]. The governor is an electromechanical device used for automatically controlling the speed of an engine depending on load by adjusting the intake fuel.

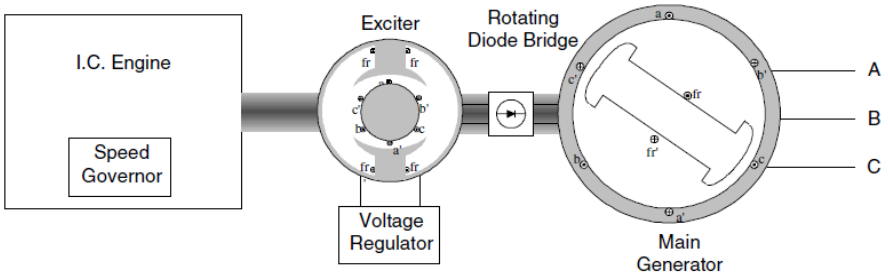

Figure 4.50: Typical structure of diesel generator set [222]

Generally, a governor can operate in two modes, i.e., the droop mode and the isochronous (constant speed) mode. The droop mode has a similar principle as discussed in the previous section on the droop control for Sunny Island inverters. That is, as the load increases, the speed or frequency decreases. In contrast, governors operating in isochronous mode will attempt to maintain the same frequency regardless of the load it is supplying up to the full rated capabilities of the diesel generator [223]. Typically, this mode of control is being used in an isolated system to maintain system frequency. However, in this work, the grid is formed by the SI inverters and therefore, the isochronous governor is not suitable to be used. Otherwise, they would fight with each other, each trying to control system frequency to its own setting. Thus, the droop mode is applied on the diesel generator controller for parallel operation with the inverters. The diesel generator is known to be running inefficiently at part load. It is recommended that diesel generators should be started only when operating at higher than 40% of its rated capacity to prolong the diesel engine lifetime. Based on this rule of thumb, this work proposed a droop control which is capable of running the diesel generator at its rated power, regardless of the load demand at that particular time. This strategy is also trying to reduce the number of start-stop sequence of the diesel generator, at the same time running at its highest efficiency. Hence, fuel saving can be achieved.

Several control strategies of the diesel generator have been proposed in the past. In literature [224], the speed control of the diesel generator has adopted the fuzzy neural network (FNN) and the genetic algorithm (GA) syncretic theory. The performance of

such controller has been compared against the conventional PID control. In another study [225], the authors have applied MPC technique to estimate the plant model parameters, with the fuzzy logic supervisor measuring the performance criteria as input variables. More recently, the authors in [226] have developed an intelligent control solution which enhance the plug-and-play capability based on time-domain system identification experiments. However, a simple diesel generator control strategy is proposed in this work and its methodology is shown in Figure 4.51. With the droop being set to a constant level, the diesel engine supplies a fixed amount of power to the generator regardless of the system frequency. The reference frequency for the governor is set to be higher than the grid frequency to ensure maximum power output is always achieved.

An emergency diesel generator which was modelled for nuclear power plant application coupled with the abovementioned droop control is implemented in this work [227]. The diesel generator modelling is shown in Figure 4.52, which includes the governor, diesel engine, synchronous generator and dump load. The control system and the actuator were represented as a second order and third order transfer functions, respectively [227]. The speed-droop or regulation characteristic was obtained by adding a steady-state feedback loop around the PI controller, as shown in Figure 4.53. The droop value, R in this case is set to 0, which effectively representing a constant level. For the engine, it can be regarded as a pure time delay due to the time taken for fuel command to result in torque applied to the shaft [222]. The value of this time delay depends on the number of active cylinders in the engine and the shaft rotational speed at the particular moment [222]. For this thesis, a time delay of 0.024s was used [227]. The gains and time constants used in this model were adjusted empirically [227].

Note that the diesel generator adopted in this work is based on a machine rated at a much higher value (3.25 MVA and 2.4 kV) than a small-scale HRES would use and it is likely to react in a much slower time frame. However, since the droop characteristic is flat (Figure 4.51); under steady state conditions it is largely unimportant what the transfer function is. Hence, the steady state model in Figure 4.52 is also then irrelevant as what is considered in this thesis is its sole purpose to

provide the fixed power reference. Therefore, the modelled diesel generator is not meant to predict the transient performance which is not being considered in this thesis. In addition, the machine parameters in this model are taken from Simulink directly and are not adjusted for a specific machine. In order to get a more accurate transient estimation of a diesel generator, experimental work should be carried out and the transfer function parameters may be fine-tuned accordingly.

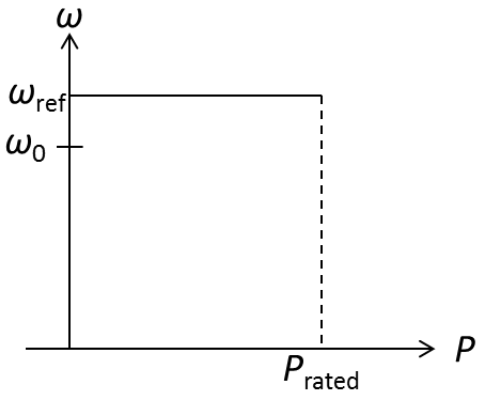

Figure 4.51: Diesel generator droop characteristics which enable constant rated power output

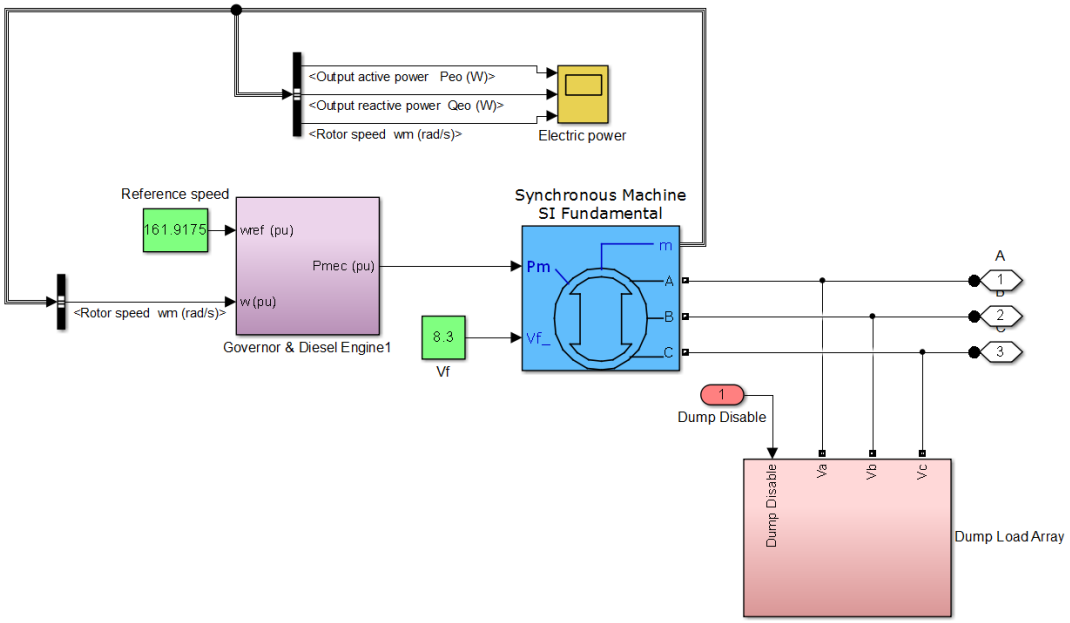

Figure 4.52: Simulink model of diesel generator set

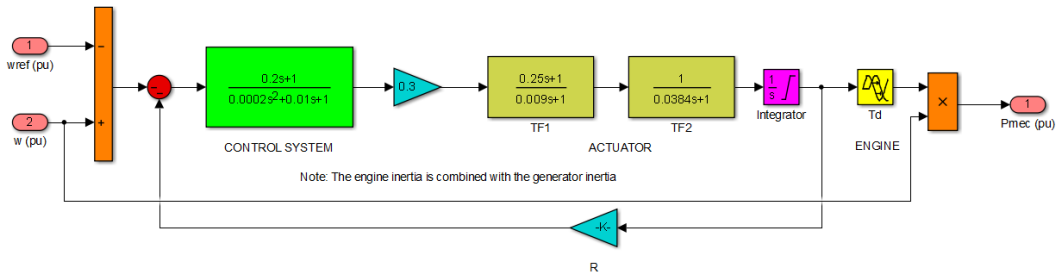

Figure 4.53: Simulink model of diesel engine and governor

Dump loads are included at the output of the diesel generator to smoothen the transition of synchronising both diesel generator and the SI inverters. If the dump load is not included, the diesel generator voltage and current transients would be seen by the inverters during synchronisation. This might cause unnecessary voltage spikes due to the sudden increase in load. When both systems are synchronised, the dump loads in the array are disconnected in stages, again to achieve a smoother transient. Note that the usage of dump loads in the system may incur additional installation and operation cost (when load is low or during the synchronisation process). The dump load disabling process can be described in the following flowchart, in Figure 4.54. Once the synchronisation and the connection between the DGs and the diesel generator are established, the dump loads are disconnected insteps. After all the dump loads are disconnected, the diesel generator operates at its rated condition, either supplying the load or charging the batteries if there is a surcharge of energy within the system.

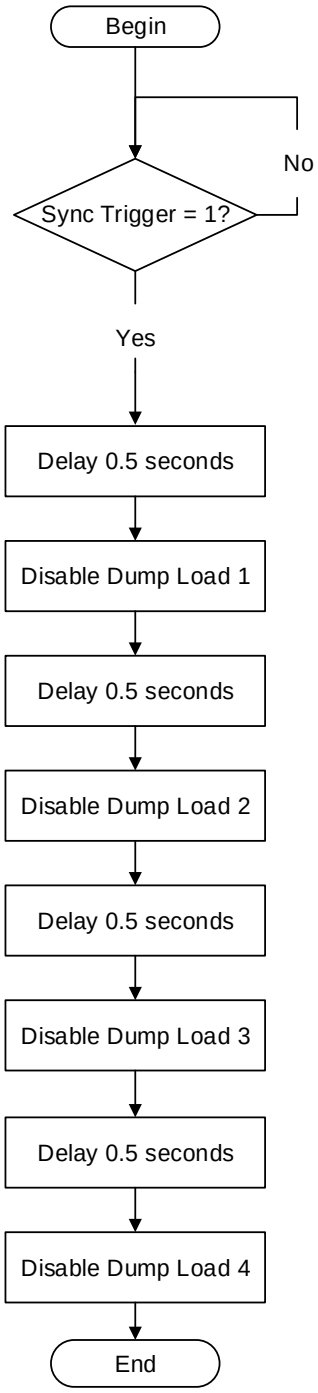

Figure 4.54: Dump load disabling process flowchart

4.6 Complete Simulation of Hybrid Wind-Diesel-Battery System

In the previous sections, the discussion has been focusing on the modelling of the hybrid components in a modular basis. Subsequently, it is vital to investigate the

performances of the hybrid system, the dynamic interactions and power flow between the components. The dynamics of the hybrid system can be examined via the disturbances taking place within the system such as the on/off switching of the loads and the turbulent wind input to the wind turbine.

The complete hybrid system simulation setup is shown in Figure 4.55. It began with the SI inverters forming the grid, which took approximately 50 s. The circuit breaker connecting the grid and the wind turbine was closed at 150 s. From this point onwards, the induction generator was started up via the soft-starter which was set to operate in current-mode control. The RMS of the start-up current was limited to 25 A. Once the wind turbine's induction generator was running at near synchronous speed, it began to generate power with a mean wind speed of 13 m/s. At 300 s, the mean wind speed dropped linearly to 5 m/s to emulate low wind condition. The diesel generator on/off state throughout the simulation was demonstrated in Table 4.11. It supplied a fixed power of 8 kW whenever it was synchronised and connected to the off-grid system. Note that the purpose of this section is to study the dynamics of the system, thus the diesel generator operation was not optimised, i.e., it was turned on even though the SOC of the battery was high. The load occurring events are shown in Table 4.12. The three-phase balanced loads were increasing in steps, followed by turning on of a highly unbalanced load at 250 s. The following simulation results were recorded after the DC link voltage was being established, which was approximately 50 s.

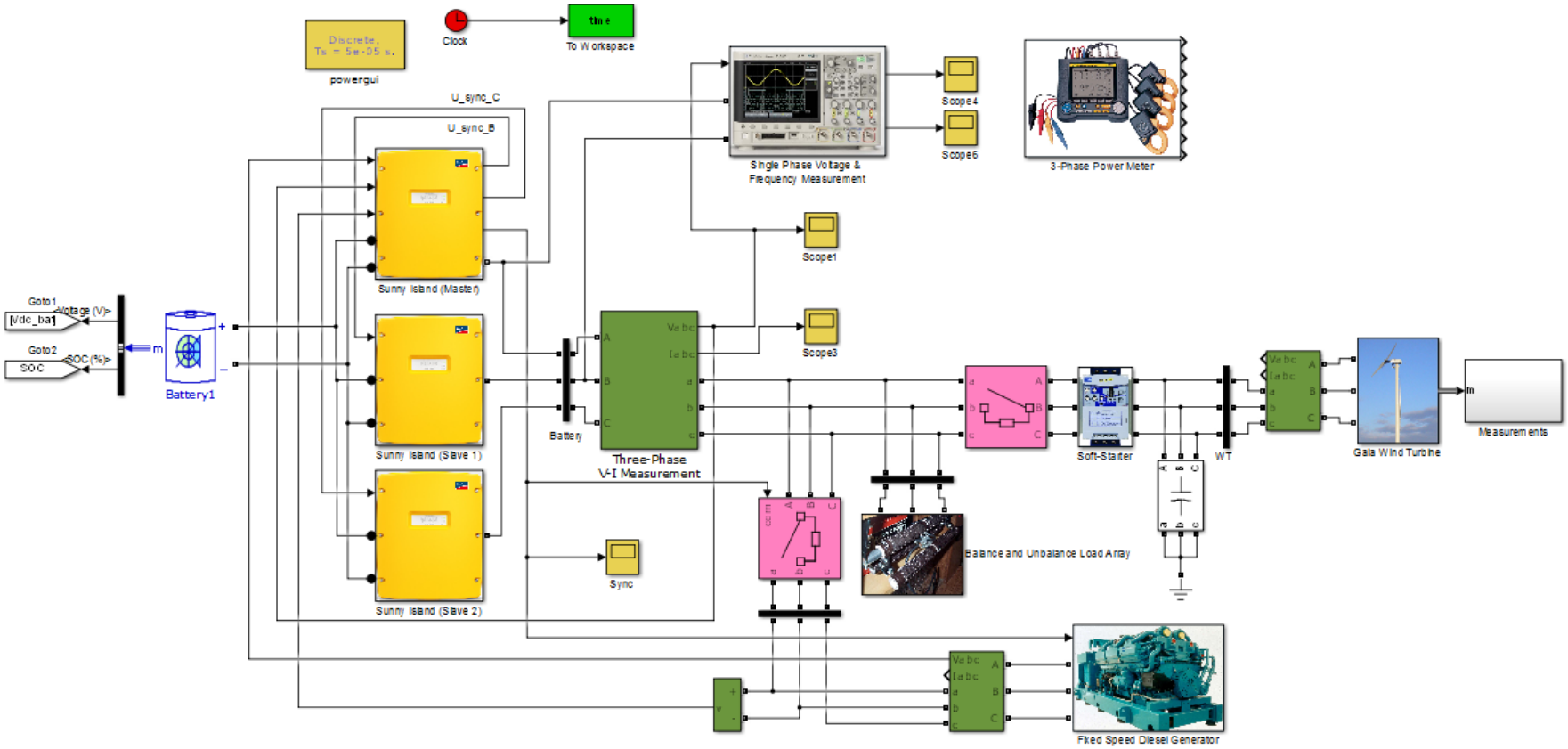

Figure 4.55: Complete Simulink model of hybrid wind-diesel-battery system

Time (s)	0 - 60	60 - 140	140 - 350	350 - 500
State of Diesel Generator	OFF	**ON**	OFF	**ON**

Table 4.11: On/off state of diesel generator for a total simulation time of 500 s

Time (s)	0 - 70	70 - 100	100 - 210	210 - 250	250 -450	450 - 500
Load 1 (3-Phase balance), 5 kW	OFF	**ON**	**ON**	**ON**	**ON**	OFF
Load 2 (3-Phase balance), 3 kW	OFF	OFF	**ON**	**ON**	**ON**	OFF
Load 3 (3-Phase balance), 6 kW	OFF	OFF	OFF	**ON**	**ON**	OFF
Load 3a (1-phase load), 1 kW Load 3b (1-phase load), 5 kW Load 3b (1-phase load), 2 kW	OFF	OFF	OFF	OFF	**ON**	OFF

Table 4.12: Load sequence for a total simulation time of 500 s

Figure 4.56 and Figure 4.57 show the RMS line-to-line voltage and frequency of the system, respectively. Voltage drop was seen to be more apparent when the wind turbine was connected to the SI inverters. This expected behaviour was generated from the soft-starter when it was configured as 25 A current limiter mode (shown in Figure 4.39). Similarly, the frequency fluctuations were also being reflected from the soft-starter (shown in Figure 4.40). However, it is important this may not be representative in a real system. The observed voltage perturbations just after 200 s can be attributed to the switching-on of several loads and the power fluctuations generated by the wind turbine. After the diesel generator was synchronised and connected to the system at about 350 s, the voltage stabilised. At 450 s, all the loads were switched off. Thereafter, the voltage and frequency of the system recovered to a level slightly higher than their rated values respectively due to the surplus energy available in the system. Overall, the system gave a satisfactory performance despite several disturbance events (wind turbulence, unbalance load, and synchronisation) took place within the time frame.

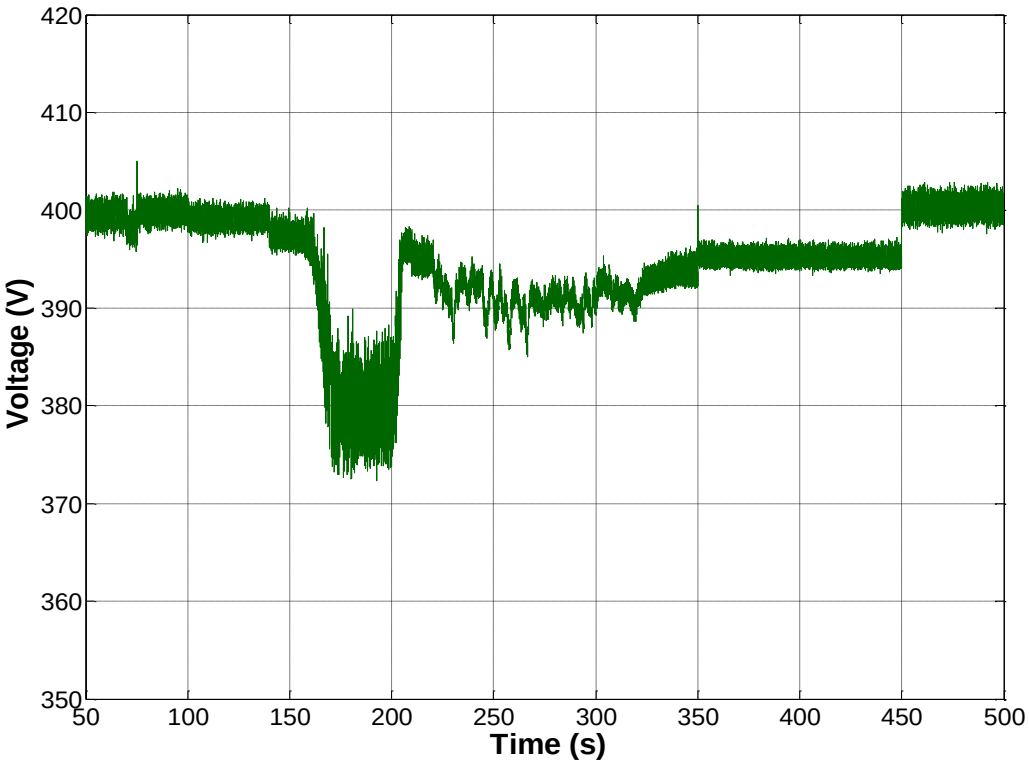

Figure 4.56: System voltage profile

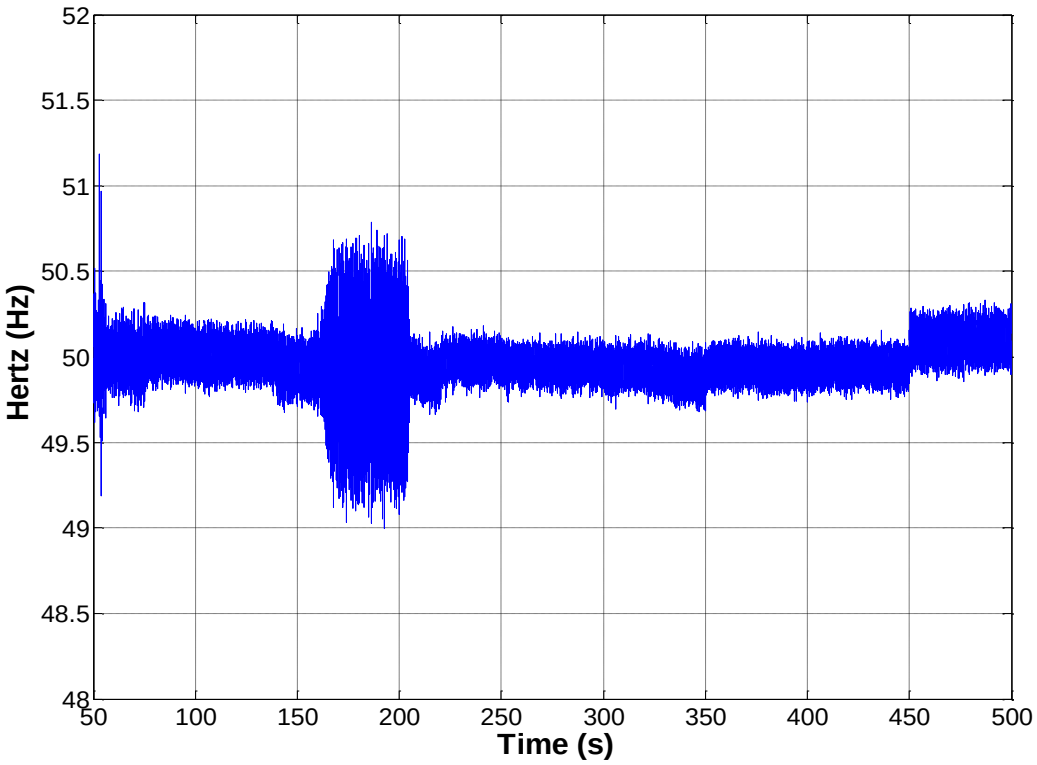

Figure 4.57: System frequency profile

Figure 4.58 shows the SOC of the batteries throughout the simulation. Between 50 s and 450 s, the batteries were discharging their energy because the total power generation in the system was lesser than the load demand most of the time. The SOC did not fluctuate significantly despite the power fluctuations experienced in the system due to turbulent wind input to the wind turbine. After all the loads were switched off at 450 s, the surplus energy from the system was stored in the batteries; hence the SOC rose quite linearly. The linear trend can also be explained by the fact that at lower mean wind speed (5 m/s), the power fluctuations output from the wind turbine was noticeably lesser.

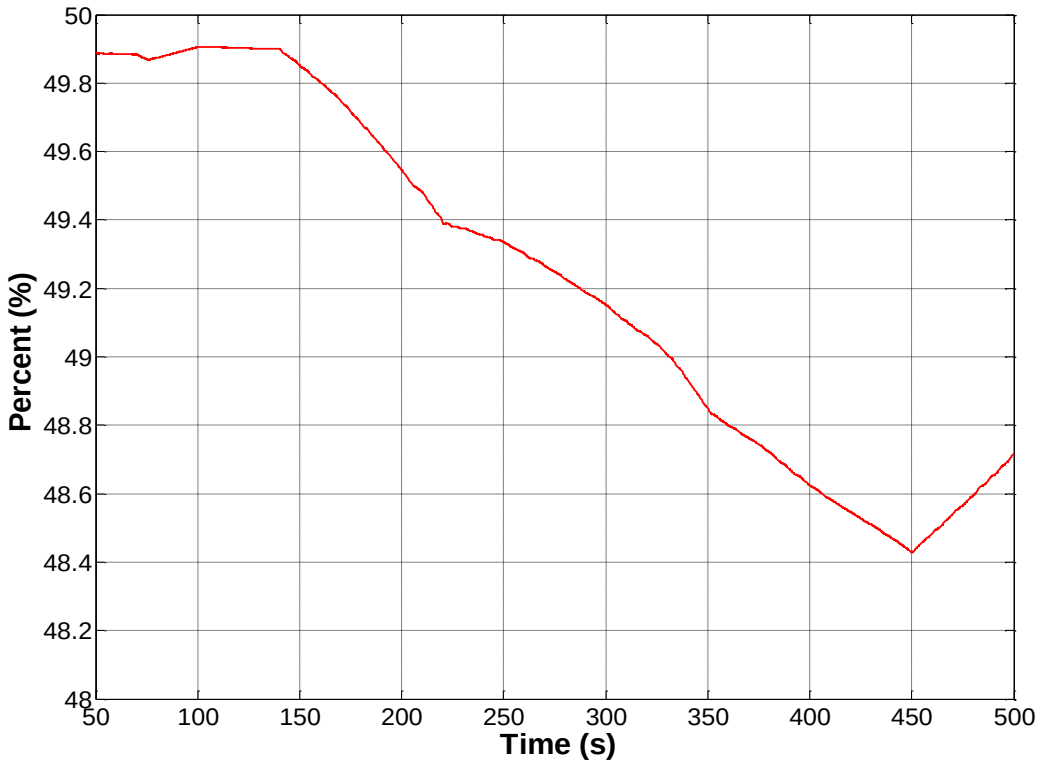

Figure 4.58: State of charge of the battery

Figure 4.59 shows the power flow within the system. From the first subplot, it can be observed that the induction machine of the wind turbine was motoring, hence consuming power. As soon as it reached near synchronous speed, it consumed minimal power. At 220 s, the wind turbine started to generate power (indicated with negative values). At 300 s, the mean wind speed dropped from 13 m/s to 5 m/s, reflecting a much lower power generation. Less power fluctuations were observed at lower mean wind speed as the turbulence intensity was smaller as mentioned previously. Subplot 2 shows the power generated by the diesel generator. In this simulation, the diesel generator was pre-set to turn on twice. The power output of the diesel generator was relatively constant with slight oscillations, despite the system frequency, load demand and power generation from the wind turbine. The power from the diesel generator was first to be utilised if the wind power was insufficient to meet the load demand requirement. On the other hand, surplus energy from the diesel generator was stored in the batteries for later use (happened between 450 s and 500 s). Subplot 3 shows the power absorbed by the loads. Between 160 s and 200 s, the

dissipated load power was reduced slightly as a result of voltage drop in the system. This event took place when the soft-starter of the wind turbine was operating within the time interval. Lastly, subplot 4 shows the charging and discharging operation of the batteries. This plot serves as an indicator of whether the system was having surplus or deficit energy. The battery supplied the power to the load via the inverters only when insufficient power was generated by the wind turbine and the diesel generator. Practically, it is important to note that the wind energy and the energy stored in the batteries should be first utilised, before turning on the diesel generator. However, this case study did turn on the diesel generator on purpose even before the SOC was low as the purpose here is to explore the dynamics of the system, rather than running it optimally. In the next chapter, the benefit of running the diesel generator with a pre-set time is demonstrated with the knowledge of optimised operation.

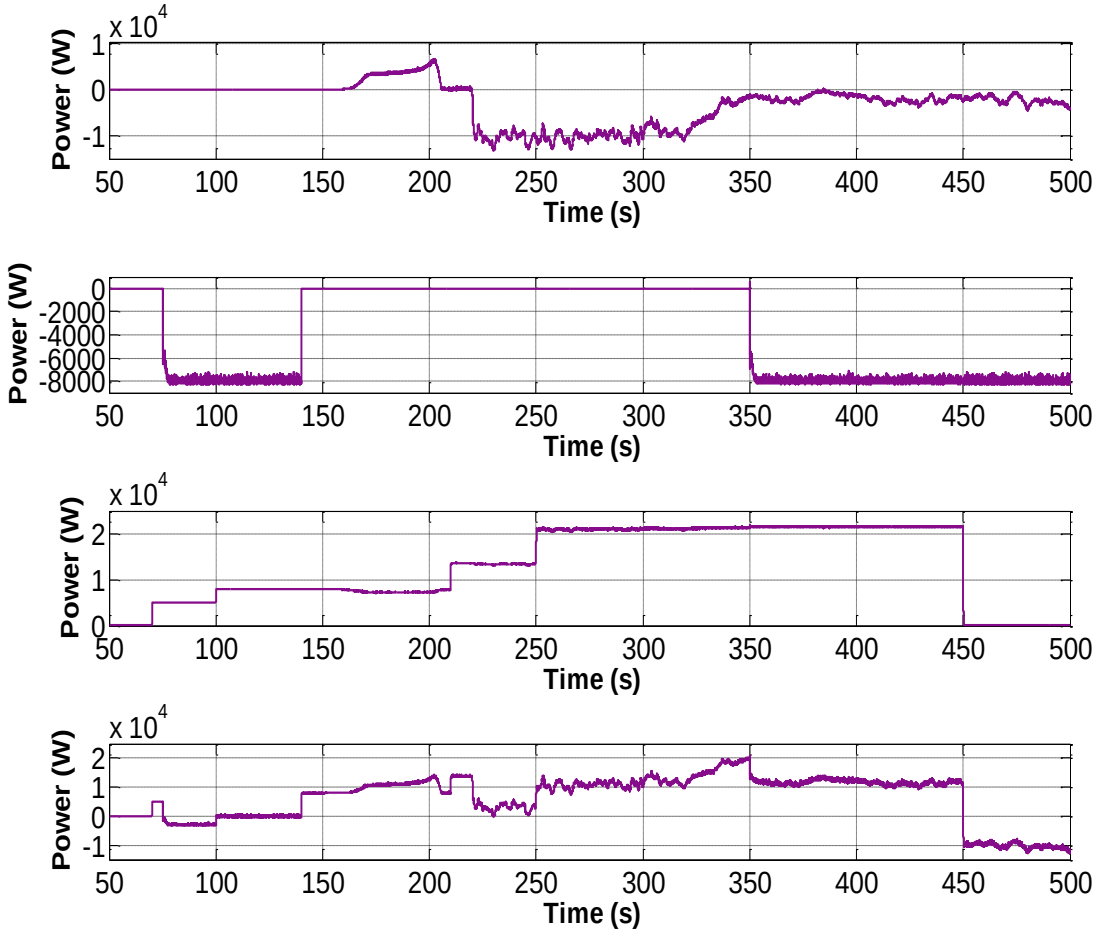

Figure 4.59: *a)* Wind turbine power *b)* Diesel generator output power *c)* Load demand *d)* Charging and discharging power of the batteries

Finally, in order to analyse the performance in a holistic approach, Figure 4.60 shows the 3D plot of fast fourier transform (FFT) analysis being done on the voltage at hybrid system. In order to observe the power quality at different stages, FFT was done with the sampling rate of 0.1 s. Note that in this plot, the zeroth order (DC) and fundamental signal (50 Hz) are not shown as the objective of this analysis is to focus on the harmonics from 2^{nd} order to 20^{th} order. The even harmonics should be extremely low in magnitude due to the selected PWM reference frequency as shown in Table 4.5. Hence, theoretically, only odd harmonics were observed. As predicted, the higher order harmonics (above 10^{th} order) were lower in magnitude. This can be explained through the fourier series formula:

$$a_n = \frac{4}{n\pi} \sin n \frac{\gamma}{2} \tag{4.31}$$

As the magnitude of *n* increased, the harmonics coefficient became lower. Also the designed harmonics filter had attenuated the high frequencies components. The harmonics were more significant between the time interval 150 s and 200 s due to the usage of a soft-starter. The thyristors switching reduced the power quality of the system. Once the induction generator was running at near synchronous speed, the harmonics were seen to be lower in magnitude. Overall, these harmonics levels were low, (peak amplitude of less than 10) relative to the fundamental signal which had a peak amplitude of 400 V.

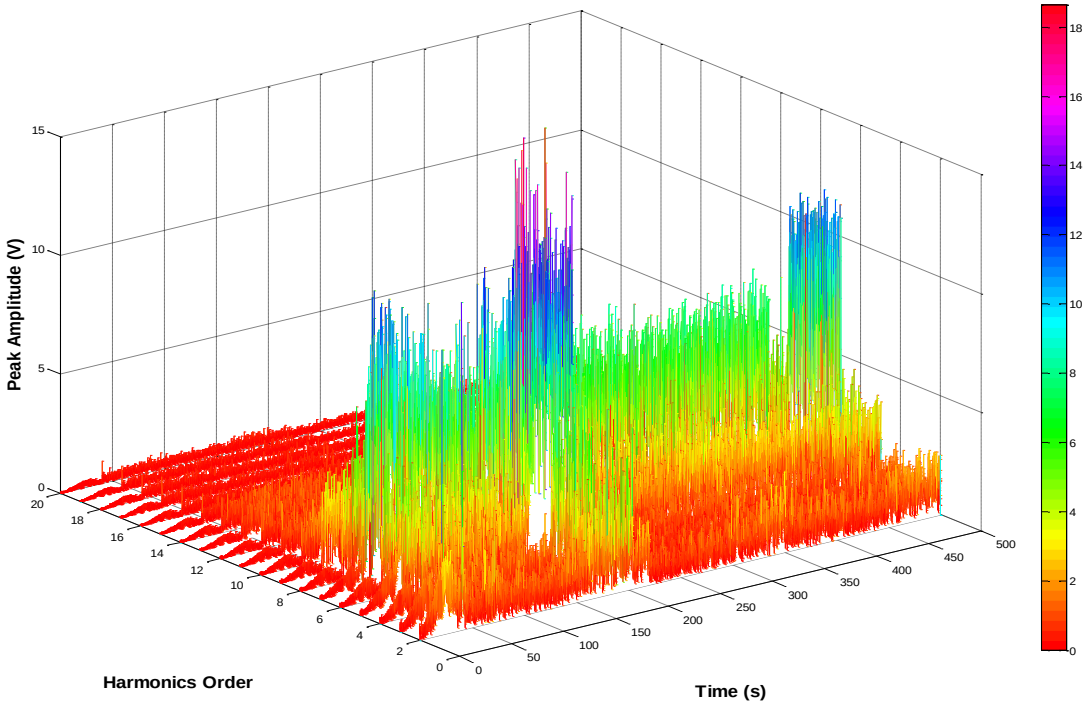

Figure 4.60: Hybrid system FFT analysis with 0.1 s sampling time

4.7 Summary

This chapter has explained the modelling and simulation results of a hybrid wind-diesel-battery system. The modelled hybrid system performs satisfactory and it provides a platform to a better understanding of the dynamic interactions between the components. It is common to use simple mathematical representations while optimising the operation of an off-grid system. However, the optimised results obtained from the mathematical modelling in the next chapter will be verified using the hybrid system model developed in this chapter. Therefore, a comparison can be made between the mathematical model and physical model. Finally, the knowledge gained through this chapter will assist the hardware development work at a later part of this thesis.

Chapter 5 Optimised Operation of Off-grid Hybrid Systems

It is well-known that a diesel generator is recommended to operate at 40% of its rated capacity or higher to prolong diesel engine lifetime. However, the user load profile is not constant throughout the day and it is often well below the suggested part-load diesel capacity. In addition, the situation becomes worse when the variability of the renewable energy sources is not taken into consideration while operating the hybrid system. The diesel generator's part loading problem can be alternatively mitigated by using a variable-speed diesel generator which was proposed in [51]. A comparison of the fuel consumption power curve between a fixed-speed and a variable-speed diesel generator has been carried out in [51]. The difference in fuel consumption between the two diesel generator types is small in the lower power ranges and non-existent above 65 kW [51]. One should evaluate the loading profile carefully as to whether or not the installed variable-speed diesel generator unit is economical as it utilises power electronics and permanent magnet generator which dramatically increases the control requirements, complexity and therefore the overall cost. In this work, the fixed-speed diesel generator is given attention to mitigate the part load.

The inclusion of batteries in a hybrid wind-diesel system allows a fixed-speed diesel generator to run at full load regardless of the load demand level at any particular time. In this case, the batteries are regarded by the diesel generator as an additional load in order to increase the power output closer to its rate capacity. In windy locations, the diesel generator is only switched on whenever there is a lack of energy from the wind and battery storage. An unknown matter in this case is the duration that the diesel generator should be operated. If a diesel generator runs for too long and charges the batteries to a high SOC, the potential available excess wind energy at a later time cannot be stored. Subsequently, excess energy is dissipated in a large dump load or wind power generation is curtailed. This scenario can be observed from the measured wind speed profile in February 2012 in Bishopton, as demonstrated in the lower plot of Figure 3.4.

As mentioned before, the RES are variable, intermittent and do not follow the trend of the consumer load profile. One way to reduce this uncertainty, and at the same time to increase customer satisfaction, is to install as much energy storage as possible to help in matching the irregular pattern of the energy supplied from the wind to the load demand profile. However, a hybrid system which has been designed in this manner will not be economical. This further emphasises the need to optimise the operation of a hybrid system, so that the energy storage system can be used efficiently to cope with drastic fluctuations in wind energy.

After sizing the hybrid system optimally as analysed in Chapter 3, the coordinated control of the hybrid system can be treated as an optimisation problem. Fortunately, if the day-ahead forecasted wind and load are available, the operation of the diesel generator can be optimised. A set of constraints such as the allowable range of battery SOC, the diesel generator capacity and the battery storage capacity are to be met within the optimisation problem. Besides, the nature of the diesel generator cost function, efficiency curve, battery degradation models and other parameters may be defined as non-linear functions, hence the non-linear optimiser is chosen in this work. These parameters can be incorporated into the optimisation problem in future if needed, although it is acknowledged that the utilisation of non-linear optimiser at this instant demands higher computational effort than the linear optimiser. Since it is desired to run the fixed-speed diesel generator at its rated power, the optimised solutions obtained from a non-binary technique need to be post-processed. This will be further described in the later sections. In most of the literature, the authors studied and investigated an optimised hybrid system operation using a mathematical approach [228] [229] [230] [231]. The main drawback of this method is the lack of mechanical and electrical considerations which take place in the real world, in particular, the physical dynamics of the system. In addition, most of the numerical optimisations are performed in an hourly discretised manner, which further decreases the accuracy of the optimised results produced.

For the first time, this work proposes a methodology to optimise the operation of the diesel generator, by considering its efficiency and also reducing the start-stop cycles in order to safeguard its lifetime. Besides that, the author puts emphasis on the

electrical and mechanical considerations, through the utilisation of physical modelling after developing an optimised control solution mathematically. The optimised solution was sought by optimising the diesel generator's operation using the Genetic Algorithm (GA) based on the forecasted wind and load profiles, which was discretised every 10 minutes. Then, the numerical optimised results were processed and being fed into the hybrid system model, which was developed using Simulink. The high-resolution simulation outputs include the system voltage and frequency, battery SOC, power flow from the wind turbine, diesel generator, load demand and batteries. The simulation ran for twenty-four hours simulation time. The simulation methodology is presented in Figure 5.1. It is uncommon to run sophisticated Simulink models with such a long simulation time due to the long central processing unit (CPU) computation time and the limitation of random access memory (RAM). It took approximately four days in real time to complete one simulation using a computer with an Intel Core i7 3.40 GHz processor, 32GB of RAM and 64-bit Windows operating system. Finally, sensitivity analyses were conducted to test the robustness of the obtained solution. The proposed methodology which thoroughly investigates an optimised hybrid system is novel and the details are to be discussed in the next sections.

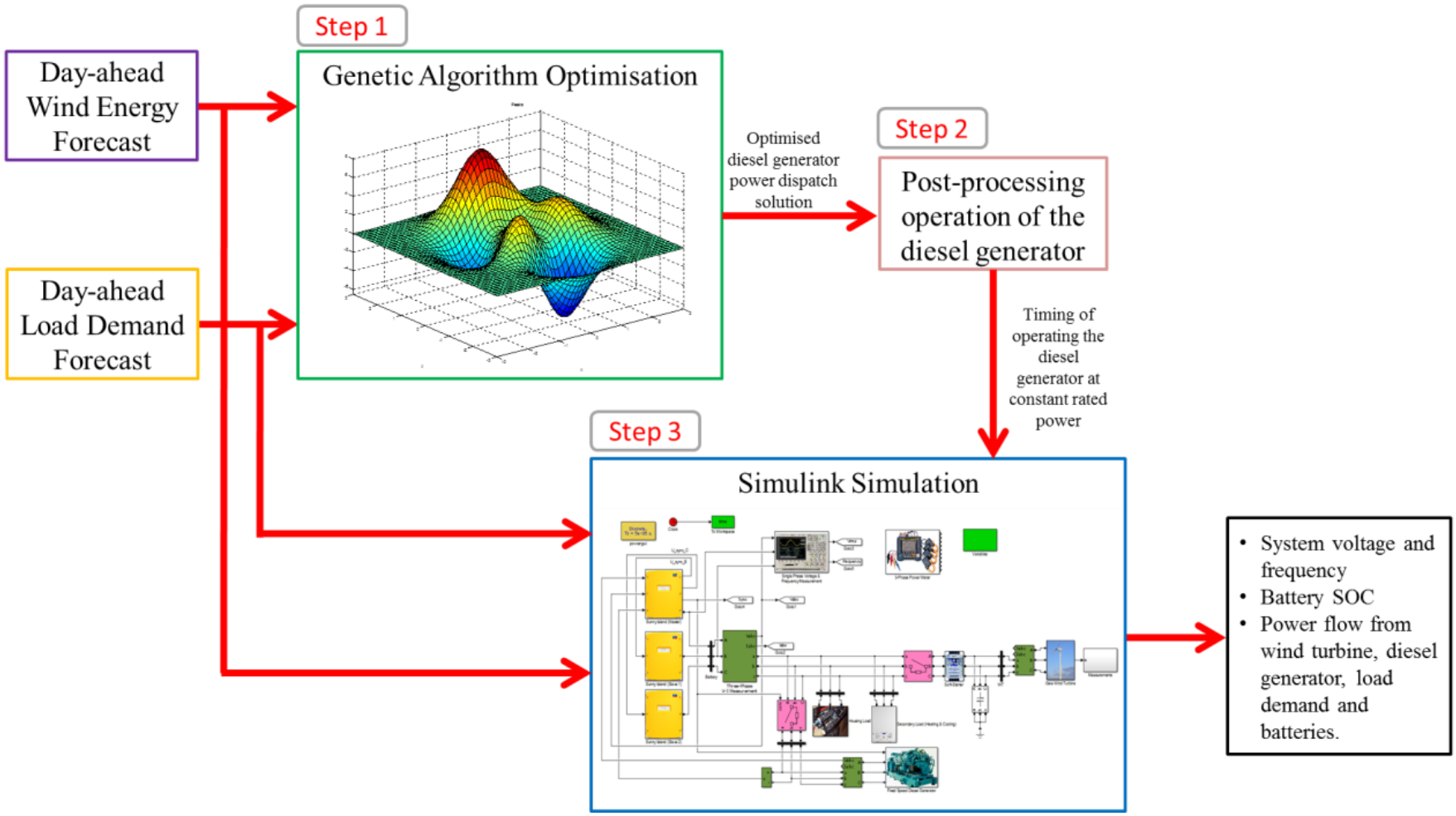

Figure 5.1: Proposed simulation methodology

5.1 Modelling and Optimisation of Hybrid System Operation using Genetic Algorithm

This section describes the modelling and optimisation methodology of the hybrid system operation. In literature, there are several optimisation algorithms which can be applied on optimising the performance of a hybrid system. GA which is classified as one of the evolutionary algorithms, is chosen in this work due to its capability of determining global optimum solutions over a series of generations throughout the search space [232] [233]. This is in contrast to local solutions determined by a continuous variable optimisation algorithm [234]. In addition, it is readily available in MATLAB's Global Optimization Toolbox and it conveniently enables the process of feeding the optimised results into Simulink software. The concept of GA was first introduced and developed in the mid-seventies. GA belongs to the class of stochastic search optimisation methods [235]. This simplified the programming process as they do not require the use of gradients of cost or constraint functions [234]. Biological evolution which is based on Darwin's theory of natural selection is comparable to the mechanics of GA, in which the language of microbiology and its application mimics genetic operations [234] [235]. It can be used to optimise multi-dimensional, non-linear engineering problems efficiently.

The basic idea of the GA is to start from a single point (or guess) within the search space and it initialises with a population of guesses. Then, the GA generates a new set of designs (population) from the current set such that the average performance (fitness) of the design is improved. The process is continued until a stopping criterion is satisfied or the number of generations exceeds a specified limit [233] [234]. In this case, the inputs to the optimisation programme are wind and load data respectively. The programme minimises diesel fuel use subject to the following constraints:

- At any point in time, the total power generated by the wind turbine, battery storage and diesel generator must be greater than or equal to the load demand
- At any point in time, the energy stored in the batteries is the energy excess between the total power generation (from wind and diesel generator) and the load demand.

- At any point in time, the minimum SOC of the batteries should be greater than or equal to 20%.
- At any point in time, the power generated from the diesel generator should be less than or equal to its capacity

5.1.1 Wind Energy Modelling

In this work, historical wind speed data was taken from the Gaia-Wind Ltd's database (LeSENSE). The main objective of this chapter is to demonstrate the decision of turning on the diesel generator optimally without charging the batteries unnecessarily as it is predicted that there is potential wind energy available at a later time. As demonstrated from the yearly battery SOC in Figure 3.18 (in Chapter 3), the SOC did reach the pre-defined lower limit. The rate of the batteries reaching low SOC is dependent on their size. With higher storage capacity, the frequency of reaching low SOC is lower and vice versa. With a near optimally sized battery capacity of 155 kWh (Figure 3.18), an extended period of low SOC occurred approximately 8 to 10 times. It is expected that similar situation may happen in other parts of UK. However, the exact figure varies depending on storage capacity. Furthermore, the occurrence of low wind speed for an extended period of time is not uncommon. The measured wind speed about the first two weeks of February 2012 in Bishopton is observed to be insufficient to generate significant power from the wind turbine to supply the load. Besides, the wind speed during the last two weeks of the month fluctuates rapidly. With this in mind, the author has selected a historical wind speed data which was measured in Aberdeen (Scotland) on 28/9/2011. Figure 5.2 shows the wind profile using the wind speed data in which each data point is averaged over 10 minutes. It can be observed that the wind speed is moderately low from midnight until 8 a.m. The highest wind speeds occur between mid-morning and mid-afternoon, reaching a peak of just over 9 m/s. In a non-optimised system, the diesel generator could turn on for a significant period of time in the morning and charge the batteries to a high SOC. Subsequently, the excess wind energy in the afternoon would be dissipated as waste energy as it cannot be stored in the batteries. The wind profile was then fed through the wind turbine power curve the power

output from the wind turbine, as shown in the lower plot of Figure 5.2. Note that power generation starts at approximately 3.5m/s wind speed.

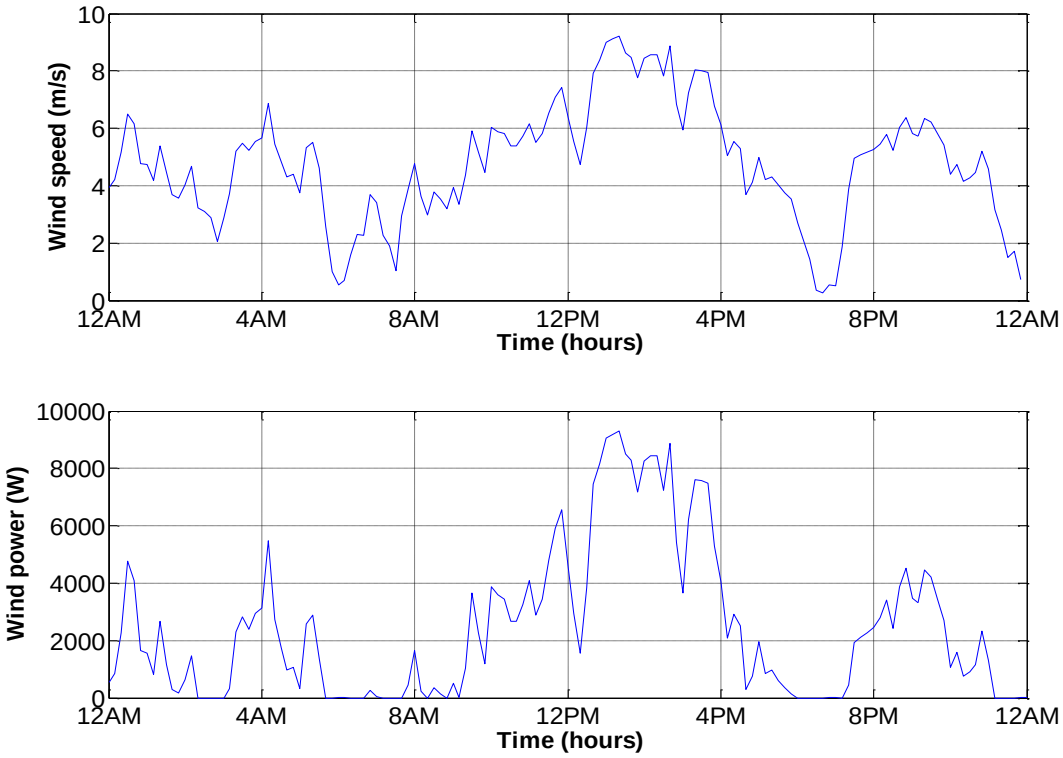

Figure 5.2: Ten-minutes average wind speed and wind power in Aberdeen measured on 28/9/2011

Typically, an energy dispatch optimisation within a hybrid system is performed in an hourly sampling time [231] [236] [137] [57]. At this resolution, the probability of losing data (peaks and troughs) is high. In this work, the optimisation is carried out with a sampling time of 10 minutes. With this defined resolution, it is important to note that each data sampling point consists of only 1/6 of the hourly energy (kWh), i.e. kW10min. Therefore, care must be taken when working with this unusual energy convention. Figure 5.3 shows the bar graph of the wind energy throughout the day. Each bar represents the absolute amount of energy generated from the wind turbine in 10-minute intervals.

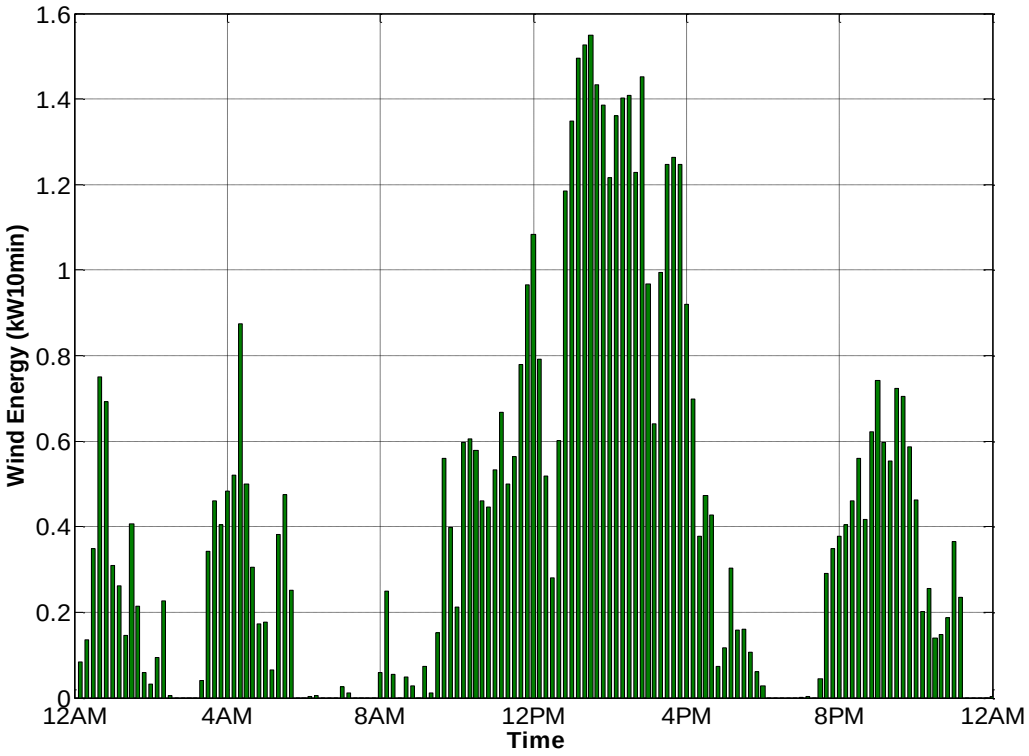

Figure 5.3: Wind energy with a sampling time of 10 minutes (28/9/2011 in Aberdeen)

5.1.2 Load Modelling

The load model used in this study can be found in Appendix A. Keeping in mind that the optimisation procedure proposed here works with 10 minutes resolution, the load profile thus needs to be translated to the same convention as the wind energy described above. In addition, the active power demand of the system is only of interest in this case. Figure 5.4 illustrates the load energy profile with 10 minutes sampling time, i.e. each bar consists of the amount of energy used by the consumer in 10 minutes. Comparing the upper figure of Figure , it is noticed there is a loss of data due to the lower sampling rate. The peak demand which was occurred just after 8am is not visible in Figure 5.4. In addition, the duration of the peak demand which happened just before 8pm was shortened as a result of the down-sampling process being taken place. A higher sampling rate is possible to capture these peaks, however this comes with the compromise of longer computation time during the optimisation process. A higher sampling rate optimisation has been attempted in this work and it

resulted in an insignificant amount of accuracy and it is thus not "economical" in this case.

It is also noted that the start-up energy of the wind turbine is not considered in this chapter for simplicity purposes. It is expected the diesel generator might be used to support the start-up of the wind turbine if the battery SOC is low. In addition, a few small dips in SOC profile should be observed if the additional starting load is considered.

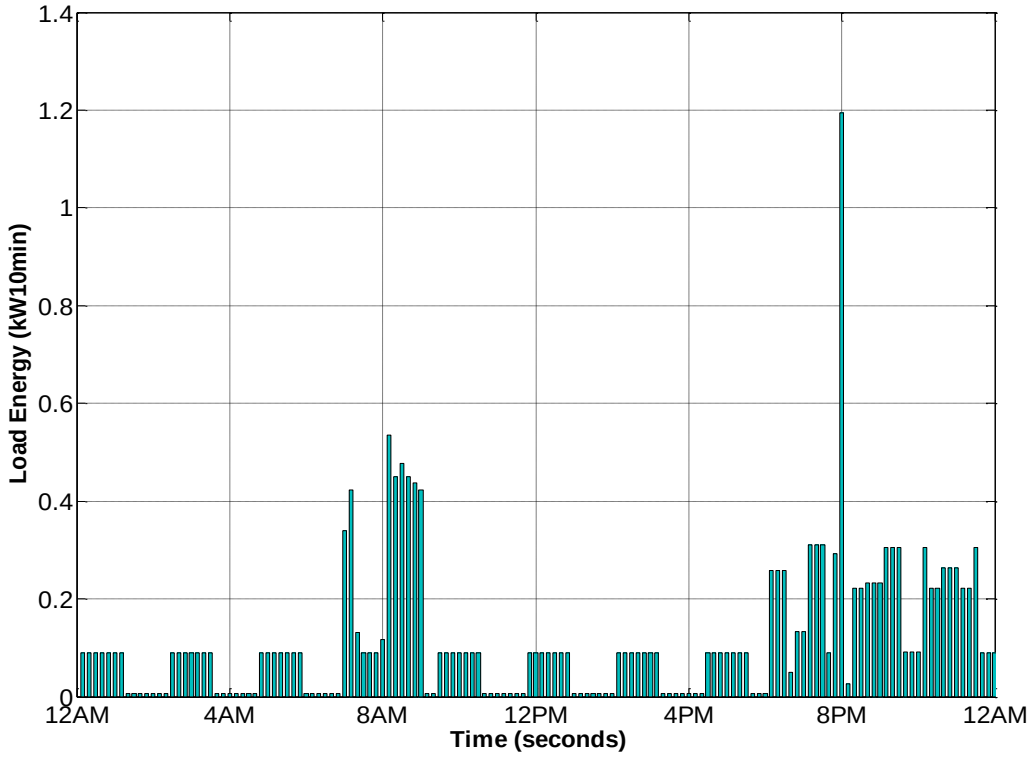

Figure 5.4: Load energy profile with a sampling of 10 minutes

5.1.3 Problem Statement, Constraints and Hybrid System Parameters

The objective of the proposed control topology is to minimise the diesel generator fuel consumption, over finite time duration:

$$\text{Objective function} = \min \sum_{n=1}^{144} E_{\text{diesel}}(n) \quad \text{subject to} \tag{5.1}$$

where:

n : sampling time of 10 minutes
$E_{diesel}(n)$: diesel generator energy output within the 10 minutes duration

Note that the objective function is minimised, subjected to the constraints of energy balance within the system, energy to store in the batteries from the excess and the minimum battery SOC.

At any point of the sample period, the total energy generated by the wind turbine, battery storage and diesel generator must be greater than or equal to the load demand. This can be written as:

$$E_{\text{wind}}(n) + E_{\text{diesel}}(n) + E_{\text{store}}(n) \geq E_{\text{load}}(n) \tag{5.2}$$

where:

n : sampling time of 10 minutes
$E_{store}(n)$: current battery energy level
$E_{wind}(n)$: wind energy output
$E_{diesel}(n)$: diesel generator energy output
$E_{load}(n)$: load energy demand

The next constraint explains that at any point of the sample period, the energy stored in the batteries is the energy excess between the total power generation (from wind and diesel generator) and the load demand.

$$E_{\text{store}}(n) = E_{\text{store}}(n-1) + E_{\text{wind}}(n) + E_{\text{diesel}}(n) - E_{\text{load}}(n) \tag{5.3}$$

where:

n : sampling time of 10 minutes
$E_{store}(n)$: current battery energy level
$E_{store}(n\text{-}1)$: previous time step of battery energy level
$E_{wind}(n)$: wind energy output
$E_{diesel}(n)$: diesel generator energy output
$E_{load}(n)$: load energy demand

Finally, the battery SOC should be greater than or equal to the pre-defined lower limit at any point of the sample period:

$$E_{\text{store}}(n) \geq SOC_{\text{min}}(n) \times battery\ storage\ capacity \tag{5.4}$$

where:

n : sampling time of 10 minutes
$E_{store}(n)$: battery energy level
$SOC_{min}(n)$: battery state-of-charge

With the wind and load data being made available, optimisation on diesel generator operation can then be performed. From Chapter 3's long-term cost analysis, a hybrid system which consists of a Gaia-Wind Turbine (11 kW power rating) is more economical to supply electricity to about two to three households. In other words, the cost of energy will increase if too little or too much load being supplied (Figure 3.15). In this case, three households were considered. Within Chapter 3, the computed optimum battery capacity based on life-cycle approach was 150 kWh with an 11 kW diesel generator. However, from Figure 3.5, it is clear that this sizing is based on a spell of low wind power including over 3 days of very low wind power (less than 3 kW). As this chapter is only concerned with a single 24 hour period, the available energy storage size has been scaled by this time period to about one third of 150 kWh to give a more realistic quantity of the energy likely to be available over an extended representative period of low wind. In addition, due to the presence of the extended period of low wind speed, the starting SOC of the battery was set to a minimum value of 20%. As demonstrated from the optimised results in the next section, the reduced battery capacity has increased the probability of the battery SOC to reach the low limit and would trigger the diesel generator to switch on. If on the other hand a bigger battery capacity is used, the diesel generator may not turn on at all as sufficient amount of energy can be sourced from the batteries during low wind conditions.

Initial sizing studies demonstrated that an 8 kW diesel generator was appropriate. However, subsequent improvements in sizing the diesel generator as shown in Chapter 3 have resulted in a change in the optimum diesel generator power rating to 11 kW. Additionally, the initial sizing studies did not relate the battery lifetime from DoD point of view. However, it is understandable that the usable battery capacity can be varied either by changing the absolute battery capacity or by modifying the allowable DoD, which both provide the same results if battery degradation is not taken into consideration. Since the focus in this chapter is to study the underlying principles of the proposed control strategy, which do not factor battery degradation as the key parameter, a different SOC limit used is tolerable. Unfortunately, time did not permit the results in this chapter to be re-done due to the significant amount of computing power required to generate a day's worth of data. It was perceived that the

change from 11 kW to 8 kW was small enough not to be deemed significant and a different allowable DoD adopted in this chapter is not expected to have a major influence in the following analyses. The specifications/conditions for the hybrid system to be optimised is summarised in Table 5.1.

Specifications/Constraints	*Values*
Gaia wind turbine power rating	11 kW
Number of household(s)	3
Total battery capacity	45 kWh
Initial battery SOC	20%
Minimum SOC at all time	20%
Diesel generator capacity	8 kW

Table 5.1: Specifications for optimised hybrid system

5.1.4 Optimisation Results

The objective of this optimisation is to minimise the diesel fuel used, subjected to various pre-defined constraints as mentioned in the previous section. The number of generations used for the simulation is 500. The results are demonstrated in Figure 5.5. The data points with reference to the y-axis on the left represent the energy production from the wind turbine and diesel generator, and the energy dissipation (consumer's load) in 10 minute intervals. To ease viewing, the graphs are plotted in lines rather than bars which were done previously in the down-sampled wind energy and load demand plot (Figure 5.3 and Figure 5.4). The right axis shows the absolute energy level of the batteries in 10 minute intervals.

The batteries began with a SOC of 20% which corresponds to 9 kWh. The GA optimisation was run for 500 generations. The optimised diesel generator energy output can be seen from Figure 5.5 (blue line). Despite having the desire of operating the diesel generator at its power rating, it is not possible to be computed through the adopted optimisation algorithm. This is because a decision variable was being utilised in the optimisation model. A decision variable is a quantity that the solver computes and user has no control over it.

At around 8am, the wind energy and the battery SOC were low while the load demand was quite high. In order to satisfy the minimal battery SOC constraint, the diesel generator started its operation to maintain the energy level of the batteries at approximately 20%. However, the diesel generator does not operate for longer than it was needed because of the significant amount of wind energy predicted to be available in the afternoon. Thereafter, the load in the evening was supplied from the charged batteries and the wind. It is noticed that the batteries started to charge at around 10am when the wind speed increased. However, it is noticed that at 11am, the control algorithm decided that the diesel generator is switched on to charge the batteries. This may be attributed to the insufficient number of generations being assigned while computing the optimised results. In this case, it can be remarked that the proposed GA control algorithm is over-complexed and it is not required. A more straightforward load following strategy (used in Chapter 3) would be more appropriate in this case. Nevertheless, it is noted that the proposed GA control algorithm may be more useful for more complex schemes of HRESs, which involves additional DGs and load types. It is important to note that the overall utilisation of wind energy (renewable) for the operation is high, which further justifies that the designed system is more sustainable and environmentally friendly.

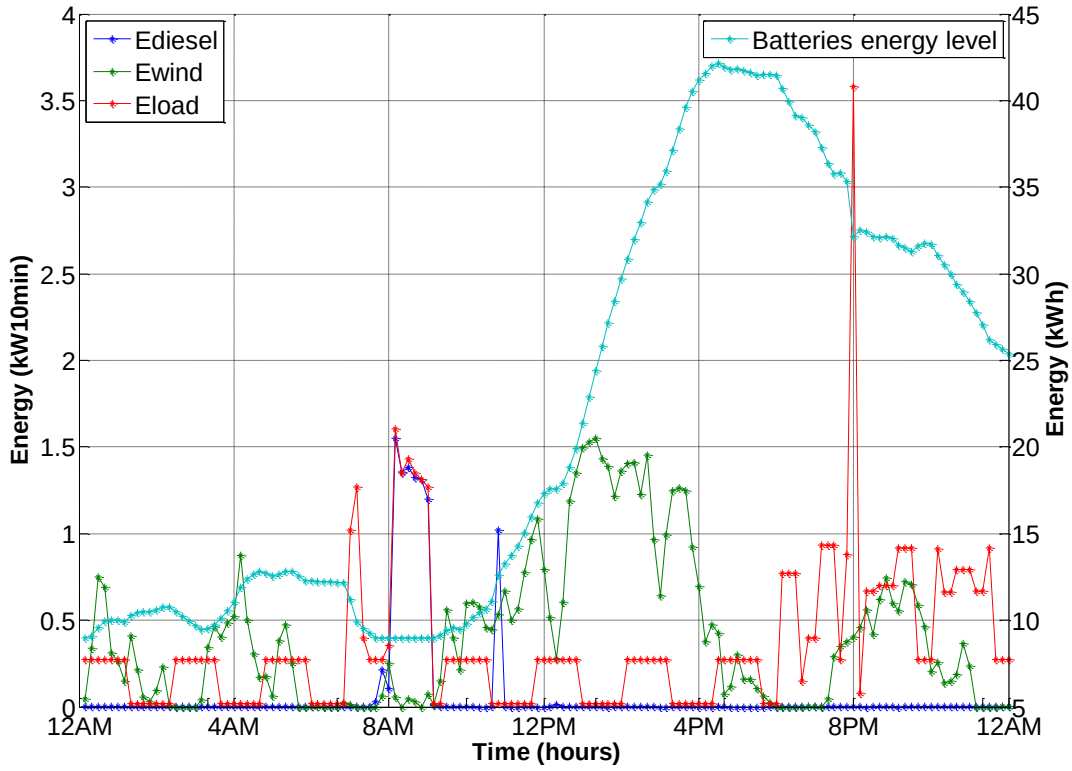

Figure 5.5: *Left axis*: energy generation from wind and diesel generator and energy consumption from the load. *Right axis*: batteries absolute energy level

The diesel generator's power dispatch control is more complex if they were to operate according to the pattern as shown previously. A sophisticated control system would need to be implemented to allow fast power output variation of the diesel generator. In addition, the lifetime of the diesel engine might be compromised if a complicated control system is employed as it will trigger the diesel generator to operate at part load condition on many occasions. Therefore, this work has proposed a method to process the diesel generator energy generation values obtained from the optimisation before putting into good use. This reduces the complexity of the control system within the diesel generator as it is programmed to operate at its rated capacity whenever it is switched on.

A two-hour time window was formed, resulting in twelve time windows throughout the day. Each time window consists of 12 data points due to the 10 minutes sampling time used here. The proposed windowing method on the diesel generator power output is illustrated in Figure 5.6. The diesel generator energy output within a

window was accumulated. If there were any energy generation within that particular time window, the diesel generator was operated for 10 minutes at its rated capacity. If the accumulated value was greater than the power rating of the diesel generator, it was set to continue its operation for the next 10 minutes. This process continued until the accumulated value was less than the total energy generated from the diesel generator at rated power. In this work, the diesel generator has a power rating of 8 kW, which is capable of generating 8 kWh of energy in one hour. The amount of energy generated in 10 minutes is thus 1.333 kWh (8 kWh divided by 6).

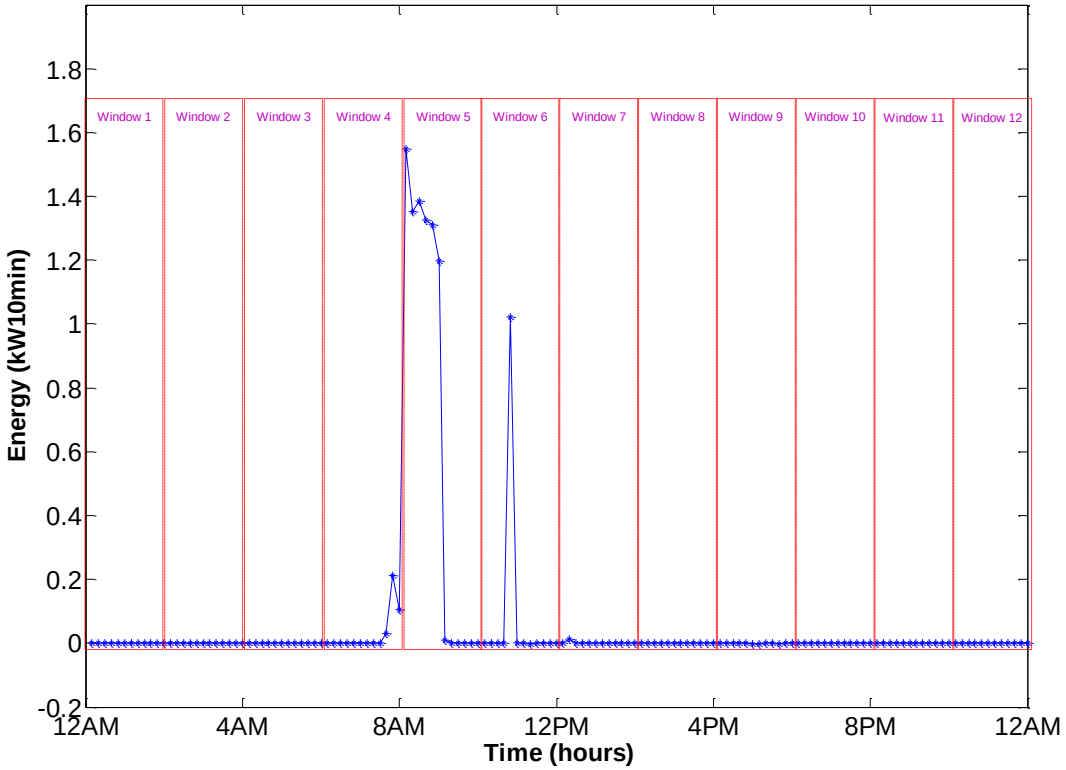

Figure 5.6: Windowing of the diesel generator output

Figure 5.7 shows the operation of the hybrid system after post-processing the diesel generator output. Notice that the diesel generator was operating at its power rating whenever it was turned on. As a result, the SOC profile within the day was also altered. As an example, considering the time frame within the fifth window (8am to 10am) in Figure 5.6, the accumulated diesel generator energy output was 6.58 kW10min. After performing the accumulation process as described above, the diesel

generator operated for 50 minutes at its full capacity, generating in a total of 6.67 kW10min. Although this was slightly more than the optimised value (6.58 kW10min), the diesel generator was believed to be able to operate more efficiently (fuel efficient) and therefore, prolonging its lifetime. The corresponding altered charging profile of the batteries is shown at the right-axis of Figure 5.7. All in all, this strategy has reduced the frequency of on/off switching (which depends on the sampling time of the optimisation and the number of windows used in a day) and has prevented the diesel generator from operating at low load condition, which potentially jeopardised its lifetime. It is worth mentioning that the start-stop frequency and period of the diesel generator can be adjusted by changing the time windows in a day or using a diesel generator which has a different power rating.

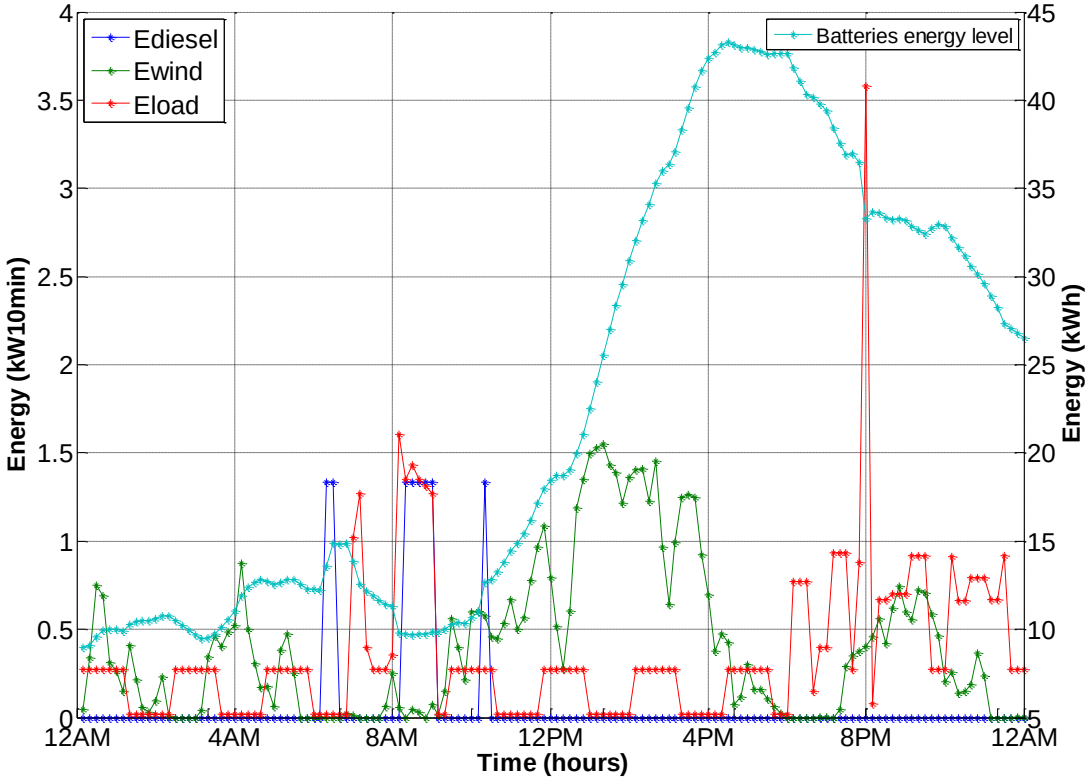

Figure 5.7: *Left axis*: post-processed diesel gen energy output. *Right axis*: post-processed batteries absolute energy level

5.2 Simulation of an Optimised Hybrid Wind-Diesel-Battery System

After optimising the hybrid system operation mathematically, it is worth testing it in the Simulink to observe the dynamics and transients of the system. If this is not being conducted, more uncertainties regarding the applicability of the optimisation results in the real system exist. Ultimately, this step is performed to give more confidence and it provides a better understanding of the results obtained from the mathematical models. Using the developed Simulink model, a simulation time of 86400 seconds (24 hours) was performed. In this work, the author has split up the simulation run time. The simulation state and the desired variables are saved after 3600 seconds (1 hour) simulation time. The variables were then cleared to free up some memory space for the next simulation run time. This can be repeated in order to extend the overall simulation time period. The sampling time of the simulation is 50 μs and the recorded data was decimated by a factor of 100. The Simulink model of the hybrid system which was used to study one day of operation is shown in Figure 5.8.

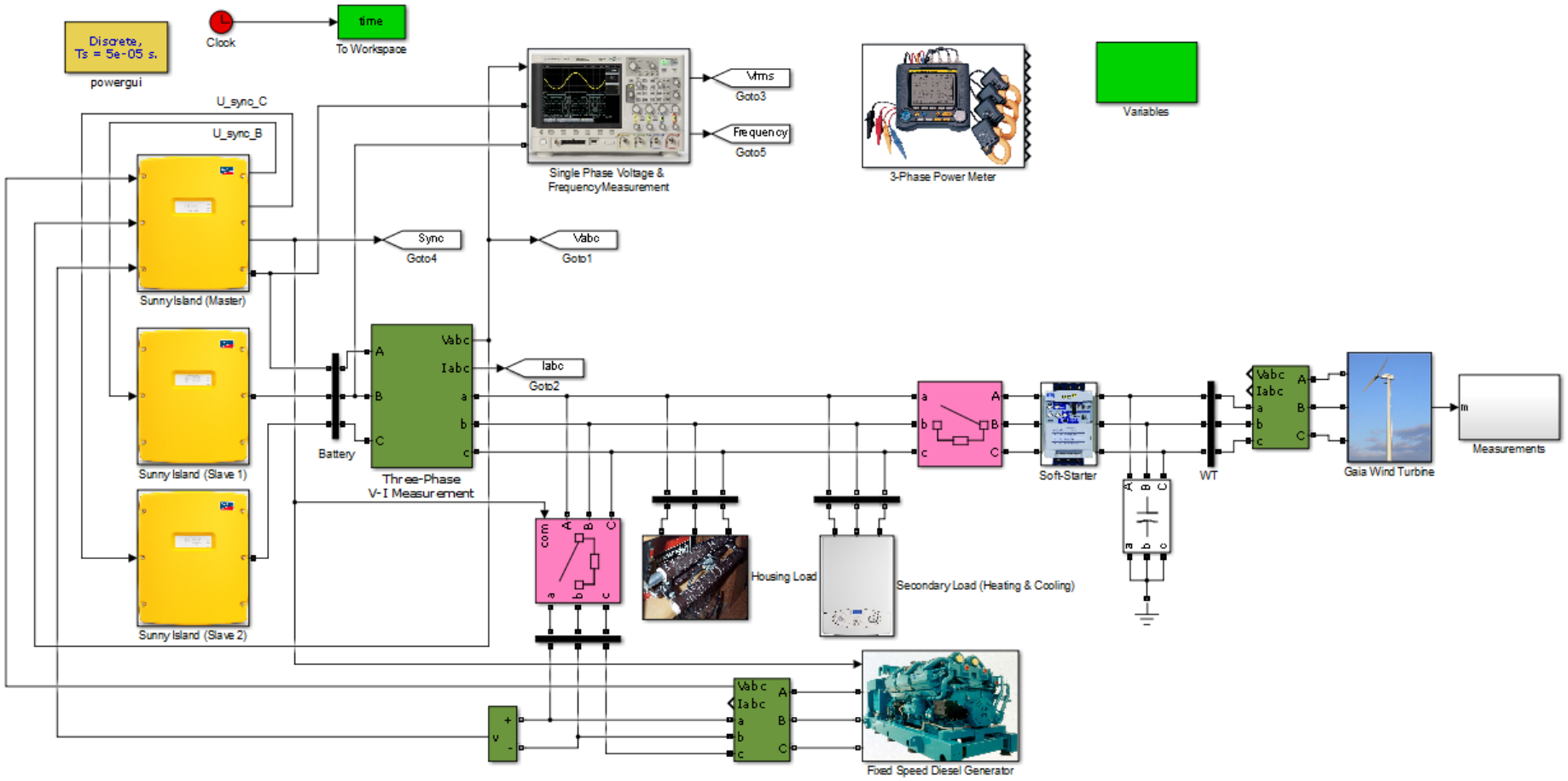

Figure 5.8: Hybrid system Simulink model used to run for 24 hours simulation time

The detailed modelling in each subsystem has been described in Chapter 4. However, several modifications have been made to accommodate this part of work. In particular, the load model is being implemented with the three-phase dynamic load block which is available in SimPowerSystems (Simulink library). The active power and reactive power were controlled by the external input. With this approach, the load profiles of Figure are emulated. In order to achieve a more realistic simulation, the 10-minutes average wind speed (Figure 5.3) was used in conjunction with the turbulent wind model described in the previous chapter, synthesising a turbulent wind profile as shown in Figure 5.9. As discussed in the previous chapter, the turbulence intensity (more fluctuations) is greater at a higher wind speed. This principle is well demonstrated in the turbulent wind profile below.

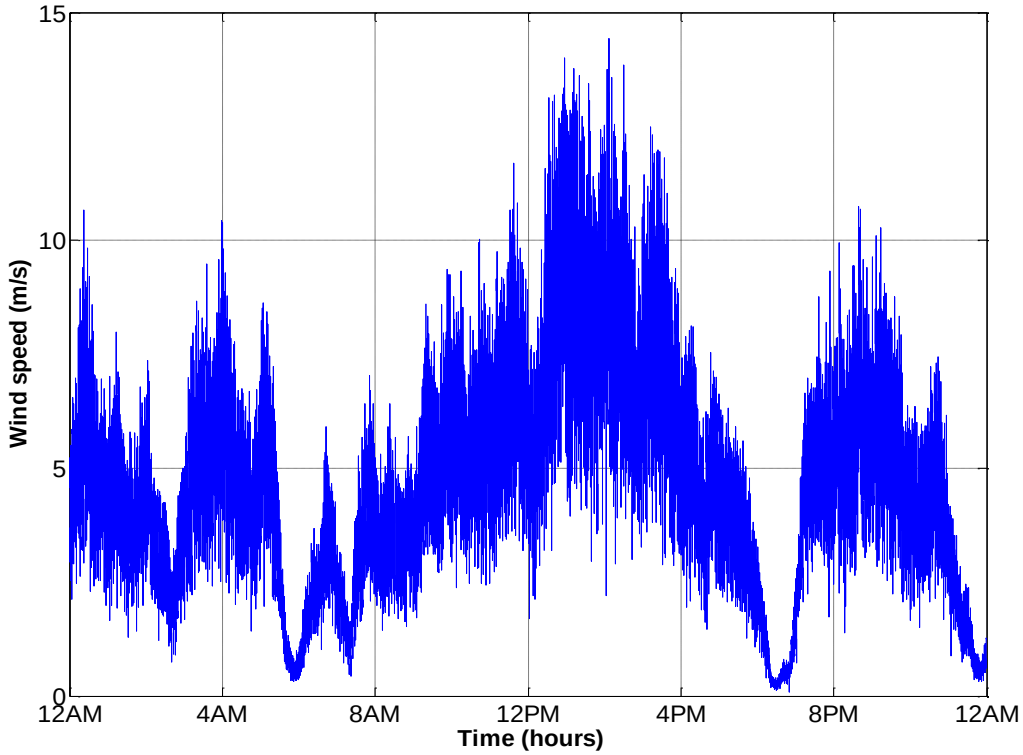

Figure 5.9: One day's synthetically generated turbulent wind profile

The start-stop cycle of the diesel generator is based on the post-processed pattern as discussed previously. The diesel generator generates 8 kW (rated power) whenever it is switched on. A safety precaution which is used to prevent the batteries from over-discharged as a result of any unexpected events or errors in wind & load forecasts

has also been implemented. In particular, the master unit of the SI reads the SOC of the batteries and switches on the diesel generator whenever the SOC is less than 15%. To prevent over-frequent start-stop cycles, a hysteresis control has been adopted. This means that the diesel generator will only switch off when the SOC of the batteries has reached 25%. It was found that the system will collapse or become unstable if the SOC of the batteries is too low.

Figure 5.10 shows the system frequency and line voltage throughout the day. Note that the frequency spikes occurred during the synchronisation and connection between the isolated grid and the diesel generator. Once the diesel generator was connected to the system, the frequency rose due to the higher availability of active power within the system. The most apparent frequency drop occurred just before 8pm, which was due to the peak in demand. At this point in time, the SI inverters were operating almost at their rated value (6 kW per phase). Several voltage drops were quite apparent and they can be associated with the higher reactive power demand during those periods. In general, the frequency and voltage were within the statutory limits throughout the simulation.

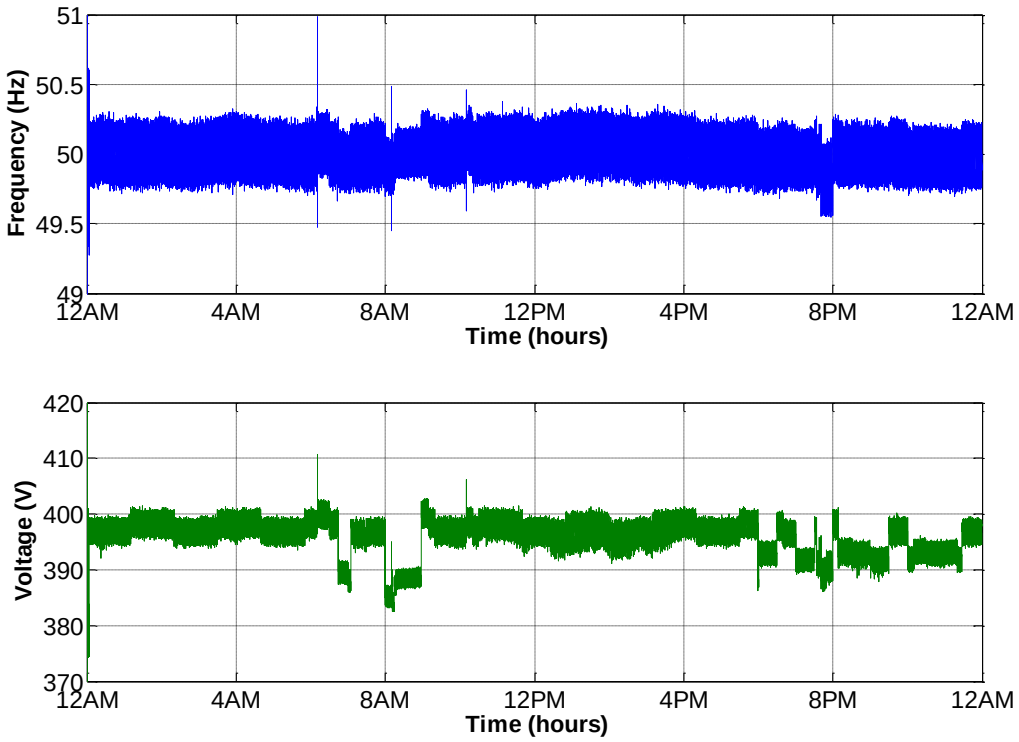

Figure 5.10: System frequency and voltage over 24 hours period

Figure 5.11 shows the comparison of batteries SOC between the GA post-processed results and the Simulink results. It can be observed that the SOC trends for both correlate well. Some small discrepancies are mainly due to the power losses in the electronics components and machines, under-sampling of load profile in the GA optimisation, turbulent wind and electrical transients (delays from control systems). Between about 1pm and 4pm, it is noticed that both of the SOC profiles began to diverge. This is due to the inability of the wind turbine to absorb the turbulent energy from the wind as a result of the disc-averaging effect possessed within a wind turbine. The high frequency components of the wind were filtered out mechanically. Another large diversion is noticed to happen at around 8pm, which can be associated with the evening peak load. Inaccuracies occur as a result of the down-sampling of the load model when performing the GA optimisation. The peak load period in the Simulink simulation is slightly longer than that of the GA and hence, more energy is being discharged in the former case as observed in Figure 5.11.

Although the optimisation has a constraint to avoid the SOC of the batteries falling below 20%, a slight outrun is observed just after 8am. It is important to note that since the Simulink model reacts to the event inputs while the GA simulation tries to look ahead and produce the power flow solutions, the discrepancies between both models are expected. In this case, the short-term peak load occurred just after 8am is averaged with 10 minutes sampling rate for the GA simulation. Even if a lower limit safety pre-cation of the diesel generator is set to 20% (currently is 15%), the outrun will still occur. This is due to the diesel generator was already coincidently determined by the GA to run just after 8am, although in GA results predicted that the SOC would be slightly above 20% at that time. It is important to note that this might not be the same for other scenarios. It is expected that a higher diesel generator power rating or the incorporation of DSM in the system may prevent the battery SOC from dropping below the pre-defined limit. Therefore, the importance to perform simulations in Simulink using the GA mathematical results is demonstrated here. In addition the Simulink model provides a platform to analyse the electrical characteristics and identify the presence of any non-ideal or unusual operating behaviour. This increases confidence and understanding of the results generated by the GA results generated from the simple mathematical model.

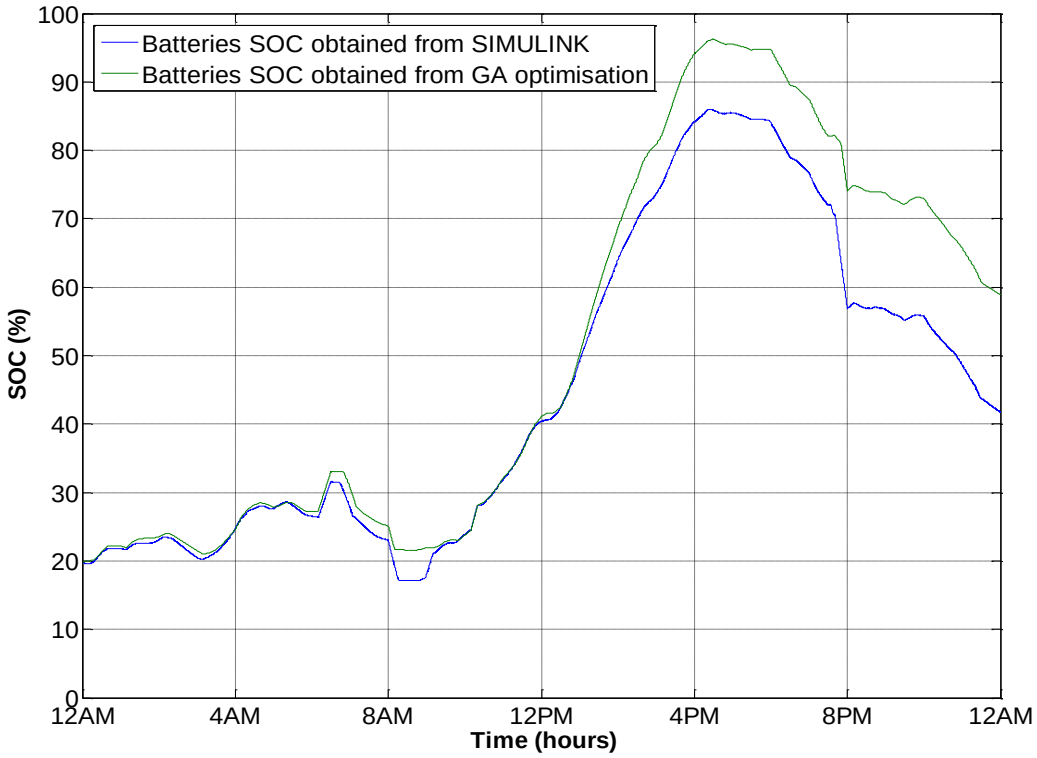

Figure 5.11: Batteries SOC comparison between measurement from Simulink and computation from mathematical model

Figure 5.12 shows the plots of the load demand and the actual power absorbed from the load and negligible difference is observed between them. This is because the system voltage is kept within a small range and the power absorbed is mainly affected by the system voltage. A similar explanation can be applied to the reactive power consumption. In general, the loads received a stable supply of power from the isolated hybrid system without any unexpected perturbation.

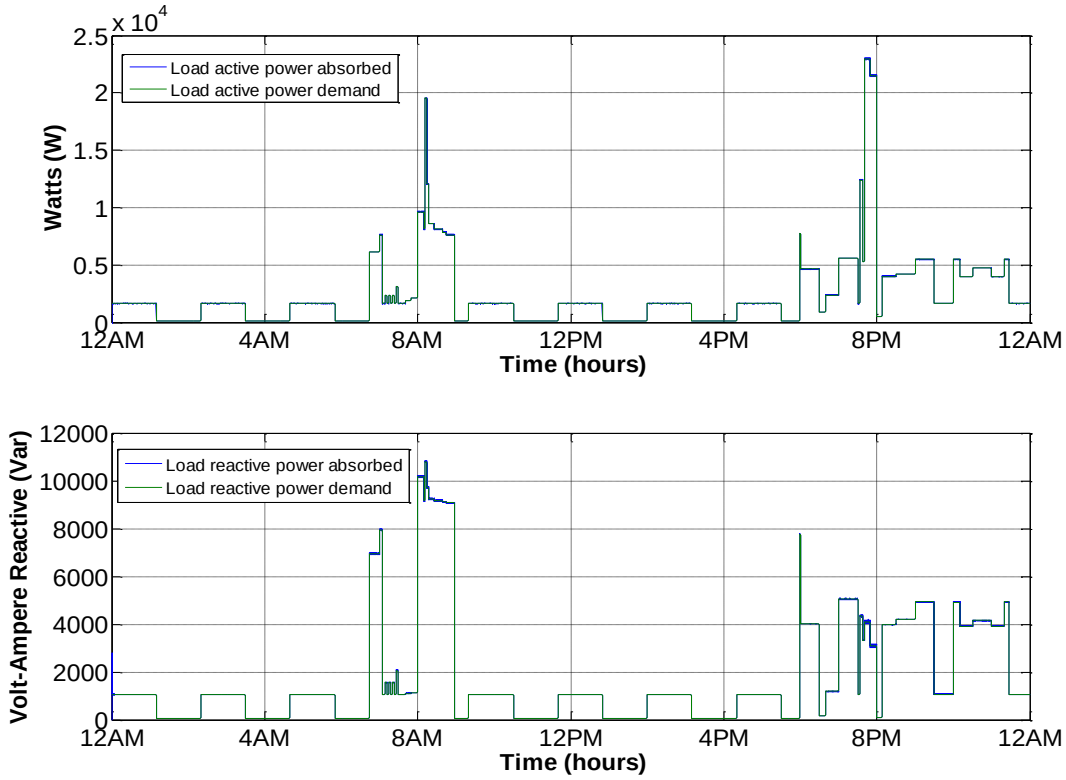

Figure 5.12: Comparison of active and reactive power demand and their absorption

Figure 5.13 shows the power flow from the wind turbine, the diesel generator and the battery storage via the SI inverters. The large fluctuations of the wind power can be linked to the turbulent effect of the wind. Despite having these variations, the hybrid system operated in a stable manner and having a good power quality which can be reflected from the system voltage and frequency (as shown in Figure 5.10). It can be shown that the power generated from the wind turbine was limited to around 11 kW despite the existence of high turbulent wind peaks (a little less than 15 m/s). This can be related to the drop in C_p when the TSR increased beyond 7. At a higher TSR, a large thrust force existed but lesser power being generated due to the smaller lift force. This is a common characteristic of a fixed-speed wind turbine [44].

The switching on/off cycle of the diesel generator was based on the optimised GA results. The diesel generator operated at its rated power whenever it was switched on. In this simulation, the safety precaution of the diesel generator was not being exploited because the SOC of the batteries never reaches to a critical level of 15%.

Finally, the power flow measured from the SI terminals is shown in the bottom plot of Figure 5.13. This also corresponds to the charge and discharge cycle of the batteries. Throughout the day, the battery charging process took place more frequently, especially in the afternoon because it was quite a windy period. The SI inverters supplied power to the load whenever the wind power was not sufficient to meet the demand. It is worth mentioning that the batteries charge and discharge cycle graph can be used for battery lifetime analysis, however it is beyond the scope of this work to do so.

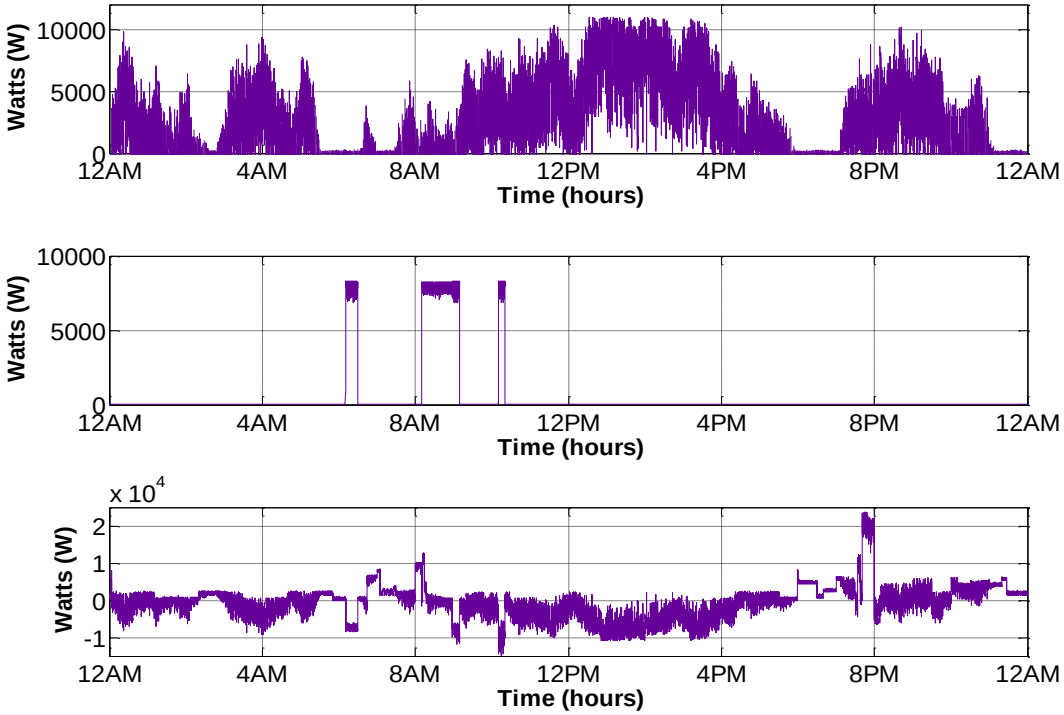

Figure 5.13: *a)* Wind turbine power *b)* Diesel generator output power *c)* Charging and discharging power of the batteries

In summary to all the analysis discussed above, the optimised hybrid system operation using GA performs well in the Simulink model. The verification from the Simulink model is a step forward to justify the feasibility of the proposed algorithm. However, it requires the fairly accurate prediction of wind and load profiles. The following section thoroughly explores the non-ideal circumstances which are more

likely to occur in real world such as under and over forecast of the wind speed and load demand. In particular, sensitivity analyses on the wind speed and on the load demand were performed.

5.3 Sensitivity Analysis on Hybrid System with Optimised Operation

A sensitivity analysis can be simply explained as the study of how a system reacts to the uncertainty in its input. In this case, it is a vital step to be performed after verifying that the hybrid system can be operated fairly well in an ideal situation (when the load and wind speed are forecasted perfectly). In reality, errors in load prediction and weather forecast can exist. These are the input to the system and therefore, their sensitivity towards the system is investigated. Typically, the errors of day-ahead load and wind speed forecast are analysed through statistical distributions [237]. In large power systems, these errors can have economic consequences as they can be a critical factor in ensuring near-optimal system operations. For the case of off-grid systems, the fast-starting, more expensive diesel generator unit will be required to fulfil the load in an energy deficit situation. On the other hand, the renewable energy generations need to be curtailed if there is excess energy exists which cannot be stored.

Load generally follows a familiar pattern, reaching its peak in the morning and evening. It was noticed from a study that the load forecasting error is accounted by numerous errors between 10% to 20% [237]. On the contrary, although wind speed displays some daily and seasonal characteristics, it follows less regular patterns compared to the load. The magnitude of the wind speed forecasting error is dependent on the length of the forecasting timescale [238]. A day-ahead wind speed forecast error has recorded values between 15% to 40%, depending on the methodology used [239]. For simplicity purposes, this paper proposes simple multiplication factors to be multiplied with the ideal load demand and wind speed forecast in order to emulate the forecast errors. Statistical models for the load demand [240] and wind speed [241] forecast can be applied if required, however, this is beyond the scope of this paper. In this section, three different sensitivity analyses are performed. The first and second sensitivity analyses have a constant multiplier

applied to the load profile (three households) and to the wind speed profile, respectively. In these analyses, it is assumed that the three households turned on their loads at the same time. Finally, the second load sensitivity analysis is performed by having the load profile being aggregated with the assumption that all three households turned on their loads at a different times. The two proposed load sensitivity analyses were also conducted for comparison purposes and as a mean of testing the hybrid system's robustness against different types of load error forecasts. Although this work considers a limited sensitivity study, other possible sensitivity analyses can be performed. These include varying the battery and DG sizing, types of battery, initial battery SOCs, wind and load patterns and the power factors of the household electrical appliances. It is expected that a significant amount of time is required to carry out these sensitivity analyses and other tasks (agreeable with Gaia-Wind Ltd. prior to starting the project) such as hybrid system laboratory development and testing (described in the next chapter) which was due to be completed before the end of year 3.

A simple add-on which had been included in the system was the secondary loads, for instance electric heater for space heating or electric boiler for water heating. They were used to avoid the batteries being charged to 100% when the wind energy was high and the load demand was low. In particular, the secondary loads were rated at 3 kW and 5 kW, respectively. Each of them was connected to the isolated grid through a circuit breaker which was controlled using a simple hysteresis approach. The 3 kW load was switched-on when the SOC of the batteries was 85% and was switched-off when the SOC was equalled to 80%. On the other hand, the 5 kW load was switched on and switched off when batteries SOC reached 95% and 90% respectively.

5.3.1 Load Sensitivity Analysis

Throughout the year, the consumer load usage varies across seasons. In this study, the load profile of the three households was varied with a multiplication factor of $\times 0.8$, $\times 1$, $\times 1.2$ and $\times 1.4$, respectively. These proposed numbers were simply suggested in this work and it is reasonable based on the typical forecast errors which were found out in the past [237]. These multiplication factors were used to inspect the performance deviation of the hybrid system from the ideal case. A multiplication

factor of ×1 represents the ideal optimised operation from the GA, while the other multiplication factors represent under- or over-prediction of the load demand. The wind speed profile and the pre-set control of turning on the diesel generator (obtained from the results of GA optimisation) did not change for all cases. However, the diesel generator might be turned on more frequently due to the abovementioned safety precaution control. In particular, the diesel generator would be running whenever the battery SOC dropped to less than 15%. It was expected that this feature would be in use when the load multiplier increased. A 15% SOC safety limit is chosen in order to prevent the battery voltage to drop to an excessively low value, which may cause system instability as a result of the converter being required to boost at a higher ratio.

Table 5.2 tabulates the simulation results and Figure 5.14 shows the SOC profiles for all the load multiplication factors. The system frequency and line-to-line voltage were averaged over the 24 hours period. In general, they are within the statutory limits for all cases. The diesel generator turned on longer when the load multiplication was higher. It can be noticed from Figure 5.14 that the batteries SOC for the case of ×1.2 and ×1.4 became quite low just after 8am, and it was dropping to about 10% despite the continuous operation of the diesel generator. The total diesel generator operation time was more than double with an additional load factor of ×0.4. However, the hybrid system was ensured to operate without failure. Therefore, the pre-included safety feature of the diesel generator increases the robustness of the optimised hybrid system operation. A higher diesel generator power rating or larger safety margin is needed if a load of that particular household is expected to have a higher usage and larger variation. The latter can be done by setting the diesel generator to be switched-on when the batteries SOC dropping to a certain level higher than 15%.

Another interesting observation from Figure 5.14 is that the SOC of different scenarios follow each other closely until the peak load occurred at about 8pm. At that time, the diesel generator did not switch on at all because the energy stored in the batteries was sufficient to supply the load for the remaining time. Thus, the largest

deviation of the SOC from the ideal case's happened only when the peak load occurred during high batteries SOC.

From Table 5.2, it can be observed that the 3 kW secondary load turn-on time reduces as the load multiplication factor increases. The batteries were prevented from being charged to 100% by switching on the secondary load. The 3 kW secondary load was switched-on about 3 times longer for the case of ×0.8 compared with multiplication factors of ×1 and ×1.2's scenarios. The batteries SOC of the former reached 85% for a relatively longer period and this can be attributed to the overall lower load demand. On all occasions, the 5 kW secondary load was not triggered to turn on because none of the batteries SOC reached 90%.

Load multiplication factor	*×0.8*	*×1*	*×1.2*	*×1.4*
Maximum frequency (Hertz)	51.17	51.12	51.13	51.03
Minimum frequency (Hertz)	49.26	49.28	49.15	49.29
Average frequency (Hertz)	50.01	50.01	50.01	50.01
Maximum line-to-line voltage (Volt)	410.02	407.49	405.89	406.59
Minimum line-to-line voltage (Volt)	374.41	374.54	373.93	373.81
Average line-to-line voltage (Volt)	396.17	395.75	395.32	394.96
Diesel generator turn-on time (minutes)	79.70	79.69	119.57	186.41
3 kW secondary load turn-on time (minutes)	156.50	54.08	49.58	0
5 kW secondary load turn-on time (minutes)	0	0	0	0

Table 5.2: Load sensitivity simulation results

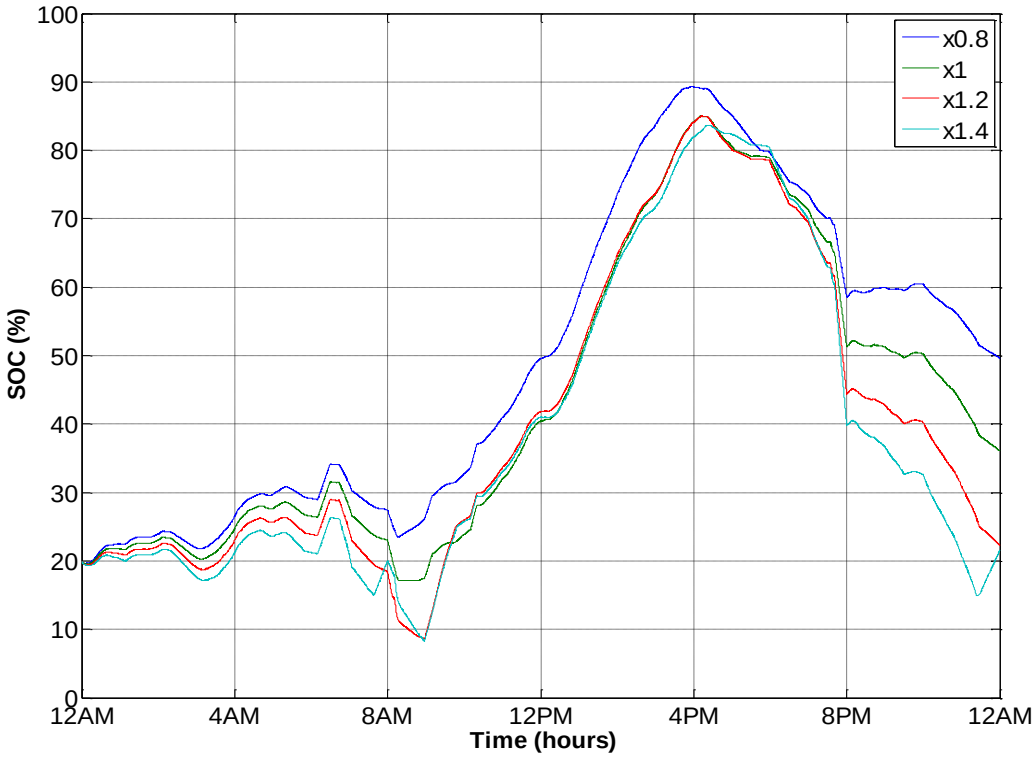

Figure 5.14: SOC profiles for different load multiplication factors

5.3.2 Wind Energy Sensitivity Analysis

In this section, the wind energy sensitivity analysis was conducted by multiplying the wind speed profile (upper plot of Figure 5.2) with a multiplication factor of ×0.8, ×1, ×1.2 and ×1.4 respectively. The load profile and the pre-set control of turning on the diesel generator (obtained from the results of GA optimisation) did not change for all cases. As mentioned before, the diesel generator and secondary loads might be utilised depending on the batteries SOC.

Table 5.3 and Figure 5.15 demonstrate the simulation results of various wind speed multiplication factors. The average frequency and the line-to-line voltage over a day were stable and were within their statutory limits. A small increase in average system frequency was observed as the multiplication factor goes up. This can be explained by the frequency versus power droop characteristic exists within the modelled SI inverters, as shown in Figure 4.9. A higher wind multiplication factor translates to a higher active power generation from the wind turbine. Therefore, the overall

frequency increased. However, the average line-to-line voltage was observed to be decreasing as the wind multiplication factor increases. This is due the fact that an induction generator consumes more reactive power when the active power generation increases. From the voltage versus reactive power droop characteristic curve (Figure 4.9), the system voltage decreases when the reactive power demand increases. The diesel generator operated for an additional 2 hours and 20 minutes when the wind speed was reduced by a factor of ×0.2. For this scenario, the secondary loads were never switched on. On all other occasions, the diesel generator runs for the same amount of time despite the additional available wind energy (higher multiplication factor). However, more energy was being dissipated in the secondary loads as it got windier throughout the day. For the case of ×1.2 and ×1.4, the 5 kW secondary load was turned-on in order to avoid the batteries being charged to 100%.

From Figure 5.15, it can be observed that the SOC deviated from the ideal case (×1) quite significantly even with just a small difference in wind speed. Comparing the load sensitivity and the wind speed sensitivity SOC results (Figure 5.14 and Figure 5.15), the battery SOC is more sensitive to the wind speed forecast error than the load forecast error. Note that this may be a specific result for this study and may not be reflected in other systems.

Wind speed multiplication factor	*×0.8*	*×1*	*×1.2*	*×1.4*
Maximum frequency (Hertz)	51.12	51.12	51.12	51.12
Minimum frequency (Hertz)	49.13	49.28	49.28	49.25
Average frequency (Hertz)	50.00	50.01	50.01	50.02
Maximum line-to-line voltage (Volt)	407.52	407.49	406.31	405.37
Minimum line-to-line voltage (Volt)	373.68	374.54	374.54	373.68
Average line-to-line voltage (Volt)	396.06	395.75	395.28	394.78
Diesel generator turn-on time (minutes)	219.80	79.69	79.70	79.71
3 kW secondary load turn-on time (minutes)	0	54.08	298.32	438.69
5 kW secondary load turn-on time (minutes)	0	0	123.92	278.25

Table 5.3: Wind speed sensitivity simulation results

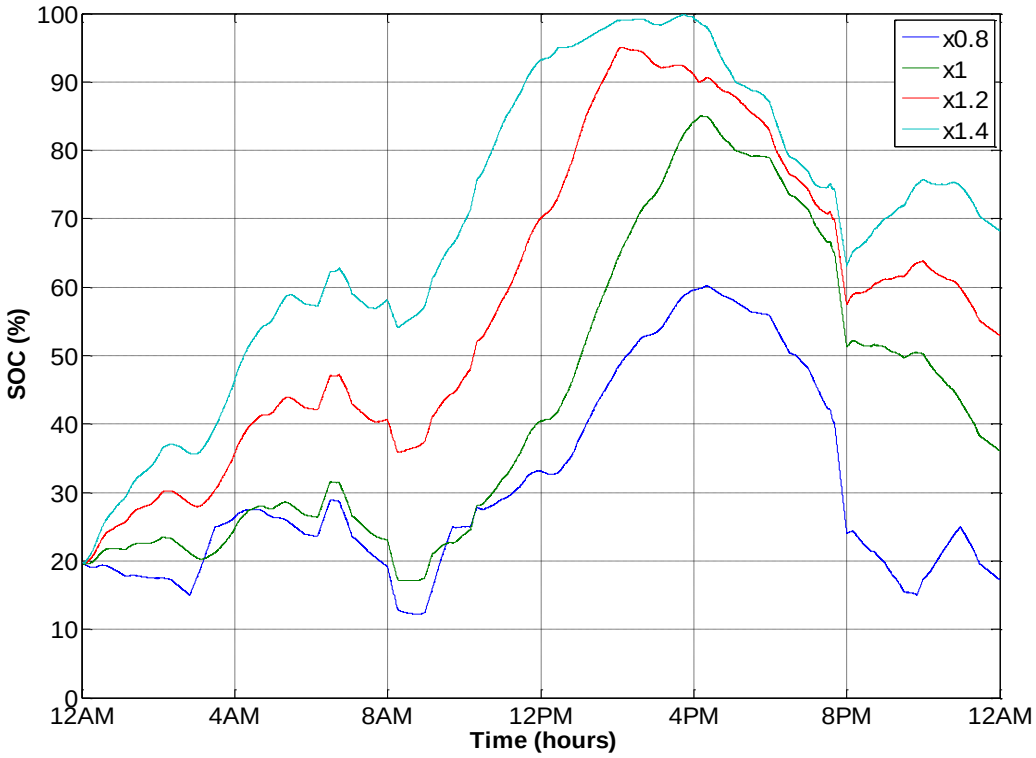

Figure 5.15: SOC profiles for different wind speed multiplication factors

5.3.3 Time-shifted Load Sensitivity Analysis

A random time-shifting approach of aggregating the three households was implemented here for the second phase of load sensitivity analysis. As shown in Figure 5.16, the load profile for the second household was obtained by delaying the load profile from the first household with a random number. The random number generator produced a random number which was set to have a mean value of 30 with a variance of 20. The sampling time of the random number generator was set to 5 minutes. Therefore, the load profile would be randomly time-shifted, however the mean delay time was set at 30 minutes. The mean value of the random number generator of the third household was 60 with a variance of 20. On average, the third household load profile had a delay of one hour relative to the first household's load profile. Finally, a summation was performed on the three households, producing an accumulated load profile as portrayed in Figure 5.17. The generated load profile here was significantly different from the previous one (direct multiplication of 3) because the morning and evening peaks of the three households did not occur at the same

time. With this in mind, the discharging rate of the batteries should be lower in this case.

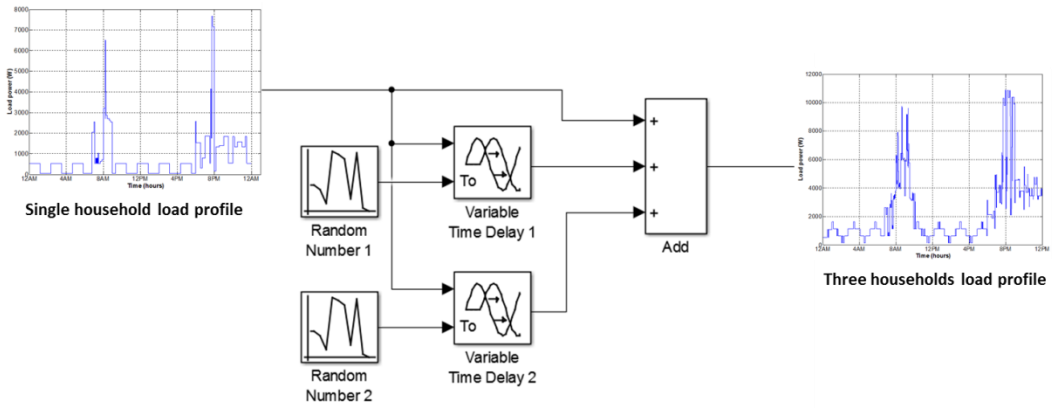

Figure 5.16: Simulink implementation of load aggregation model with random number generators

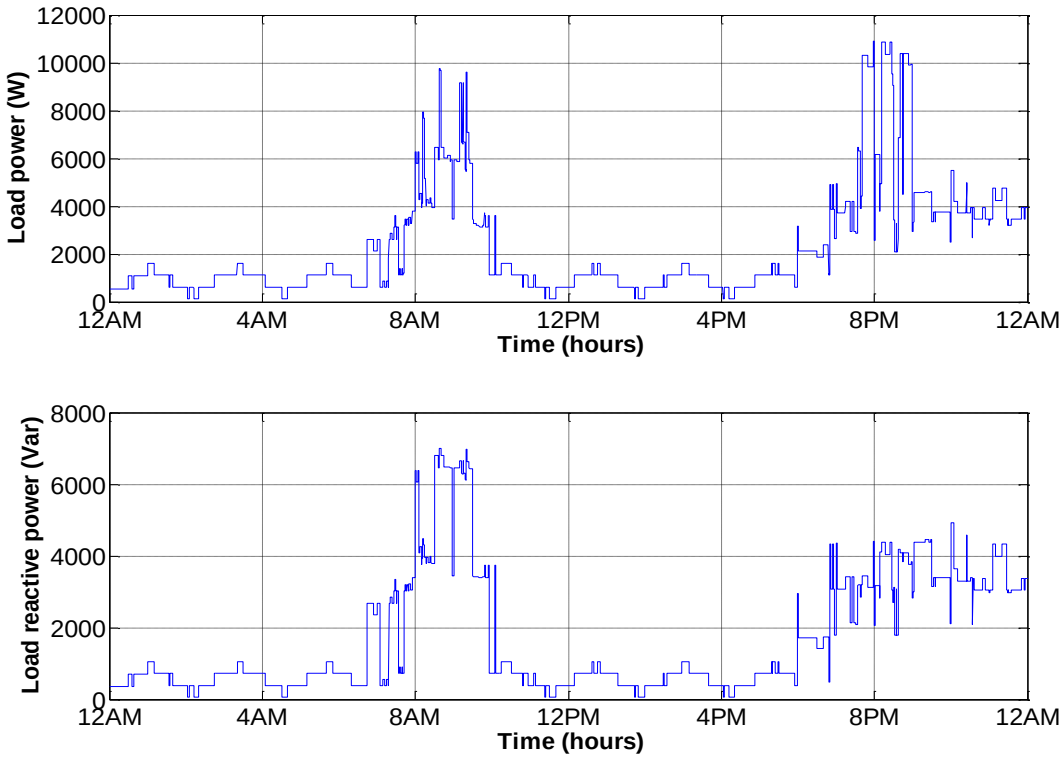

Figure 5.17: Load profile for three households (time-shifted for second and third household)

Using the load profile mentioned above, a sensitivity analysis was carried out on the hybrid system. Multiplication factors of ×0.8, ×1, ×1.2 and ×1.4 were applied to the

new load profile in Figure 5.17 with 24 hours of simulation performed for each scenario. Table 5.4 and Figure 5.18 show the simulation results and SOC profiles for all scenarios, respectively. The average frequency and average voltage show that the hybrid system operated in a stable manner. The diesel generator's running time for the case of ×1.2 and ×1.4 tabulated in Table 5.4 is observed to be less than that in Table 5.2. This was due to the morning peak magnitude in new load profile being significantly less than the previous case which reduced the discharging rate of the batteries. In addition, it decreased the risk of having the SOC to fall below the pre-set safety threshold level. In addition, it was apparent that the discharging rate of the batteries for the evening peak load at 8pm was smaller for the case in Figure 5.18 than the results shown in Figure 5.14. Overall, the SOCs for both studies are similar despite the differences between the load profile patterns. It is acknowledged that the robustness of the system cannot be fully proven through simulation studies as some of the parasitic effects are not being modelled, such as the battery temperature and ageing effect. In order to thoroughly test the robustness of the proposed control algorithm, it is suggested that more sensitivity studies may be performed but more importantly hardware prototyping followed by testing the platform under various conditions (for example different climate and load characteristics) are essential.

Load multiplication factor	*×0.8*	*×1*	*×1.2*	*×1.4*
Maximum frequency (Hertz)	51.17	51.10	51.52	51.08
Minimum frequency (Hertz)	49.25	49.30	49.23	49.21
Average frequency (Hertz)	50.01	50.01	50.01	50.01
Maximum line-to-line voltage (Volt)	406.93	405.68	406.71	405.22
Minimum line-to-line voltage (Volt)	375.10	375.35	375.26	374.93
Average line-to-line voltage (Volt)	396.19	395.77	395.34	394.97
Diesel generator turn-on time (minutes)	79.70	79.70	79.70	151.07
3 kW secondary load turn-on time (minutes)	166.75	69.83	0	0
5 kW secondary load turn-on time (minutes)	0	0	0	0

Table 5.4: Time-shifted load sensitivity simulation results

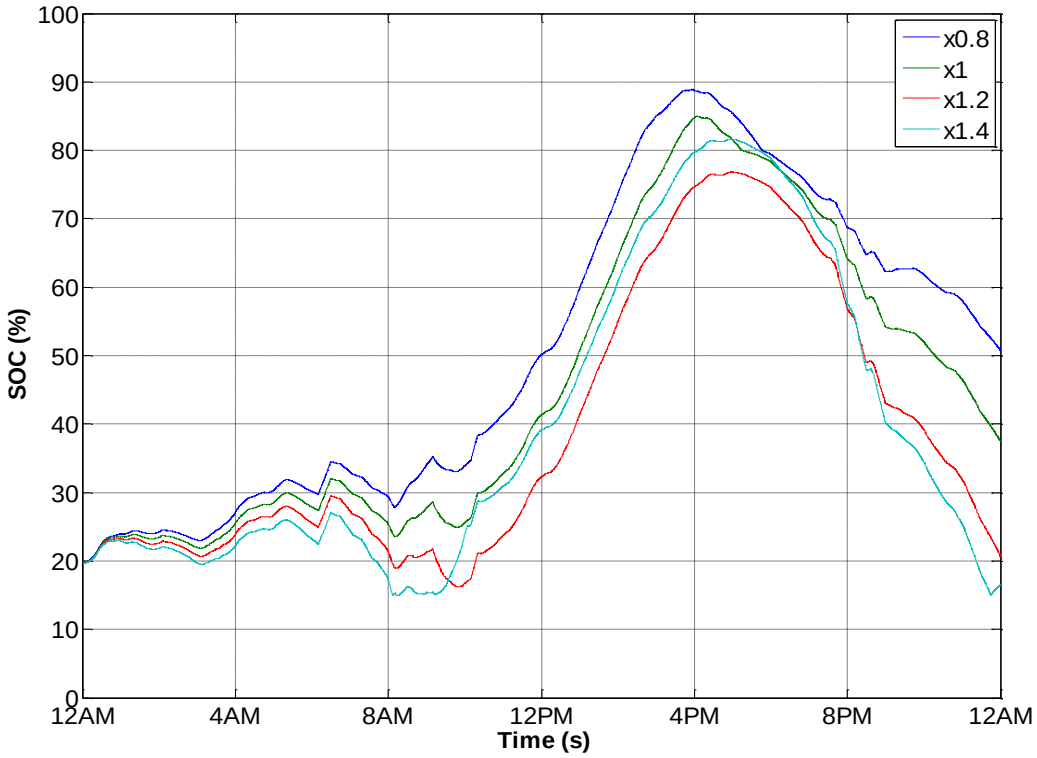

Figure 5.18: SOC profiles for different time-shifted load multiplication factors

5.4 Summary

To summarise, the proposed optimisation algorithm to optimise the operation of a hybrid wind-diesel-battery system has been tested with various load and wind scenarios. As pointed out earlier, some safety pre-cautions are needed to ensure the hybrid system operates in a stable manner during any unexpected events. The lifetime of a diesel generator is potentially prolonged with the reduction in start-stop cycles and operating at its rated capacity whenever it is running. The proposed methodology (illustrated in Figure 5.1) of testing the optimised results (from GA) using the developed Simulink model has highlighted the importance of such an approach when comparisons are made between them. In particular, this technique allows the hybrid system designers to investigate the factors which contribute to the non-ideal behaviours of the hybrid system in the real world.

The next chapter attempts to explain the process of setting up the hybrid system test rig in the laboratory. However, it is important to emphasise that the studies

performed in this chapter will not be realised experimentally due to the control limitation lies within the hardware. It is believed that the necessity to test the proposed algorithm using the test rig is minimal as it only involves the timing of switching on/off the diesel generator. Dynamic issues which can be potentially observed in the hardware implementation can be fine-tuned with the lower level controller and it is beyond the scope of this project to carry this out.

Chapter 6 Laboratory Development of an Off-grid Hybrid System

This chapter discusses the laboratory setup of the proposed hybrid system which, on the whole, uses off-the-shelf components to reduce the development time. The construction of a hybrid system in the laboratory provides a low cost, safer testing and verification of the wind turbine, which would otherwise be costly in the field. Since the hybrid system involves the rotation of the wind turbine blades, additional protection and risk assessment would be required if it was tested in the field. This is due to the lack of initial understanding of the level of operational safety of a newly proposed system. In addition, the repeatability is a challenge in the field, for instance, it is nearly impossible to obtain the exact same wind speed profile in the field to be used as a test input. This adds to the challenge while tuning the controller or to troubleshoot any faults within the system. The additional time which is required to perform certain tests in the field further justify the additional human resource cost in the project development.

The process of designing the system is described together with the results of characterising on each component are shown in the following sections. In addition, the test procedures are described. Subsequently, the discussion leads to a complete off-grid hybrid system setup for the lab environment. The discussion in this chapter can serve as a reference for any similar laboratory setup. It presents the challenges and considerations which need to be taken into account whilst developing a complex test rig involving various hardware components. The block diagram in Figure 6.1 shows the hybrid system setup in the laboratory. It is important to note that due to the use of off-the-shelf components in this work, the comparison between the simulated and measured results are performed whenever possible. This is due to the fact that the specifications of these devices are not fully obtainable from the manufacturers and results variations are expected in this case.

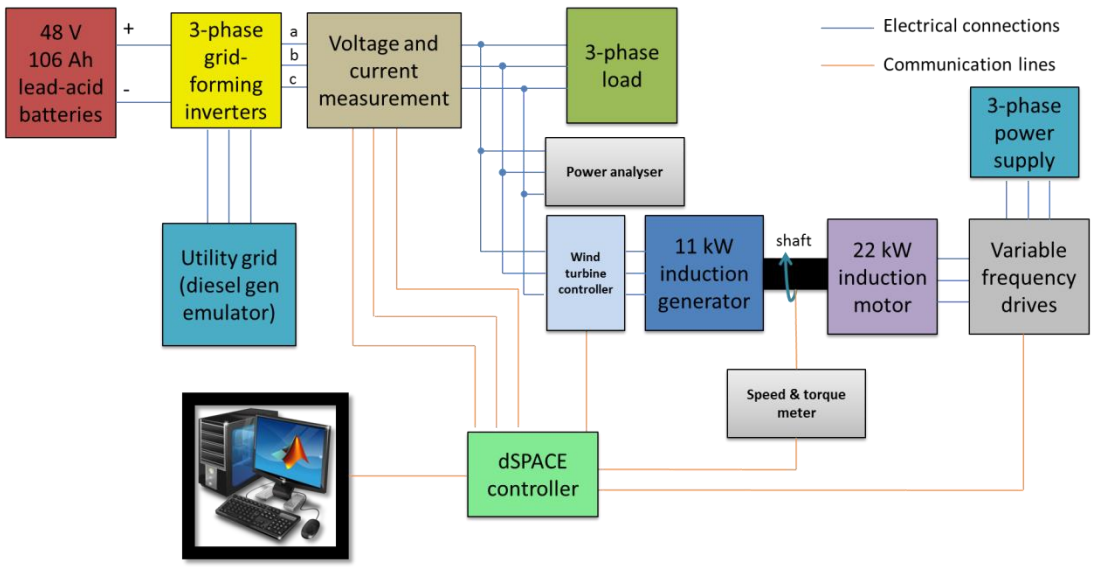

Figure 6.1: Hybrid wind-diesel-battery laboratory setup

The discussion of this chapter begins with the characterisation of the 3-phase grid-forming inverters, i.e., the SI 8.0H inverters. The steady-state analysis of the voltage and current profiles for different load conditions is performed alongside dynamic analysis of the droop concept within the grid-forming inverters. The SI grid-forming inverters are then characterised with its efficiency being measured and compared with the efficiency profile given in the datasheet.

It is known that a wind turbine which utilises an induction machine requires energy from the grid to start the wind turbine. During the start-up process, high in-rush current is accompanied. The induction machine needs to rotate at near synchronous speed before it starts to generate power from the wind. The utility grid is able to supply this amount of current, although a soft-starter is frequently used to mitigate the voltage dip effect as a result of high in-rush current. However, for an off-grid system, the supply current is limited by the current limit of the grid-forming inverters. Therefore, the use of a start-starter to enable the induction machine being start-up successfully is of interest. In this work, the operation of a soft-starter on starting up the Gaia's 11 kW induction machine using utility grid (strong grid) and a battery-formed grid (weak grid) is compared. The start-up current and voltage profiles using different control mode (voltage ramp and current limiter) are studied.

After identifying the suitable settings of the soft-starter, the discussion is then focused on the wind turbine emulator. The main objective of developing the wind turbine emulator is to test its operating conditions in an off-grid scenario. The wind turbine emulator should be able simulate the control and power generation characteristics of the Gaia wind turbine while the wind turbine is operating in the field. The wind turbine controller, namely IC1100 Mita-Teknik is used in conjunction with the induction machine. As such, a more realistic test rig is developed. Note that the wind turbine controller (in Figure 6.1) consists of a soft-starter, with its estimated model referred from Chapter 4 (in Figure 4.55). A load bank is connected in parallel with the induction generator output. Then, a complete software interface between the dSPACE controller and the Simulink is developed using the ControlDesk. ControlDesk is a user-friendly software that has a front panel which allows developer to control and monitor the test rig in real time. These include varying the mean wind speed, torque demand and observe the corresponding voltage, current, frequency and power waveforms.

Note that in this work, the diesel generator is emulated using the utility grid. The diesel generator and the utility grid connect to the same terminal at the SI inverters and therefore they are seen as being electrically similar as viewed by the inverter. The utility grid will be used as a backup automatically whenever the batteries SOC is low. The SOC threshold to start the backup can be set by the user through the SI control panel. At the last part of this chapter, a complete hybrid system test is conducted and the results are discussed, before a final concluding remark is given.

6.1 Characterisation of Overall Battery Grid-forming Inverter System

6.1.1 Instrumentation Setup

This section describes the instruments used for the following experimental work, as shown in Figure 6.2. The key parameters to measure were mainly voltages, currents, torque and the rotational speed of the generator. An in-house developed voltage and current measurement tool were used to measure the three-phase voltage and current at the output terminals of the SI inverters. The fundamental components include the

voltage and current transducers. The measured values were transmitted to the dSPACE controller. Subsequently, these voltage and current values were used to calculate the power and frequency using Simulink software. The Voltech three-phase Power Analyzer (PM 3000A) is an instrument used for measuring voltage, current, power, total harmonic distortion etc.

A Magtrol torque transducer (TM 312), as shown in Figure 6.3 was used to measure the torque and rotational speed of the shaft which couples two of the induction machines. The torque and speed meter was used for display purposes. At the same time, the measured torque and rotational speed were sent to the dSPACE controller. In short, the dSPACE controller was used as a central device to acquire all the measured values so that the dynamics of these parameters can be captured and linked with each other. In addition, it is also being used as part of the wind turbine emulator which is explained in later section.

The three-phase load was used to absorb the power generated by the induction generator and/or batteries via the SI inverters. Note the load in each phase can be turned on individually and in steps.

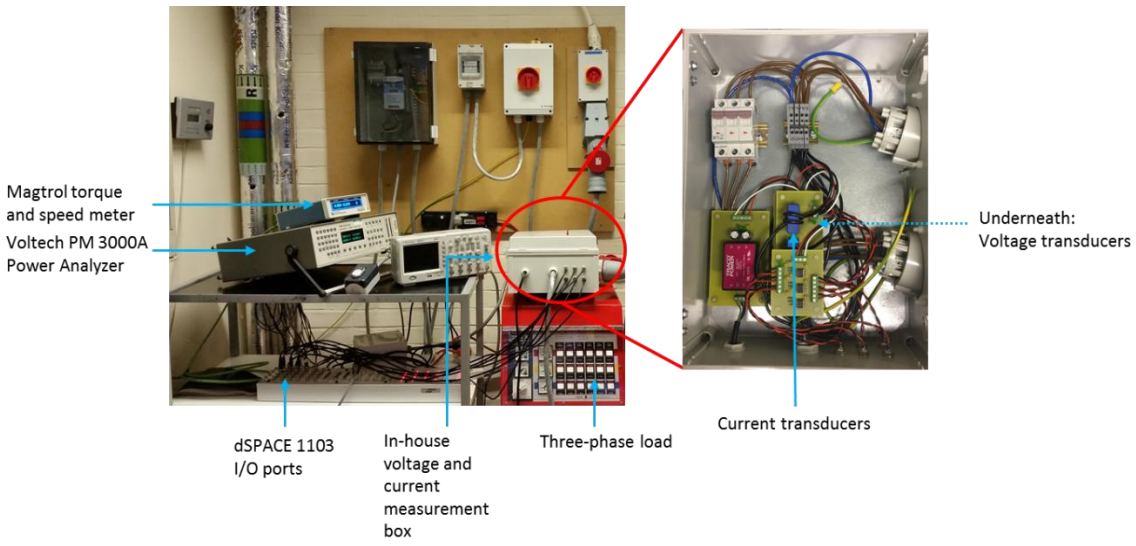

Figure 6.2: Lab instrumentations

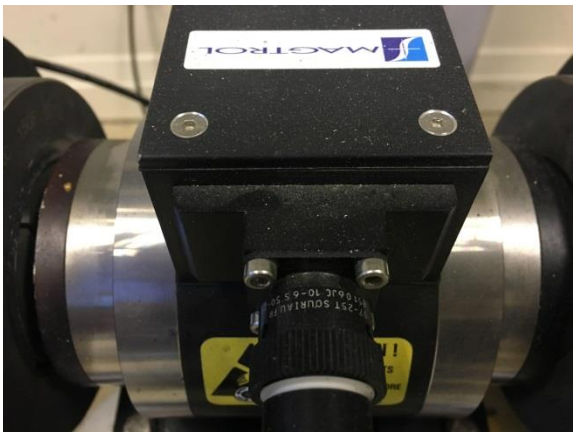

Figure 6.3: Magtrol TM 312 torque transducer

6.1.2 Characterisation of Inverters

This section describes the hardware testing of the grid-forming SI 8.0H inverters, which was previously modelled in Simulink in Chapter 4. The specifications, functionalities of the sub-blocks of the inverter were discussed and therefore will not be repeated here.

Four Rolls lead-acid batteries, each with a nominal voltage of 12 V and capacity of 106 Ah were connected in series as shown in Figure 6.4. This gives a nominal voltage of 48 V and a capacity of 106 Ah at the terminals. These batteries were connected to the SI inverters via a DC fuse box. The inverters were commissioned and the parameters of the hybrid system configuration were set through the SI Remote Control, which was connected to the SI via a communication interface of RS485. This remote control allows the user to control and visualise the operation of the SI inverters. An SD card was inserted to store measured data. Figure 6.5 shows a single-phase SI 8.0H inverter and its labelled internal circuitry.

Figure 6.4: Rolls lead acid batteries

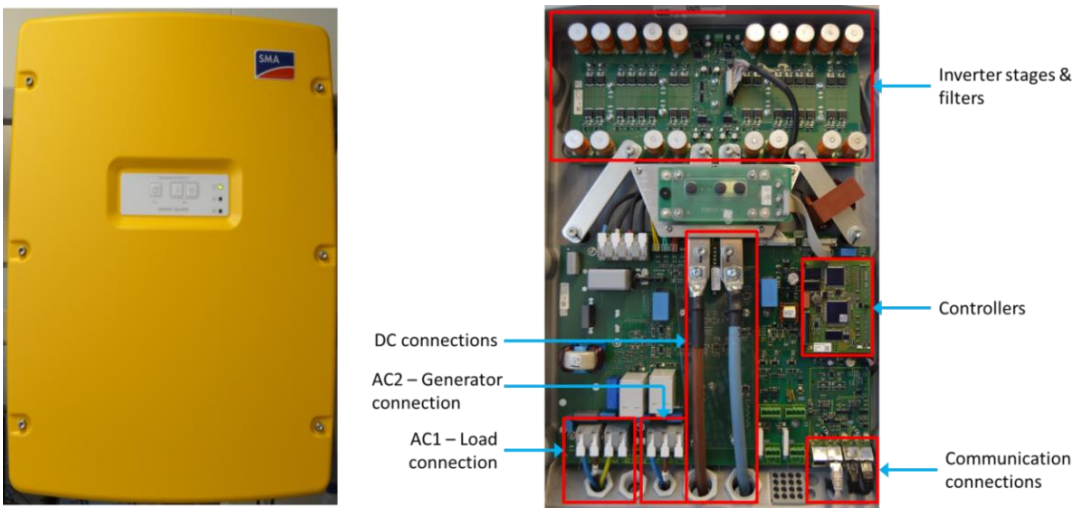

Figure 6.5: SMA Sunny Island 8.0H and its connections

A standalone three-phase grid supply was formed with the three units of SI inverters, one being the master and the remaining two acting as slave. The synchronisation of these inverters was performed by linking them with data cables, RJ45. A three-phase resistive load bank was connected to system. The system setup block diagram for the following test is shown in Figure 6.6.

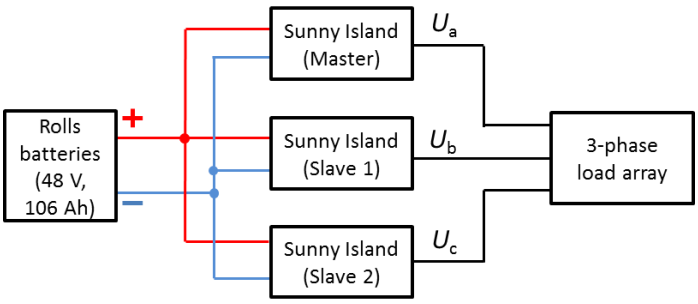

Figure 6.6: Battery-formed grid with load array connected

An unbalanced load test was performed by switching-on and switching-off 0.3 kW, 1.7 kW and 0.7 kW one after another. A similar test was performed using the Simulink model setup, as described in Chapter 4 for comparison purposes. The corresponding measured and simulated voltage and current waveforms are demonstrated in Figure 6.7. Qualitatively, it can be observed that both experimental and simulated are well correlated. The waveforms are of high quality sinusoidal waveforms while the system was supplying an unbalanced resistive load.

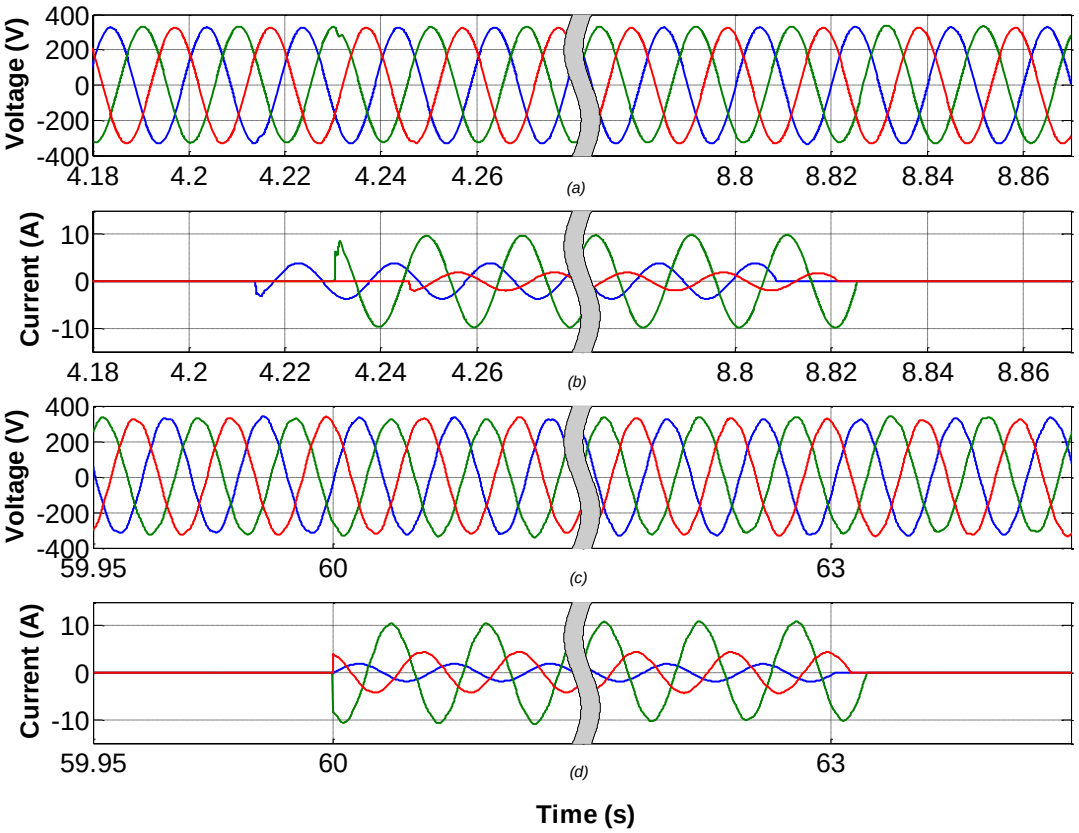

Figure 6.7: *a)* measured voltage *b)* measured current *c)* simulated voltage *d)* simulated current waveforms for unbalanced load

In order to analyse and verify the droop concept within the grid-forming inverters, 10 kW loads were turned on in steps of 1 kW, 3 kW, 5 kW and 10 kW. Figure 6.8 shows the measured line-line RMS voltage, frequency and power absorbed by the loads. The voltage and frequency transients were more significant when a higher load was switched-on. In this case, the highest occurred at 5 kW. In addition, the steady-state voltage and frequency were dropping as the load demand increases. This have proven and validated the discussed droop concept (Figure 4.9), which exists within the SI inverters.

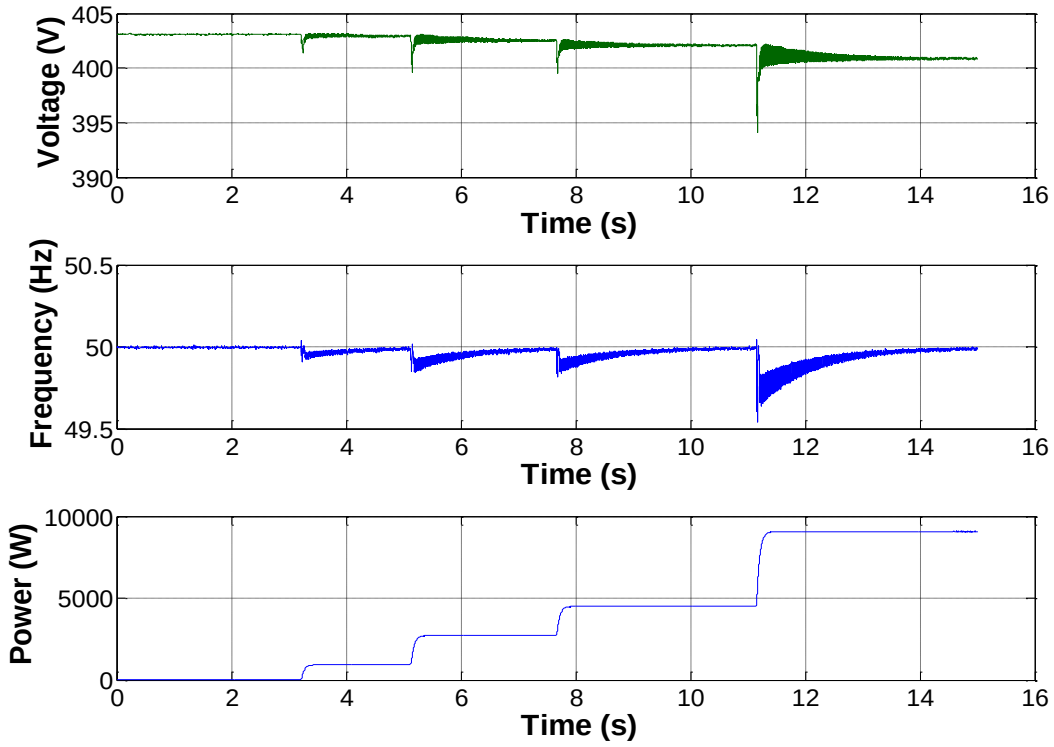

Figure 6.8: Voltage and frequency dynamics from load steps

The performance of the SI inverters was evaluated by comparing its efficiency profile with manufacturer data. The efficiency of the system can be determined by using the following equation:

$$\eta_{\text{inverter}} = \left(\frac{P_{\text{out,AC}}}{P_{\text{in,DC}}}\right) \times 100\% \tag{6.1}$$

In this test, the inverters were electrically loaded from approximately 5% to 60% of their three-phase rated power (18 kW). Since the battery capacity being used in the setup was minimal, higher loadings were not performed in order to avoid high discharging current from the batteries. Otherwise, the battery lifetime would be compromised. The output AC power and input DC power were measured for each loading. Figure 6.9 portrays the measured efficiencies at various load conditions, which was compared with the manufacturer's efficiency profile obtained from datasheet. From inspection, the efficiency curves highlight the importance of performing the correct sizing of an inverter. The inverters would be operated at its

lower efficiency region if the load to be supplied is much smaller than its power rating.

Further observation shows that both of the efficiency profiles have a similar trend. The efficiency rises from low to mid-loading conditions, and drops when the loading continues to increase. However, the peak efficiency for both curves is different. Therefore, in order to obtain an accurate understanding in the efficiency performance of the inverters, they should be characterised accordingly.

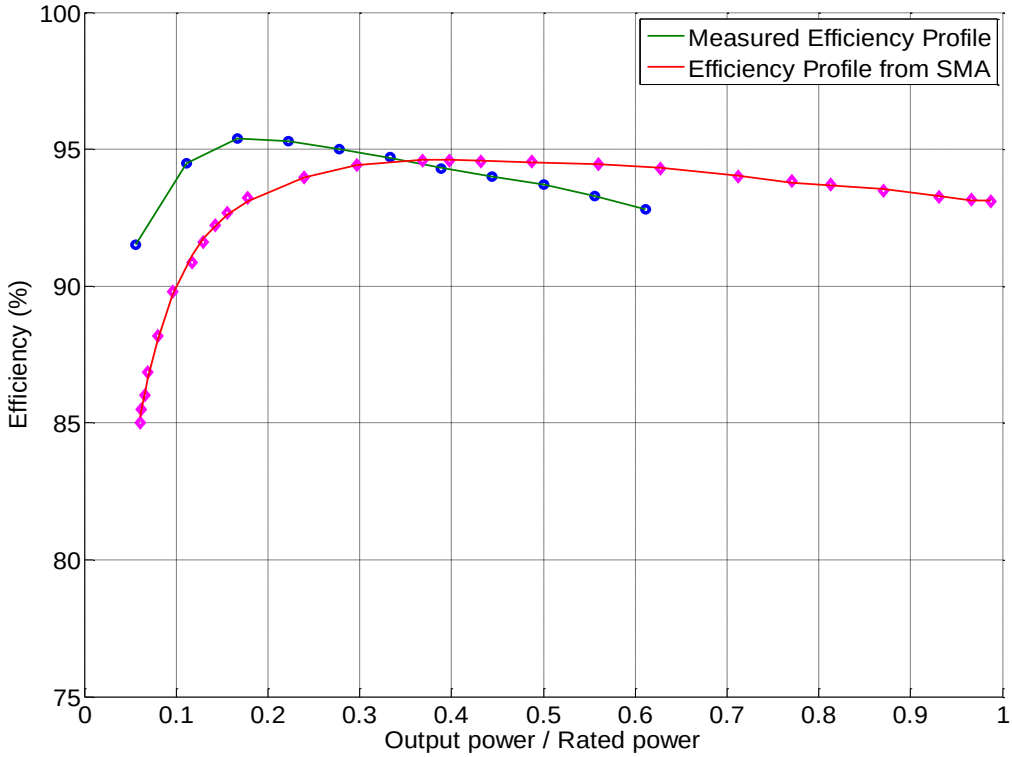

Figure 6.9: Comparison of SMA inverter measured efficiency with its manufacturer's data

6.2 Characterisation of the Soft-starter

A soft-starter is required to reduce the inrush current when starting the induction machine. In an off-grid system, it prevents high discharging current from the batteries. This reduces the stress being imposed on the batteries, which is beneficial for its lifetime. The description and simulation of the soft-starter are discussed previously, in Chapter 4. In this section, the three-phase WEG SSW-07 soft-starter

is considered [212]. The current limiter control and voltage ramp control were tested on the 11 kW induction machine. Both control methodologies of the soft-starter were tested with the power sources from the utility grid and the SI inverters. The start-up profiles were compared with each other and the most appropriate settings for the off-grid application were identified.

The WEG SSW-07 soft-starter front panel with its description is shown in Figure 6.10. The fundamental feature of this soft-starter is its capability of operating either current limiter control or voltage ramp control, depending on applications. The trimpots allow user to adjust the kick-start time, acceleration time and deceleration time. Additional features such as the motor current protection, thermal protection and status indicators are also available.

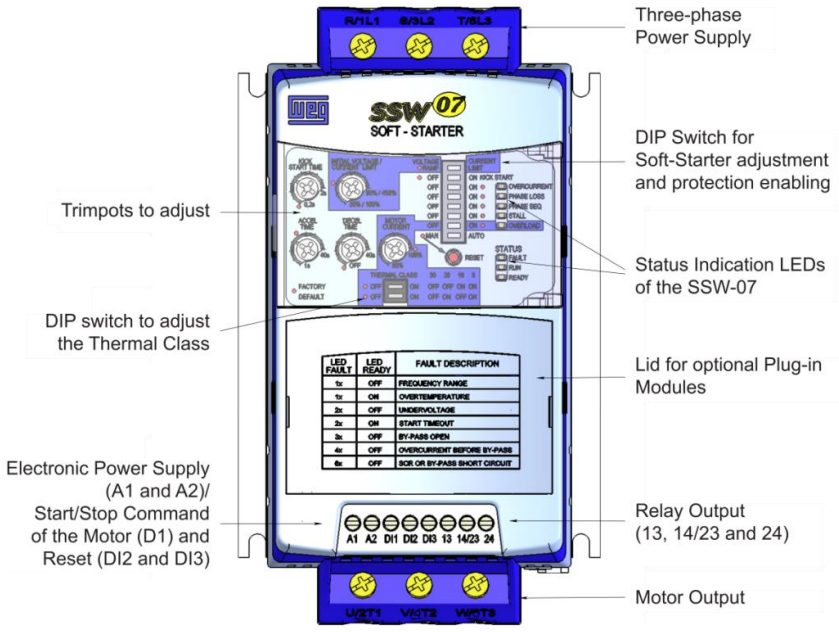

Figure 6.10: Frontal view of the SSW-07 [212]

The block diagram of the soft-starter's architecture is shown in Figure 6.11. The digital signal processor generates the firing pulses to the thyristors and handles the digital inputs and outputs. Each pair of anti-paralleled thyristors is connected with a snubber to suppress voltage spikes and to damp the ringing caused by circuit inductance during switching operation takes place.

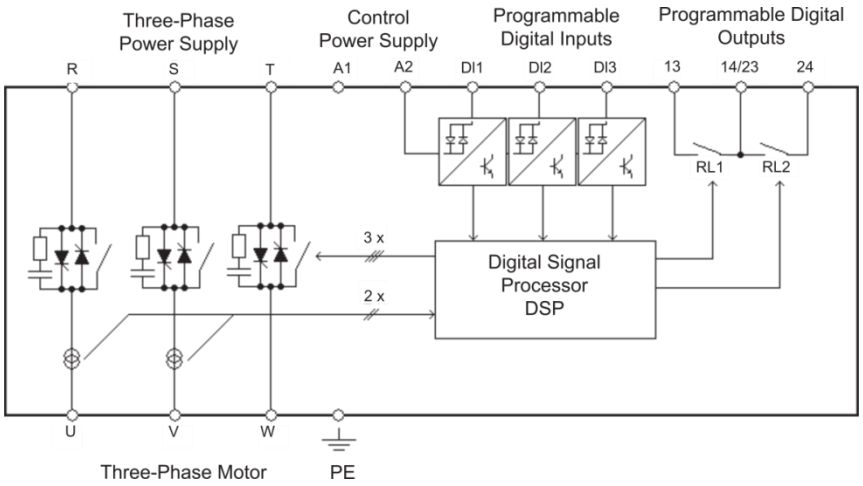

Figure 6.11: Soft-Starter SSW-07 block diagram [212]

The test setup block diagram in this section is shown in Figure 6.12. The start-up of the induction machine was tested with the SI inverters and the utility grid. The current limiter control and voltage ramp control were tested with power sources from both the inverters and utility, respectively. The 10 kVAr compensator was turned-on at a pre-set time, which was determined by the Mita-Teknik controller. Typically, it was after the induction machine reached near synchronous speed and after the soft-starter was bypassed. The inertia of the wind turbine blades were not taken into consideration in the following tests. With a larger inertia, only the start-up time would be extended with no changes on the current magnitude experienced by the generator.

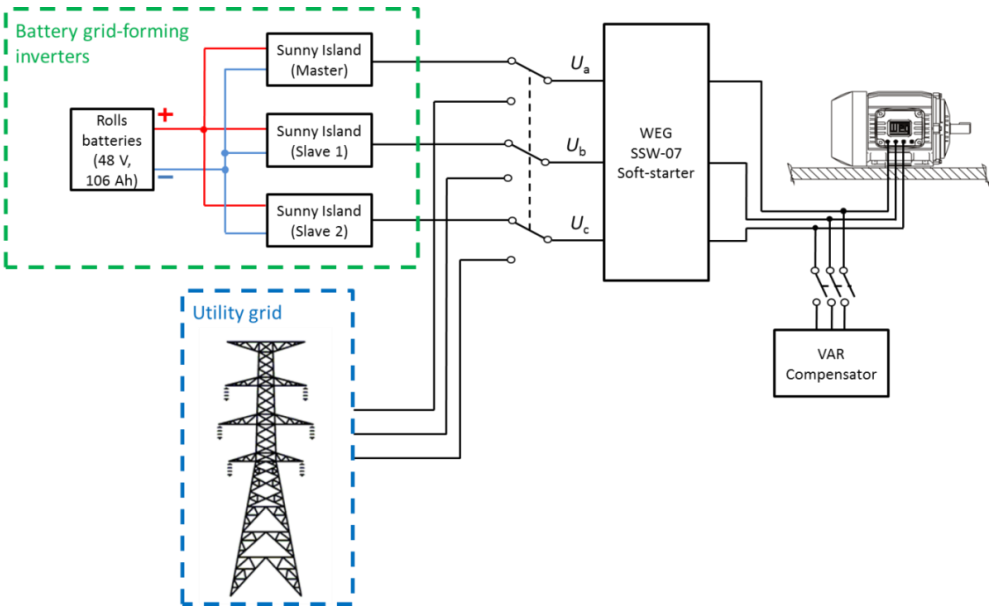

Figure 6.12: Test setup for WEG SSW-07 soft-starter

Within the current limiter control and voltage ramp control topologies, the WEG soft-starter allows a maximum current and initial voltage to be pre-set, respectively. In the following tests, the maximum limit of the current was tuned to be 200% of the nominal current of the soft-starter, whereas the initial voltage was set to be 40% of the rated input voltage of the soft-starter when voltage ramp control was utilised. Figure 6.13 and Figure 6.14 portray the measured start-up profile of the induction generator using the current limiter control with the utility power source and SI inverters, respectively. It is observed that the voltage and current profiles are slightly different for both cases. However, the maximum power achieved a peak of 10 kW in both cases. In addition, the generator took approximately the same amount of time to accelerate from stationary to near synchronous speed as observed from the rotational speeds (subplot 4 of Figure 6.13 and Figure 6.14). At about 17.5 s, the perturbation experienced from bypassing the soft-starter was observed to be more significant when the power source was from the SI inverters. The generator was stopped at about 32.5 s. It is noticed that little differences exist between Figure 6.13 and Figure 6.14 compared to the simulation results (Figure 4.39 and Figure 4.41) and this may be attributed to several reasons. Firstly, the integrated soft-start mechanism within the SI inverters [242] is not modelled in Chapter 4. It is unclear with regards to the architecture and the predefined settings of the integrated soft-start mechanism as very

limited information is found in the literature. Therefore, the combined effect of the SI soft-start mechanism and the WEG soft-starter is hard to be predicted analytically. Secondly, discrepancies between the modelled and real WEG soft-starter may also contribute to the differences. It is acknowledged that the use of the off-the-shelf components accelerate development time. However, the detailed control algorithm and architecture are usually very limited in the literature.

In general, the measured ramp up time of the induction machine is shorter in the experiments compared to the longer time being taken for simulations because the inertia of the rotor blades were not modelled in the test-rig during the start-up process. In other words, more energy is required when the rotor inertia included and hence the longer time. It is recognised that this is a limitation of the test-rig design. However, after start-up process is completed, the wind turbine model which is installed in dSPACE (explained in the next section) is activated and the wind turbine emulation begins thereafter.

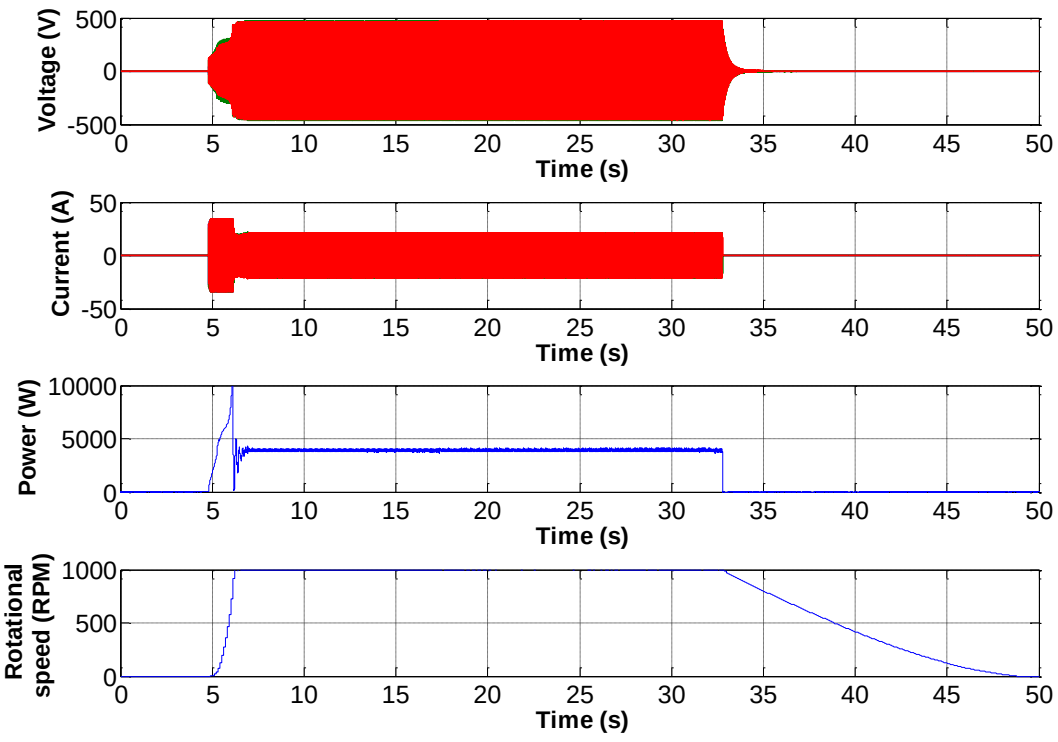

Figure 6.13: Generator start-up profile with current limited control using utility grid - *a)* Three-phase voltages *b)* Three-phase currents *c)* Power absorbed by the generator *d)* Rotational speed of the generator

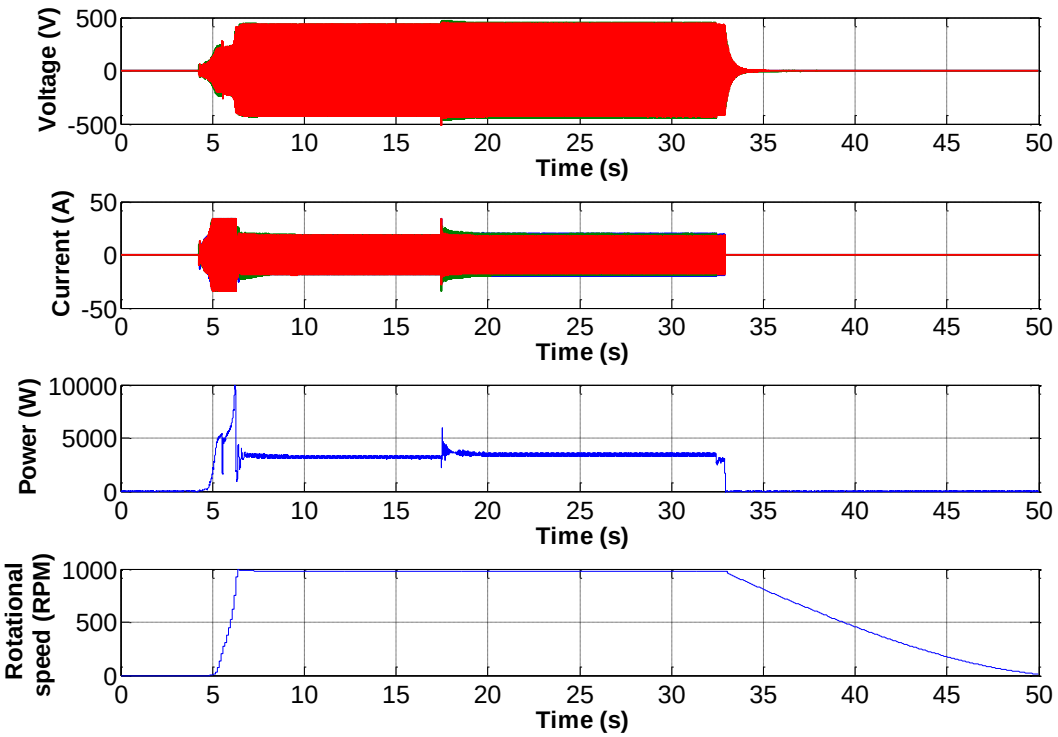

Figure 6.14: Generator start-up profile with current limited control using SI inverters - *a)* Three-phase voltages *b)* Three-phase currents *c)* Power absorbed by the generator *d)* Rotational speed of the generator

The start-up profile using voltage ramp control from both utility grid and SI inverters can be seen from Figure 6.15 and Figure 6.16. Despite having the same soft-starter settings, discrepancy in terms of voltage ramp rate can be observed from the graphs. The ramping profiles took relatively longer to reach their nominal values when the power was sourced from the SI inverters. As explained earlier, the integrated soft-start mechanism within the SI inverters may potentially affect the ramping profile compared to the utility grid which does not have a soft-start mechanism. A perturbation was observed when the soft-starter was bypassed at approximately 36.5 s for the case of grid-forming inverters. The generator was stopped at about 32.5 s for the utility grid case and at about 40 s for the SI inverters case.

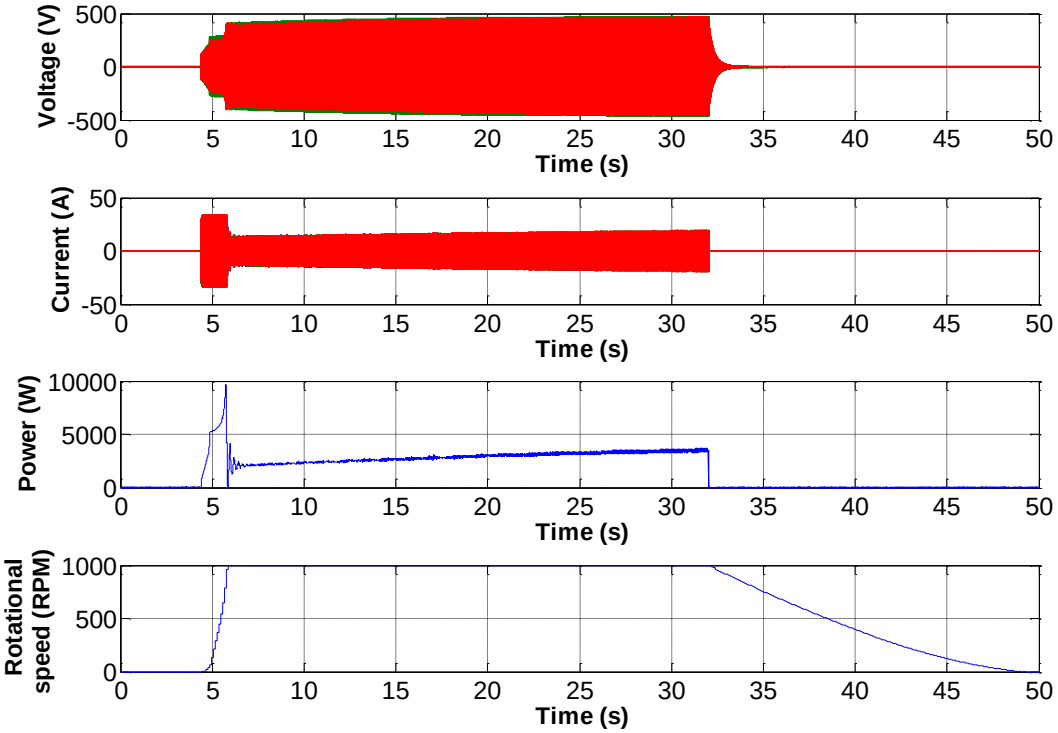

Figure 6.15: Generator start-up profile with voltage ramp control using utility grid - *a)* Three-phase voltages *b)* Three-phase currents *c)* Power absorbed by the generator *d)* Rotational speed of the generator

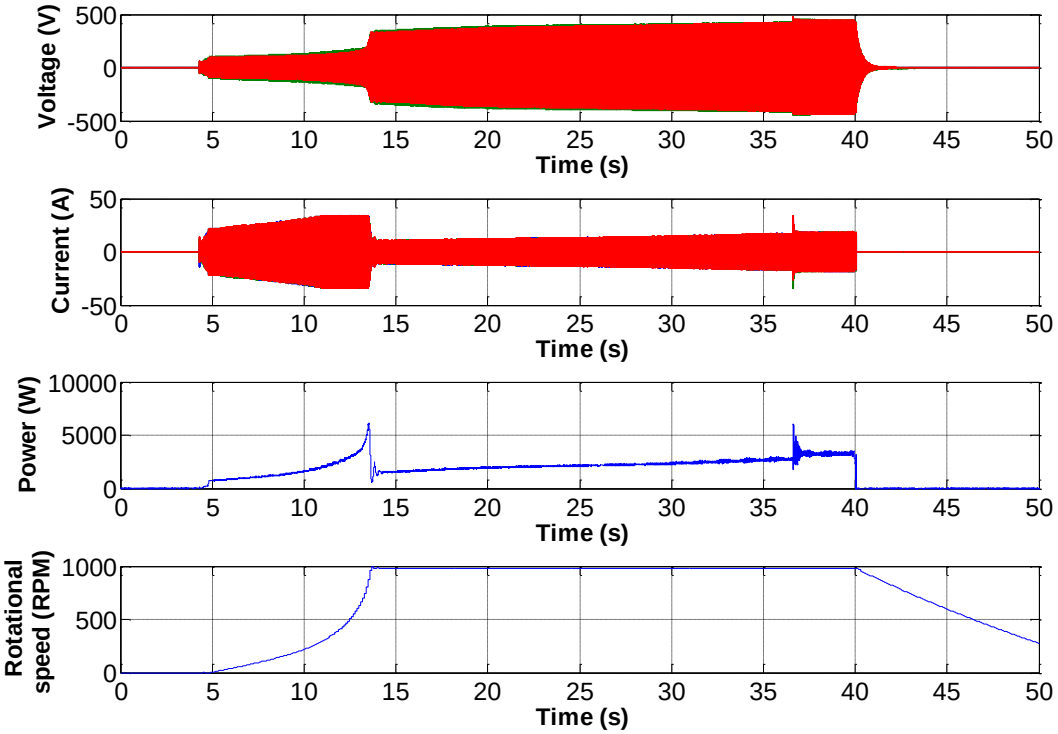

Figure 6.16: Generator start-up profile with voltage ramp control using SI inverters - *a)* Three-phase voltages *b)* Three-phase currents *c)* Power absorbed by the generator *d)* Rotational speed of the generator

The above study concluded that for the same soft-starter settings, the start-up profile can vary depending on the source of electricity, i.e. from the utility grid or from the SI inverters. Therefore, the settings which were determined using the utility grid cannot be directly used for the case of an off-grid scenario. A separate soft-starter test with the suggested setup needs to be conducted independently in order to select suitable parameters within a soft-starter.

Comparing the start-up profile of the current limiter control (Figure 6.14) and voltage ramp control (Figure 6.16) in the SI inverters setup, the former appeared to be the preferred choice as the latter took much longer to complete the start-up process. The objective of not exceeding the power rating of the inverter (18 kW) during start-up was achieved. In this case, the peak power during start-up was 10 kW and this translated to about 44% safety margin in terms of power rating. In addition, it has provided the shortest possible start-up time compared to other settings.

6.3 Development and Characterisation of a Wind Turbine Emulator

This section describes the development and the process of characterising a wind turbine emulator in the laboratory environment. The inductor generator is driven by an induction motor which is powered by a variable speed inverter drive using torque control. With this approach, the induction generator is able to operate at fixed speed with either positive or negative slip, depending on whether it is running as motoring or generating mode.

In a real wind turbine system, a braking mechanism with sensors exists to ensure safe operation of the wind turbine at all times. The Mita-Teknik controller is designed to operate with various inputs/outputs (I/Os) from the wind turbine system. Since the test rig was developed to study the electrical characteristics of the wind turbine, the braking operation I/Os input with the signals being emulated from the assistance of external circuitry. Therefore, the sophisticated mechanical parts can be avoided throughout the test rig development whilst having the Mita-Teknik controller to operate in conjunction at the same time. The detailed development work of the emulated brake operation can be referred in Appendix E.

The components layout of the wind turbine controller is shown in Figure 6.17. The Mita-Teknik IC1100 is the main controller of the system. It reads signals from the transducers, such as voltage, current, rotational speed of the turbine and generator, brake release status, vibration, cable twist and wind speed from the anemometer. These information are evaluated and the output signals such as tripping, emergency brake, solenoid for braking mechanism, on-off of VAr compensator and soft-starter bypass are generated accordingly.

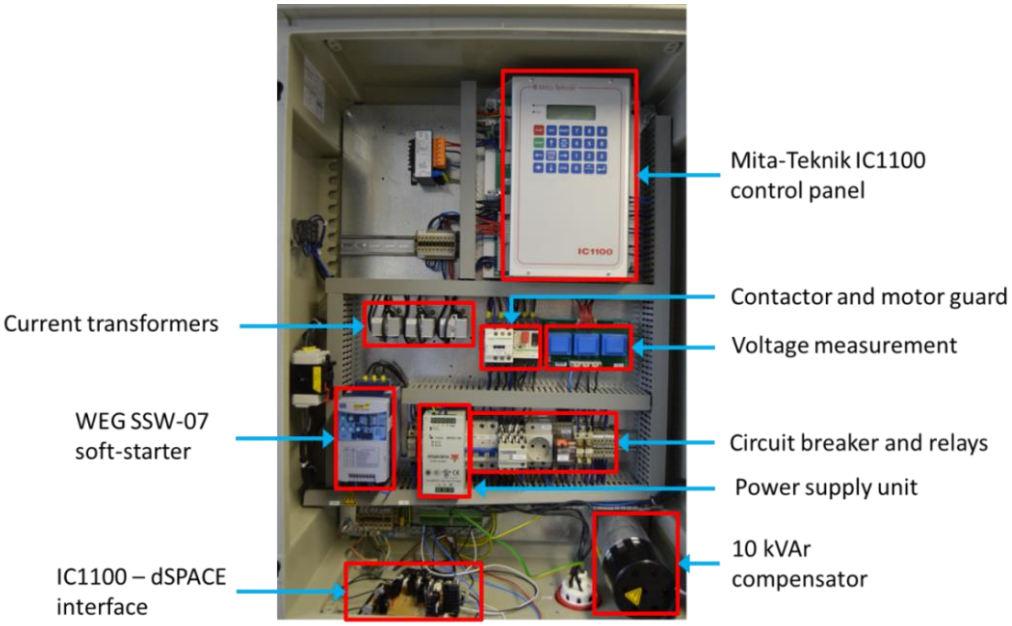

Figure 6.17: Wind turbine controller cabinet

As the wind turbine controller's I/Os are operating within the range of 0 – 24 V, a signal conditioning circuitry is needed to interface these I/Os with the dSPACE's analogue-to-digital converter (ADC), which operates from -10 V to 10 V. In order to achieve this, the open collector circuits are utilised as level shifters. In this work, the DC voltages from the wind turbine controller are shifted from 24 V to 5 V and vice versa. The dSPACE is programmed to read 5 V as high logic level and 0 V as low logic level. Therefore, the schematic shown in Figure 6.18 is designed to interface between the wind turbine controller and the dSPACE controller.

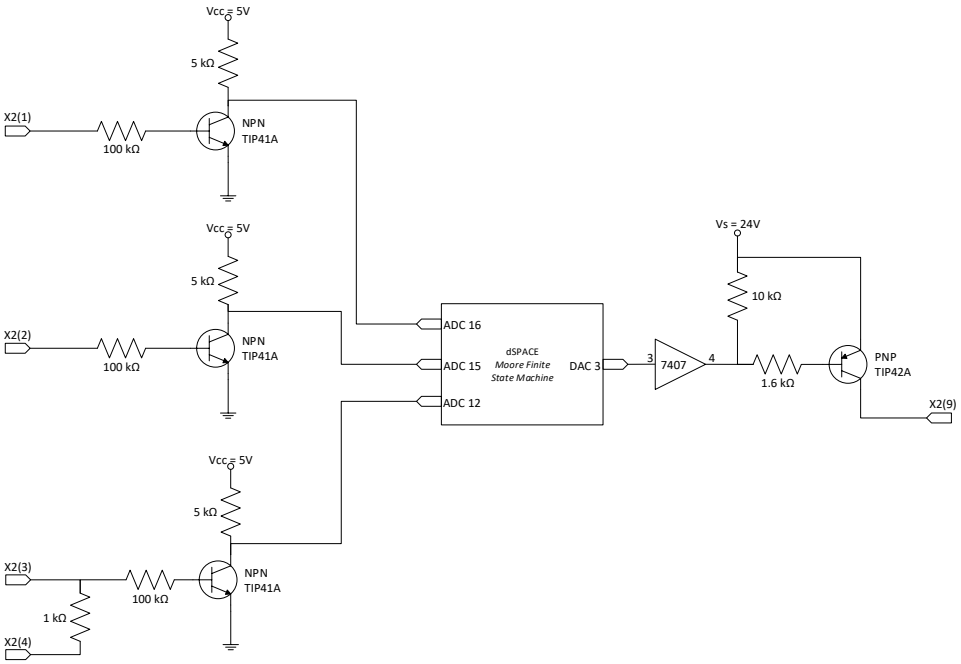

Figure 6.18: Interface circuit for the wind turbine controller and the dSPACE DS1103 with Moore FSM

Another input signal required by the wind turbine controller is the rotational speed of the wind turbine. In the laboratory environment, the induction generator is not intended to be driven by the wind turbine blades. Therefore, the gearbox can be omitted in this case. Since the generator's speed can be measured using the proximity sensor, it can be multiplied with the gear's ratio (1:18) in order to obtain the rotational speed of the wind turbine. Similarly, this will be performed by the dSPACE controller and the schematic is shown in Figure 6.19. The modelling of the divide-by-18 pulse generator in Simulink is shown in Figure 6.20.

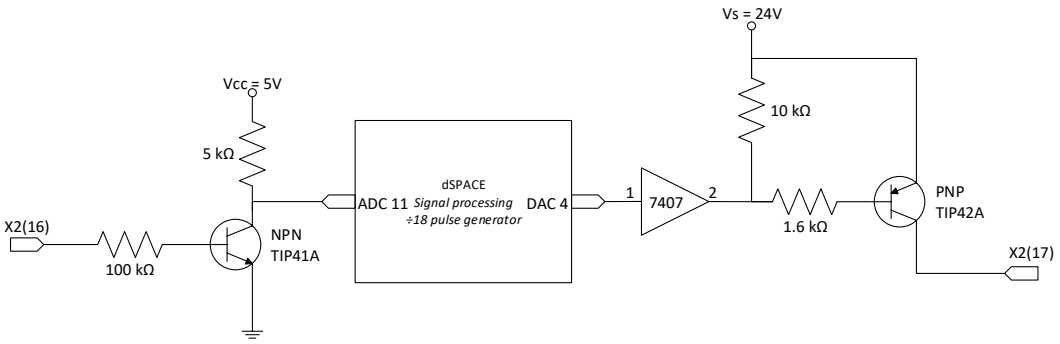

Figure 6.19: Interface circuit for the wind turbine controller and the dSPACE DS1103 with divide-by-18 pulse generator

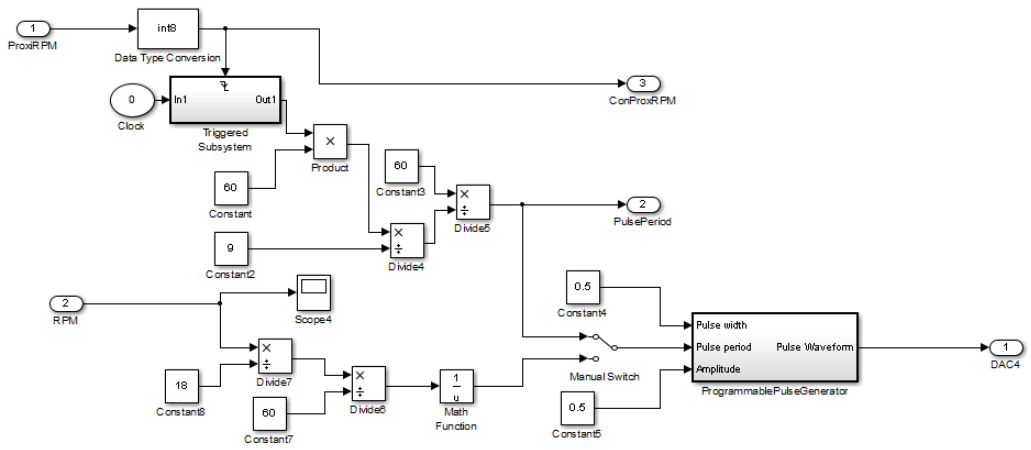

Figure 6.20: Divide-by-18 pulse generator block diagram

The hardware implementation of the interface in Figure 6.18 and Figure 6.19 is shown in Figure 6.21.

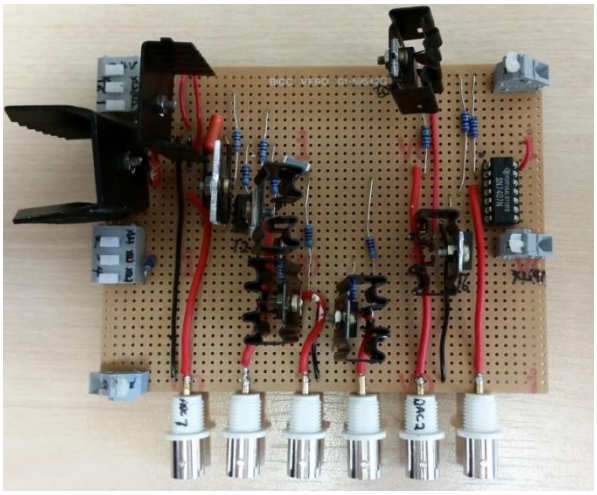

Figure 6.21: Hardware interfacing circuit between wind turbine controller and dSPACE board.

In the past, one of the popular choices to form a wind turbine simulator is based on a DC motor [243]. However, such simulator requires a relatively largely sized DC motor. In addition, the DC system is unattractive due to its unavailability, maintenance requirement and relatively more expensive [243]. On the other hand, the induction machine is well known for its robustness, simplicity and ease of control. In this work, the step-up gearbox is represented by a simple mathematical function with the mechanical torque at the low-speed shaft and the rotational speed of the generator

as inputs. A 1:18 ratio gives the rotational speed at the rotor blades; the input power at the low-speed shaft is then used to calculate the mechanical torque at the high-speed shaft. A 22 kW induction motor is used to emulate the wind energy, driving the induction generator. The reason for using the 22 kW induction machine is that it was readily available in the lab. The motor is powered by a variable-speed drive, Parker SSD Drive [244] as shown in Figure 6.22. The corresponding functional block diagram is shown in Figure 6.23 [244]. The power module consists of DC link capacitors which are used to smooth the DC voltage output prior to the power stage. The IGBTs converts the DC input to a three phase output, driving the motor. The processor performs the arithmetic operations and provides a range of analogue and digital inputs and outputs. Finally, a Speed Feedback Technology Board is fitted into the Technology Option Interface which provides speed feedback for the HTTL encoder.

Figure 6.22: Variable speed AC drive – Parker SSD Drive

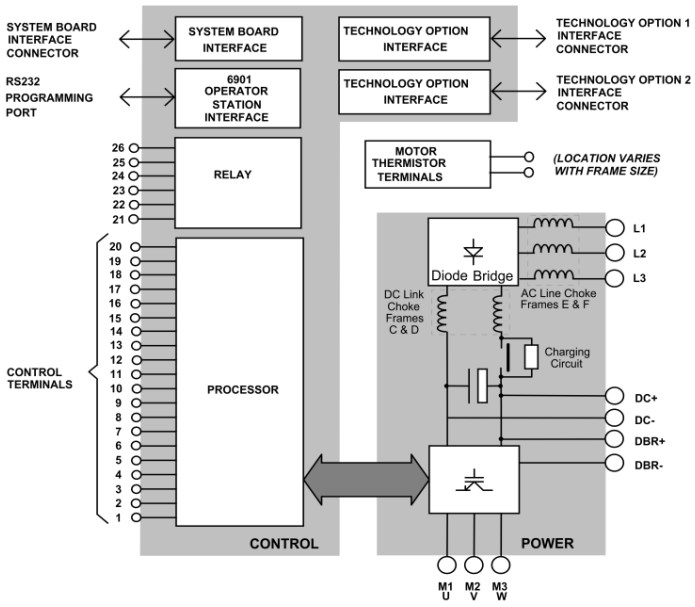

Figure 6.23: Functional block diagram of the Parker SSD Drive [244]

The SSD drive is capable of controlling the motor with two control topologies. These are speed control and torque control. As the Gaia wind turbine is a fixed speed wind turbine, torque control topology of the SSD drive is adopted in driving the 22 kW induction motor. With the generator running at a near-constant speed, the torque can be varied, hence emulating different strength from the wind. In addition, the phase synchronisation between the generator and the motor can be ensured with torque control topology. The motor control block diagram of the SSD Drive is shown in Figure 6.24 [244]. In this case, the speed control loop is bypassed. The torque control is enabled and the torque demand can be directly inputted through the analogue port. Note that the implemented torque control within the SSD drive is an open-loop control system.

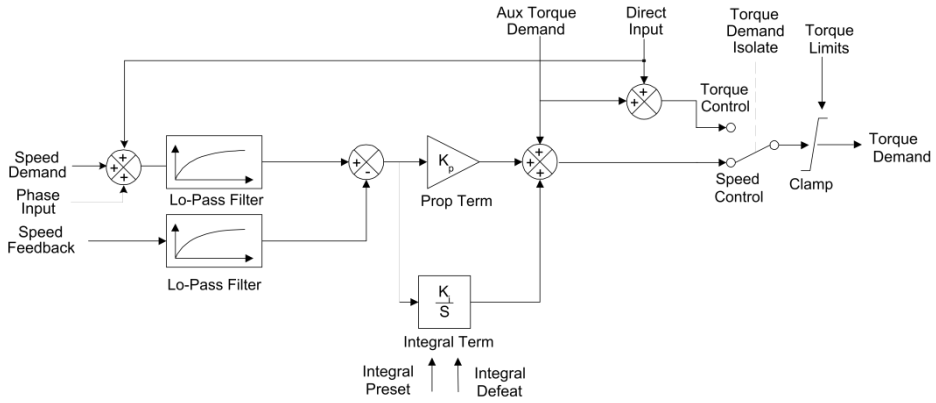

Figure 6.24: Speed loop control of the SSD Drive [244]

With the capability of programming different torque demand at the drive, the wind energy resulted from the variation in wind speed can be modelled. The coupling of the induction motor and induction generator is shown in Figure 6.25. The structure of the wind turbine emulator is portrayed in Figure 6.26.

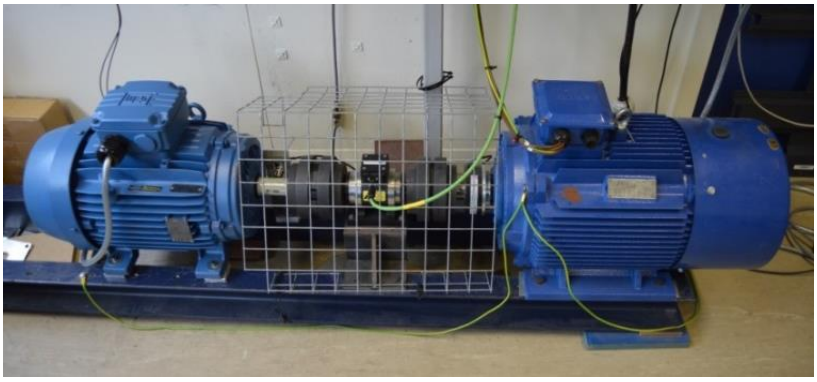

Figure 6.25: Coupling of the 22 kW induction motor (right) and the 11 kW induction generator (left)

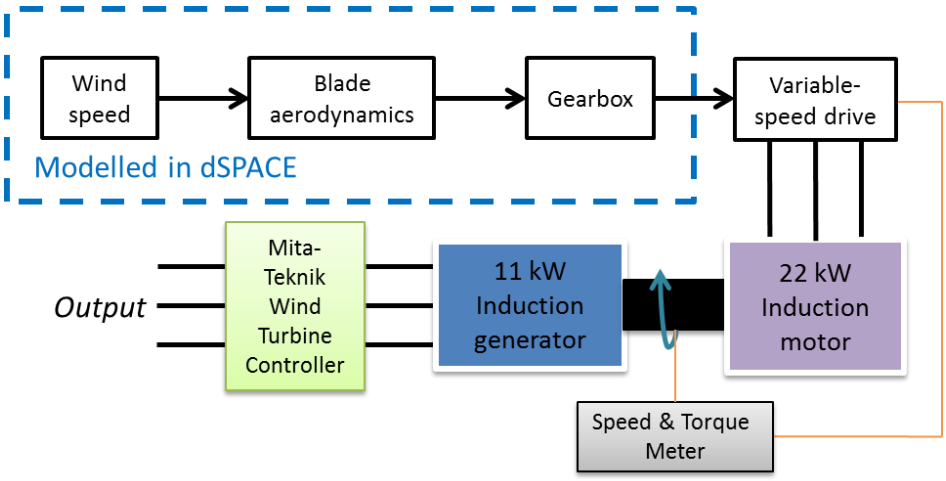

Figure 6.26: Setup of wind turbine emulator

Figure 6.27 shows the comparison of wind turbine power curves generated from the test rig, Simulink model and TUV NEL. The TUV NEL's power curve was formulated based on the characterisation of the Gaia wind turbine in the field. It can be observed that the curves are correlating well at low wind speed. At higher wind speed, the error from the test rig is more significant. From the wind turbine power equation (4.7), the power is a cubic function of the wind speed. As a result, the computed power at higher wind speed is more responsive. Secondly, the deviation

can be attributed to the slight difference of the rotational speed being assumed in the model and the real rotational speed observed within the setup.

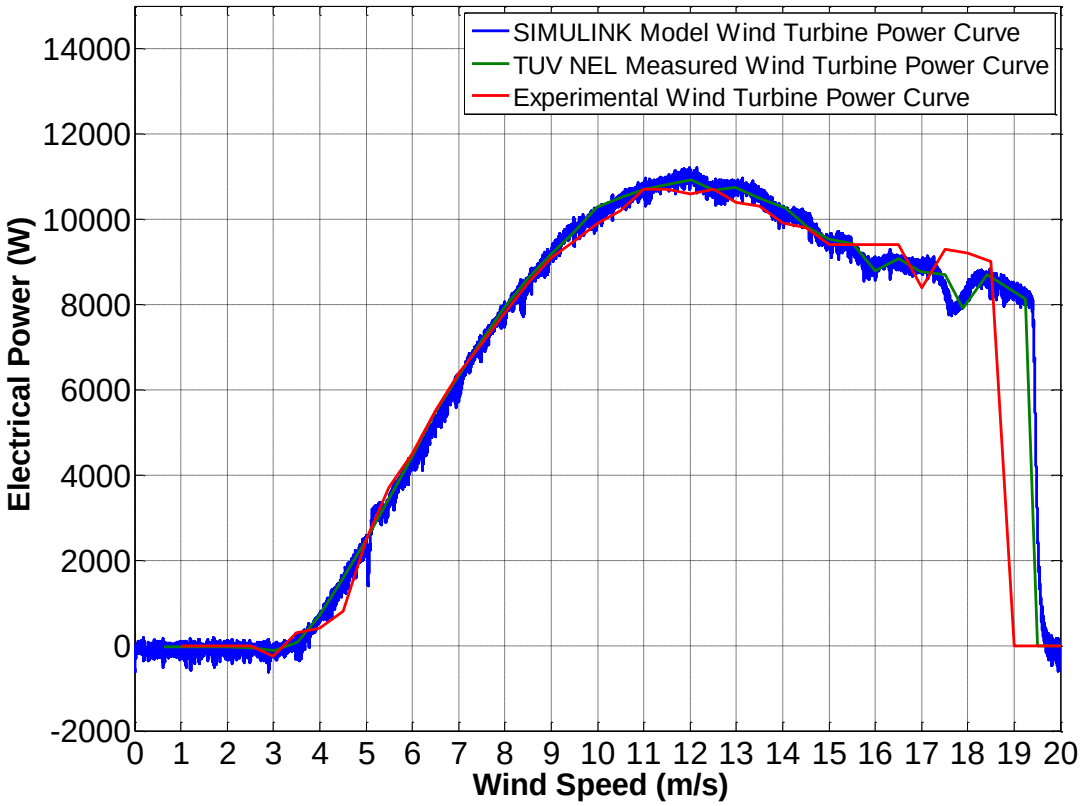

Figure 6.27: Wind emulator power curve comparison

6.4 Software Interface

The ControlDesk is a software programme which acts as an interface between the Simulink and the dSPACE controller. The implemented ControlDesk front panel interface for the test rig application is shown in Figure 6.28. It allows the user to set the wind speed, select the wind turbine tower configuration (which will be described in Chapter 7) in addition to displaying the desired waveforms (voltage, current, power, frequency etc). The corresponding Simulink coding which emulates the aerodynamics of the wind turbine, gearbox, braking mechanism, tower shadow profiles (which will be described in Chapter 7) and the calculations on system power and frequency is shown in Figure 6.29.

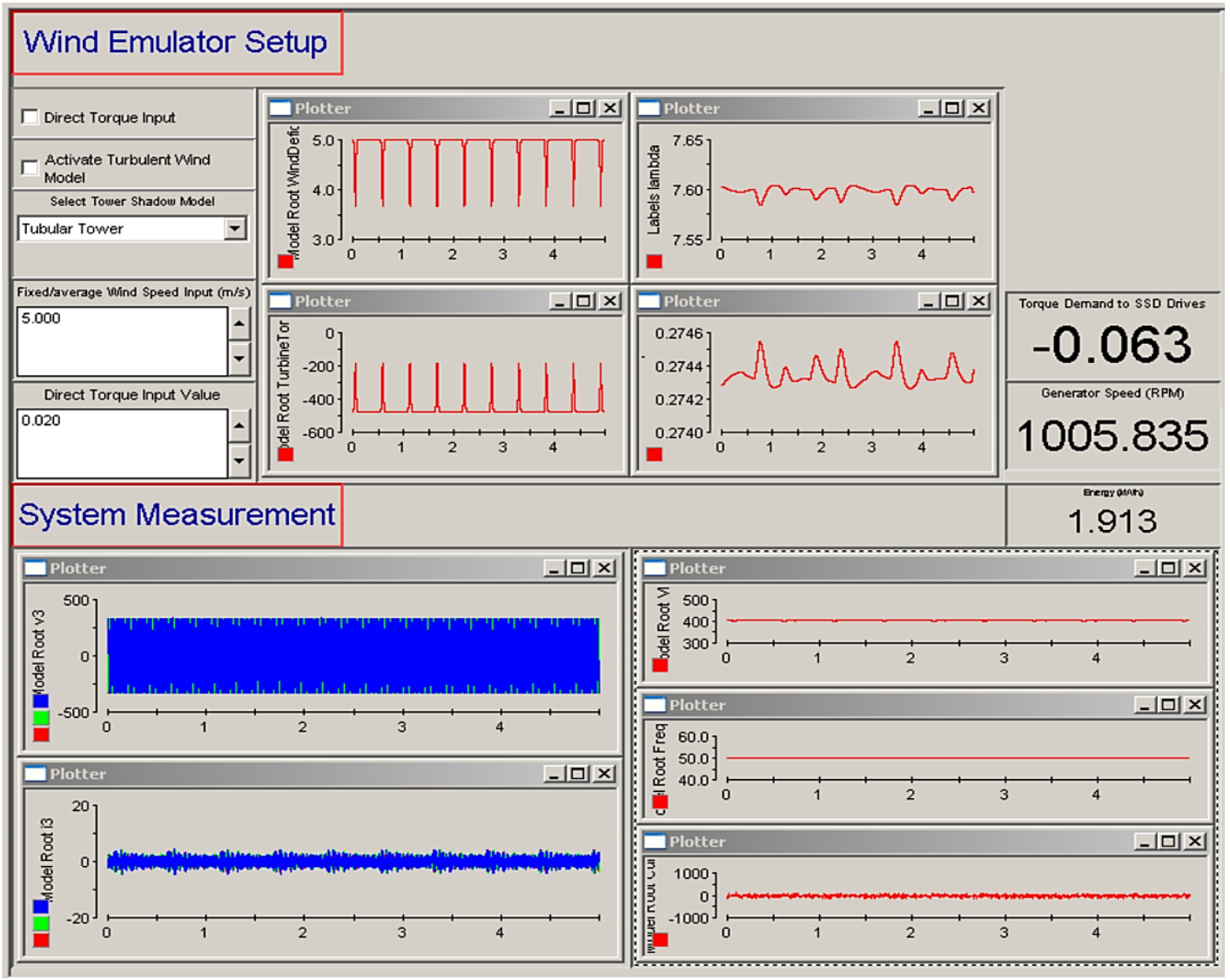

Figure 6.28: ControlDesk front panel

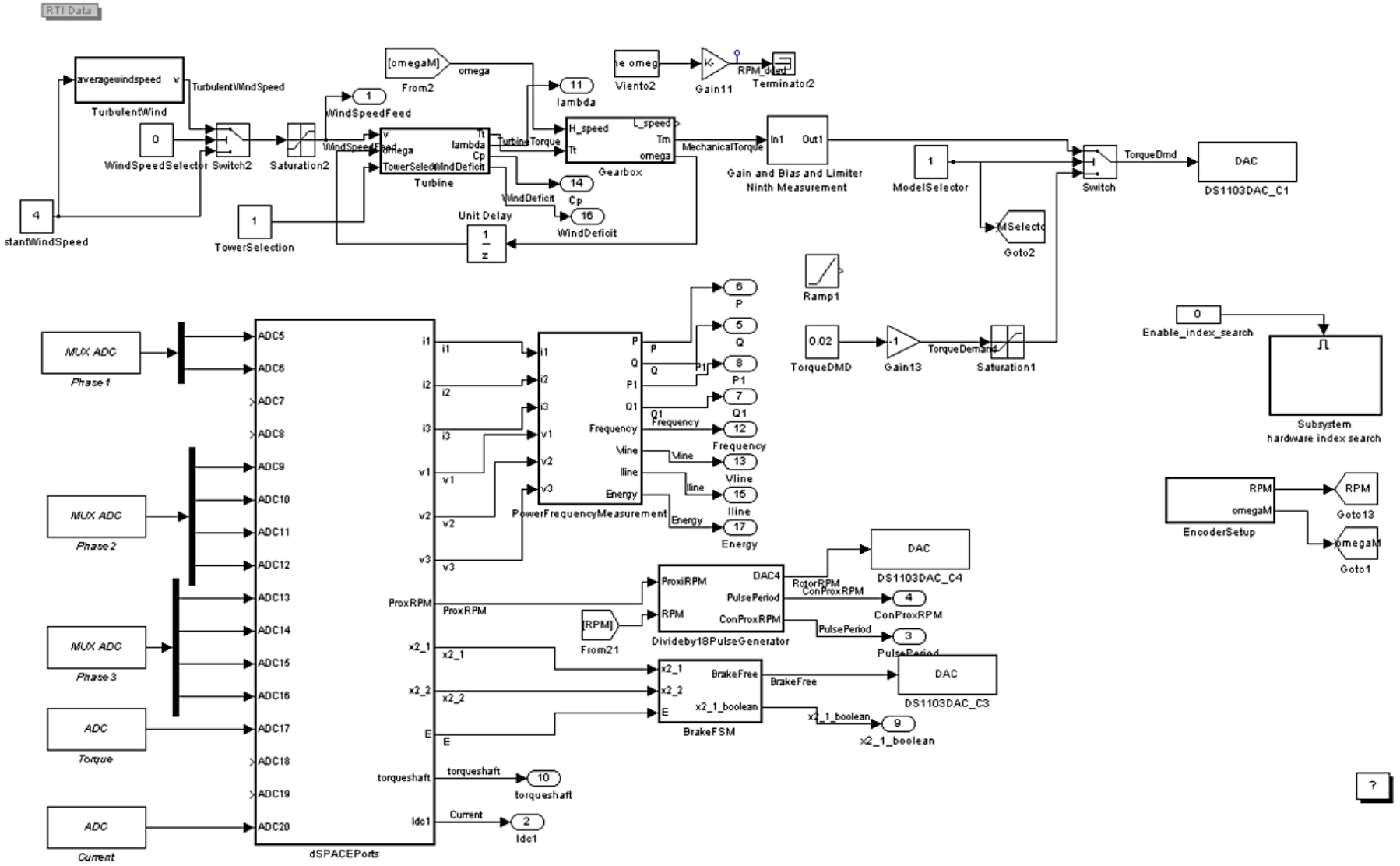

Figure 6.29: Simulink coding linked by the ControlDesk

6.5 Complete System Experimental Test and Results

The dynamics of the hybrid system test rig is analysed through several test scenarios. These include step changes in the wind speed, load demand and the utilisation of a turbulent wind profile as the reference wind speed. Figure 6.30 and Figure 6.31 show the measurement results. The system began with the wind turbine emulator generating electricity at wind speed 4.5 m/s and a load demand of 4 kW. At 4.5 m/s, the power generation was less than 4 kW. Therefore, this power deficit was met by the batteries. The fourth and fifth subplot of Figure 6.30 shows the power and current being supplied and absorbed from the batteries, respectively. Positive values indicated that the power or current being delivered from the battery to the load and vice versa. The first plot of Figure 6.30 shows the wind speed increment from 4.5 m/s to 6.5 m/s and decrement from 6.5 m/s to 4.5 m/s at the designated time at a step change of 0.5 m/s. Note that due to the limitation of the inverters in absorbing high power in charging the batteries, reduced wind speeds were used in this study. The line-to-line RMS voltage and its frequency and its frequency transients are demonstrated at the second and third subplot, respectively. The observed perturbations were within the statutory limits. As the wind speed increased beyond 6 m/s, the power generation exceeded the load demand; hence energy storing process began thereafter.

The second, third and fourth subplots of Figure 6.31 demonstrate the corresponding power coefficient (C_p), tip speed ratio (λ), mechanical torque demand at the generator shaft and the rotational speed of the generator. The power coefficient and tip speed ratio variations are within the range of the curve shown in Figure 4.20. In this scenario, it is observed that the optimum power coefficient occurs when the tip speed ratio was approximately 7.5, which corresponds to the wind speed of 5 m/s. As the wind speed increased to 6.5 m/s, the power coefficient reduced slightly. However, as the power is a cubic function of the wind speed, the power generated from the wind turbine was mainly affected by the magnitude of the wind speed. From the last subplot of Figure 6.31, the induction generator was operating at super-synchronous mode (exceeding synchronous speed of 1000 rpm) when it was generating electricity.

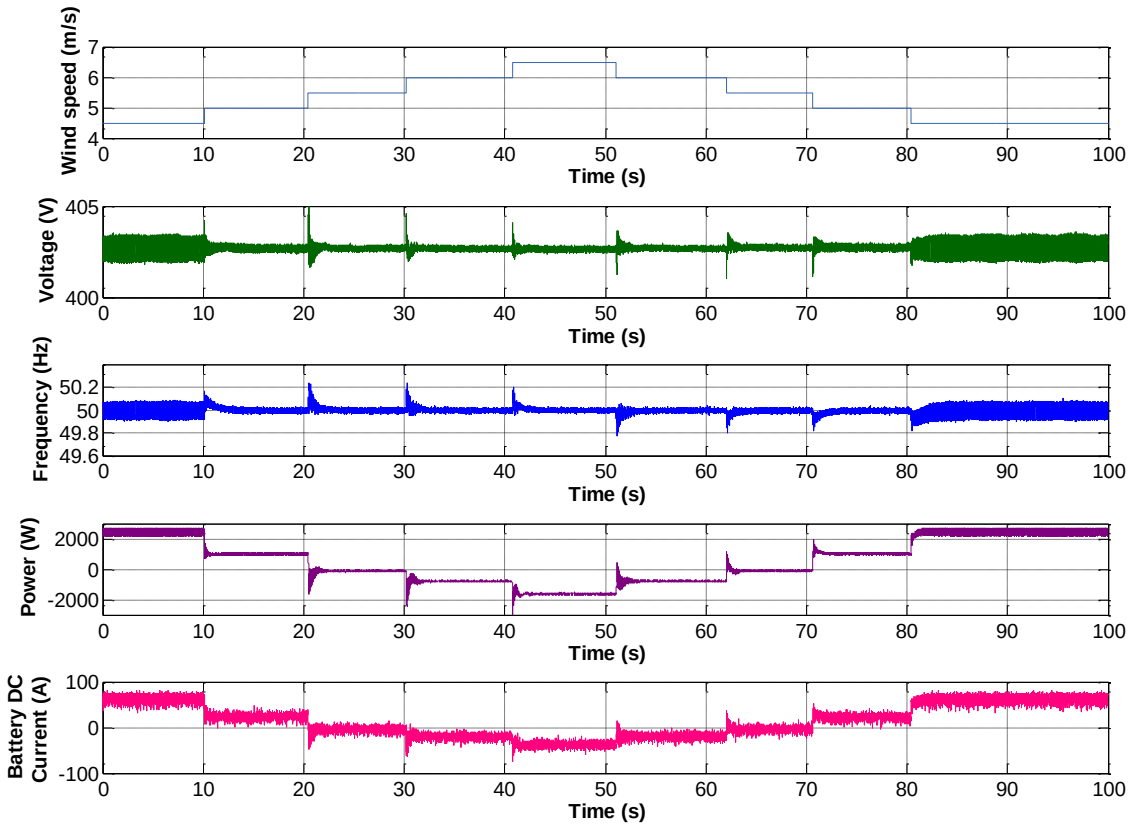

Figure 6.30: Experimentally measured wind emulator dynamic analysis with wind speed steps - *a)* Wind speed *b)* Grid line-to-line voltage *c)* Grid frequency *d)* Charging and discharging power of the batteries *e)* Battery DC current

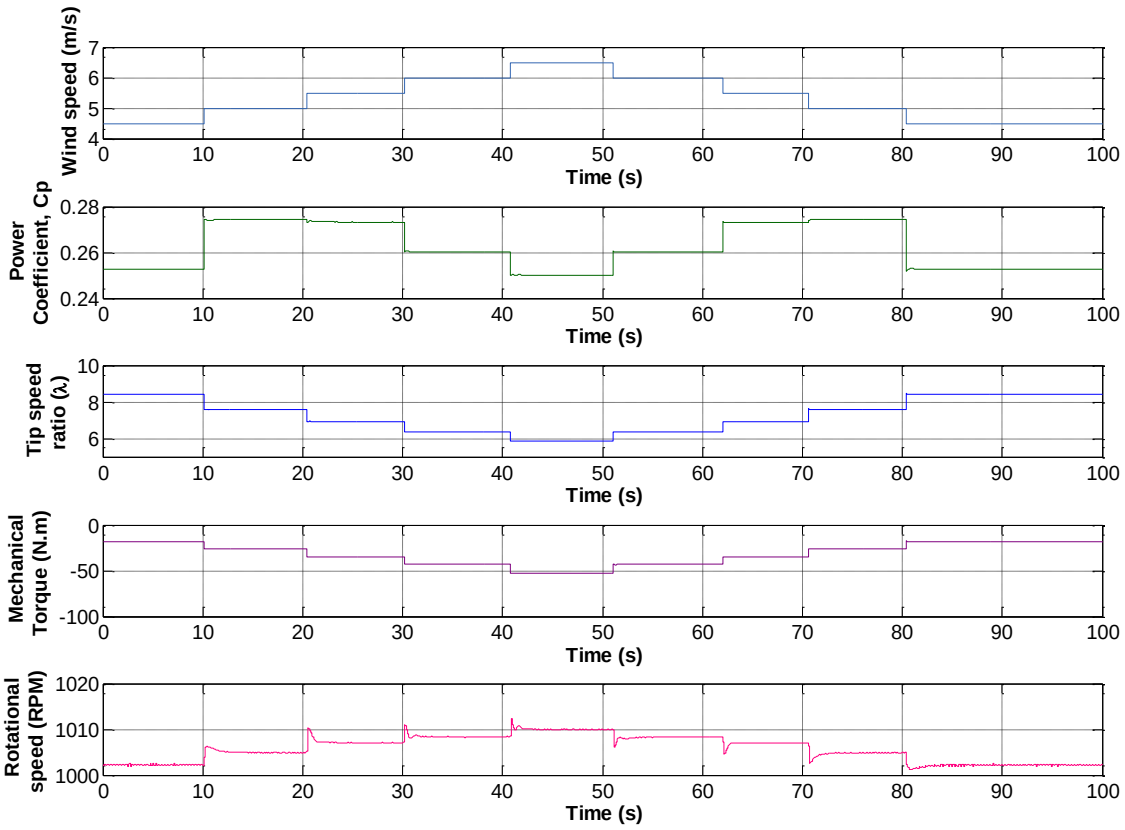

Figure 6.31: Experimentally measured wind emulator dynamic analysis with wind speed steps - *a)* Wind speed *b)* Power coefficient *c)* Tip speed ratio *d)* Input torque of the induction generator *e)* Rotational speed of the induction generator

In order to validate the measured results against the hybrid system model in Chapter 4, a simulation has been performed using the same test inputs as outlined above. Figure 6.32 shows the simulated results of stepping the wind speed with constant values. In general, it possesses similar dynamics as demonstrated from the experimental results in Figure 6.30, except that there is more settling time being observed for the experiment case. Theoretically, the simulated and experimentally measured grid voltage and frequency are correlated in terms of the magnitude change. However, the discrepancy in power flow can be associated with the electrical losses from power converters, cables and batteries not being taken into consideration in the simulation model.

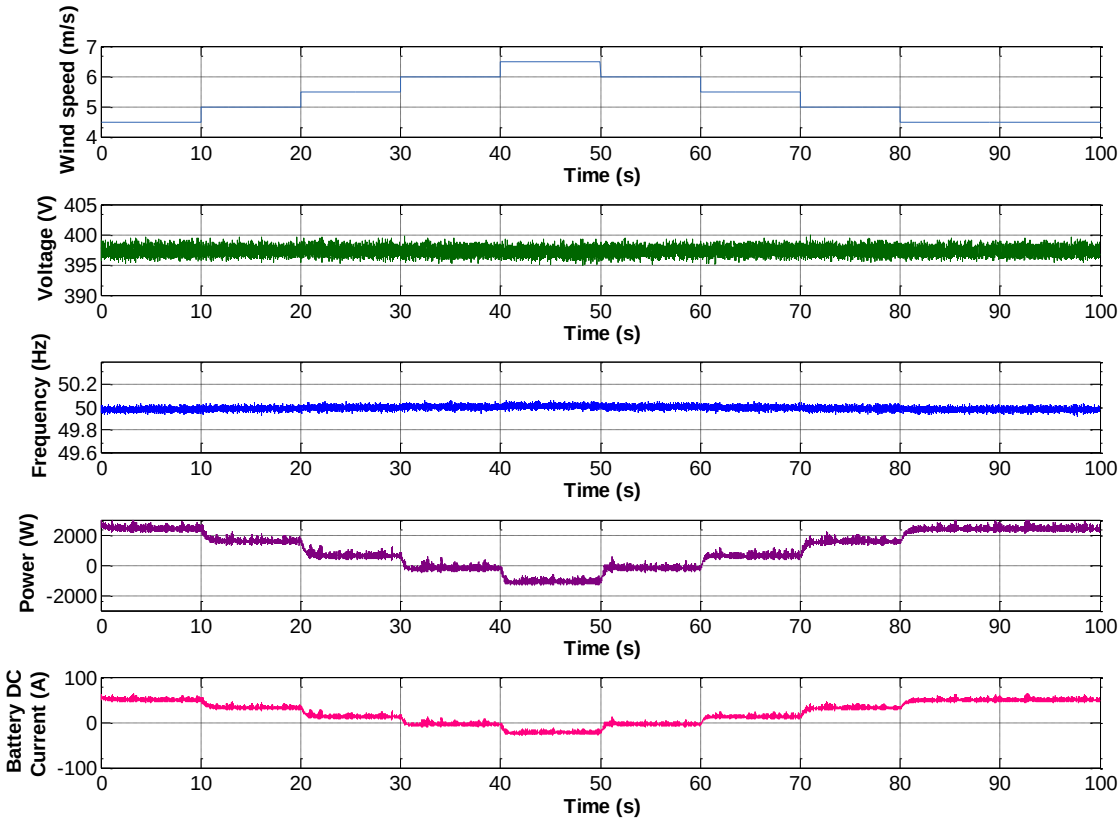

Figure 6.32: Simulated dynamic analysis with wind speed steps - *a)* Wind speed *b)* Grid line-to-line voltage *c)* Grid frequency *d)* Charging and discharging power of the batteries *e)* Battery DC current

Next, the investigation was carried out on the effect of load switching on the hybrid system. The test began with a load of 5 kW. The load was reduced to 3 kW and 1 kW at about 11 s and 20 s, respectively. At approximately 30 s, the load was completely turned-off. After that, the load was switched-on in the same sequence, with the running load of 1 kW, 3 kW and 5 kW at about 40 s, 50 s and 60 s, respectively. Throughout this test, the wind speed is given as 5 m/s.

Figure 6.33 shows the system dynamics of the test. The system voltage rose when the loads were switched-off in steps and vice versa. However, minimal changes in the frequency level were perceived, except that it has experienced some perturbations. Similar as before, the excess energy from the generator was being stored in the batteries which can be observed from the direction of the power flow. Figure 6.34 shows the dynamics of the wind energy system. Small perturbations on the generator rotational speed, TSR and hence the power coefficient were seen when the step load

occurred. However, they recovered to their original level within 1 to 2 s. The power generation from the induction generator remained the same throughout the test period despite the occurrence of load steps. This can be attributed to the capability of the SI inverters in "holding" the system frequency, however, with minimal frequency droop.

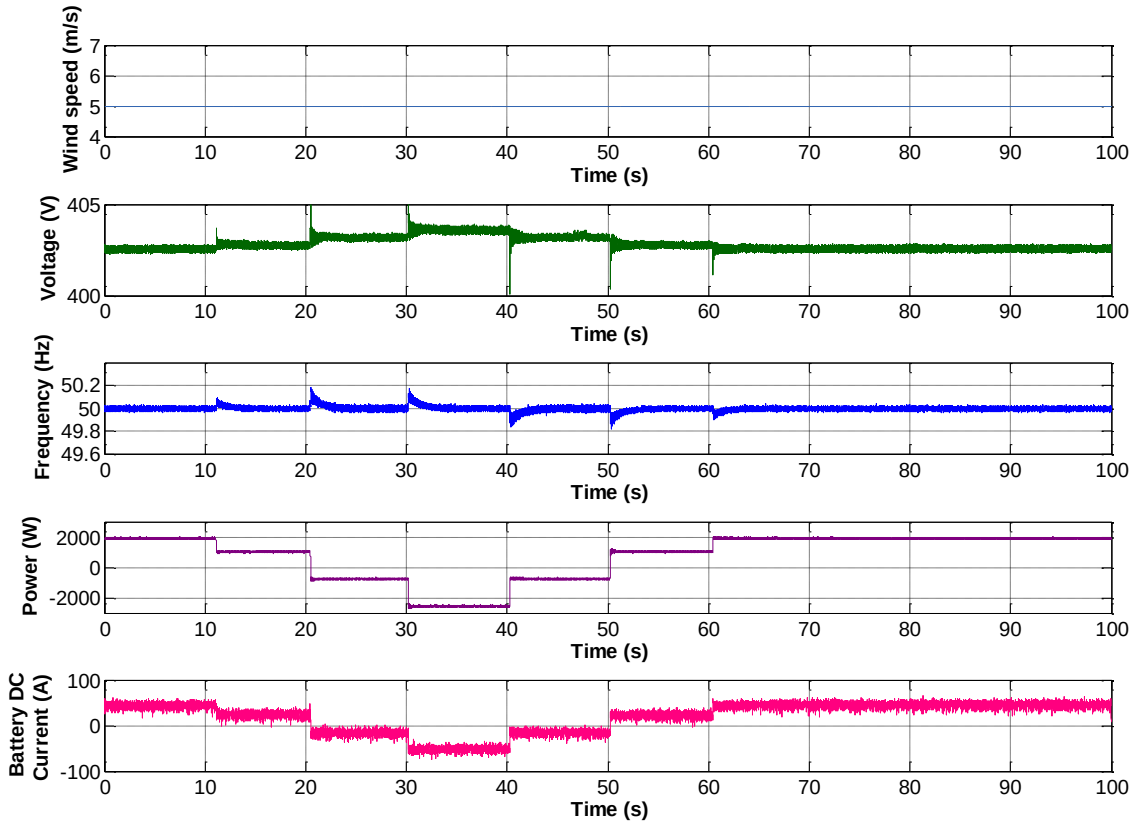

Figure 6.33: Experimentally measured wind emulator dynamic analysis with load steps - *a)* Wind speed *b)* Grid line-to-line voltage *c)* Grid frequency *d)* Charging and discharging power of the batteries *e)* Battery DC current

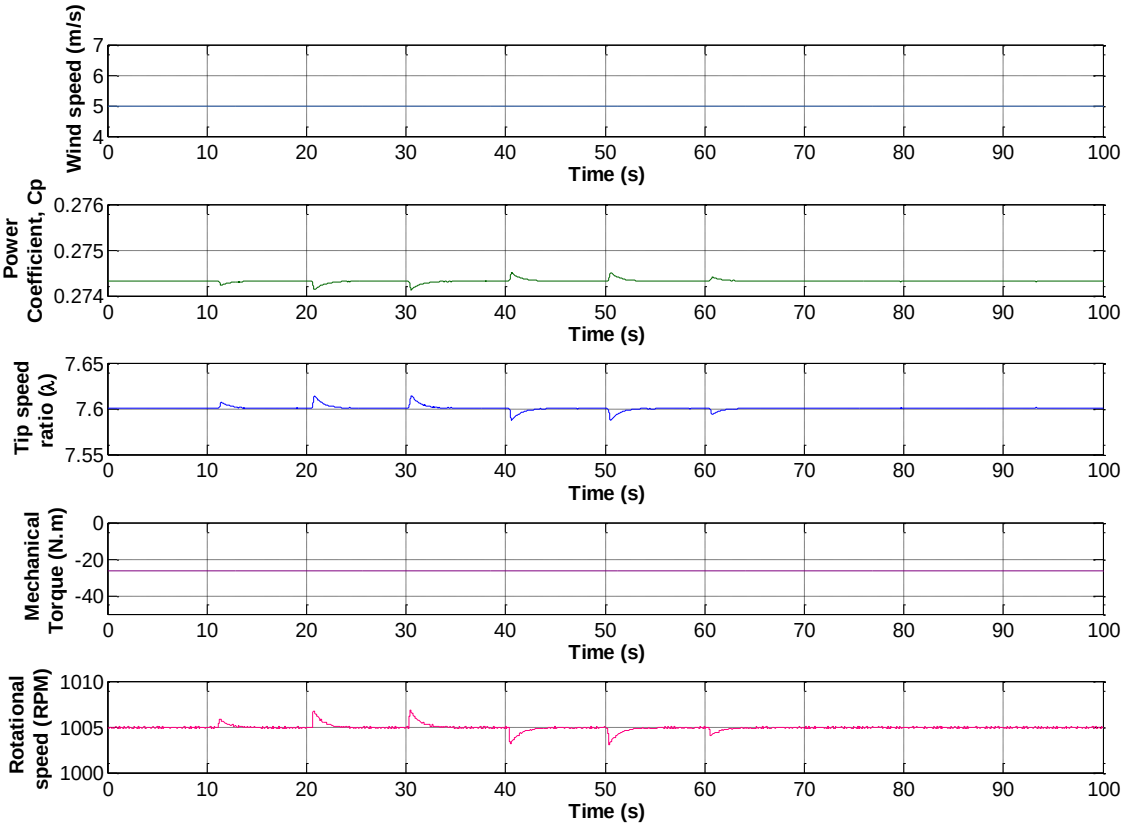

Figure 6.34: Experimentally measured wind emulator dynamic analysis with load steps - *a)* Wind speed *b)* Power coefficient *c)* Tip speed ratio *d)* Input torque of the induction generator *e)* Rotational speed of the induction generator

Similarly, a simulation of the load step changes was performed using the model developed from Chapter 4. The simulation results are shown in Figure 6.35. Once again, the simulated voltage, frequency, battery power flow and its DC current profiles is relatively similar to the measured results as shown in Figure 6.33.

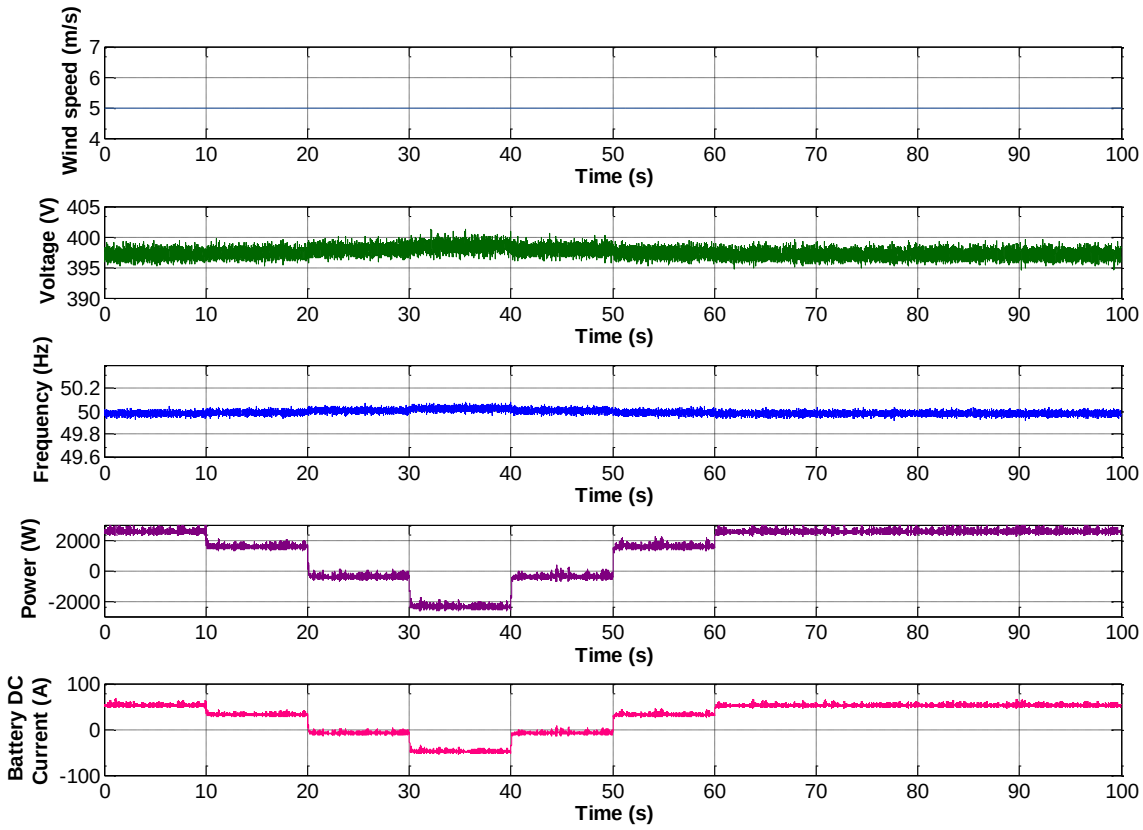

Figure 6.35: Simulated dynamic analysis with load steps - *a)* Wind speed *b)* Grid line-to-line voltage *c)* Grid frequency *d)* Charging and discharging power of the batteries *e)* Battery DC current

In order to establish a more realistic test rig, the turbulent wind speed model which was developed in Section 4.4 is adopted instead of a fixed wind speed input. A test using the turbulent wind model with an average wind speed of 5 m/s was conducted with a fixed load demand of 4 kW. The first subplot of Figure 6.36 demonstrates the turbulent wind speed profile. At about 52 s, the wind speed reached a peak of 8 m/s within the entire measured period. At this time, an excess power of 4 kW existed within the system. The frequency reached the highest value after a delay of about 3 s. The inverters were also being tested if they were able to handle the fluctuations from the wind by reacting quickly between the charging and discharging modes seamlessly. Figure 6.37 shows the corresponding variations in the power coefficient, TSR, mechanical torqued demand at the shaft and the rotational speed of the induction generator.

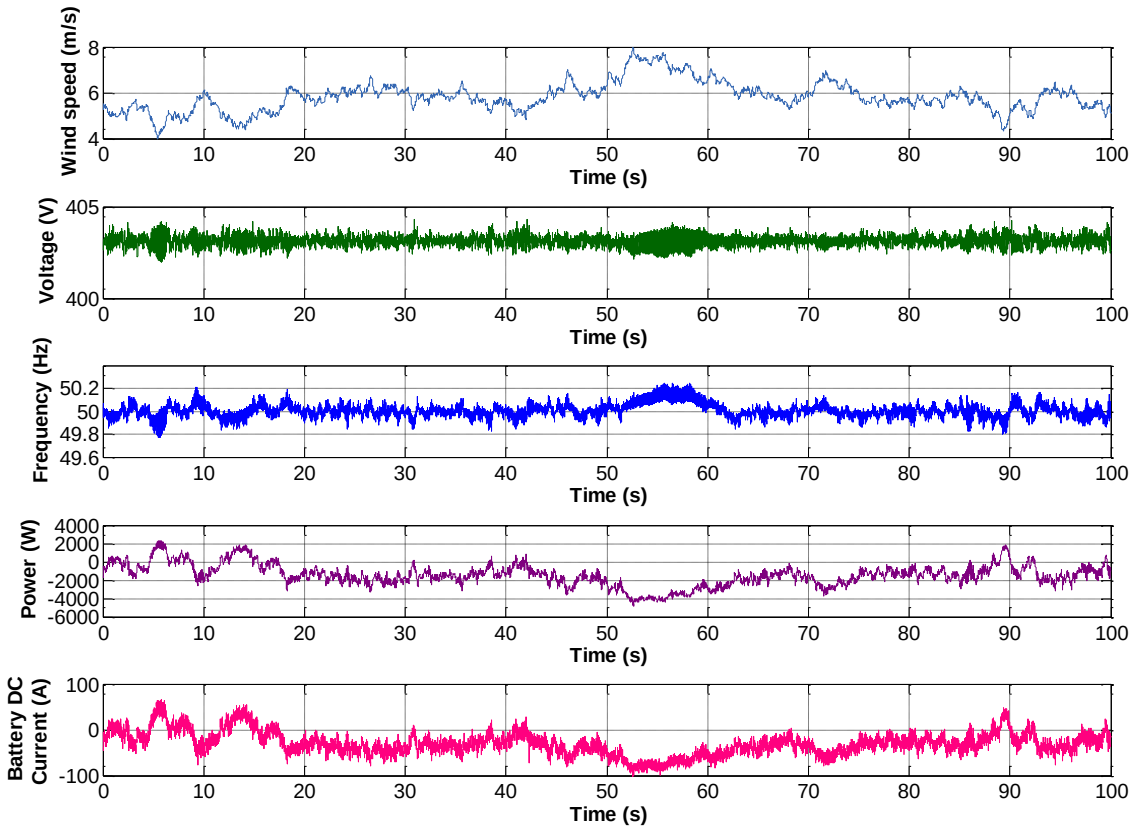

Figure 6.36: Experimentally measured wind emulator dynamic analysis with turbulent wind - *a)* Wind speed *b)* Grid line-to-line voltage *c)* Grid frequency *d)* Charging and discharging power of the batteries *e)* Battery DC current

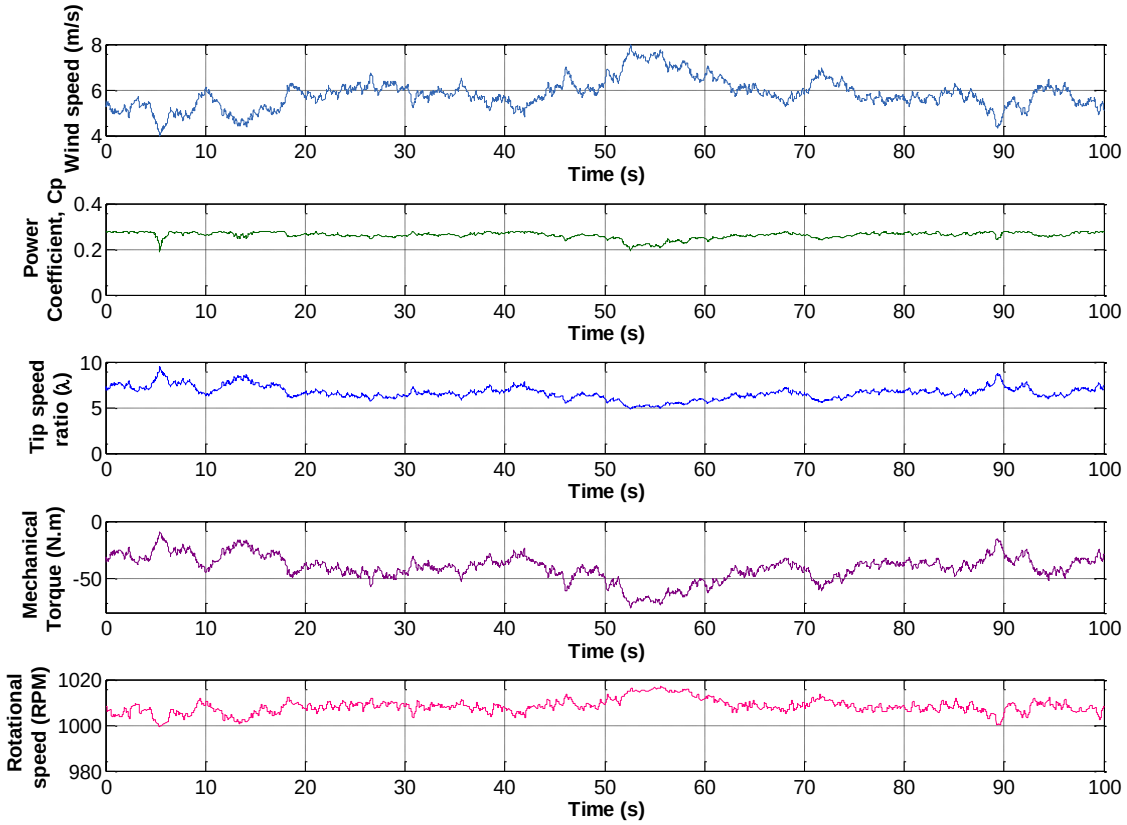

Figure 6.37: Experimentally measured wind emulator dynamic analysis with turbulent wind - *a)* Wind speed *b)* Power coefficient *c)* Tip speed ratio *d)* Input torque of the induction generator *e)* Rotational speed of the induction generator

Using the hybrid system model which was developed in Chapter 4, the simulation results using the same turbulent wind profile is shown in Figure 6.38. Comparing both Figure 6.36 and Figure 6.38, it is noticed that the experimental measured voltage and frequency fluctuate more rapidly compared to the simulation results. Although the fluctuations are kept within the statutory limits, as expected, it is observed that a single distributed generator (wind turbine in this case) can have a significant influence in the system voltage and frequency perturbations.

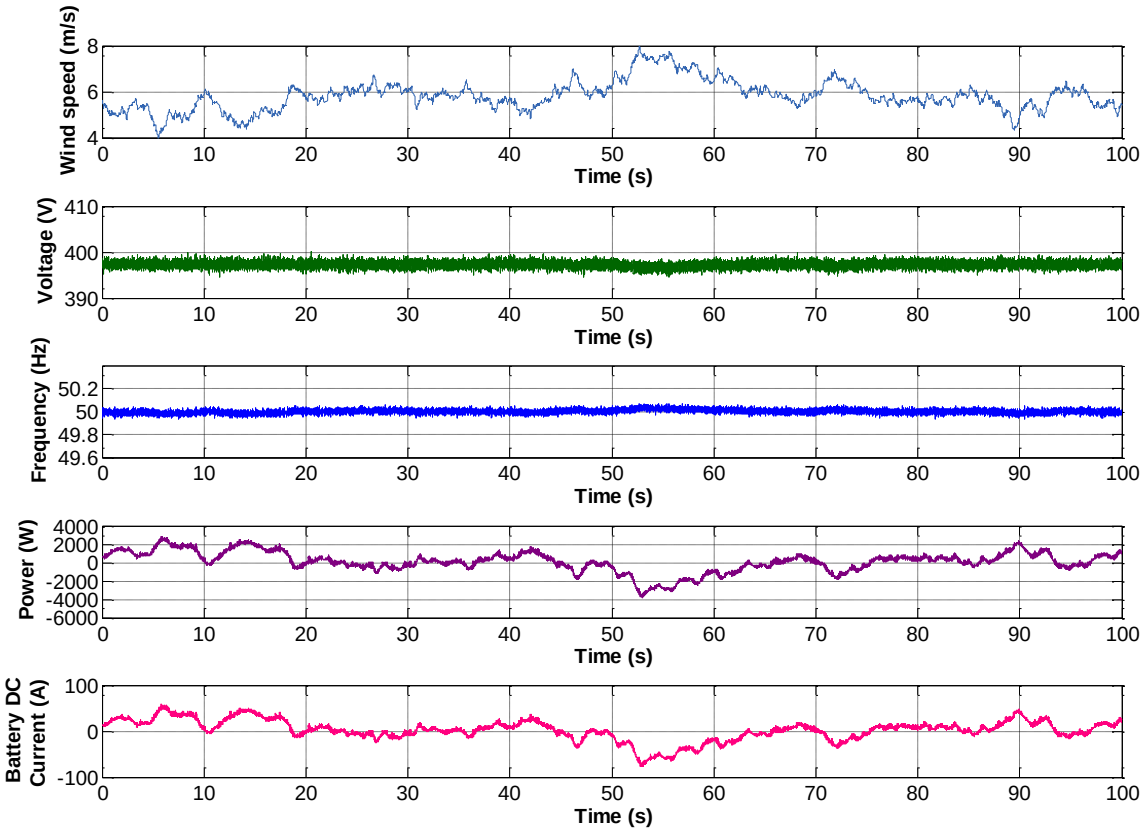

Figure 6.38: Simulated dynamic analysis with turbulent wind - *a)* Wind speed *b)* Grid line-to-line voltage *c)* Grid frequency *d)* Charging and discharging power of the batteries *e)* Battery DC current

6.6 Summary

In conclusion, this chapter has highlighted the steps and considerations whilst developing an off-grid hybrid wind-diesel-battery system in a laboratory environment. The understanding of the characteristics of inverters is crucial in an off-grid design as their sizing and capacity have a relative effect on the overall system efficiency. In addition, the soft-starter performs differently with the power source from the utility grid and the SI inverters. Separate tests should be conducted to identify the appropriate settings for the off-grid case. The steps to adapt an off-the-shelf wind turbine system (controller and generator) were also demonstrated. Appropriate integrated circuit designs can assist in accommodating the use of an off-the-shelf wind turbine controller without having the actual braking system being installed which would otherwise be complicated. Finally, the system's dynamics are studied. Stability of the system with various perturbations (wind speed and load steps)

is investigated and verified. Through appropriate experimental procedures, this chapter has also demonstrated the validation of the simulation of relevant modelling components from Chapter 4.

The realistic situation in the field is not much being compromised if a carefully designed test rig is utilised in the laboratory environment. The next chapter investigates the effects of tower shadow in an off-grid hybrid system with a downwind wind turbine.

Chapter 7 The Tower Shadow Effects on Off-grid Hybrid Systems

In the horizontal axis wind turbine technology, the rotor orientation may be either upwind or downwind of the tower. Following the wind direction, the former has the rotor upwind of the tower, whereas the latter has the rotor downwind of the tower where the rotor rotates through the disturbed air produced by the tower's aerodynamic shadow. Generally, the upwind rotor requires stiffer blades because the wind bends the rotor towards the tower. Due to this reason, the rotor weight is increased which also lead to an increase in load applied to the bearing and the tower. In addition, an active yaw mechanism is essential to keep the rotor facing the wind. On the other hand the centrifugal forces which tend to counteract moments due to thrust reduce the blade root flap bending moments for the downwind configuration [44]. A significant advantage of the downwind wind turbine is that the rotor blades may bend at high wind speeds and therefore reduce the load being passed to the tower [245]. However, the tower produces a wake in the downwind direction, and the blades must go through that wake every revolution. Effects that occur once per revolution are commonly referred as having a frequency of 1P [44]. For a three-bladed wind turbine, this effect occurs at three times per revolution and hence it is being referred as 3P [44]. This pressure fluctuation of airflow is a source of periodic loads which may impose high fatigue load on the blades and propagate the ripple on the electrical power produced. This phenomenon is known as 'tower shadow'. Although this effect is more significant in the downwind configuration, occurrence of tower shadow in the upwind configuration counterpart is apparent.

On an upwind wind turbine, the perturbation of the flow is caused by a redirection of the incoming flow as a result of the presence of the tower. As such, the tower shadow on the upwind turbines is not very severe, and it gives rise to a quasi-steady aerodynamic response on the blades. On a downwind turbine, the rotor passes the highly unsteady airflow as a result of high Reynold number flow over the circular cylinders [246]. The interaction of the blade with the tower wake is therefore

dominated by two effects: firstly, the presence of the tower that creates a velocity deficit, which will cause the blade to experience sudden drop in wind speed when it travels through the wake, and secondly, the blade will occasionally encounter the vortices which are shed from the tower. Figure 7.1 portrays the flow situation for the two types of turbines [246]. From the literature, it was quantified that regardless the number of blades and rotor speed, the peak-to-mean torque variation is about 6% to 12% for the upwind cases and 24% to 38% for the downwind cases [245].

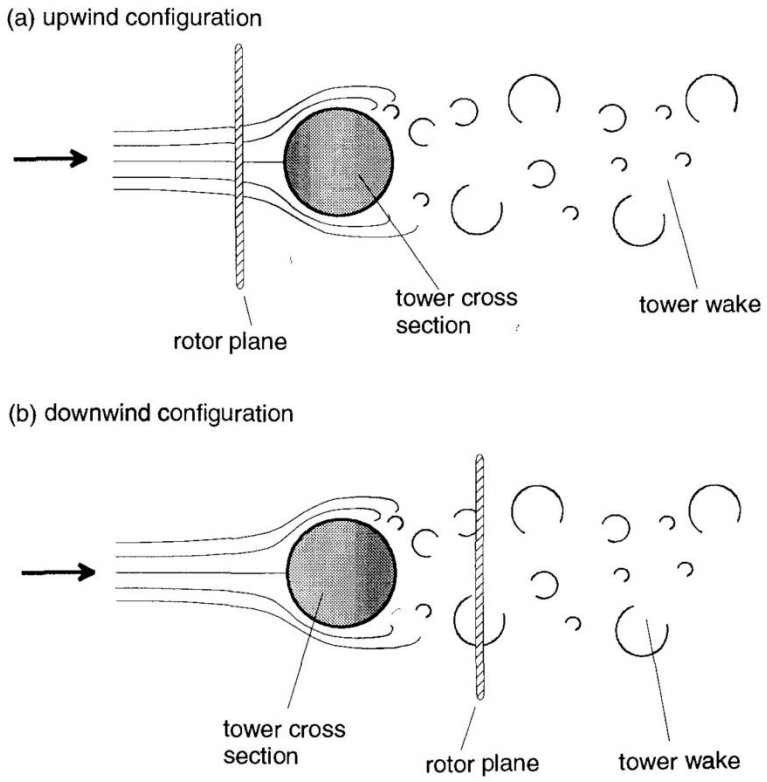

Figure 7.1: Schematic of the flow in the vicinity of the tower on an upwind and downwind wind turbine [247]

In the literature [245], an investigation has been performed on the rotor performance for the upwind and downwind wind turbines, with three-bladed and two-bladed turbines at the same rotor RPM and the same power rating. The general conclusion made was that if the same rotor speed is maintained, changing the number of blades from three to two reduces the rotor total power and torque by around 17% in both upwind and downwind turbines. However, a slightly higher torque is produced from the individual blade in the two-bladed turbines than in the three-bladed turbines. This

is due to more uniform inflow in the two-bladed design [245]. Regardless of the configurations, that is, three-bladed versus two-bladed or upwind versus downwind, the blade hub bending moments are not significantly affected. However, for the same power rating, the higher rotor RPM in the two-bladed design experiences a significant increase of blade hub bending moment of 40% to 70% in upwind and downwind, respectively. In terms of the tower shadow effect, the oscillation occurs more frequently in the three-bladed turbines than in the two-bladed case. The above discussion shows the merits and demerits of the rotor and tower for different wind turbine designs, which may have contradicting features.

In [248], Dale has presented an analytical formulation of the generated aerodynamic torque of a three-bladed upwind wind turbine, including the effects of wind shear and tower shadow. The model developed as an input function of turbine-specific parameters such as the radius, height, tower dimensions, as well as the site parameter, the wind shear exponent. The main advantage of this model is that it is suitable for time-domain simulation. In addition, the model was formulated based on an "equivalent wind speed" which has been developed by Sørensen [249]. Dale's simulation studies have found out that the presence of the wind-shear-induced 3P oscillations is masked by much larger tower-shadow-induced oscillations. It contributed to approximately a 1% dc reduction in average torque [248]. This work was then adopted by [250] to characterise the presence of shaft speed ripples in wind turbines as a result of wind shear and tower shadow. A mathematical conclusion was made from the literature was that the relative amount of shaft speed ripples caused by wind shear and tower shadow is independent of the turbine size [250]. The authors in [251] and [252] have brought forward Dale's equivalent wind speed model in studying the impact of wind shear and tower shadow on wind farms and large scale grid-connected wind power systems. A variable speed wind turbine emulator has been successfully developed with the incorporation of Dale's equivalent wind speed model [253]. Experimental results showed that wind shear and tower shadow were able to be emulated in the laboratory environment [253]. More recently, the author in [254] has integrated Dale's model and a generic yaw error model to investigate the effects of yaw error on wind turbine running characteristics at different stages of operation. Interestingly, the literature has shown in simulation that the yaw errors can

restraint the 3P torque pulsation. Such restraining effect became more severe when the yaw error increases [254]. In literature [255], the mechanical and aerodynamic aspects of the wind turbine system were simulated and the effects of tower shadow, wind shear, yaw error and turbulence on the power quality of a wind-diesel system were shown individually. Others such as [256] and [257] have represented the tower shadow effect as cosine waveform with an empirical coefficient. This approach reduces the modelling complexity but the accuracy and the correctness have yet to be characterised against other analytical models.

In most applications, batteries are clearly operating in either charging or discharging mode. Consequently, these charge-discharge cycles can cause battery wear, which can be characterised by its depth of discharge (DoD) [258]. However, in renewable energy systems, whereby there are generators and loads often operate concurrently, short-term charge-discharge cycling occurs [20]. These battery current fluctuations can also be caused by the renewable sources. In particular, rapid turbulence from the wind and its corresponding wind turbine output power is a non-linear function of the wind speed cubed which can generate considerable power fluctuations into the system at frequencies up to several Hertz [20]. However, battery currents in autonomous renewable energy systems are generally predicted or measured in terms of mean values over an interval of 1 minute or longer. As a result, the short charge-discharge cycles or microcycles are often overlooked. This leads to an underestimation of the battery wear and consequently having an optimistic prediction of battery lifetime. Microcycles are defined as a fast and continuous charge of battery current with a change of direction, typically with a period in the range of seconds [19]. At any particular time interval, the battery current can be broken down into two components, the mean or DC value, and a spectrum of frequencies that cause no net flow of current when integrated over time [20]. For instance, battery current microcycles resulted from the high-frequency noise from the power electronics converters can be easily removed by implementing appropriate filtering circuits. If the AC current is a sufficiently high frequency and low amplitude, it can be supplied or absorbed by the supercapacitors [147]. On the other hand, it was analysed that lower frequency AC components can cause charge-discharge cycling of the active material, resulting increase in battery wear [20] [259].

Experiments in the past have indicated that the battery current microcycles have a detrimental effect on the battery performance [19] [260] [261]. In this work, the focus is given to investigate the effect of unsteady aerodynamic phenomena from the wind turbine on the battery storage system within an off-grid hybrid renewable energy system. Hypothetically, the oscillations generated from the wind shear and the tower shadow effects are believed to have negative consequences on the battery lifetime. As far as the author is aware, other studies on the wind shear and tower shadow effects have not given attention to the off-grid systems. In addition, many have considered the tower shadow modelling of an upwind, three-bladed configuration wind turbine. The downwind tower shadow effect has been modelled and verified with CFD, but yet to be used experimentally.

7.1 Modelling of tower shadow effect in downwind wind turbines

7.1.1 Downwind Configuration – Tubular Tower

The abovementioned studies of the tower shadow effect on power quality are mainly focused on the upwind wind turbine configuration. In this work, the Gaia's 11 kW wind turbine is configured as downwind and therefore, an alternative analytical solution is referenced. Reiso has highlighted several steady wake models which were used to describe the mean velocity deficit for downwind turbines; the Powles', Blevins', Schlichtings' and the jet wake models [262]. In 1983, Powles formulated a tower shadow model for downwind mounted rotors [263]. Through the experiments, he has found out that a cosine squared model predicted the tower shadow fairly accurately in the region of 3 - 6 tower diameters downstream [263]. Blevins' model has some similar features to Powles' model, however, it was originated from fluid dynamics to describe the wake behind a cylinder [264]. The Schlichtings' wake model originates from boundary layer theory with the idea of a frictional surface in the interior of the flow [265]. The Powles, Blevins, Schlichting and jet wake models are simple algebraic equations which often include some flow dependent parameters for the downwind tower shadow, such as the wake width, velocity deficit, drag coefficient or less physical factors. In addition, these models are less computationally demanding compared to the CFD simulations. The jet wake model [266] in particular will be adopted in this work for modelling, simulation and experimental work as it

was developed for time-series simulation. It can be implemented in Simulink and uploaded to dSPACE controller to emulate tower shadow effect in real-time. The jet wake model also has been verified against CFD and the results can be referred in the literature [246, 266].

The jet wake model [266] was established to represent a quasi-steady reference for the time varying CFD wake velocity behind a cylindrical tower. This model is based on the boundary layer solution for a jet flowing into a fluid at rest [266]. The axial and lateral velocity components were developed as:

$$u(x,\eta) = \frac{\sqrt{3}}{2}\sqrt{\frac{K\sigma}{x}}(1 - tanh^2(\eta)) \tag{7.1}$$

$$v(x,\eta) = \frac{\sqrt{3}}{4}\sqrt{\frac{K\sigma}{x}}(2\eta(1 - tanh^2(\eta) - \tanh(\eta)) \tag{7.2}$$

where $\eta = \sigma\frac{y}{x}$, x and y are non-dimensional (with respect to tower radius) Cartesian co-ordinates in the tower cross section, as demonstrated in Figure 7.2.

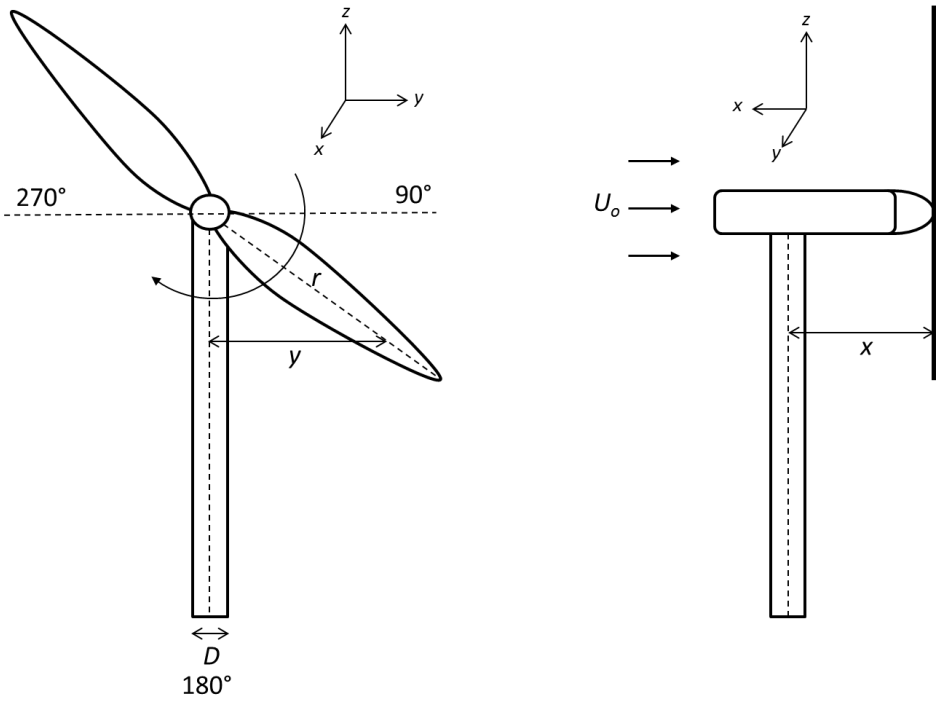

Figure 7.2: Dimensions used in jet wake tower shadow formula

σ is an empirical constant equal to 7.67 [266]. K is the kinematic momentum defined as:

$$K = \frac{J_{\mathrm{m}}}{\rho} \tag{7.3}$$

where:

ρ: Air density (kg/m^3)
J_{m}: momentum deficit behind the tower

The derived J_{m} expression [266] in terms of tower parameters can be written as:

$$J_{\mathrm{m}} = \frac{U_0^2 D}{2}\frac{\rho}{\pi}\left[\frac{1}{8} + \frac{16}{3\pi}\right] C_{\mathrm{d}}^2 \tag{7.4}$$

where:

D: Tower diameter (m)
U_0^2: Free stream velocity (m/s)
C_{d}: Drag coefficient of the tower

In order to ease the implementation of time-series simulation, equation (7.1) can be converted from a function of *y* (lateral distance) to a function of *r* (radial distance) and θ (azimuthal angle) as follows:

$$u(x,r,\theta) = \frac{\sqrt{3}}{2}\sqrt{\frac{K\sigma}{x}}(1 - tanh^2\left(\sigma\frac{r\sin\theta}{x}\right)) \tag{7.5}$$

It should be noted that this equation only valid for 90° ≤ θ ≤ 270° as above the horizontal, the tower shadow effects should be absent.

Using the Gaia wind turbine dimensions which were obtained from [267] and assuming that parameter values as tabulated in Table 7.1, a simulation was performed to compare the tower shadow profiles at different blade elements from the tower midline. The tower shadow profile was evaluated at radii 1 m from the hub, all the way to the tip of the blade (6.5 m) with an increment distance of 0.5 m, as shown in Figure 7.3. It is observed that the blade elements closer to the hub experienced tower shadow for a longer period. However, the wind deficit was the same when the blade was pointing downward (180°), which corresponds to about 27% drop in magnitude. For all other wind speeds, a drop of 27% will be observed when evaluating the tower shadow for this turbine at an azimuthal angle of 180°. A similar tower shadow profile was observed for the upwind counterpart [248]. However, the wind deficit is 8% for the upwind case when the azimuthal angle is 180°. The wind deficit percentage acquired from the downwind wind turbine using a jet wake model falls within the range of results obtained from [245] which were performed using a high-fidelity CFD analysis, further validated the results from this work.

Parameters	***Values***
Undisturbed wind speed, U_0	8 m/s
Blade radius, R	6.5 m
Hub height	18 m
Tower type	Tubular
Air density, ρ (kg/m^3)	1.225
Tower drag coefficient, C_d	0.4
Tower diameter, D	0.8 m
Distance from the blade to tower midline, x	3.0 m
Sigma, σ	7.67

Table 7.1: Gaia wind turbine parameters for tower shadow computations

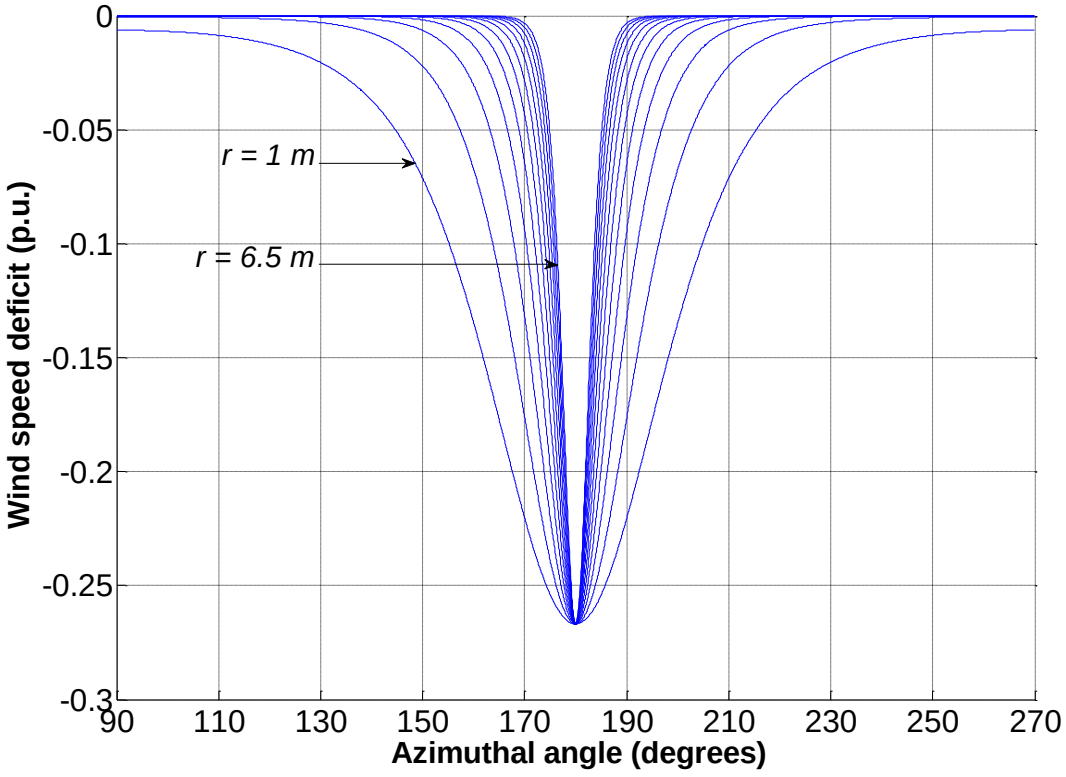

Figure 7.3: Comparison of downwind tower shadow profiles at different radii from the tower midline

Figure 7.4 shows the tower shadow profiles with different longitudinal distances between the tower and the blades. As expected, the wind speed deficit is less pronounced when the blades are further away (larger x) from the tower. This is due to the larger allowable distance for the airflow to accelerate and increases its velocity after being blocked by the tower. On the other hand, if the rotor plane was closer to the tower, the influence of the tower shadow effect would be more severe, as demonstrated in Figure 7.4. In this case, the tower clearance is varied from 1 m to 10 m. It is noticed that the tower shadow effect reduced algebraically whilst the tower clearance was increased linearly. The tower clearance increment from 1 m to 2 m was more effective in reducing the tower shadow effect than increasing the tower clearance from 9 m to 10 m. Since a much higher tower clearance was needed to reduce the tower shadow effect, it is often not a viable solution as the additional cost will be incurred. This is due to the use of a stronger material for the tower construction to support a higher moment or loading as a result of the higher tower clearance. Literature [246] has investigated the influence of tower clearance on tower shadow effects, for the standard downwind configuration. The author has found out that an increase in tower distance from 10 m to 13.44 m resulted in a 4% decrease in tower shadow. The small decrease indicated that it is not feasible to reduce tower shadow effects with such approach [246]. Another way of reducing the tower shadow effect can be achieved by reducing the drag coefficient of the tower by using a different built material. However, this will incur additional cost and an economic analysis will be required to justify its advantages. Furthermore, the unsteady vortex shedding can be reduced by streamlining the body into an aerofoil shape in order to make a downwind concept viable [246]. It is beyond of the scope of this project to perform these studies.

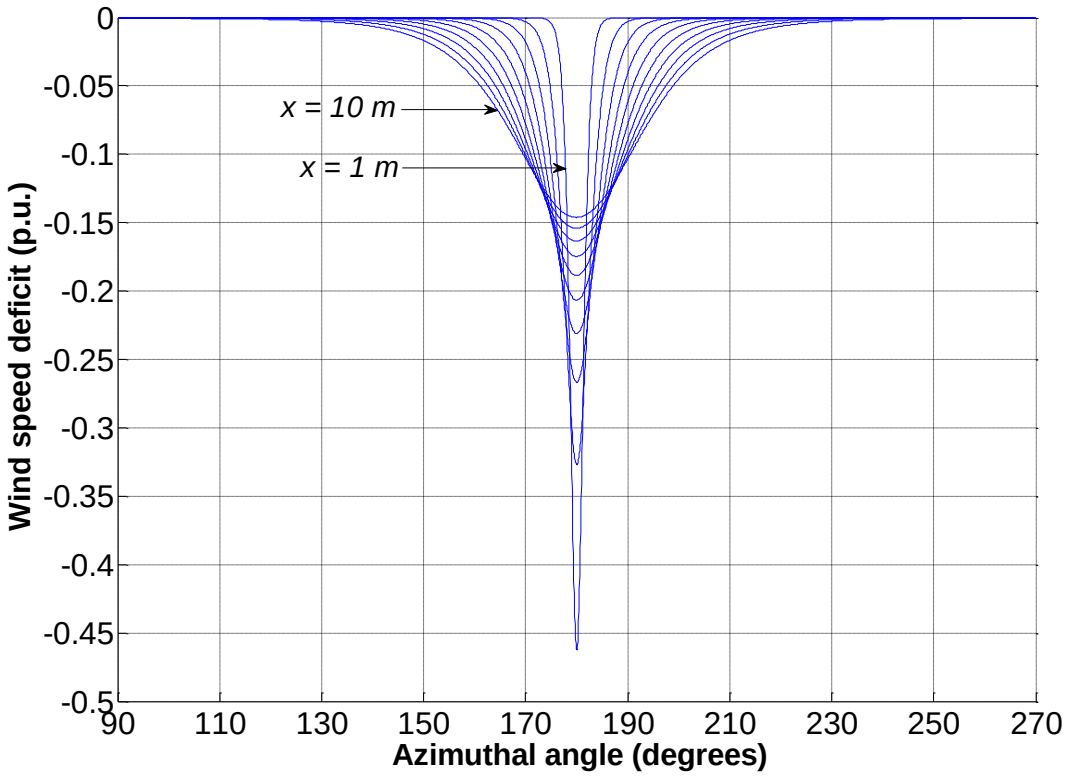

Figure 7.4: Comparison of tower shadow profiles with different distances between the tower and the blades

7.1.2 Downwind Configuration – Four-leg Tower

An alternative tower configuration for small wind turbines is the four leg tower (also known as lattice tower), connected by diagonal beams. An illustration of the Gaia wind turbine with this tower configuration is shown Figure 7.5. In 2D and for simplification purposes, only the four main legs were considered in this work, although the diagonal beams are likely to contribute to the wind deficit and cause unsteadiness of the flow [246]. In addition, each leg was assumed to be cylindrical in shape. The authors in [246] have performed the CFD simulations on the axial wind velocity for the tubular and four-leg tower configurations. With these assumptions, the jet wake model described above was programmed in Simulink and it was used to estimate the tower shadow profile of the four-leg tower. For illustration purposes, Figure 7.6 shows the extracted CFD snapshots [246] of the predicted wind flow patterns behind the towers.

Figure 7.5: Gaia wind turbine with lattice tower configuration

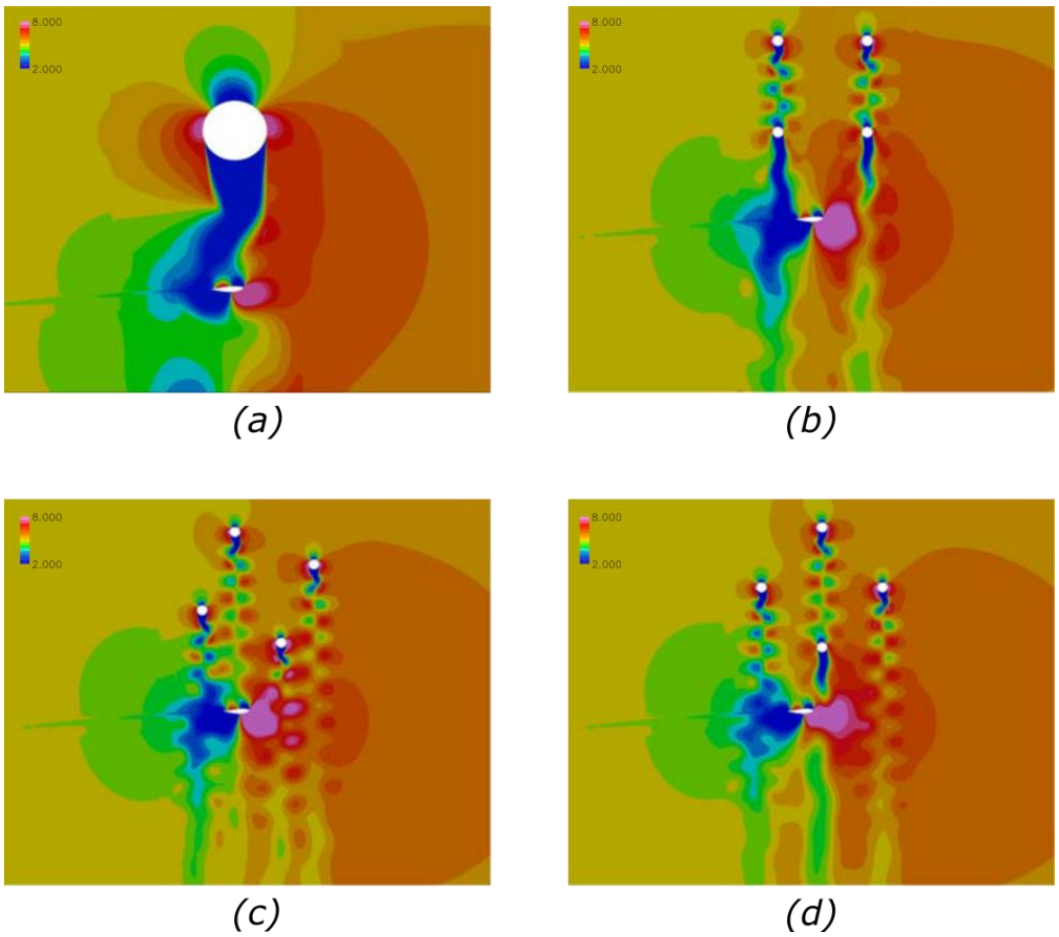

Figure 7.6: CFD snapshot of axial wind velocity for a) tubular tower b) four-leg 0° orientation c) four-leg 22.5° orientation d) four-leg 45° orientation to the tower at 80% radius blade section [246]

As the Gaia downwind wind turbine simply utilises free-yaw mechanism, it is free to move around the tower according to the wind directions. As a result, different tower shadow profiles will be experienced due to different yaw angles relative to the rotor plane. In this work, three orientations of the tower with respect to the rotor plane were considered. These were 0°, 22.5°and 45°, respectively. Figure 7.7 shows the top view of the wind turbine with three different orientations. The estimated Gaia wind turbine lattice tower dimension is shown in Figure 7.7 (a). The distance between each leg was approximated as 1.2 m. Each leg was represented as a cylindrical shape with a diameter of 0.2 m. For the sake of direct comparing with the tubular tower case described above, the distance between the lattice tower centre and the rotor plane was set to 3 m. Figure 7.7 (b) and (c) show the tower orientations of 22.5°and 45°, respectively.

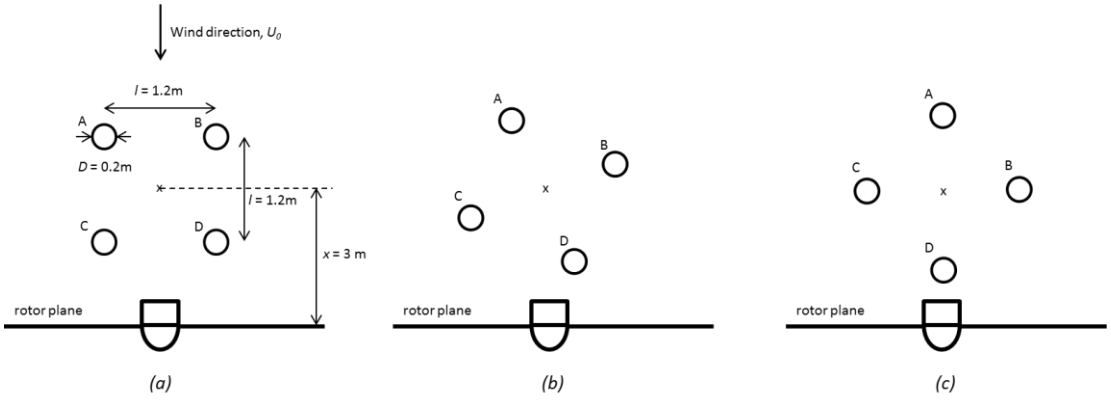

Figure 7.7: Four-leg configurations with *a)* 0° orientation *b)* 22.5° orientation and *c)* 45° orientation relative to the rotor plane, respectively.

Using the illustrated dimensions in Figure 7.7 (a), the dimensions for the case of 22.5° and 45° orientations can be derived easily through the Pythagorean Theorems. Then, the jet wake model was utilised to estimate the wind deficit resulted from each leg, at 70% radius blade section. At 70% radius of the blade section, half of the rotor area was outside this radius and half was inside. Therefore, the velocity profile was represented. The simulated tower shadow profiles for these orientations are shown in Figure 7.8. Intuitively, the analytically formulated tower shadow profiles captured the qualitative behaviour for all the three tower orientations. The tubular tower

shadow profile is shown to serve as magnitude comparison with the four-leg orientations.

The 0° lattice configuration (Figure 7.8 (b)) produced a narrower width of wind deficits than the tubular configuration's due to the smaller leg diameter of the former. At 0° lattice orientation, the two legs in upwind (A & B) were positioned in-line with the other two legs (C&D), respectively. The wind speed deficit due to the front leg was further reduced by the second leg. Therefore, an accumulated of wind speed deficit was experienced when the blade passes these legs. Two wind speed dips of the tower shadow profile were experienced by the blade (Figure 7.8 (b)) as it rotated from position 90° to 270° (refer to Figure 7.2). At 180°, the wind speed experienced by the blade recovered to the maximum value before it was moving towards to the next leg. Similar explanations can be used for the 22.5° and 45° orientations. The maximum wind speed deficit for these orientations occurred when the blade passes through leg D (Figure 7.7 (b) & (c)). This can be attributed to the shortest distance between leg D and the rotor plane compared to other legs. In addition, at 45° orientation, two legs (A & D) are positioned in-line with the direction of the wind. Therefore, an accumulated of wind speed deficit was experienced when the blade passes these legs at 180°. Nevertheless, it is noted that only 2 peaks occurred for the 22.5° orientation. This may be attributed to the small horizontal distance between leg B and leg D, which resulting insufficient time for the wind speed to recover before the turbine blade approaches leg B from leg D. Similar explanation can be applied when the blade moves from leg A to leg C. Intuitively the horizontal distance between leg D and leg A is greater than the horizontal distance BD and AC, thus allowing additional time for the wind speed to recover.

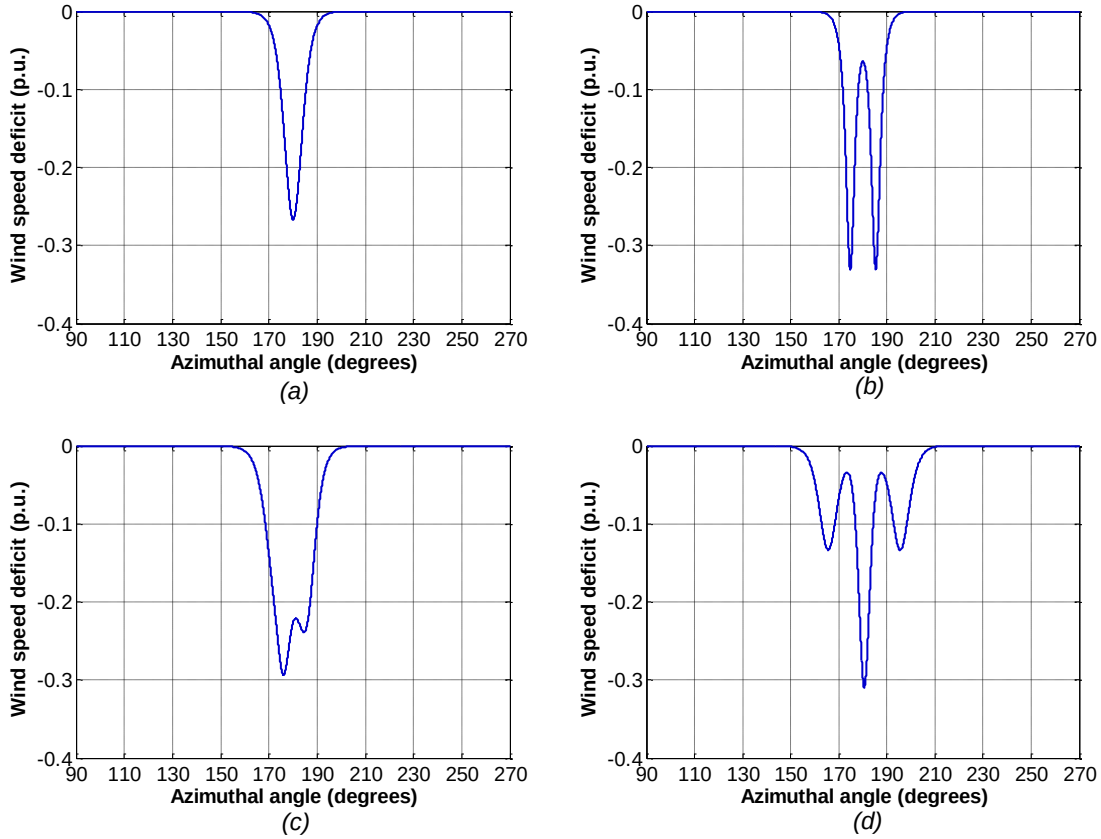

Figure 7.8: Analytically derived downwind tower shadow profiles with *l* = 1.2 m for *a)* tubular tower *b)* four-leg 0° orientation *c)* four-leg 22.5° orientation *d)* four-leg 45° orientation to the tower

The corresponding FFT analysis as shown in Figure 7.9 further revealed existence of the harmonics contents within these tower shadow profiles. The FFT was performed with the simulated tower shadow profiles for 10 s. Since the rotational speed of the two-bladed wind turbine was approximately 55.6 rpm, the tower shadow profile was generated at a rate of about 1.85 Hz. Therefore, the first peak of each plot corresponds to the fundamental frequency of the tower shadow profile, which was 1.85 Hz. For the case of tubular tower (Figure 7.9 (a)), the harmonics decreased algebraically in magnitude. These plots further indicated that the representation of tower shadow using a sinusoidal waveform in the past [256, 257] was oversimplified. For the case of lattice tower configuration, the harmonics profile was dependent on its orientation against the wind direction. For the 0° and 45° orientations, the high frequency harmonics were more apparent. This can also be reflected from the time-

series profile from Figure 7.8. It can be visualised that the lattice configuration generates a more sophisticated of tower shadow profile at varying degree of orientations, compared to its tubular counterpart. Therefore, it is the interest of this research to compare and contrast the effect of these tower shadow profiles on the batteries lifetime as a result of microcycles. It is important to note that the model considers two blades of which only one at a time is affected by the tower shadow.

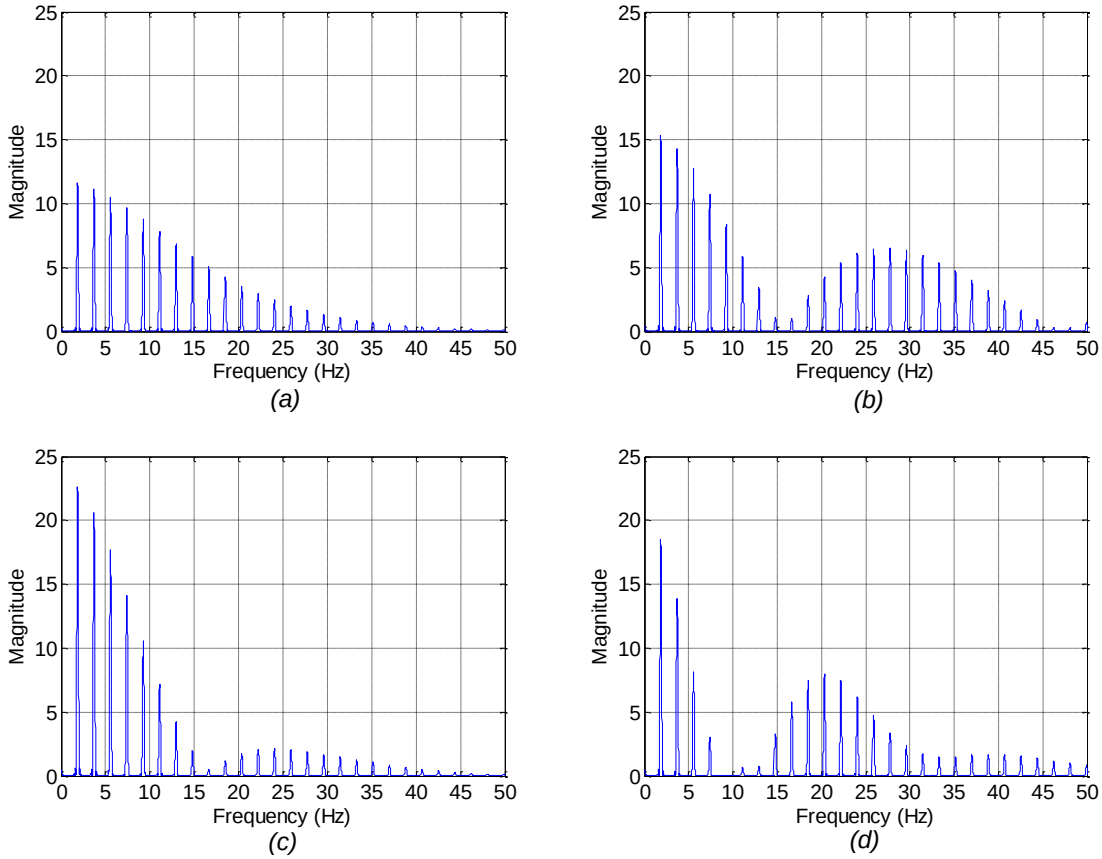

Figure 7.9: FFT analysis on the tower shadow profile of *a)* tubular tower *b)* four-leg 0° orientation *c)* four-leg 22.5° orientation *d)* four-leg 45° orientation

7.2 Characterisation of Tower Shadow Profile Using a Wind Turbine Emulator

This section describes the characteristics and limitations of the tower shadow profile generated from the wind turbine emulator described in the previous chapter. As the induction machine was used to emulate the wind speed experienced by the blades of the wind turbine, it was required to investigate the capability of the machine in

responding the pulses as a result tower shadows. As highlighted earlier, for the case of the Gaia wind turbine, the tubular tower can cause a wind speed deficit of about 27%. In addition, the wind speed deficit took a short period of time to recover to the nominal wind speed level, usually in the order of hundreds of milliseconds. Figure 7.10 shows the block diagram with the designated measuring points throughout the test rig during the characterisation process.

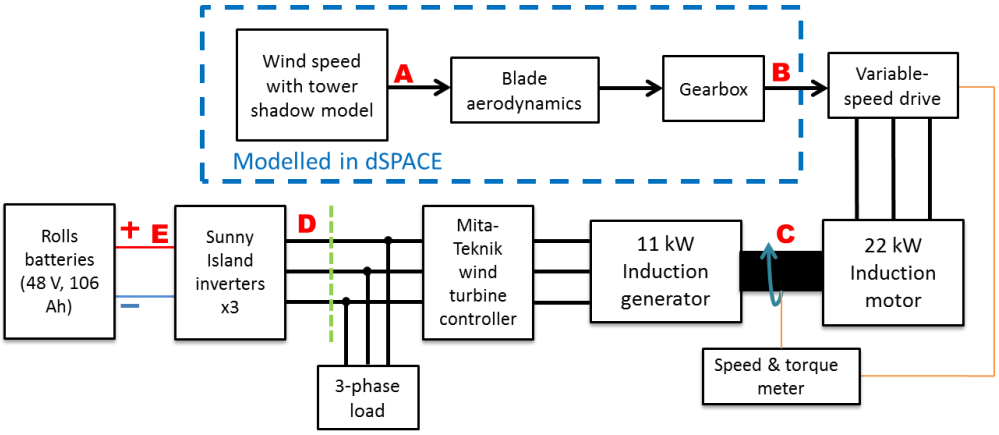

Figure 7.10: Block diagram of wind turbine emulator setup with the highlighted measurement points

The test was carried out with an input wind speed of 8 m/s, coupled with the tower shadow profile which is shown in Figure 7.11 (a). In order to avoid high charging current on the batteries, a three-phase load of 7 kW was switched-on to absorb the power generated from the 11 kW induction machine. The torque demand for the variable speed drive corresponding to this wind speed profile is depicted in Figure 7.11 (b). The 22 kW induction machine generated a torque and a speed profile at the shaft connecting to the generator, as shown in Figure 7.11 (c) and (d), respectively. The rotational speed sampling rate was limited by the speed & torque meter, which in this case it was 0.1 s. It is noticed that an oscillation occurred on the torque profile during the transition to steady-state. This recovery period took place for about 1.5 s. It is an undesirable scenario as the torque fluctuations have exceeded the machine's full-load torque. It is known that when an induction machine operates beyond its full-load region, the leakage flux becomes dominant and this induces high reactive power. As a result, the machine would be operated at low power factor. Figure 7.11 (e) shows the measured power at point D of Figure 7.10. This power corresponds to the

difference between the generated power from the 11 kW machine and the constant load demand. However, the focus here was to analyse the power output profile. As expected, the oscillation from the shaft was propagated to the power output produced by the generator. The high magnitude power oscillations can cause additional thermal stress on the windings and iron core laminations of the machine. Eventually, the machine may fail. Finally, the batteries current profile (Figure 7.11(f)), which was measured at point E, possessed the similar transients compared to the power output of the generator. High power losses and thermal stresses were imposed on batteries due to the existence of internal resistances.

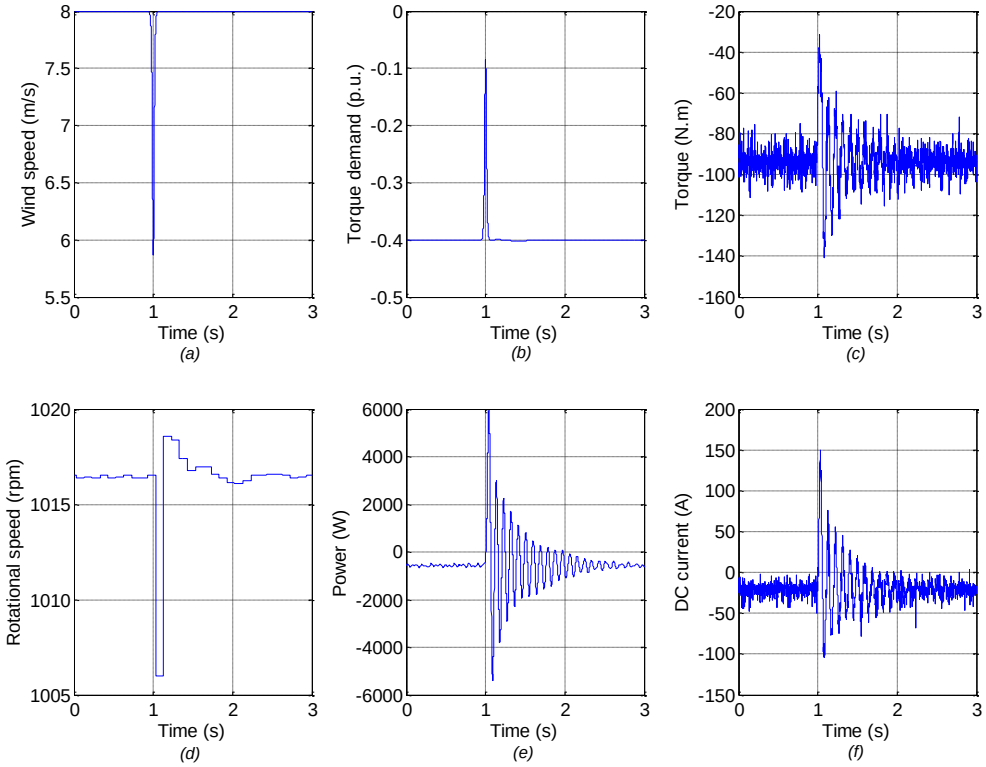

Figure 7.11: *a)* Point A - simulated wind speed experienced by the blade with tower shadow profile *b)* Point B – simulated torque demand on the variable speed drive. Measurement results at various stages of the test rig *c)* Point C – measured torque at the shaft *d)* Point C – measured rotational speed at the shaft *e)* Point D – measured power at the terminals of the induction generator *f)* Point E – batteries DC current flow

A FFT analysis was performed (shown in Figure 7.12) on the power output (Figure 7.11(e)) in order to analyse the frequency contents of the oscillation. The peak

magnitude of the oscillation was identified to be located at just below 11 Hz. Analysing the tubular tower shadow FFT profile (Figure 7.9(a)), it was noticed that the fifth harmonic of the fundamental frequency coincides with the oscillation frequency of the output power. At this point, it can be hypothetically concluded that the induction motor drive system was highly responsive to this frequency input.

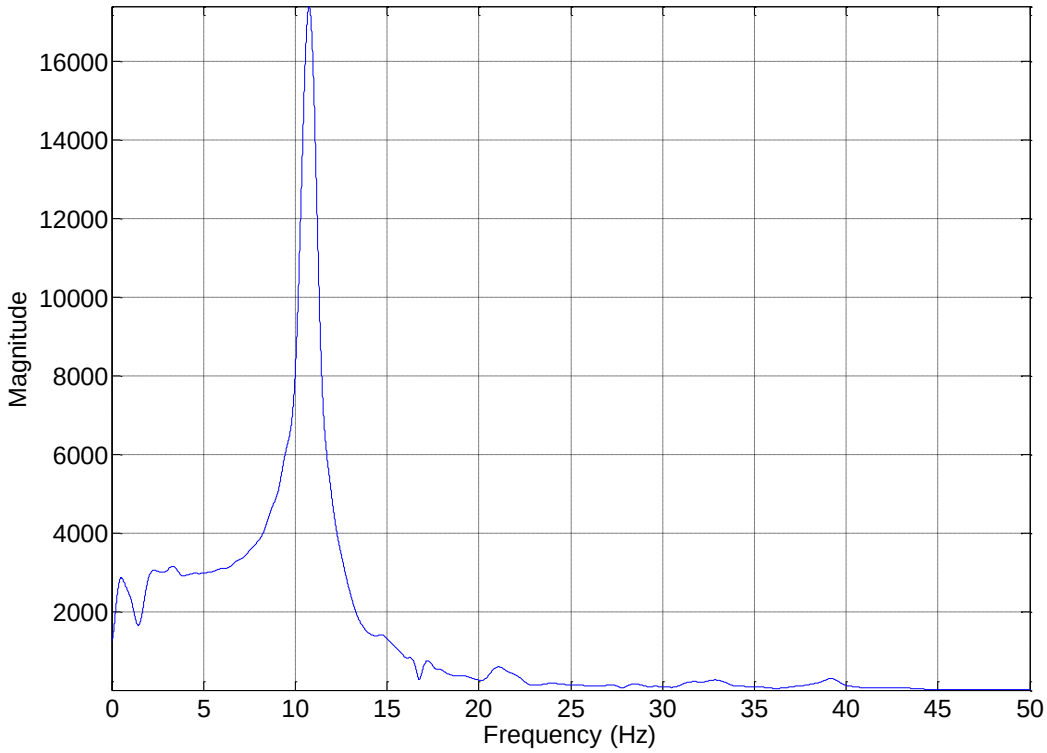

Figure 7.12: FFT analysis of the emulated tower shadow power transient (Figure 7.11(e))

A simplified test on the system frequency response was designed and carried in order to verify the hypothesis mentioned above. The wind speed was formulated as a sinusoidal waveform with a frequency of 7 Hz and a mean wind speed of 5 m/s. The peak-to-peak of this sinusoidal waveform was 1 m/s. Subsequently, the test was repeated with the frequencies of 9 Hz, 11 Hz, 13 Hz, 15 Hz and 20 Hz. The measured shaft rotational speed, torque and power output from the 11 kW generator for all these tests are shown in Figure 7.13. From Figure 7.13, it can be observed that the measured shaft torque was experiencing sustained oscillations, with its magnitude increasing as the frequency is increased from 7 Hz to 9 Hz. Another test was

conducted with an input frequency of 10 Hz and the results are shown in Figure 7.14. At this frequency, the induction machine drive system became unstable at approximately 7.8 second. The rotational speed accelerated and the system tripped at about 8.5 second. The load demand (constant power) was fully supplied by the grid-forming inverter system as soon as the generator became unstable (acceleration began). However, the oscillation decreased (as shown in Figure 7.13) with the input frequency increases. This can be observed when the input frequency was set to 11 Hz, 13 Hz, 15 Hz and 20 Hz, respectively.

The stability problem in induction motor drive system has been studied in the past [268, 269]. Authors in [268, 269] have highlighted that the stability problem can be viewed from the interactions between the electric transients and the rotor dynamics. It was mentioned that a stability problem could never occur if the electromagnetic torque is precisely controlled as to be kept, without delay, at the desired value required from the load side. However, this condition can only be achieved by an ideal induction motor which has zero resistances and leakage inductances in both stator and rotor windings. Therefore, the oscillatory behaviour of the system can be directly linked to the existence of the wind resistances and leakage inductances. In addition, the unstable phenomena (also known as hunting phenomena) can be associated with the variation of slip frequency. This undesirable rotor motion also leads to a phase angle variation of the magnetic flux in the air-gap. Even under a constant rotor speed circumstance, the abrupt variation of the stator voltage or current not accompanied by right control of the air-gap flux can cause oscillation [268]. Literature [268] has also simulated a scenario where the fluctuations of rotor speed can cause nonlinear and parametric oscillation within the system. When the real part of a dominant eigenvalue becomes positive, the system will be in an unstable state, as demonstrated by the case of 10 Hz input frequency in this work. Moving beyond 11 Hz cases, the decay in oscillation magnitudes can be attributed to the slower response time of the machine due to its inertia. The machine can be seen as a “low pass filter”, therefore has a little reaction against the high-frequency inputs.

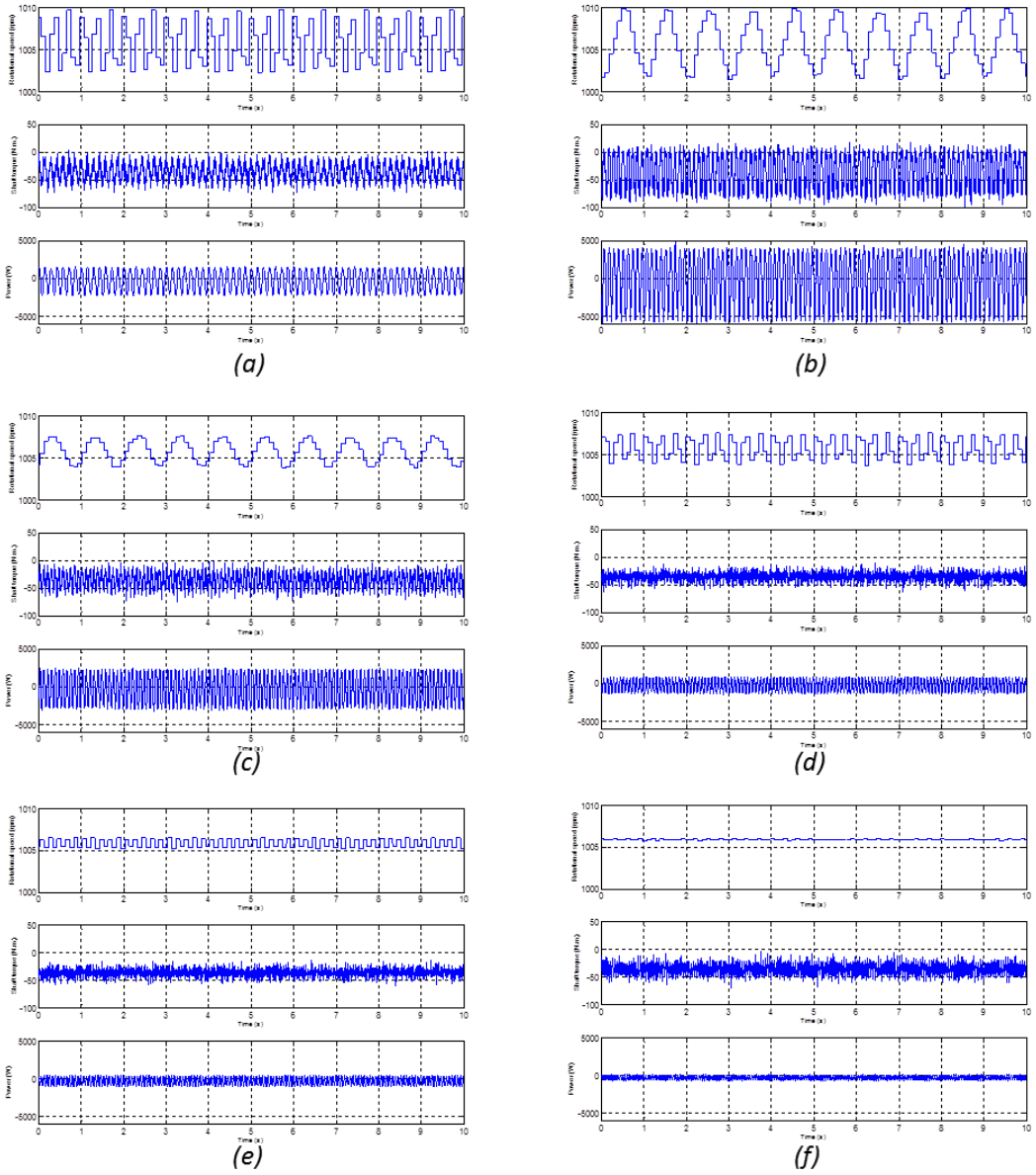

Figure 7.13: Measurement of the shaft rotational speed, torque and the power difference between the generator and the load with *a)* 7 Hz *b)* 9 Hz *c)* 11 Hz *d)* 13 Hz *e)* 15 Hz and *f)* 20 Hz of wind speed input

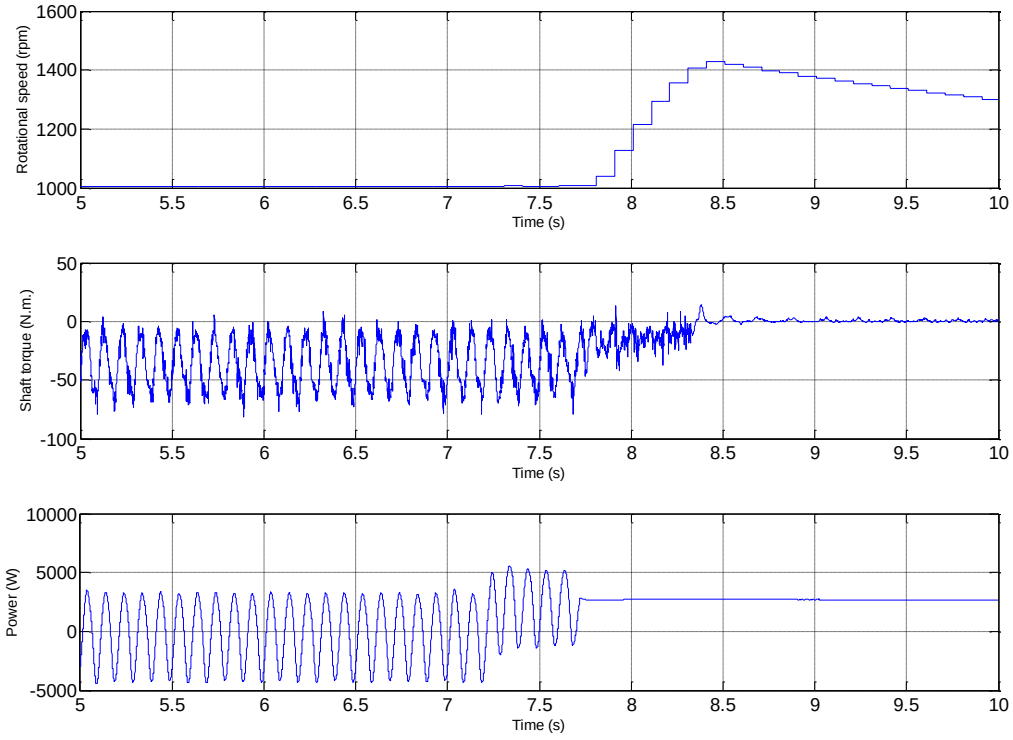

Figure 7.14: Measurement of the shaft rotational speed, torque and the power difference between the generator and the load with a 10 Hz of wind speed input. Unstable operation began at approximately 7.7 second

In order to further understand the test rig's characteristics in respond to the modelled tower shadow profiles, two sensitivity analyses have been carried out. The impact of tower shadow's widths and its magnitude on the oscillations were studied respectively. Since the purpose of the test was to observe the generator output power profile given an input tower shadow profile, only the wind speed with tower shadow profile and its corresponding output power are shown in the following results.

The results of different tower shadow widths with their corresponding oscillating power output are shown in Figure 7.15. By taking the tower shadow experienced at different blade section, various widths for the same magnitude can be obtained. As expected, the tower shadow profile experienced by the blade section closer to the hub has a wider width compared to the sections near the tip. From the measured output power profiles, it can be stated that tower shadow profile with wider width

contributes to a higher magnitude of oscillation compared to the smaller width counterpart, despite having the same peak magnitude of tower shadow. However, it can be seen that the oscillation frequency is the same for all cases and they decayed at a same rate.

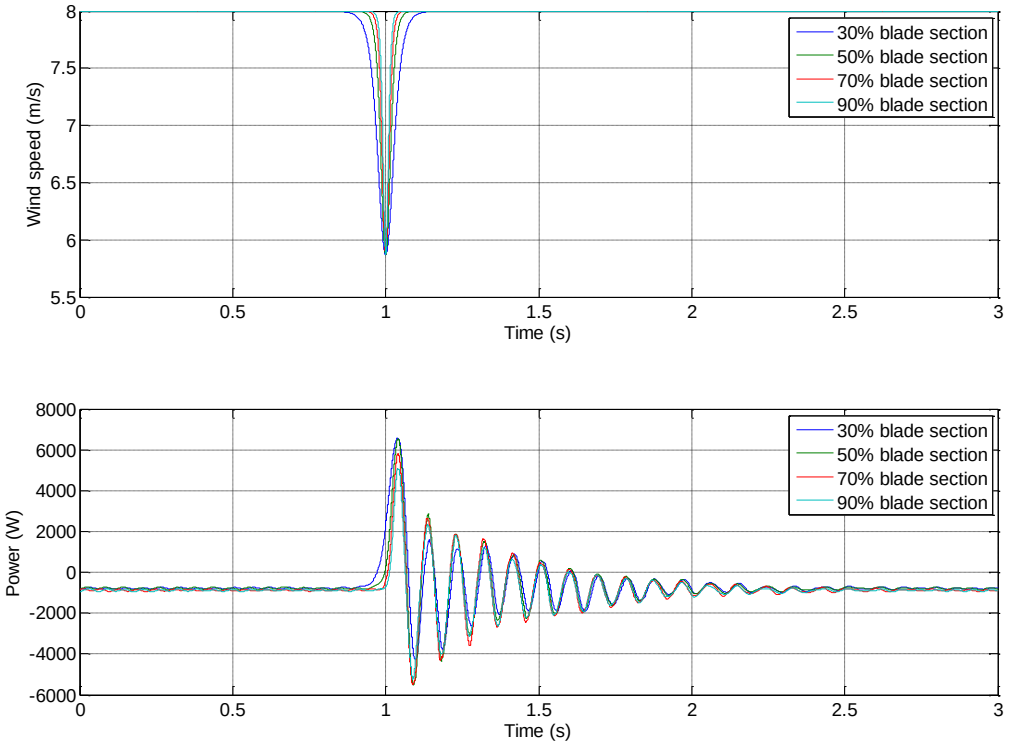

Figure 7.15: Sensitivity analysis on the tower shadow widths against the power oscillations

Next, the power oscillations as a result of different tower shadow magnitudes are shown in Figure 7.16. In this case, the tower shadow profiles were generated by varying the distance between the centre of the tower and the rotor plane, *x*. Note that the width of the profile changes as the distance between the tower and the rotor plane is varied. Interestingly, the highest magnitude of tower shadow (smallest width) did not produce the highest oscillation in terms of magnitude. This can be attributed to the very small width of the tower shadow profile, where the energy of the high-frequency components was "not seen" by the induction motor drive system. When the distance, *x* moved from 3 m to 5 m, the tower shadow magnitude was reduced and this was correctly being reflected at the power output of the generator. Therefore,

this test has highlighted the limitation of the induction machine drive system in responding to the tower shadow profiles which have relatively small widths.

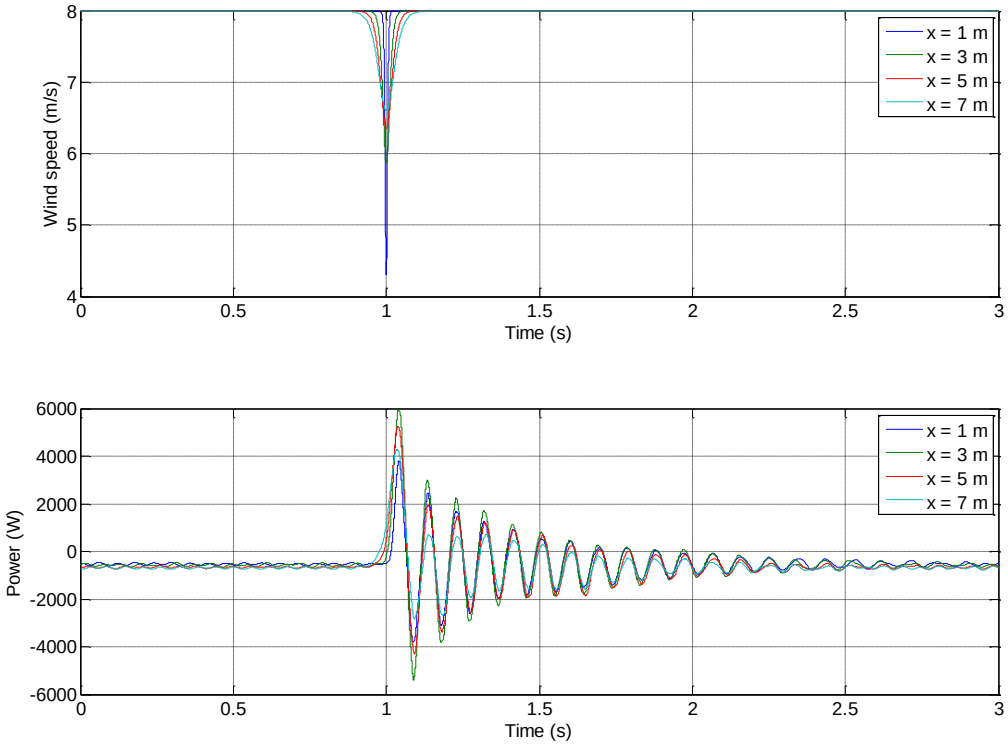

Figure 7.16: Sensitivity analysis on the tower shadow magnitudes against the power oscillations

From the experiments described above, it can be concluded that the tower shadow profiles from a wind turbine can be emulated, whilst being aware that the abovementioned limitations do exists when analysing the results in the following sections.

7.3 The Effect of Tower Shadow on Battery Lifetime

This section investigates the tower shadow effect of the downwind wind turbine on the batteries lifetime in off-grid systems. The following subsections are dedicated to discussing the experimental measurement results of the emulated tower shadow using the described test rig and the process of estimating the batteries lifetime reduction as a consequence of these tower shadow effects. Specifically, the power oscillation from the emulated tower shadow and its contribution to the charging and

discharging microcycles on the batteries profiles are discussed. Comparisons were carried out between the tubular tower and the lattice tower which was positioned at different orientations. Then, a sensitivity analysis on battery lifetime is conducted through various load scenarios. Finally, the effect of lattice tower dimension (which directly influence the tower shadow profile) on the batteries lifetime is studied.

7.3.1 Experimental Results of Tower Shadow Effect

Utilising the analytically derived tubular and lattice tower shadow profiles in Figure 7.8 and feeding them as the wind inputs to the test rig, the power outputs which took into consideration of tower shadow effect were produced. Typically, the battery microcycles throughput would be the largest when the level of power generation within the system is approximately equal to the load. In this experiment, the wind speed of the system was set as 8 m/s, which corresponded to a power generation of about 8 kW. In this case, the load demand was set to match this figure as close as possible so that the optimum number of microcycles can be computed for this scenario. Therefore, the load demand was set to be 8 kW. Any small energy excess or deficit was balanced by the batteries. For comparison purposes, the measurement results without including the tower shadow effect is shown in Figure 7.17. It can be observed that the measured torque at the shaft (Figure 7.17 (a)) was rather constant, with minimal torque transient at the shaft (Figure 7.17 (b)). Within the measurement period, the batteries DC current waveform did not have a zero-crossing, which is indicated in Figure 7.17 (c). Thus, the microcycle throughput is zero for this case. A closer inspection on the waveform revealed that the DC current was slightly shifted towards negative values. This negative sign convention indicates the batteries were undergoing charging process.

Same parameters were acquired for the case of the tubular tower, lattice tower with 0° degree orientation, lattice tower with 22.5° degree orientation and lattice tower with 45° degree orientation which is illustrated in Figure 7.18 to Figure 7.21, respectively. Looking at DC current plots of these figures, it can be noticed that the batteries in all scenarios were subjected to rapid charge-discharge reversals. In addition, the oscillation after each tower shadow effect was clearly demonstrated within the period of measurement, except for the case of lattice tower with 45° degree orientation. This

issue has been previously discussed and it can be attributed to the unstable operation of the generator, due to the presence of resonant frequency of approximately 10 Hz. The analytically derived tower shadow waveform of lattice tower with 45° degree orientation generated low amplitude of harmonics at around 10 Hz, thus the oscillation was not apparent in this particular scenario.

In order to have a fair comparison while computing the battery lifetime reduction due to the effect of tower shadow, the contribution of microcycles from the 10 Hz oscillation was subtracted from the equation. These include the tubular tower and lattice 0° and 22.5° orientations. The microcycles contributed by the 10 Hz oscillation was characterised separately and is shown in Figure 7.22. Using this approach, the battery lifetime caused only by the tower shadow effect can be computed relatively more accurate.

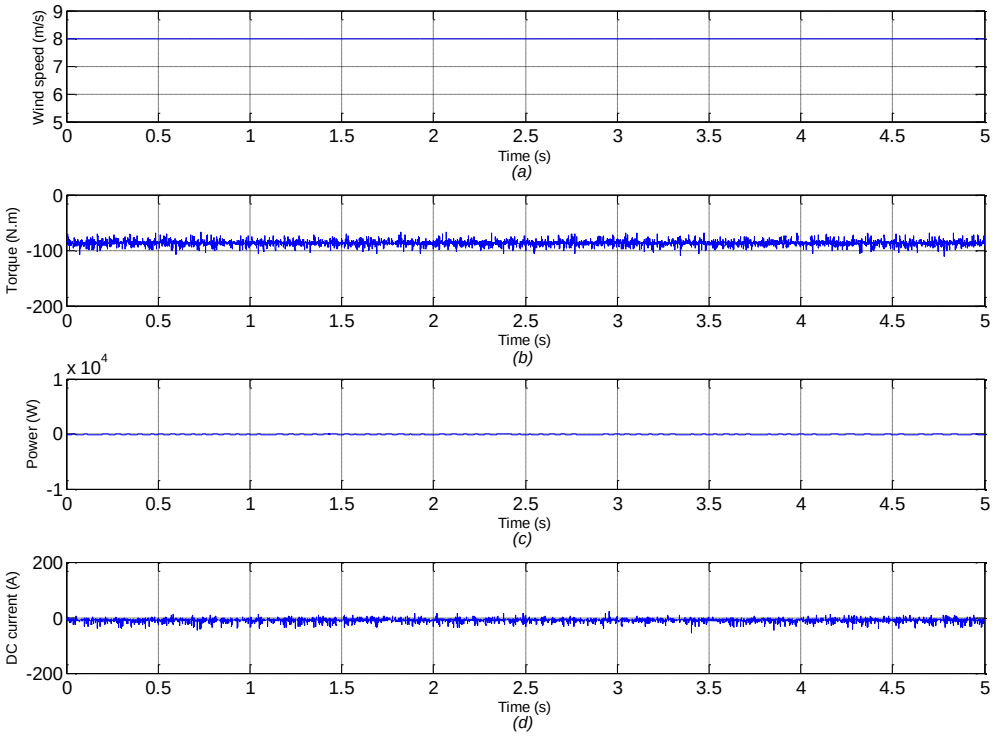

Figure 7.17: Measurement results without tower shadow effect *(a)* fixed wind speed (Point A) experienced by the blades *(b)* torque at the shaft (Point C) *(c)* power difference between the generator and the load (Point D) *(d)* batteries DC current (Point E)

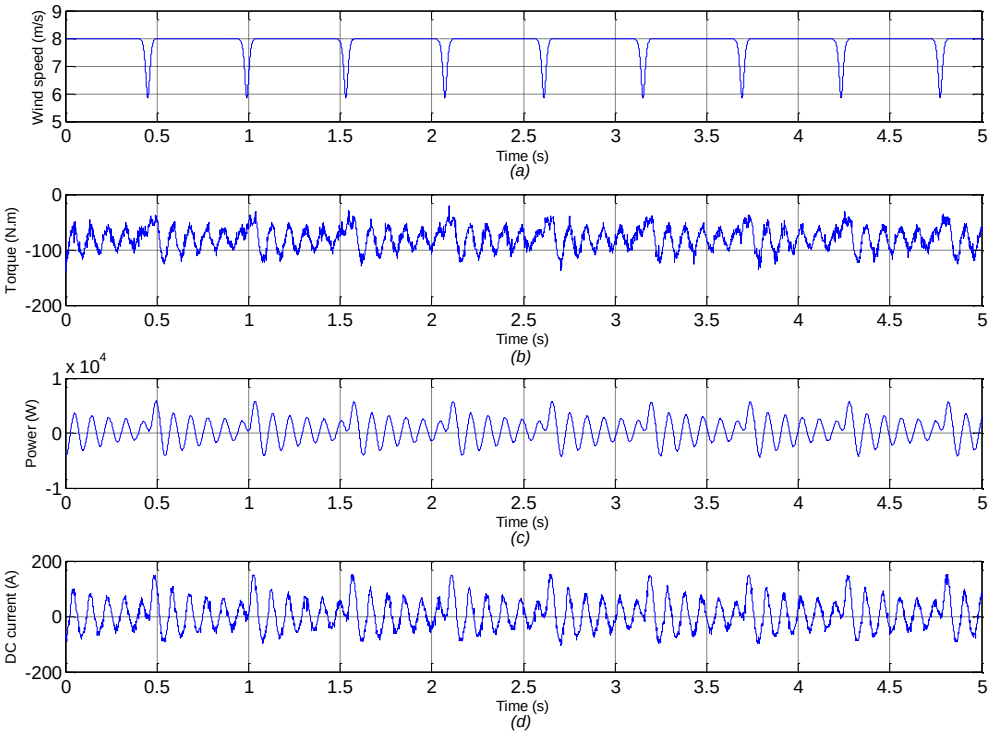

Figure 7.18: Measurement results with tubular tower shadow effect *(a)* modelled wind speed (Point A) experienced by the blades *(b)* torque at the shaft (Point C) *(c)* power difference between the generator and the load (Point D) *(d)* batteries DC current (Point E)

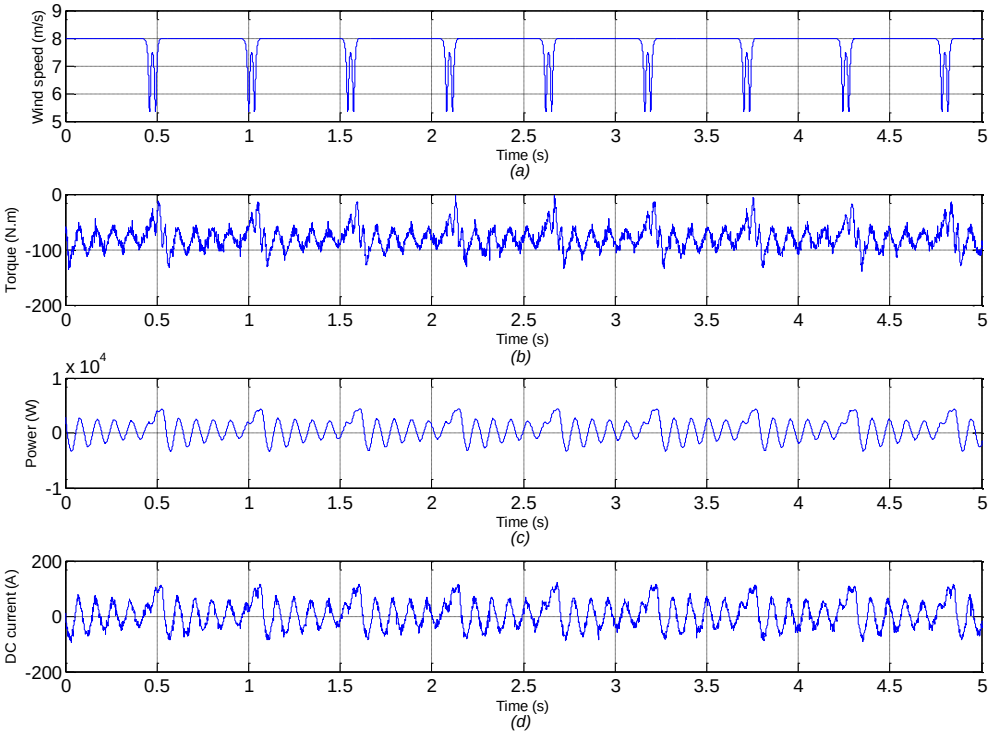

Figure 7.19: Measurement results with lattice 0° orientation tower shadow effect *(a)* modelled wind speed (Point A) experienced by the blades *(b)* torque at the shaft (Point C) *(c)* power difference between the generator and the load (Point D) *(d)* batteries DC current (Point E)

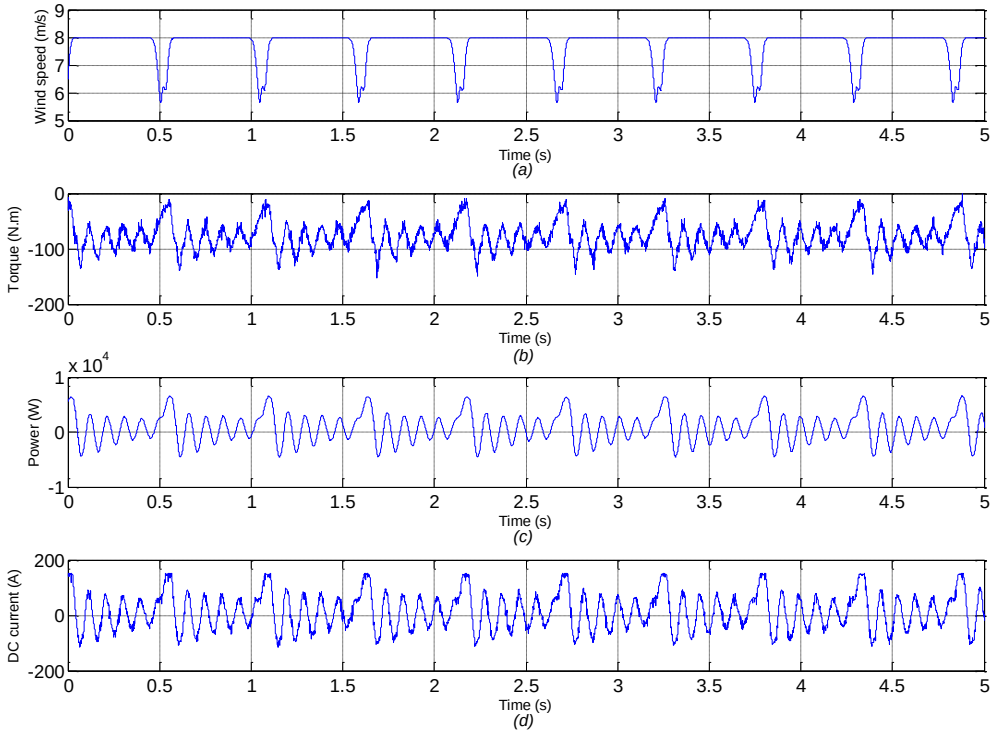

Figure 7.20: Measurement results with lattice 22.5° orientation tower shadow effect *(a)* modelled wind speed (Point A) experienced by the blades *(b)* torque at the shaft (Point C) *(c)* power difference between the generator and the load (Point D) *(d)* batteries DC current (Point E)

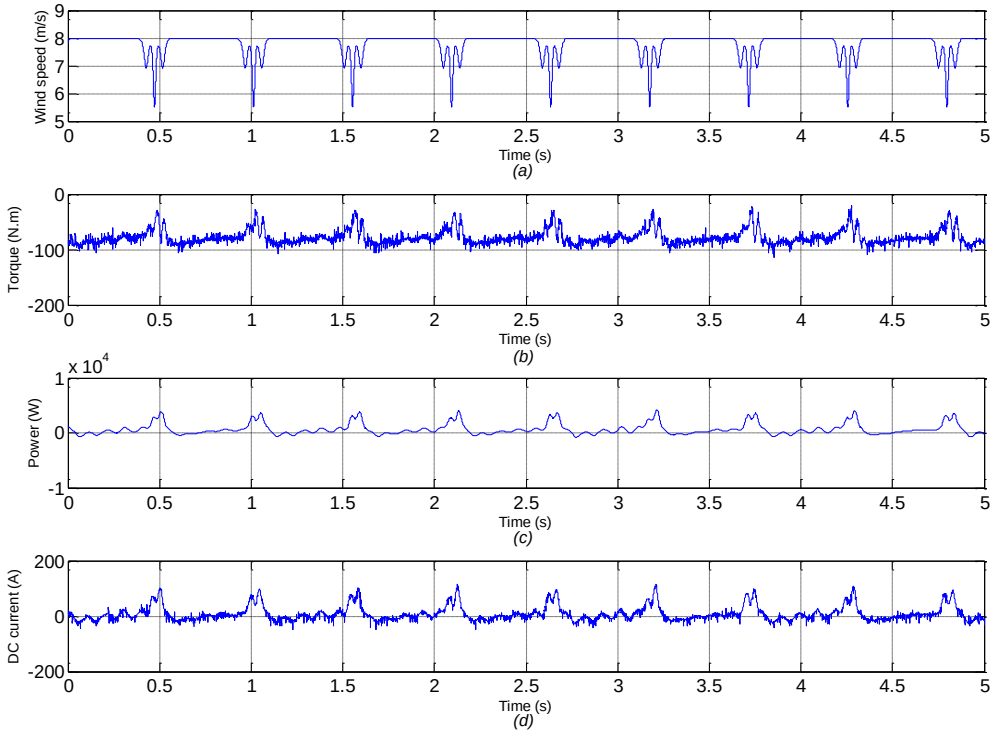

Figure 7.21: Measurement results with lattice 45° orientation tower shadow effect *(a)* modelled wind speed (Point A) experienced by the blades *(b)* torque at the shaft (Point C) *(c)* power difference between the generator and the load (Point D) *(d)* batteries DC current (Point E)

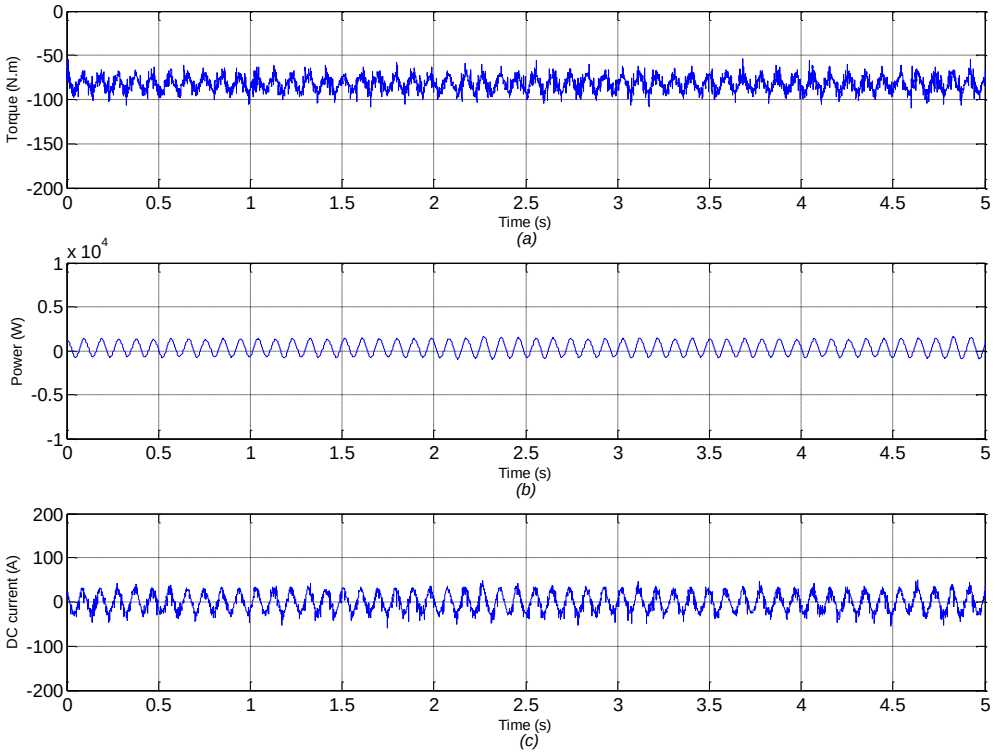

Figure 7.22: Microcycles induced by 10 Hz harmonic which will be subtracted from the calculation of battery lifetime

7.3.2 Battery Lifetime Modelling

In this work, a cycle-to-failure versus depth of discharge curve which was discussed in Chapter 3, Section 3.1.3 is employed and it is shown in Figure 7.23 (a) [173]. The fractional discharge cycles within the range less than 0.1 was extrapolated so that battery lifetime due to microcycles can be included, as depicted in Figure 7.23 (b). An adjusted cycle-to-failure curve was resulted, which effectively allows the microcycles to be evaluated. The corresponding relationship which was approximated by a polynomial curve fit is shown as [173]:

$$C_d = -1.345e^{-12}d^{-4} + 1.495e^{-7}d^{-3} - 0.001507d^{-2} + 601.5d^{-1} - 122.5 \quad (7.6)$$

where:

C_d: Cycles to failure at depth of discharge d
d: Depth of discharge

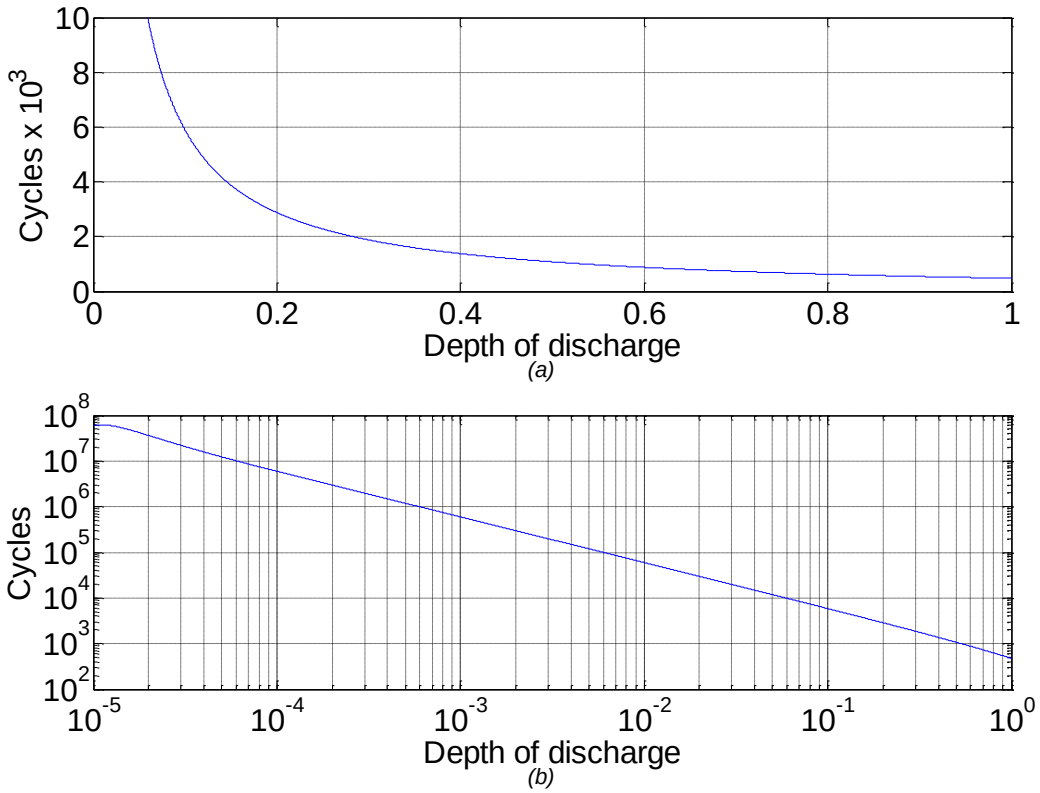

Figure 7.23: (a) Cycles-to-failure versus depth of discharge for a typical deep-cycle lead-acid battery (b) Extrapolated cycles to failure versus depth of discharge for the same battery on a logarithmic scale [173]

In reality, it is challenging to measure the fine changes in batteries SOC caused by the occurrence of microcycles. Furthermore, an extended period of experimental running time coupling with the highly sensitive transducers is required to produce an accurate measurement in the SOC changes. In order to facilitate this analysis, a computer simulation was utilised as it is a cost-effective method of investigating the small changes in batteries SOC. This can be achieved by feeding the recorded battery charge and discharge currents into the model, as shown in Figure 7.24. The current controlled source would emulate the measured current profile by acting as the current supply and demand from the battery. Then, the battery would generate the SOC profile accordingly.

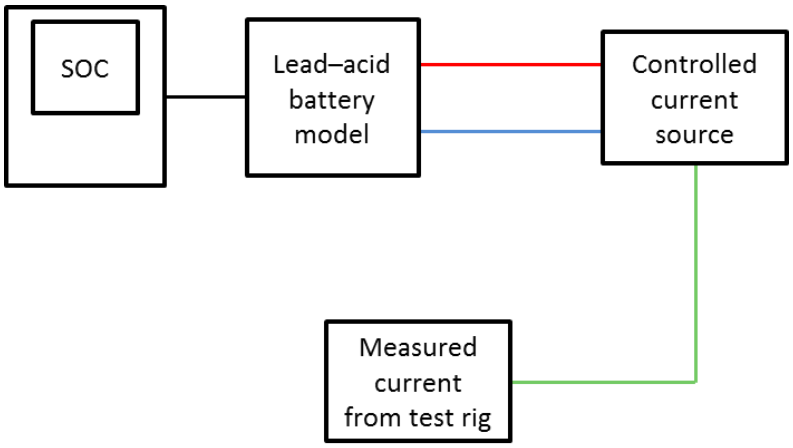

Figure 7.24: Methodology to simulate batteries SOC using Simulink

A more useful quantification on the battery lifetime is to consider a longer term operation of the system. However, as mentioned before, this is not a practical solution and therefore, several assumptions were made in this work. First, the overall objective was set upon finding the impact of the microcycles had on the battery lifetime for a period of 1 year. At the end of the year of operation, the percentage damage on the batteries lifetime due to only the effect tower shadow was sought. In this work, it was assumed that on average, the total power generation matches the load demand for 30 minutes within a day. Therefore, the battery lifetime reduction due to the tower shadow effect was anticipated to only occur for 30 minutes within a day.

The experimental measurement was conducted for a period of 10 s, although the results demonstrated from Figure 7.18 to Figure 7.22 only show 5 seconds of measurement results. Hence, the first step was to calculate the microcycles undergone by the battery within the period of 10 seconds. This was performed by the rain-flow cycle counting algorithm. The corresponding total cycle-to-failure was then computed using equation (7.6) and equation (3.9), based on the depth of discharge as a result of these microcycles.

From the sizing study in Chapter 3, it was determined that the optimum storage size of a hybrid wind-diesel system is 150 kWh, taking into the consideration the lower COE of the system can achieve. This corresponds to 3125 Ah for a 48 V system. Therefore, the battery capacity in the Simulink model was set to these figures in

order to simulate a more practical situation. Figure 7.25 to Figure 7.28 demonstrate the simulated results of the SOC profiles which have taken into consideration of the effect of tubular, lattice 0° orientation, lattice 22.5° orientation and lattice 45° orientation tower shadows, respectively. Comparison of all these SOC profiles shows that the batteries undergone fewer polarity reversals when the lattice tower was positioned 45° against the rotor plane.

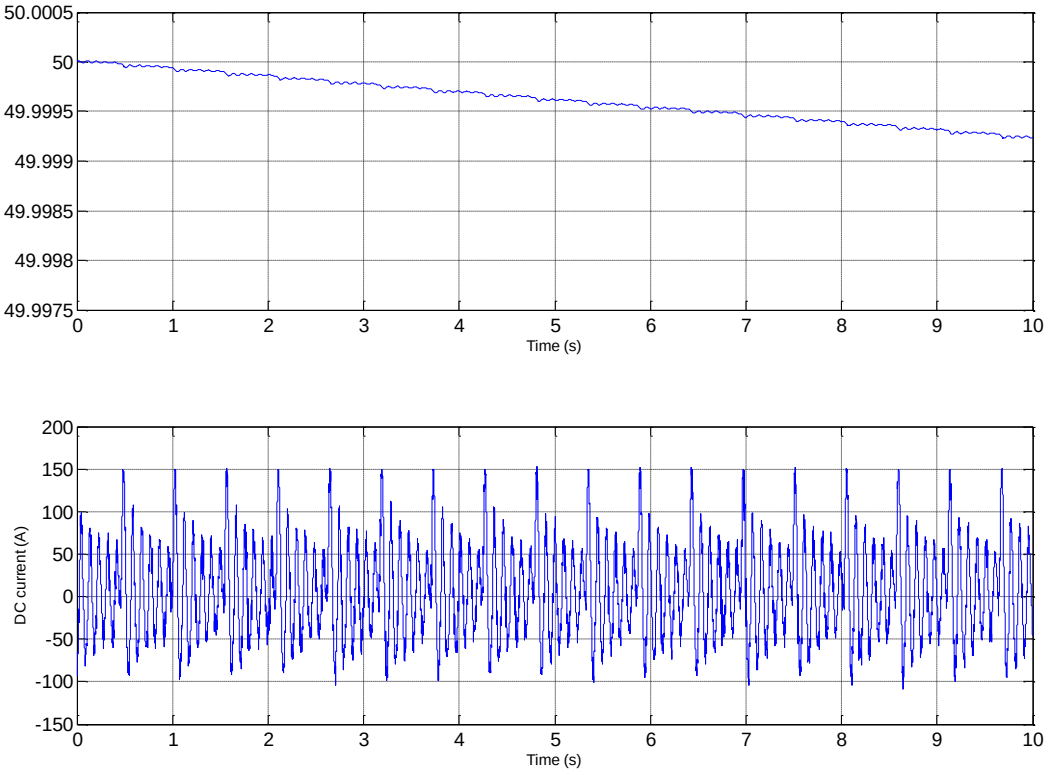

Figure 7.25: Tubular tower simulated *(a)* battery SOC with measured *(b)* battery current

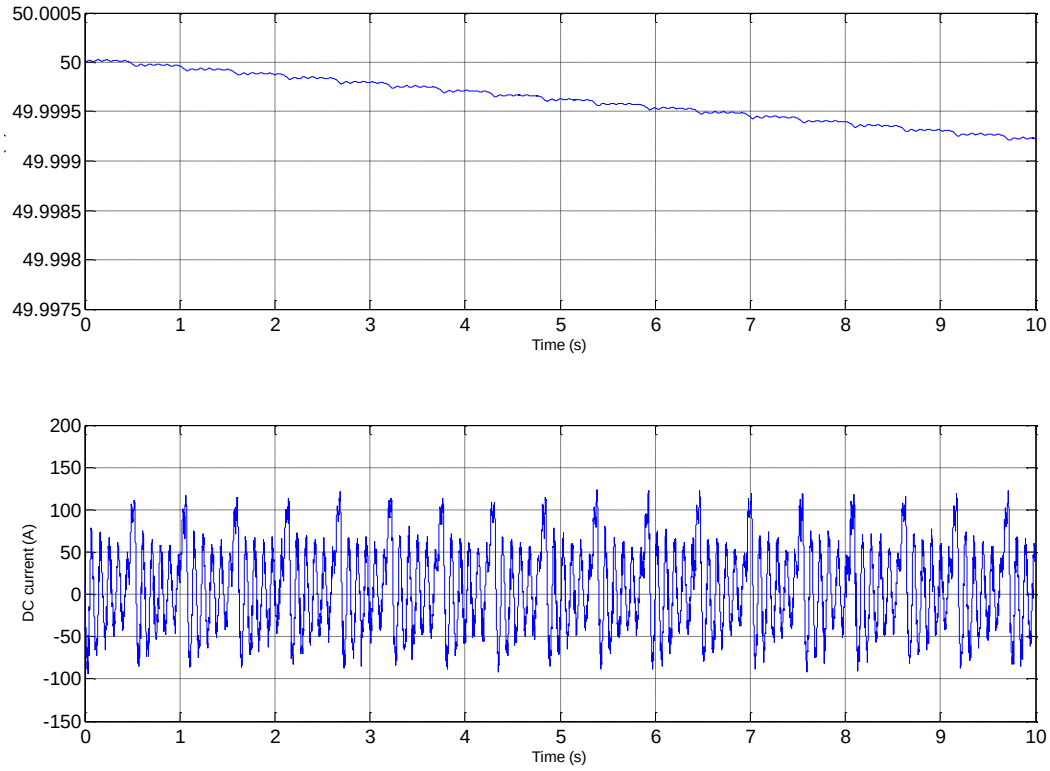

Figure 7.26: Lattice 0° orientation tower simulated *(a)* battery SOC with measured *(b)* battery current

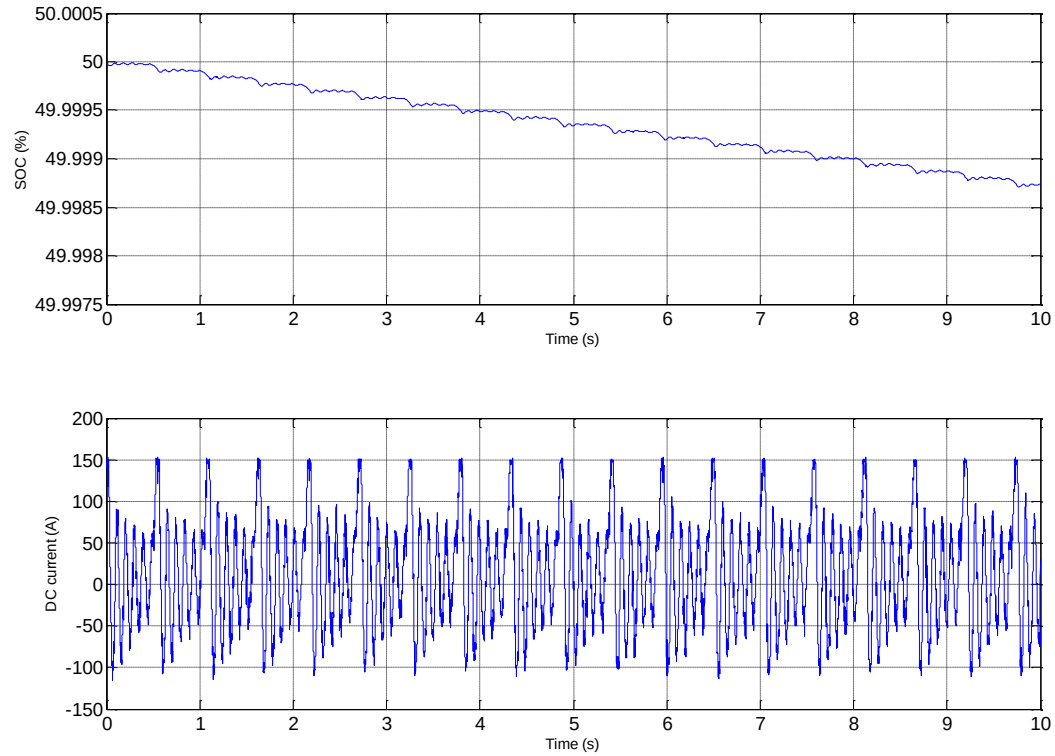

Figure 7.27: Lattice 22.5° orientation tower simulated *(a)* battery SOC with measured *(b)* battery current

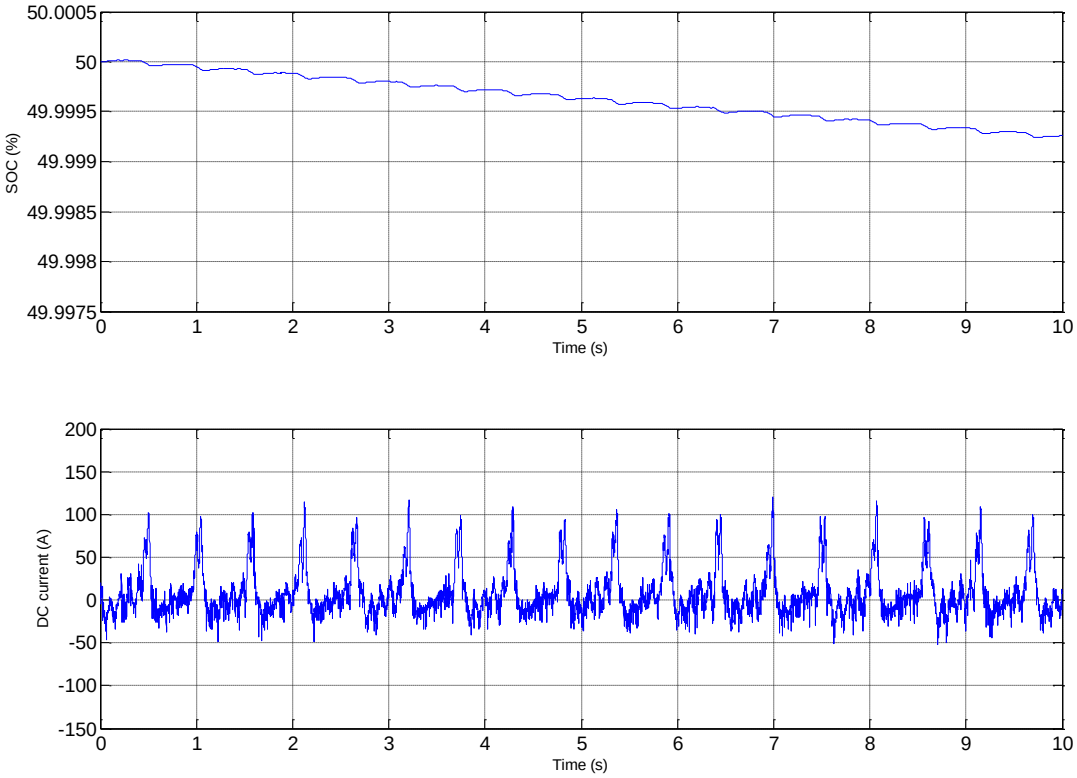

Figure 7.28: Lattice 45° orientation tower simulated *(a)* battery SOC with measured *(b)* battery current

Using the above described modelling approach and the assumptions made, the contribution of the tower shadow in reducing the battery lifetime in a year can be computed. It was determined that the contribution of the 10 Hz oscillation in battery lifetime in a year worked out to be about 6%. This needs to be discounted from the calculated reduction battery lifetime, in particular for the tubular, lattice 0° orientation and lattice 22.5° orientation tower configurations as they were subjected to the influence of the 10 Hz oscillation. Note that this was specific only for test rig in the lab. Other test rigs might be influenced by other oscillation frequencies and this depends heavily on the drive system response.

Figure 7.29 shows the comparison of the battery lifetime reduction for the tubular, lattice 0° orientation, lattice 22.5° and lattice 45° orientation tower configurations, respectively. The estimated battery lifetime reductions in a period of one year, which are expressed in percentages, were solely attributed to the tower shadow effect. It can be observed that the lattice tower incurred a more complex effect on the battery

lifetime, which highly depends on its orientation. The 22.5° orientation has the most detrimental effect on the battery lifetime, recording about 11% in a year, as opposed to about 3% for the case when the tower is positioned 45° against the rotor place. In reality, the orientation of the wind turbine varies significantly depending on the wind direction. Although there is a possibility that the lattice tower has a lower impact on the battery lifetime, it is not significantly lower than the tubular tower counterpart if no appropriate planning on the lattice tower's position is taken into consideration. In particular, the wind direction of the specific site has to be studied. It is believed that by placing the lattice tower in an optimum way towards the wind direction, there is a higher probability that minimal tower shadow effect can be imposed on the batteries. In this way, the benefits of using a lattice tower in an off-grid system can be maximised, in addition to its lower cost structure compared to the tubular counterpart. However, the lattice tower is potentially more dangerous for the birds as they might be exposed to the rotational motion of the blades due to the availability of resting steels for them to get near to. In addition, it is perceived to have a higher visual impact compared to the tubular towers. Therefore, many considerations need to be assessed before making the choice of tower configuration.

Some remarks on the obtained results in this section should be made. First of all, battery degradation of up to 11% due to the tower shadow effect is believed to be a significant value. However, the presented analysis did provide a relative insight on the battery degradation of different tower configurations. Several shortcomings of the analysis are recognised. These include the use of simulation model in estimating the drop of battery SOC. Furthermore, the real battery degradation may not be accurately estimated with the analytical battery degradation model used in this work. In order to provide concrete evidence on the significance of tower shadow effect on battery degradation, more experimental work needs to be carried out. For instance, different types of batteries may be used as test samples under the same microcycles involved. However, experimental work on battery degradation is known to be costly in terms of time, person-hours and equipment [270]. Finally, the assumption of the microcycles occurring 30 minutes in one day may be over-simplified and a thorough renewable resource and load analysis should be conducted to formulate a more

accurate estimate on this. Again, this requires significant amount of data acquisition which involves a considerable amount of time and money.

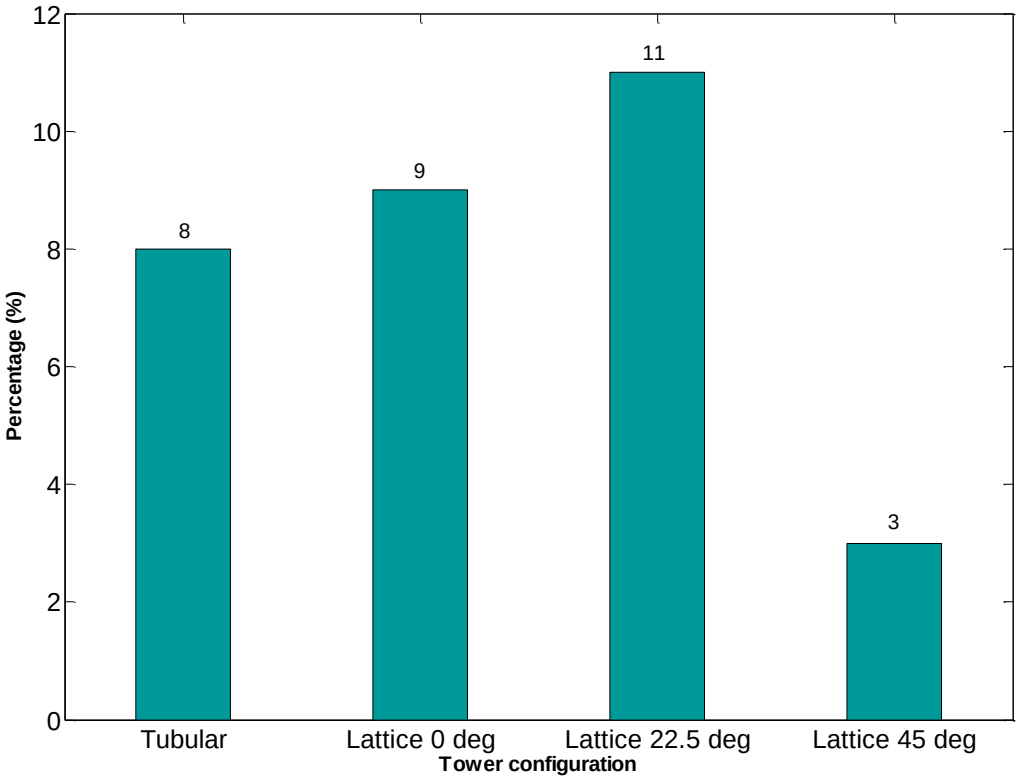

Figure 7.29: Estimated battery lifetime reduction in a year from microcycles for different tower configurations

7.3.3 Sensitivity Analysis of Tower Shadow Effects on Battery Lifetime

As mentioned before, the battery microcycles throughput will be the largest when the power generation closely matches the load [20]. However, the previous study focused on the occurrence of microcycles as a result of variability of renewable resources and load fluctuations. In this section, the objective is to investigate if this concept holds true when the microcycles are generated from the tower shadow effect. The assumption used in this work is that the microcycles due to tower shadow effect on average occur 30 minutes every day. Finally, the battery lifetime reduced in a year is determined.

In order to study the effect of the microcycles at different load conditions, a sensitivity analysis has been carried out to facilitate this. Different offset current

values were artificially added to the measured current profiles to emulate different load conditions. This approach simplifies the analysis and the exact same current profile with only the difference in magnitude can be compared to each other. An example of demonstrating the addition of an offset current to the tubular tower's generated current profile is shown in Figure 7.30. In this case, a fixed value of -40 A was added to the current profile. This translates to a reduction in load demand of about 2 kW.

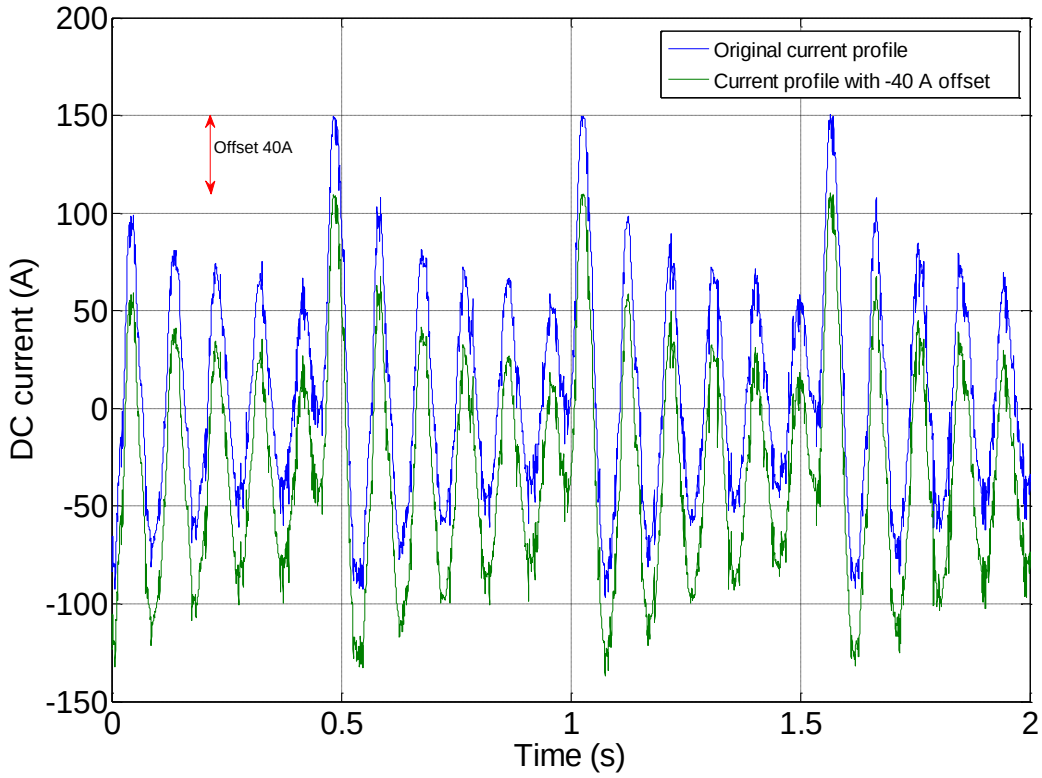

Figure 7.30: An example to demonstrate an offset current being added to the original current profile

In this work, it was proposed that the current values of 10 A, 20 A, 30 A, -10 A, -20 A, -30 A, -40 A and -50 were added to all the current profiles of all the tower configurations. In addition, these current values were being taken into consideration from the 10 Hz oscillation current profile, while determining the microcycles contribution to the tubular, lattice 0° orientation, lattice 22.5° orientation emulated tower shadows from the test rig. Figure 7.31 shows the percentages of the battery

lifetime reduced as a result of microcycles with the assumption that the microcycles occur 30 minutes in each day in a year. It can be observed that the battery lifetime reduction trend varied in a non-linear fashion despite the linear changed in current magnitude. Interestingly, the battery lifetime for lattice 22.5° orientation and lattice 45° orientation were most severely affected when the current profiles were reduced at 20 A (load reduction of about 1 kW). For the lattice 0° orientation, the worst battery lifetime reduction occurred when the current was reduced 10 A (load reduction of about 500 W). For tubular tower configuration, it was found that an incremental load of 10 A (correspond to 500 W) can result in most significant battery degradation. These results were contrasting to the previous fact which was stated that the highest battery throughput due to microcycles should occur when the load matches the generation [20]. This can be explained by the difference in the shape of the tower shadow profiles generated from different tower configurations. As expected, the battery throughput due to microcycles reduces as the difference between the power generation and the load becomes larger. Using the assumptions mentioned, the reduction in battery lifetime lies within the range of about 2% to 28%, depending on the tower's configuration in a single year of operation.

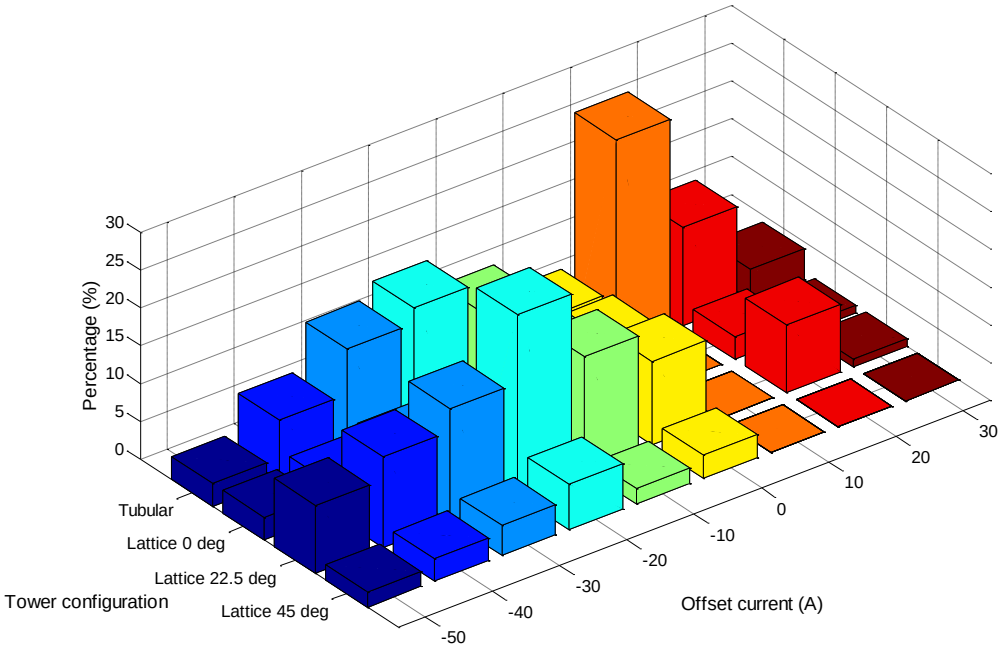

Figure 7.31: Battery lifetime reduction in a year from microcycles for different tower configurations and load conditions

The study in this chapter has opened up research questions such as:

- What is the optimum tower structure design for a small wind turbine in an off-grid system which minimises the effect of tower shadow on the battery systems?
- In what way a controller can help to minimise the effect of tower shadow?
- Can power electronics technologies solve the problem of tower shadow and is it worth implementing it in a hybrid system?

7.4 Summary

In conclusion, this chapter has described and discussed the modelling approach and the experimental work which focused on the battery lifetime reduction due to the tower shadow effect in an off-grid hybrid wind-diesel-battery system. The non-ideal behaviour, such as the oscillation of the test rig was characterised and the approach to "compensate" this through post-processing are demonstrated. The characteristics of the tower shadow profiles from both tubular and lattice towers perspective were

clearly demonstrated. In particular, their individual effect on the battery lifetime was studied. It was found out that the microcycles indeed reduce the battery lifetime in a considerable manner. The finding here is important for system designers whilst sizing the hybrid system during planning stages as it is very often the battery lifetime is assumed to last optimistically longer than in reality.

Chapter 8 Conclusions and Future Work

This chapter summarises the steps taken towards achieving the aim of this thesis and the importance in which it contributes to the knowledge of the off-grid hybrid systems. In addition, the limitations of this research will be highlighted. Finally, recommendations for future work are given which further extend the scope of the research presented in this thesis.

8.1 Conclusions and contribution to knowledge

The reasons for developing an affordable and reliable off-grid system and its significance to society have been outlined in Chapter 1. The identified off-grid HRES issues include the sizing trade-offs between the batteries and diesel generator fuel used, non-optimised operation of the diesel generator, the need to develop an off-grid HRES in the laboratory and the battery lifetime reduction as a result of microcycles. The proposed hypotheses were made accordingly to solve the mentioned problems. In order to achieve this, the associated aims were set out and discussed. Finally, Chapter 1 also provided the outline of this thesis.

In Chapter 2, the background and literature review of the HRESs were given. The discussion in this chapter was aimed at providing the fundamentals of the off-grid HRESs discipline and it is important for one to understand these basics before embarking into more detailed research topics. A comparison between grid-connected HRES and an off-grid HRES was made. It can be concluded that the knowledge of one system cannot be directly applied to another as they possess different characteristics in terms of fault handling, protection scheme, control strategy and communication system. Then, the discussion was continued with the elaboration on the design considerations at component level which exists within an off-grid hybrid wind-diesel-battery system. By understanding the operating characteristics of the batteries, inverters and diesel generators, they can be utilised more efficiently. Three possible architectures of off-grid systems were compared and contrasted. They were the AC system, DC system and the mixed AC-DC system. The choice of system architecture is dependent on several considerations, such as the characteristics of the

DGs, types of loads to be supplied and the complexity of the system, the types of batteries and their suitability for off-grid systems. From the discussion, it was found out that the limitations of any battery technology typically lean towards either higher power density or higher energy density. Therefore, it is vital for designers to select the appropriate batteries to be used in the HRES, depending on the applications. Although the hybrid system topology chosen in this work was pre-determined with the project collaborator (Gaia-Wind), a literature review on different topologies of HRES schemes was carried out for both modelled and implemented systems. The study has provided some justifications on the load size and community considered in this project. Then, a brief review on the off-the-shelf hybrid system component and their associated costs were conducted. The obtained information was used for the sizing studies in Chapter 3. A brief overview on the battery degradation model is also discussed. Finally, the energy management systems proposed by other authors were reviewed and they are referenced from the studies in Chapter 5.

In Chapter 3, the methodology of modelling a sizing tool, specifically for off-grid HRESs has been demonstrated. The main capability of this tool is its ability to provide an instant visualisation and evaluation on the trade-offs between batteries and the diesel generator usage, given a site-specific resource availability and load demand. Its simplicity to size an off-grid system can be attributed to the design methodology which was specific to off-grid systems. In addition, the algorithm and the process of building such a sizing tool were explained and this will assist other researchers in understanding them rather than treating the tool as a "black box", which often is the case for other commercial sizing tools. The optimal configuration was sought by considering the life-cycle cost of the system, assumed to be over a 20-year period in this research. This in turn translates to the lowest COE from an optimally sized system can produce. From the load sensitivity analysis performed in this chapter, it was found that a load of three households should be supplied from the hybrid wind-diesel-battery system which is based on the Gaia wind turbine (power rating of 11 kW) as the main source of renewable energy production. Otherwise, the "unbalance" between the energy generated from the wind turbine and the energy consumption will increase the COE over a life-cycle of 20 years. This is shown in Figure 3.15(a). In addition to considering the COE, the performance of the batteries

also varied considerably for different installed capacity. It was shown that the batteries encountered higher battery throughput if the installed capacity is smaller and vice versa.

A complete hybrid wind-diesel-battery system modelled in Simulink was developed and its simulation results were discussed in Chapter 4. The model comprised of a battery grid-forming inverter system, wind turbine, diesel generator, soft-starter and a turbulent wind generator. The simulation proved that the operation of the modelled hybrid wind-diesel-battery system was capable of operating in a stable condition through the steady-state and dynamic analysis. In particular, the power flow and power quality of the system were assessed. From this assessment, it showed that the load power demand was first met by the wind turbine and the diesel generator. Any amount of energy deficit was supplied by the batteries via the three-phase inverter system. Finally, the power flow study also showed that the three-phase SI inverter system was able to cope with the load and turbulent wind perturbations. In addition, a comparison of starting-up the generator through the soft-starter using the battery grid-forming inverter system and the utility grid was carried out. They produced different start-up characteristics from both the voltage control mode and current limiter mode control which were being applied on the soft-starter. This understanding allowed one to evaluate the control modes appropriately, based on the application's specifications such as the start-up speed and the allowable torque pulsations during start-up process. In addition, the control modes also determined the grid performance in terms of voltage dip and frequency perturbations during the start-up process. Hence, the selected control mode should also ensure that the voltage and frequency were kept within the statutory limits. As far as the author is aware, no previous literature was found that conducted such a test. Despite the simplicity of the topology of a soft-starter, it is important to differentiate the performance between the voltage control mode and current limited mode control while starting-up a high power rated induction machine using the power source either from the battery grid-forming inverter system or from the utility grid. This is a step that any designers would not want to avoid as it justifies the capability of a battery grid-forming system in starting-up a fixed-speed wind turbine, without exceeding the inverter's current

rating. Typically, an appropriate current margin within the inverter's current rating is intended to avoid the protection system being triggered.

In Chapter 5, the objective of optimising the operation of the hybrid system was achieved through the use of GA. A slightly different approach was taken in this work where the diesel generator operation was optimised by having a controlled number of start-stop cycles in addition to a fixed power output whenever it was switched on. This proposed control algorithm required the forecasted wind speed and the load demand to be part of the input data, besides defining the constraints during the optimisation process. In order to simulate a more realistic scenario, measured wind speed was utilised. For the load profile, a single household bottom-up load model which was developed from previous work was adopted. In order to perform a more realistic study, a load capacity of three households was used to carry out the optimisation studies in Chapter 5. The choice of this load capacity was again justified from the lowest COE supplied from the hybrid wind-diesel-battery system. The optimised results generated mathematically were post-processed and verified using the hybrid system developed from Chapter 4. Through this, the contrast in results between the simple mathematical modelling and the physical modelling were clearly demonstrated. It was shown that there were discrepancies between the two and it has proven the importance of the latter. The physical models built from the SimPowerSystems contain the electrical and mechanical information, whereas simple mathematical models only describe the system operation through arithmetic operations. Therefore, more confidence can be gained by verifying the mathematical modelling using the physical models. However, the physical simulation demands a large computation effort and therefore it incurs much longer simulation time. Ultimately, it was shown that the diesel generator was able to operate in a stable manner in the off-grid scenario, with a fixed power output whenever it was switched on. It is believed that such optimised operation can prolong the lifetime of the diesel generator significantly, although it is beyond the scope of this work to demonstrate that.

An off-grid system was developed in the laboratory with hardware setup to demonstrate the operation of a full-scale system. The experimental performance was

verified against the simulation results. These were being discussed in Chapter 6. A good correlation of wind emulator power curve, voltage and current profiles between the measured and simulated results were obtained. Experimentally, it was shown that the SI inverter system was able to balance the power requirement through the batteries utilisation. This has also been demonstrated from the simulation results. In addition, the soft-starter was also proven to be an important device to reduce the in-rush current of an induction generator to enable its operation in off-grid scenarios. From both simulation and experimental perspective, it appeared that the current limiter control is a preferred choice compared to the voltage mode control. This can be attributed to the fast acceleration, lower voltage dip and lower peak power during start-up. The hybrid system components were characterised individually before the complete system was being tested. Some components of the wind turbine, such as the aerodynamics of the blade, the gearbox which coupled the turbine and the generator, the tower and the braking mechanism were modelled in Simulink. The resulted test rig was more compact from the removal of real wind turbine blades and tower. However, an induction motor drive system was needed to emulate the wind energy. With an appropriate software model, a turbulent wind speed was being emulated successfully. The benefit of using the off-the-shelf components was that the reliability can be ensured from each of them. Hybrid system manufacturers who adopted this approach can expedite the product development cycle and reduce the need of human resources to perform testing prior to product rollout. Due to the limited control and flexibility within the SI inverter system, the optimised start-stop cycles of the diesel generator could not be implemented with the test rig. However, the necessity to test the algorithm using the test rig was minimal as the success of such scheme depends on the lower level control implementation. As a result, a more flexible hardware was justifiably needed if such an algorithm was used. From the industrial point of view, the developed test rig served as a platform to investigate the performances and issues of the off-grid hybrid system. It assists testing to be carried out in a more controlled manner, which would otherwise be costly in the field. In the lab environment, a particular test scenario can be repeated many times and this eases the process of identifying potential problems which compromise the reliability of the overall system.

In Chapter 7, a non-ideal effect of the wind turbine was investigated for an off-grid system scenario. In this case, the tower shadow effect of a downwind wind turbine has been modelled for both tubular tower and lattice tower configurations. They have been emulated successfully using the test rig developed in Chapter 6. However, they were subjected to some oscillations which have been discussed. The chapter achieved the aim of quantifying the battery lifetime reduction due to the tower shadow effect, which occurred when the load matched closely with the power generation within the designated period of time. Under this scenario, the frequent charging and discharging cycles appeared, in this case at a rate of 1.85 Hz (two-bladed wind turbine rotating at 55.5 rpm). With the assumption that these tower shadow microcycles occurred half an hour a day, it was determined that its contribution to the battery lifetime reduction should not be disregarded. The magnitude varied significantly, within the range of about 5% to 27%, which is dependent on the tower's configuration. This study uncovered the fact that the non-ideal effect of a wind turbine can be detrimental to other components (in this case the batteries) and it should not be underestimated while designing such system. While the tower shadow effects have been studied in the past, research that relates this effect to the reduction of battery lifetime is absent. The findings in the chapter bridge the knowledge gap and provide a new insight for off-grid system designers to incorporate the tower shadow effect whilst designing an off-grid hybrid system. This is to avoid the situation where the system designers are often being too optimistic in predicting the battery lifetime.

Together, the work of this thesis aims to design an affordable off-grid hybrid wind-diesel-battery system, without compromising the system's reliability. First, an optimally sized system can be sought for a particular site based on its historical renewable resource assessment, load demand, the life-cycle cost of the hybrid system components and the projected diesel fuel price. Then, the operation of the hybrid system can be optimised with the objective of maximising the utilisation of wind energy. At the same time, the diesel generator start-stop cycles and operating at part load condition is minimised to prolong its lifetime. This requires the forecasted wind speed and load demand as part of the optimisation process. The reliability of the system is ensured by utilising off-the-shelf components as they are thoroughly tested

by their corresponding manufacturers. The testing and characterisation work performed in this research has allowed a hybrid system to be setup and operated successfully in the laboratory. This reduces the knowledge gap in terms of design considerations and testing methodologies which involved in developing an off-grid hybrid system using existing technologies. Finally, a new design consideration which was developed towards the end of this thesis has proven to be important awareness for hybrid system manufacturers. Particularly, the existence of microcycles due to tower shadow from the wind turbine should be taken consideration while estimating the battery lifetime within an off-grid system. The magnitude of the microcycles was quantified to be dependent on the tower configuration and how closely the load demand matches the power generation. In the long run, the performance of the battery, and hence the economics of the hybrid system will be affected if appropriate measures are not taken to overcome these microcycles. All in all, various aspects of the hybrid system have been studied throughout this research, which can be summarised in the area of economics, optimised operation, hardware design considerations and prototyping in the laboratory.

8.2 Future work

The sizing tool developed in this work utilised a year of historical RES data and a fixed load demand profile while seeking the optimum configuration of the hybrid system. As part of the expansion work, more historical data and load growth estimation throughout the hybrid system's life cycle can be taken into consideration. More historical weather data can provide more confidence in understanding the local climate condition; however this comes at the expense of higher cost in data acquisition and data analysis. Although the load growth effect on power system is more significant in the national level, it is possible to be considered in an off-grid scenario in order to obtain a more accurate sizing solution. Furthermore, consumer electronics will be more affordable over time, which can increase the overall electricity consumption. From another point of view, the battery throughput due to the tower shadow effects can be incorporated into the cost assessment to increase accuracy. Two types of tower should be considered in this case, the tubular and the lattice tower, respectively. It was known that the lattice tower generates a different

set of tower shadow profiles, depending on the position of the rotor plane. In most scenarios, the rotor plane should be facing towards the wind direction to extract as much energy from the wind as possible. Therefore, a more sophisticated sizing tool which involved the battery throughput calculations due to the tower shadow effects at different wind conditions can be developed. Besides that, a life cycle analysis which includes the cost of the emissions from the fossil fuel can be integrated into this sizing tool in order to reflect the environmental cost involved. Finally, the economics of the DSM can be included in the future as they are not being considered in the sizing tool developed here. In this case, the loads are acting as virtual storage via load shifting. The load is shed at the critical time and the process has to catch up later [271]. Usually, the DSM is being associated with larger power systems and very little attention has been given to off-grid power systems. Potentially, with the DSM being implemented, the reliance on batteries as the main storage can be relaxed.

The sizing studies in Chapter 3, the proposed optimised operation control algorithm in Chapter 5 and the studies of non-ideal effects of the wind turbine in Chapter 7 were applied to the selected hybrid system architecture. However, these can be utilised on other HRES technologies. First of all, the grid-forming system in this work is based on the conventional two-level converter topology and a simple LCL filter design. The power quality can possibly be improved by using other converter topologies, filter topologies and control strategies [272] [273]. However, the increased number of components (for more inverting stages) and the complexity of the controller design will be the trade-off compared to the simplicity of the two-level converter. In addition, other wind turbine technologies such as the doubly-fed induction generator and permanent magnet-based topologies can be investigated along with an off-grid scenario. All these can be compared and contrasted to provide more understanding on their respective advantages and limitations. For instance, the switching, conduction losses and other performance indicators can be parametrised accordingly, working in conjunction with other renewable power generators in an off-grid scenario.

Following from the successful implementation of the hybrid system test rig in the laboratory environment, a long-term field demonstration project in an actual

community should be carried out to assess the real-life performance of the proposed system. Reliability issues can be identified and the lessons learned through the field operation will be invaluable for future improvements. To take a step further, the concept of hybrid systems can be extended to incorporate other renewable energy technologies such as solar photovoltaic and run-of-river hydropower. These are relatively well-established technologies; however, the lack of real life examples which demonstrate their optimal operation in an off-grid scenario still exists. The sizing, optimisation of hybrid system operation and laboratory testing in this research can be utilised to maximise the potential of these technologies. .

The last part of this thesis has shown that the tower shadow effects can negatively impact the battery lifetime, under the circumstances of power generation closely matching the load demand. It is believed that the magnitude of the tower shadow effects can be mitigated mechanically or electronically. In terms of the mechanical approach, the tower can be redesigned with a different architecture. Electronically, for instance, a power electronics module coupled with the appropriate filters can theoretically attenuate the magnitude of the power dip as a result of tower shadow. One potential solution to absorb the power fluctuations is through the utilisation of hybrid energy storage systems (HESS). In the scale of laboratory and in terms of practicality purposes, the hybrid battery-supercapacitor energy storage system is a promising solution to begin with. The aim of such solution is to introduce the supercapacitor to absorb high-frequency power surges while reducing the required battery power rating, degree of discharge and power losses of the overall system. The hybrid approach takes advantage of the two complementing technologies to provide large power and energy capacities. Some simulation and experimental work have been dedicated to the development of power electronics interfaces and energy managements for the hybrid battery-supercapacitor ESS technology [274], [275], [276], [277]. The battery lifetime gained from the additional components involved would require an economic analysis to be carried out. In addition, the methodology of sizing of the supercapacitors can be developed to achieve the optimum financial and technical performances.

8.3 Summary

As a final concluding remark, the work presented in this thesis has contributed to the knowledge gap in the field of hybrid wind-diesel-battery systems, without forgetting its limitations and its potential improvements which can be explored in the future. The fundamental pillars of sustainability i.e. environment, economic and social are believed to be achievable with the utilisation of hybrid renewable energy systems in supplying electricity to the isolated communities. The success of an energy system is highly dependent on how well it presents itself technically and at the same time not neglecting the sustainability aspects. Therefore, the sustainability concept should serve as the core driver and the basic awareness while developing the future generations of off-grid renewable energy systems.

Publications

[1] L. K. Gan, J. K. H. Shek, and M. A. Mueller, “Hybrid wind-photovoltaic-diesel-battery system sizing tool development using empirical approach, life-cycle cost and performance analysis: A case study in Scotland,” *Energy Conversion and Management*, vol. 106, pp.479-494, 2015.

[2] L. K. Gan, J. K. H. Shek, and M. A. Mueller, "Modelling and experimentation of grid-forming inverters for standalone hybrid wind-battery systems," in International Conference on Renewable Energy Research and Applications (ICRERA), 2015, pp. 449-454

[3] L. K. Gan, J. K. H. Shek, and M. A. Mueller, "Optimised operation of an off-grid hybrid wind-diesel-battery system using genetic algorithm," Energy Conversion and Management, vol. 126, pp. 446-462, 2016.

[4] L. K. Gan, J. K. H. Shek, and M. A. Mueller, “Modeling and Laboratory Development of an Off-grid Hybrid Wind-Battery System,” Submitted to IEEE Transactions on Industry Applications

[5] L. K. Gan, J. K. H. Shek, and M. A. Mueller, “Modeling and Characterization of Downwind Tower Shadow Effects using a Wind Turbine Emulator,” in IEEE Transactions on Industrial Electronics, vol. PP, no. 99, pp. 1-1

[6] L. K. Gan, J. K. H. Shek, and M. A. Mueller, “Analysis of Tower Shadow Effects on Battery Lifetime in Standalone Hybrid Wind-Diesel-Battery Systems,” in IEEE Transactions on Industrial Electronics, vol. PP, no. 99, pp. 1-1

References

[1] "CO_2 Emissions from Fuel Combustion Highlights," *International Energy Agency (IEA)*, Paris, France, 2015.

[2] IPCC, "Climate Change 2014: Synthesis Report. Contribution of Working Groups I, II and III to the Fifth Assessment Report of the Intergovernmental Panel on Climate Change," *[Core Writing Team, R.K. Pachauri and L.A. Meyer (eds.)]*, Geneva, Switzerland, 2014.

[3] A. de Oliveira, A. M. de Morais, O. S. Valente, and J. R. Sodré, "Combustion characteristics, performance and emissions from a diesel power generator fuelled by B7-ethanol blends," *Fuel Processing Technology,* vol. 139, pp. 67-72, 2015.

[4] IEA, "Energy, Climate Change and Environment: 2016 Insights," *International Energy Agency*, Paris, France, 2016.

[5] IEA, "World Energy Outlook 2015," *International Energy Agency*, Paris, France, 2015.

[6] REN21, "Renewables 2016 Global Status Report," Paris, France, 2016.

[7] "Poor people's energy outlook 2016: National Energy Access Planning from the Bottom Up," *Practical Action Publishing*, Rugby, UK.

[8] OPEC, "World Oil Outlook," *Organization of the Petroleum Exporting Countries*, Vienna, Austria, 2016.

[9] BP, "BP Statistical Review of World Energy 2016," 2016.

[10] S. Mišák, J. Stuchlý, J. Platoš, and P. Krömer, "A heuristic approach to Active Demand Side Management in Off-Grid systems operated in a Smart-Grid environment," *Energy and Buildings,* vol. 96, pp. 272-284, 2015.

[11] C. Spataru and P. Bouffaron, "Chapter 22 - Off-Grid Energy Storage A2 - Letcher, Trevor M," in *Storing Energy*, ed Oxford: Elsevier, 2016, pp. 477-497.

[12] S. Speidel and T. Bräunl, "Leaving the grid—The effect of combining home energy storage with renewable energy generation," *Renewable and Sustainable Energy Reviews,* vol. 60, pp. 1213-1224, 2016.

[13] P. Bajpai and V. Dash, "Hybrid renewable energy systems for power generation in stand-alone applications: A review," *Renewable and Sustainable Energy Reviews,* vol. 16, pp. 2926-2939, 2012.

[14] X. Luo, J. Wang, M. Dooner, and J. Clarke, "Overview of current development in electrical energy storage technologies and the application potential in power system operation," *Applied Energy,* vol. 137, pp. 511-536, 2015.

[15] H. Belmili, M. Haddadi, S. Bacha, M. F. Almi, and B. Bendib, "Sizing stand-alone photovoltaic–wind hybrid system: Techno-economic analysis and optimization," *Renewable and Sustainable Energy Reviews,* vol. 30, pp. 821-832, 2014.

[16] A. Cano, F. Jurado, H. Sánchez, L. M. Fernández, and M. Castañeda, "Optimal sizing of stand-alone hybrid systems based on PV/WT/FC by using several methodologies," *Journal of the Energy Institute,* vol. 87, pp. 330-340, 2014.

[17] M. Sechilariu and F. Locment, *Urban DC Microgrid: Intelligent Control and Power Flow Optimization*: Butterworth-Heinemann, 2016.

[18] A. Saengprajak, "Efficiency of Demand Side Management Measures in Small Village Electrification Systems " Doktor der Ingenieurwissenschaften, Faculty of Electrical Engineering and Computer Science, University of Kassel, Germany, 2006.

[19] C. Ropeter, H. Wenzl, H. P. Beck, E. A. Wehrmann, J. W. Twidell, and D. U. Sauer, "The impact of microcycles on batteries in different applications," in *18th Electric Vehicle Symposium (EVS18)*, Berlin, 2001.

[20] A. J. Ruddell, A. G. Dutton, H. Wenzl, C. Ropeter, D. U. Sauer, J. Merten, C. Orfanogiannis, J. W. Twidell, and P. Vezin, "Analysis of battery current microcycles in autonomous renewable energy systems," *Journal of Power Sources,* vol. 112, pp. 531-546, 2002.

[21] "Gaia-Wind 133-11kW Data Sheet," *Gaia-Wind Ltd*, Glasgow, United Kingdom.

[22] J. K. Kaldellis, E. Kondili, and A. Filios, "Sizing a hybrid wind-diesel stand-alone system on the basis of minimum long-term electricity production cost," *Applied Energy,* vol. 83, pp. 1384-1403, 2006.

[23] B. Grieser, Y. Sunak, and R. Madlener, "Economics of small wind turbines in urban settings: An empirical investigation for Germany," *Renewable Energy,* vol. 78, pp. 334-350, 2015.

[24] J. J. Justo, F. Mwasilu, J. Lee, and J. W. Jung, "AC-microgrids versus DC-microgrids with distributed energy resources: A review," *Renewable and Sustainable Energy Reviews,* vol. 24, pp. 387-405, 2013.

[25] P. Asmus, "Microgrids, Virtual Power Plants and Our Distributed Energy Future," *The Electricity Journal,* vol. 23, pp. 72-82, 2010.

[26] N. L. and M. J., "Virtual power plants - General review: Structure, application and optimization," *Journal of Power Technologies,* vol. 92, pp. 135-149, 2012.

[27] K. De Brabandere, B. Bolsens, J. Van den Keybus, A. Woyte, J. Driesen, and R. Belmans, "A voltage and frequency droop control method for parallel inverters," *IEEE Transactions on Power Electronics,* vol. 22, pp. 1107-1115, 2007.

[28] M. P. Kazmierkowski and L. Malesani, "Current control techniques for three-phase voltage-source PWM converters: a survey," *IEEE Transactions on Industrial Electronics,* vol. 45, pp. 691-703, 1998.

[29] M. Monfared and S. Golestan, "Control strategies for single-phase grid integration of small-scale renewable energy sources: A review," *Renewable and Sustainable Energy Reviews,* vol. 16, pp. 4982-4993, 2012.

[30] E. Pouresmaeil, O. Gomis-Bellmunt, D. Montesinos-Miracle, and J. Bergas-Jané, "Multilevel converters control for renewable energy integration to the power grid," *Energy,* vol. 36, pp. 950-963, 2011.

[31] T. S. Ustun, C. Ozansoy, and A. Zayegh, "Modeling of a Centralized Microgrid Protection System and Distributed Energy Resources According to IEC 61850-7-420," *IEEE Transactions on Power Systems,* vol. 27, pp. 1560-1567, 2012.

[32] D. Salomonsson, L. Soder, and A. Sannino, "Protection of low-voltage DC microgrids," *IEEE Transactions on Power Delivery,* vol. 24, pp. 1045-1053, 2009.

[33] Y. Kumar, J. Ringenberg, Soma S. Depuru, V. K. Devabhaktuni, Jin W. Lee, E. Nikolaidis, B. Andersen, and A. Afjeh, "Wind energy: Trends and enabling technologies," *Renewable and Sustainable Energy Reviews,* vol. 53, pp. 209-224, 2016.

[34] "IEC 61400-1:2005," *International Electrotechnical Commission*, Switzerland, 2005.

[35] T. K. Saha and D. K. Kastha, "Design Optimization and Dynamic Performance Analysis of a Stand-Alone Hybrid Wind-Diesel Electrical Power Generation System," *IEEE Transactions on Energy Conversion,* vol. 25, pp. 1209-1217, 2010.

[36] V. Carpentiero, R. Langella, T. Manco, and A. Testa, "A Markovian Approach to Size a Hybrid Wind-Diesel Stand Alone System," in *Proceedings of the 10th International Conference on Probabilistic Methods Applied to Power Systems (PMAPS)*, 2008, pp. 1-8.

[37] M. Kefayat, A. Lashkar Ara, and S. A. Nabavi Niaki, "A hybrid of ant colony optimization and artificial bee colony algorithm for probabilistic optimal placement

and sizing of distributed energy resources," *Energy Conversion and Management,* vol. 92, pp. 149-161, 2015.

[38] M. Stiebler, *Wind Energy Systems for Electric Power Generation*: Springer Berlin Heidelberg, 2008.

[39] F. O. Hocaoglu, O. N. Gerek, and M. Kurban, "The effect of model generated solar radiation data usage in hybrid (wind–PV) sizing studies," *Energy Conversion and Management,* vol. 50, pp. 2956-2963, 2009.

[40] "IEC 61400-2:2013," *International Electrotechnical Commission*, Switzerland, 2013.

[41] "Small and Medium Wind UK Market Report," *RenewableUK*, United Kingdom, 2015.

[42] M. Malinowski, A. Milczarek, R. Kot, Z. Goryca, and J. T. Szuster, "Optimized Energy-Conversion Systems for Small Wind Turbines: Renewable energy sources in modern distributed power generation systems," *IEEE Power Electronics Magazine,* vol. 2, pp. 16-30, 2015.

[43] R. Spée, S. Bhowmik, and J. H. R. Enslin, "Novel control strategies for variable-speed doubly fed wind power generation systems," *Renewable Energy,* vol. 6, pp. 907-915, 1995.

[44] J. F. Manwell, J. G. McGowan, and A. L. Rogers, *Wind Energy Explained: Theory, Design and Application*: Wiley-Blackwell, 2009.

[45] S. Muller, M. Deicke, and R. W. D. Doncker, "Doubly fed induction generator systems for wind turbines," *IEEE Industry Applications Magazine,* vol. 8, pp. 26-33, 2002.

[46] M. Rolak, R. Kot, M. Malinowski, Z. Goryca, and J. T. Szuster, "Design of Small Wind Turbine with Maximum Power Point Tracking Algorithm," in *IEEE International Symposium on Industrial Electronics*, 2011, pp. 1023-1028.

[47] G. Léna, "Rural Electrification with PV Hybrid Systems - Overview and Recommendations for Further Deployment," *International Energy Agency (IEA)*, July 2013.

[48] S. Rolland and G. Glania, "Hybrid Mini-Grids for Rural Electrification: Lessons Learned," *Alliance for Rural Electrification (ARE)*, Brussels, Belgium, March 2011.

[49] W. Peukert, "Über die Abhängigkeit der Kapazität von der Entladestromstärke bei Bleiakkumulatoren," *Elektrotechnische Zeitschrift,* vol. 20, pp. 20-21, 1897.

[50] D. Doerffel and S. A. Sharkh, "A critical review of using the Peukert equation for determining the remaining capacity of lead-acid and lithium-ion batteries," *Journal of Power Sources,* vol. 155, pp. 395-400, April 2006.

[51] P. A. Stott, "Renewable Variable Speed Hybrid System," PhD Thesis, The University of Edinburgh, Edinburgh, 2010.

[52] G. Zenginobuz, I. Cadirci, M. Ermis, and C. Barlak, "Soft starting of large induction motors at constant current with minimized starting torque pulsations," *IEEE Transactions on Industry Applications,* vol. 37, pp. 1334-1347, 2001.

[53] G. Lu, Y. Ji, H. Yu, and K. Zhang, "Analysis of a novel topology of soft starter for induction motors," in *The 29th Annual Conference of the IEEE Industrial Electronics Society (IECON)*, 2003, pp. 662-667 vol.1.

[54] (2012). "Sunny Island 8.0H / 6.0H installation manual," *SMA.* Available: http://www.sma.de/en/products/battery-inverters/sunny-island-60h-80h.html#Downloads-229866

[55] A. Driesse, P. Jain, and S. Harrison, "Beyond the curves: Modeling the electrical efficiency of photovoltaic inverters," in *33rd IEEE Photovoltaic Specialists Conference (PVSC)*, 2008, pp. 1-6.

[56] F. Spertino, F. Corona, and P. D. Leo, "Limits of Advisability for Master-Slave Configuration of DC-AC Converters in Photovoltaic Systems," *IEEE Journal of Photovoltaics,* vol. 2, pp. 547-554, 2012.

[57] A. Malheiro, P. M. Castro, R. M. Lima, and A. Estanqueiro, "Integrated sizing and scheduling of wind/PV/diesel/battery isolated systems," *Renewable Energy,* vol. 83, pp. 646-657, 2015.

[58] R. Siddaiah and R. P. Saini, "A review on planning, configurations, modeling and optimization techniques of hybrid renewable energy systems for off grid applications," *Renewable and Sustainable Energy Reviews,* vol. 58, pp. 376-396, 2016.

[59] M. H. Nehrir, C. Wang, K. Strunz, H. Aki, R. Ramakumar, J. Bing, Z. Miao, and Z. Salameh, "A Review of Hybrid Renewable/Alternative Energy Systems for Electric Power Generation: Configurations, Control, and Applications," *IEEE Transactions on Sustainable Energy,* vol. 2, pp. 392-403, 2011.

[60] M. Saeedifard, M. Graovac, R. F. Dias, and R. Iravani, "DC power systems: Challenges and opportunities," in *IEEE Power and Energy Society General Meeting*, 2010, pp. 1-7.

[61] Y. Li and F. Nejabatkhah, "Overview of control, integration and energy management of microgrids," *Journal of Modern Power Systems and Clean Energy,* vol. 2, pp. 212-222, 2014.

[62] A. Tuladhar, J. Hua, T. Unger, and K. Mauch, "Control of parallel inverters in distributed AC power systems with consideration of line impedance effect," *IEEE Transactions on Industry Applications,* vol. 36, pp. 131-138, 2000.

[63] R. Majumder, B. Chaudhuri, A. Ghosh, R. Majumder, G. Ledwich, and F. Zare, "Improvement of stability and load sharing in an autonomous microgrid using supplementary droop control loop," *IEEE Transactions on Power Systems,* vol. 25, pp. 796-808, 2010.

[64] T. L. Lee and P. T. Cheng, "Design of a New Cooperative Harmonic Filtering Strategy for Distributed Generation Interface Converters in an Islanding Network," *IEEE Transactions on Power Electronics,* vol. 22, pp. 1919-1927, 2007.

[65] A. Chauhan and R. P. Saini, "A review on Integrated Renewable Energy System based power generation for stand-alone applications: Configurations, storage options, sizing methodologies and control," *Renewable and Sustainable Energy Reviews,* vol. 38, pp. 99-120, 2014.

[66] S. Mishra, G. Mallesham, and A. N. Jha, "Design of controller and communication for frequency regulation of a smart microgrid," *IET Renewable Power Generation,* vol. 6, pp. 248-258, 2012.

[67] J. Alonso-Martinez, J. E. Carrasco, and S. Arnaltes, "Table-based Direct Power Control: A critical review for microgrid applications," *IEEE Transactions on Power Electronics,* vol. 25, pp. 2949-2961, 2010.

[68] J. M. Guerrero, J. Matas, V. Luis Garcia de, M. Castilla, and J. Miret, "Decentralized control for parallel operation of distributed generation inverters using resistive output impedance," *IEEE Transactions on Industrial Electronics,* vol. 54, pp. 994-1004, 2007.

[69] K. Yukita, "Chapter 10 - AC/DC microgrids," in *Integration of Distributed Energy Resources in Power Systems*, ed: Academic Press, 2016, pp. 236-260.

[70] (1/6/2015). "IEEE Smart Grid Experts Roundup: AC vs. DC Power," *IEEE Smart Grid.* Available: http://smartgrid.ieee.org/resources/interviews/368-ieee-smart-grid-experts-roundup-ac-vs-dc-power

[71] G. A. Laudani and P. Mitcheson, "Comparison of cost and efficiency of DC versus AC in office buildings," *Imperial College London*, 2014.

[72] H. Kakigano, M. Nomura, and T. Ise, "Loss evaluation of DC distribution for residential houses compared with AC system," in *The 2010 International Power Electronics Conference - ECCE ASIA -*, 2010, pp. 480-486.

[73] E. Unamuno and J. A. Barrena, "Hybrid ac/dc microgrids—Part I: Review and classification of topologies," *Renewable and Sustainable Energy Reviews,* vol. 52, pp. 1251-1259, 2015.

[74] P. Basak, S. Chowdhury, S. Halder nee Dey, and S. P. Chowdhury, "A literature review on integration of distributed energy resources in the perspective of control, protection and stability of microgrid," *Renewable and Sustainable Energy Reviews,* vol. 16, pp. 5545-5556, 2012.

[75] A. R. Haron, A. Mohamed, and H. Shareef, "A review on protection schemes and coordination techniques in microgrid system," *Journal of Applied Sciences,* vol. 12, pp. 101-112, 2012.

[76] S. P. Chowdhury, S. Chowdhury, and P. A. Crossley, "Islanding protection of active distribution networks with renewable distributed generators: A comprehensive survey," *Electric Power Systems Research,* vol. 79, pp. 984-992, 2009.

[77] H. J. Laaksonen, "Protection principles for future microgrids," *IEEE Transactions on Power Electronics,* vol. 25, pp. 2910-2918, 2010.

[78] P. Kou, L. Deliang, and L. Gao, "Distributed Coordination of Multiple PMSGs in an Islanded DC Microgrid for Load Sharing," *IEEE Transactions on Energy Conversion,* vol. PP, pp. 1-1, 2017.

[79] H. Kakigano, Y. Miura, and T. Ise, "Low-Voltage Bipolar-Type DC Microgrid for Super High Quality Distribution," *IEEE Transactions on Power Electronics,* vol. 25, pp. 3066-3075, 2010.

[80] M. A. Redfern, "Smart DC micro-grids," in *Proceedings of the 2014 15th International Scientific Conference on Electric Power Engineering (EPE)*, 2014, pp. 173-178.

[81] M. Starke, L. M. Tolbert, and B. Ozpineci, "AC vs. DC distribution: A loss comparison," in *IEEE/PES Transmission and Distribution Conference and Exposition*, 2008, pp. 1-7.

[82] P. Wang, L. Goel, X. Liu, and F. H. Choo, "Harmonizing AC and DC: A hybrid AC/DC future grid solution," *IEEE Power and Energy Magazine,* vol. 11, pp. 76-83, 2013.

[83] G. Wu, Y. Ono, and M. Alishahi, "Development of a resilient hybrid microgrid with integrated renewable power generations supplying DC and AC loads," in *2015 IEEE International Telecommunications Energy Conference (INTELEC)*, 2015, pp. 1-5.

[84] Y. Xia, Y. Peng, P. Yang, M. Yu, and W. Wei, "Distributed Coordination Control for Multiple Bidirectional Power Converters in a Hybrid AC/DC Microgrid," *IEEE Transactions on Power Electronics,* vol. PP, pp. 1-1, 2016.

[85] P. Maher, N. P. A. Smith, and A. A. Williams, "Assessment of pico hydro as an option for off-grid electrification in Kenya," *Renewable Energy,* vol. 28, pp. 1357-1369, 2003.

[86] A. A. Lahimer, M. A. Alghoul, F. Yousif, T. M. Razykov, N. Amin, and K. Sopian, "Research and development aspects on decentralized electrification options for rural household," *Renewable and Sustainable Energy Reviews,* vol. 24, pp. 314-324, 2013.

[87] (6/6/2015). "Comparison of energy storage technologies," *Energy Storage Association.* Available: http://energystorage.org/

[88] H. Ibrahim, A. Ilinca, and J. Perron, "Energy storage systems—Characteristics and comparisons," *Renewable and Sustainable Energy Reviews,* vol. 12, pp. 1221-1250, 2008.

[89] I. Hadjipaschalis, A. Poullikkas, and V. Efthimiou, "Overview of current and future energy storage technologies for electric power applications," *Renewable and Sustainable Energy Reviews,* vol. 13, pp. 1513-1522, 2009.

[90] J. K. Kaldellis, *Stand-Alone and Hybrid Wind Energy Systems: Technology, Energy Storage and Applications*: Woodhead Publishing Ltd, 2010.

[91] Y. Kim, J. Koh, Q. Xie, Y. Wang, N. Chang, and M. Pedram, "A scalable and flexible hybrid energy storage system design and implementation," *Journal of Power Sources,* vol. 255, pp. 410-422, 2014.

[92] R. K. Akikur, R. Saidur, H. W. Ping, and K. R. Ullah, "Comparative study of stand-alone and hybrid solar energy systems suitable for off-grid rural electrification: A review," *Renewable and Sustainable Energy Reviews,* vol. 27, pp. 738-752, 2013.

[93] D. Saheb-Koussa, M. Haddadi, and M. Belhamel, "Economic and technical study of a hybrid system (wind–photovoltaic–diesel) for rural electrification in Algeria," *Applied Energy,* vol. 86, pp. 1024-1030, 2009.

[94] P. Dalwadi, V. Shrinet, C. R. Mehta, and P. Shah, "Optimization of solar-wind hybrid system for distributed generation," in *Nirma University International Conference on Engineering*, 2011, pp. 1-4.

[95] M. A. Elhadidy, "Performance evaluation of hybrid (wind/solar/diesel) power systems," *Renewable Energy,* vol. 26, pp. 401-413, 2002.

[96] E. M. Nfah and J. M. Ngundam, "Modelling of wind/Diesel/battery hybrid power systems for far North Cameroon," *Energy Conversion and Management,* vol. 49, pp. 1295-1301, 2008.

[97] E. S. Sreeraj, K. Chatterjee, and S. Bandyopadhyay, "Design of isolated renewable hybrid power systems," *Solar Energy,* vol. 84, pp. 1124-1136, 2010.

[98] A. H. Mondal and M. Denich, "Hybrid systems for decentralized power generation in Bangladesh," *Energy for Sustainable Development,* vol. 14, pp. 48-55, 2010.

[99] D. O. Akinyele and R. K. Rayudu, "Community-based hybrid electricity supply system: A practical and comparative approach," *Applied Energy,* vol. 171, pp. 608-628, 2016.

[100] S. Tselepis, "12 years operation of the Gaidouromantra Microgrid in Kythnos island," in *5th International Conference on Integration of Renewable and Distributed Energy Resources*, Berlin, 2012.

[101] B. Bhandari, K.-T. Lee, C. S. Lee, C.-K. Song, R. K. Maskey, and S.-H. Ahn, "A novel off-grid hybrid power system comprised of solar photovoltaic, wind, and hydro energy sources," *Applied Energy,* vol. 133, pp. 236-242, 2014.

[102] S. B. Silva, M. A. G. de Oliveira, and M. M. Severino, "Economic evaluation and optimization of a photovoltaic–fuel cell–batteries hybrid system for use in the Brazilian Amazon," *Energy Policy,* vol. 38, pp. 6713-6723, 2010.

[103] R. H. Kemsley, P. McGarley, S. Wade, and F. Thim, "Making small high-penetration renewable energy systems work - Scottish Island experience," in *IET Conference on Renewable Power Generation (RPG)*, 2011, pp. 1-7.

[104] Z. Chmiel and S. C. Bhattacharyya, "Analysis of off-grid electricity system at Isle of Eigg (Scotland): Lessons for developing countries," *Renewable Energy,* vol. 81, pp. 578-588, 2015.

[105] "User Manual - Gaia-Wind 11 kW Turbine," *Gaia-Wind Ltd.*, United Kingdom, August 2008.

[106] "Britwind R9000 - 5 kW Wind Turbine," *Britwind Ltd*, United Kingdom.
[107] (6/11/2016). "Payback for an Evance R9000," *Anemos Renewables.* Available: http://www.anemos.org.uk/index.php/finance/payback-for-an-evance-r9000
[108] "Kingspan Wind KW6 - Technical Information," *Kingspan*, United Kingdom.
[109] "Kingspan KW6 Price," *Natural Energy Renewables Ltd.* Available: http://www.naturalenergyuk.co.uk/kingspan-kw6/
[110] (6/11/2016). "AirForce 10 Technical Specifications," *FuturEnergy Ltd.* Available: http://www.futurenergy.co.uk/10kwturbine.html
[111] (6/11/2016). "FuturEnergy Airforce-10 Price Information," *Renugen.*
[112] "Fortis Alizé Technical Specifications," *Fortis Wind Energy*, The Netherlands.
[113] "Fortis Wind Energy price list 2012-1," *Fortis Energy*, The Netherlands.
[114] "Bergey Excel 10 Technical Specifications," *Bergey Windpower*, United States.
[115] (6/11/2016). "Bergey Wind Turbine Price Information," *Bergey Windpower.* Available: http://bergey.com/documents/2013/10/bwc-retail-price-list-10-01-13.pdf
[116] "Small Wind Turbine General Information - Gaia-Wind 11kW Turbine," *Gaia-Wind Ltd*, United Kingdom.
[117] "OutBack radian Price Information " *Wind & Sun Ltd.* Available: http://www.windandsun.co.uk/products/Inverters/OutBack-Inverters/OutBack-Radian#.WBp7q_qLSUl
[118] (26/11/2016). "SMA Sunny Island Off Grid Inverters Price Information," *Wind & Sun Ltd.* Available: http://www.windandsun.co.uk/products/Inverters/SMA-Inverters/SMA-Sunny-Island-Off-Grid-Inverters#.VaxARcdVhBc
[119] (26/11/2016). "Studer Xtender Price Information," *Off-grid Europe.* Available: http://www.off-grid-europe.com/inverters/inverter-chargers/studer-innotec/studer-xtender-xth-6000-48-inverter-charger?
[120] (26/11/2016). "Scheneider Conext Price Information," *Wholesale Solar.* Available: http://www.wholesalesolar.com/2430013/schneider/inverters/schneider-conext-xw-6848-inverter
[121] (26/11/2016). "Victron Inverter Price Information," *Wind & Sun Ltd.* Available: http://www.windandsun.co.uk/products/Inverters/Victron-Inverters/Victron-InverterChargers#.WBqADvqLSUk
[122] M. Braun, "Models for Transient Simulations of Decentral Power Generation - Implementation and Verification in PowerFactory," Universität Stuttgart & Institut für Solare Energieversorgungstechnik (ISET), Stuttgart, Germany, 2005.
[123] S. M. Cuk, "Modelling, Analysis and Design of Switching Converters," PhD thesis, California Institute of Technology Pasadena, California, 1977.
[124] P. Strauss and A. Engler, "AC coupled PV hybrid systems and microgrids-state of the art and future trends," in *Proceedings of 3rd World Conference on Photovoltaic Energy Conversion*, 2003.
[125] "Off-Grid Inverter Sunny Island 8.0H/6.0H Installation Manual - Circuitry Overview," *SMA*.
[126] (26/11/2016). "Diesel Generator Price Information," *Generators Direct.* Available: http://www.generators-direct.co.uk/?gclid=Cj0KEQiAguXBBRCE_pbQ5reuq8MBEiQANji2LfWWreOuObJhtAoLVCWz_9TvX-GmSkhlVAY9fxlZm48aAgpS8P8HAQ
[127] O. Skarstein and K. Uhlen, "Design considerations with respect to long-term diesel saving in wind/diesel plants," *Wind Engineering,* vol. 13, pp. 72-87, 1989.

[128] (26/11/2016). "Rolls Batteries Price Information," *Wind & Sun Ltd.* Available: http://www.windandsun.co.uk/products/Batteries/Rolls-Batteries#.WH06SRuLTcs

[129] (26/11/2016). "Victron Lithium Ion Batteries Price Information," *Wind & Sun Ltd.* Available: http://www.windandsun.co.uk/products/Batteries/Lithium-Ion-Batteries/Victron-Lithium-Ion-Batteries#.WH07LhuLTcs

[130] (26/11/2016). "LG Chem Lithium Ion Batteries Price Information," *Wind & Sun Ltd.* Available: http://www.windandsun.co.uk/products/Batteries/Lithium-Ion-Batteries/LG-Chem-Lithium-Ion-Batteries#.WH06rBuLTcs

[131] Y. Zhang, C.-Y. Wang, and X. Tang, "Cycling degradation of an automotive LiFePO4 lithium-ion battery," *Journal of Power Sources,* vol. 196, pp. 1513-1520, 2011.

[132] E. Meissner and G. Richter, "The challenge to the automotive battery industry: the battery has to become an increasingly integrated component within the vehicle electric power system," *Journal of Power Sources,* vol. 144, pp. 438-460, 2005.

[133] F. Huet, "A review of impedance measurements for determination of the state-of-charge or state-of-health of secondary batteries," *Journal of Power Sources,* vol. 70, pp. 59-69, 1998.

[134] J. Guo, Z. Li, and M. Pecht, "A Bayesian approach for Li-Ion battery capacity fade modeling and cycles to failure prognostics," *Journal of Power Sources,* vol. 281, pp. 173-184, 2015.

[135] A. Barré, B. Deguilhem, S. Grolleau, M. Gérard, F. Suard, and D. Riu, "A review on lithium-ion battery ageing mechanisms and estimations for automotive applications," *Journal of Power Sources,* vol. 241, pp. 680-689, 2013.

[136] K. Takei, K. Kumai, Y. Kobayashi, H. Miyashiro, N. Terada, T. Iwahori, and T. Tanaka, "Cycle life estimation of lithium secondary battery by extrapolation method and accelerated aging test," *Journal of Power Sources,* vol. 97–98, pp. 697-701, 2001.

[137] H. Tazvinga, B. Zhu, and X. Xia, "Energy dispatch strategy for a photovoltaic–wind–diesel–battery hybrid power system," *Solar Energy,* vol. 108, pp. 412-420, 2014.

[138] B. Zhu, H. Tazvinga, and X. Xia, "Model Predictive Control for Energy Dispatch of a Photovoltaic-Diesel-Battery Hybrid Power System," *IFAC Proceedings Volumes,* vol. 47, pp. 11135-11140, 2014.

[139] C. Dennis Barley and C. Byron Winn, "Optimal dispatch strategy in remote hybrid power systems," *Solar Energy,* vol. 58, pp. 165-179, 1996.

[140] Y. Hu, J. M. Morales, S. Pineda, M. J. Sánchez, and P. Solana, "Dynamic multi-stage dispatch of isolated wind–diesel power systems," *Energy Conversion and Management,* vol. 103, pp. 605-615, 2015.

[141] X. Wang, A. Palazoglu, and N. H. El-Farra, "Operational optimization and demand response of hybrid renewable energy systems," *Applied Energy,* vol. 143, pp. 324-335, 2015.

[142] E. Dursun and O. Kilic, "Comparative evaluation of different power management strategies of a stand-alone PV/Wind/PEMFC hybrid power system," *International Journal of Electrical Power & Energy Systems,* vol. 34, pp. 81-89, 2012.

[143] D. Ipsakis, S. Voutetakis, P. Seferlis, F. Stergiopoulos, S. Papadopoulou, and C. Elmasides, "The effect of the hysteresis band on power management strategies in a stand-alone power system," *Energy,* vol. 33, pp. 1537-1550, 2008.

[144] T. Alnejaili, S. Drid, D. Mehdi, L. Chrifi-Alaoui, R. Belarbi, and A. Hamdouni, "Dynamic control and advanced load management of a stand-alone hybrid renewable power system for remote housing," *Energy Conversion and Management,* vol. 105, pp. 377-392, 2015.

[145] D. Feroldi, L. N. Degliuomini, and M. Basualdo, "Energy management of a hybrid system based on wind–solar power sources and bioethanol," *Chemical Engineering Research and Design,* vol. 91, pp. 1440-1455, 2013.

[146] M. Dali, J. Belhadj, and X. Roboam, "Theoretical and experimental study of control and energy management of a hybrid wind-photovoltaic system," in *8th International Multi-Conference on Systems, Signals & Devices*, 2011, pp. 1-7.

[147] A. Tani, M. B. Camara, and B. Dakyo, "Energy Management in the Decentralized Generation Systems Based on Renewable Energy-Ultracapacitors and Battery to Compensate the Wind/Load Power Fluctuations," *IEEE Transactions on Industry Applications,* vol. 51, pp. 1817-1827, 2015.

[148] M. R. Basir Khan, R. Jidin, and J. Pasupuleti, "Multi-agent based distributed control architecture for microgrid energy management and optimization," *Energy Conversion and Management,* vol. 112, pp. 288-307, 2016.

[149] R. Palma-Behnke, C. Benavides, F. Lanas, B. Severino, L. Reyes, J. Llanos, and D. Sáez, "A Microgrid Energy Management System Based on the Rolling Horizon Strategy," *IEEE Transactions on Smart Grid,* vol. 4, pp. 996-1006, 2013.

[150] S. N. Laboratories, "Stand-alone Photovoltaic Systems - A Handbook of Recommended Design Practices," *National Technical Information Service*, United States of America, 1991.

[151] A. M. Abd-el-Motaleb and S. K. Bekdach, "Optimal sizing of distributed generation considering uncertainties in a hybrid power system," *International Journal of Electrical Power & Energy Systems,* vol. 82, pp. 179-188, 2016.

[152] S. Sinha and S. S. Chandel, "Review of software tools for hybrid renewable energy systems," *Renewable and Sustainable Energy Reviews,* vol. 32, pp. 192-205, 2014.

[153] W. D. Kellogg, M. H. Nehrir, G. Venkataramanan, and V. Gerez, "Generation unit sizing and cost analysis for stand-alone wind, photovoltaic, and hybrid wind/PV systems," *IEEE Transactions on Energy Conversion,* vol. 13, pp. 70-75, 1998.

[154] L. K. Gan, J. K. H. Shek, and M. A. Mueller, "Optimisation sizing of hybrid wind-diesel systems using linear programming technique," in *7th IET International Conference on Power Electronics, Machines and Drives (PEMD)*, 2014, pp. 1-6.

[155] M. K. Deshmukh and S. S. Deshmukh, "Modeling of hybrid renewable energy systems," *Renewable and Sustainable Energy Reviews,* vol. 12, pp. 235-249, 2008.

[156] H. C. Chen, "Optimum capacity determination of stand-alone hybrid generation system considering cost and reliability," *Applied Energy,* vol. 103, pp. 155-164, 2013.

[157] Y. Luo, L. Shi, and G. Tu, "Optimal sizing and control strategy of isolated grid with wind power and energy storage system," *Energy Conversion and Management,* vol. 80, pp. 407-415, 2014.

[158] X. Hu, S. J. Moura, N. Murgovski, B. Egardt, and D. Cao, "Integrated Optimization of Battery Sizing, Charging, and Power Management in Plug-In Hybrid Electric Vehicles," *IEEE Transactions on Control Systems Technology,* vol. 24, pp. 1036-1043, 2016.

[159] J. Rurgladdapan, K. Uthaichana, and B. Kaewkham-ai, "Li-Ion battery sizing and dynamic programming for optimal power-split control in a hybrid electric vehicle," in *9th International Conference on Electrical Engineering, Electronics, Computer, Telecommunications and Information Technology*, 2012, pp. 1-5.

[160] J. V. Roy, S. D. Breucker, and J. Driesen, "Analysis of the optimal battery sizing for plug-in hybrid and battery electric vehicles on the power consumption and V2G availability," in *16th International Conference on Intelligent System Applications to Power Systems*, 2011, pp. 1-6.

[161] V. Carpentiero, R. Langella, and A. Testa, "Hybrid wind-Diesel stand-alone system sizing accounting for fuel price uncertainty," in *2010 IEEE 11th International Conference on Probabilistic Methods Applied to Power Systems (PMAPS)*, 2010, pp. 101-106.

[162] B. Viswanathan, "Chapter 12 - Batteries," in *Energy Sources*, ed Amsterdam: Elsevier, 2017, pp. 263-313.

[163] D. A. J. Rand and P. T. Moseley, "Chapter 13 - Energy Storage with Lead–Acid Batteries," in *Electrochemical Energy Storage for Renewable Sources and Grid Balancing*, ed: Elsevier, pp. 201-222, 2015.

[164] R. Belfkira, L. Zhang, and G. Barakat, "Optimal sizing study of hybrid wind/PV/diesel power generation unit," *Solar Energy,* vol. 85, pp. 100-110, 2011.

[165] L. Zhang, R. Belfkira, and G. Barakat, "Wind/PV/diesel energy system: Modeling and sizing optimization," in *Proceedings of the 14th European Conference on Power Electronics and Applications (EPE)*, 2011, pp. 1-10.

[166] (10/9/2013). "The British Atmospheric Data Centre (BADC)," Available: http://badc.nerc.ac.uk/home/index.html

[167] S. Rusck, "The simultaneous demand in distribution network supplying domestic consumers," *ASEA Journal,* vol. 10, pp. 59-61, 1956.

[168] J. Dickert and P. Schegner, "Residential load models for network planning purposes," in *Modern Electric Power Systems*, 2010, pp. 1-6.

[169] P. Boait, V. Advani, and R. Gammon, "Estimation of demand diversity and daily demand profile for off-grid electrification in developing countries," *Energy for Sustainable Development,* vol. 29, pp. 135-141, 2015.

[170] H. Wenzl, I. Baring-Gould, R. Kaiser, B. Y. Liaw, P. Lundsager, J. Manwell, A. Ruddell, and V. Svoboda, "Life prediction of batteries for selecting the technically most suitable and cost effective battery," *Journal of Power Sources,* vol. 144, pp. 373-384, 2005.

[171] H. Bindner, T. Cronin, P. Lundsager, J. F. Manwell, U. Abdulwahid, and I. Baring-Gould, "Lifetime modelling of lead acid batteries," Risø National Laboratory, Roskilde, Denmark, April 2005.

[172] J. F. Manwell, A. Rogers, G. Hayman, C. T. Avelar, and J. G. McGowan, "Hybrid2- A hybrid system simulation model -Theory Manual," Renewable Energy Research Laboratory, Department of Mechanical Engineering, University of Massachusetts, November 1998.

[173] A. M. Gee, F. V. P. Robinson, and R. W. Dunn, "Analysis of Battery Lifetime Extension in a Small-Scale Wind-Energy System Using Supercapacitors," *IEEE Transactions on Energy Conversion,* vol. 28, pp. 24-33, 2013.

[174] J. Li, A. M. Gee, M. Zhang, and W. Yuan, "Analysis of battery lifetime extension in a SMES-battery hybrid energy storage system using a novel battery lifetime model," *Energy,* vol. 86, pp. 175-185, 2015.

[175] E. Hittinger, T. Wiley, J. Kluza, and J. Whitacre, "Evaluating the value of batteries in microgrid electricity systems using an improved Energy Systems Model," *Energy Conversion and Management,* vol. 89, pp. 458-472, 2015.

[176] R. A. Messenger and J. Ventre, *Photovoltaic Systems Engineering*: CRC Press, 2010.

[177] H. Yang, Z. Wei, and L. Chengzhi, "Optimal design and techno-economic analysis of a hybrid solar–wind power generation system," *Applied Energy,* vol. 86, pp. 163-169, 2009.

[178] (2015). "Approximate Fuel Consumption Chart," *Diesel Service and Supply Ltd.* Available: http://www.dieselserviceandsupply.com/Diesel_Fuel_Consumption.aspx

[179] (2014). "Data Sheet - Generator Set Model DGDB," *Cummins Power Generation Inc.* Available: https://powersuite.cummins.com/PS5/PS5Content/SiteContent/en/Binary_Asset/pdf/Commercial/Diesel/d-3425.pdf

[180] (1/5/2013). "Fuel Burn Calculator," *Hardy Diesel Generators Ltd.* Available: http://www.hardydiesel.com/generator-fuel-consumption-calculator.html

[181] (9/5/2013). "Monthly and annual prices of road fuels and petroleum products," *Department of Energy & Climate Change (DECC).* Available: www.gov.uk/government/statistical-data-sets/oil-and-petroleum-products-monthly-statistics

[182] *Sunny Island 4500 - Installation & operating instructions*: SMA, 2004.

[183] G. Ding, F. Gao, S. Zhang, P. C. Loh, and F. Blaabjerg, "Control of hybrid AC/DC microgrid under islanding operational conditions," *Journal of Modern Power Systems and Clean Energy,* vol. 2, pp. 223-232, 2014.

[184] A. Engler, "Regelung von Batteriestromrichtern in modularen und erweiterbaren Inselnetzen," PhD thesis, Universität Gesamthochschule Kassel, 2001.

[185] M. K. Kazimierczuk, *Pulse-width Modulated DC-DC Power Converters*: Wiley-Blackwell, September 2008.

[186] M. H. Rashid, *Power Electronics Handbook*, Third ed.: Butterworth-Heinemann Ltd, Jan 2011.

[187] A. Ioinovici, *Power Electronics and Energy Conversion Systems: Fundamentals and Hard-switching Converters* vol. 1: Wiley-Blackwell, May 2013.

[188] P. Pany, R. K. Singh, and R. K. Tripathi, "Bidirectional DC-DC converter fed drive for electric vehicle system," *International Journal of Engineering, Science and Technology,* vol. 3, pp. 101-110, April 2011.

[189] P. Cominos and N. Munro, "PID controllers: recent tuning methods and design to specification," *IEE Proceedings - Control Theory and Applications,* vol. 149, pp. 46-53, 2002.

[190] (3/2/2017). "MathWorks R2013b SimPowerSystems Documentation - Battery," *MathWorks.* Available: https://uk.mathworks.com/help/releases/R2013b/physmod/sps/powersys/ref/battery.html?searchHighlight=battery;jsessionid=65c142f0e613a995cb638abede82

[191] J. A. Peas Lopes, C. L. Moreira, and A. G. Madureira, "Defining control strategies for microgrids islanded operation," *IEEE Transactions on Power Systems,* vol. 21, pp. 916-924, 2006.

[192] Q. C. Zhong and G. Weiss, "Synchronverters: Inverters That Mimic Synchronous Generators," *IEEE Transactions on Industrial Electronics,* vol. 58, pp. 1259-1267, 2011.

[193] C. C. L. Moreira, "Identification and Development of Microgrids Emergency Control Procedures," PhD Dissertation, Faculty of Engineering, University of Porto, 2008.

[194] H. Han, X. Hou, J. Yang, J. Wu, M. Su, and J. M. Guerrero, "Review of Power Sharing Control Strategies for Islanding Operation of AC Microgrids," *IEEE Transactions on Smart Grid,* vol. 7, pp. 200-215, 2016.

[195] J. Rocabert, A. Luna, F. Blaabjerg, and P. Rodriguez, "Control of Power Converters in AC Microgrids," *IEEE Transactions on Power Electronics,* vol. 27, pp. 4734-4749, 2012.

[196] P. Wang, C. Jin, D. Zhu, Y. Tang, P. C. Loh, and F. H. Choo, "Distributed Control for Autonomous Operation of a Three-Port AC/DC/DS Hybrid Microgrid," *IEEE Transactions on Industrial Electronics,* vol. 62, pp. 1279-1290, 2015.

[197] A. Gkika, "Microgrid Operation for Remote Rural Communities," MSc Dissertation, School of Engineering, The University of Edinburgh, 2010.

[198] J. Chi, L. Poh Chiang, W. Peng, M. Yang, and F. Blaabjerg, "Autonomous operation of hybrid AC-DC microgrids," in *IEEE International Conference on Sustainable Energy Technologies (ICSET)*, 2010, pp. 1-7.

[199] H. H. Zeineldin and J. L. Kirtley, Jr., "Micro-grid operation of inverter based distributed generation with voltage and frequency dependent loads," in *IEEE Power & Energy Society General Meeting (PES).* , 2009, pp. 1-6.

[200] C. L. Moreira, F. O. Resende, and J. A. Peas Lopes, "Using low voltage microgrids for service restoration," *IEEE Transactions on Power Systems,* vol. 22, pp. 395-403, 2007.

[201] A. Tuladhar, K. Jin, T. Unger, and K. Mauch, "Parallel operation of single phase inverter modules with no control interconnections," in *IEEE Applied Power Electronics Conference and Exposition (APEC)*, 1997, pp. 94-100.

[202] (15/1/2017). "Engineering Recommendation G59 (Issue 3 Amendment 1 August 2014)," *Energy Networks Association (ENA).* Available: http://www.amps.org.uk/static/assets/downloads/DraftG5931_170914updatev1280115trackchangev4.pdf?attach

[203] P. Jain, *Wind Energy Engineering*: McGraw-Hill, 2010.

[204] I. Paraschivoiu, *Wind Turbine Design: With Emphasis on Darrieus Concept*: Polytechnic International Press, 2002.

[205] REUK. "Wind Turbine Tip Speed Ratio," Available: http://www.reuk.co.uk/Wind-Turbine-Tip-Speed-Ratio.htm

[206] "Power Performance Certification Test of a Model GW 133-11 Wind Turbine," *TUV NEL Ltd., Report No. 2010/204,* , 2010.

[207] "Design Aeroelastic Loads Gaia-Wind 11kW Turbine 18[m] Tubular Tower," *Gaia Wind Ltd., Report No. GWTD0028*, 2011.

[208] J. Andringa, "Gaia-Wind GW133-11 kW Summary Report for UK MSC," *Gaia-Wind Ltd*, United Kingdom, 2010.

[209] J. Rees, M. Kjellberg, and S. Kling, "Softstarter Handbook," *ABB*, ,2010.

[210] R. Ferraz and E. C. d. Nascimento, "Soft-starter Application Guide," *WEG*, 2009.

[211] M. Ghadimi, A. Ramezani, and M. Mohammadimehro, "Soft starter modeling for an induction drive starting study in an industrial plant," in *Fifth UKSim European Symposium on Computer Modeling and Simulation (EMS)*, 2011, pp. 245-250.

[212] "Soft-starter SSW-07 User's Guide," *WEG Electric Corporation*, United States.

[213] "BS EN 61000-3-3:2013 - Electromagnetic compatibility (EMC) - Part 3-3: Limits - Limitation of voltage changes, voltage fluctuations and flicker in public low-voltage supply systems, for equipment with rated current $\leqslant$ 16 A per phase and not subject to conditional connection," 2013.

[214] W. S. E. Abdel-Latif, A. H. K. Alaboudy, H. E. Mostafa, and M. Y. Fekry, "Evaluation and mitigation of voltage flicker caused by constant speed wind turbines," in *IEEE PES Conference on Innovative Smart Grid Technologies - Middle East*, 2011, pp. 1-6.

[215] D. A. Spera, *Wind Turbine Technology: Fundamental Concepts in Wind Turbine Engineering*. New York: ASME Press, 1994.

[216] N. Stannard and J. R. Bumby, "Performance aspects of mains connected small-scale wind turbines," *IET Generation, Transmission & Distribution,* vol. 1, pp. 348-356, 2007.

[217] C. Nichita, D. Luca, B. Dakyo, and E. Ceanga, "Large band simulation of the wind speed for real time wind turbine simulators," *IEEE Transactions on Energy Conversion,* vol. 17, pp. 523-529, 2002.

[218] E. Welfonder, R. Neifer, and M. Spanner, "Development and experimental identification of dynamic models for wind turbines," *Control Engineering Practice,* vol. 5, pp. 63-73, 1997.

[219] I. Van der Hoven, "Power spectrum of horizontal wind speed in frequency range from 0.0007 to 900 cycles per hour," *Journal of Meteorology,* vol. 14, pp. 160-164, 1957.

[220] A. P. Prudnikov, Y. A. Brychkov, and O. I. Marichev, *Integrals and Series: Elementary Functions Vol 1*: Gordon and Breach SA, 1991.

[221] *European Standard for Wind Loads – Eurocode EN 1991-1-4 WIND ACTIONS*.

[222] S. Krishnamurthy, T. M. Jahns, and R. H. Lasseter, "The operation of diesel gensets in a CERTS microgrid," in *IEEE Power and Energy Society General Meeting - Conversion and Delivery of Electrical Energy in the 21st Century*, 2008, pp. 1-8.

[223] S. D. Alley, "Generator Basics: Applied to Field Problems," *ANNA Inc.*, 1993.

[224] M. J. Hu and G. F. Yang, "Simulation of Speed Controlling System on Diesel Engine Based on FN," in *Fourth International Symposium on Knowledge Acquisition and Modeling (KAM)*, 2011, pp. 358-361.

[225] J. Mamboundou and N. Langlois, "Application of indirect adaptive model predictive control supervised by fuzzy logic to a diesel generator," in *9th IEEE International Conference on Control and Automation (ICCA)*, 2011, pp. 1037-1043.

[226] C. Mai, K. Jepsen, Y. Zhenyu, L. Hansen, and K. K. Madsen, "Intelligent control of diesel generators using gain-scheduling: Based on online external-load estimation," in *International Electronics and Application Conference and Exposition (PEAC)*, 2014, pp. 966-971.

[227] K. E. Yeager and J. R. Willis, "Modeling of emergency diesel generators in an 800 megawatt nuclear power plant," *IEEE Transactions on Energy Conversion,* vol. 8, pp. 433-441, 1993.

[228] M. S. Ismail, M. Moghavvemi, and T. M. I. Mahlia, "Genetic algorithm based optimization on modeling and design of hybrid renewable energy systems," *Energy Conversion and Management,* vol. 85, pp. 120-130, 2014.

[229] F. Garcia and C. Bordons, "Optimal economic dispatch for renewable energy microgrids with hybrid storage using Model Predictive Control," in *39th Annual Conference of the IEEE Industrial Electronics Society (IECON)*, 2013, pp. 7932-7937.

[230] J. Zeng, M. Li, J. F. Liu, J. Wu, and H. W. Ngan, "Operational optimization of a stand-alone hybrid renewable energy generation system based on an improved genetic algorithm," in *IEEE Power and Energy Society General Meeting*, 2010, pp. 1-6.

[231] H. Dagdougui, R. Minciardi, A. Ouammi, M. Robba, and R. Sacile, "A dynamic decision model for the real-time control of hybrid renewable energy production systems," *IEEE Systems Journal,* vol. 4, pp. 323-333, 2010.

[232] A. Messac, *Optimization in Practice with MATLAB®: For Engineering Students and Professionals*: Cambridge University Press, 2015.

[233] D. A. Coley, *An Introduction to Genetic Algorithms for Scientists and Engineers*: World Scientific, 1999.

[234] J. Arora, *Introduction to Optimum Design*, 3rd ed.: Academic Press, 2011.

[235] P. Venkataraman, *Applied Optimization with MATLAB Programming*, 2nd ed.: John Wiley & Sons, 2009.

[236] A. Bianchini, N. Magnelli, G. Ferrara, E. A. Carnevale, and L. Ferrari, "Optimization of a PV-wind-Diesel Hybrid System for a Remote Stand-alone Application," *Energy Procedia,* vol. 81, pp. 133-145, 2015.

[237] B.-M. Hodge, A. Florita, K. Orwig, D. Lew, and M. Milligan, "A Comparison of Wind Power and Load Forecasting Error Distributions," presented at the 2012 World Renewable Energy Forum Denver, Colorado, 2012.

[238] B.-M. Hodge and M. Milligan, "Wind Power Forecasting Error Distributions over Multiple Timescales," presented at the Power & Energy Society General Meeting, Michigan, 2011.

[239] M. Brower, "Wind Energy Forecasting," ed. Cambridge, United States: Massachusetts Institute of Technology (MIT), 2011.

[240] A. E. Clements, A. S. Hurn, and Z. Li, "Forecasting day-ahead electricity load using a multiple equation time series approach," *European Journal of Operational Research*.

[241] J. Wu, B. Zhang, H. Li, Z. Li, Y. Chen, and X. Miao, "Statistical distribution for wind power forecast error and its application to determine optimal size of energy storage system," *International Journal of Electrical Power & Energy Systems,* vol. 55, pp. 100-107, 2014.

[242] (4/2/2017). "Sunny Island 6.0H / 8.0H Brochure," *SMA Solar Technology AG.* Available: http://files.sma.de/dl/2485/SI_6H8H-AEN131411W.pdf

[243] B. Neammanee, S. Sirisumrannukul, and S. Chatratana, "Development of a wind turbine simulator for wind generator testing," *International Energy Journal 8,* pp. 21-28, 2007.

[244] "Parker 690+ Series AC Drive - Product Manual," *Parker Hannifin Ltd.*, 2010.

[245] Q. Y. Zhao, C. H. Sheng, and A. Afjeh, "Computational Aerodynamic Analysis of Offshore Upwind and Downwind Turbines," *Journal of Aerodynamics,* vol. 2014, p. 13, 2014.

[246] F. Zahle, H. A. Madsen, and N. N. Sørensen, "Research in Aeroelasticity EFP-2007-II," *Danmarks Tekniske Universitet, Risø Nationallaboratoriet for Bæredygtig Energi*.

[247] S. Wagner, R. Bareiβ, and G. Guidati, *Wind Turbine Noise*: Springer-Verlag, 1996.

[248] D. S. L. Dolan and P. W. Lehn, "Simulation model of wind turbine 3p torque oscillations due to wind shear and tower shadow," *IEEE Transactions on Energy Conversion,* vol. 21, pp. 717-724, 2006.

[249] P. Sørensen, A. D. Hansen, and P. A. C. Rosas, "Wind models for simulation of power fluctuations from wind farms," *Journal of Wind Engineering and Industrial Aerodynamics,* vol. 90, pp. 1381-1402, 2002.

[250] J. D. M. De Kooning, T. L. Vandoorn, J. Van de Vyver, B. Meersman, and L. Vandevelde, "Shaft speed ripples in wind turbines caused by tower shadow and wind shear," *IET Renewable Power Generation,* vol. 8, pp. 195-202, 2014.

[251] H. Weihao, S. Chi, and C. Zhe, "Impact of wind shear and tower shadow effects on power system with large scale wind power penetration," in *37th Annual Conference on IEEE Industrial Electronics Society (IECON)*, 2011, pp. 878-883.

[252] J. Tan, W. Hu, X. Wang, and Z. Chen, "Effect of Tower Shadow and Wind Shear in a Wind Farm on AC Tie-Line Power Oscillations of Interconnected Power Systems," *Energies,* vol. 6, p. 6352, 2013.

[253] J. M. Nye, J. G. de la Bat, M. A. Khan, and P. Barendse, "Design and implementation of a variable speed wind turbine emulator," in *International Conference on Electrical Machines (ICEM)*, 2012, pp. 2060-2065.

[254] S. Wan, L. Cheng, and X. Sheng, "Effects of Yaw Error on Wind Turbine Running Characteristics Based on the Equivalent Wind Speed Model," *Energies,* vol. 8, p. 6286, 2015.

[255] R. Fadaeinedjad, G. Moschopoulos, and M. Moallem, "The Impact of Tower Shadow, Yaw Error, and Wind Shears on Power Quality in a Wind-Diesel System," *IEEE Transactions on Energy Conversion,* vol. 24, pp. 102-111, 2009.

[256] E. Sakasegawa, K. Shinohara, K. Yamamoto, and M. Hombu, "Characteristic analysis of a wind power system with doubly fed induction generator in considering of the tower shadow effect," in *International Power Electronics Conference (IPEC)*, 2010, pp. 3225-3229.

[257] A. G. Abo-Khalil, "A new wind turbine simulator using a squirrel-cage motor for wind power generation systems," in *IEEE Ninth International Conference on Power Electronics and Drive Systems (PEDS)*, 2011, pp. 750-755.

[258] C. Zhou, K. Qian, M. Allan, and W. Zhou, "Modeling of the Cost of EV Battery Wear Due to V2G Application in Power Systems," *IEEE Transactions on Energy Conversion,* vol. 26, pp. 1041-1050, 2011.

[259] C. J. Zhan, X. G. Wu, S. Kromlidis, V. K. Ramachandaramurthy, M. Barnes, N. Jenkins, and A. J. Ruddell, "Two electrical models of the lead-acid battery used in a dynamic voltage restorer," *IEE Proceedings - Generation, Transmission and Distribution,* vol. 150, pp. 175-182, 2003.

[260] G. Lutzemberger, "Cycle life evaluation of lithium cells subjected to micro-cycles," in *5th International Youth Conference on Energy (IYCE)*, 2015, pp. 1-5.

[261] M. Ceraolo, A. D. Donato, C. Miulli, and G. Pede, "Microcycle-based efficiency of hybrid vehicle batteries," in *IEEE Conference Vehicle Power and Propulsion*, 2005, pp. 233-237.

[262] M. Reiso, "The Tower Shadow Effect in Downwind Wind Turbines," PhD Thesis, Department of Civil and Transport Engineering, Norwegian University of Science and Technology (NTNU), Norway, May 2013.

[263] S. R. J. Powles, "The effects of tower shadow on the dynamics of a horizontal axis wind turbine," *Wind Engineering,* vol. 7, pp. 26-42, 1983.

[264] R. D. Blevins, *Flow-Induced Vibrations*. New York: Van Nostrand Reinhold, 1990.

[265] H. Schlichting and K. Gersten, *Boundary-Layer Theory*. Berlin: Springer, 2000.

[266] H. A. Madsen, J. Johansen, N. N. Sørensen, G. C. Larsen, and M. H. Hansen, "Simulation of low frequency noise from a downwind wind turbine rotor," in *45th AIAA Aerospace Sciences Meeting and Exhibit*, pp. 1-12, 2007.

[267] M. Molinari, M. Pozzi, D. Zonta, and L. Battisti, "In-field testing of a steel wind turbine tower," in *International Modal Analysis Conference (IMAC) XXVIII*, Florida USA, 2010.

[268] K. Koga, R. Ueda, and T. Sonoda, "Stability problem in induction motor drive system," in *IEEE Industry Applications Society Annual Meeting*, 1988, pp. 129-136.

[269] R. Ueda, T. Sonoda, K. Koga, and M. Ichikawa, "Stability analysis in induction motor driven by v/f controlled general-purpose inverter," *IEEE Transactions on Industry Applications,* vol. 28, pp. 472-481, 1992.

[270] J. C. Forman, S. J. Moura, J. L. Stein, and H. K. Fathy, "Optimal Experimental Design for Modeling Battery Degradation," pp. 309-318, 2012.

[271] P. Palensky and D. Dietrich, "Demand Side Management: Demand Response, Intelligent Energy Systems, and Smart Loads," *IEEE Transactions on Industrial Informatics,* vol. 7, pp. 381-388, 2011.

[272] Z. Zeng, H. Yang, R. Zhao, and C. Cheng, "Topologies and control strategies of multi-functional grid-connected inverters for power quality enhancement: A comprehensive review," *Renewable and Sustainable Energy Reviews,* vol. 24, pp. 223-270, 2013.

[273] M. Büyük, A. Tan, M. Tümay, and K. Ç. Bayındır, "Topologies, generalized designs, passive and active damping methods of switching ripple filters for voltage source inverter: A comprehensive review," *Renewable and Sustainable Energy Reviews,* vol. 62, pp. 46-69, 2016.

[274] L. Wei and G. Joos, "A power electronic interface for a battery supercapacitor hybrid energy storage system for wind applications," in *IEEE Power Electronics Specialists Conference (PECS)*, 2008, pp. 1762-1768.

[275] L. Wei, G. Joos, and J. Belanger, "Real-Time Simulation of a Wind Turbine Generator Coupled With a Battery Supercapacitor Energy Storage System," *IEEE Transactions on Industrial Electronics,* vol. 57, pp. 1137-1145, 2010.

[276] G. Guidi, T. M. Undeland, and Y. Hori, "An Interface Converter with Reduced VA Ratings for Battery-Supercapacitor Mixed Systems," in *Power Conversion Conference (PCC)*, Nagoya, 2007, pp. 936-941.

[277] Z. Haihua, T. Bhattacharya, T. Duong, T. S. T. Siew, and A. M. Khambadkone, "Composite Energy Storage System Involving Battery and Ultracapacitor With Dynamic Energy Management in Microgrid Applications," *IEEE Transactions on Power Electronics,* vol. 26, pp. 923-930, 2011.

[278] I. Richardson, M. Thomson, D. Infield, and C. Clifford, "Domestic electricity use: A high-resolution energy demand model," *Energy and Buildings,* vol. 42, pp. 1878-1887, 2010.

[279] A. Capasso, W. Grattieri, R. Lamedica, and A. Prudenzi, "A bottom-up approach to residential load modeling," *IEEE Transactions on Power Systems,* vol. 9, pp. 957-964, 1994.

[280] R. Yao and K. Steemers, "A method of formulating energy load profile for domestic buildings in the UK," *Energy and Buildings,* vol. 37, pp. 663-671, 2005.

[281] M. Newborough and P. Augood, "Demand-side management opportunities for the UK domestic sector," *IEE Proceedings on Generation, Transmission and Distribution,* vol. 146, pp. 283-293, 1999.

[282] L. K. Gan, "Synchronisation Control and Operation of Microgrids for Rural/Island Applications," MSc Dissertation, University of Edinburgh, Edinburgh, 2012.

[283] L. Chia-Tse, J. Ruei-Pei, and C. Po-Tai, "A Grid Synchronization Method for Droop-Controlled Distributed Energy Resource Converters," *IEEE Transactions on Industry Applications,* vol. 49, pp. 954-962, 2013.

[284] C. Changhee, J. Jin-Hong, K. Jong-Yul, K. Soonman, P. Kyongyop, and K. Sungshin, "Active synchronizing control of a microgrid," *IEEE Transactions on Power Electronics,* vol. 26, pp. 3707-3719, 2011.

[285] K. S. Parlak, "Synchronization of an inverter to a distributed power network," in *International Symposium on Power Electronics Electrical Drives Automation and Motion (SPEEDAM)*, 2010, pp. 599-602.

[286] L. Freris and D. Infield, *Renewable Energy in Power Systems*: John Wiley & Sons, 2008.

[287] N. Jenkins, R. Allan, P. Crossley, D. Kirchen, and G. Strbac, *Embedded Generation*. London: IEE Power and Engineering Series 31, Institution of Engineering and Technology, 2000.

[288] "Gaia Wind 133 Technical Guide," *Gaia-Wind Ltd.*, United Kingdom, July 2012.

[289] N. B. Venkateswarlu, *Computer Science and Information Technology for GATE*: Tata McGraw-Hill Education.

Appendix A – Load Modelling

Due to the measured load data is not freely available, this work has adopted a detailed "bottom-up" load model which was developed in [51] and it will be briefly described here for the sake of completeness. In addition, the load model in reference [51] was developed using Simulink software, which further reduces the complexity of utilising it in this research. Other similar "bottom-up" load modelling methodologies can be referred from the work in [278] [279] [280].

In the load model of this work, a defined time window has been associated for each action/event to take place (e.g. waking up, washing dishes, watching television and etc). A random number which was created for each activity, was then added onto the window starting time to determine exactly when the action will be started [51]. In addition, this model has assigned attributes to individuals so that they cannot perform irrational activity such as vacuuming while using the computer and listening to the radio.

Each electrical device consumes active power and reactive power. Since the power factor (PF) of a device can be related as:

$$\mathrm{PF} = \cos\theta = \frac{P}{S} \tag{A1}$$

and the vector triangle of P, Q and S can be expressed as:

$$S = \sqrt{P^2 + Q^2} \tag{A2}$$

The reactive power of a device is obtained as:

$$\mathrm{Q} = \sqrt{\left(\frac{P}{\cos\theta}\right)^2 - P^2} \tag{A3}$$

Typically, a household contains several electrical devices which can be categorised as [51]:

- Electronics and entertainment
- Lighting
- Motors
- Heating

Electronic and entertainment devices such as televisions, personal computers, radios, game consoles generally contain switch mode power supplies (SMPS). The smaller power ratings SMPS (below 75W) do not require power factor corrections whereas devices above 75W are required by law to maintain a given power factor under regulation standard EN61000-3-2. Therefore, it can be concluded that the smaller SMPS loads have lower PF. Several lighting options for a typical household are the incandescent, compact fluorescent light, and fluorescent lamp. Small single phase motors (usually induction) which can be found in fridges, washing machines, dishwashers and other small pumps and fans throughout the property. Finally, the electrical devices for heating purposes consist of electric heaters, kettles, water heaters, microwave and irons. Table tabulates the power factors being associated for various electrical devices modelled in this work. Using equation (A3), the reactive power of an electrical device can be computed by using its real power and power factor. Note that the power factor of the electrical devices modelled in this work may be lower than reality due to the change/improvement in power conversion technologies. Figure A1 shows the comparison between the measured and simulated power factor from aggregated loads (56 dwellings) throughout the day [278]. The measured power factor was observed to fluctuate between 0.86 and 0.99. During the night, the power factor is reduced and fluctuated more significantly because cooling appliances (which utilise induction machines) are at a higher proportion of the overall load demand.

Category	Electronics		Lighting			Motors	Heating	
Type	SMPS (< 75W)	SMPS (> 75W)	Incandescent	CFL	Fluorescent Lamp	1-phase Induction	Space / Water	Microwave / Iron
Power factor	0.63	0.98	0.99	0.95	0.9	0.83	0.99	0.83

Table A1: Electrical devices power factor [51]

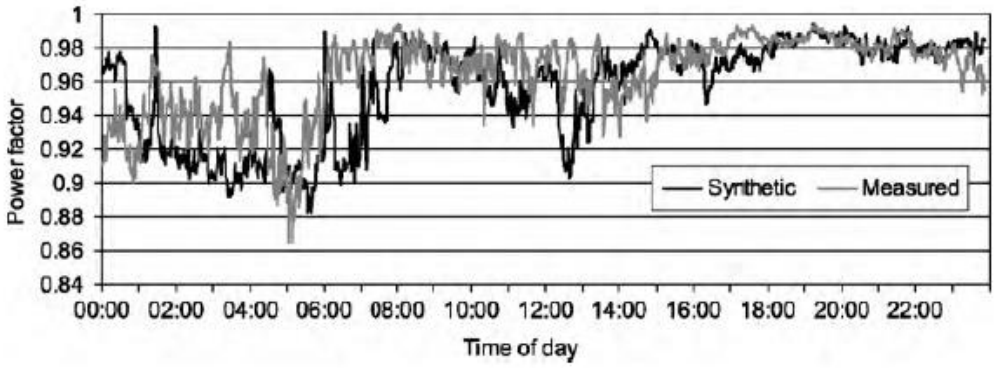

Figure A1: Power factor comparison from the aggregated loads throughout the day

Figure shows the overview of the load model which was implemented in Simulink. It consists of daily scheduling block, elapsed time activities block, and various electrical devices which consume a different level of active and reactive powers based on their power factors and power ratings. It is important to emphasise that this model was built based on two full-time (9am to 6pm) working adults occupancy in mind, therefore no activities were taken place in the afternoon.

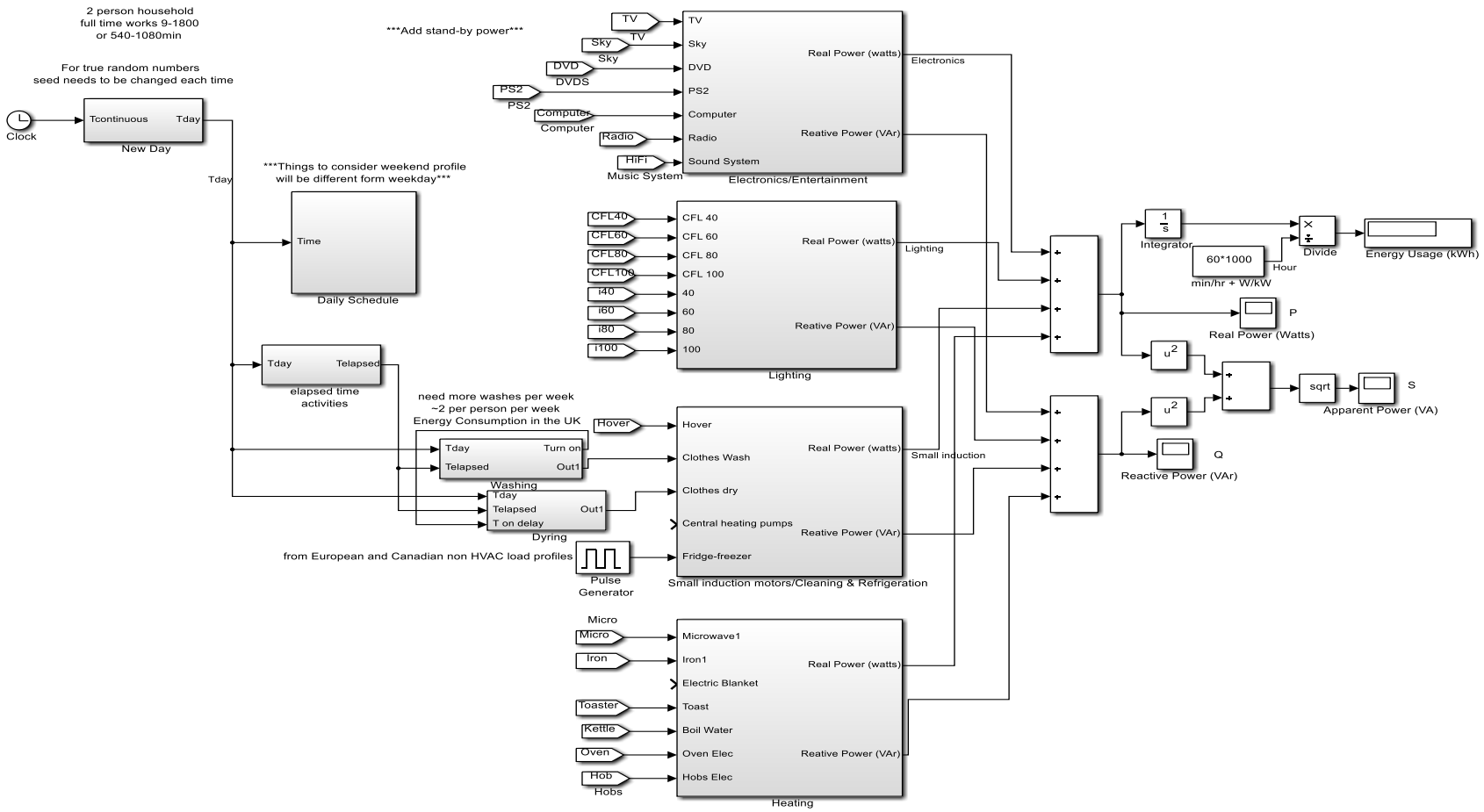

Figure A2: Overview of load Simulink model

The scheduling block controls the household member's waking up and sleeping time. This information is then used for the device usage and task execution in the household. In addition, the design of the building and layout of the devices in each room has been considered in the scheduling process. It means that the links has been made between the electrical appliances and the rooms. For example, when the TV in the living room is switched-on during night time, the lights in the living room will be turned on and the lights in the kitchen will be off if no one is using any appliances there. Links can also be made between devices so that the DVD players and the game consoles require the TV to be on.

Furthermore, most of the electrical appliances usage is directly linked to the human attributes which consist of ears, eyes and hands. Some appliances such as the computer and game console require hands, eyes and sometimes ears. Other tasks are effectively obstructing the use of some human attributes [51]. For instance, vacuuming requires the use of hands and eyes but hinder the use of ears for other activities. On the other hand, some devices can be used by multiple people at the same time for example watching TV, playing games and listening music together. In short, the scheduling block takes care of the concerns mentioned with the implementation of some logics [51]. Certain tasks require no continued human attributes once started. These are known as time elapsed/non-effort driven tasks. The examples are washing machines, dishwashers and some cooking appliances like ovens and microwaves. In this model, they are controlled by elapsed time logics.

Some devices are programmed to work in a more complex manner and require more detailed analysis. Figure A3 shows the load pattern of a washing machine on a 40ºC cycle [281]. The first large load period can be attributed to the initial water heating process. The amplitude and period will increase or decrease based on the temperature setting. Subsequently, the load spikes are the cleaning cycles with the larger spinning cycle at the end [51]. In addition, the power factor varies throughout the washing period. The initial water heating will be more resistive and hence the power factor will be close to unity. During the wash and spin cycles, single phase induction motor is mainly utilised, thus having a power factor of approximately 0.83. The refrigerator has a distinct load behaviour compared to other types of load. Its working principle is

based on the hysteresis control of compressors. The thermistor reads the temperature of the fridge and turns on the compressor when the upper pre-set temperature threshold is met. The same principle applies to the turn-off sequence. Therefore, a pulsing sequence will be observed from the refrigerator especially during the night when the inside temperature is not disrupted.

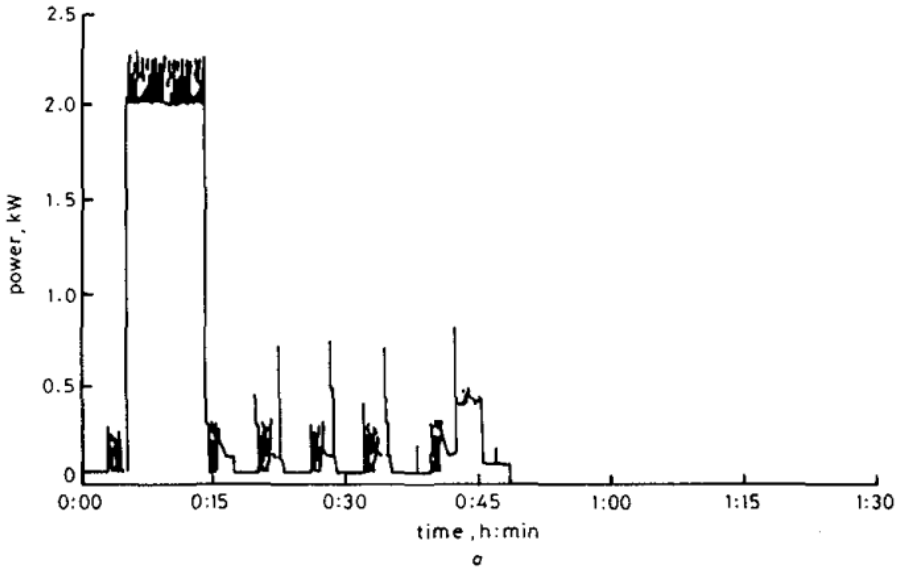

Figure A3: Washing machine load signature on 40ºC cycle [281]

A single household load profile (Figure A4) was generated by running the complete load model in Simulink. The resulted energy used per day was 18.69 kWh, which is close to UK's typical single household usage.

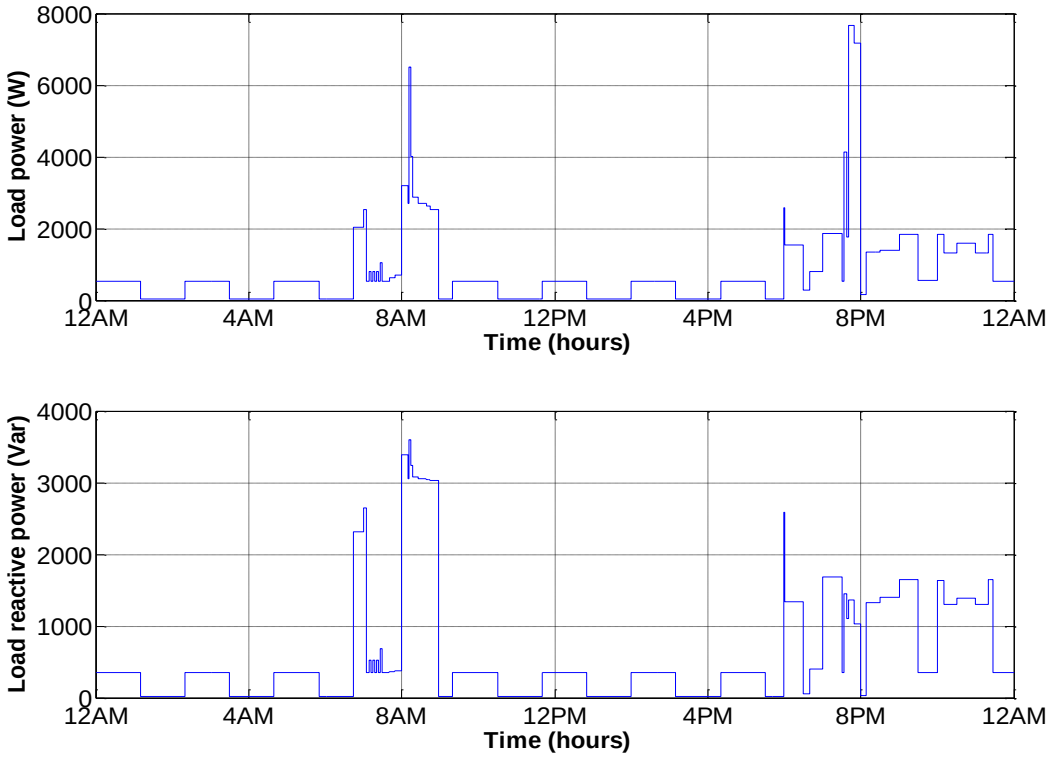

Figure A4: Single household load profile (active and reactive power) [51]

A closer examination of the load profile shows that there are several distinct phases throughout the day. From midnight until about 7am, only the base load is noticed, which consists mainly the refrigeration compressor cycles and the standby loads. The next phase occurs between 7am and 9am where people wake up, turn on the lights, make breakfast and get ready to work. The final phase is the post-work period which the peak load commonly occurs. Various activities such as doing domestic chores (washing, ironing, vacuuming and cooking for dinner) and enjoying in-house entertainments (TV, PC, radio and video games) took place during the night period. As mentioned before, this model was built for two people who are working full-time and thus no activities are involved during lunch time at home. All in all, the resulting load profile is sufficiently realistic as the main objective of this work lies on the optimal operation of the hybrid system as a whole.

Appendix B – Synchronisation Controller

This appendix describes the technical aspect of achieving synchronisation criteria and to incorporate them into the existing microgrid $P - f$, $Q - V$ droop control. The synchronisation algorithm used in this research has been previously developed in [282] as part of a MSc dissertation project. It is being repeated here for the sake of completeness.

The synchronisation criteria to be achieved are to make the values of phase-angle, frequency and voltage difference as minimal as possible. Another consideration when designing the controller is its capability to work with the conventional $P - f$, $Q - V$ droop controlled DG. During the transition of the grid synchronisation, the power flows should be controlled in such a way that it is similar to the autonomous droop controllers in islanded mode with minimal transients.

In this work, the proposed synchronisation process is realised with the utilisation of Main Controller and Synchronisation Controller. The Main controller top level block diagram is shown in Figure B1.

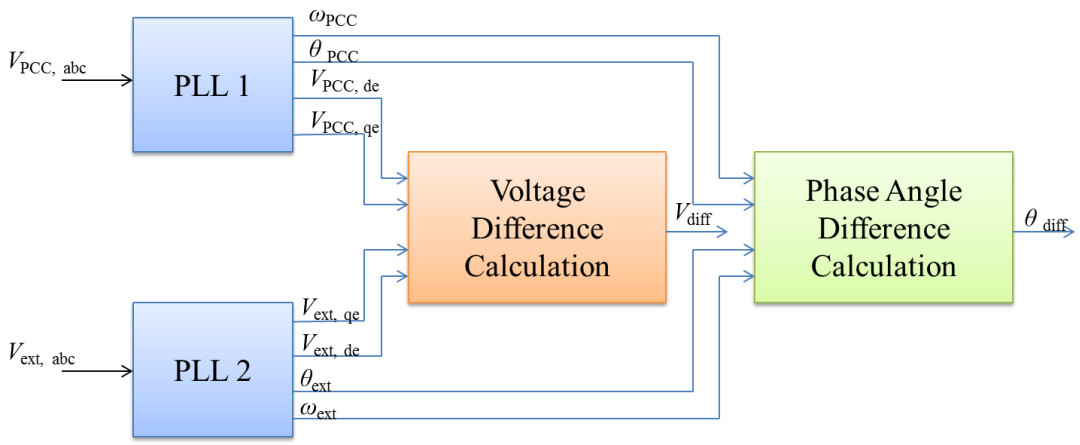

Figure B1: Main Controller block diagram

The Main Controller inputs the feedback signals, $V_{PCC,\ abc}$ and $V_{ext,\ abc}$ and calculate the information required for synchronisation. The desired information is measured at the point of common coupling (PCC) and at the external source frequency, ω_{PCC} and ω_{ext}. The external source in this case is defined as a diesel generator or utility grid. Ultimately, the phase angle difference θ_{diff} and the voltage magnitude difference, V_{diff}

information between the PCC and the external source are required to verify if both sources are synchronised. The two three-phase phase-locked loops (PLL) with each obtain the voltage from the PCC and the external voltage source, respectively. These PLLs provide instantaneous frequencies, phases and dq-voltages. The voltage difference between the two voltage sources can be derived as [283]:

$$\begin{aligned} V_{\text{diff}} &= V_{\text{PCC}} - V_{\text{ext}} \\ V_{\text{PCC}} &= \sqrt{V_{\text{PCC,qe}}^2 + V_{\text{PCC,de}}^2} \\ V_{\text{ext}} &= \sqrt{V_{\text{ext,qe}}^2 + V_{\text{ext,de}}^2} \end{aligned} \tag{B1}$$

The phase angle difference can be written as [283]:

$$\theta_{\text{diff}} = (\omega_{\text{PCC}} - \omega_{\text{ext}})t + (\theta_{\text{PCC}} - \theta_{\text{ext}}) \tag{B2}$$

The model developed in Simulink is shown in Figure B2. The two ideal programmable voltage sources represent the external voltage and the PCC voltage respectively. Both of the PLLs track the voltages and compute its corresponding phase angles, frequencies and voltages in dq-frame. The *Voltage Magnitude Difference* and *Phase Angle Difference* blocks are implemented with equation (B1) and (B2), respectively. An interesting feature which has been incorporated in this simulation is the light emitting diode (LED) indicator to detect the PLL locking state. If the PLL has locked to the input signal, the LED will become green. On the other hand, if the PLL fails to be locked to the input signal due to wrong settings or defects, the LED will become red. This functions to assist the designer to detect if there are any faults occurred within the PLL system. However, the existence of LED incurs additional simulation time and the user should eliminate it when the PLL is stable for a particular application or if not needed.

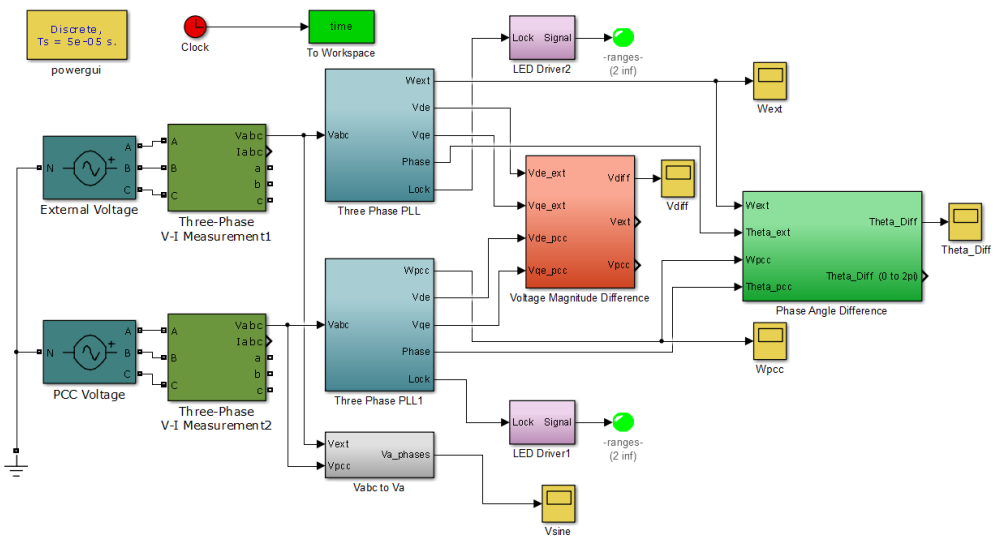

Figure B2: Main Controller Simulink setup

The external voltage was set as 400 $V_{rms,\ ph\text{-}ph}$ and 50 Hz all the time. Initially, the PCC voltage source was programmed with 390 $V_{rms,\ ph\text{-}ph}$ and 49.8 Hz with 50 degrees phase shifted. At 7 s, the PCC frequency was stepped up to 50 Hz until the end of simulation time.

Some measurement points of the Main Controller are demonstrated in Figure B3. Initially, the external source was started to operate at 50 Hz (314.16 rad/s) whereas the PCC voltage was at 49.8 Hz (312.9 rad/s). Due to a phase shift of 50 degrees which was set upon PCC voltage, a start-up phase difference of 0.8727 radian (50 degrees) can be observed. The frequency deviation between the external source (50 Hz) and the PCC (49.8 Hz) have contributed to the phase angle difference, θ_{diff} which continuously varied between $-\pi$ to π.

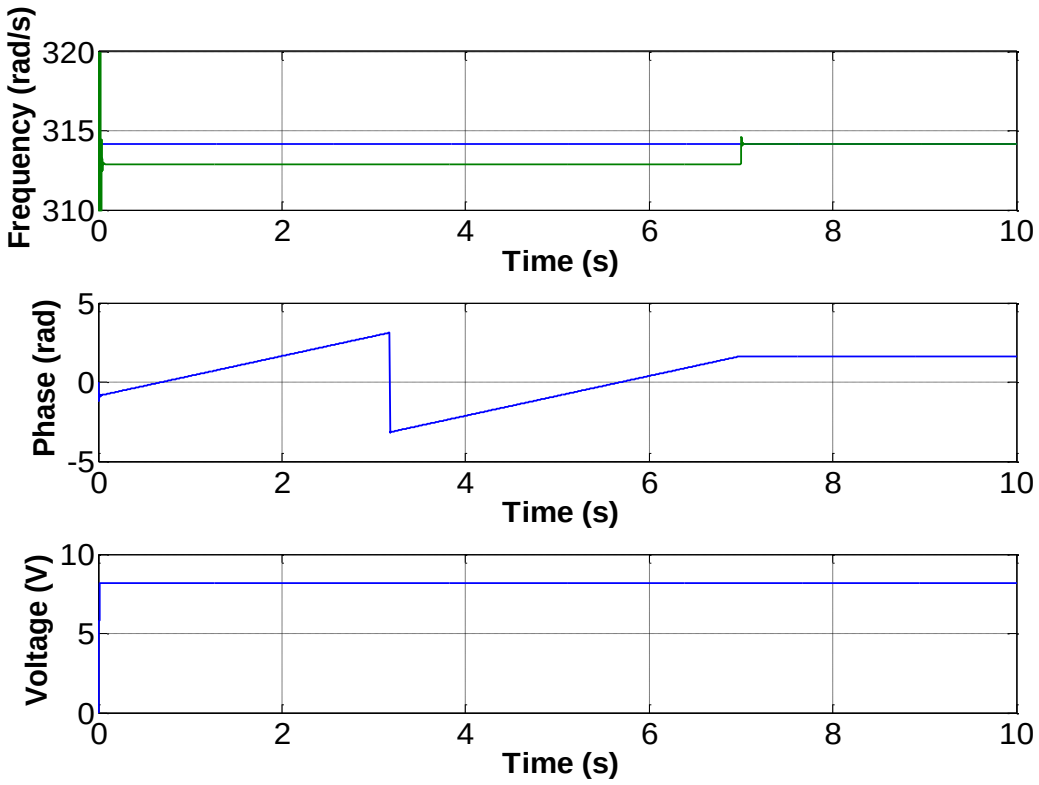

Figure B3: Main Controller output: External voltage and PCC frequencies, phase angle and voltage difference

At 7 s, the PCC frequency was programmed with a step of 0.2 Hz, hence operating at 50 Hz. This was artificially created to test if the *Phase Angle Difference* block was working accordingly. Indeed, from this point onwards, the phase angle difference was fixed at a constant level and stopped varying. The pre-set voltage difference between the external voltage source and the PCC voltage was 10 $V_{rms,\ ph\text{-}ph}$, which was equivalent to $10\left(\sqrt{2}/\sqrt{3}\right) = 8.165\ V_{peak,\ line-line}$. From Figure B3, third subplot, it can be observed that the *Voltage Difference* block was providing the correct value of about 8.16 V, which was the difference between the external and the PCC voltages. The next step was to explore the methodology to incorporate this into the power-electronics based inverter controller.

As the operation of the SI inverters should not be disturbed during islanding or even grid-connecting, the main controller which was obtaining the phase difference and

voltage difference information should not be connected to the droop controller without an interface. It was only during the synchronisation process which this information are allowed to be fed into the system. Figure B4 demonstrates the flowchart of synchronisation controller algorithm which was to be interfaced between the Main Controller and droop controller.

The controller begins by detecting the synchronisation switch's status which can be manually controlled by the user. Then, the controller will observe the phase difference between the two networks which were to be synchronised. It is important to note at this stage the phase difference should be as small as possible before proceeding it to droop controller [284] [285]. This minimum phase difference which is to be set in the controller is denoted as $\varepsilon\theta$. In this work, the $\varepsilon\theta$ value is set to 0.5 radian. This was determined empirically and was selected minimally to avoid output voltage frequency perturbation from inverter as a result of large phase difference seen in the droop controller. Yet, the value was chosen to allow synchronisation process to be carried successfully. This is a design trade-off that one should consider carefully as the optimum value varies, depending on the system.

After satisfying the two conditions (enabling synchronisation switch and obtaining small phase difference between the networks), a delay of 1.5 s took place to allow settling down of output power transient before circuit breaker switch was being closed. Latching of the synchronisation signal commences immediately in a digital manner with the D flip-flop to ensure the circuit breaker does not trip off unintentionally. Finally, the phase and voltage difference outputs were disabled to allow the remaining operation to take place naturally.

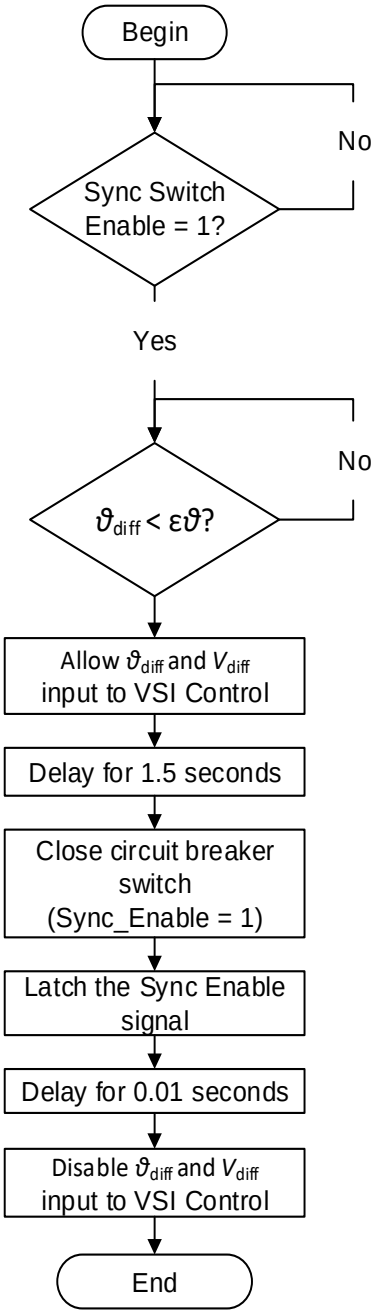

Figure B4: Synchronisation Algorithm Flowchart

The top level logic structure for this synchronisation controller was implemented based on the flowchart in Figure in Simulink as shown in Figure B5.

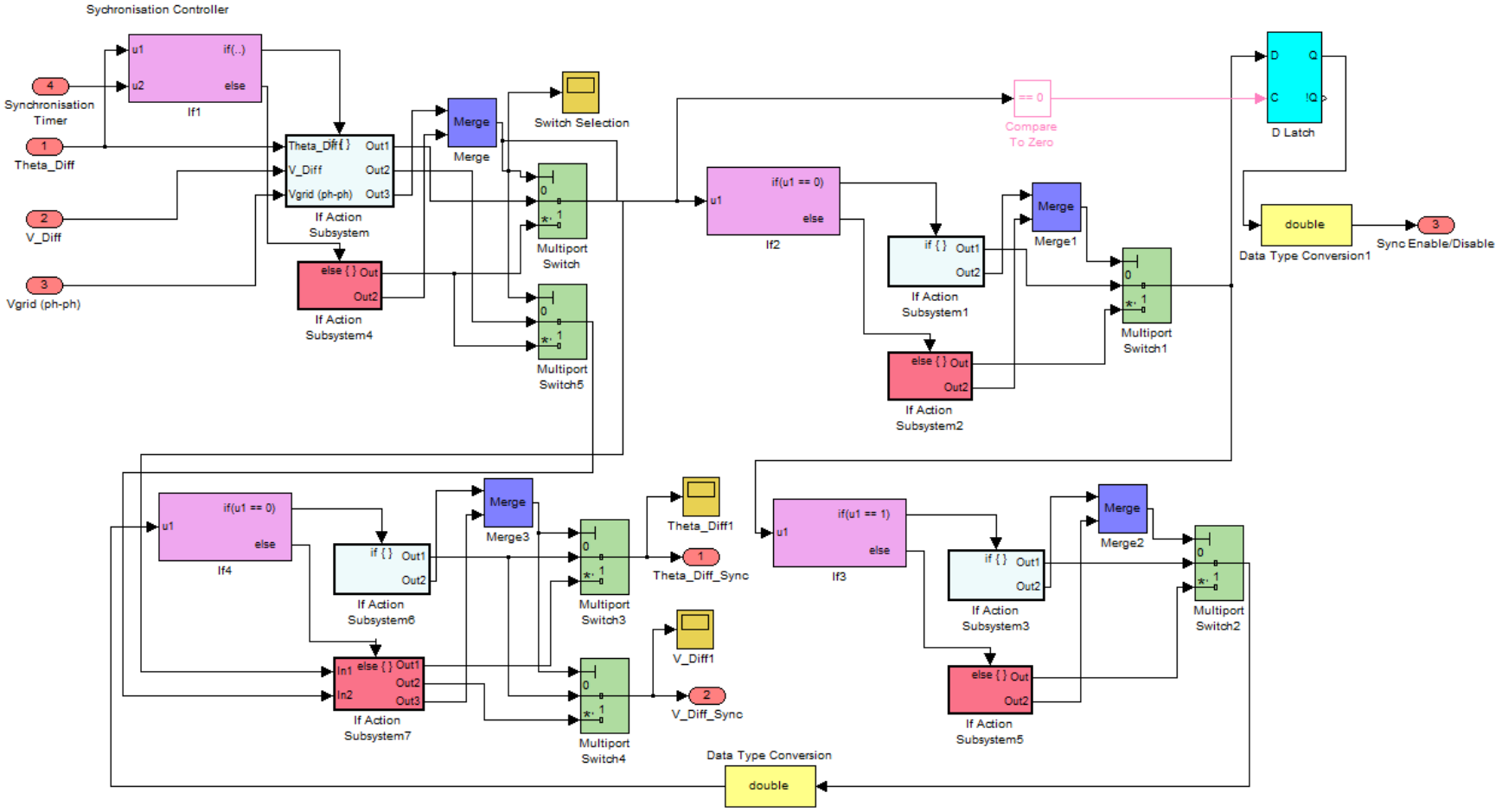

Figure B5: Synchronisation Controller Simulink setup

The Main Controller and Synchronisation Controller described above were tested with an external AC source as shown in Figure B6. The focus of this simulation was to analyse the transients and performances of the synchronisation process. The SI and the external source were connected through impedance which was modelled with a PI section. The Main Controller obtained the PCC and the external voltages at both ends and computed the necessary information, i.e. θ_{diff} and V_{diff} for synchronisation process. Initially, the three-phase circuit breaker was opened circuited and was closed once the enabling signal from Synchronisation Controller was obtained. The Simulink model of the integration of the synchronisation module into the droop controller is shown in Figure B7. The SI stabilised its DC link and fed a three-phase load of 6 kW at 70 s. An additional load of 14 kW was switched on at 90 s, overloading the SI inverters. Thus synchronisation algorithm was started from then onwards to obtain additional energy support from the external source.

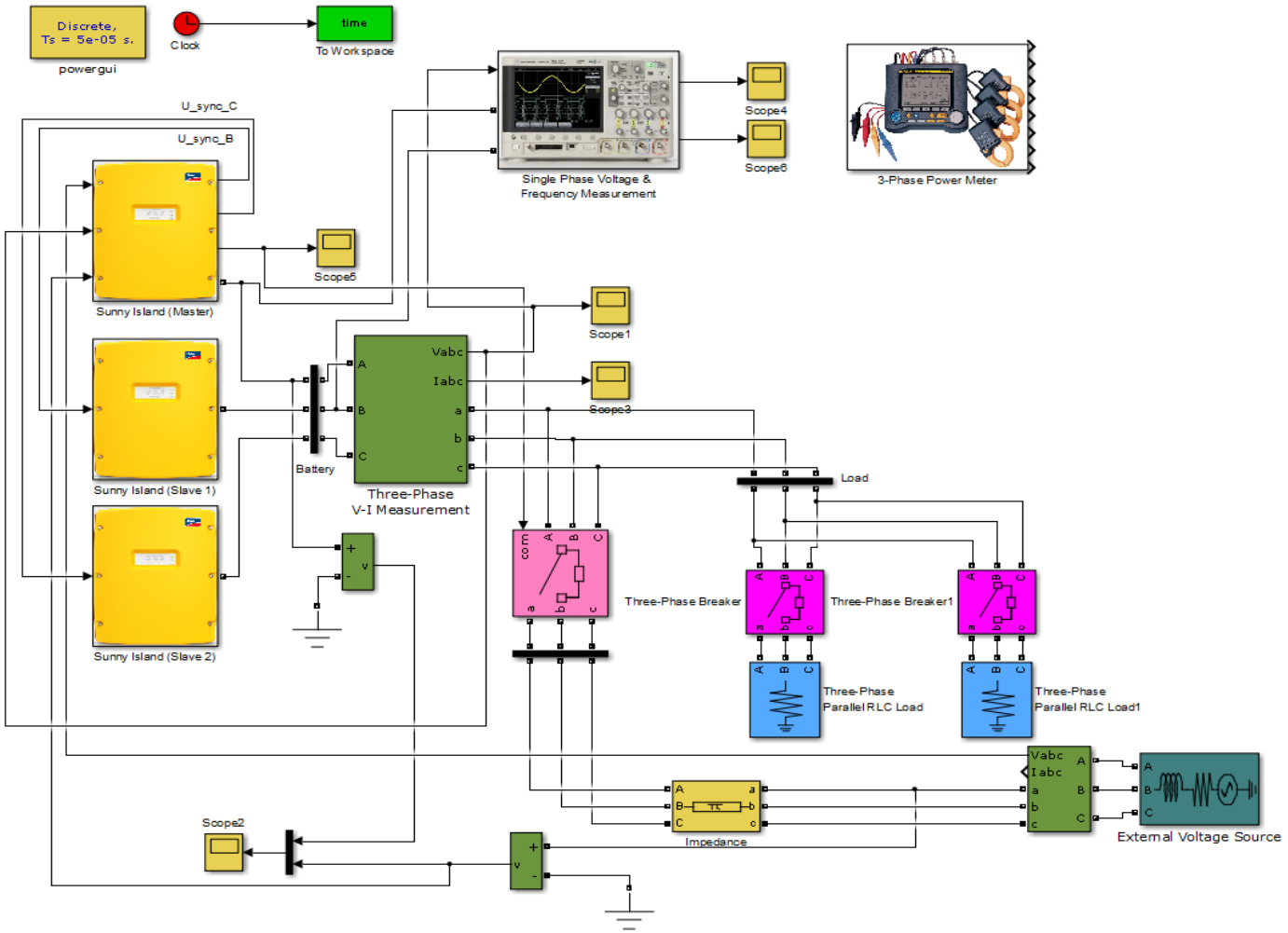

Figure B6: Main Controller and Synchronisation Controller modelling

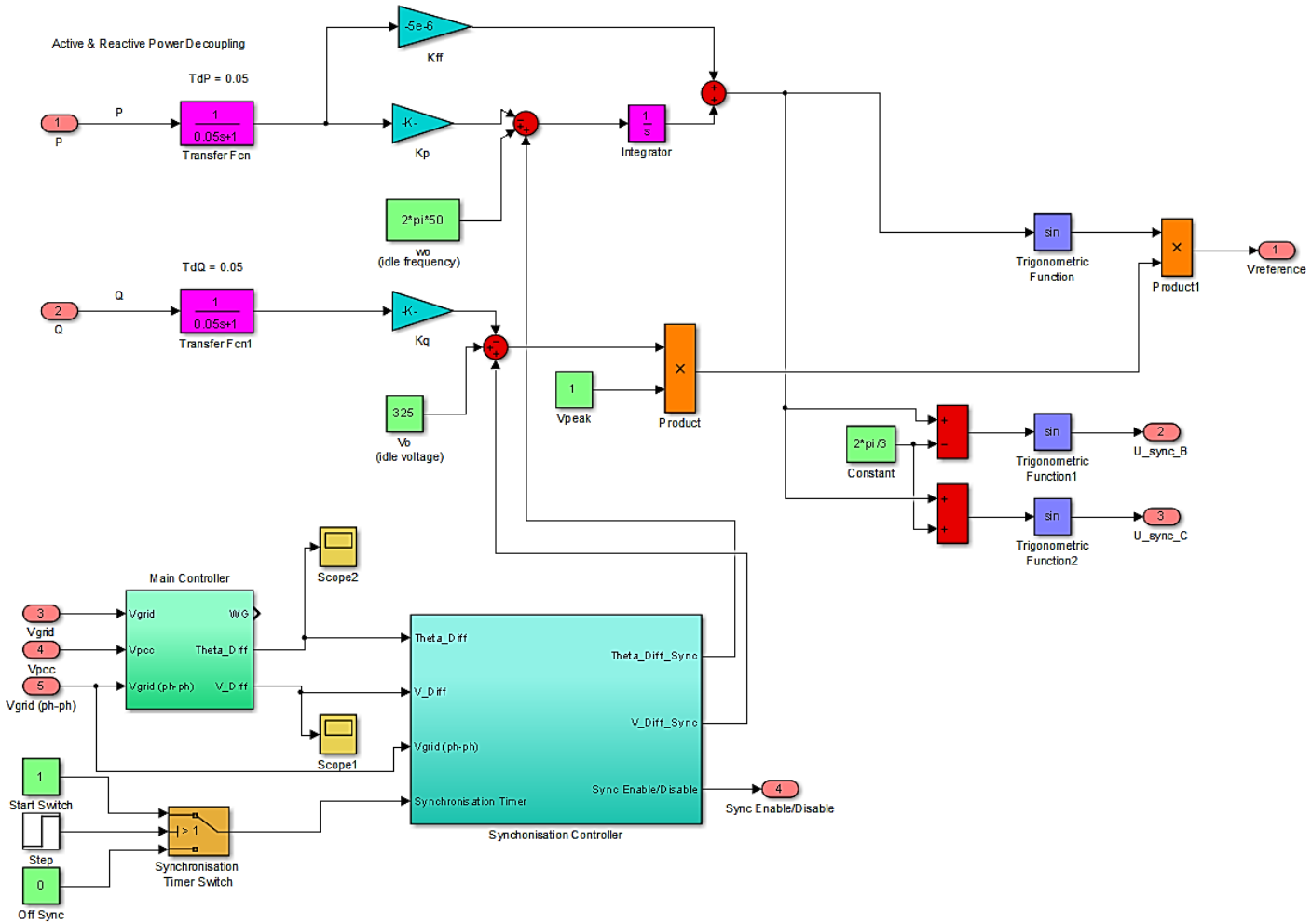

Figure B7: Incorporation of Synchronisation Controller into droop controller

Figure B8 shows the phase angle difference, the voltage difference and the synchronisation signal. As described before, the phase angle varies between $-\pi$ to π before the synchronisation algorithm is started. It can be noticed that there was a change of slope in the phase angle difference once the additional load was switched-on at 90 s. Then, the Synchronisation Controller was *pooling* until the two conditions were met, i.e. the synchronisation switch was enabled and the phase angle difference was less than 0.5 rad before synchronisation algorithm was started. Note that these information were not allowed to have any influence on the droop controller prior to this. At about 100.8 s (when the phase angle difference was less than 0.5 rad), the droop controller started to receive these signals and the transient took place for 1.5 seconds. The three-phase breaker was triggered to close at approximately 102.3 s. In addition, the phase angle difference at this time was approximately zero. The SI inverters and the external voltage source were eventually connected. The phase angle difference and the voltage difference information was stopped being fed to the system and this has permitted the power flow to happen naturally. The positive constant phase difference after 102.3 s indicated that there was a certain fixed amount of power being transferred from the external source to the load, supplying additional load. This amount was highly influenced by the required order of active power transfer if X >> R as described in equation (B3):

$$P_R = \left(\frac{V_R}{X}\right) V_S \sin\delta \tag{B3}$$

The voltage difference between the two systems before and after synchronisation was relatively small compared to their phase voltage magnitudes (in this case 230 V). The voltage difference was about less than or equal to 15 V as opposed to their peak-to-peak amplitude which was in the order of hundreds. During the synchronisation transient process, the voltage difference between the two systems was being brought down to a minimal level which helps to smooth synchronisation transition. After connecting the two systems, the voltage difference was fixed at about constant level to allow effective power transfer. This level is highly affected by the required amount of reactive power transfer between the two systems if X >> R as highlighted in equation (B4):

$$Q_R = \left(\frac{V_R}{X}\right)(V_S \cos\delta - V_R) \tag{B4}$$

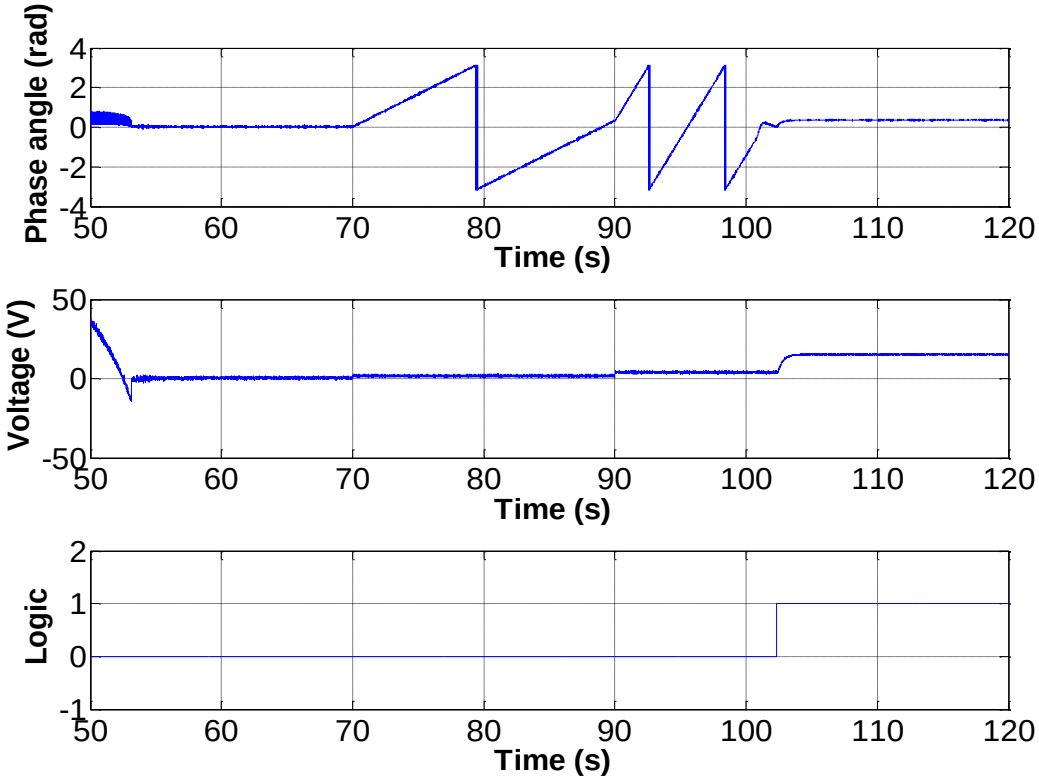

Figure B8: Phase angle difference, voltage difference and synchronisation signal between Sunny Island and external voltage source

To further visualise the synchronisation process in time series, Figure B9 portrays the SI inverter's and the external source phase voltages before, at and after synchronisation took place. The first subplot shows the two voltages before synchronisation. Between 92.5 s and 92.6 s, the phase angle difference shown in Figure B9 was about 180 degrees and this subplot shows the corresponding phase voltages. At about 102.3 s, their phase angle difference was approximately zero and these voltages were synchronised with each other as shown in subplot 2. Subplot 3 in Figure B9 demonstrates that the phase angle difference exists between the two voltage sources after connection. A phase angle difference of 0.36 rad (from Figure B9, subplot 1), equivalent to 20.6 degrees was displayed between the two voltages. At this time, a constant power transfer occurs.

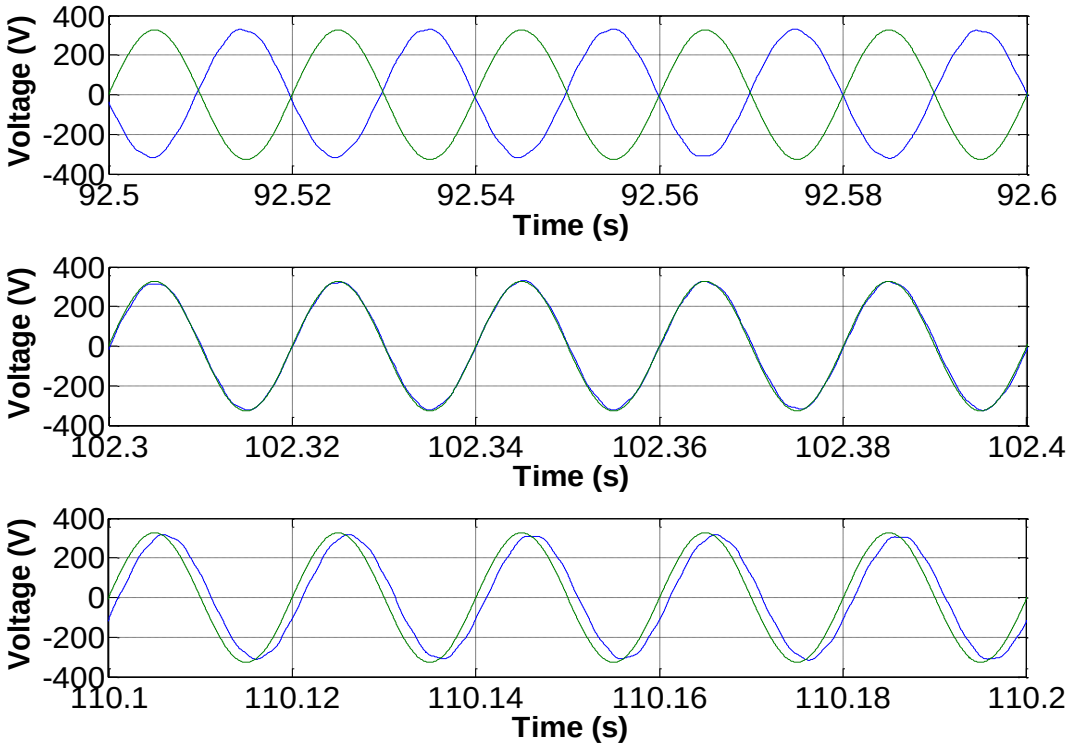

Figure B9: Sunny Island and external voltage before, at and after synchronisation

The system frequency and voltage are shown in Figure B10 and Figure B11 respectively. An additional load occurring at 90 s has caused the frequency to drop significantly due to the power deficit. After connection took place between the two power sources at 102.3 s, the frequency gradually recovered to 50 Hz as a result of obtaining additional power from the external source. From Figure B11, it was noticed that the voltage drops after additional loads were connected at 70 s and 90 s, respectively. In addition, voltage drop was noticed after synchronisation took place due to the additional impedance between the SI inverters and the external voltage source. The approximate formula to calculate the voltage drop across the impedance is [286], [287]:

$$\Delta V \approx \frac{PR + QX}{V} \tag{B5}$$

However, it is important to stress that the synchronisation process has taken place successfully with minimal transient based on the above analysis on frequency and voltage.

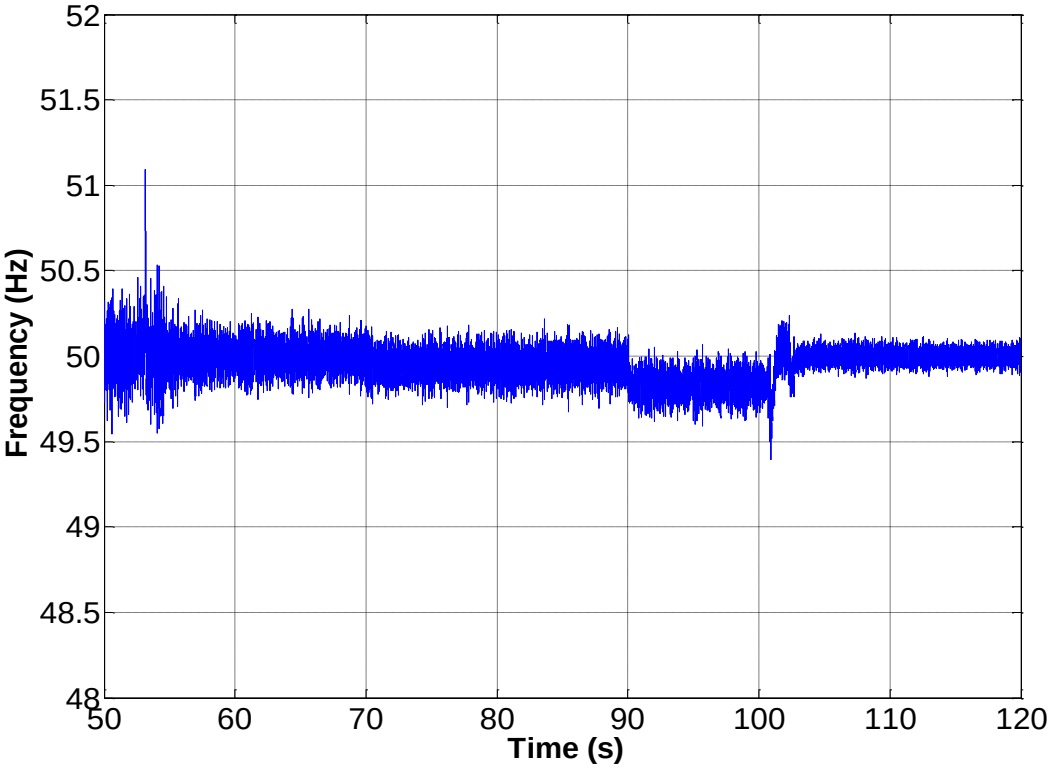

Figure B10: System frequency profile

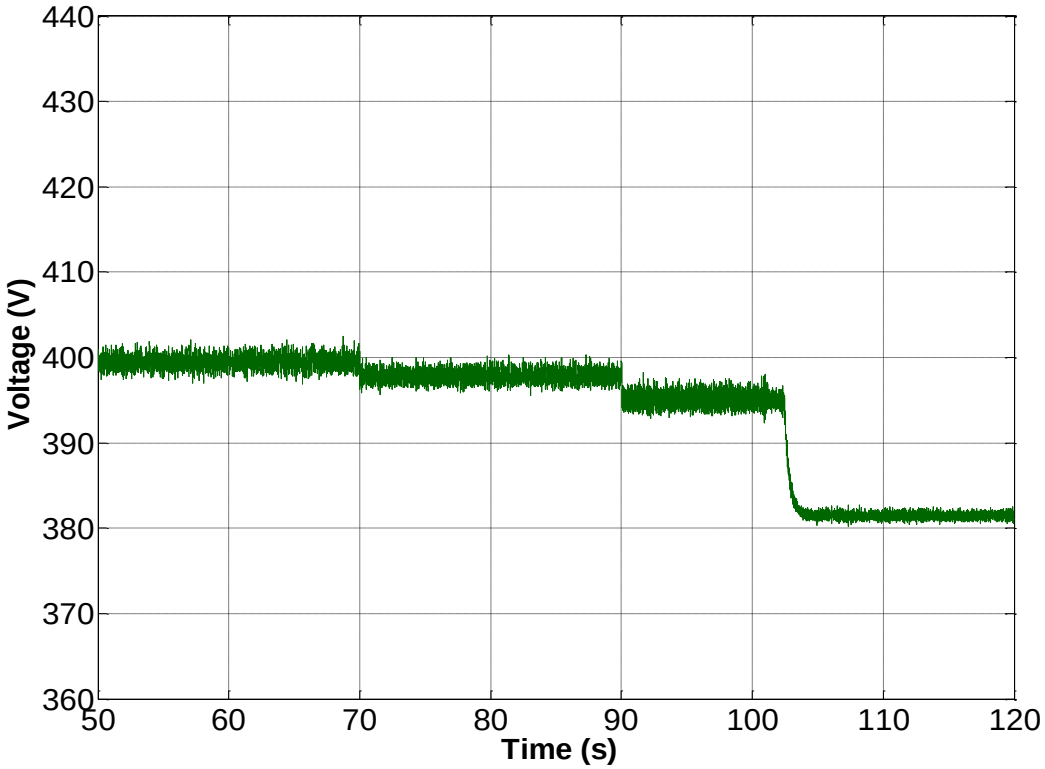

Figure B11: System voltage profile

Appendix C – Maintenance and Cost Calculations

Given that:

$i = 0.03$

$d = 0.04$

$$x = \left(\frac{1+i}{1+d}\right)$$

$$x = \left(\frac{1+0.03}{1+0.04}\right)$$

$$x = 0.9904$$

Considering $n = 20$ years:

$$P_a = \left(\frac{1-x^n}{1-x}\right)$$

$$P_a = \left(\frac{1-0.9904^{20}}{1-0.9904}\right)$$

$$P_a = 18.277$$

$$P_{a1} = xP_a$$

$$P_{a1} = 0.9904 \times 18.277$$

$$P_{a1} = 18.1015$$

Present worth wind turbine maintenance cost for 20 years:

$$PW\_wind = P_{a1}(C_o)$$

$$PW\_wind = 18.1015 \times £\,500$$

$$\underline{PW\_wind = £\,9{,}050}$$

Present worth batteries replacement (depending on computed replacement period from battery degradation model):

$$P_{\mathrm{r(n)}} = \left(\frac{1+i}{1+d}\right)^{n}$$

$$PW\_battery(n) = P_{\mathrm{r(n)}} \times (£\,1{,}108)$$

$$\underline{PW\_battery(n) = £\,47.64}$$

Present worth diesel generator replacement (depending on computed replacement period from the number of running hours):

$$P_{\mathrm{r(m)}} = \left(\frac{1+i}{1+d}\right)^{m}$$

$$PW\_diesel(m) = P_{\mathrm{r(m)}} \times (£\,521.72)$$

Present worth SMA inverters replacement for year 10:

$$P_{\mathrm{r10}} = 0.9079$$

$$PW\_inverter10 = 0.9079 \times (£\,10{,}806)$$

$$\underline{PW\_inverter10 = £\,9{,}811}$$

Appendix D – Gaia-Wind Turbine Field Measured Power Curve Data

Measured power curve (database B)							
Reference Air Density: 1.225 kg/m3					Category A	Category B	Combined uncertainty
Bin no.	Hub Height Wind Speed (m/s)	Power Output (kW)	C_p	No. of data sets (1 min. Avg.)	Standard Uncertainty s_I (kW)	Standard Uncertainty u_I (kW)	Standard Uncertainty u_d (kW)
1	0.64	-0.03	-1.40	23	0.0001	0.1300	0.1300
2	1.06	-0.03	-0.30	150	0.0002	0.1299	0.1299
3	1.53	-0.03	-0.10	404	0.0001	0.1299	0.1299
4	2.01	-0.03	-0.05	826	0.0010	0.1299	0.1299
5	2.50	-0.05	-0.04	1316	0.0028	0.1300	0.1300
6	3.01	-0.12	-0.05	1499	0.0050	0.1312	0.1313
7	3.51	0.08	0.02	1767	0.0099	0.1427	0.1430
8	4.00	0.71	0.14	1983	0.0153	0.2372	0.2377
9	4.49	1.56	0.21	2055	0.0187	0.3170	0.3176
10	4.99	2.46	0.24	1777	0.0226	0.3386	0.3393
11	5.49	3.44	0.26	1467	0.0256	0.3824	0.3833
12	5.99	4.43	0.25	1261	0.0310	0.3979	0.3991
13	6.49	5.44	0.24	1034	0.0329	0.4254	0.4267
14	6.98	6.30	0.23	793	0.0353	0.3943	0.3959
15	7.48	7.14	0.21	596	0.0383	0.4006	0.4024
16	7.98	7.91	0.19	380	0.0458	0.3805	0.3833
17	8.49	8.61	0.17	248	0.0561	0.3674	0.3717
18	8.98	9.16	0.16	165	0.0607	0.3177	0.3234
19	9.46	9.67	0.14	105	0.0677	0.3131	0.3203
20	9.99	10.29	0.13	73	0.0813	0.3549	0.3641
21	10.50	10.51	0.11	67	0.0677	0.2022	0.2132
22	11.02	10.69	0.10	39	0.0682	0.1888	0.2007
23	11.51	10.81	0.09	42	0.0791	0.1791	0.1958
24	12.02	10.93	0.08	41	0.0629	0.1762	0.1871
25	12.51	10.67	0.07	45	0.1287	0.2302	0.2637
26	12.97	10.74	0.06	29	0.0779	0.1675	0.1848
27	13.52	10.47	0.05	32	0.0761	0.2309	0.2432
28	14.06	10.26	0.05	36	0.0657	0.2132	0.2231
29	14.53	9.82	0.04	47	0.0669	0.3766	0.3825
30	14.98	9.54	0.03	50	0.1331	0.2841	0.3137
31	15.52	9.42	0.03	35	0.1062	0.1757	0.2053
32	16.00	8.79	0.03	17	0.3461	0.5527	0.6521
33	16.50	9.07	0.02	22	0.1154	0.2836	0.3061
34	16.98	8.76	0.02	15	0.1102	0.3165	0.3351
35	17.50	8.69	0.02	6	0.0000	0.1620	0.1620
36	17.89	7.91	0.02	3	0.0000	0.8911	0.8911
37	18.42	8.69	0.02	4	0.0000	0.6871	0.6871
38	19.24	8.12	0.01	1	0.0000	0.3612	0.3612
39	19.50	0.00	0.00	0	0.0000	0.1299	0.1299
40	20.00	0.00	0.00	0	0.0000	0.1299	0.1299
41	20.50	0.00	0.00	0	0.0000	0.1299	0.1299
42	21.00	0.00	0.00	0	0.0000	0.1299	0.1299
43	21.50	0.00	0.00	0	0.0000	0.1299	0.1299
44	22.00	0.00	0.00	0	0.0000	0.1299	0.1299
45	22.50	0.00	0.00	0	0.0000	0.1299	0.1299
46	23.00	0.00	0.00	0	0.0000	0.1299	0.1299
47	23.50	0.00	0.00	0	0.0000	0.1299	0.1299
48	24.00	0.00	0.00	0	0.0000	0.1299	0.1299
49	24.50	0.00	0.00	0	0.0000	0.1299	0.1299
50	25.00	0.00	0.00	0	0.0000	0.1299	0.1299

Table D1: Performance at sea-level air density, 1.225 kg/m^3

Appendix E – Braking Mechanism of Gaia-Wind Turbine

The Gaia wind turbine brake mechanism is shown in Figure E1 and its component labels are listed in Table E1 [288]

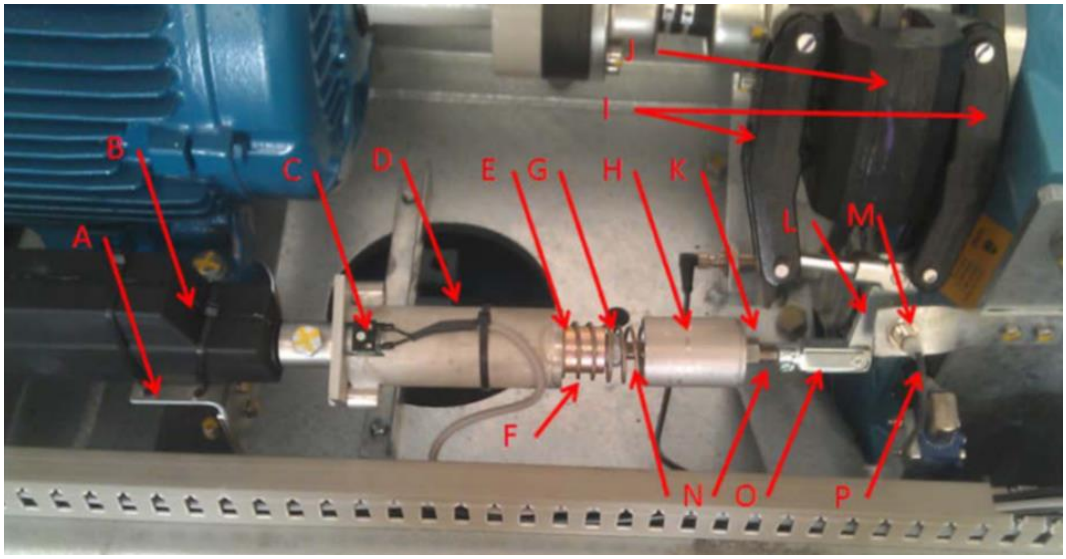

Figure E1: Brake parts [288]

Item	Description
A	Brake support bracket
B	Brake motor
C	Brake electromagnet (solenoid)
D	Chassis
E	Inner sleeve
F	Spring
G	Rod lock nut
H	Spring collar
I	Pad adjustment screws
J	Calliper body
K	Spring tension lock nut
L	Brake lever
M	Brake released switch
N	Brake rod
O	Clevis pin and chip
P	Pad worn

Table E1: Brake parts description [288]

The operation of the brake system in Figure E1 can be simply described as a state machine. The linear (forward and backward) motion of the solenoid can be converted

mechanically from the bi-directional rotation of the DC motor. The solenoid would be energised and acted as a magnet to get hold of the spring. From the controller's schematic, it was analysed that the output ports which control the DC motor were namely *X2(1)* and *X2(2)*. Due to commercial confidential purposes, the schematic of the Mita-Teknik controller will not be shown in this thesis. The operation of the DC motor can be written as:

X2(1)	***X2(2)***	**Motor action**
0V	0V	Motor stop
24V	0V	Motor forward
0V	24V	Motor reverse
24V	24V	Motor stop

Table E2: DC motor operation

In addition, the electromagnetic outputs were identified as *X2(3)* and *X2(4)*. These outputs were connected to a loading resistor and the signal was taken at the positive terminal, which was named as *E* in this case. In order to emulate the braking mechanism, a Moore finite state machine (FSM) was designed to accomplish this. Figure E2 shows the state transition diagram of the FSM. The sequence begins with an initial state of the motor being in idle position and the solenoid is not magnetised. Then, the state is transited to motor forward. The next state (motor is reversed) is activated when the solenoid is magnetised. This step releases the brake, leaving the rotor in freewheeling state when the motor is stopped. With this, the brake release output is triggered at the IC1100 controller.

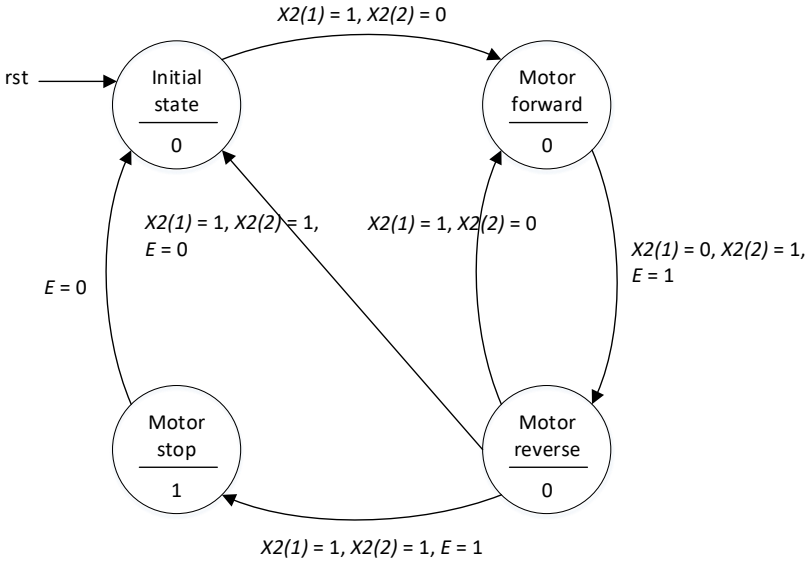

Figure E2: Braking mechanism of Moore finite state machine

The words that describe the different states of the diagram in Figure E2 were replaced with binary numbers, as shown in Figure E3. Finally, the diagram was converted to a state transition table as depicted in Table E3.

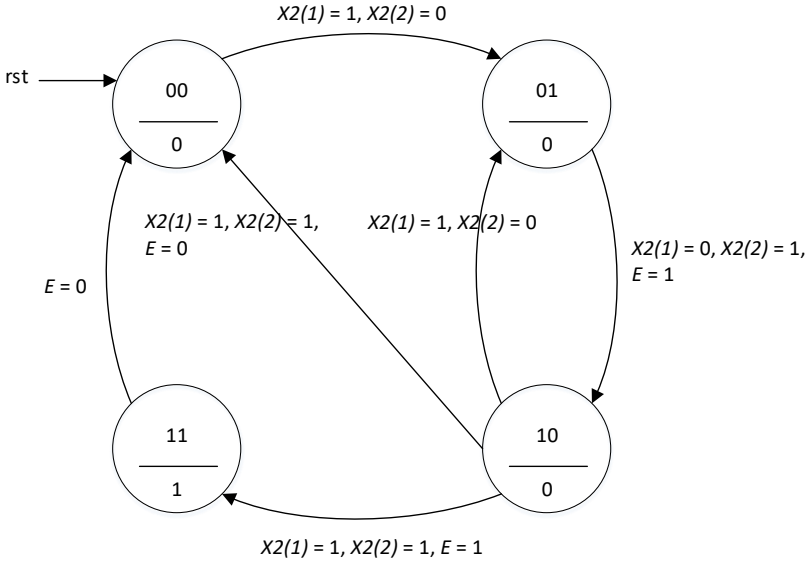

Figure E3: Braking mechanism state diagram with coded states

Current State		Inputs			Next State		Output
A	B	*X2(1)*	*X2(2)*	*E*	D_A	D_B	*Y*
0	0	0	0	0	0	0	0
		0	0	1	0	0	0
		0	1	0	0	0	0
		0	1	1	0	0	0
		1	0	0	0	0	0
		1	0	1	0	0	0
		1	1	0	0	0	0
		1	1	1	0	0	0
0	1	0	0	0	0	1	0
		0	0	1	0	1	0
		0	1	0	0	1	0
		0	1	1	1	0	0
		1	0	0	0	1	0
		1	0	1	0	1	0
		1	1	0	0	1	0
		1	1	1	0	1	0
1	0	0	0	0	1	0	0
		0	0	1	1	0	0
		0	1	0	1	0	0
		0	1	1	1	0	0
		1	0	0	0	1	0
		1	0	1	0	1	0
		1	1	0	0	1	0
		1	1	1	0	1	0
1	1	0	0	0	0	0	1
		0	0	1	1	1	1
		0	1	0	0	0	1
		0	1	1	1	1	1
		1	0	0	0	0	1
		1	0	1	1	1	1
		1	1	0	0	0	1
		1	1	1	1	1	1

Table E3: Truth table of the braking mechanism FSM

Since the FSM involves five input variables, namely *A, B, E, X2(1)* and *X2(2)*, the 5 – variable overlay Karnaugh map was utilised to derive the output functions [289]. The derivation steps can be referred in Figure E4 to E6.

Output function, D_A

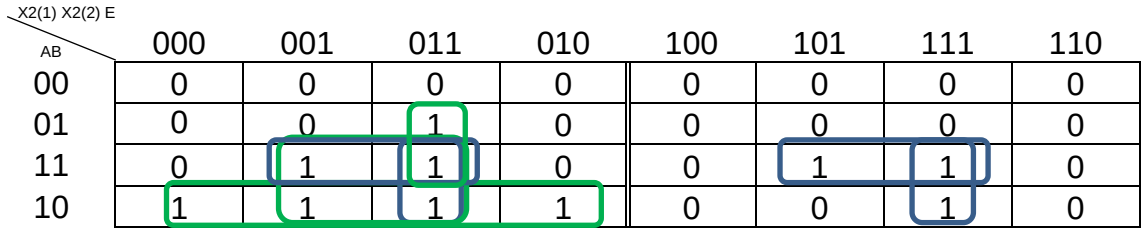

Figure E4: Overlay Karnaugh map for output function, D_A

Output function, D_B

AB \ X2(1) X2(2) E	000	001	011	010	100	101	111	110
00	0	0	0	0	1	1	0	0
01	1	1	0	1	1	1	1	1
11	0	1	1	0	0	1	1	0
10	0	0	0	0	1	1	1	0

Figure E5: Overlay Karnaugh map for output function, D_B

Output function, Y

AB \ X2(1) X2(2) E	000	001	011	010	100	101	111	110
00	0	0	0	0	0	0	0	0
01	0	0	0	0	0	0	0	0
11	1	1	1	1	1	1	1	1
10	0	0	0	0	0	0	0	0

Figure E6: Overlay Karnaugh map for output function, Y

The corresponding output functions are derived as:

$$D_A = B\overline{X_2(1)}X_2(2)E + A\overline{X_2(1)}E + A\bar{B}\overline{X_2(1)} + AX_2(2)E + ABE \quad \text{(E1)}$$

$$D_B = AB\overline{X_2(1)}E + BX_2(1)\overline{X_2(2)} + \bar{A}BX_2(1) + AX_2(1)E + \bar{A}B\overline{X_2(2)} + \bar{A}BX_2(2)\bar{E} \quad \text{(E2)}$$

$$Y = AB \quad \text{(E3)}$$

The implemented FSM circuitry which was based on the equation E1 to E3 using the Simulink software is shown in Figure E7.

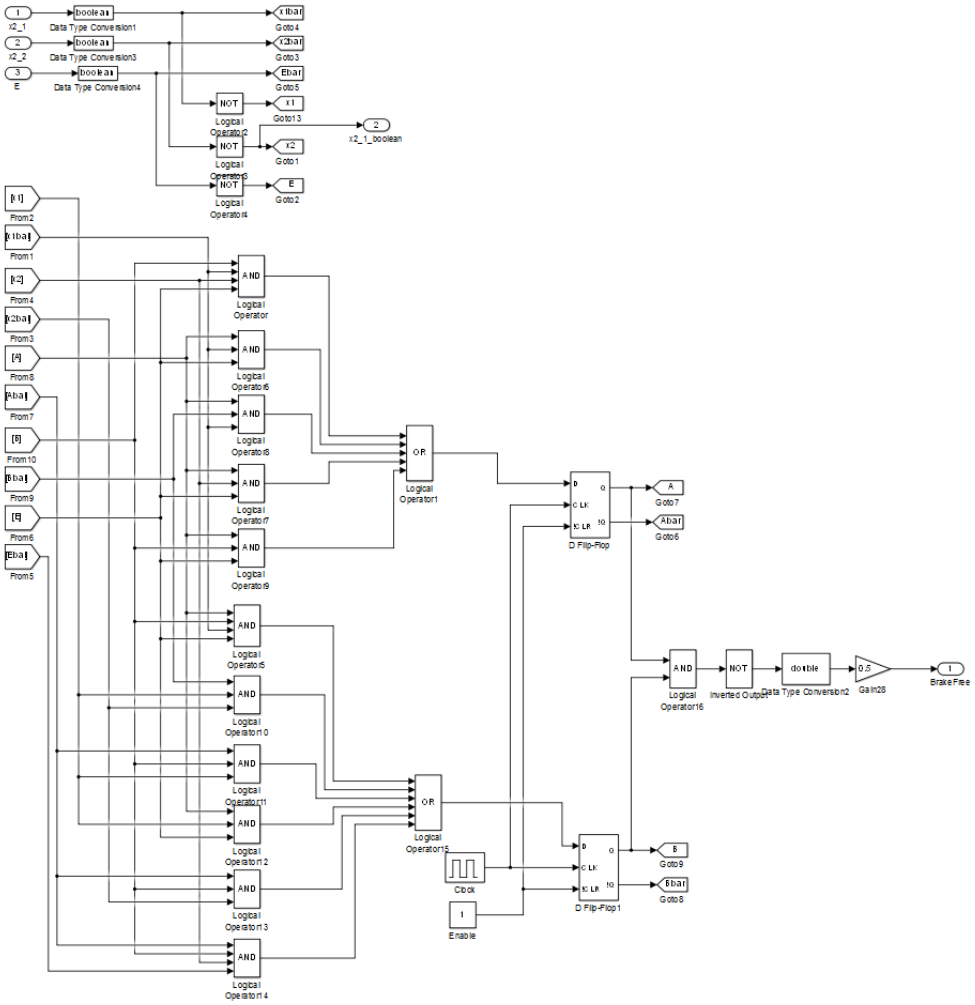

Figure E7: Braking mechanism logic diagram